INSTRUMENTATION TEP

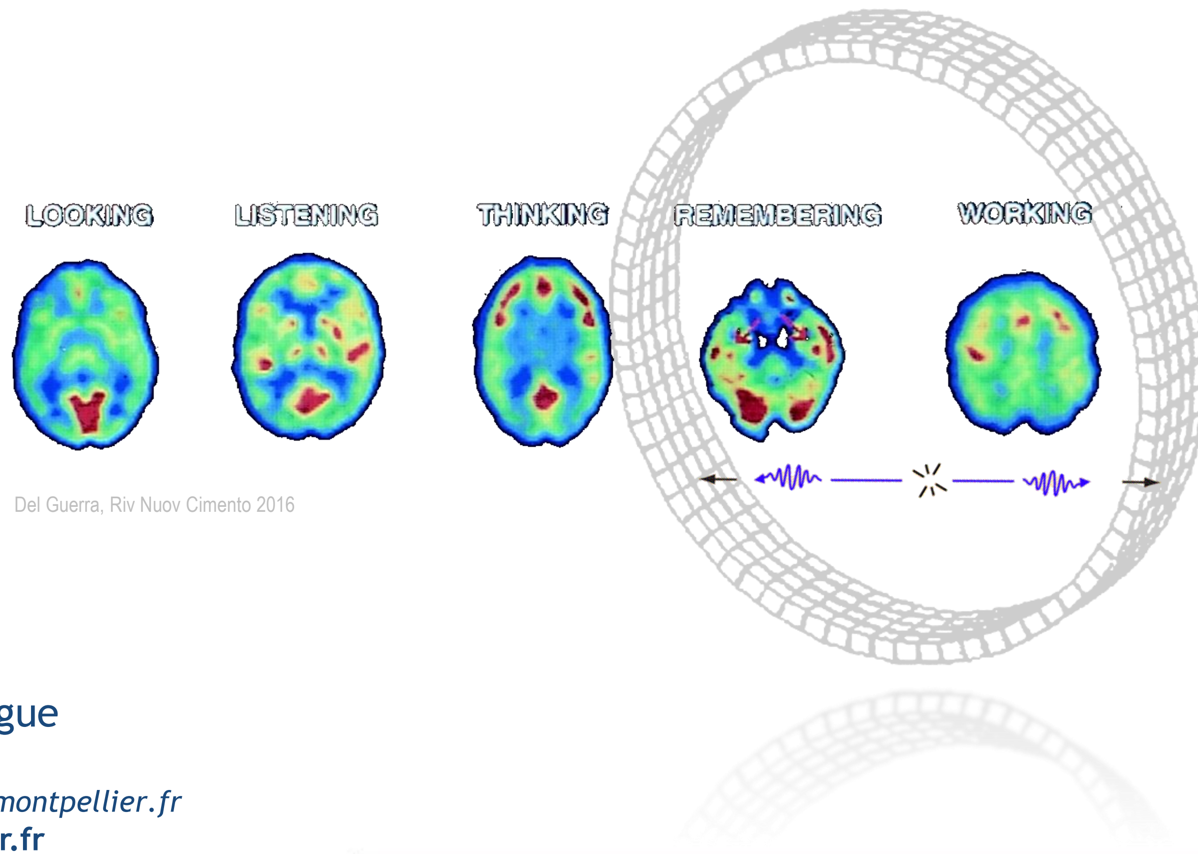

Del Guerra, Riv Nuov Cimento 2016

Fayçal Ben Bouallègue
CHU Montpellier
faycal.ben-bouallegue@umontpellier.fr
scinti.edu.umontpellier.fr

Imagerie moléculaire

^{18}F-FDG

Oncologie

- *Caractérisation*
- *Staging TNM*
- *Guidage biopsique*
- *Optimisation RT*
- *Réponse thérapeutique*
- *Récidive*

Poumon

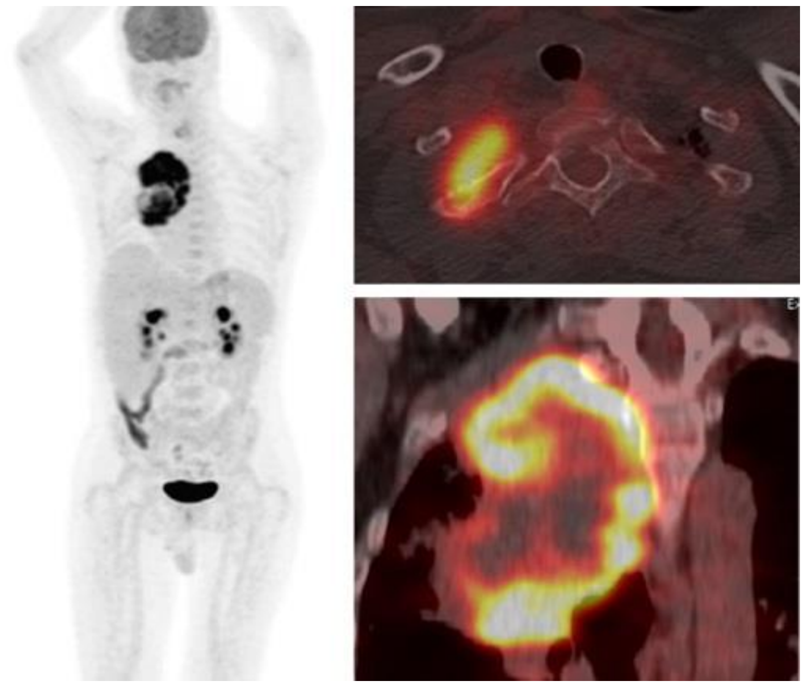

Groheux, Diagn Interv Imaging 2016

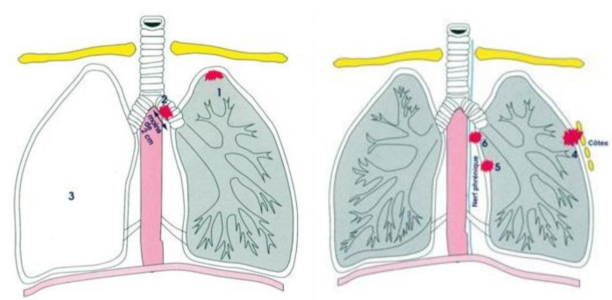

D'après A Paumier (CHU Angers)

Imagerie moléculaire

^{18}F-FDG

Oncologie

- *Caractérisation*
- *Staging TNM*
- *Guidage biopsique*
- *Optimisation RT*
- *Réponse thérapeutique*
- *Récidive*

Poumon
Lymphome

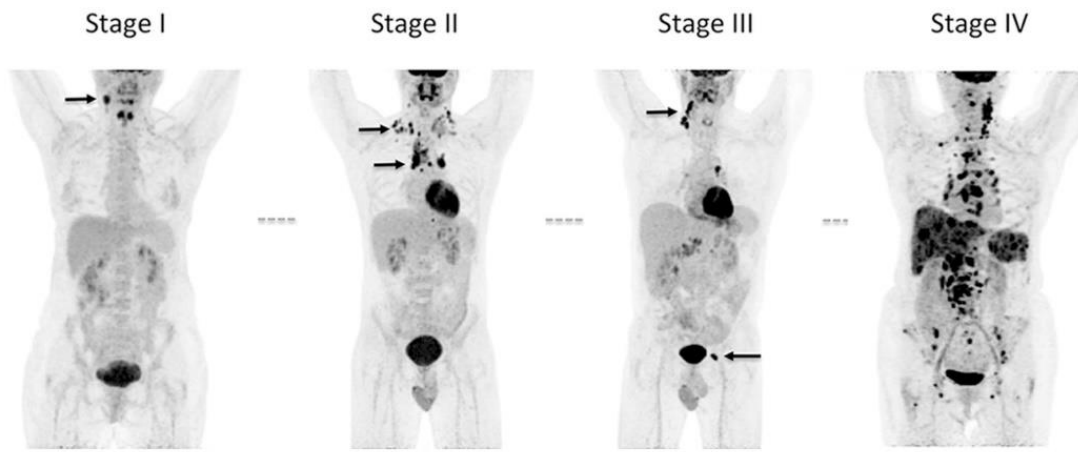

El-Galaly, Semin Nucl Med 2018

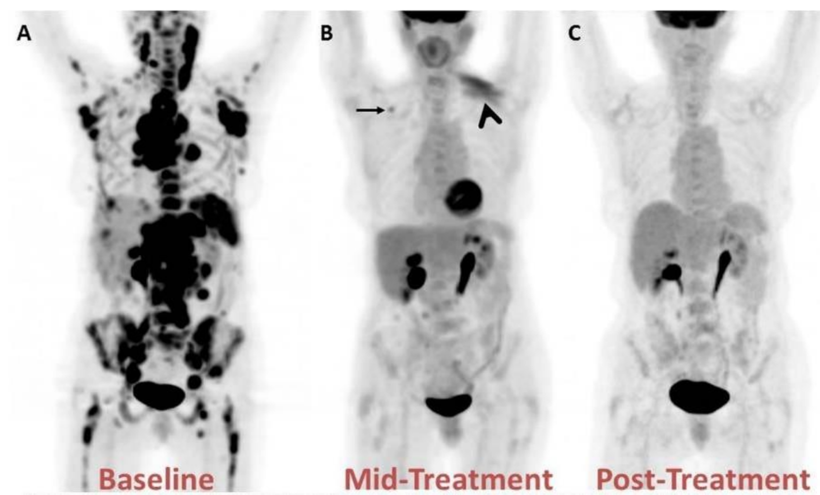

Han, J Nucl Med 2017

Imagerie moléculaire

^{18}F-FDG

Oncologie

- *Caractérisation*
- *Staging TNM*
- *Guidage biopsique*
- *Optimisation RT*
- *Réponse thérapeutique*
- *Récidive*

Poumon
Lymphome
Sein
ORL
Gynéco
Oeso-gastrique
Mélanome

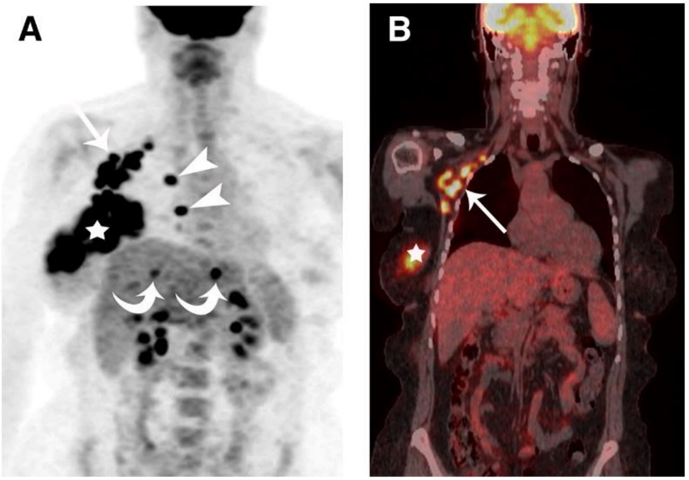

S Carkaci, J Nucl Med 2009

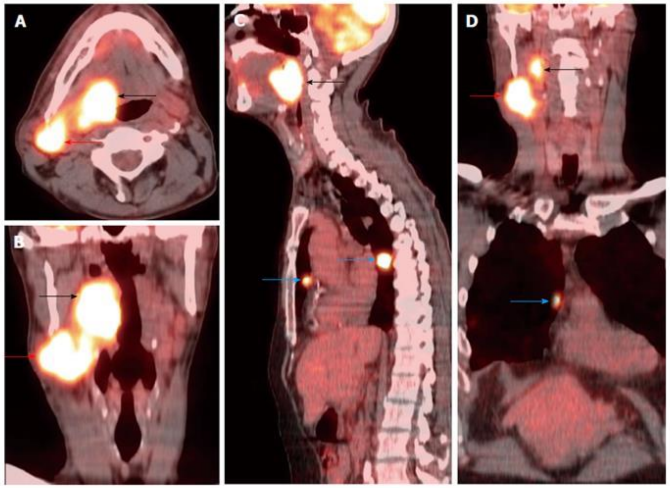

Tantiwongkosi, World J Radiol 2014

Imagerie moléculaire

^{18}F-FDG

Hors-oncologie

Démences

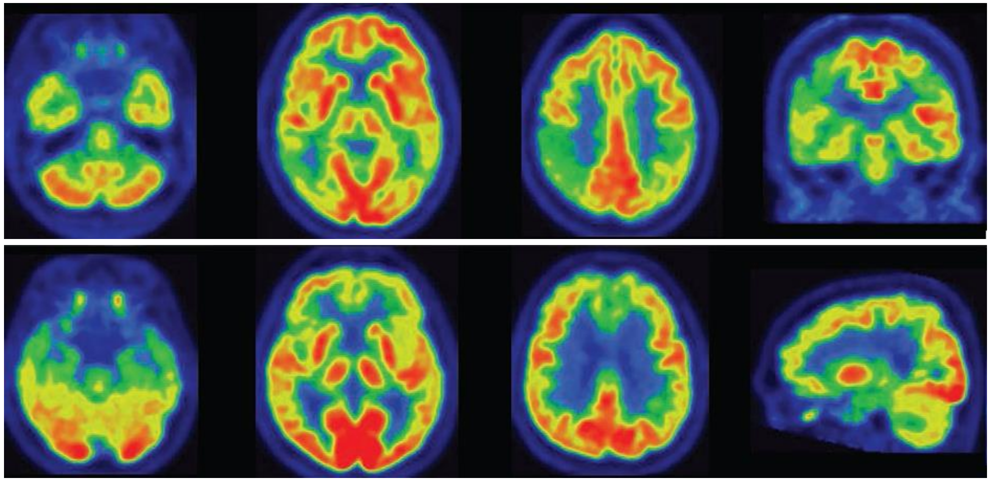

Martin-Macintosh, Am J Roentgenol 2016

Imagerie moléculaire

^{18}F-FDG

Hors-oncologie

- Démences
- Viabilité

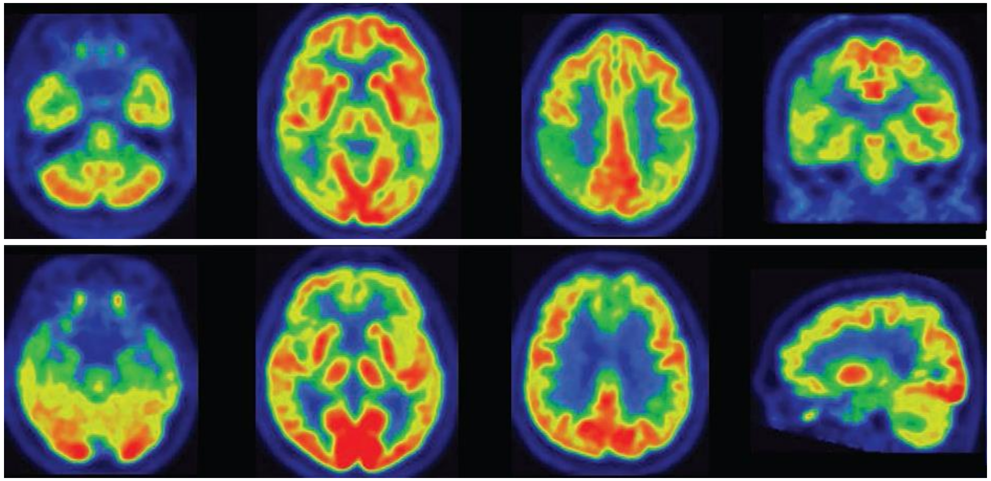

Martin-Macintosh, Am J Roentgenol 2016

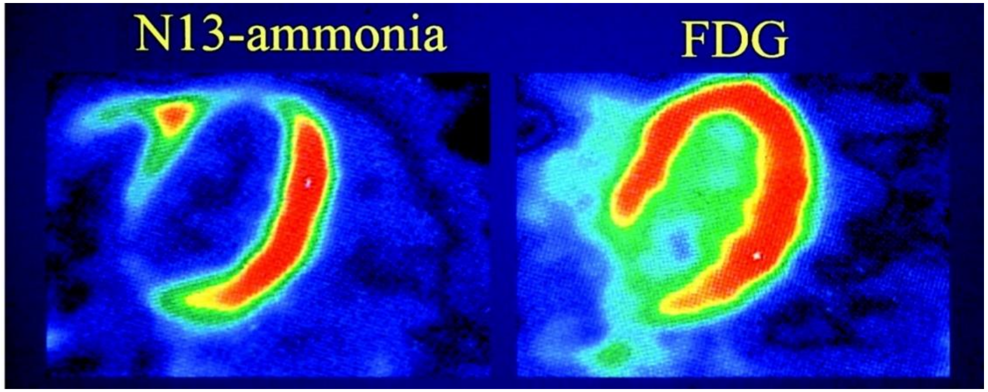

Schinkel, J Nucl Med 2007

Imagerie moléculaire

^{18}F-FDG

Hors-oncologie

- Démences
- Viabilité
- Infection

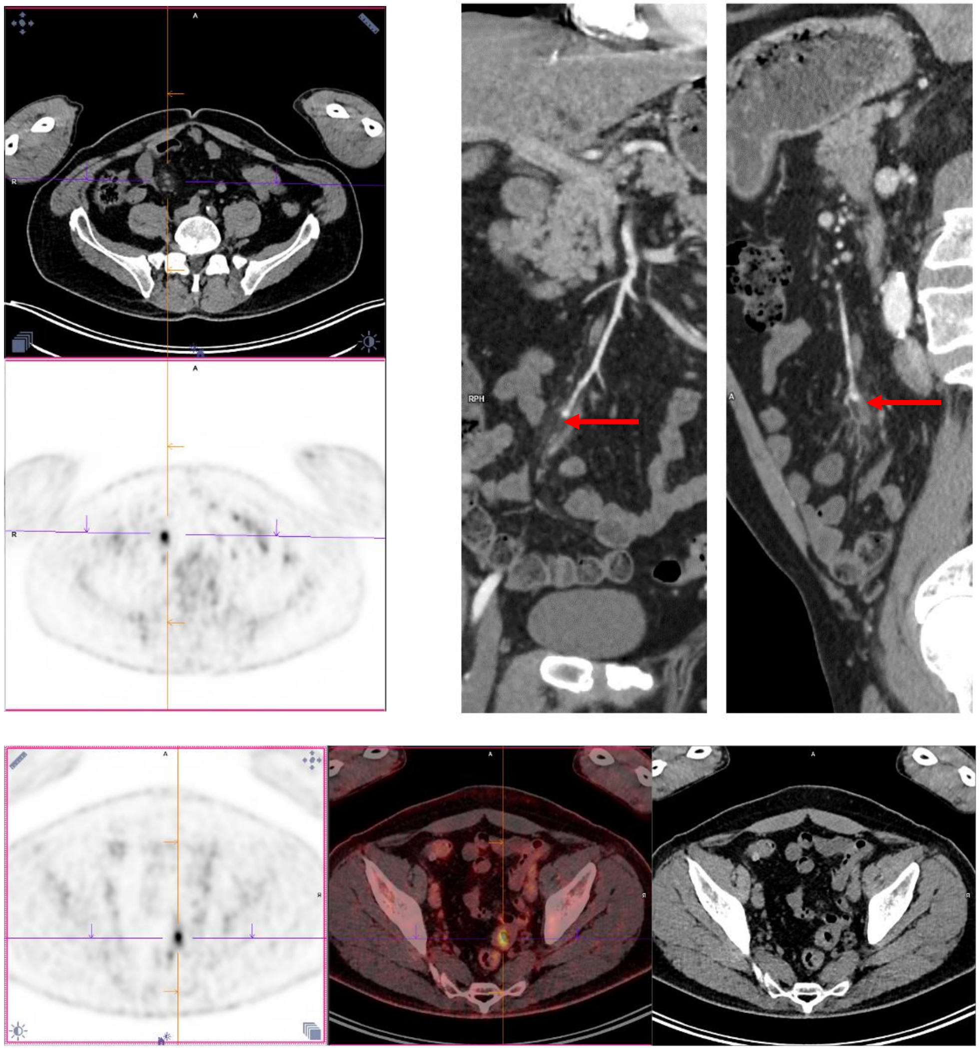

CHU Montpellier

Imagerie moléculaire

^{18}F-FDG

Hors-oncologie

- Démences
- Viabilité
- Infection
- Vascularite

Pooled performances	Value
Sensitivity	0.80
Specificity	0.89
Accuracy	0.84
Positive LR	6.73
Negative LR	0.25

Besson, Eur J Nucl Med Mol Imaging 2011

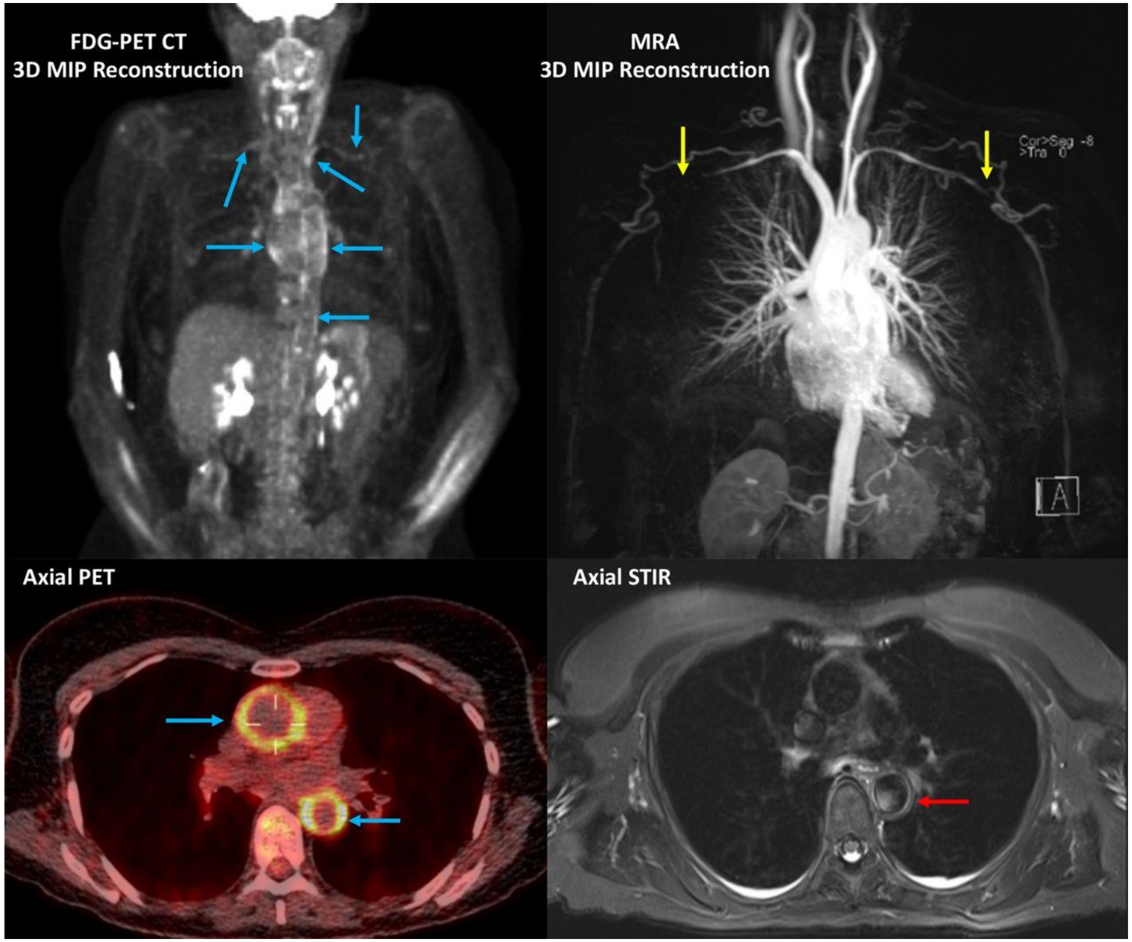

Quinn, Ann Rheum Dis 2018

Imagerie moléculaire

^{18}F-FDG

^{18}F-choline

ADK prostate

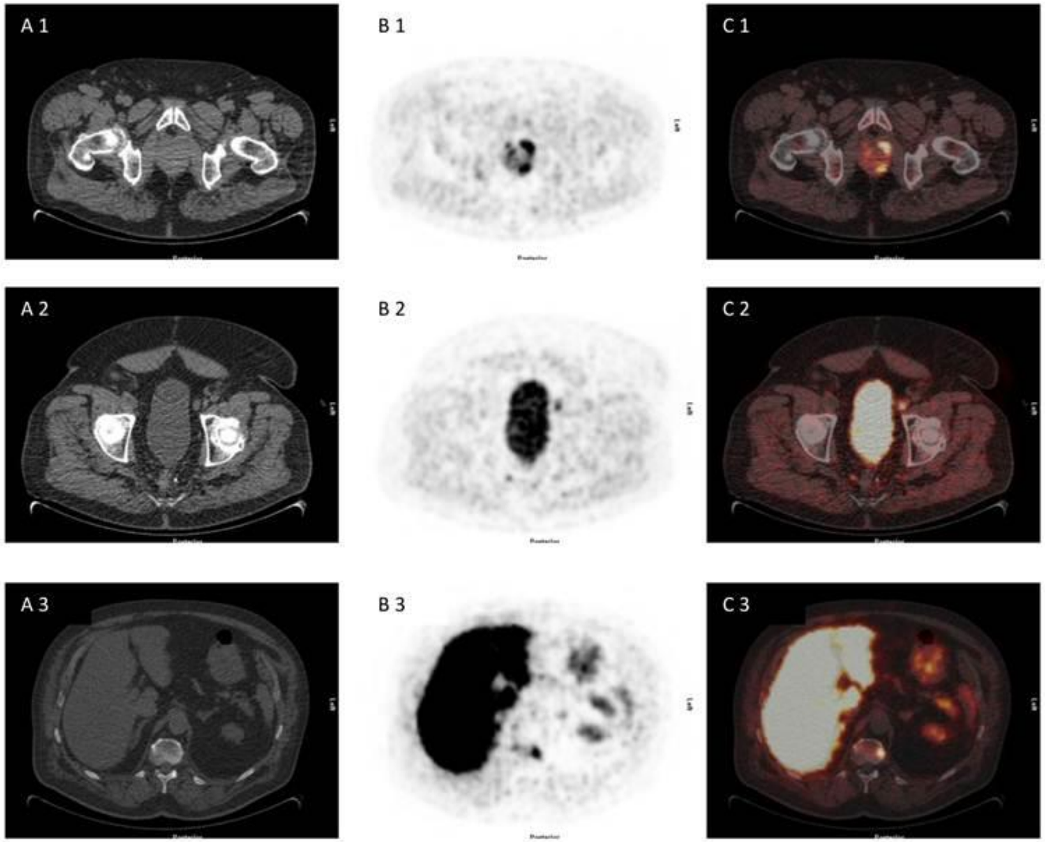

Schwarzenböck, Theranostics 2012

Imagerie moléculaire

^{18}F-FDG

^{18}F-choline

ADK prostate
CHC

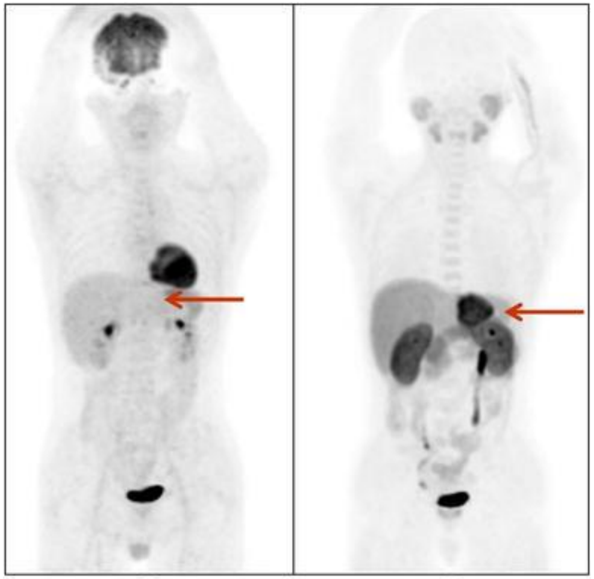

A B

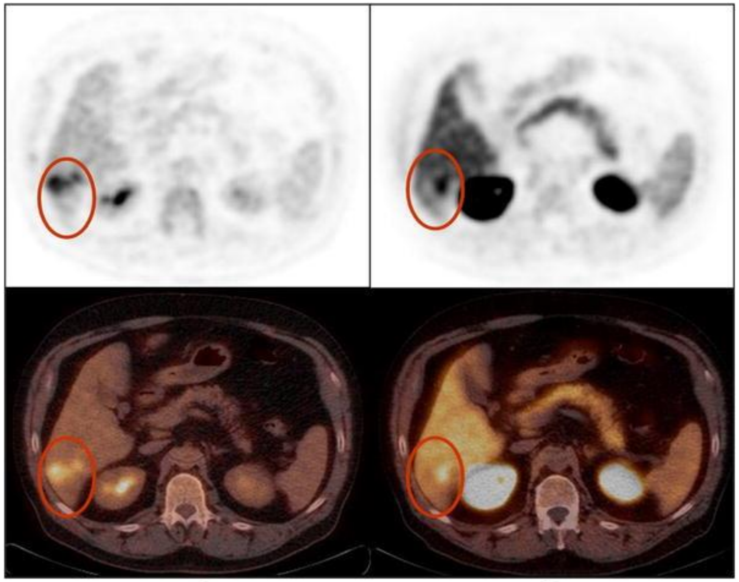

A B

Talbot, Clin Transl Imaging 2014

Imagerie moléculaire

^{18}F-FDG

^{18}F-choline

- ADK prostate
- CHC
- Adénome parathyr.

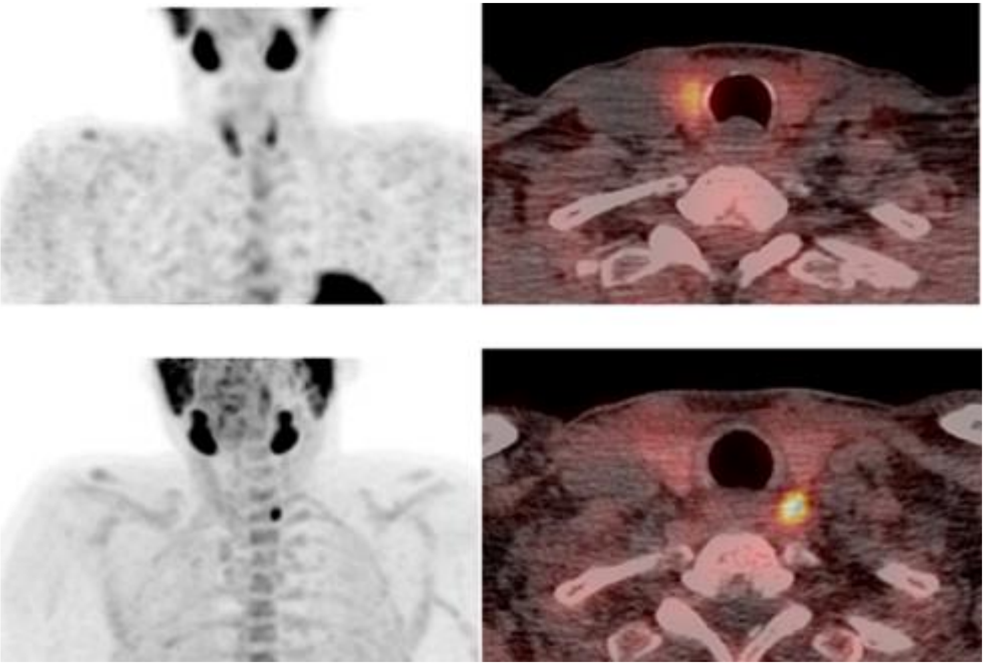

Kluijfhout, Int J Surg Case Rep 2015

Imagerie moléculaire

^{18}F-FDG

^{18}F-choline

^{18}F-Na

Poumon / sein / prostate

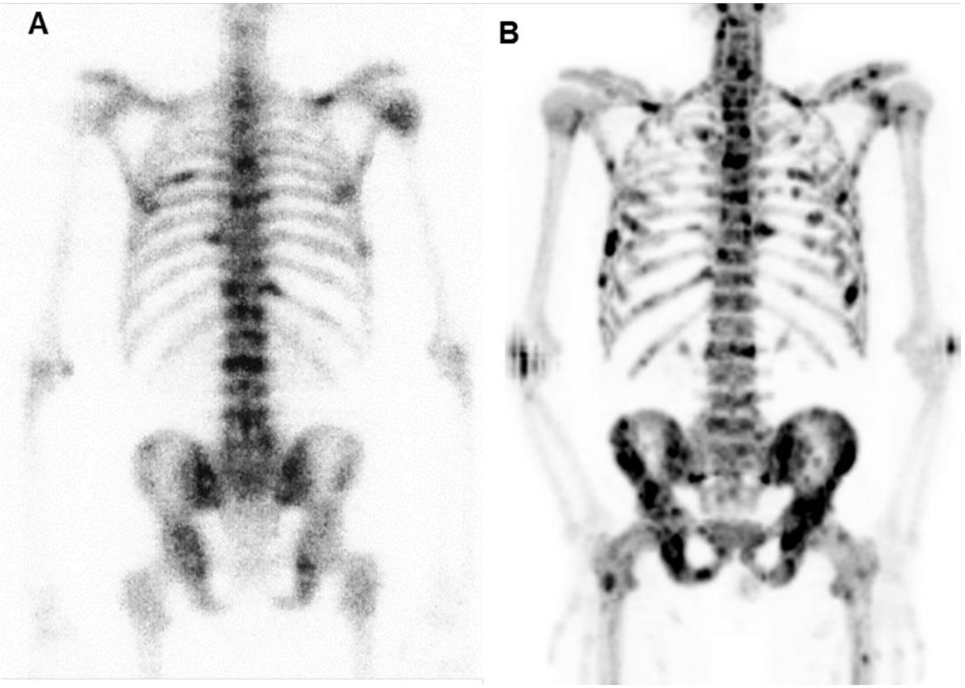

Langsteger, Semin Nucl Med 2016

Imagerie moléculaire

^{18}F-FDG

^{18}F-choline

^{18}F-Na

^{18}F-DOPA

Syndrome PK

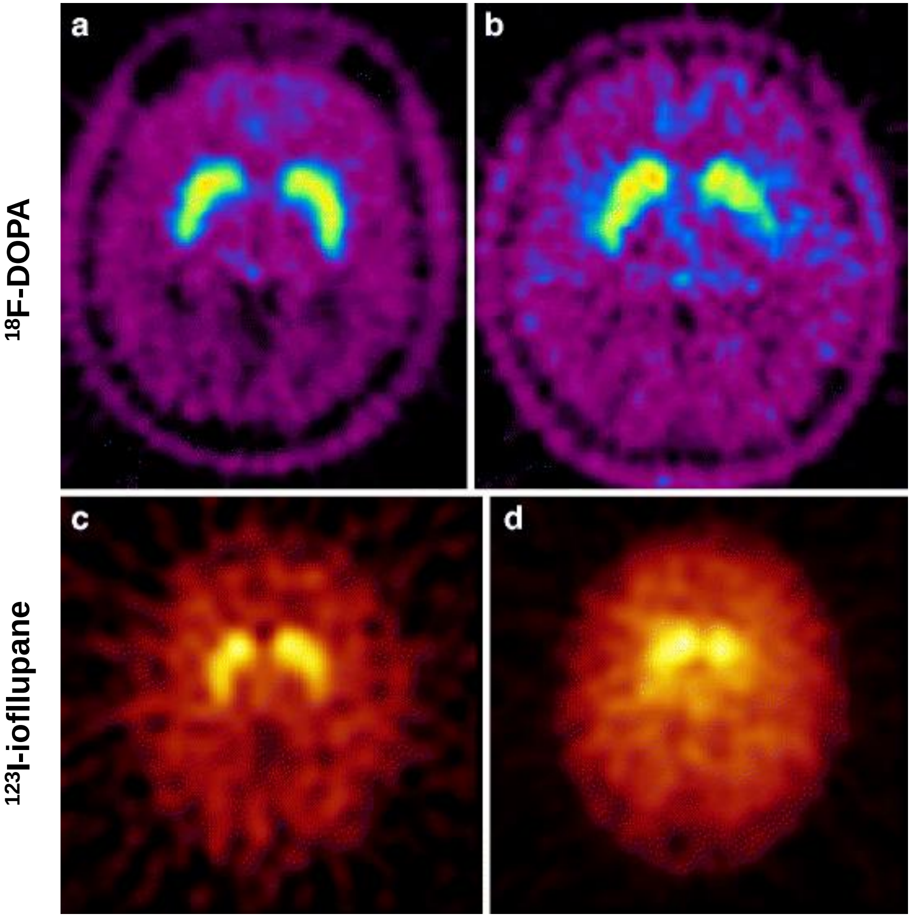

Eshuis, Eur J Nucl Med Mol Imaging 2009

Imagerie moléculaire

^{18}F-FDG

^{18}F-choline

^{18}F-Na

^{18}F-DOPA

- Syndrome PK
- Neuro-oncologie

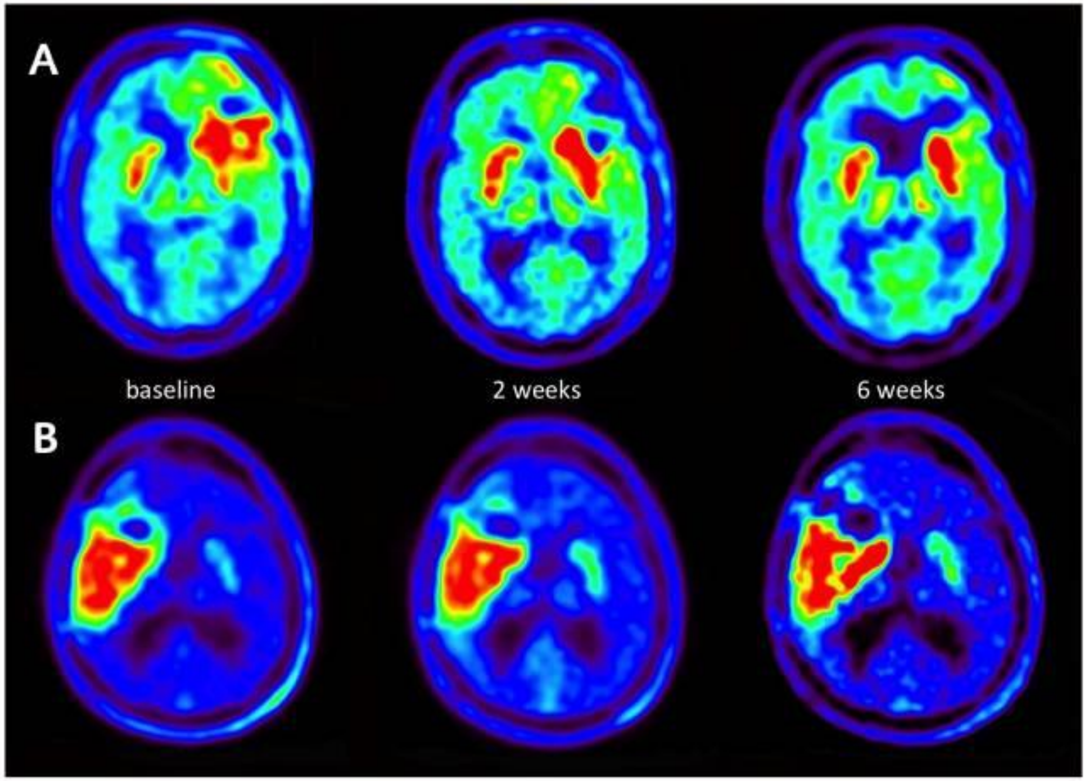

Schwarzenberg, Clin Cancer Res 2015

Imagerie moléculaire

^{18}F-FDG

^{18}F-choline

^{18}F-Na

^{18}F-DOPA

Syndrome PK
Neuro-oncologie
TNE

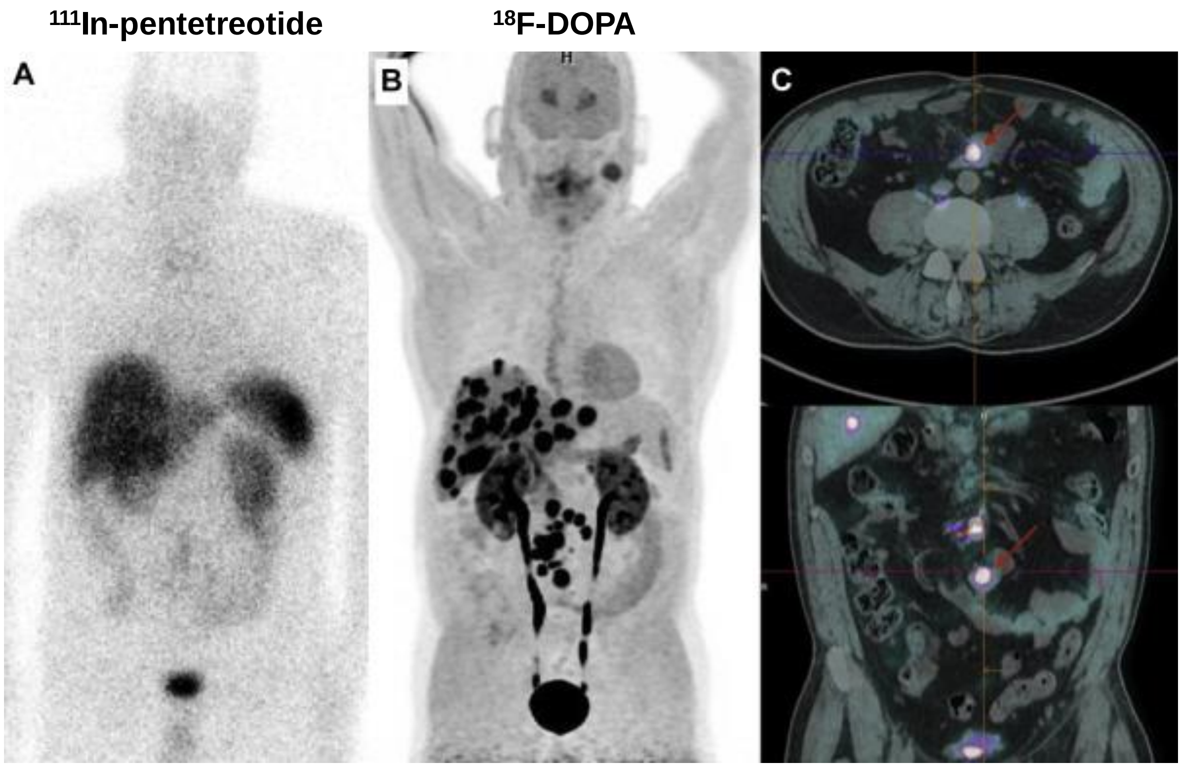

Lussey-Lepoutre, Médecine Nucléaire 2016

Imagerie moléculaire

^{68}Ga

^{68}Ga-peptides

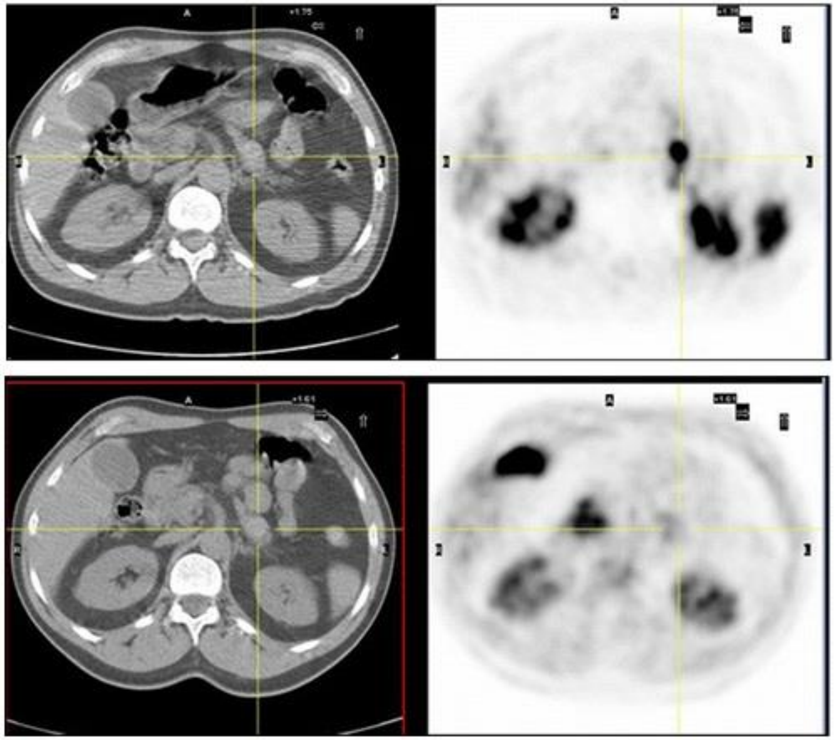

^{68}Ga-DOTANOC

^{18}F-DOPA

Ambrosini, Eur J Nucl Med Mol Imaging 2008

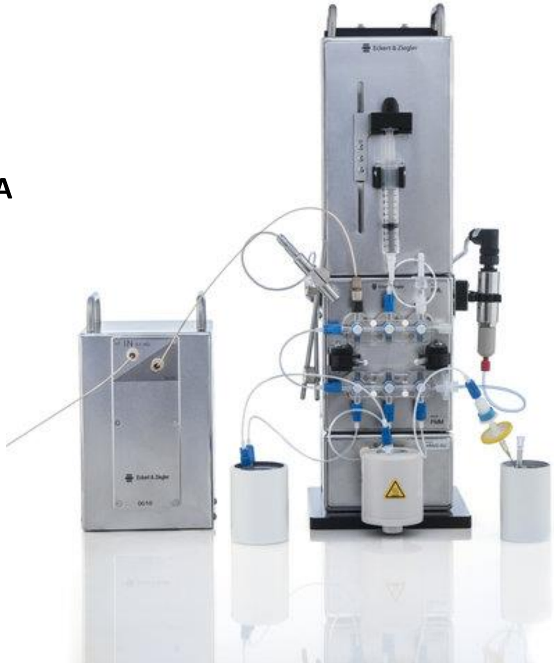

Imagerie moléculaire

^{68}Ga

^{68}Ga-peptides

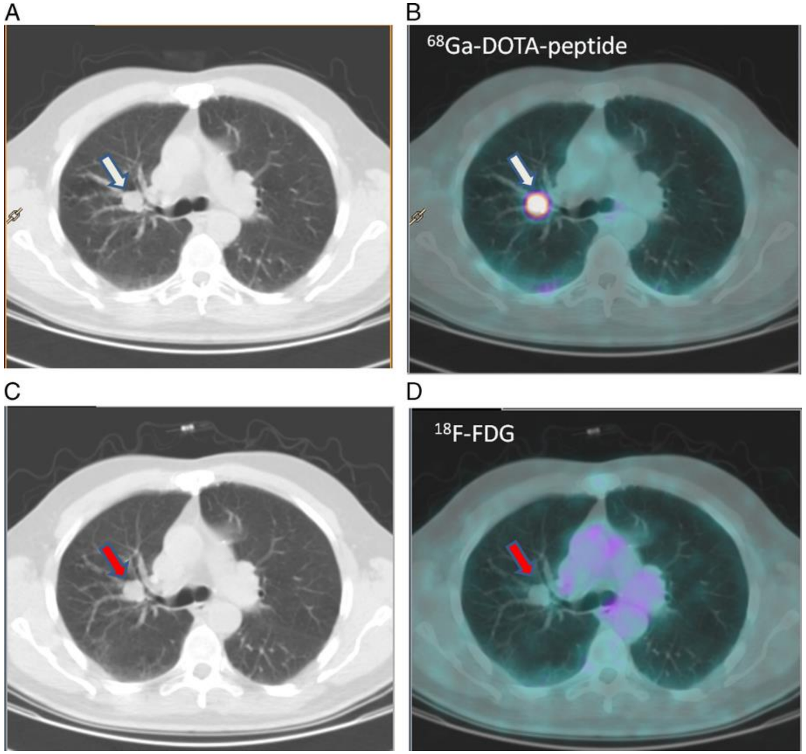

Lococo, Clin Nucl Med 2015

^{68}Ga

^{68}Ga-peptides

^{68}Ga-PSMA

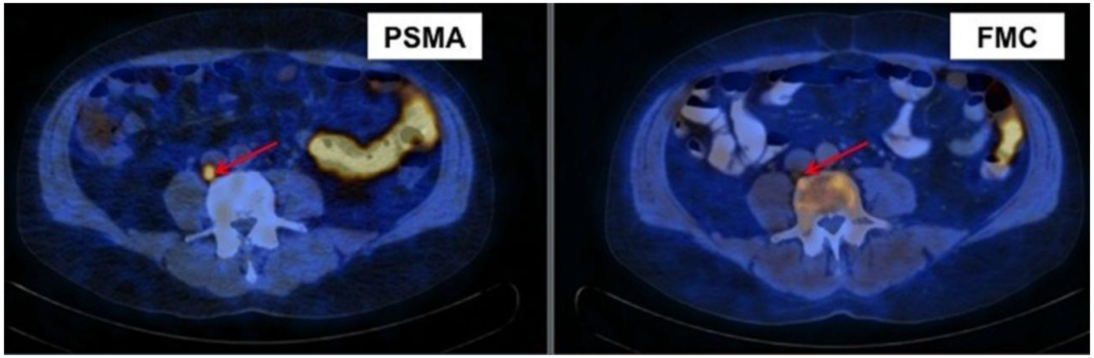

Morigi, J Nucl Med 2015

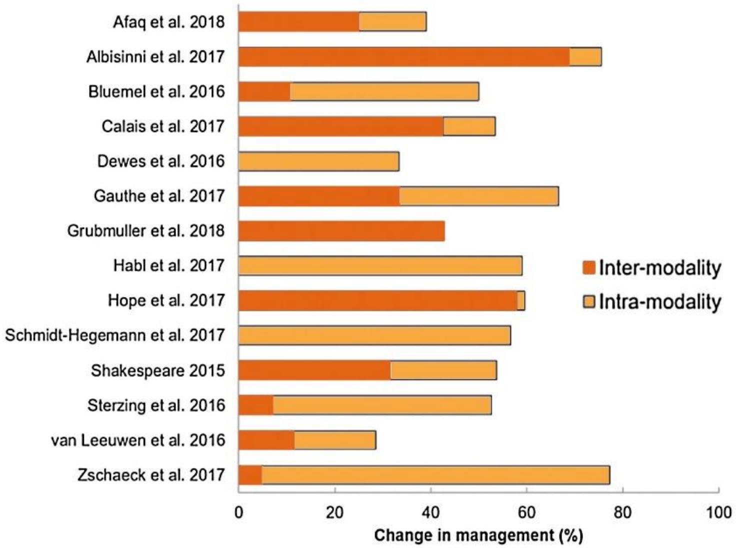

Han, Eur Urol 2018

^{15}O

^{15}O-water : perfusion
^{15}O-CO : RBV

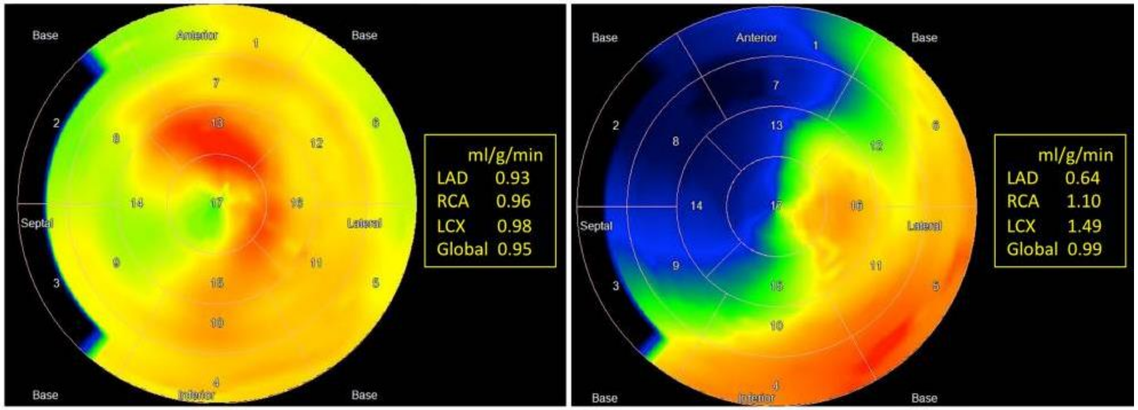

Williams, Eur Radiol 2017

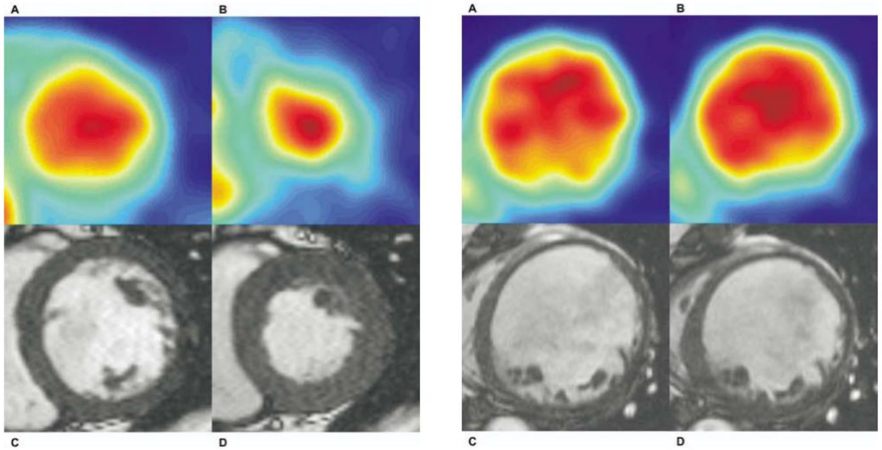

Hofman, J Nucl Cardiol 2005

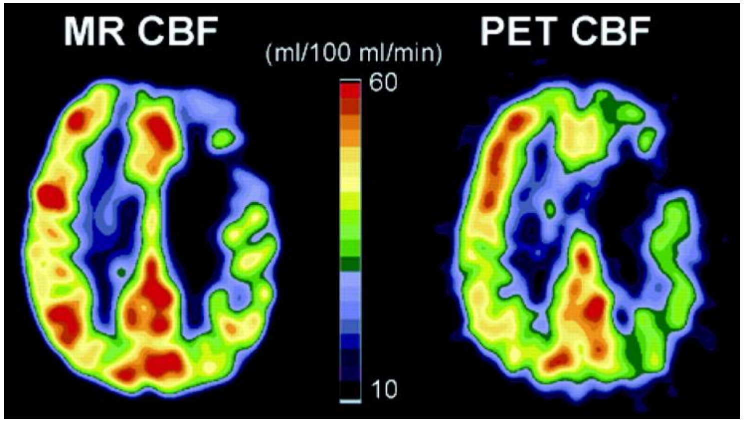

Mukherjee, AJNR Am J Neuroradiol. 2003

Imagerie moléculaire

$^{13}N\text{-}NH_3$, ^{82}Rb

Perfusion myocardique

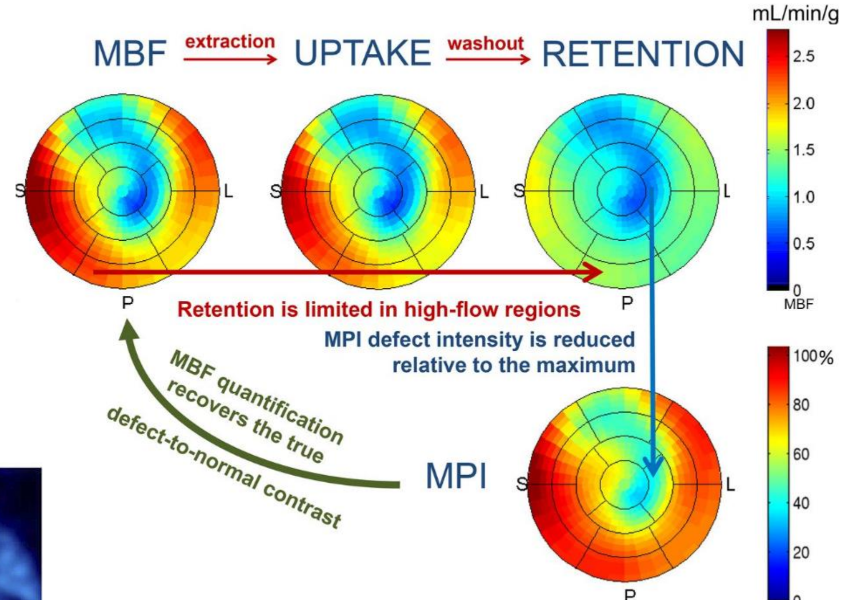

Murthy, J Nucl Med 2018

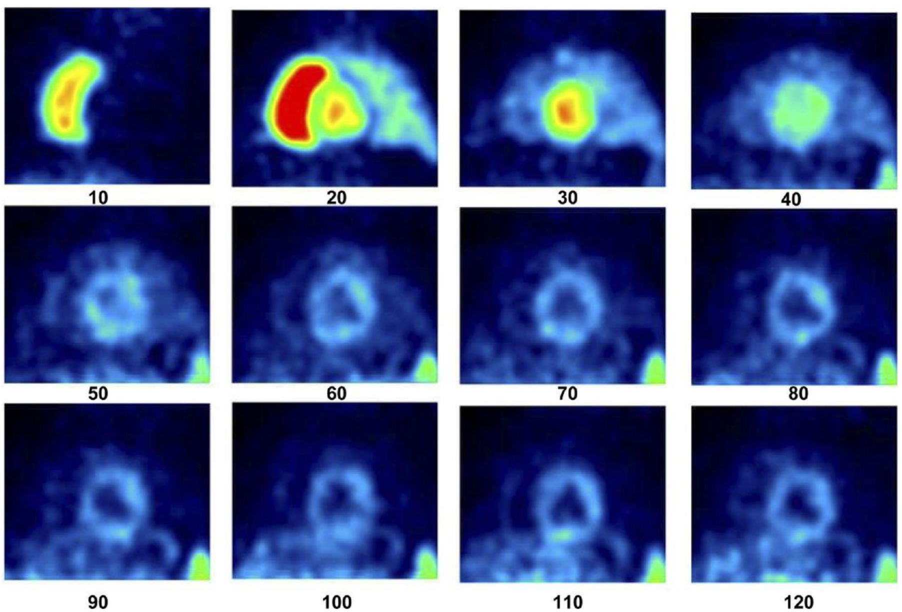

Schindler, JACC Cardiovasc Imaging 2010.

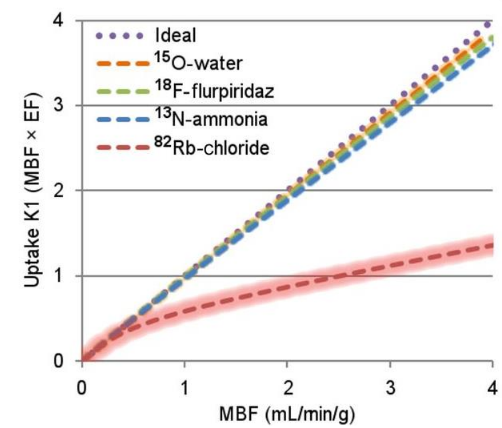

Imagerie moléculaire

^{11}C

- ^{11}C-glucose
- ^{11}C-PIB
- ^{11}C-choline
- ^{11}C-acetate
- ^{11}C-methionine

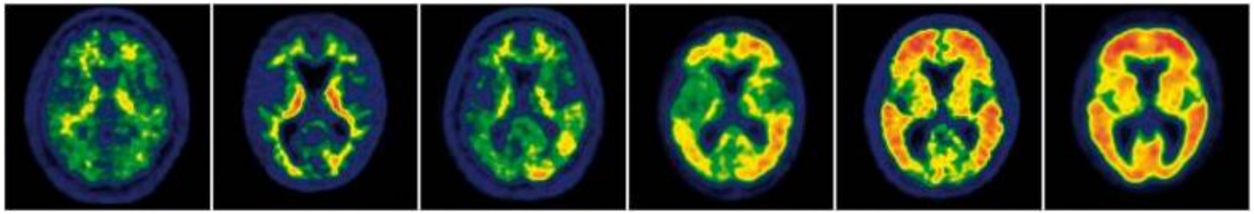

Murray, Brain 2015

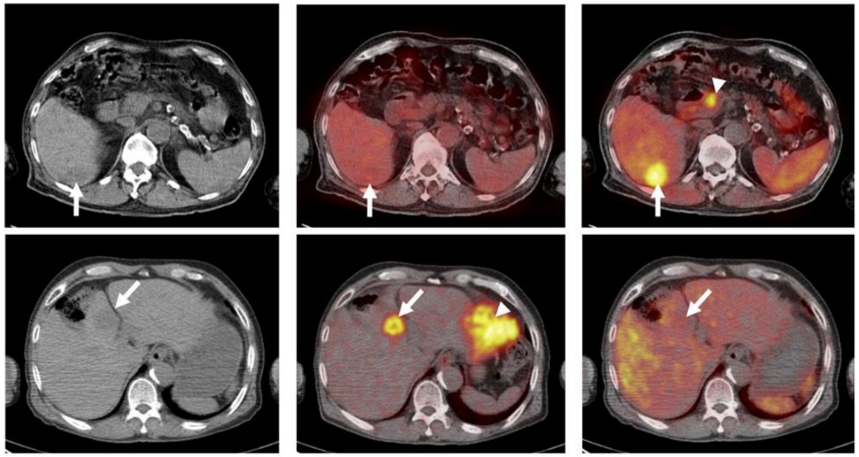

Park, J Nucl Med 2008.

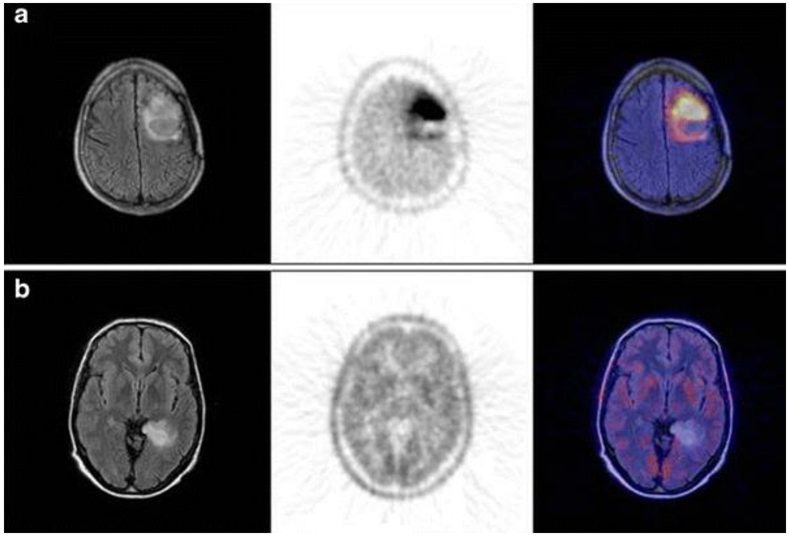

Glaudemans, Eur J Nucl Med Mol Imaging 2013

Désintégration β+

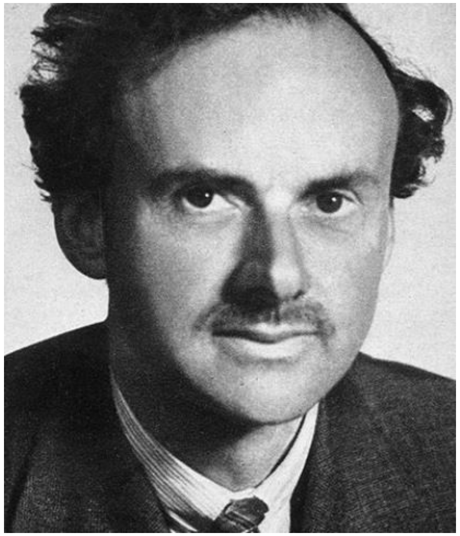

Paul Adrien Maurice Dirac

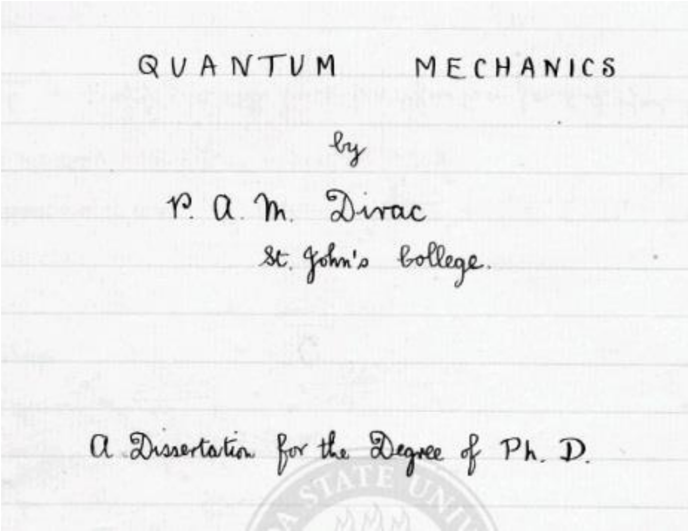

$$\left(\beta mc^2 + \sum_{k=1}^{3} \alpha_k p_k\, c\right) \psi(\mathbf{x},t) = i\hbar \frac{\partial \psi(\mathbf{x},t)}{\partial t}$$

"This balancing on the dizzying path between genius and madness is awful"
A. Einstein

Désintégration β+

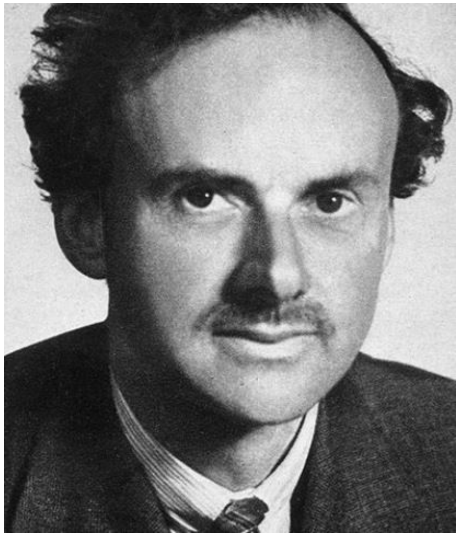

Paul Adrien Maurice Dirac

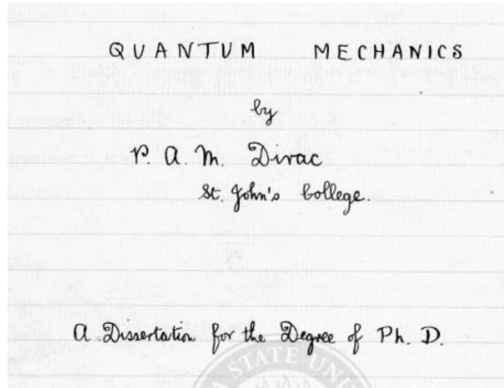

QUANTUM MECHANICS

by

P. A. M. Dirac
St. John's College.

A Dissertation for the Degree of Ph. D.

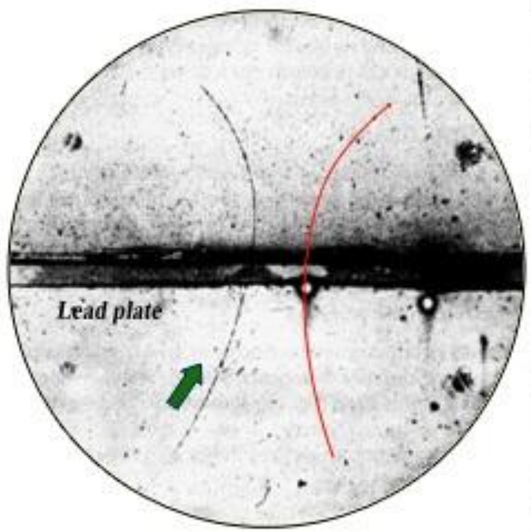

Cloud (Wilson) chamber

Carl Anderson

Désintégration β+

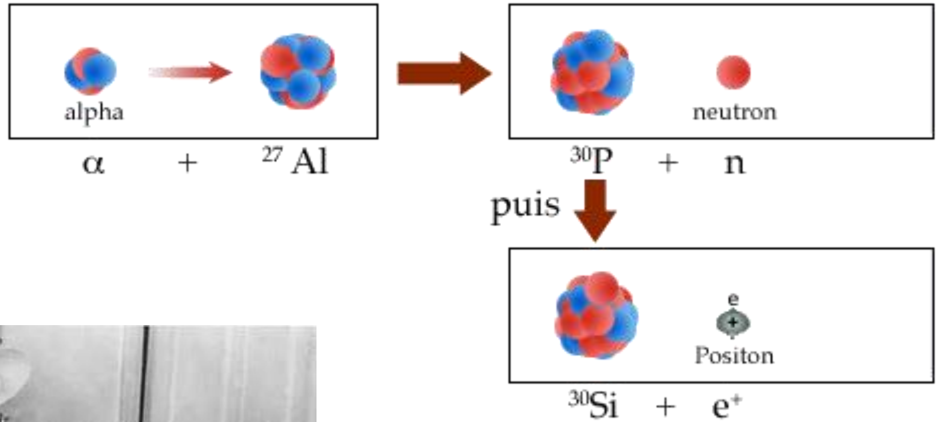

Frédéric et Irène Joliot-Curie, Institut du Radium 1934

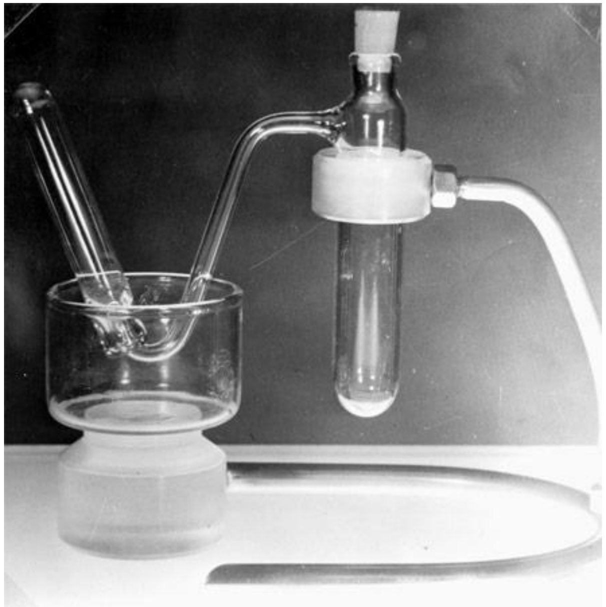

Désintégration β+

Frédéric et Irène Joliot-Curie, Institut du Radium 1934

Ces radioéléments pourront recevoir des ***applications médicales*** *et peut-être d'autres applications pratiques.*

Introduits dans l'organisme, ces corps doivent se comporter ***très différemment des radioéléments ordinaires*** *en raison de leurs* ***propriétés chimiques différentes*** *et de leur* ***destruction sans résidu.***

Certains des radioéléments nouveaux sont émetteurs de rayons γ. ***Ceux qui émettent des positons*** *produisent avec une grande intensité dans la matière voisine le* ***rayonnement d'annihilation de 511 KeV*** *et, par conséquent, ils constitueront des* ***sources de rayons γ homogènes*** *et pourront être utilisés à ce titre.*

Enfin, on doit prévoir un ***développement considérable*** *de l'emploi de ces noyaux radioactifs, en tant qu'****indicateurs*** *pour étudier le comportement de leurs isotopes inactifs dans certaines réactions chimiques ou dans les* ***phénomènes biologiques.***

F. Joliot, Londres 1934

Désintégration β+

$$ {}^{A}_{Z}X \rightarrow {}^{\;\;A}_{Z-1}Y + e^{+} + \nu $$

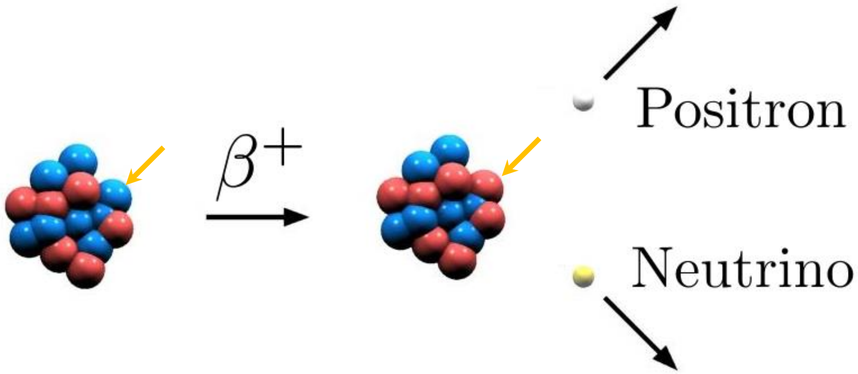

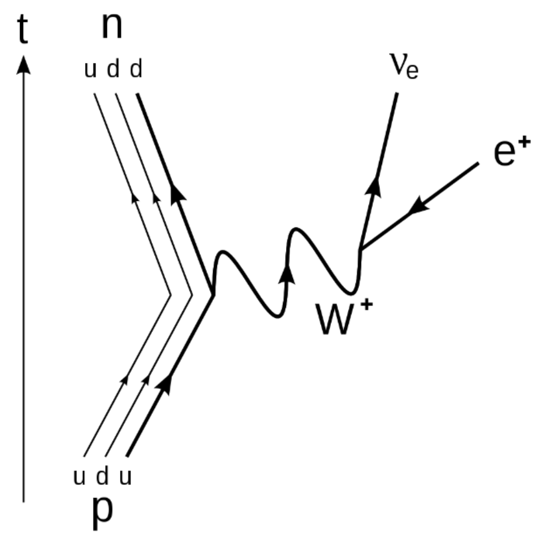

Désintégration β+

$$^{A}_{Z}X \rightarrow {}^{A}_{Z-1}Y + e^{+} + \nu$$

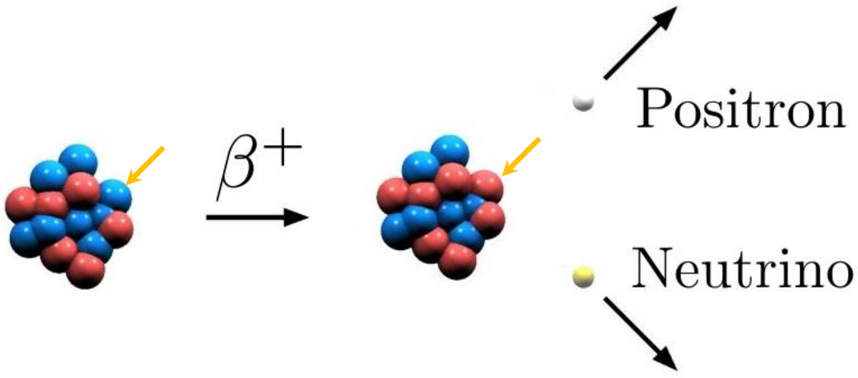

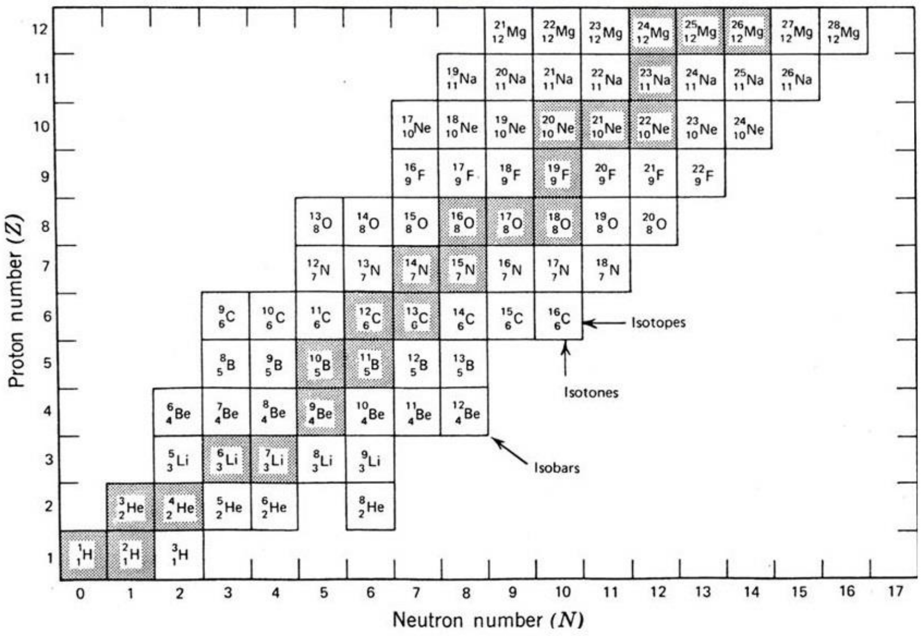

Désintégration β+

$$^{A}_{Z}X \rightarrow {}_{Z-1}^{\;\;A}Y + e^{+} + \nu$$

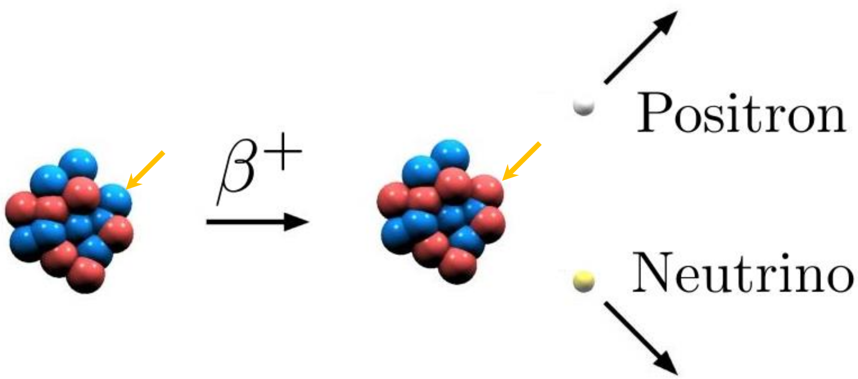

beta+

beta+ , $t_{1/2}$ > 1 min

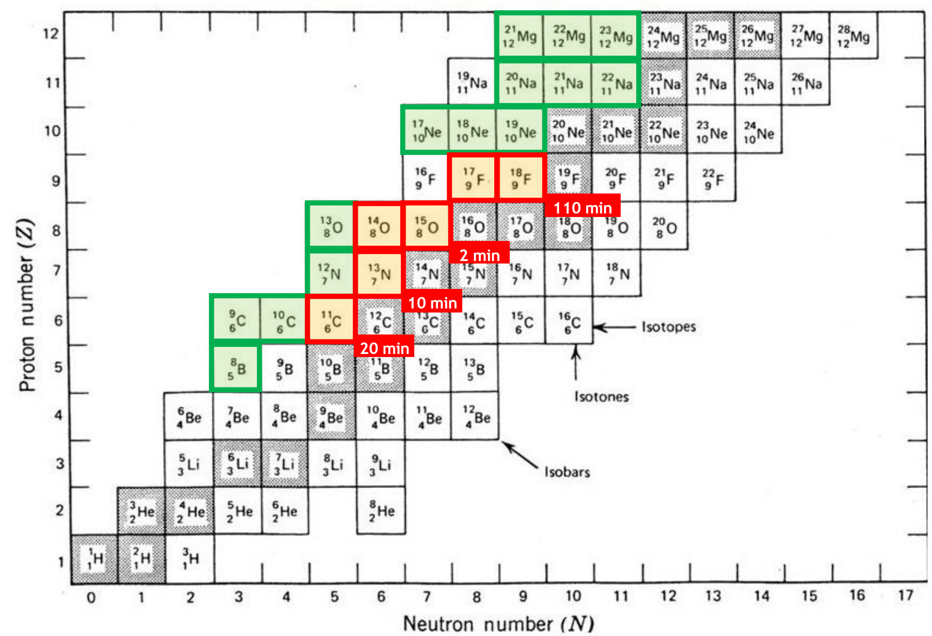

Désintégration β+

$$ {}_{Z}^{A}X \rightarrow {}_{Z-1}^{A}Y + e^{+} + \nu $$

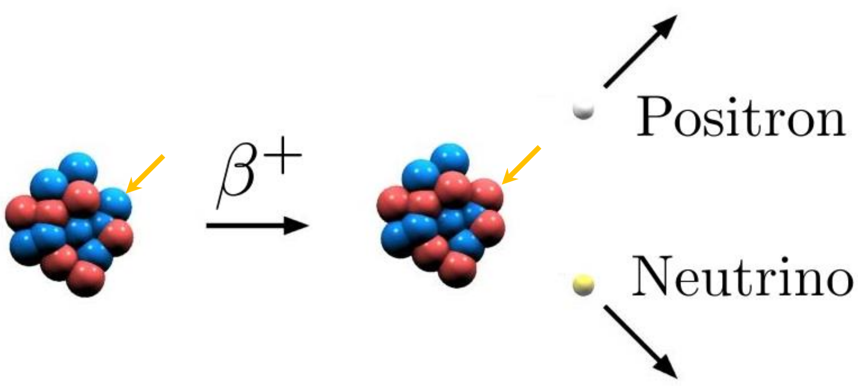

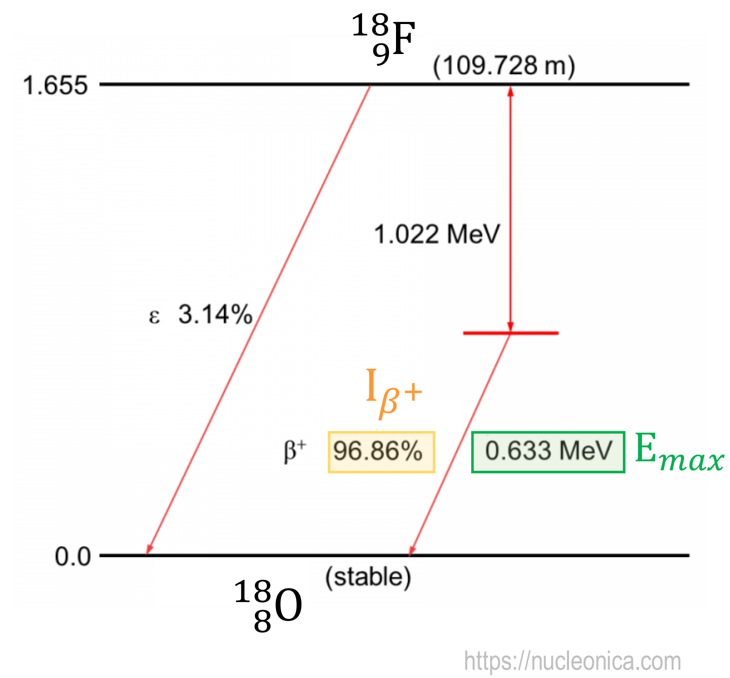

Désintégration β+

$$^{A}_{Z}X \rightarrow {}^{A}_{Z-1}Y + e^{+} + \nu$$

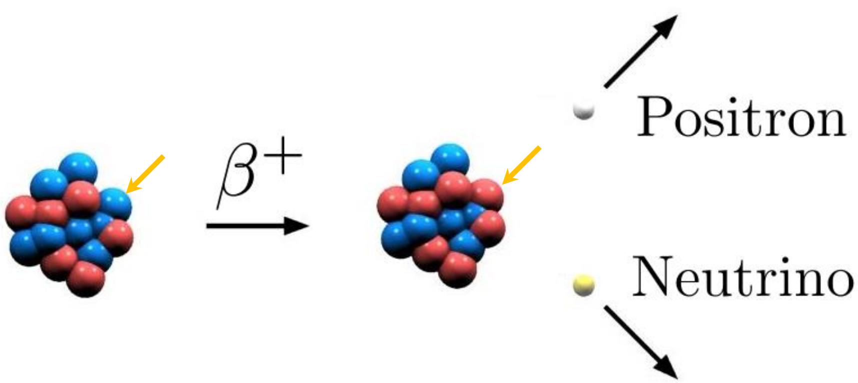

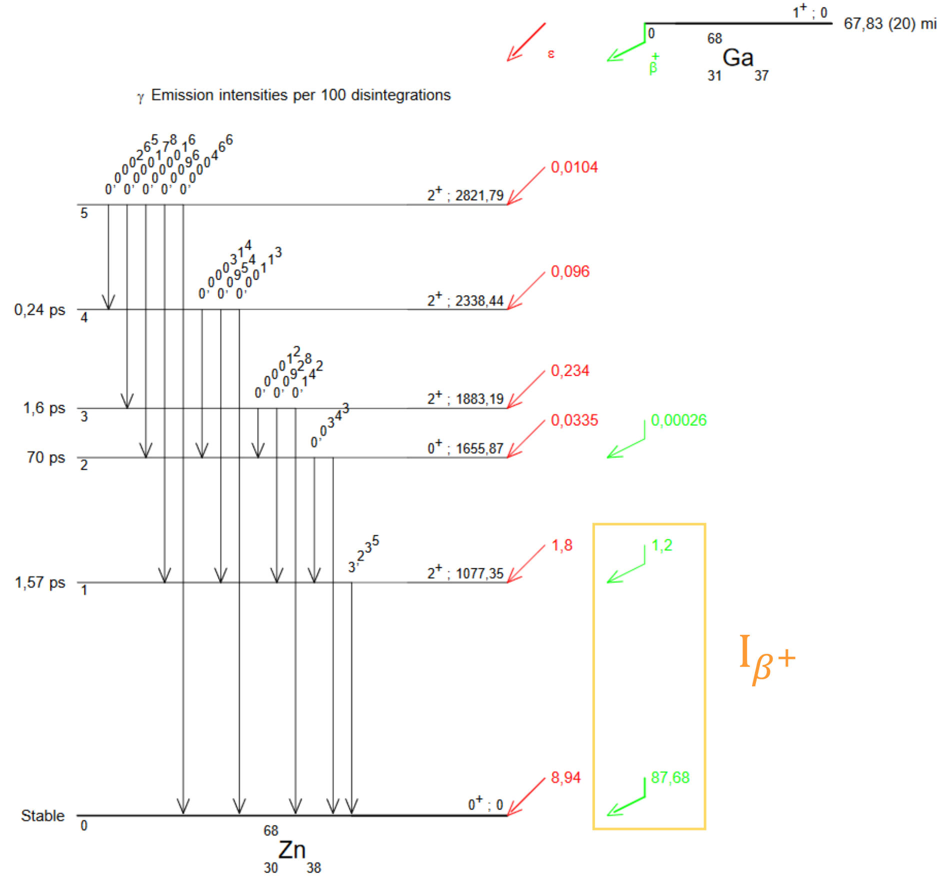

Nucleide.org

Désintégration β+

$$ {}^{A}_{Z}X \rightarrow {}_{Z-1}^{\;\;\;A}Y + e^{+} + \nu $$

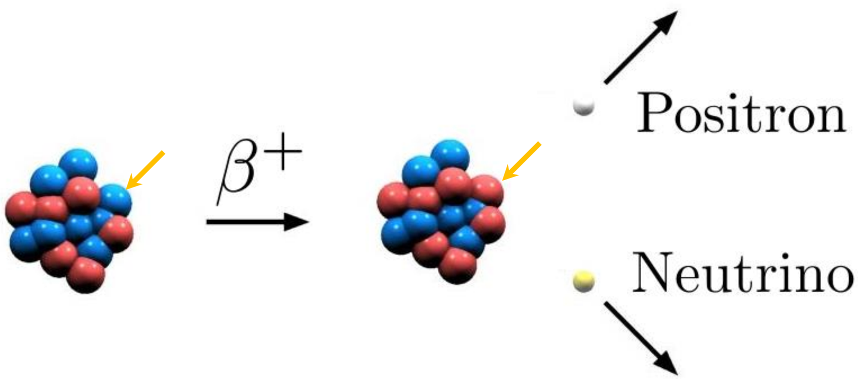

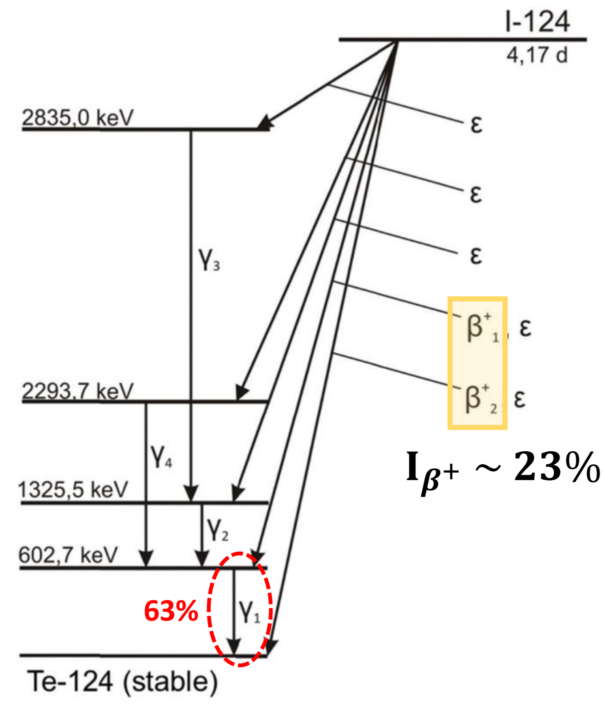

Preylowski, Plos One 2013

Désintégration β+

$$^A_ZX \rightarrow {}_{Z-1}^{\ A}Y + e^+ + \nu$$

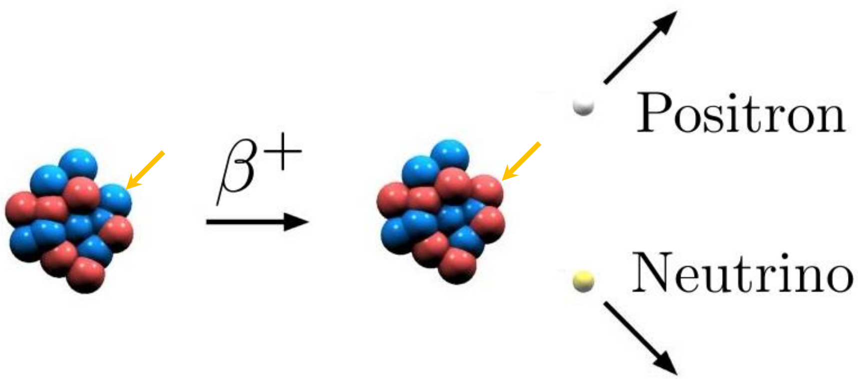

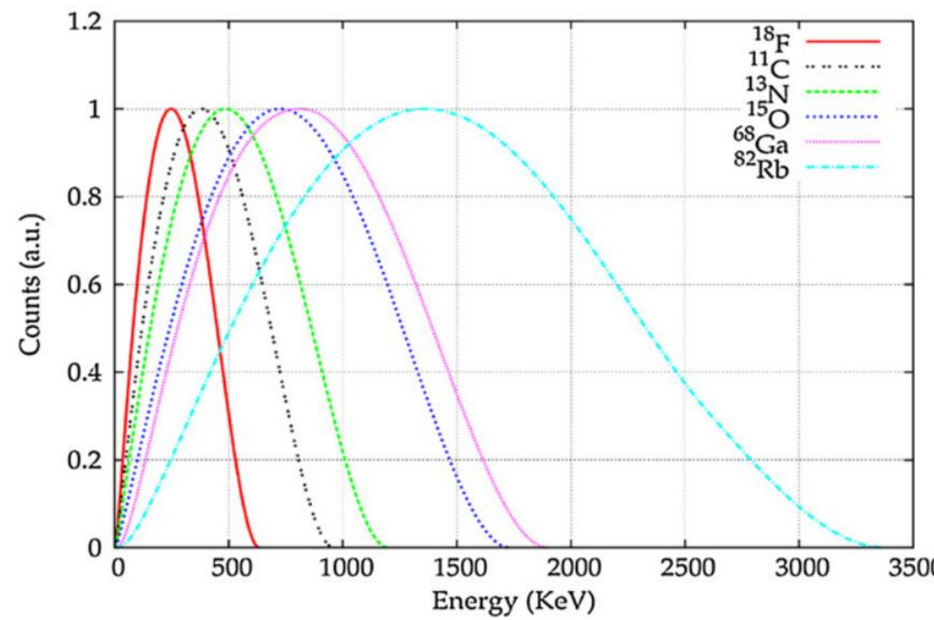

Cal-Gonzalez, Phys Med Biol 2013

Désintégration β+

$$ {}^{A}_{Z}X \rightarrow {}^{\;\;A}_{Z-1}Y + e^{+} + \nu $$

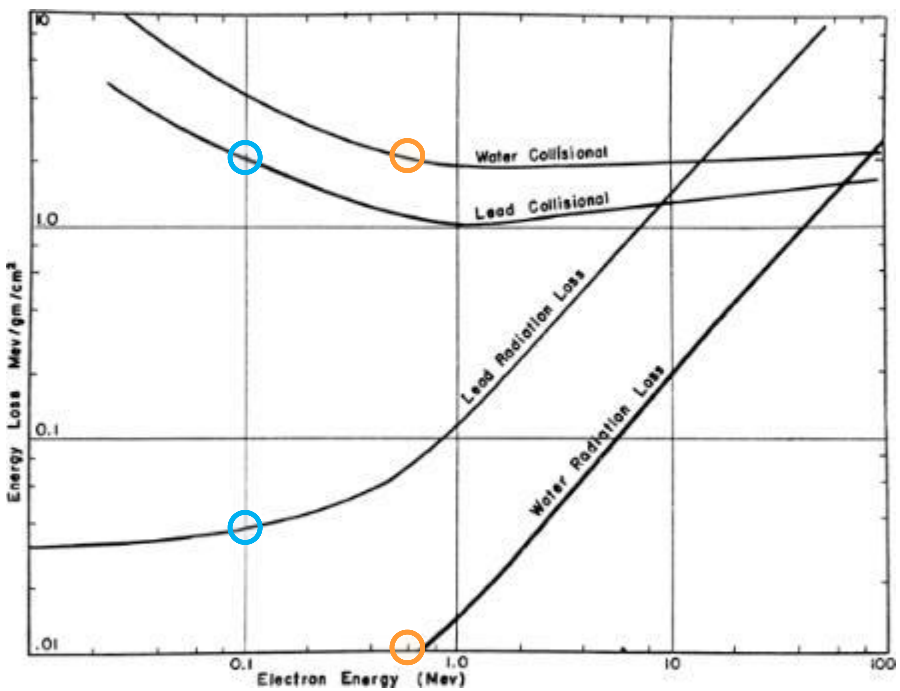

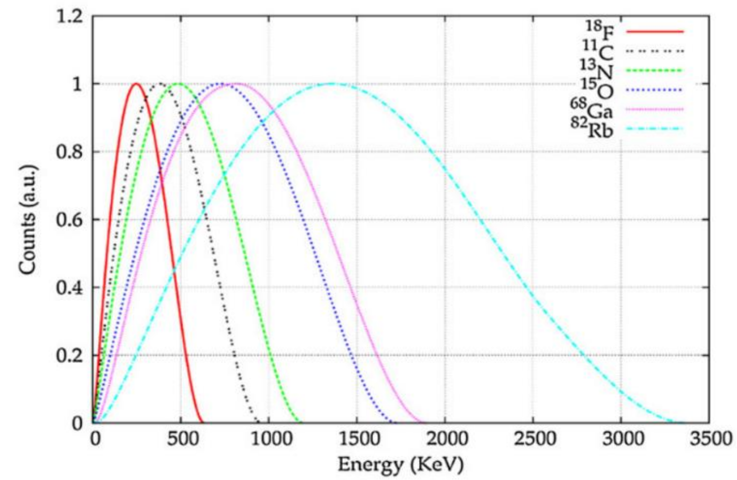

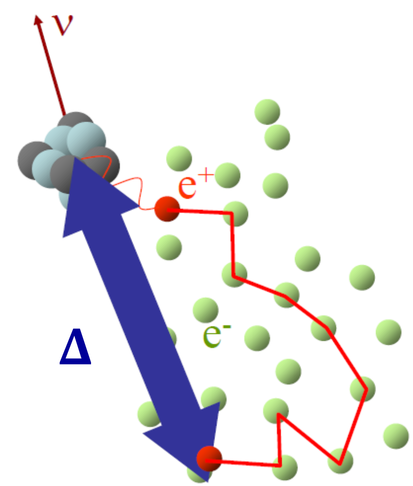

	E moy. (KeV)	Portée (mm)
^{11}C	390	1,1
^{13}N	490	1,5
^{15}O	730	2,5
^{18}F	250	0,6
^{68}Ga	850	2,9
^{82}Rb	1550	5,9

Jødal, Phys Med Biol 2012
Conti, EJNMMI Physics 2016

Désintégration β+

$$ {}^{A}_{Z}X \rightarrow {}^{\;\;\;A}_{Z-1}Y + e^{+} + \nu $$

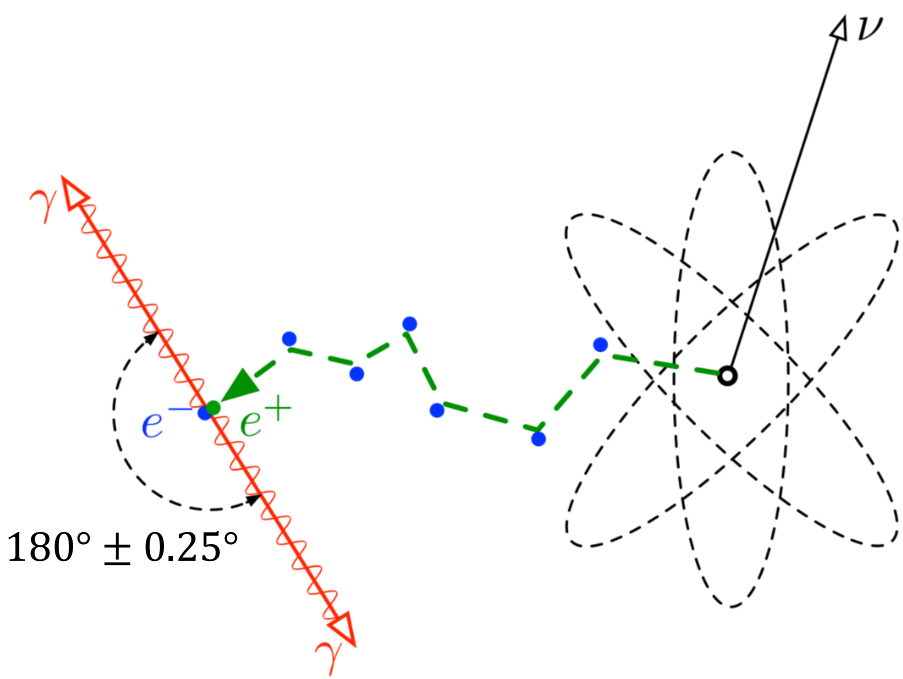

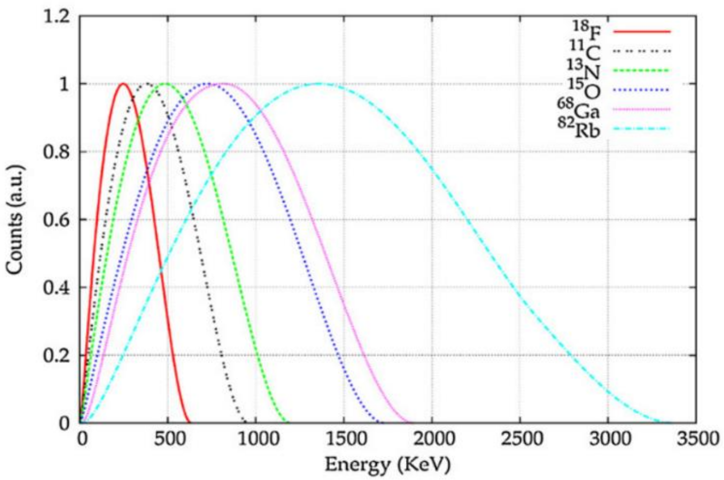

	E moy. (KeV)	Portée (mm)
^{11}C	390	1,1
^{13}N	490	1,5
^{15}O	730	2,5
^{18}F	250	0,6
^{68}Ga	850	2,9
^{82}Rb	1550	5,9

Jødal, Phys Med Biol 2012
Conti, EJNMMI Physics 2016

Désintégration β+

$$ {}^{A}_{Z}X \rightarrow {}^{\ \ \ A}_{Z-1}Y + e^{+} + \nu $$

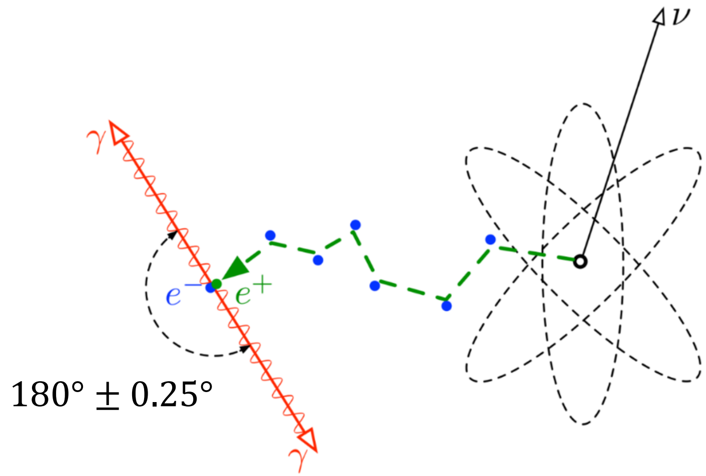

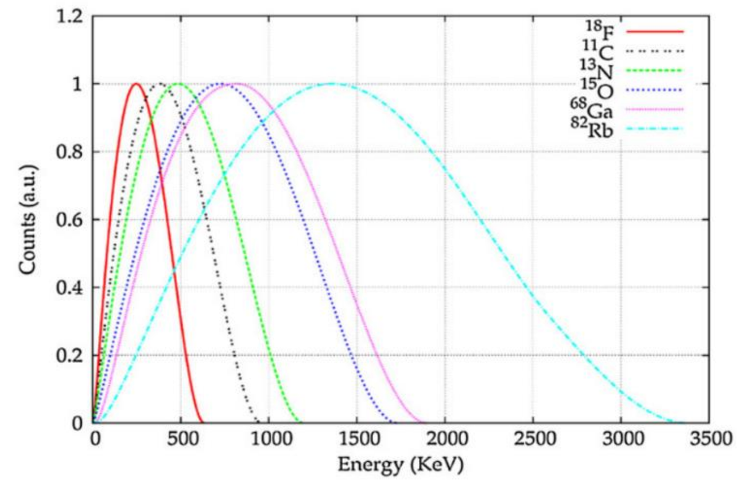

	E moy. (KeV)	Portée (mm)
^{11}C	390	1,1
^{13}N	490	1,5
^{15}O	730	2,5
^{18}F	250	0,6
^{68}Ga	850	2,9
^{82}Rb	1550	5,9

Jødal, Phys Med Biol 2012
Conti, EJNMMI Physics 2016

annihilation directe 60%

Para-positonium 10%

Ortho-positonium <1%

Ortho-positonium / pick-off 30%

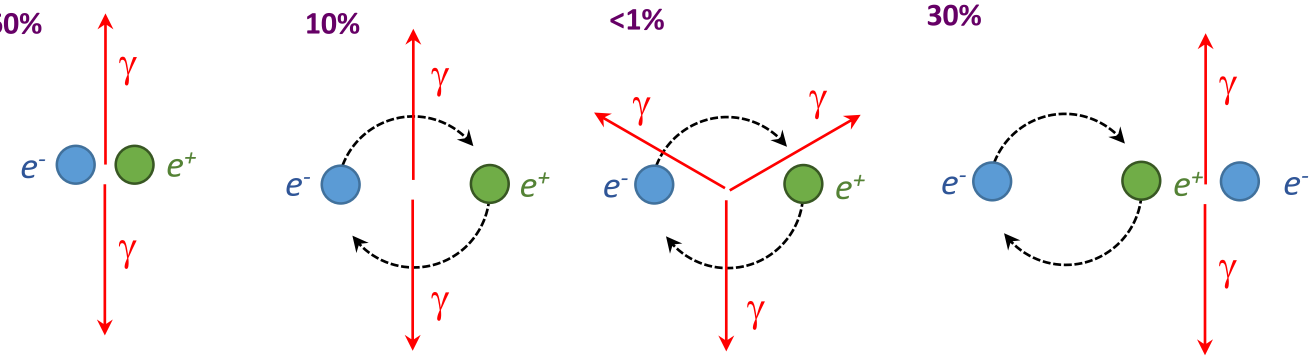

Désintégration β+

TABLE IV. – *Summary of the positron annihilation processes*

State	Annihilation process	Comments	Lifetime	Ang. dev.
non-bound	in-flight via 2γ emission	of the order of 2%, coulomb interactions and bremsstrahlung preferred	$\sim$ 1 ps	narrow
	at rest via 2γ emission	standard PET situation	$\sim$ 1 ns	narrow
	at rest via 3γ emission	improbable		
	at rest via more than 3γ emission	more and more improbable		
Positronium	para-positronium self-annihilation	1/4 of the bound states, preferred annihilation for para-positronium	$\sim$ 100 ps	narrow
	para-positronium pick-off	improbable	$\sim$ 1 ns	narrow
	ortho-positronium self-annihilation	via 3γ, it is anticipated by pick-off	$\sim$ 100 ns	narrow
	ortho-positronium pick-off	3/4 of the bound states	$\sim$ 1 ns	large

Del Guerra, Riv Nuov Cimento 2016

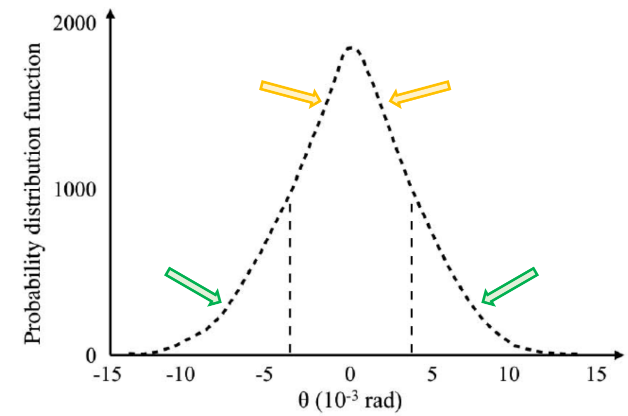

	E moy. (KeV)	Portée (mm)
^{11}C	390	1,1
^{13}N	490	1,5
^{15}O	730	2,5
^{18}F	250	0,6
^{68}Ga	850	2,9
^{82}Rb	1550	5,9

Jødal, Phys Med Biol 2012
Conti, EJNMMI Physics 2016

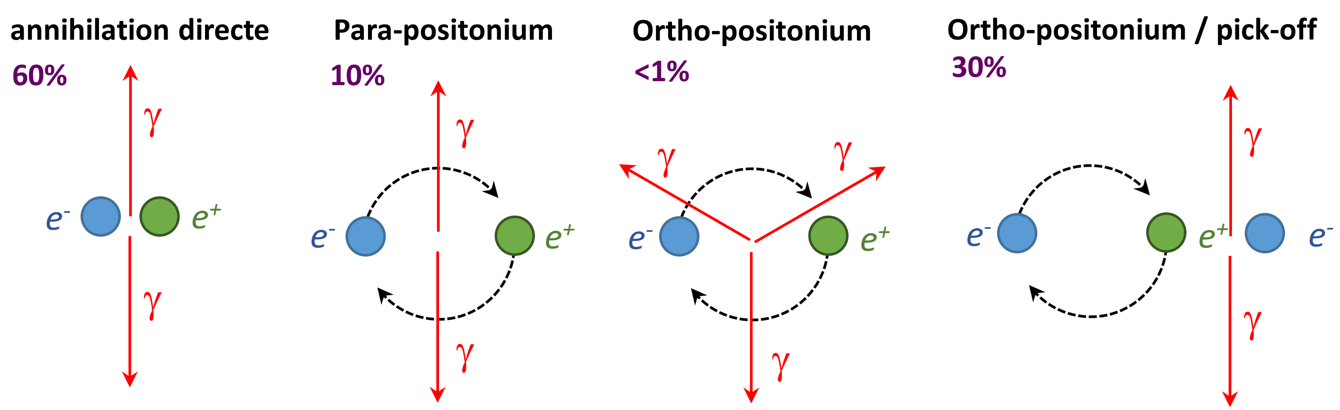

Désintégration $\beta+$

Choix d'un radionucléide

Isotope	$t_{1/2}$ [min]	E_{moy} [KeV]	Portée [mm]	$I_{\beta+}$	γ	Prod.
^{11}C	20	390	1,1	100%	–	Cycl.
^{13}N	10	490	1,5	100%	–	Cycl.
^{15}O	2	730	2,5	100%	–	Cycl.
^{18}F	110	250	0,6	97%	–	Cycl.
^{68}Ga	68	850	2,9	90%	1080 KeV (3%)	Gén.
^{82}Rb	1,25	1550	5,9	96%	780 KeV (15%)	Gén.
^{124}I	4 j	700 - 1000	3 – 4	23%	600 KeV (63%)	Cycl.

Désintégration β+

Cyclotron

Centre TEP Cyceron, Caen

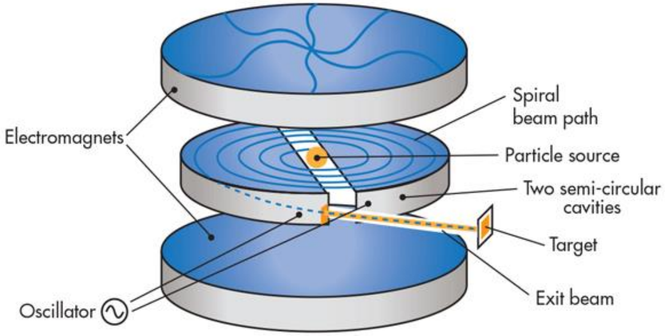

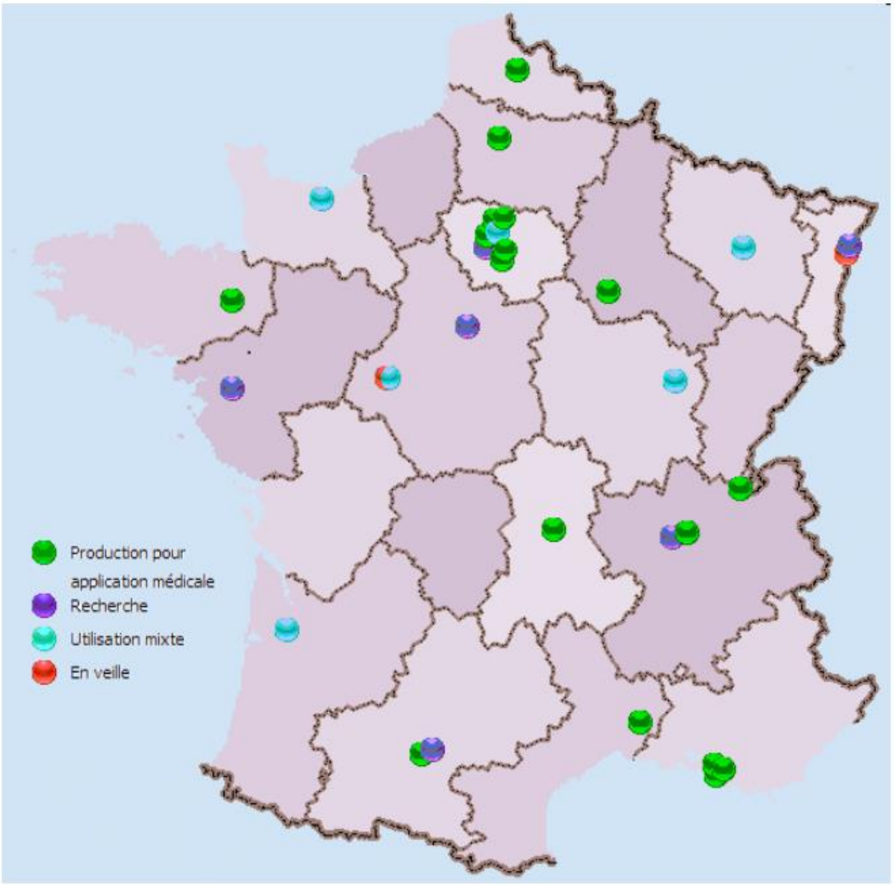

Désintégration β+

Cyclotron

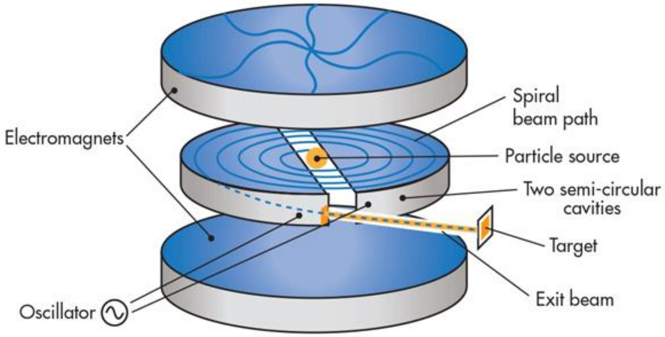

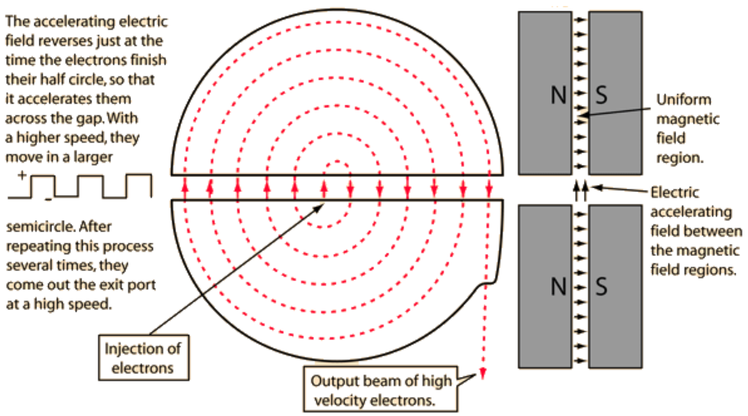

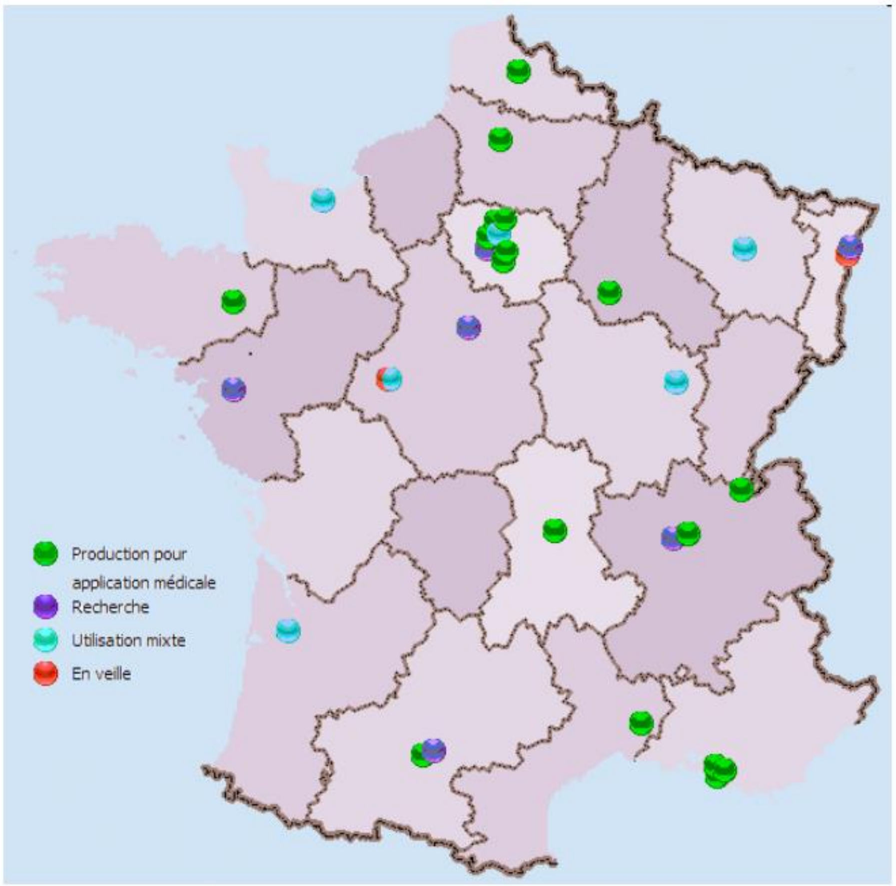

Désintégration β+

Cyclotron

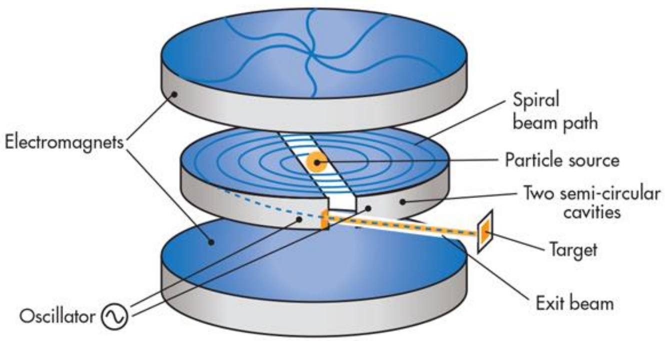

Nuclear Reactions Used to Produce Fluorine-18

$\boxed{^{18}O(p,n)^{18}F}$	$^{20}Ne(d,\alpha)^{18}F$	$^{6}Li(n,\alpha)3H,\ ^{16}O(^{3}H,n)^{18}F$
$^{16}O(^{3}He,p)^{18}F$	$^{20}Ne(p,2n)^{18}F$	
$^{16}O(\alpha,pn)^{18}F$	$^{20}Ne(^{3}He,n)^{18}Ne,\ ^{18}Ne\text{-}^{18}F$	

Cole, Top Med Chem 2014

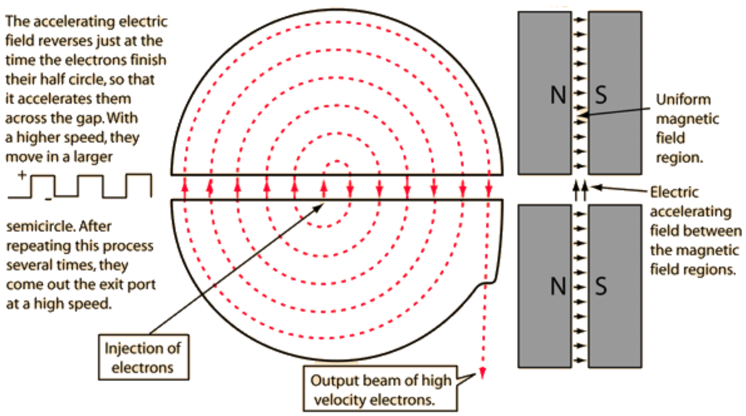

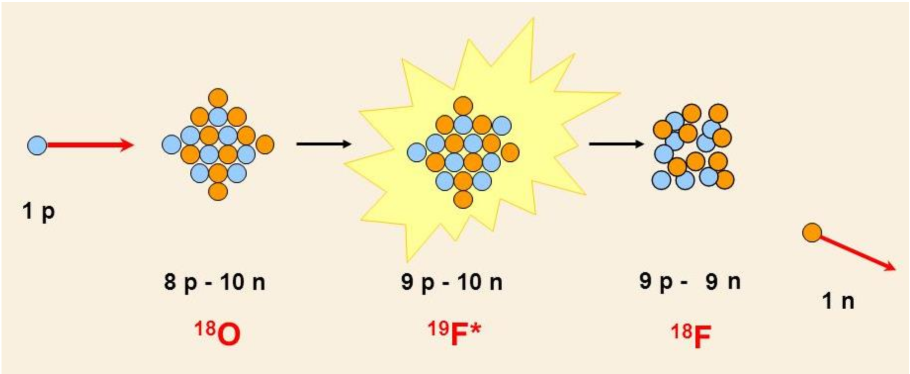

Désintégration β+

Générateur

Marganiec-Galazka, Appl Radiat Isot 2018

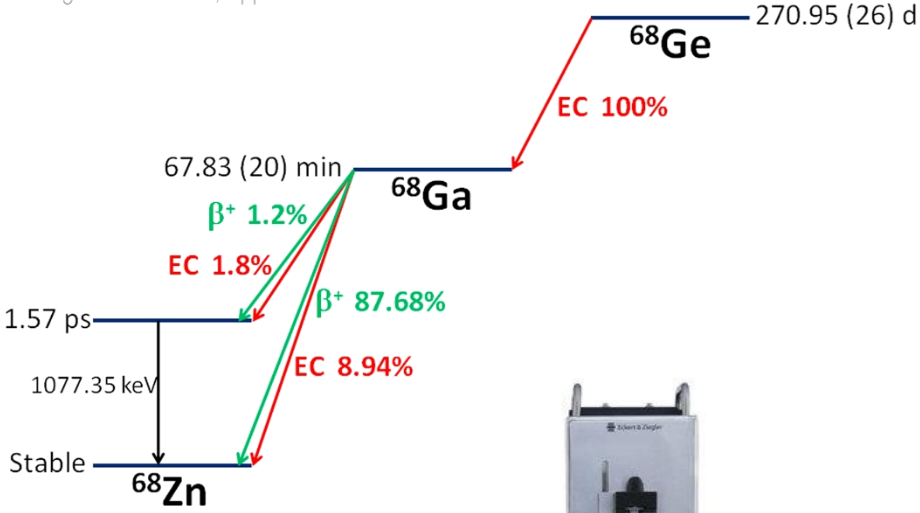

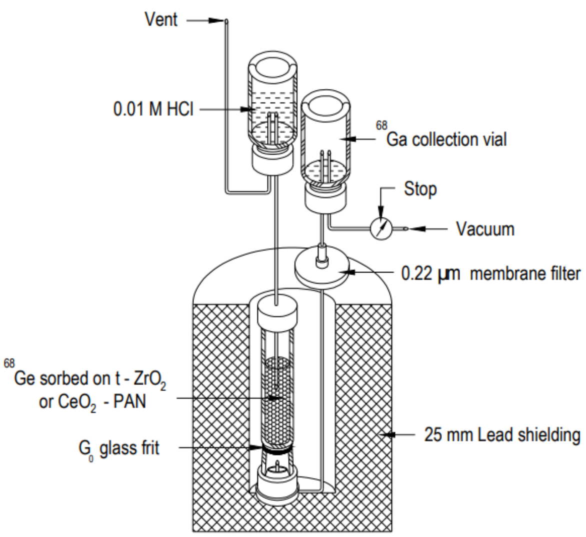

Technique de détection

Géométrie

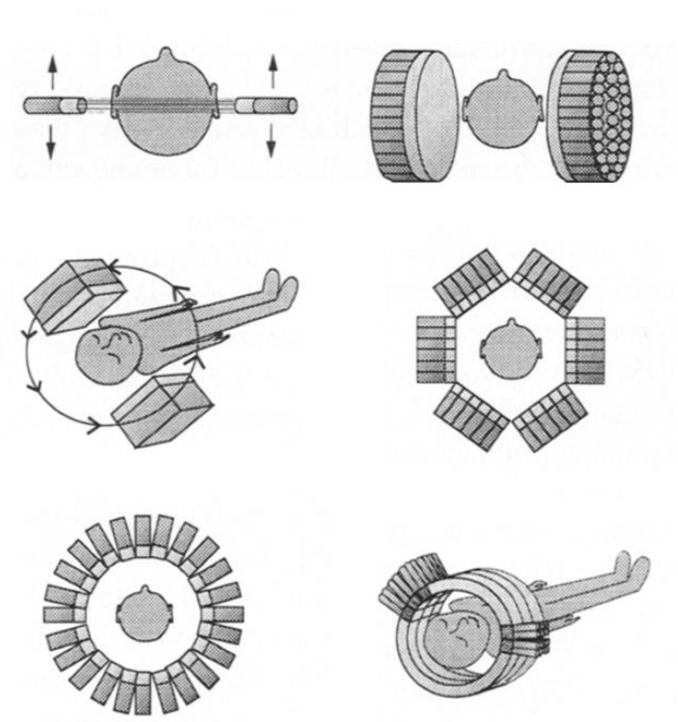

Budinger, Semin Nucl Med 1998

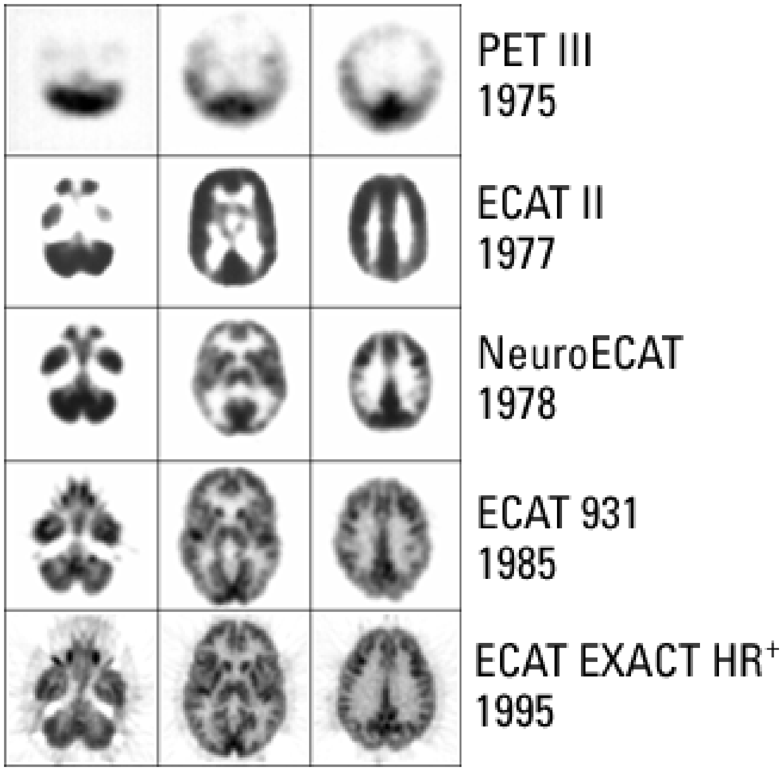

Technique de détection

Géométrie

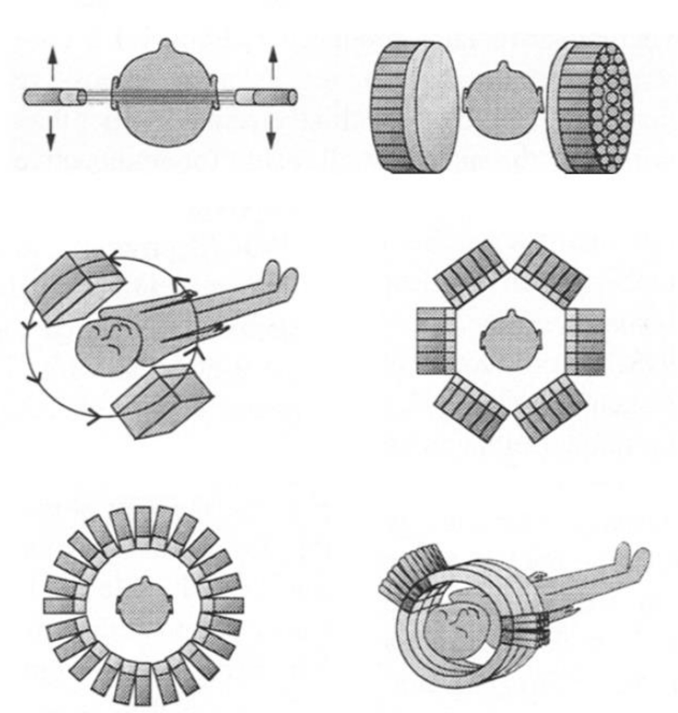

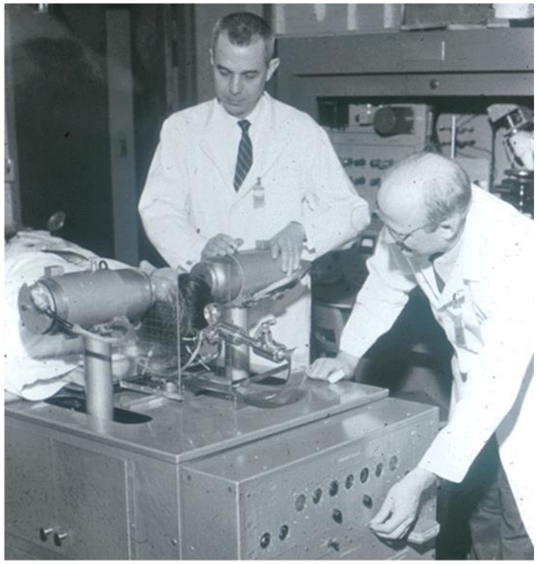

Massashusetts General Hospital. Boston 1952

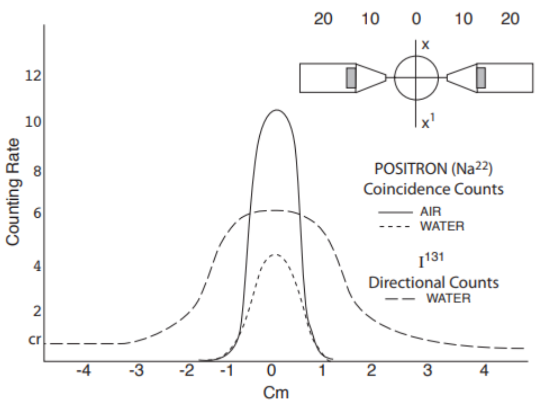

Figure 1. Gordon Brownell's diagram demonstrating higher specificity and sensitivity of positron coincidence counting, now used in positron emission tomography (PET), compared to directional detection of gamma radiation, now used in single photon emission tomography (SPECT).

Redrawn from Sweet, NEJM 1951; 245:875-8.

Technique de détection

Géométrie

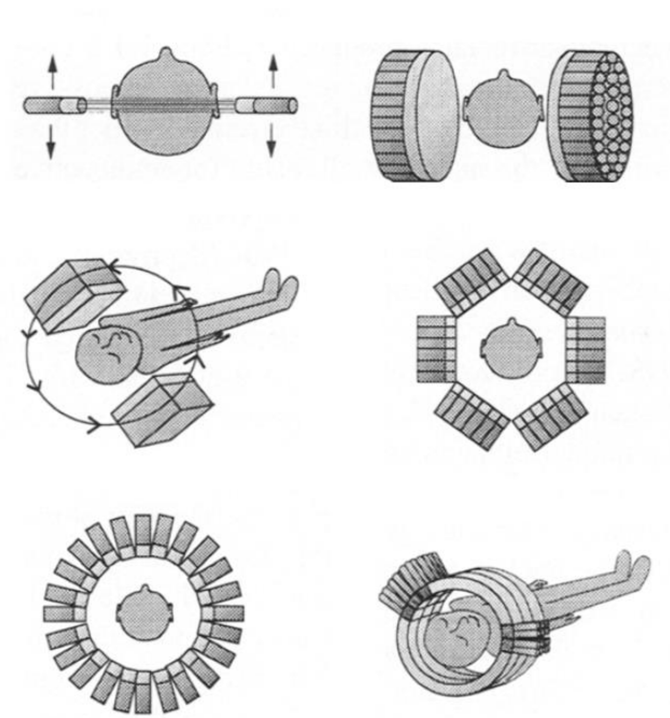

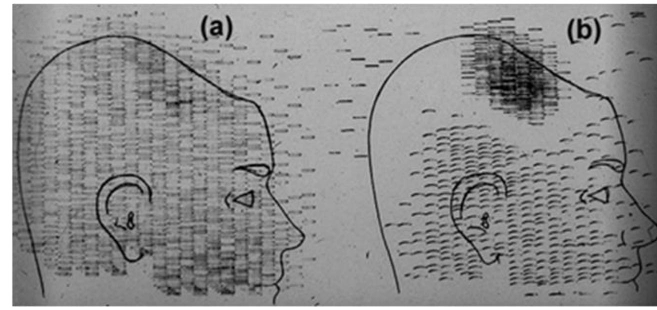

Sweet., N Engl J Med 1951

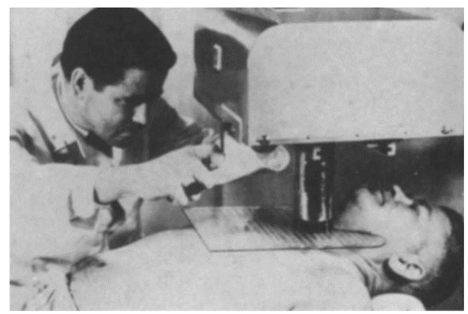

Blahd, Semin Nucl Med 1996

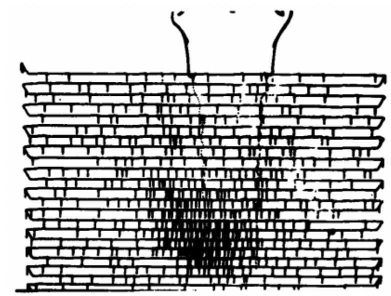

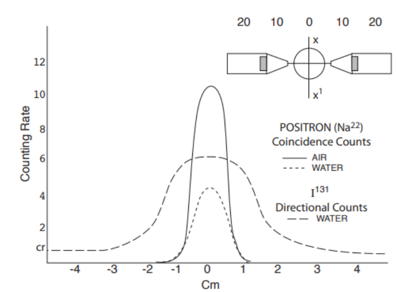

Figure 1. Gordon Brownell's diagram demonstrating higher specificity and sensitivity of positron coincidence counting, now used in positron emission tomography (PET), compared to directional detection of gamma radiation, now used in single photon emission tomography (SPECT).

Redrawn from Sweet, NEJM 1951; 245:875-8.

Technique de détection

Géométrie

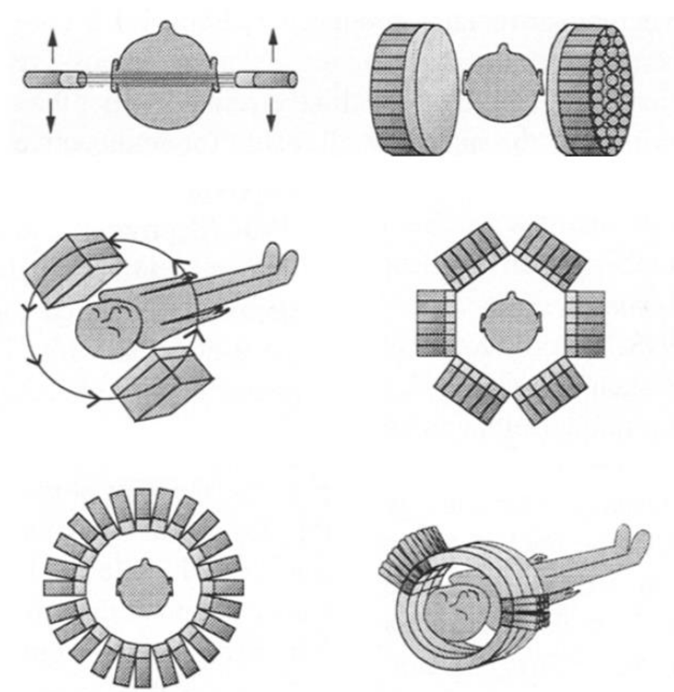

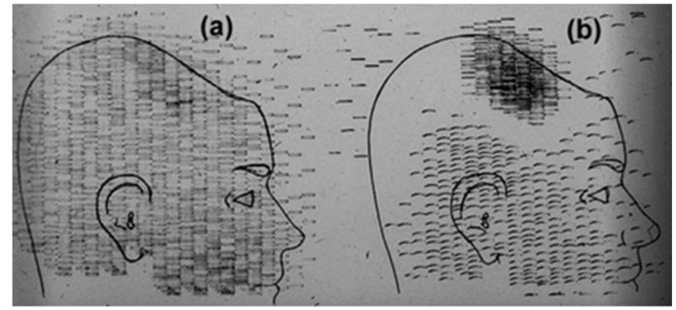

Sweet., N Engl J Med 1951

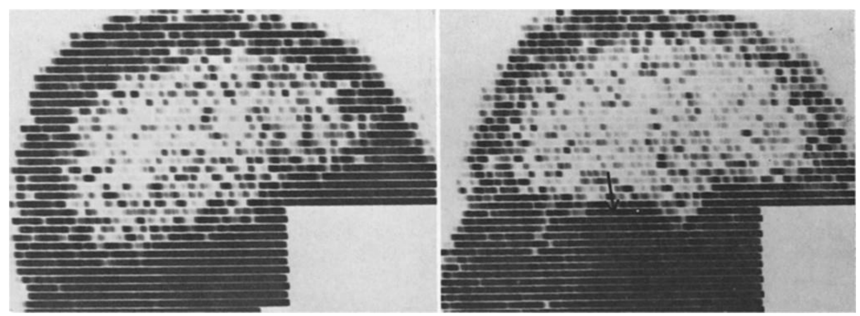

Baum, J Neurosurg 1972

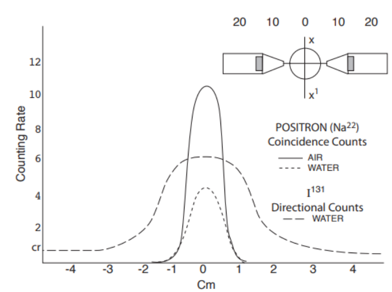

Figure 1. Gordon Brownell's diagram demonstrating higher specificity and sensitivity of positron coincidence counting, now used in positron emission tomography (PET), compared to directional detection of gamma radiation, now used in single photon emission tomography (SPECT).

Redrawn from Sweet, NEJM 1951; 245:875-8.

Technique de détection

Géométrie

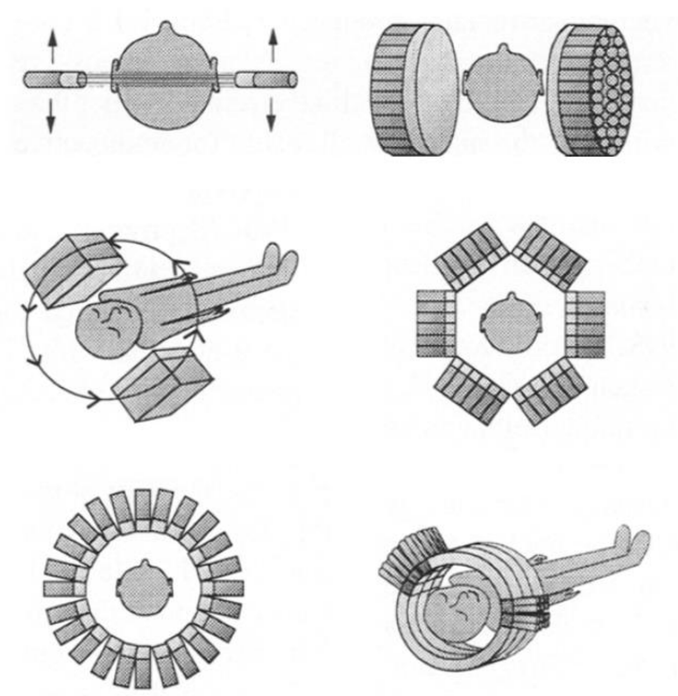

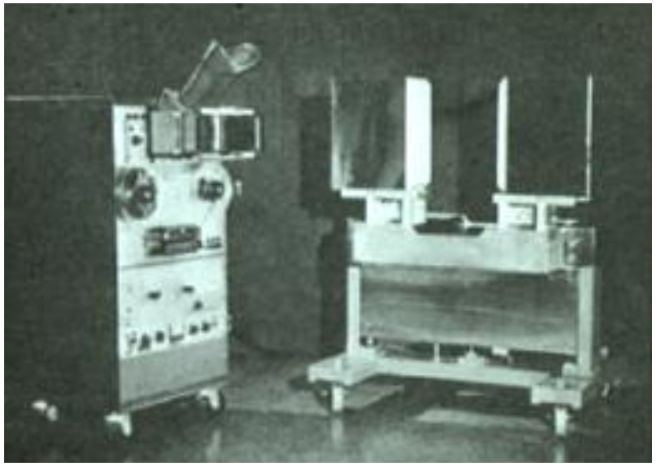

Hybrid Positron Scanner 1962 (Brownell, 1999)

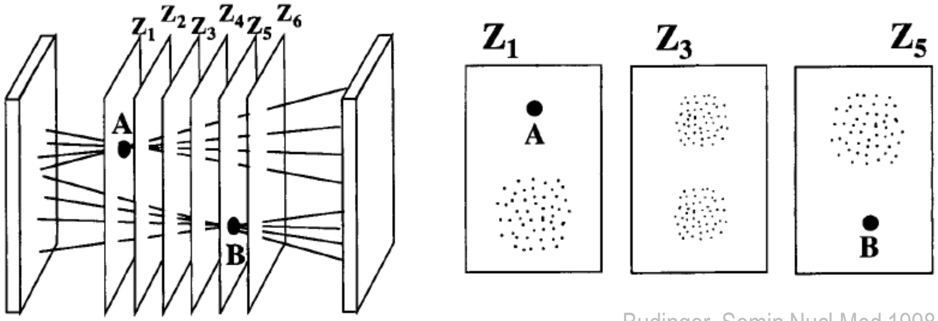

Budinger, Semin Nucl Med 1998

Technique de détection

Géométrie

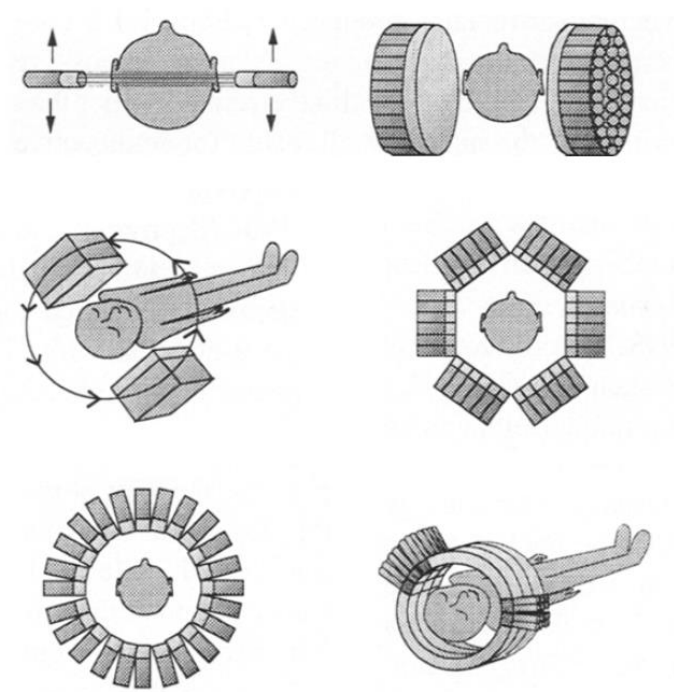

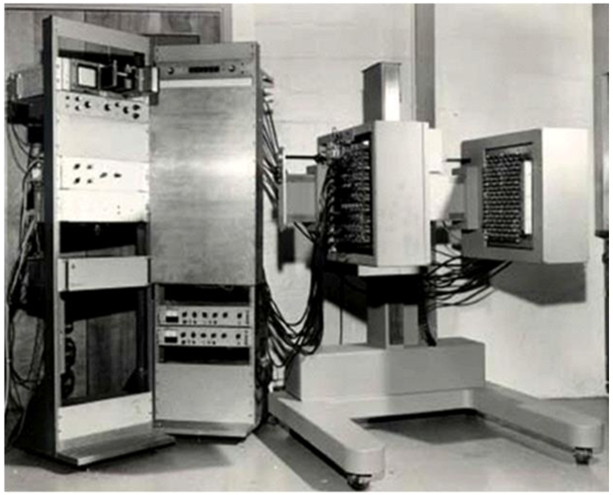

PC-I 1968-1971 (Brownell, 1999)

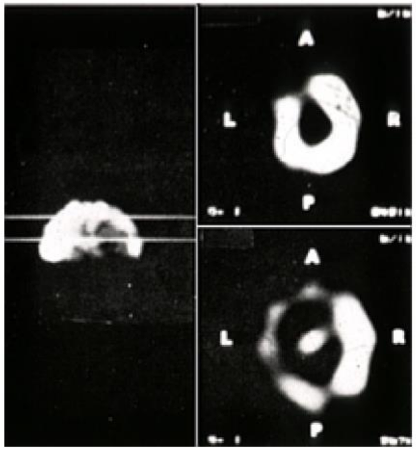

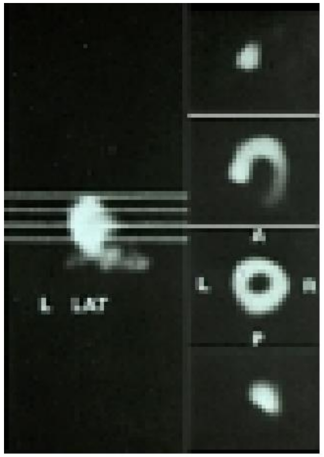

Technique de détection

Géométrie

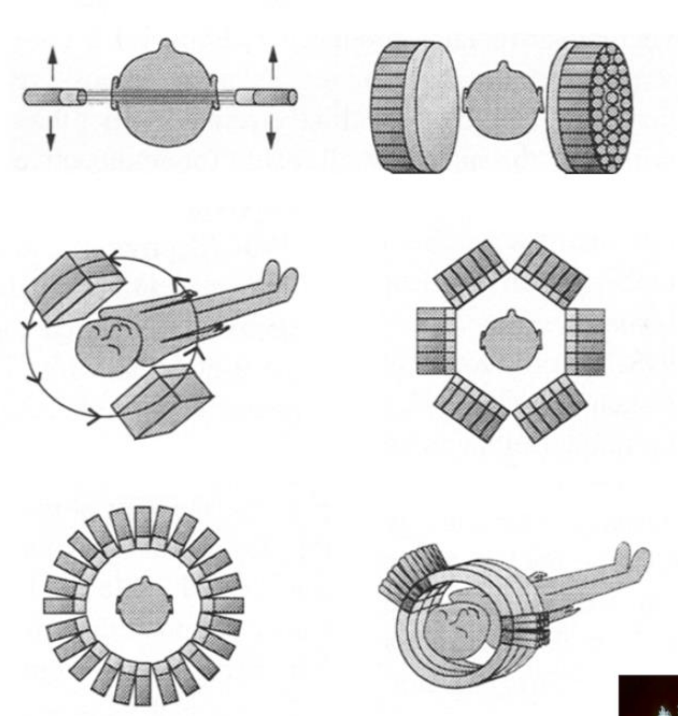

PC-II 1971-1976 (Brownell, 1999)

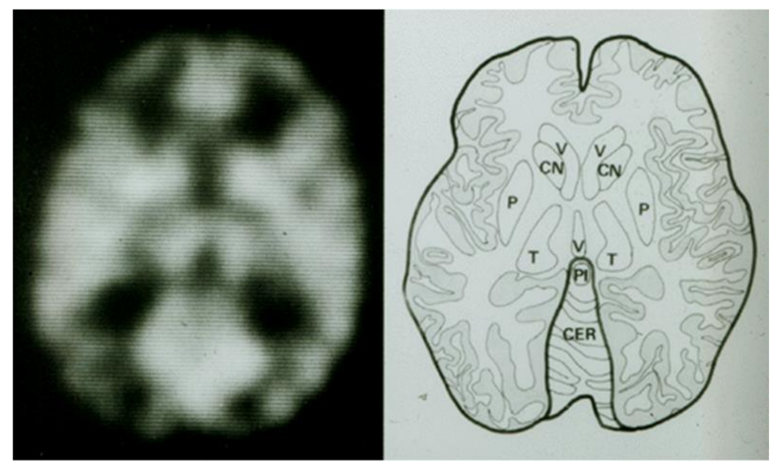

Technique de détection

Géométrie

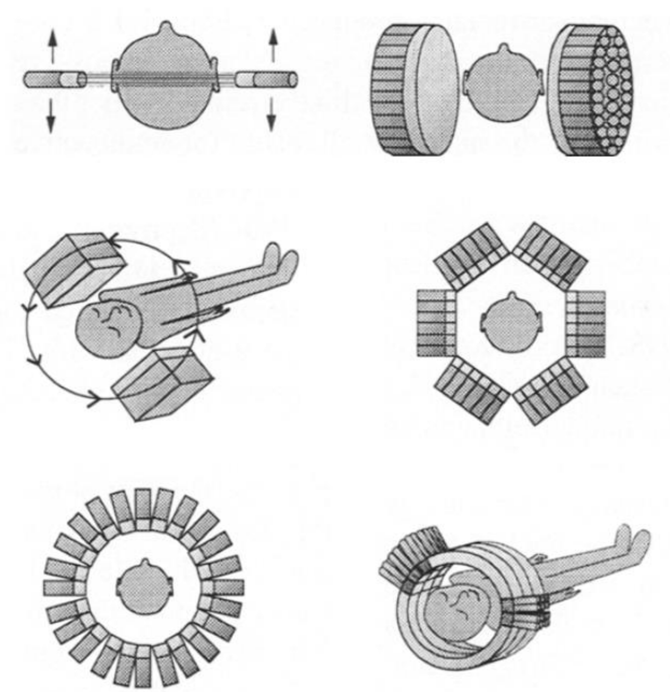

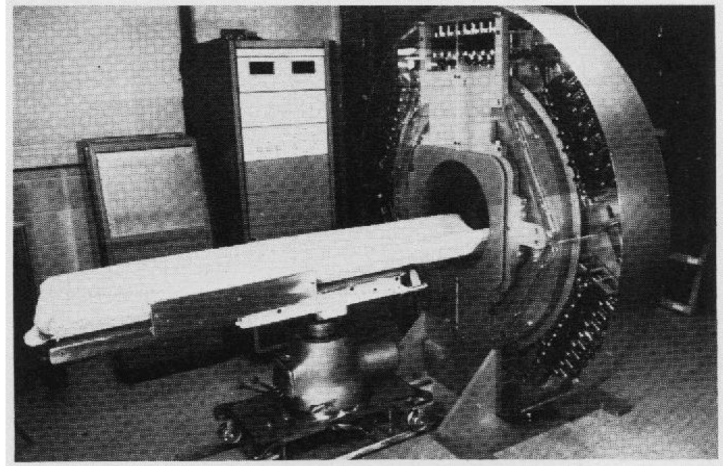

Figure 1. Photograph of PETT III.

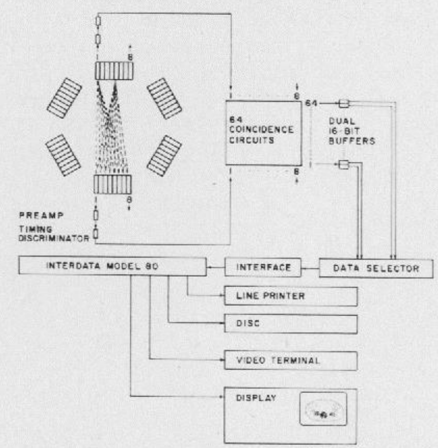

PETT III 1976 (Phelps, IEEE Trans Nucl Sci 1976)

Technique de détection

Géométrie

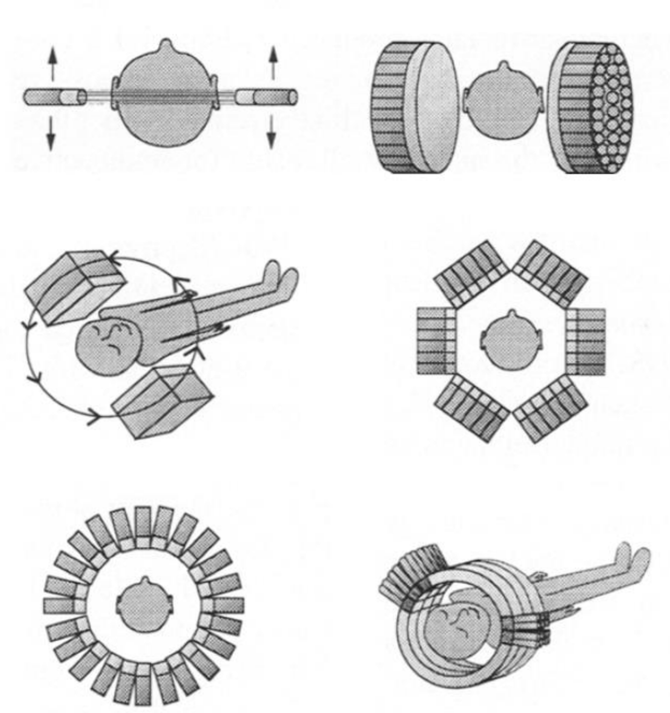

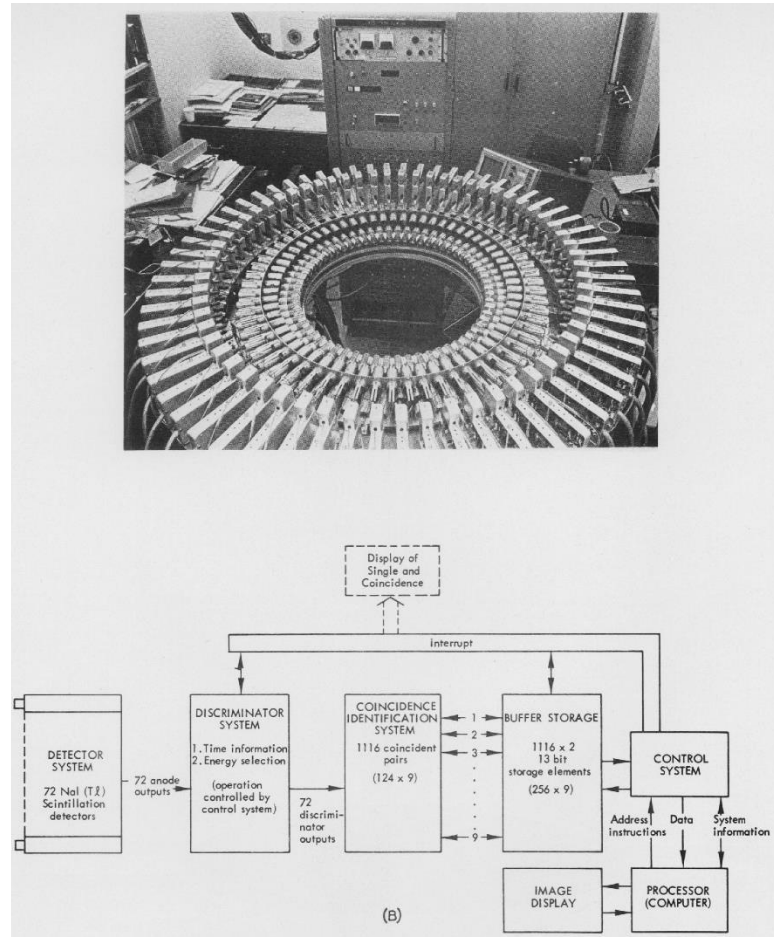

Fig. 5. a) Picture of the positron camera system.
b) Schematic diagram of the 72 x-tal system electronics.

Cho, IEEE Trans Nucl Sci 1976

Technique de détection

Géométrie

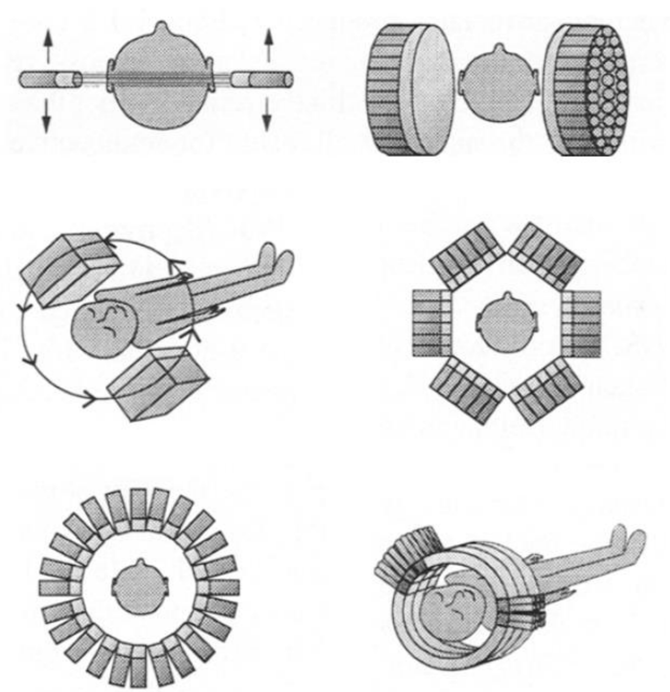

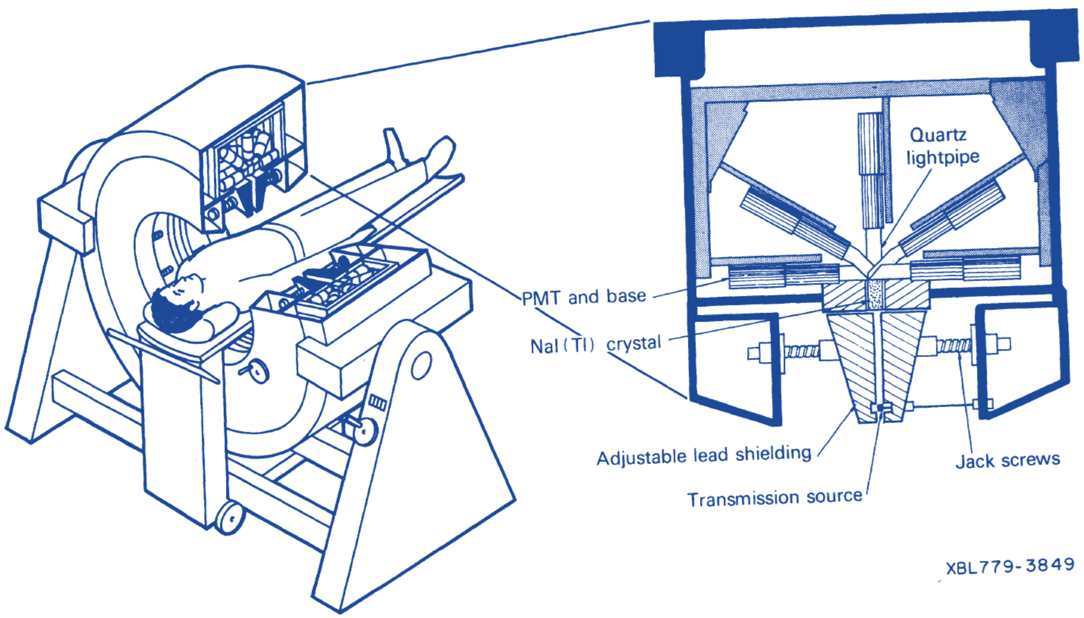

Figure 1. Schematic of Donner 280-Crystal Positron Tomograph. Crystals are mounted behind adjustable lead shielding and are individually coupled to phototubes via quartz lightpipes.

Derenzoo, IEEE Trans Nucl Sci 1979

Technique de détection

Géométrie

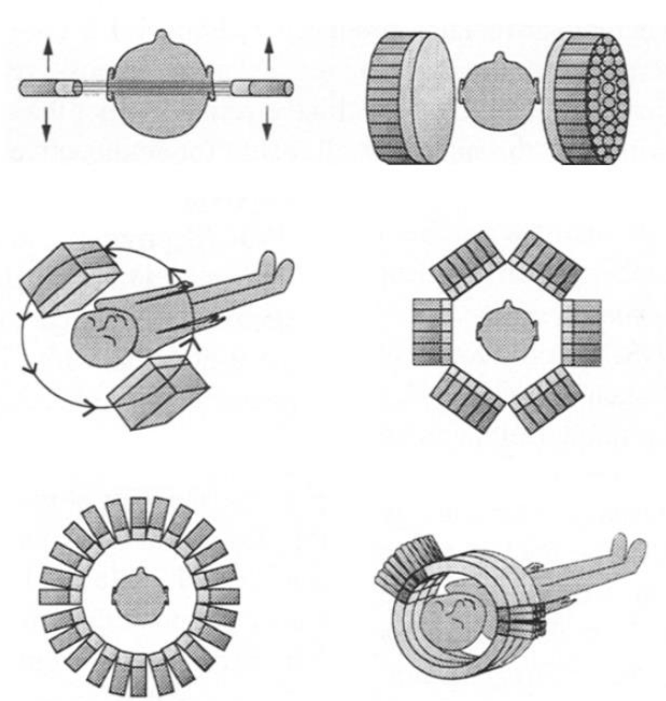

FIG. I

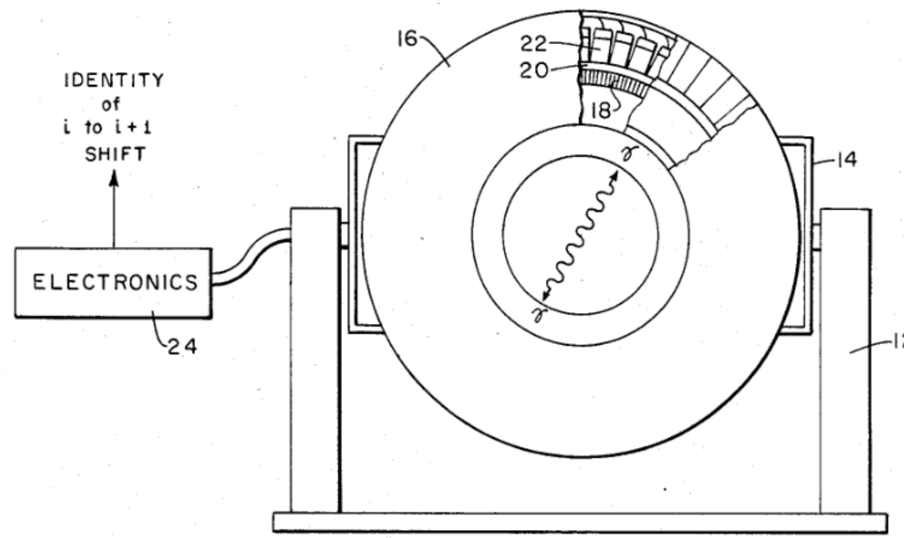

FIG. 5

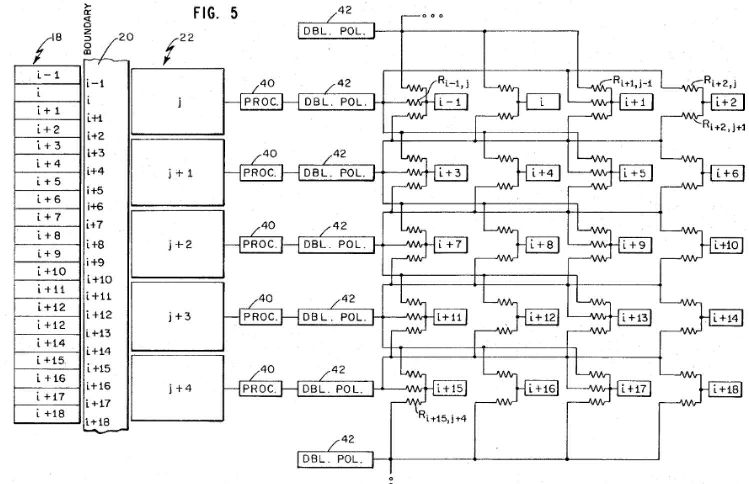

Burnham 1985 (patents.google)

Technique de détection

Géométrie

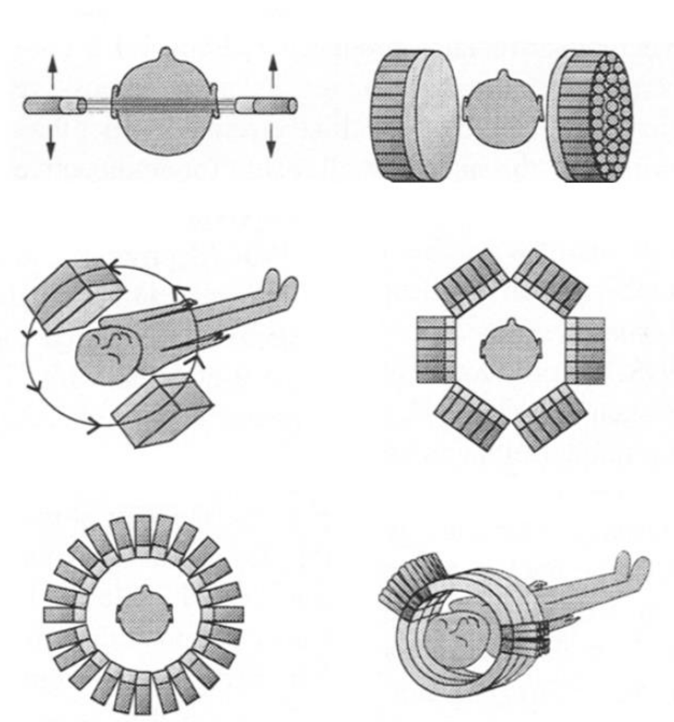

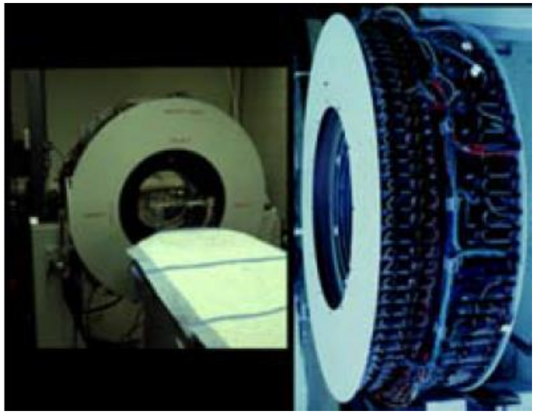

PCR-I et PCR-II 1985-1988 (Brownell, 1999)

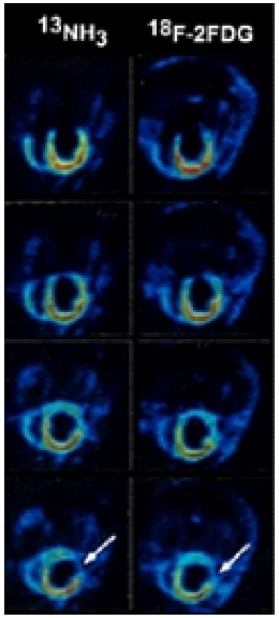

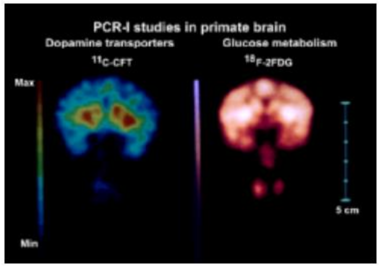

Technique de détection

Géométrie

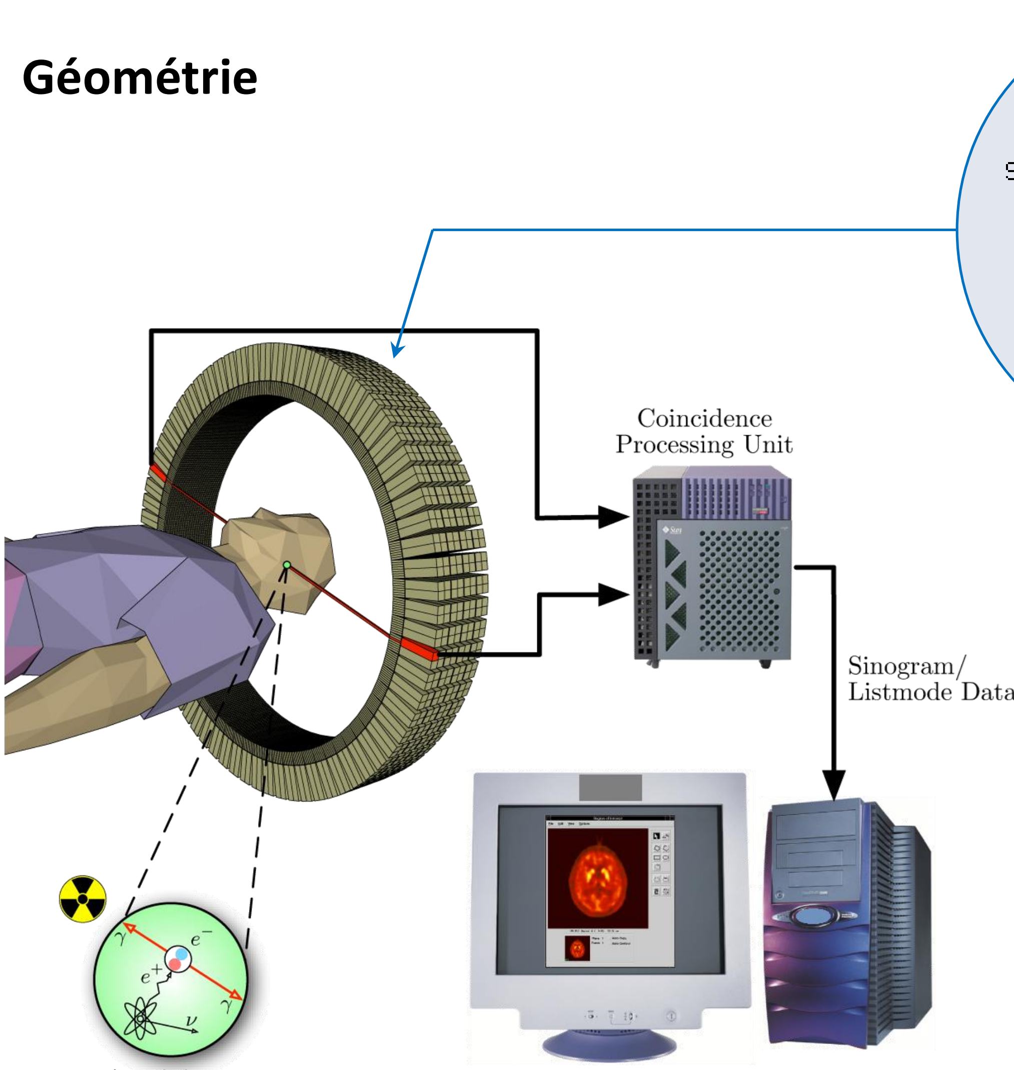

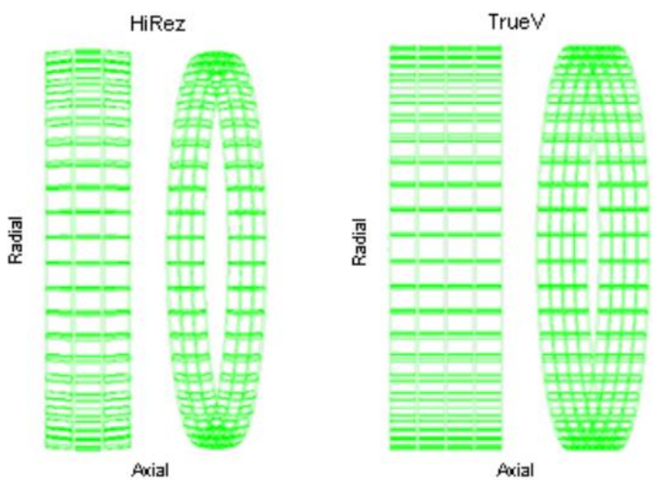

Kotasidis, Phys Med Biol 2011

Technique de détection

Géométrie

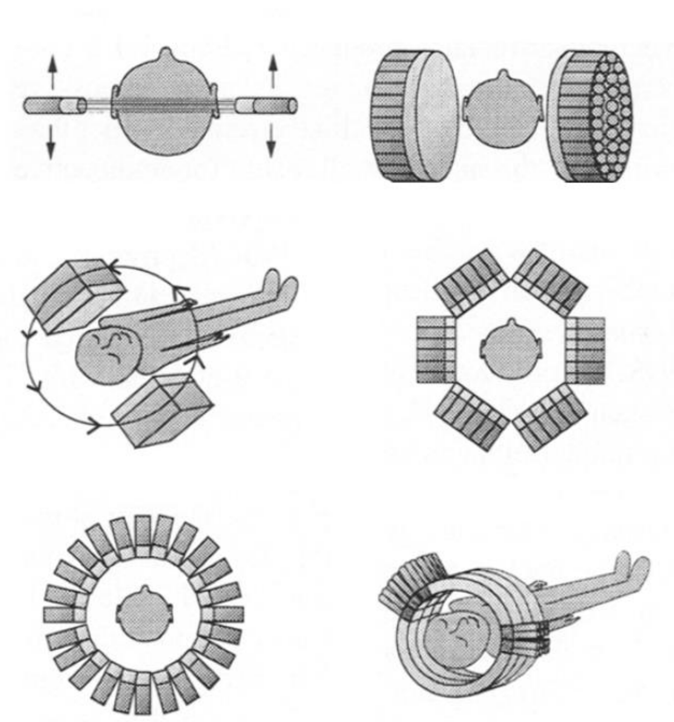

Budinger, Semin Nucl Med 1998

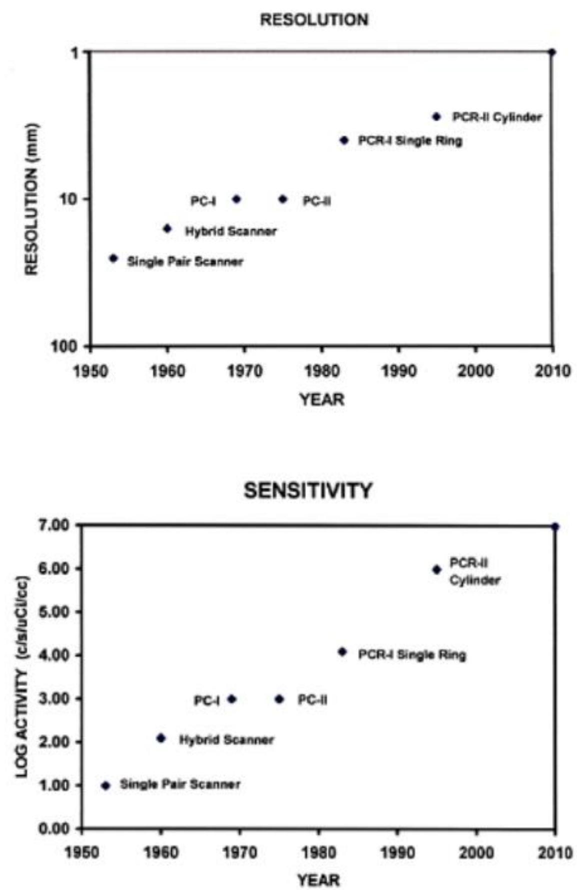

Brownell, 1999

Technique de détection

Géométrie

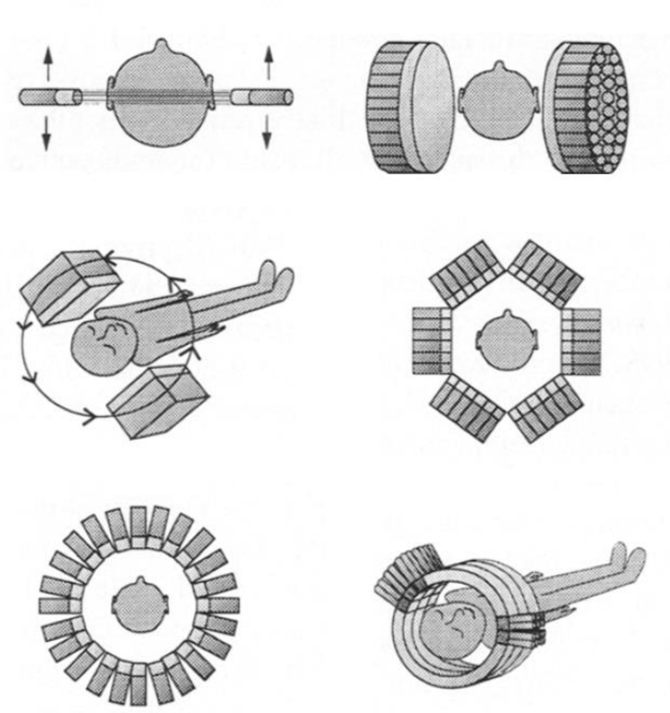

Budinger, Semin Nucl Med 1998

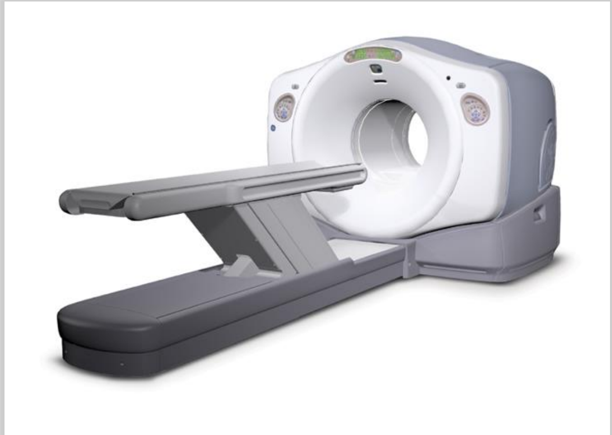

TEP-TDM, 1998

TEP-IRM, 2010

Technique de détection

Collimation

SPECT : collimation mécanique
Compromis résolution / sensibilité

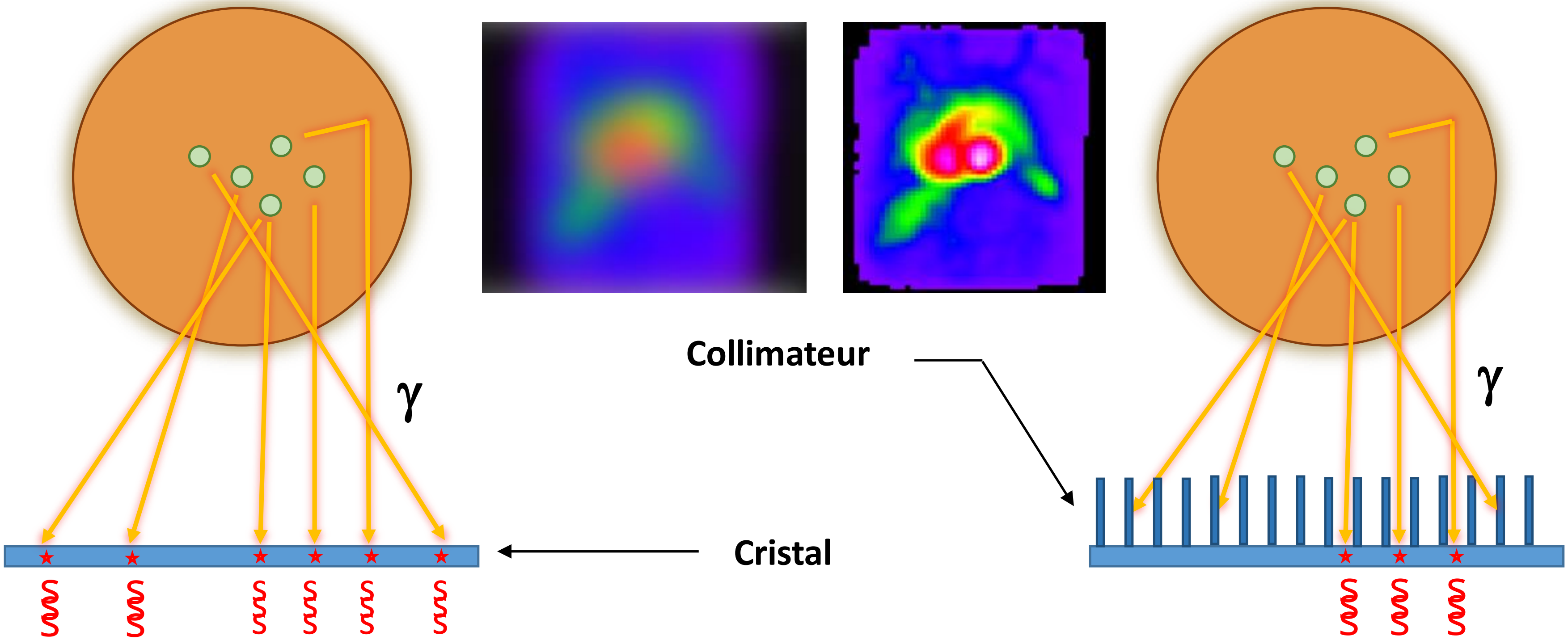

Collimation

TEP : collimation électronique
Détection en coïncidence

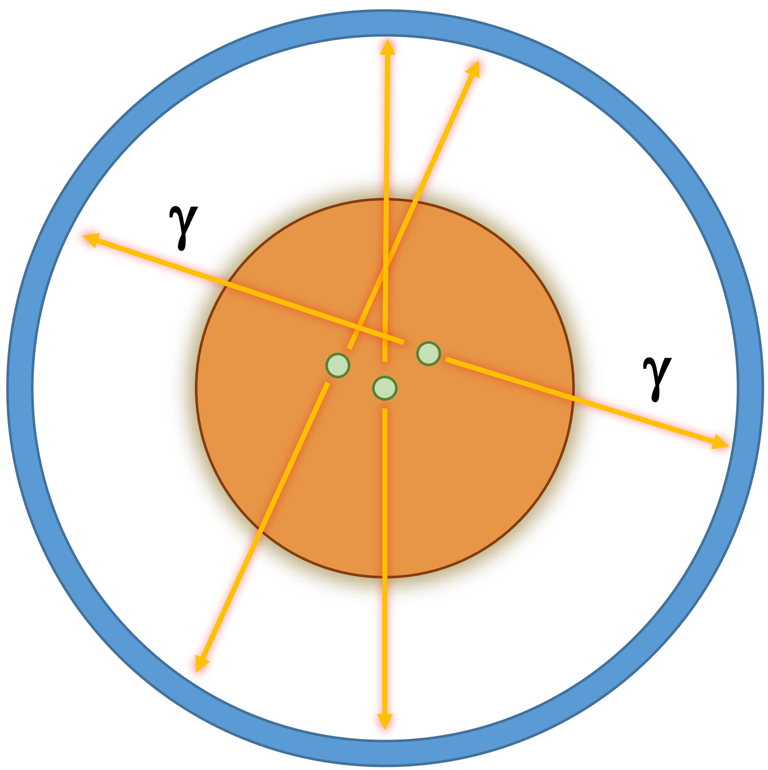

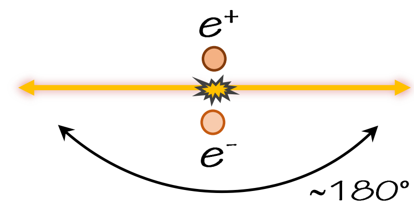

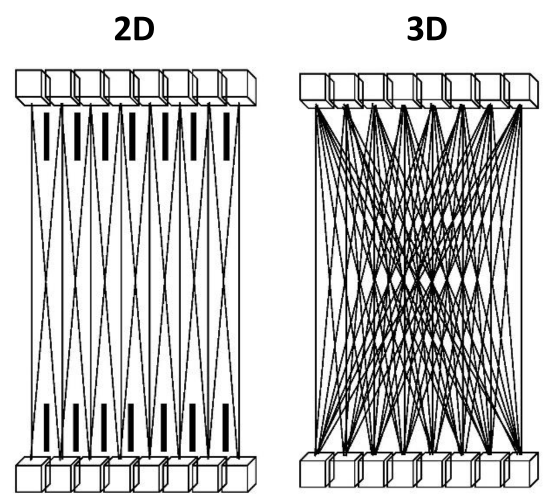

Slomka, Prog Cardiovasc Dis 2015

Technique de détection

Détecteur

Détection indirecte

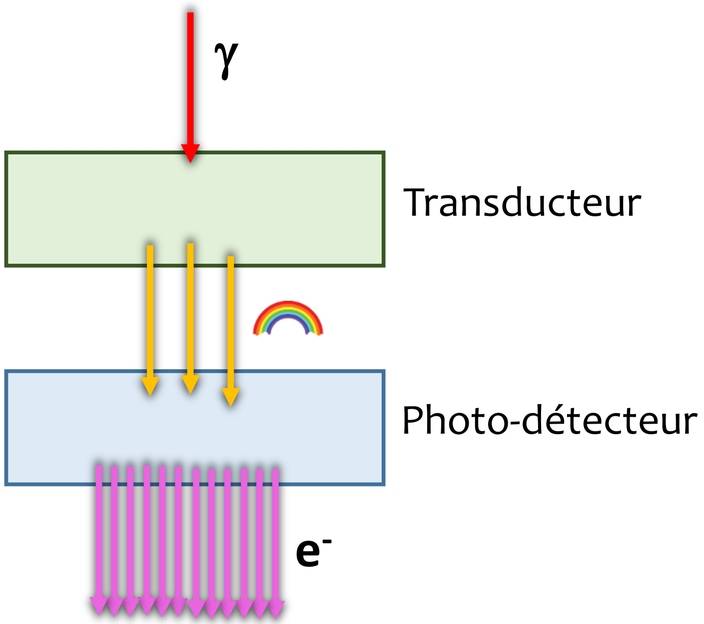

Détection directe

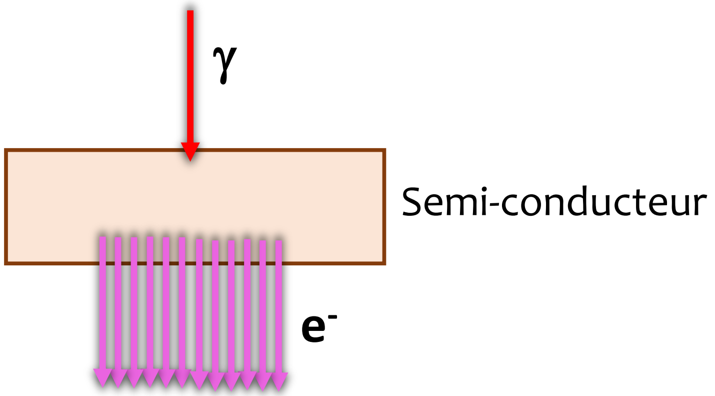

Technique de détection

Détecteur

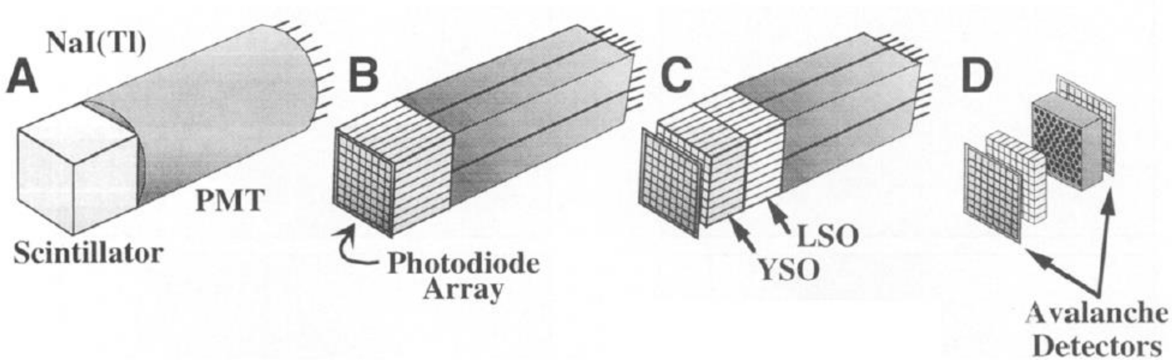

Fig 4. Scintillation detectors have evolved from single scintillator–single photomultiplier couples to multiplex systems. Contemporary ring PET systems use the block design of B but without the photodiode array. The potential for the future is replacement of the photomultiplier tubes by electronic devices such as the avalanche detector.

Budinger, Semin Nucl Med 1998

Technique de détection

■ Scintillateur

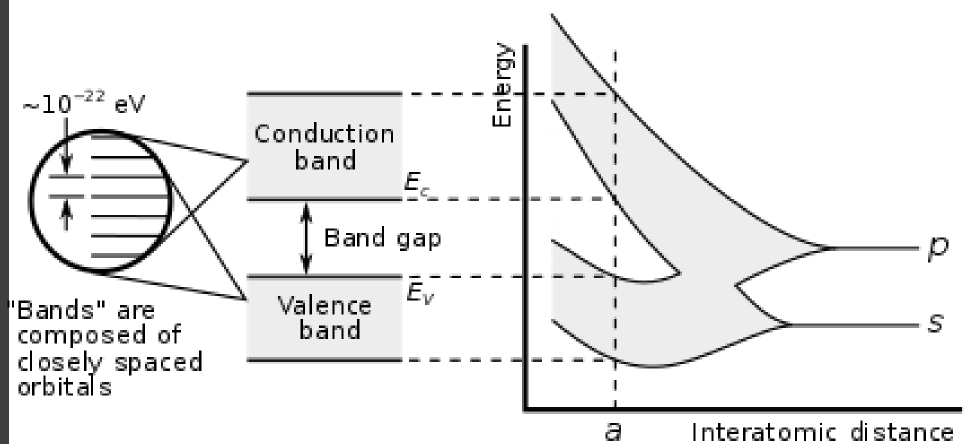

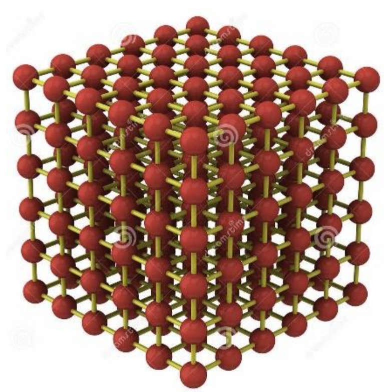

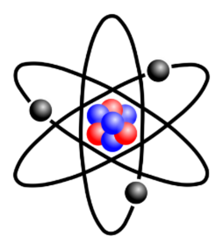

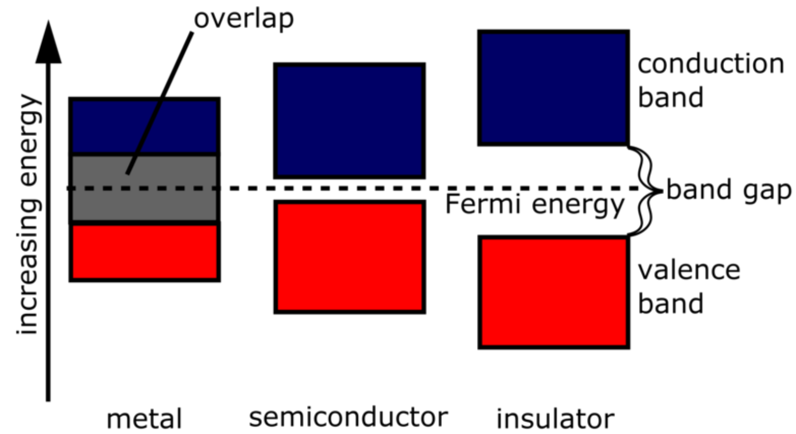

Technique de détection

■ **Scintillateur**

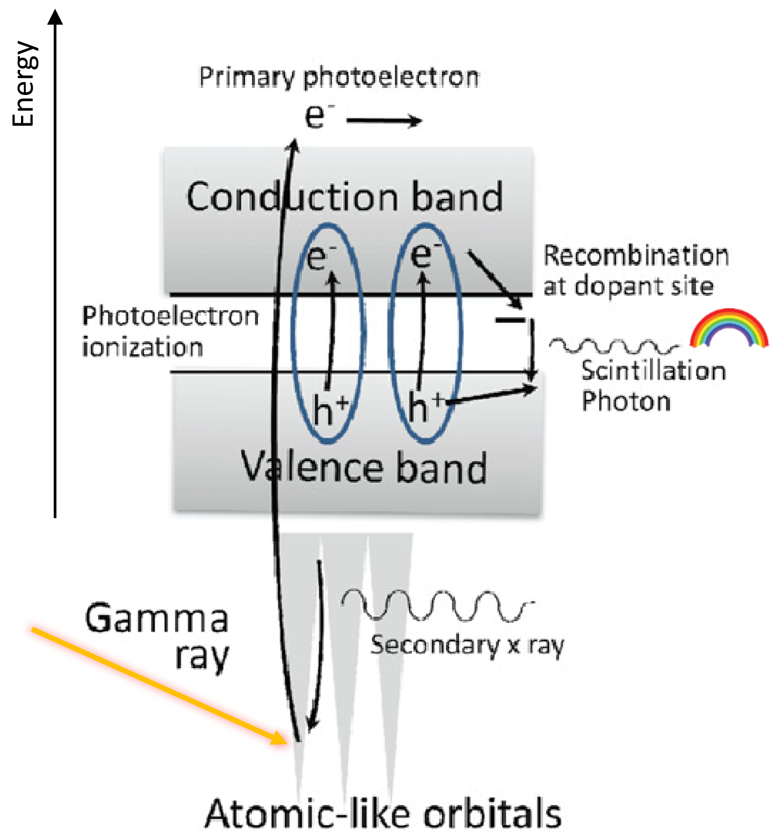

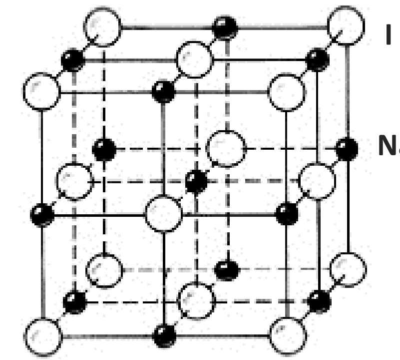

NaI(Tl)

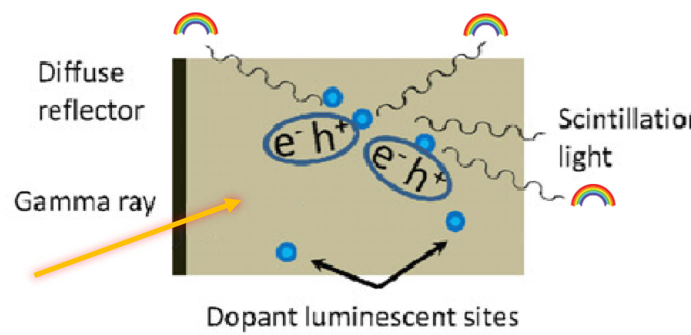

■ **Scintillateur**

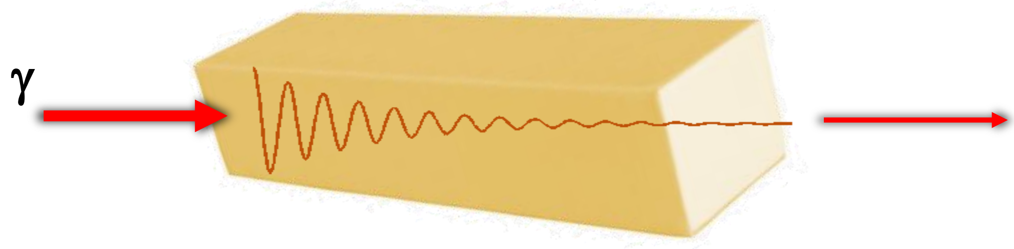

Pouvoir d'arrêt : densité ρ, Z. Couche de demi-atténuation (CDA) mm.

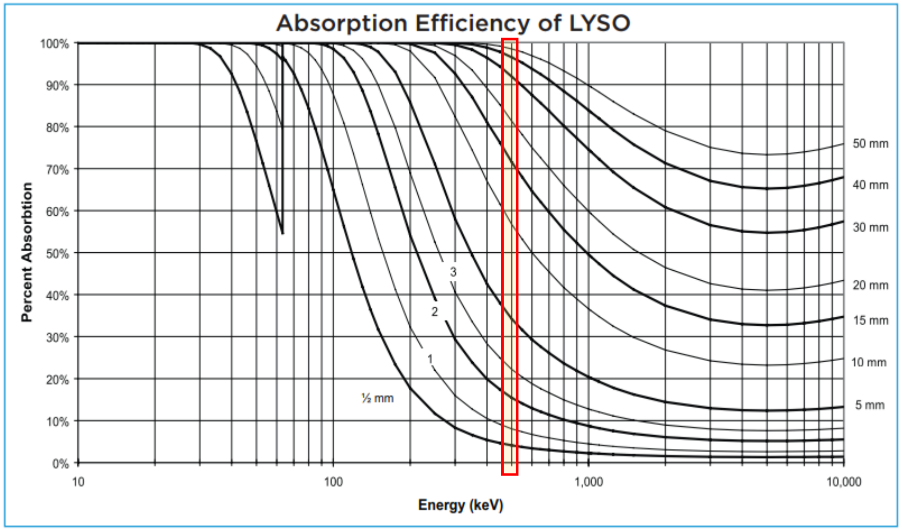

crystals.saint-gobain.com

Technique de détection

■ **Scintillateur**

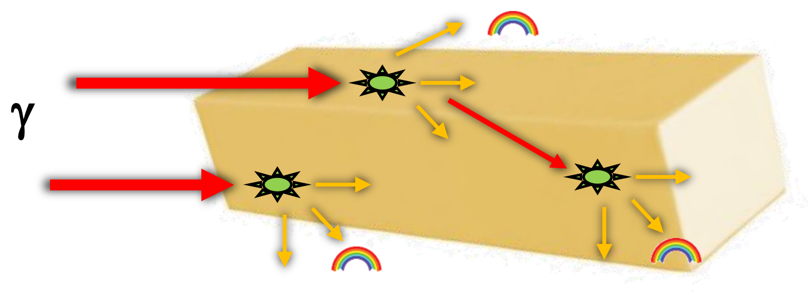

Pouvoir d'arrêt : densité ρ, Z. Couche de demi-atténuation.
Photo-fraction : PE / Compton.

Technique de détection

■ **Scintillateur**

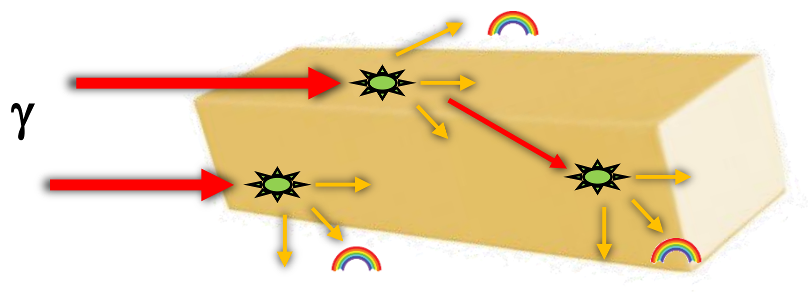

Pouvoir d'arrêt : densité ρ, Z. Couche de demi-atténuation.
Photo-fraction : PE / Compton.
Spectre d'émission : transparence, couplage photoK.

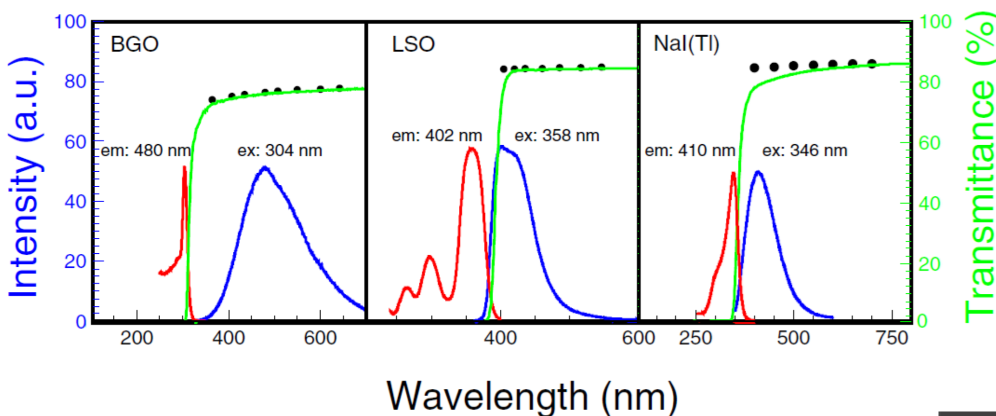

Mao, IEEE Ncul Sci Symp 2007

Technique de détection

■ Scintillateur

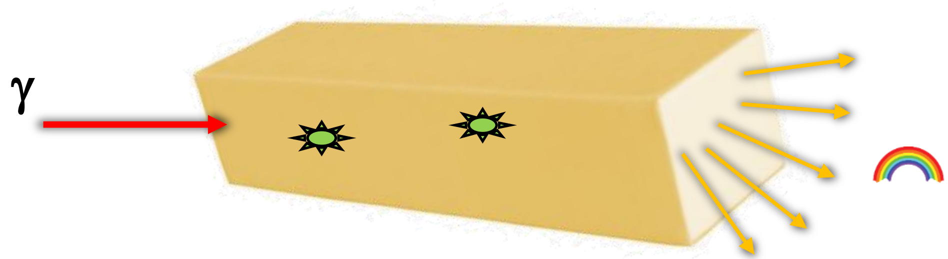

Pouvoir d'arrêt : densité ρ, Z. Couche de demi-atténuation.
Photo-fraction : PE / Compton.
Spectre d'émission : transparence, couplage photoK.
Rendement lumineux : photons / KeV.
ΔE/E

Technique de détection

■ Scintillateur

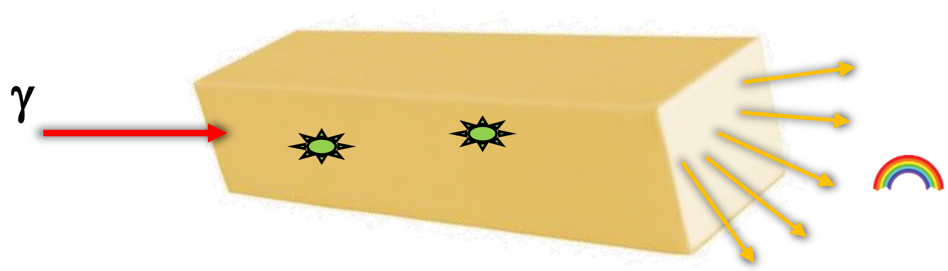

Mao, IEEE Ncul Sci Symp 2007

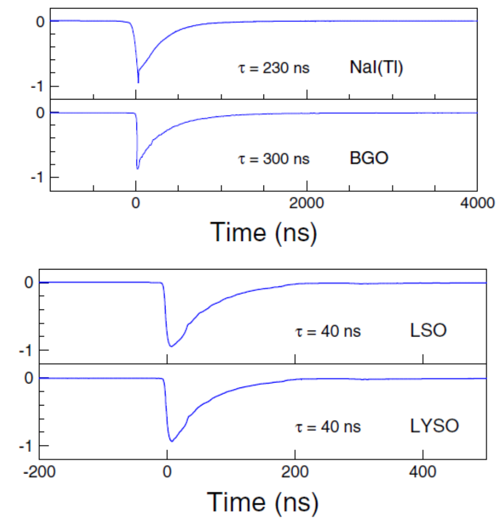

Pouvoir d'arrêt : densité ρ, Z. Couche de demi-atténuation.
Photo-fraction : PE / Compton.
Spectre d'émission : transparence, couplage photoK.
Rendement lumineux : photons / KeV.
ΔE/E
Pulse : rise / decay.

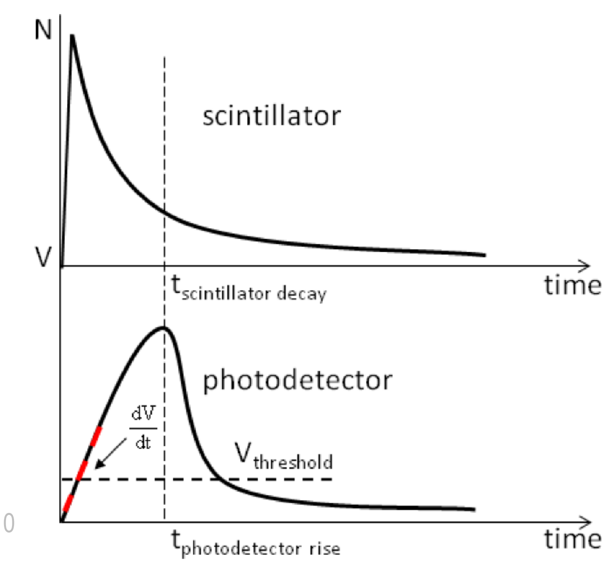

Spanoudaki, Sensors 2010

■ Scintillateur

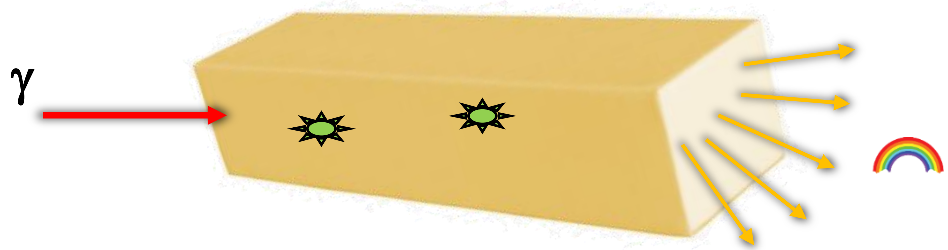

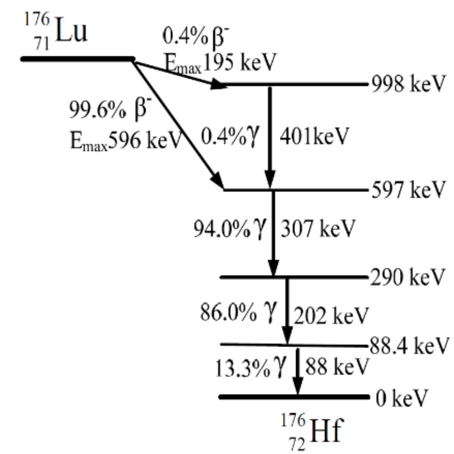

Pouvoir d'arrêt : densité ρ, Z. Couche de demi-atténuation.
Photo-fraction : PE / Compton.
Spectre d'émission : transparence, couplage photoK.
Rendement lumineux : photons / KeV.
ΔE/E
Pulse : rise / decay.
Rayonnement intrinsèque : L(Y)SO (^{176}Lu 3%)

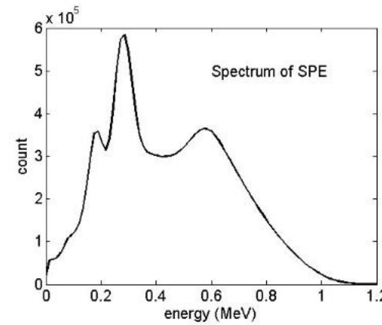

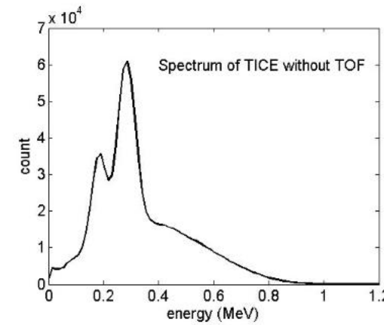

Wei (arxiv.org)

Technique de détection

■ Scintillateur

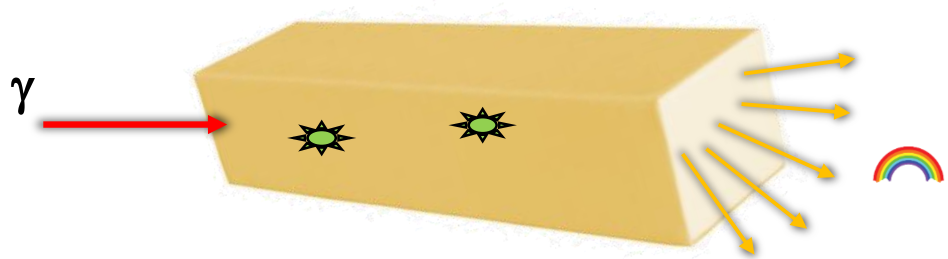

Pouvoir d'arrêt : densité ρ, Z. Couche de demi-atténuation.
Photo-fraction : PE / Compton.
Spectre d'émission : transparence, couplage photoK.
Rendement lumineux : photons / KeV.
ΔE/E
Pulse : rise / decay.
Rayonnement intrinsèque : L(Y)SO (^{176}Lu 3%)
Dépendance T°C

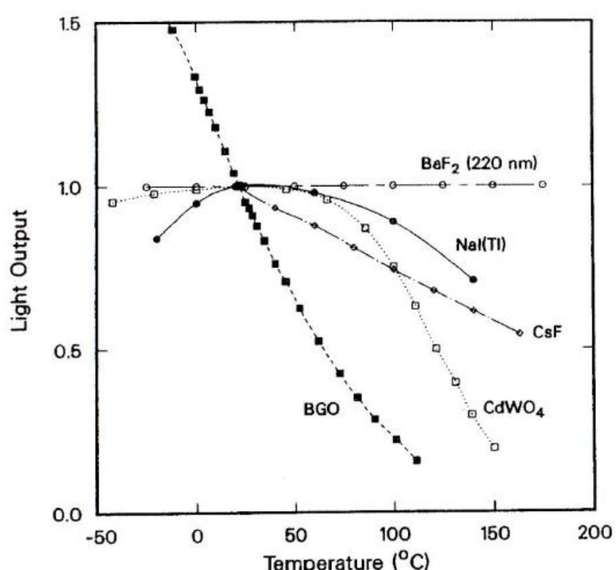

astro.rug.nl

Technique de détection

■ **Scintillateur**

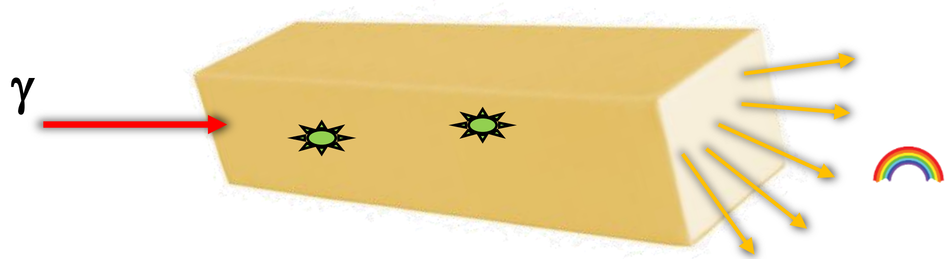

Pouvoir d'arrêt : densité ρ, Z. Couche de demi-atténuation.
Photo-fraction : PE / Compton.
Spectre d'émission : transparence, couplage photoK.
Rendement lumineux : photons / KeV.
ΔE/E
Pulse : rise / decay.
Rayonnement intrinsèque : L(Y)SO (^{176}Lu 3%)
Dépendance T°C
Hygroscopicité
Prix, disponibilité

Technique de détection

■ Scintillateur

Properties of Scintillators with Application in Nuclear Medicine

Scintillator	ρ (g/cm^3)	Atten. Length (mm)	Photoelectric Fraction (%)	Hygroscopicity	Luminosity (photons/keV)	Decay Const. (ns)	Emission Peak (nm)	$\Delta E/E$ (% FWHM)	Refractive Index	Clinical Application
NaI: Tl	3.67	29.1	17	Yes	41	230	410	5.6	1.85	SPECT
CSI: Na	4.51	22.9	21	Yes	40	630	420	7.4		XII
CSI: Tl	4.51	22.9	21	Little	66	>800	420	6.6		PET, SPECT, CT
CSF	4.64	20	23	High	2	3	390		1.48	TOF-PET
BaF_2	4.89	20.5	17	Little	2	0.7	220	10	1.54	TOF-PET
BGO ($Bi_4Ge_3O_{12}$)	7.13	10.1	40	No	9	300	480	9	2.15	PET
LSO (Lu_2SiO_5:Ce)	7.4	11.4	32	No	26	40	420	7.9	1.82	TOF-PET
$Lu_{1.8}Y_{0.2}SiO_5$:Ce	7.1	11.5		No	26	41	420	7–9	1.81	TOF-PET
$LuYSiO_5$: Ce	6	16.7	21	No	26		420	7–9		TOF-PET
LuAP ($LuAlO_3$:Ce)	8.3	10.5	30	No	12	18	365	~ 15	1.94	TOF-PET
LPS ($Lu_2Si_2O_7$:Ce)	6.2	14.1	29	No	30	30	380	~10	1.74	TOF-PET
GSO (Gd_2SiO_5:Ce)	6.7	14.1	25	No	8	60	440	7.8	1.85	PET
YAP ($YalO_3$)	5.5	21.3	4.2	No	21	30	350	4.3	1.95	PET
$LaCl_3$:Ce	3.86	27.8	14	Yes	46	25 (65%)	353	3.3	1.9	SPECT
$LaBr_3$:Ce	5.3	21.3	13	Yes	61	35 (90%)	358	2.9	1.9	SPECT
$CeBr_3$	5.2	21.5	14	Yes	68	17	370	3.4		TOF-PET
LXe (liquid xenon)	3.06	30.4	21	—	11	27 (30%)	165	22/16		DOI-PET
Ideal (PET)	>6	<12	>30	No	>8	<300	300–500	<10		

De Lima, CRC Press 2010

Technique de détection

■ **Photo-détecteur : PMT**

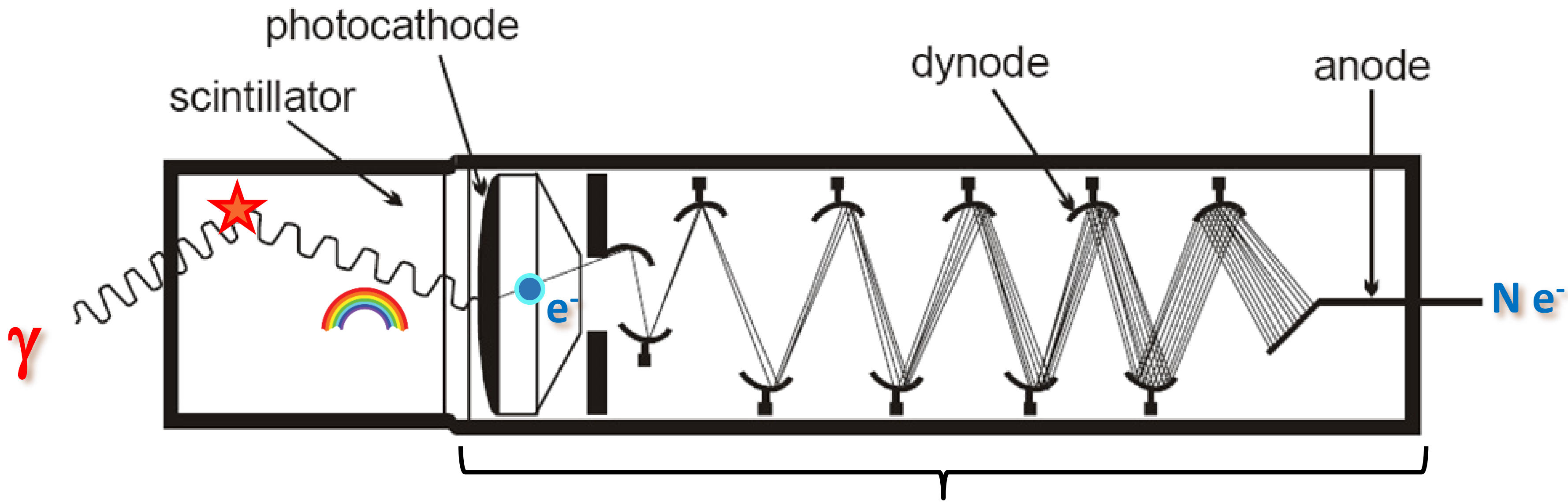

Technique de détection

■ **Photo-détecteur : PMT**

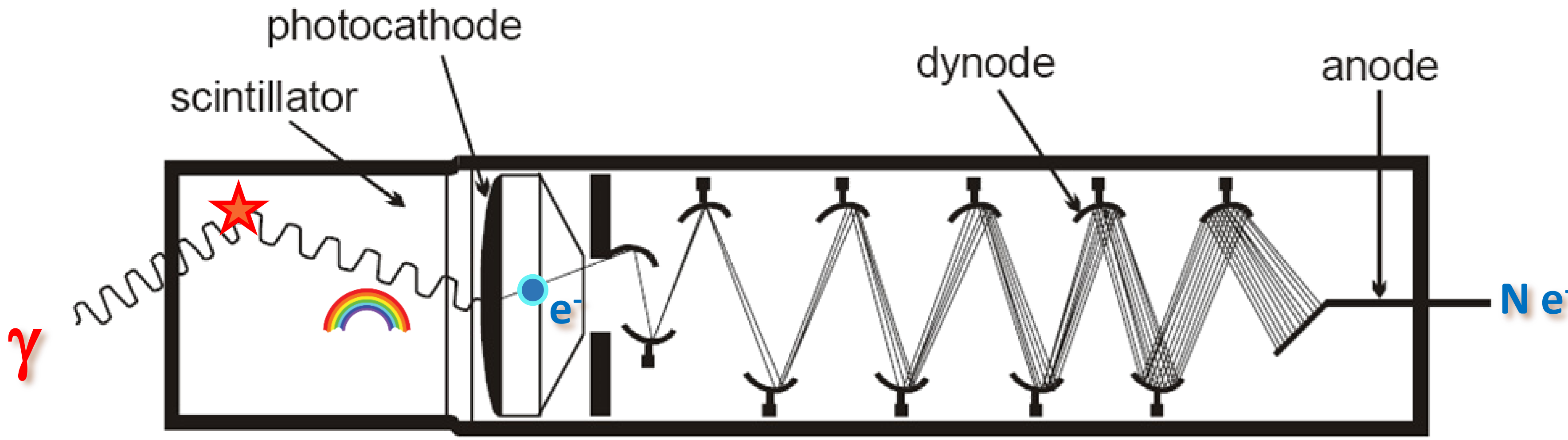

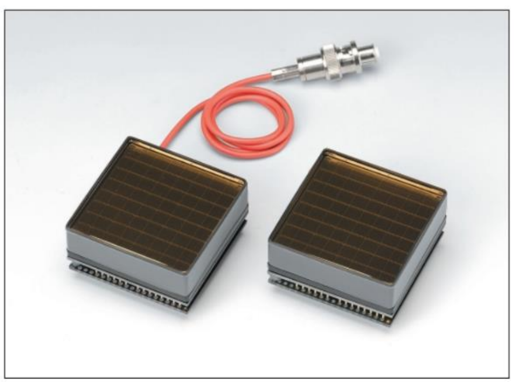

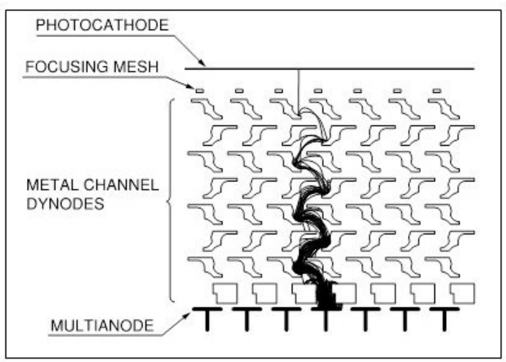

Type	Metal Channel Dynode Multianode Photomultiplier Tubes					
	Matrix			Linear		Matrix
	M4	M16	M64	L16	L32	M64
Anode Shape						
Number of Anodes	4	16	64	16	32	64
Pixel Size (mm)	9 × 9	4 × 4	2 × 2	0.8 × 16	0.8 × 7	5.8 × 5.8

hamamatsu.com

■ Photo-détecteur : PMT

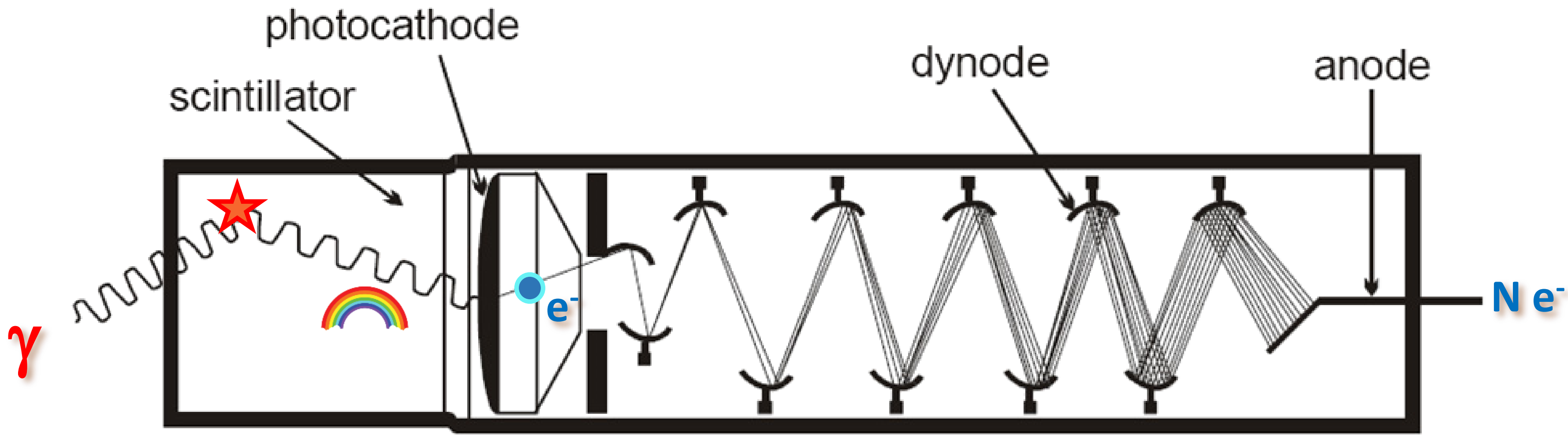

Gain : N ~ 10^6.
Rapidité : < 1 ns.

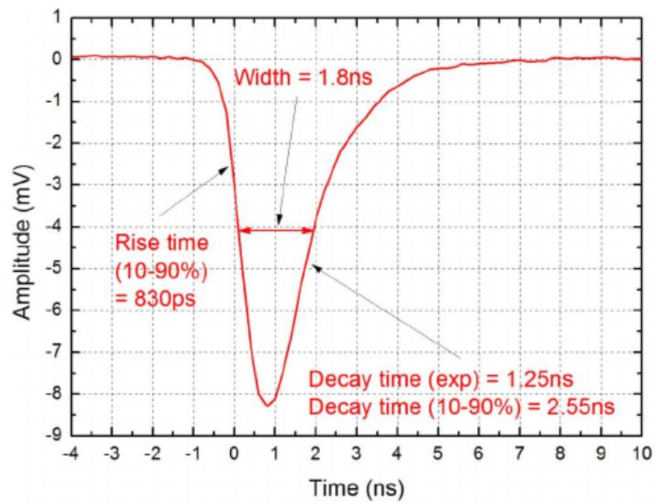

Szczęśniak, IEEE Nucl Sci Symp 2013

■ **Photo-détecteur : PMT**

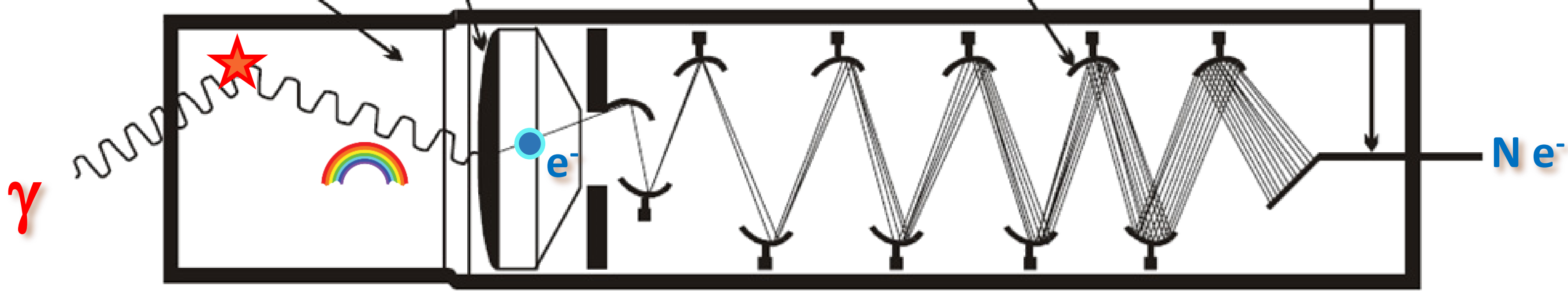

Gain : N ~ 10^6.
Rapidité : < 1 ns.
Efficacité quantique : QE ~ 15–25%.

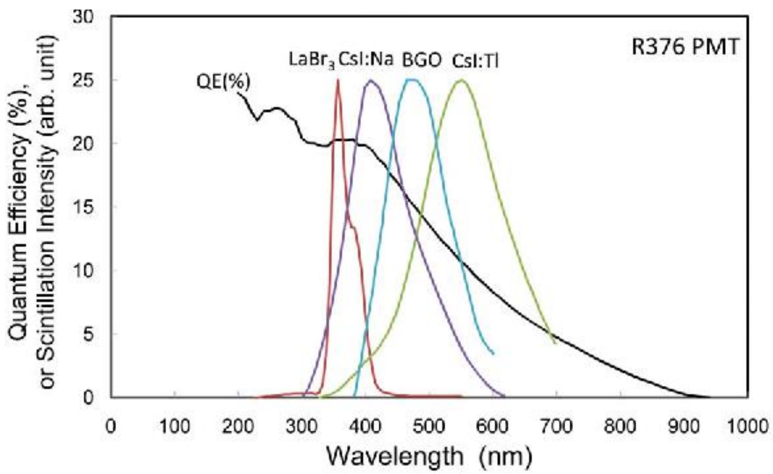

Sasaki, IEEE Trans Nucl Sci 2010

Technique de détection

■ **Photo-détecteur : PMT**

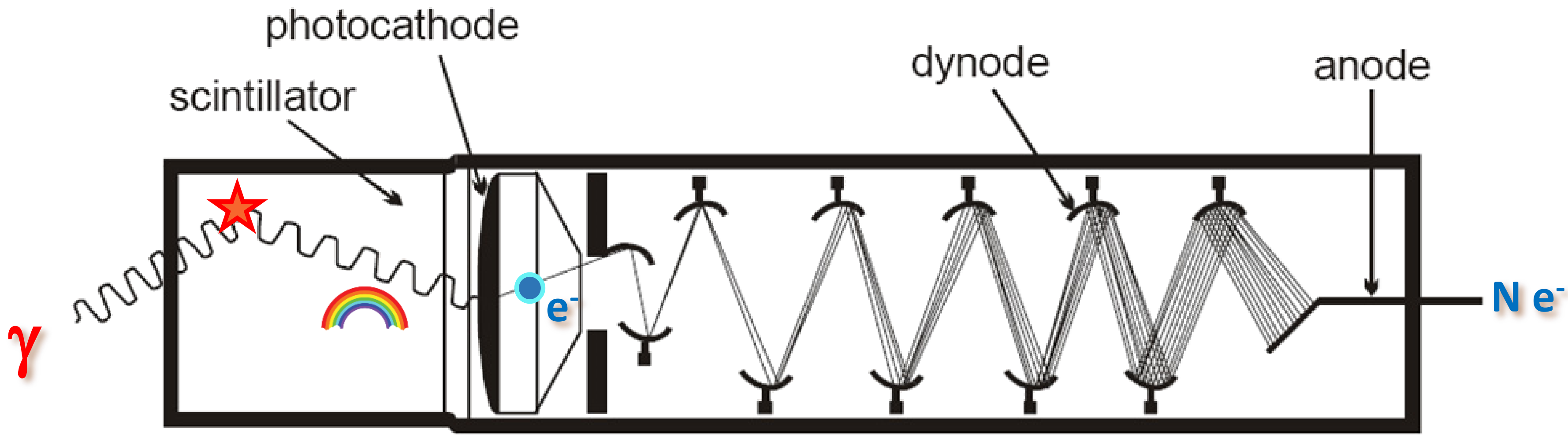

Gain : N ~ 10^6.
Rapidité : < 1 ns.
Efficacité quantique : QE ~ 15–25%.
Bruit faible (Stat. Poisson)
T°C indépendant
Encombrement
Incompatibilité IRM

■ Photo-détecteur : photodiode

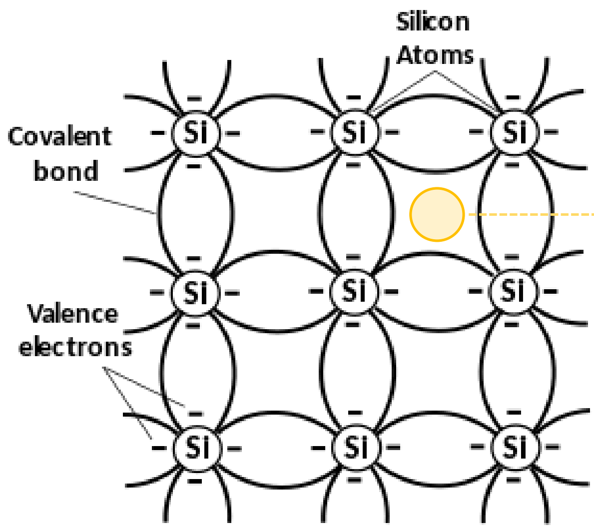

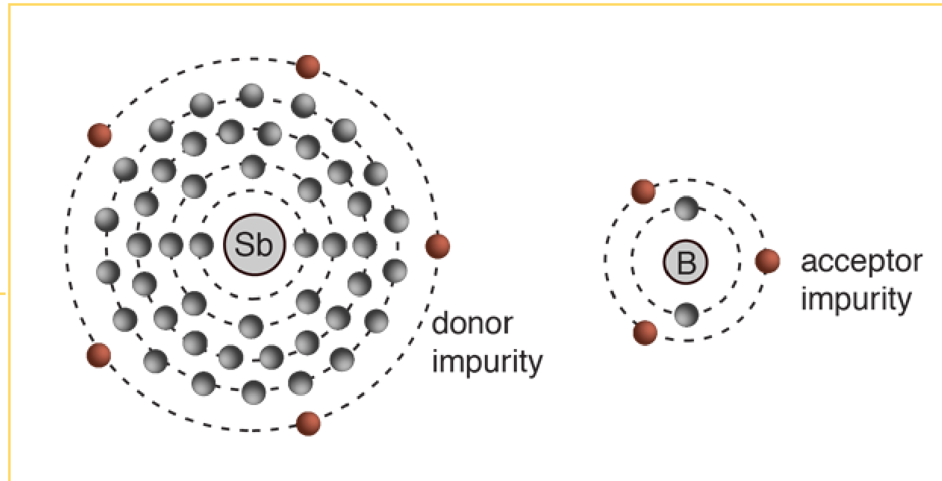

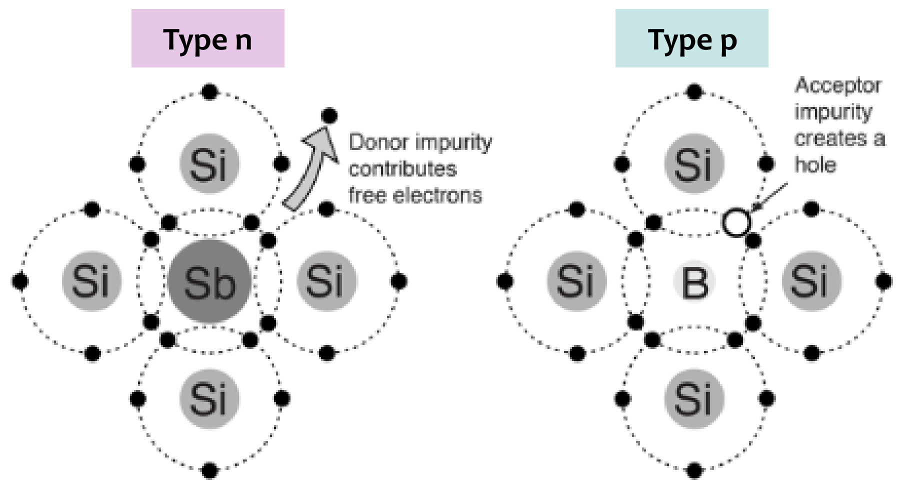

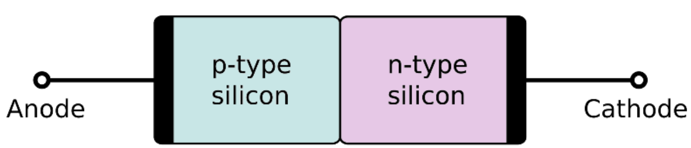

hyperphysics.phy-astr.gsu.edu

Technique de détection

■ Photo-détecteur : photodiode

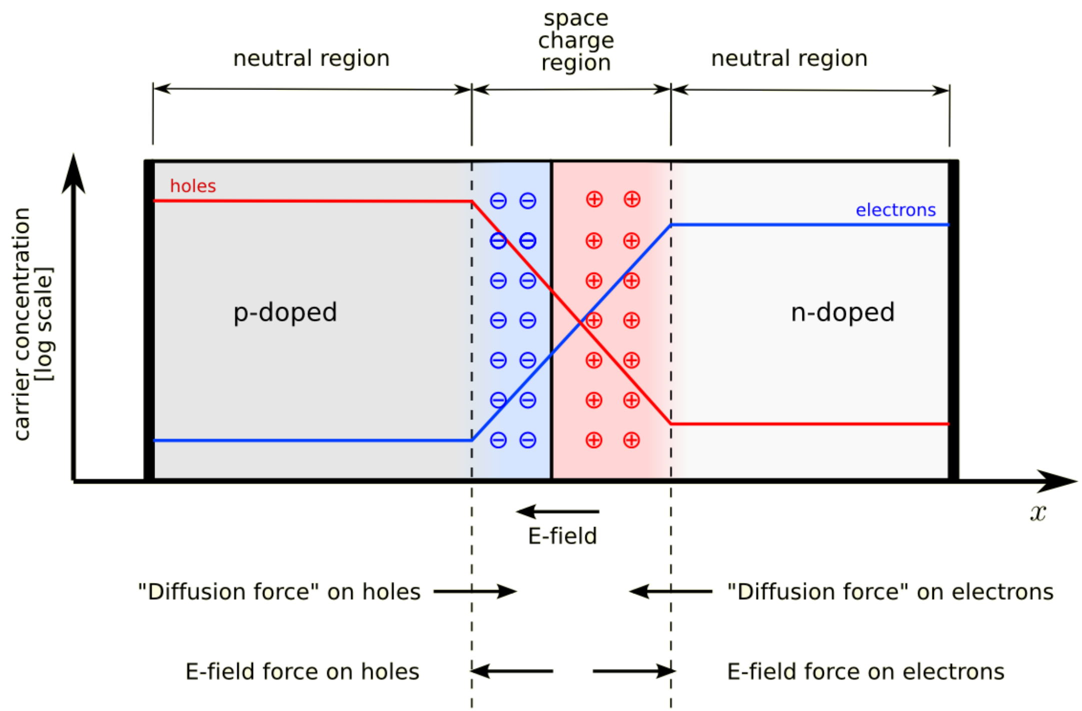

■ Photo-détecteur : photodiode

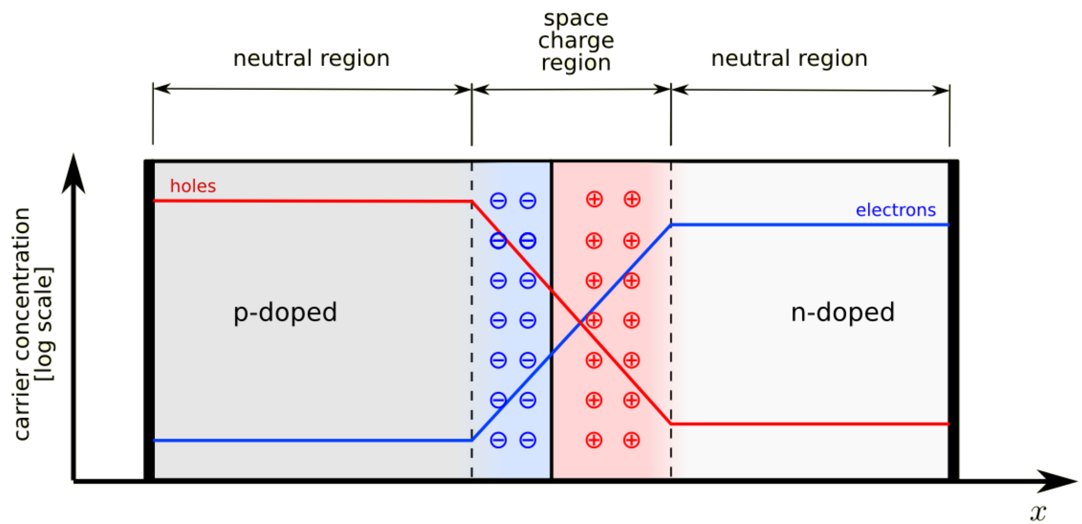

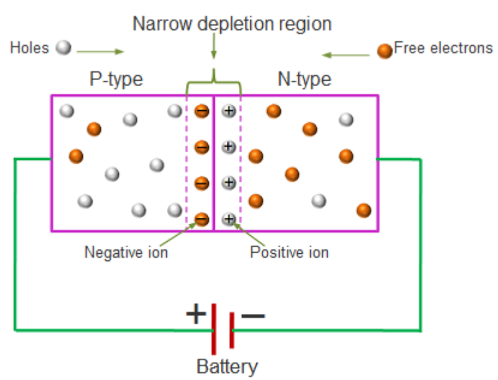

Forward bias

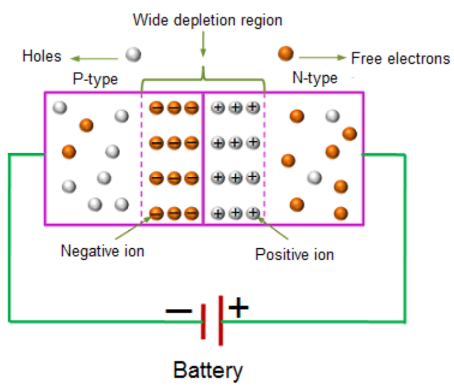

Reverse bias

physics-and-radio-electronics.com

■ Photo-détecteur : photodiode

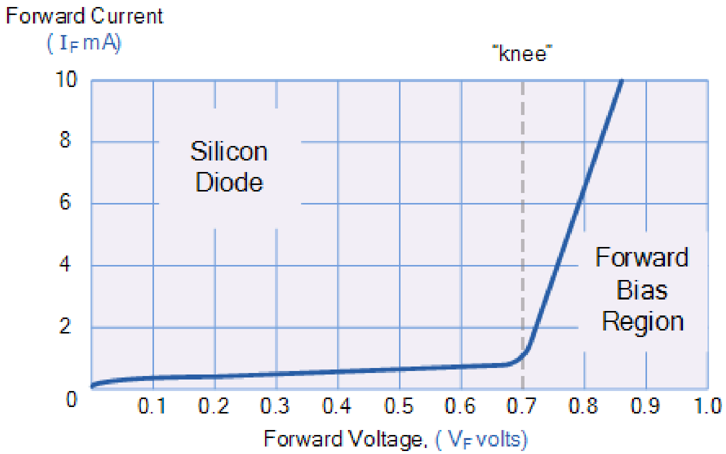

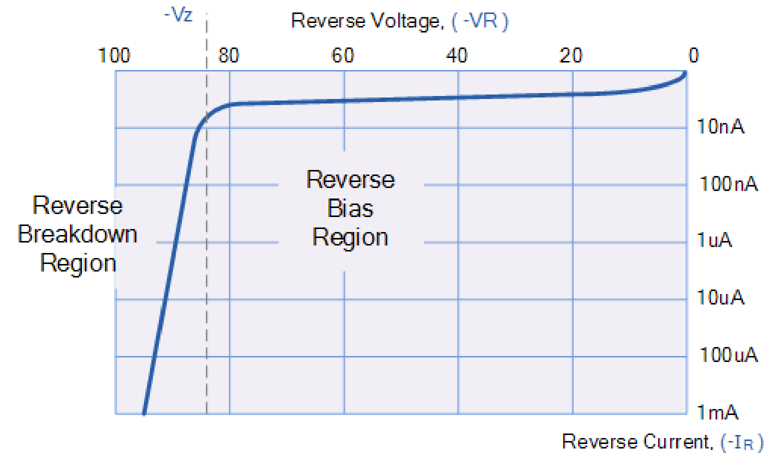

electronics-tutorials.ws

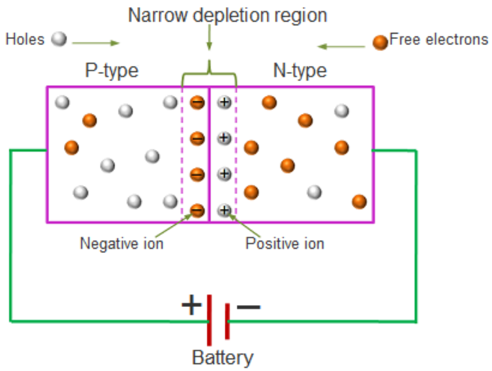

Forward bias

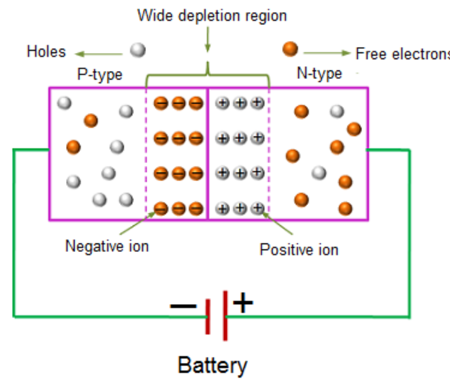

Reverse bias

physics-and-radio-electronics.com

Technique de détection

■ **Photo-détecteur : photodiode**

APD
Compact
QE ~ 70%
Compatible IRM

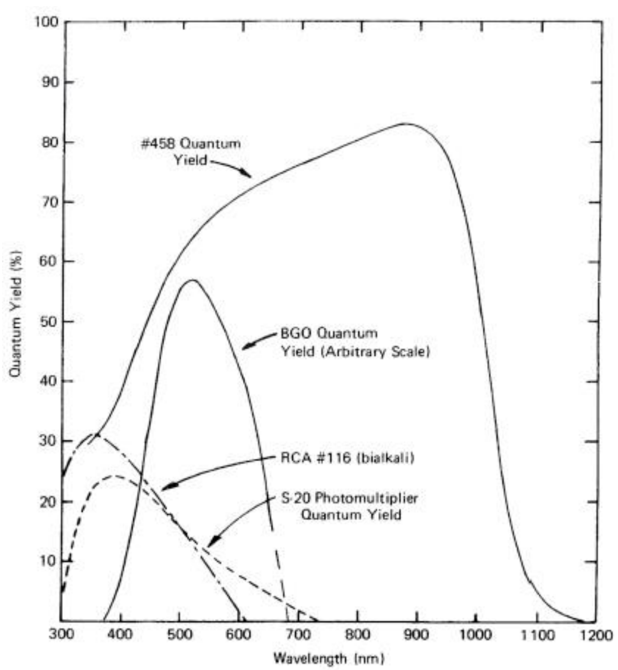

astro.rug.nl

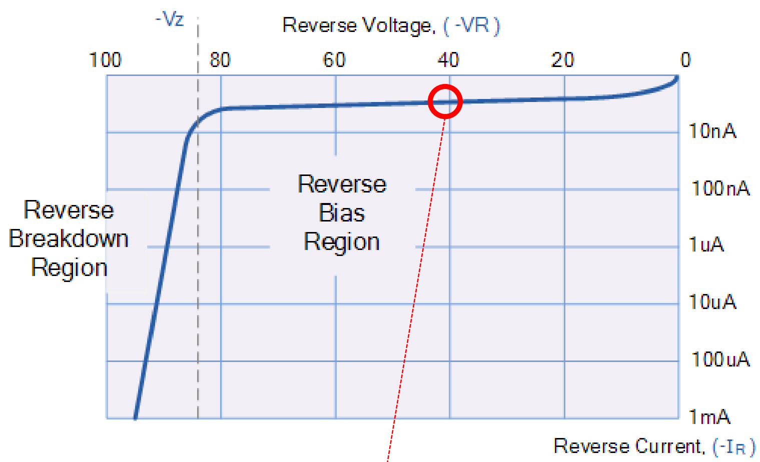

Proportional mode

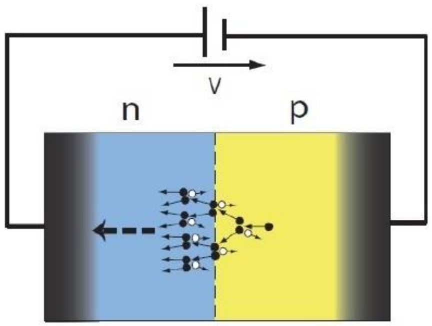

Spanoudaki, Sensors 2010

Technique de détection

■ Photo-détecteur : photodiode

APD
Compact
QE ~ 70%
Compatible IRM
Réponse 5 ns
Gain < 1000, T°C dépendant
Bruit ∝ surface

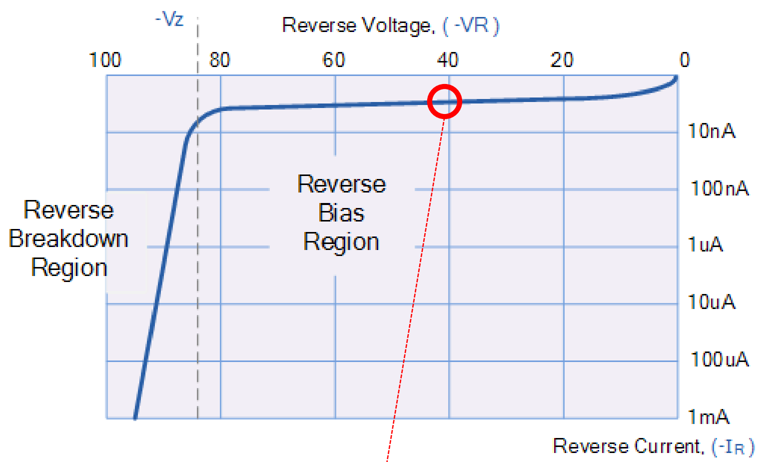

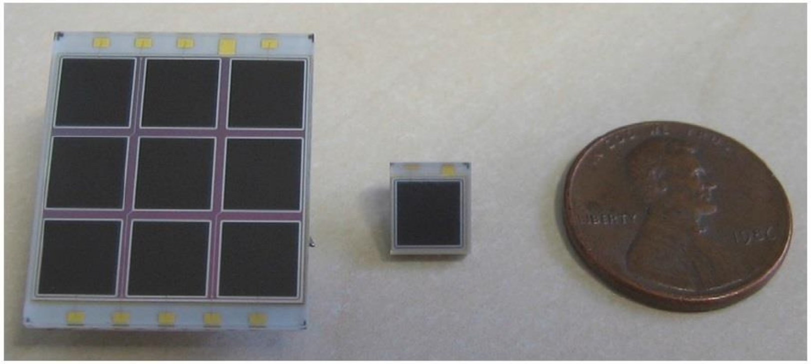

Pichler, J Nucl Med 2008

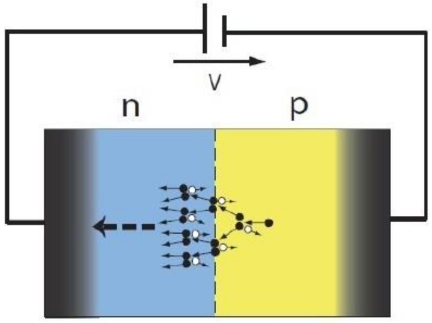

Spanoudaki, Sensors 2010

Technique de détection

■ **Photo-détecteur : photodiode**

SPAD / SiPM

Compact

QE ~ 70%

Compatible IRM

Réponse < 1 ns

Gain ~ 10^6

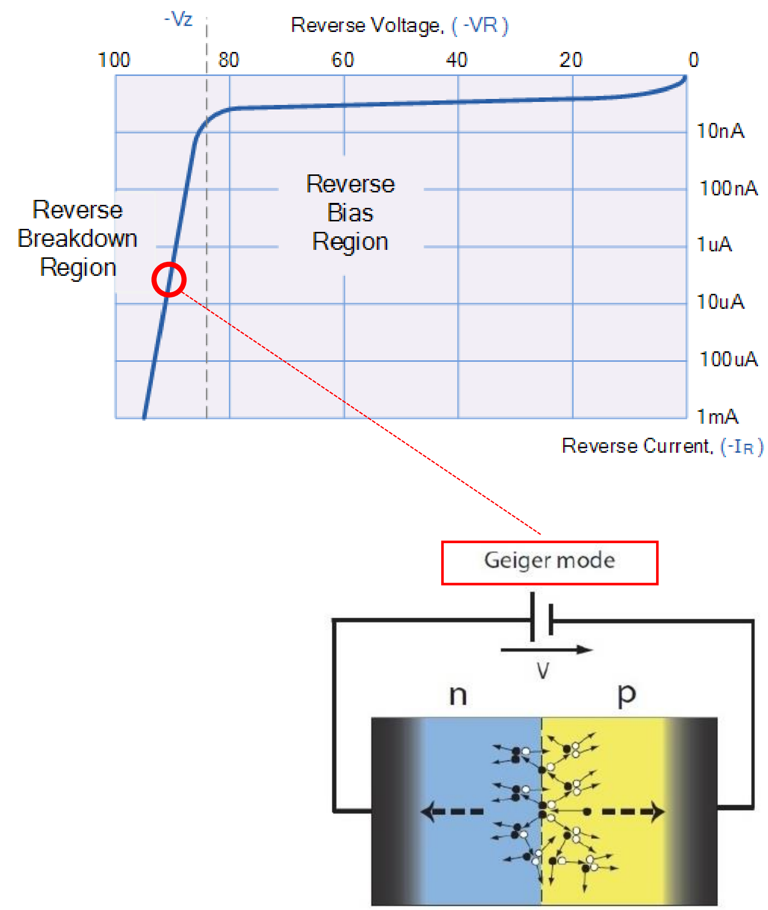

Spanoudaki, Sensors 2010

Technique de détection

■ **Photo-détecteur : photodiode**

SPAD / SiPM

Compact
QE ~ 70%
Compatible IRM
Réponse < 1 ns
Gain ~ 10^6

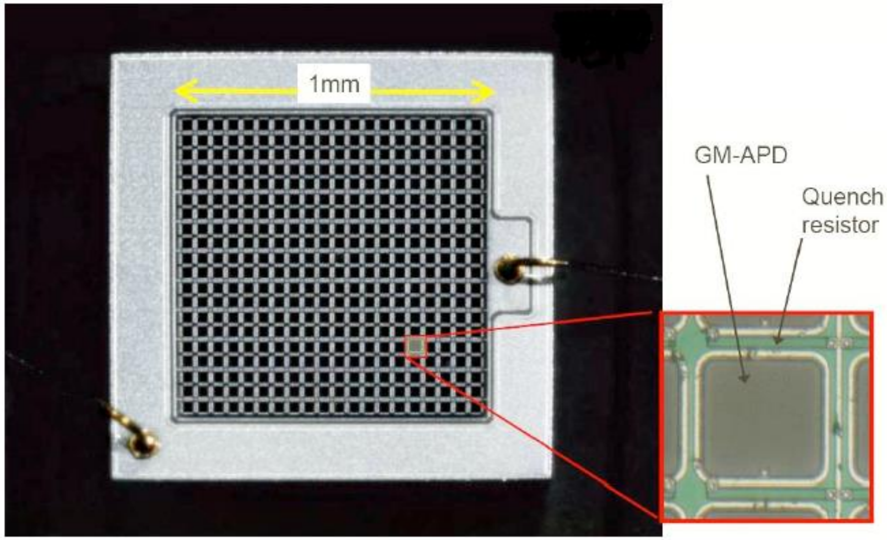

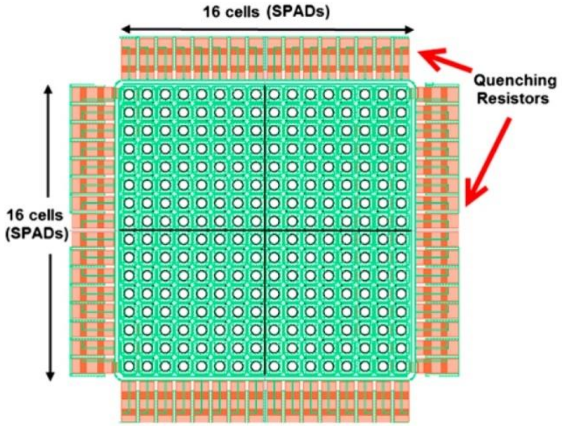

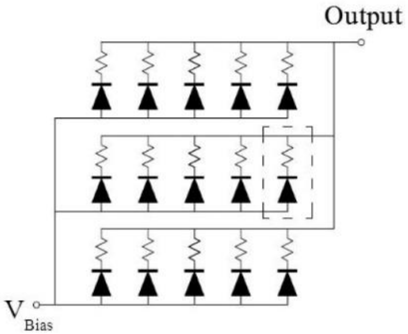

Zou, J Mod Opt 2015

Technique de détection

■ **Bloc détecteur**

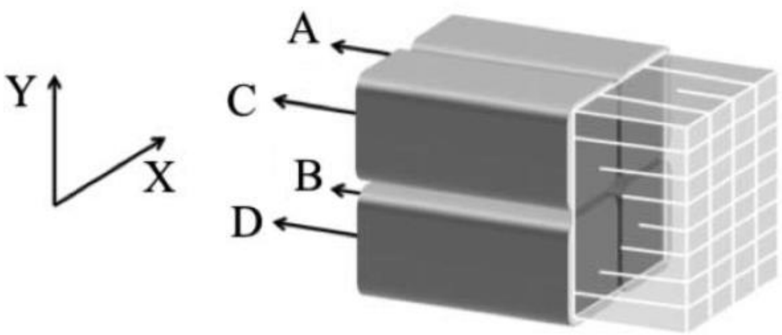

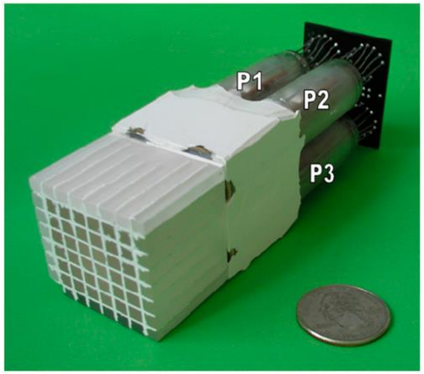

Pichler, J Nucl Med 2008

$$X = \frac{(S_A + S_B) - (S_C + S_D)}{(S_A + S_B + S_C + S_D)}$$

$$Y = \frac{(S_A + S_C) - (S_B + S_D)}{(S_A + S_B + S_C + S_D)}$$

Del Guerra, Riv Nuov Cimento 2016

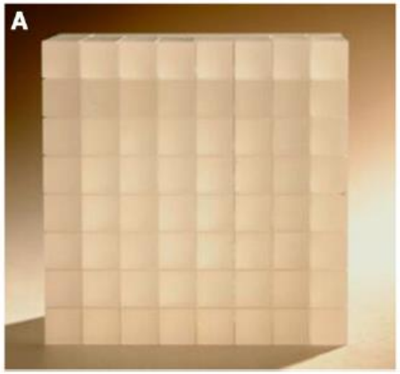

8×8 BGO 6×6 mm²

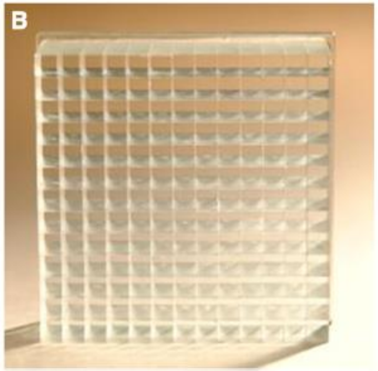

13×13 LSO 4×4 mm²

C

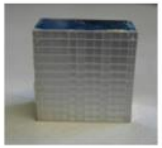

12×12 LSO
1,5×1,5 mm²

Technique de détection

■ **Bloc détecteur**

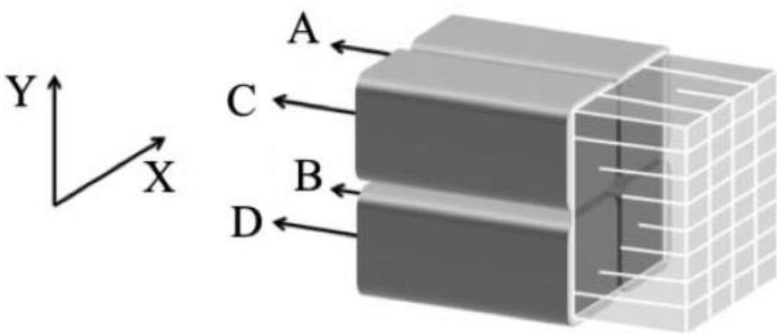

$$X = \frac{(S_A + S_B) - (S_C + S_D)}{(S_A + S_B + S_C + S_D)}$$

$$Y = \frac{(S_A + S_C) - (S_B + S_D)}{(S_A + S_B + S_C + S_D)}$$

Del Guerra, Riv Nuov Cimento 2016

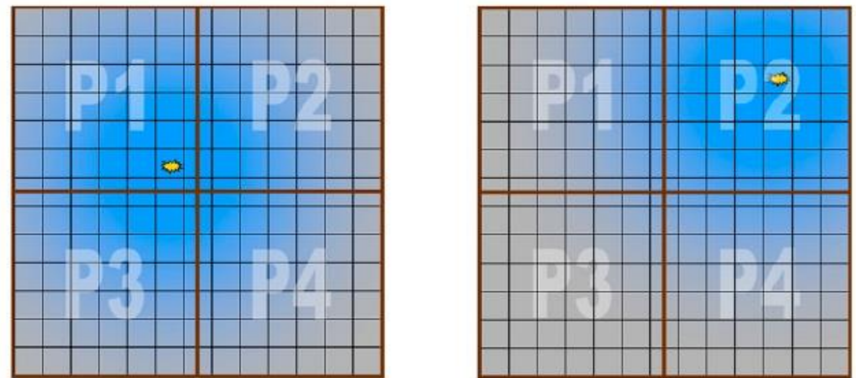

Codage Anger : $X = \frac{P_2 + P_4 - P_1 - P_3}{P_1 + P_2 + P_3 + P_4}$ $Y = \frac{P_1 + P_2 - P_3 - P_4}{P_1 + P_2 + P_3 + P_4}$

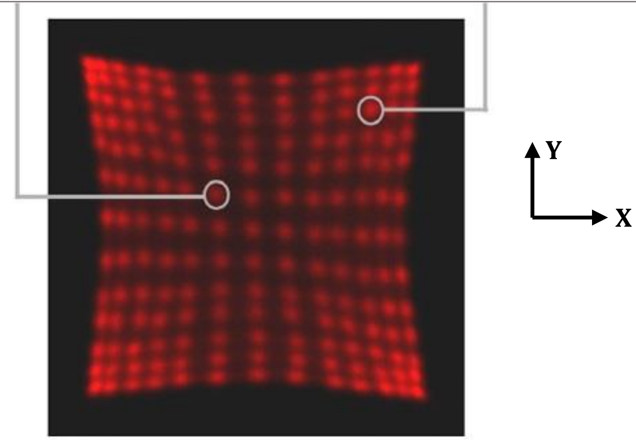

Pichler, J Nucl Med 2008

Technique de détection

■ **Bloc détecteur**

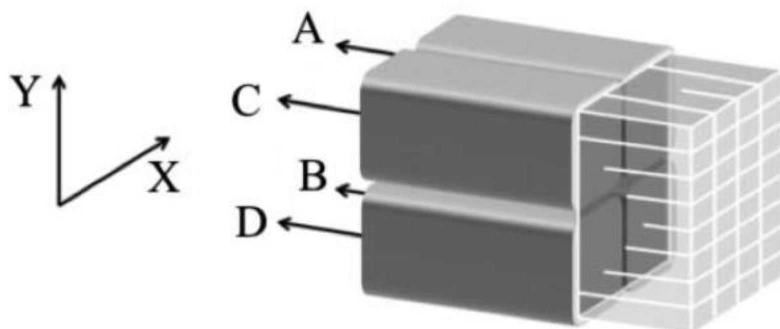

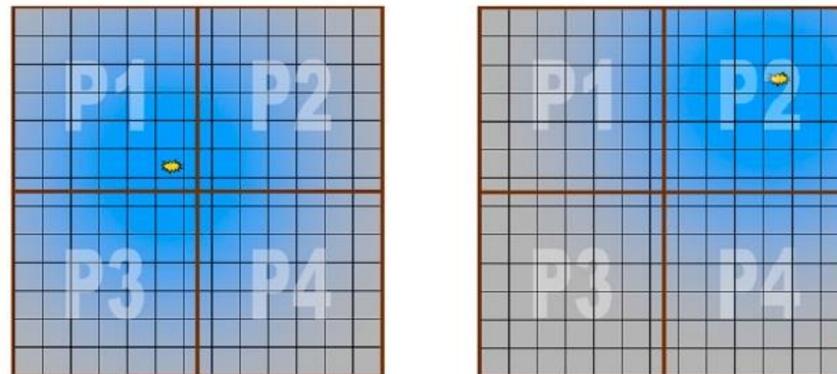

Codage Anger : $X = \frac{P_2+P_4-P_1-P_3}{P_1+P_2+P_3+P_4}$ $Y = \frac{P_1+P_2-P_3-P_4}{P_1+P_2+P_3+P_4}$

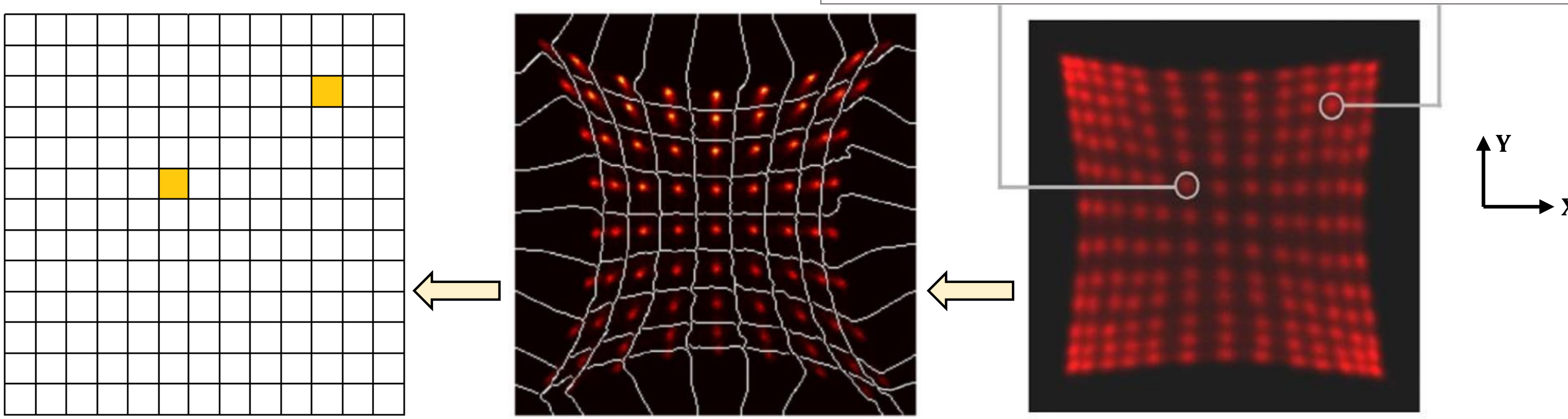

Chaudhari, Phys Med Biol 2008

Pichler, J Nucl Med 2008

SPECT

Sensibilité

~ 0,01 %
Collimateur : angle d'acceptance
géométrie

Résolution spatiale

Collimateur

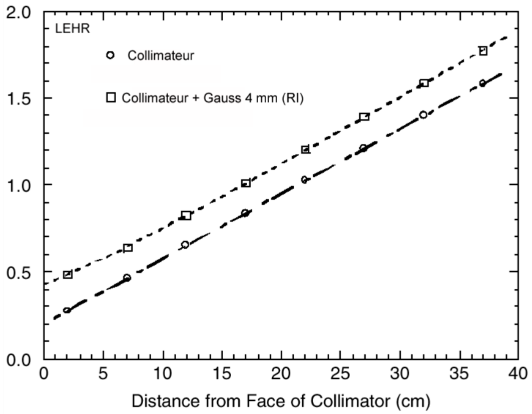

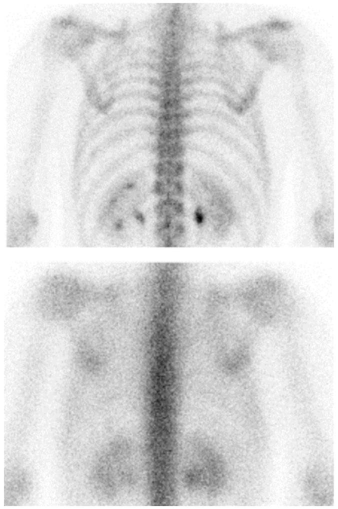

Résolution énergie

Rendement lumineux

Performances

TEP

Sensibilité Point source au centre du FOV

$$E_s = E_g \times E_i \quad \sim 1\ \%$$

Efficacité géométrique E_g

Géométrie : angle solide (FOV axial, diamètre)
Packing fraction
2D / 3D (max ring difference)

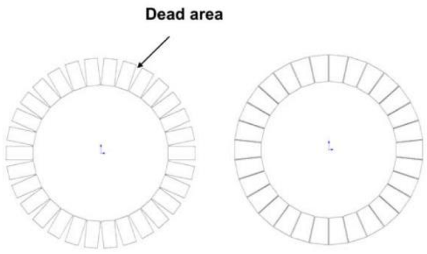

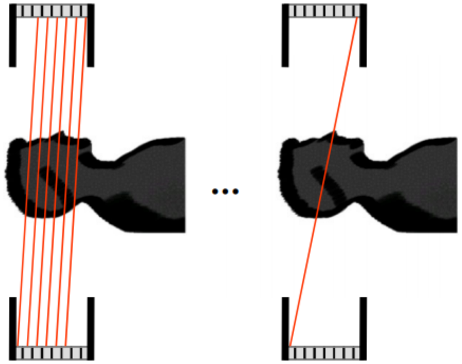

Performances

TEP

Sensibilité Point source au centre du FOV

$$E_s = E_g \times E_i \quad \sim 1\ \%$$

Efficacité géométrique E_g

Géométrie : angle solide (FOV axial, diamètre)
Packing fraction
2D / 3D (max ring difference)

Efficacité intrinsèque E_i

Probabilité d'interaction : ρ, Z, longueur
Fenêtre coïncidence, fenêtre énergie

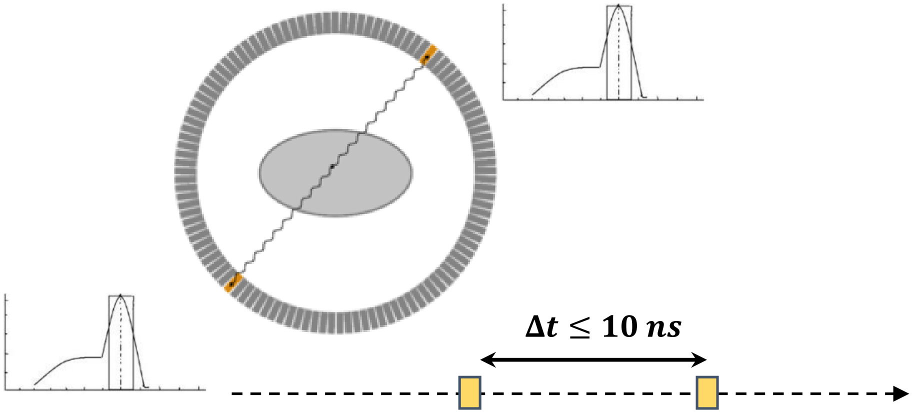

TEP

Sensibilité Point source au centre du FOV

$$E_s = E_g \times E_i \quad \sim 1\ \%$$

Efficacité géométrique E_g

Géométrie : angle solide (FOV axial, diamètre)
Packing fraction
2D / 3D (max ring difference)

Efficacité intrinsèque E_i

Probabilité d'interaction : ρ, Z, longueur
Fenêtre coïncidence, fenêtre énergie

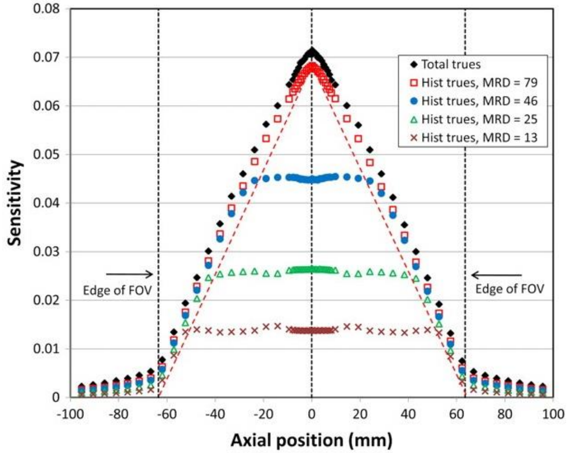

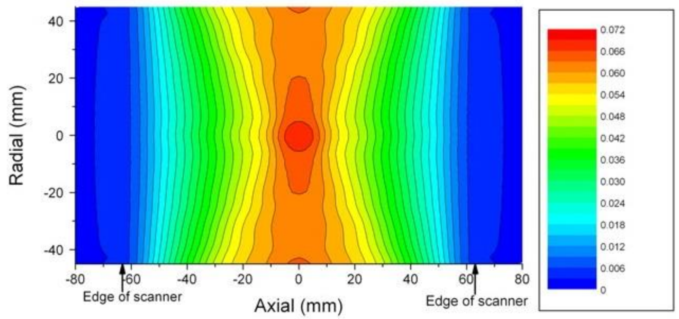

Visser, J Nucl Med 2009

Performances

TEP

Sensibilité Point source au centre du FOV

$$E_s = E_g \times E_i \quad \sim 1\ \%$$

Efficacité géométrique E_g

- Géométrie : angle solide (FOV axial, diamètre)
- Packing fraction
- 2D / 3D (max ring difference)

Efficacité intrinsèque E_i

- Probabilité d'interaction : ρ, Z, longueur
- Fenêtre coïncidence, fenêtre énergie

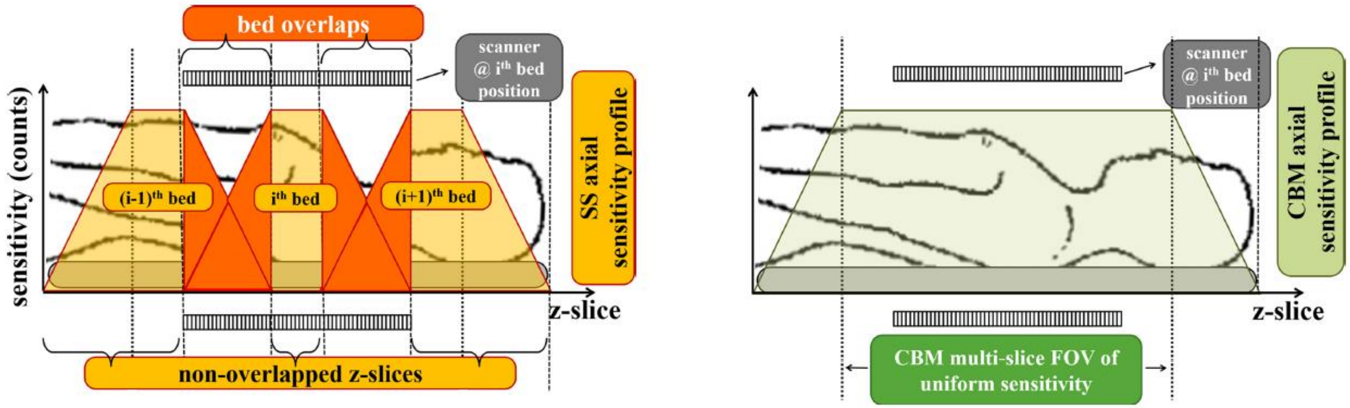

Zaidi, Br J Radiol 2018

Performances

TEP

Résolution spatiale

$$\mathrm{FWHM} = 1.25\sqrt{(d/2)^2 + b^2 + (0.0022D)^2 + r^2 + p^2}$$

Portée du positon r

Acolinéarité $0{,}0022\ D$

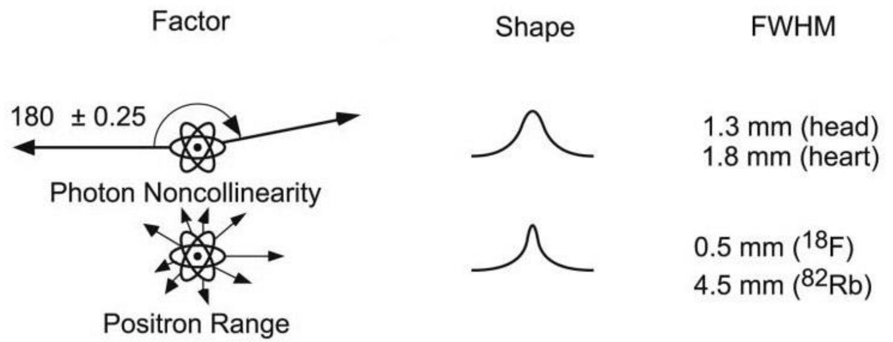

Moses, Nucl Instrum Methods Phys Res 2011

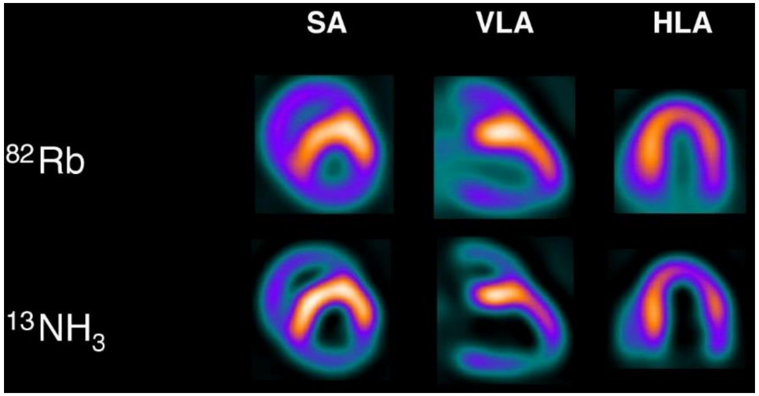

Bengel, JACC 2009

Performances

TEP

Résolution spatiale

$$\mathrm{FWHM} = 1.25\sqrt{(d/2)^2 + b^2 + (0.0022D)^2 + r^2 + p^2}$$

Portée du positon r
Acolinéarité $0{,}0022\ D$

Taille du détecteur d
Erreur de codage $b \sim d/3$

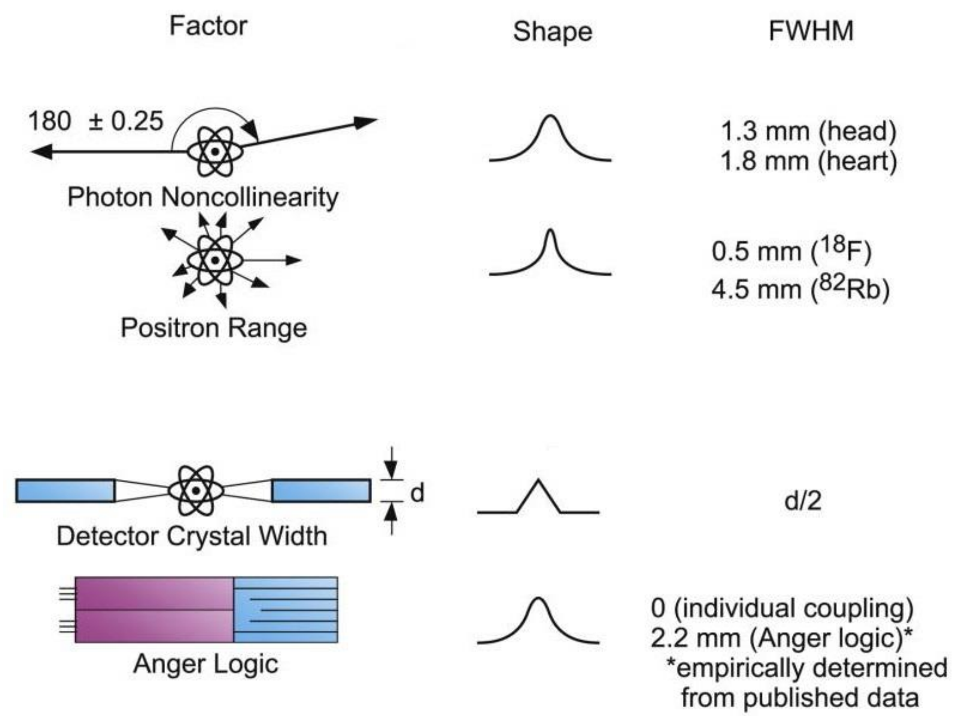

Moses, Nucl Instrum Methods Phys Res 2011

Performances

TEP

Résolution spatiale

$$\mathrm{FWHM} = 1.25\sqrt{(d/2)^2 + b^2 + (0.0022D)^2 + r^2 + p^2}$$

Portée du positon r
Acolinéarité $0{,}0022\ D$

Taille du détecteur d
Erreur de codage $b \sim d/3$

Erreur de parallaxe

$$p = \alpha \frac{r}{\sqrt{r^2 + R^2}}$$

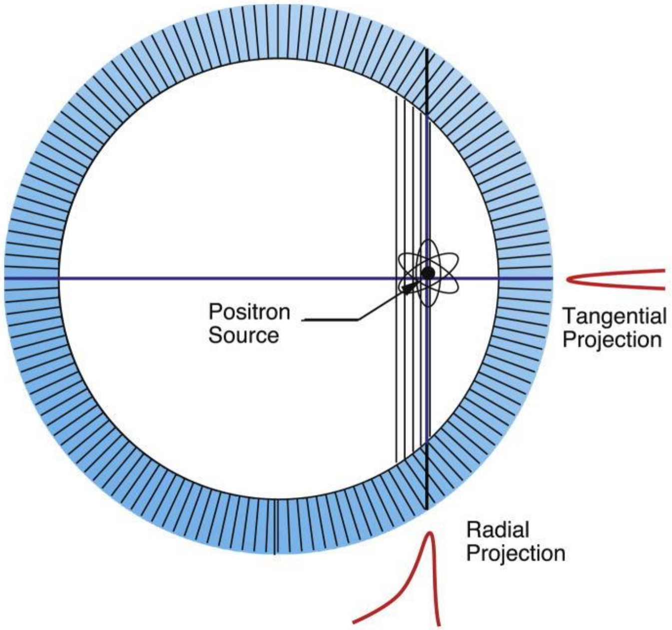

Moses, Nucl Instrum Methods Phys Res 2011

Performances

TEP

Résolution spatiale

$$\mathrm{FWHM} = 1.25\sqrt{(d/2)^2 + b^2 + (0.0022D)^2 + r^2 + p^2}$$

Portée du positon r
Acolinéarité $0{,}0022\ D$

Taille du détecteur d
Erreur de codage $b \sim d/3$

Erreur de parallaxe

$$p = \alpha \frac{r}{\sqrt{r^2 + R^2}}$$

Echantillonnage / reconstruction (1.25)

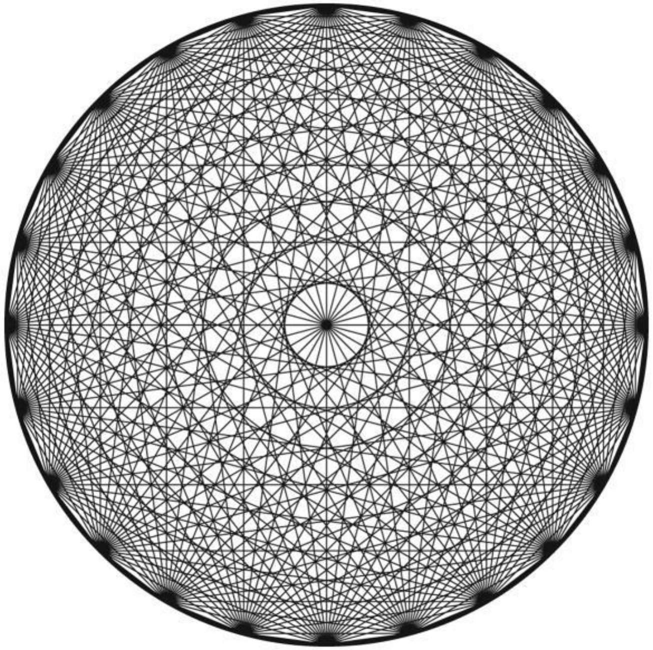

Moses, Nucl Instrum Methods Phys Res 2011

Performances

TEP

Résolution spatiale

$$\mathrm{FWHM} = 1.25\sqrt{(d/2)^2 + b^2 + (0.0022D)^2 + r^2 + p^2}$$

Portée du positon r

Acolinéarité $0{,}0022\ D$

Taille du détecteur d

Erreur de codage $b \sim d/3$

Erreur de parallaxe

$$p = \alpha \frac{r}{\sqrt{r^2 + R^2}}$$

Echantillonnage / reconstruction (1.25)

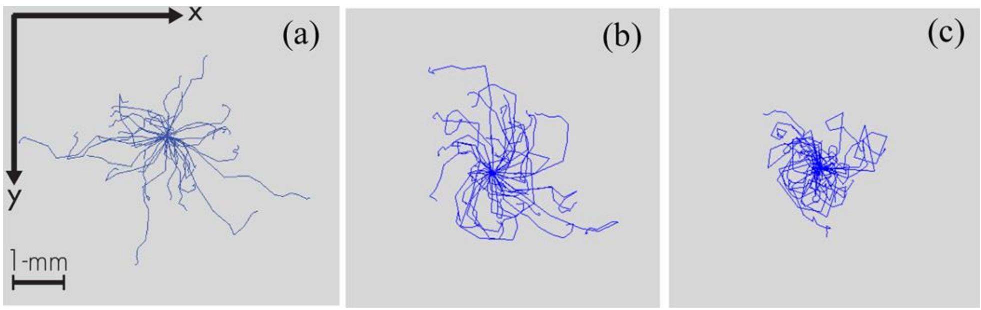

Sy, IEEE Nucl Sci Symp 2014

Table 1. Mean 3-D Positron range (mm)

B_0	0 T	1.5 T	3 T	9.5 T
^{18}F	0.56	0.56	0.54	0.43
^{11}C	1.05	1.03	0.96	0.67
^{15}O	2.44	2.31	2.00	1.41
^{68}Ga	2.62	2.47	2.12	1.50
^{82}Rb	5.21	4.77	3.90	2.88

Soultanidis, J Phys Conf Ser 2011

Performances

TEP

Résolution spatiale

$$\mathrm{FWHM} = 1.25\sqrt{(d/2)^2 + b^2 + (0.0022D)^2 + r^2 + p^2}$$

Portée du positon r
Acolinéarité $0{,}0022\ D$

$$\Gamma = \sqrt{(d/2)^2 + r^2 + (0.0044R)^2}\ (\mathrm{mm\ fwhm})$$

^{18}F 0,7 mm (pré-clinique)
1,8 mm (clinique)

Taille du détecteur d
Erreur de codage $b \sim d/3$

Erreur de parallaxe

$$p = \alpha \frac{r}{\sqrt{r^2 + R^2}}$$

Echantillonnage / reconstruction (1.25)

Performances

TEP

Résolution spatiale

$$\mathrm{FWHM} = 1.25\sqrt{(d/2)^2 + b^2 + (0.0022D)^2 + r^2 + p^2}$$

Portée du positon r

Acolinéarité $0{,}0022\ D$

$$\Gamma = \sqrt{(d/2)^2 + r^2 + (0.0044R)^2}\ (\mathrm{mm\ fwhm})$$

^{18}F 0,7 mm (pré-clinique)
1,8 mm (clinique)

Taille du détecteur d

Erreur de codage $b \sim d/3$

$d = 3\ mm$ $\mathrm{FWHM} = 2{,}4\ mm$

$d = 2\ mm$ $\mathrm{FWHM} = 2{,}1\ mm$

Coating 0,1 mm

Erreur de parallaxe

$$p = \alpha \frac{r}{\sqrt{r^2 + R^2}}$$

Echantillonnage / reconstruction (1.25)

Performances

TEP

Résolution spatiale

$$\mathrm{FWHM} = 1.25\sqrt{(d/2)^2 + b^2 + (0.0022D)^2 + r^2 + p^2}$$

Portée du positon r

Acolinéarité $0{,}0022\ D$

Taille du détecteur d

Erreur de codage $b \sim d/3$

Erreur de parallaxe

$$p = \alpha \frac{r}{\sqrt{r^2 + R^2}}$$

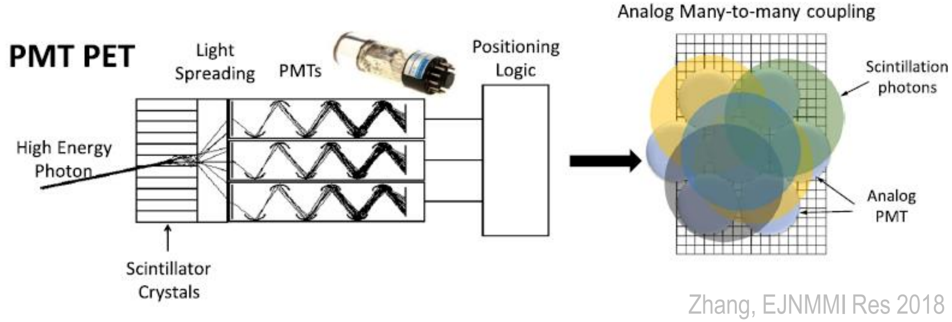

Zhang, EJNMMI Res 2018

Echantillonnage / reconstruction (1.25)

Performances

TEP

Résolution spatiale

$$\mathrm{FWHM} = 1.25\sqrt{(d/2)^2 + b^2 + (0.0022D)^2 + r^2 + p^2}$$

Portée du positon r
Acolinéarité 0,0022 D

Taille du détecteur d
Erreur de codage $b \sim d/3$

Erreur de parallaxe

$$p = \alpha \frac{r}{\sqrt{r^2 + R^2}}$$

Echantillonnage / reconstruction (1.25)

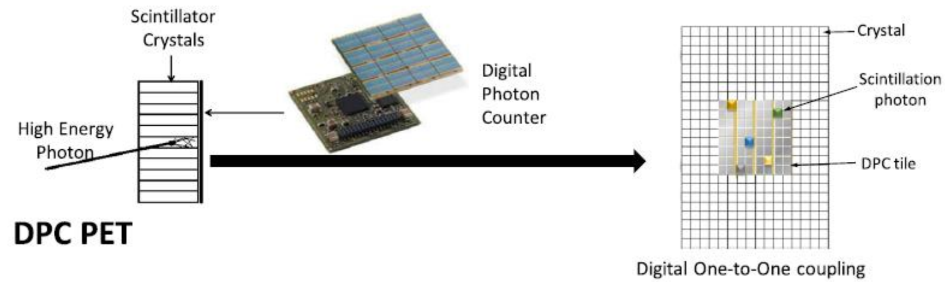

Zhang, EJNMMI Res 2018

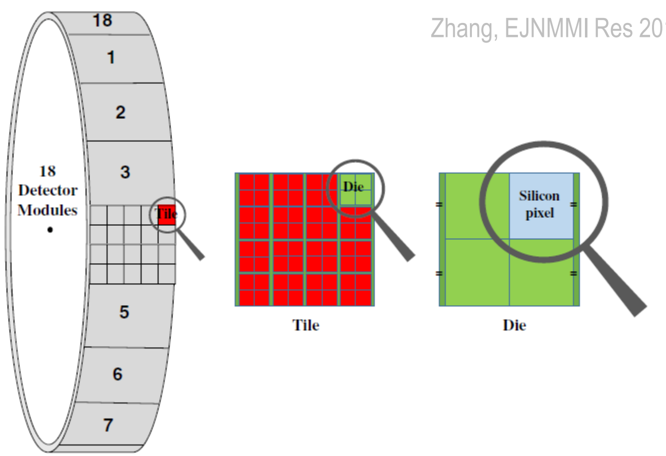

Performances

TEP

Résolution spatiale

$$\mathrm{FWHM} = 1.25\sqrt{(d/2)^2 + b^2 + (0.0022D)^2 + r^2 + p^2}$$

Portée du positon r
Acolinéarité $0{,}0022\ D$

Taille du détecteur d
Erreur de codage $b \sim d/3$

Erreur de parallaxe

$$p = \alpha \frac{r}{\sqrt{r^2 + R^2}}$$

Echantillonnage / reconstruction (1.25)

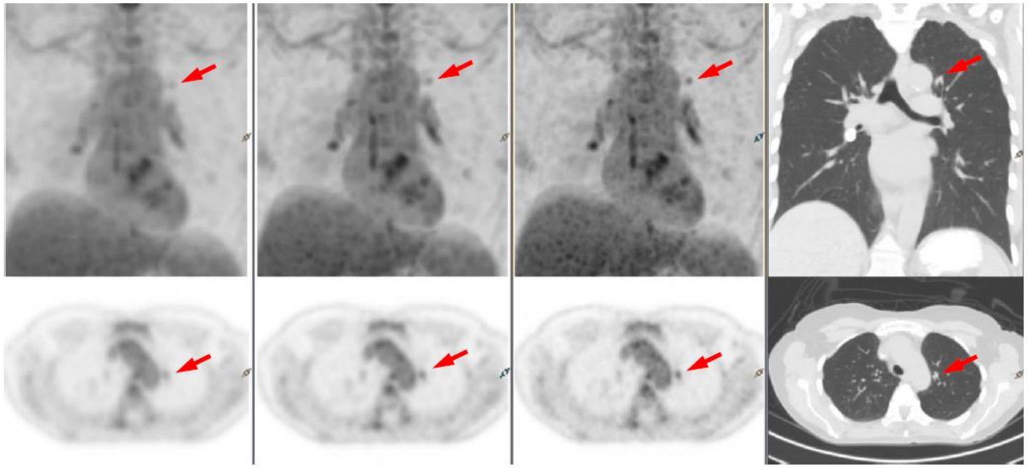

SD PET (4x4x4 mm³) HD (2x2x2 mm³) UHD (1x1x1 mm³)

Zhang, EJNMMI Res 2018

Performances

TEP

Résolution spatiale

Portée du positon r
Acolinéarité $0{,}0022\ D$

Taille du détecteur d
Erreur de codage $b \sim d/3$

Erreur de parallaxe

$$p = \alpha \frac{r}{\sqrt{r^2 + R^2}}$$

Echantillonnage / reconstruction (1.25)

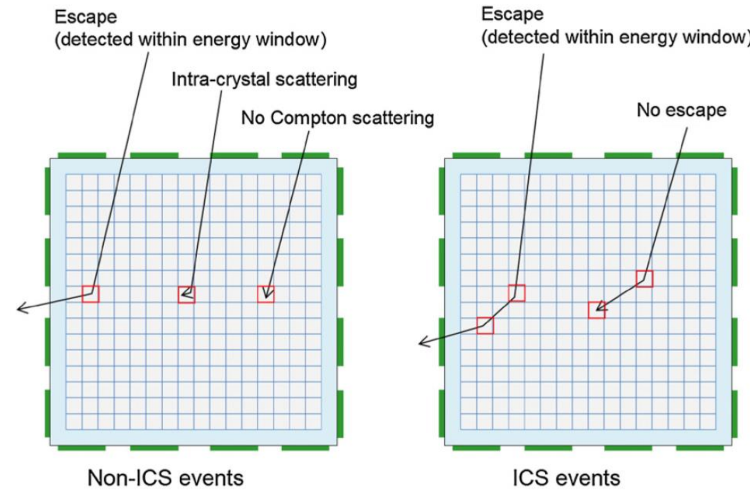

Yamaya, Phys Med Biol 2011

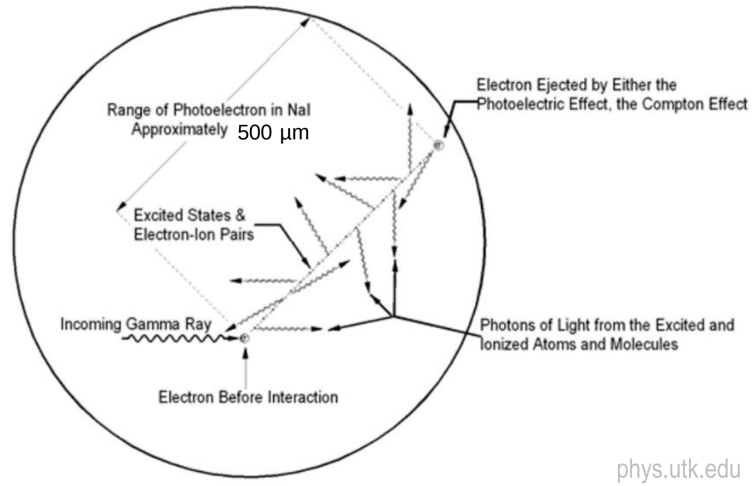

phys.utk.edu

Performances

TEP

Résolution spatiale

Portée du positon r
Acolinéarité $0{,}0022\ D$

Taille du détecteur d
Erreur de codage $b \sim d/3$

Erreur de parallaxe

$$p = \alpha \frac{r}{\sqrt{r^2 + R^2}}$$

Echantillonnage / reconstruction (1.25)

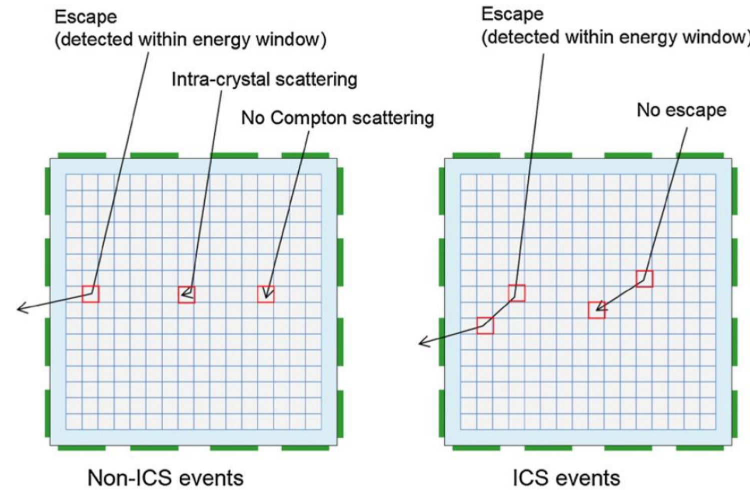

Yamaya, Phys Med Biol 2011

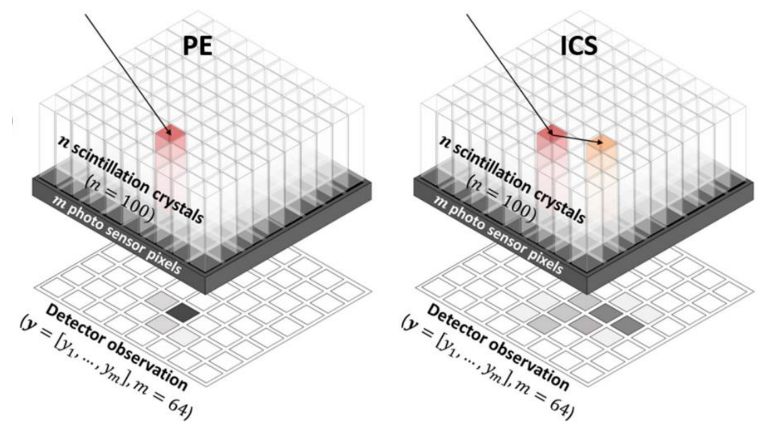

Lee, Phys Med Biol 2018

Performances

TEP

Résolution spatiale

$$\mathrm{FWHM} = 1.25\sqrt{(d/2)^2 + b^2 + (0.0022D)^2 + r^2 + p^2}$$

Portée du positon r
Acolinéarité 0,0022 D

Taille du détecteur d
Erreur de codage $b \sim d/3$

Erreur de parallaxe
$$p = \alpha \frac{r}{\sqrt{r^2 + R^2}}$$

Echantillonnage / reconstruction (1.25)

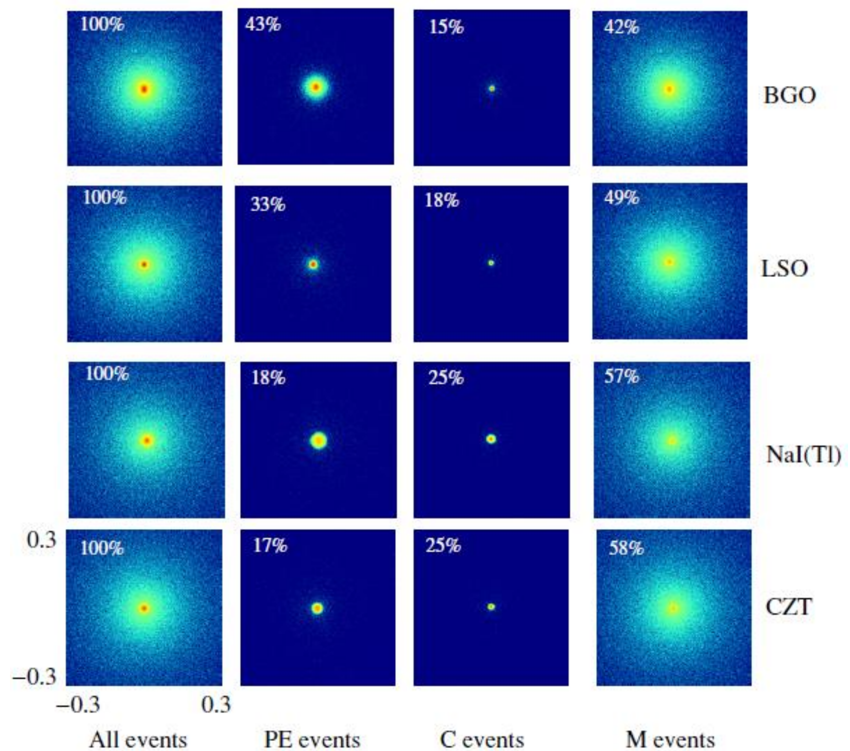

Stickel, Phys Med Biol 2005

Performances

TEP

Résolution spatiale

Portée du positon r
Acolinéarité $0{,}0022\ D$

Taille du détecteur d
Erreur de codage $b \sim d/3$

Erreur de parallaxe

$$p = \alpha \frac{r}{\sqrt{r^2 + R^2}}$$

Echantillonnage / reconstruction (1.25)

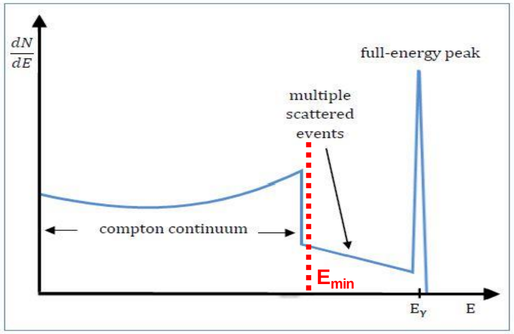

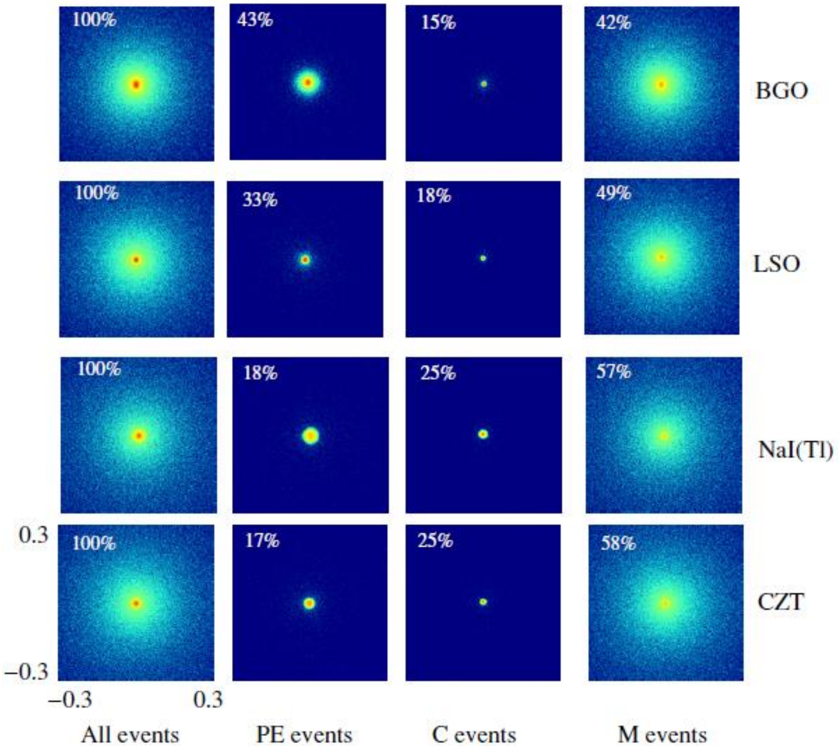

Stickel, Phys Med Biol 2005

Performances

TEP

Résolution spatiale

$$\mathrm{FWHM} = 1.25\sqrt{(d/2)^2 + b^2 + (0.0022D)^2 + r^2 + p^2}$$

Portée du positon r
Acolinéarité $0{,}0022\ D$

Taille du détecteur d
Erreur de codage $b \sim d/3$

Erreur de parallaxe

$$p = \alpha \frac{r}{\sqrt{r^2 + R^2}}$$

Echantillonnage / reconstruction (1.25)

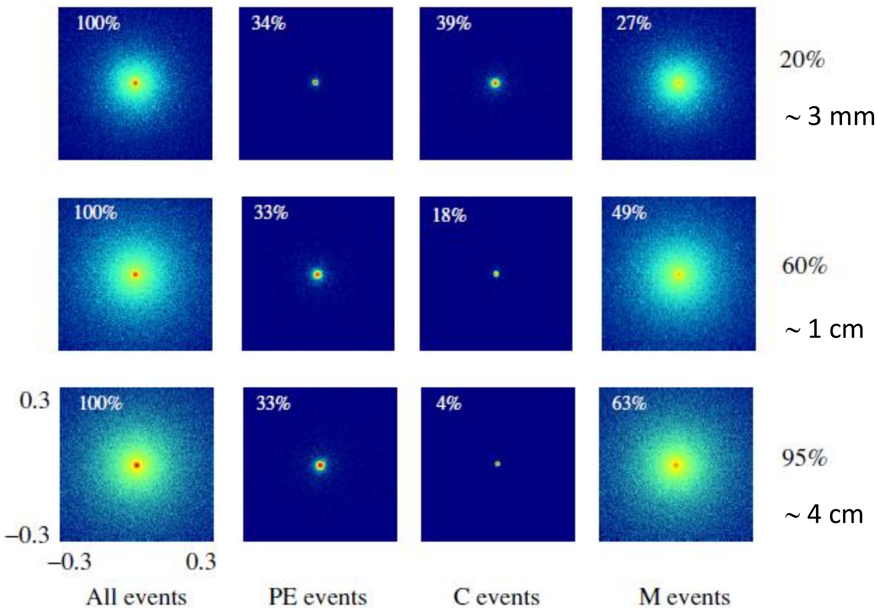

Stickel, Phys Med Biol 2005

Performances

Institut National des Sciences et Techniques Nucléaires

TEP

Résolution spatiale

$$\mathrm{FWHM} = 1.25\sqrt{(d/2)^2 + b^2 + (0.0022D)^2 + r^2 + p^2}$$

Portée du positon r
Acolinéarité $0{,}0022\ D$

Taille du détecteur d
Erreur de codage $b \sim d/3$

Erreur de parallaxe

$$p = \alpha \frac{r}{\sqrt{r^2 + R^2}}$$

Echantillonnage

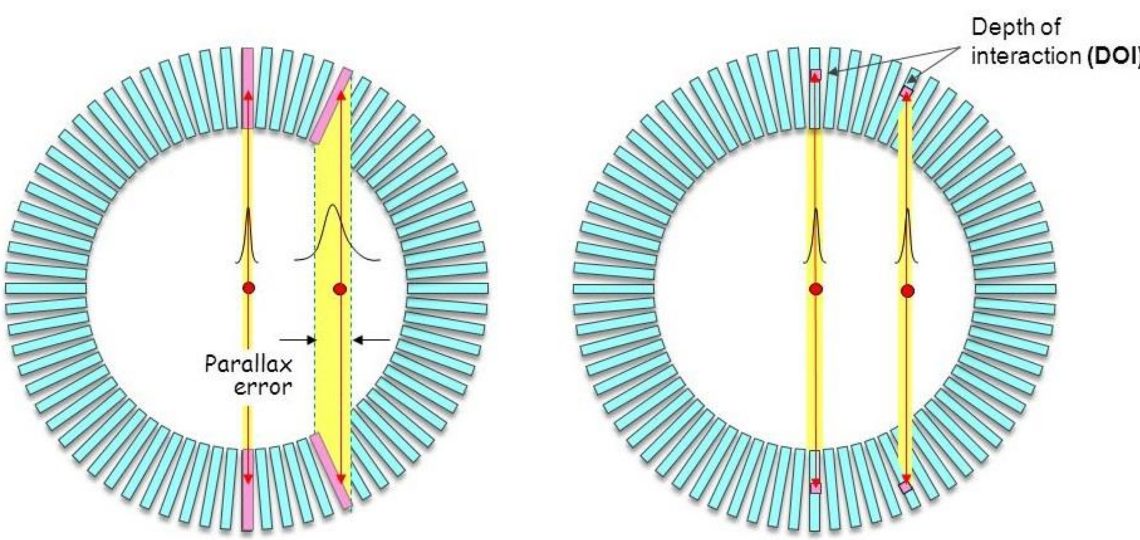

If the DOI position is unknown — If the DOI position is known

TEP

Résolution spatiale

$$\mathrm{FWHM} = 1.25\sqrt{(d/2)^2 + b^2 + (0.0022D)^2 + r^2 + p^2}$$

Portée du positon r
Acolinéarité $0{,}0022\ D$

Taille du détecteur d
Erreur de codage $b \sim d/3$

Erreur de parallaxe

$$p = \alpha \frac{r}{\sqrt{r^2 + R^2}}$$

Echantillonnage

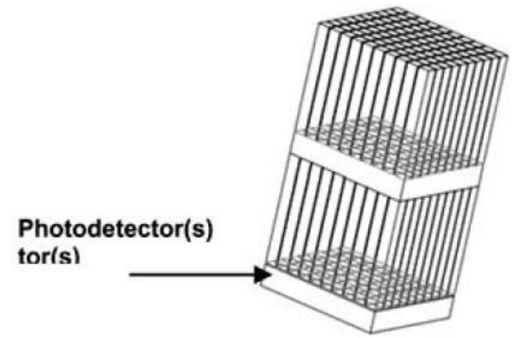

Peng, Curr Pharm Biotechnol 2010

Multiple crystal-photodetector layers

Performances

TEP

Résolution spatiale

$$\mathrm{FWHM} = 1.25\sqrt{(d/2)^2 + b^2 + (0.0022D)^2 + r^2 + p^2}$$

Portée du positon r

Acolinéarité $0{,}0022\ D$

Taille du détecteur d

Erreur de codage $b \sim d/3$

Erreur de parallaxe

$$p = \alpha \frac{r}{\sqrt{r^2 + R^2}}$$

Echantillonnage

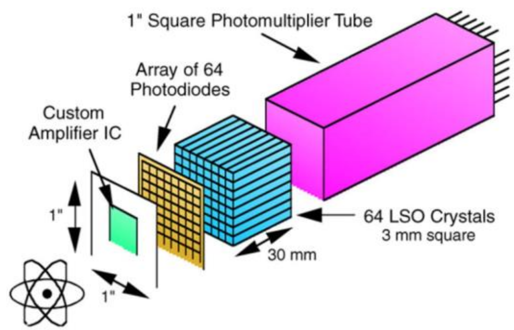

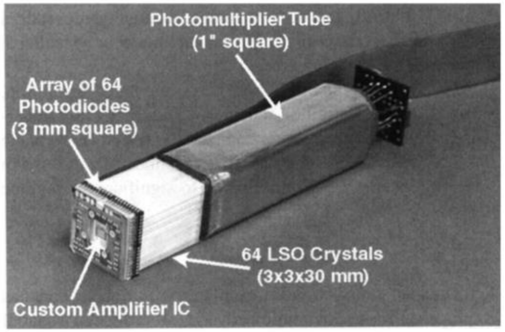

Lewellen, Phys Med Biol 2010

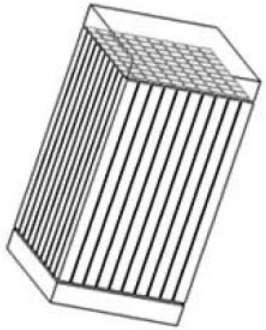

Peng, Curr Pharm Biotechnol 2010

Single crystal layer
+ dual ended photodetectors

Performances

TEP

Résolution spatiale

$$\mathrm{FWHM} = 1.25\sqrt{(d/2)^2 + b^2 + (0.0022D)^2 + r^2 + p^2}$$

Portée du positon r
Acolinéarité 0,0022 D

Taille du détecteur d
Erreur de codage $b \sim d/3$

Erreur de parallaxe

$$p = \alpha \frac{r}{\sqrt{r^2 + R^2}}$$

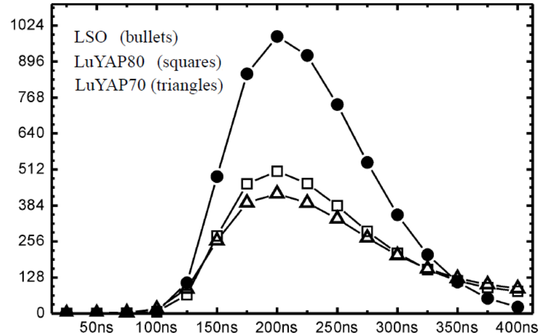

Streun, IEEE Trans Nucl Sci 2003

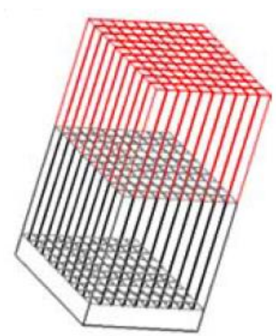

Peng, Curr Pharm Biotechnol 2010

Echantillonnage

Photoswich design
Pulse shape discrimination

Performances

TEP

Résolution spatiale

$$\mathrm{FWHM} = 1.25\sqrt{(d/2)^2 + b^2 + (0.0022D)^2 + r^2 + p^2}$$

Portée du positon r
Acolinéarité $0{,}0022\ D$

Taille du détecteur d
Erreur de codage $b \sim d/3$

Erreur de parallaxe

$$p = \alpha \frac{r}{\sqrt{r^2 + R^2}}$$

Echantillonnage

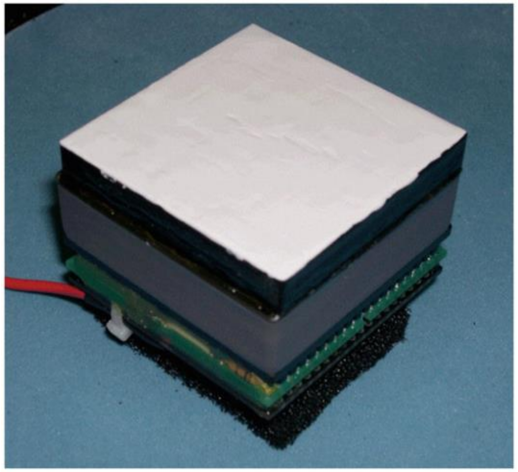

Lewellen, Phys Med Biol 2010

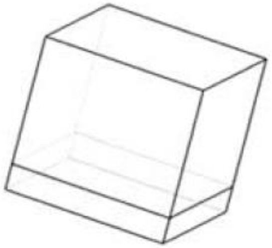

Peng, Curr Pharm Biotechnol 2010

Monolithic cristal
Statistical positionning

Performances

TEP

Résolution spatiale

Portée du positon r
Acolinéarité $0{,}0022\ D$

Taille du détecteur d
Erreur de codage $b \sim d/3$

Erreur de parallaxe

$$p = \alpha \frac{r}{\sqrt{r^2 + R^2}}$$

Echantillonnage

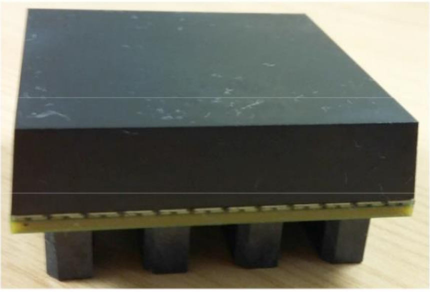

Gonzalez, IEEE Trans Nucl Sci 2016

Monolithic cristal
Statistical positionning

Performances

TEP

Résolution spatiale

Portée du positon r
Acolinéarité $0{,}0022\ D$

Taille du détecteur d
Erreur de codage $b \sim d/3$

Erreur de parallaxe

$$p = \alpha \frac{r}{\sqrt{r^2 + R^2}}$$

Echantillonnage

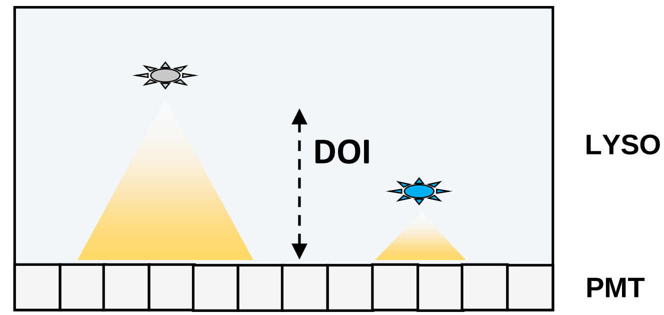

Gonzalez, IEEE Trans Nucl Sci 2016

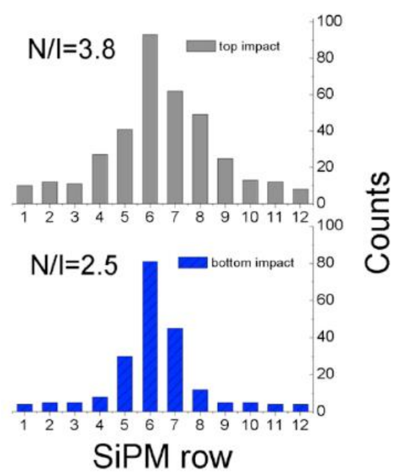

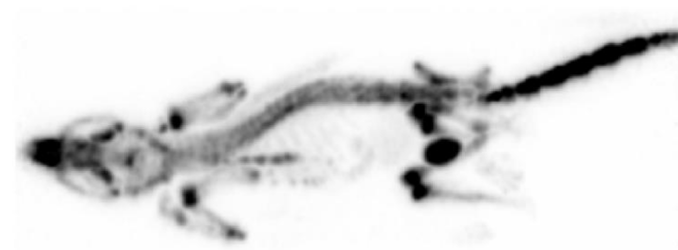

Monolithic cristal
Statistical positionning

Performances

TEP

Résolution spatiale

$$\mathrm{FWHM} = 1.25\sqrt{(d/2)^2 + b^2 + (0.0022D)^2 + r^2 + p^2}$$

Portée du positon r
Acolinéarité $0{,}0022\ D$

Taille du détecteur d
Erreur de codage $b \sim d/3$

Erreur de parallaxe

$$p = \alpha \frac{r}{\sqrt{r^2 + R^2}}$$

Echantillonnage

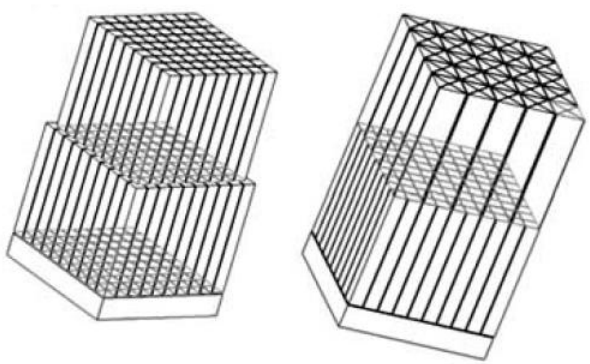

Peng, Curr Pharm Biotechnol 2010

Dual layer crystals
Offset positions
Mixed shapes

Performances

TEP

Résolution spatiale

$$\mathrm{FWHM} = 1.25\sqrt{(d/2)^2 + b^2 + (0.0022D)^2 + r^2 + p^2}$$

Portée du positon r
Acolinéarité $0{,}0022\ D$

Taille du détecteur d
Erreur de codage $b \sim d/3$

Erreur de parallaxe

$$p = \alpha \frac{r}{\sqrt{r^2 + R^2}}$$

Echantillonnage

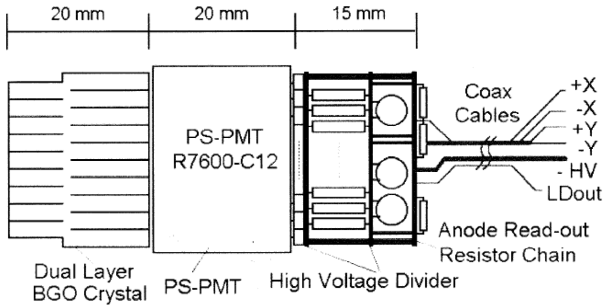

Zhang, IEEE Trans Nucl Sci 2002

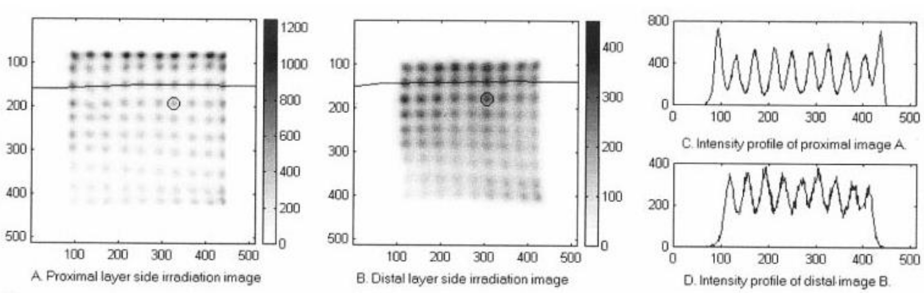

Dual layer crystals - *Offset positions*

Performances

TEP

Résolution spatiale

$$\mathrm{FWHM} = 1.25\sqrt{(d/2)^2 + b^2 + (0.0022D)^2 + r^2 + p^2}$$

Portée du positon r
Acolinéarité 0,0022 D

Taille du détecteur d
Erreur de codage $b \sim d/3$

Erreur de parallaxe

$$p = \alpha \frac{r}{\sqrt{r^2 + R^2}}$$

Echantillonnage

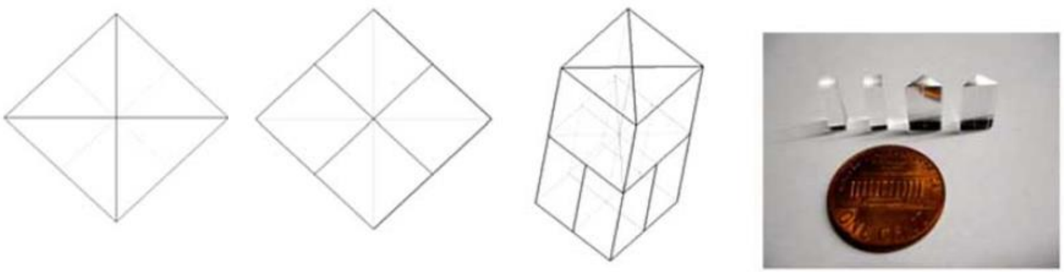

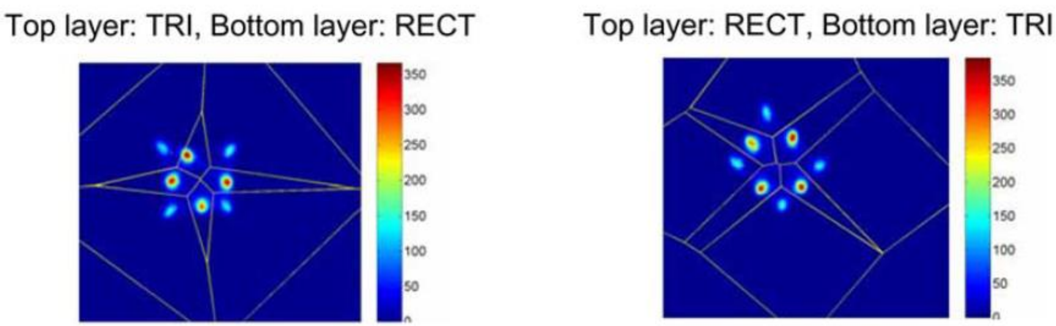

Peng, Curr Pharm Biotechnol 2010

Dual layer crystals - *Mixed shapes*

Performances

TEP

Résolution spatiale

Portée du positon r
Acolinéarité $0{,}0022\,D$

Taille du détecteur d
Erreur de codage $b \sim d/3$

Erreur de parallaxe

$$p = \alpha \frac{r}{\sqrt{r^2 + R^2}}$$

Echantillonnage

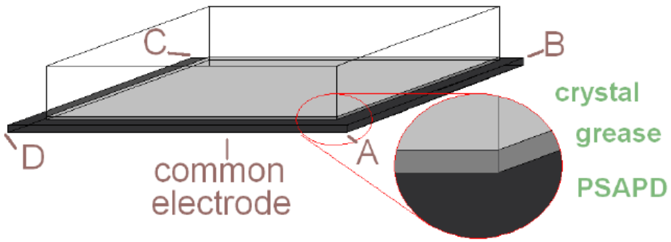

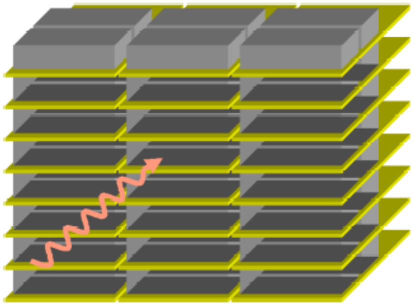

8x3 LSO 1x1x3 mm^3

Foudray, IEEE Nucl Sci Symp 2006

Performances

TEP

Résolution spatiale

Portée du positon r
Acolinéarité $0{,}0022\ D$

Taille du détecteur d
Erreur de codage $b \sim d/3$

Erreur de parallaxe

$$p = \alpha \frac{r}{\sqrt{r^2 + R^2}}$$

Echantillonnage

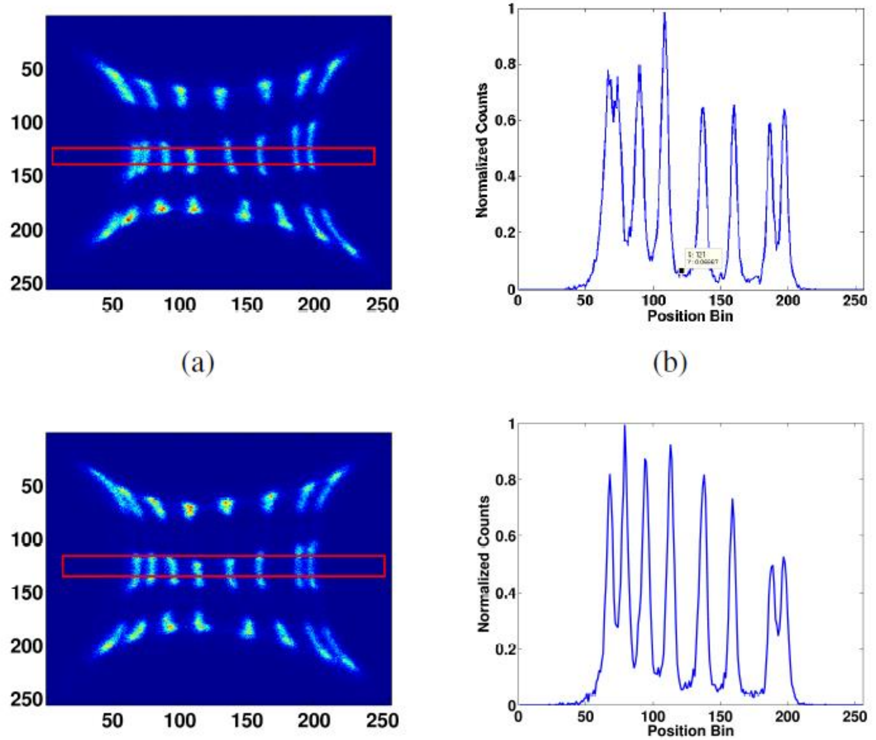

(a) (b)

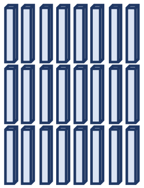

8x3 LSO 1x1x3 mm^3

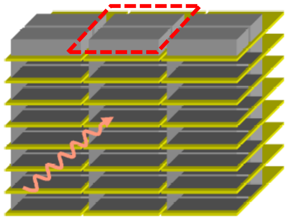

Foudray, IEEE Nucl Sci Symp 2006

Performances

TEP

Résolution spatiale

Portée du positon r
Acolinéarité $0{,}0022\ D$

Taille du détecteur d
Erreur de codage $b \sim d/3$

Erreur de parallaxe

$$p = \alpha \frac{r}{\sqrt{r^2 + R^2}}$$

Echantillonnage

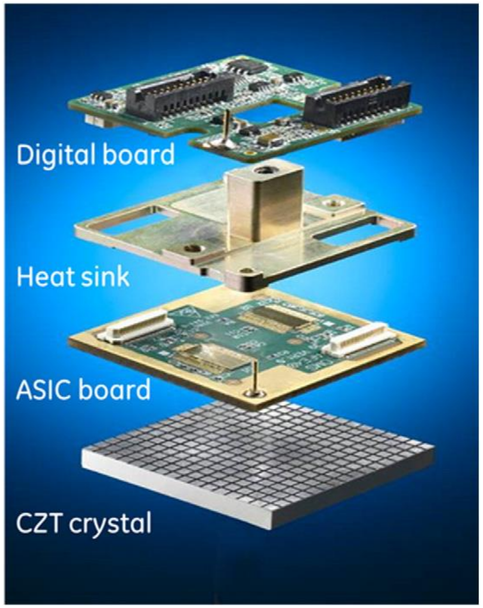

Slomka, Prog Cardiovasc Dis 2015

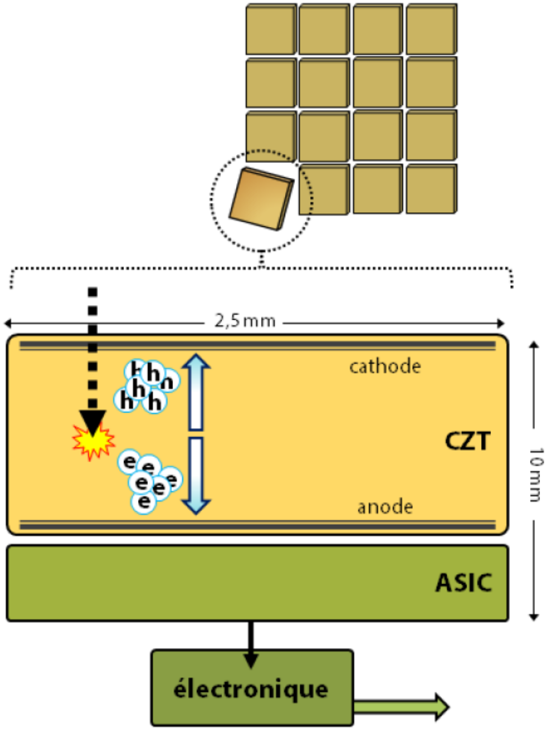

Ben Bouallègue, Med Nucl 2015

TEP

Résolution spatiale

Portée du positon r
Acolinéarité $0{,}0022\ D$

Taille du détecteur d
Erreur de codage $b \sim d/3$

Erreur de parallaxe

$$p = \alpha \frac{r}{\sqrt{r^2 + R^2}}$$

Echantillonnage

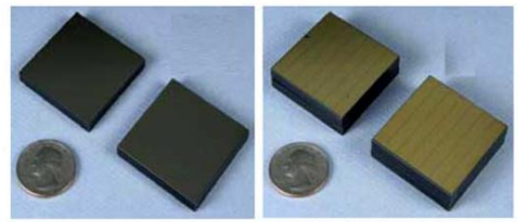

Anode side	Cathode side

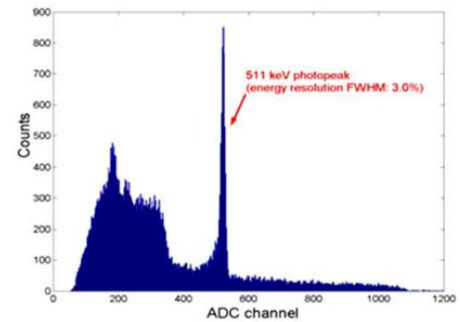

Scintillator	Density (g/cm^3)	Effective Atomic Number (Z)	Linear Attenuation Coefficient (cm^{-1})	Decay Time (ns)	Light output (light photons/MeV Annihilation Photon)
NaI	3.67	50.8	0.35	230	41,000
$Bi_4(GeO_4)_3$ (BGO)	7.06	75.2	0.96	300	7,000
$Lu_2(SiO_4)O:Ce$ (LSO)	7.40	66.4	0.86	40	26,000
$Gd_2(SiO_4)O:Ce$ (GSO)	6.71	59.4	0.70	60	10,000
$Cd_{0.9}Zn_{0.1}Te$ (CZT)	5.61	48	0.50	N/A	200,000

Peng, Curr Pharm Biotechnol 2010

Pouvoir d'arrêt : 86% à 4cm (LSO 82% à 2 cm)
ΔE/E ~ 2-3% (100000 e^- / LSO 2500 e^-)

Performances

TEP

Résolution spatiale

Portée du positon r
Acolinéarité $0{,}0022\ D$

Taille du détecteur d
Erreur de codage $b \sim d/3$

Erreur de parallaxe

$$p = \alpha \frac{r}{\sqrt{r^2 + R^2}}$$

Echantillonnage

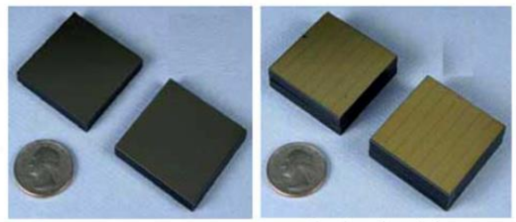

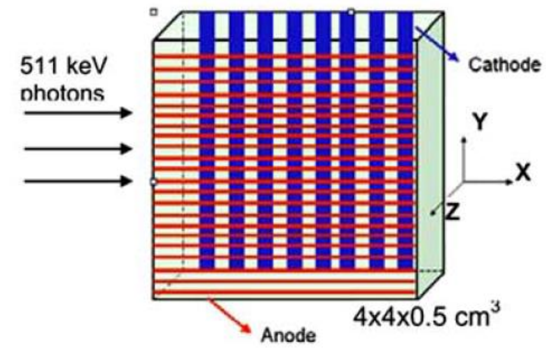

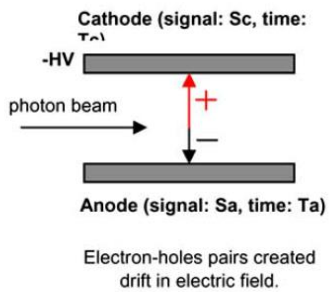

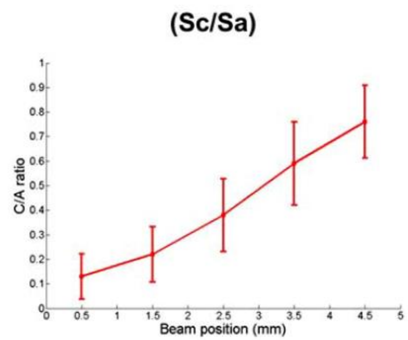

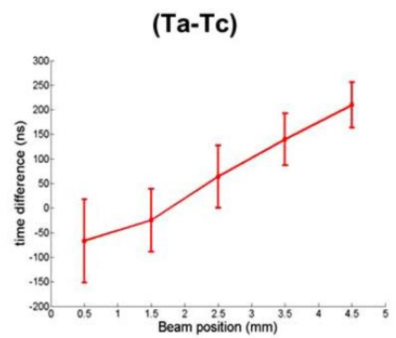

Peng, Curr Pharm Biotechnol 2010

Pouvoir d'arrêt : 86% à 4cm (LSO 82% à 2 cm)
ΔE/E ~ 2-3% (100000 e$^-$ / LSO 2500 e$^-$)
Résolution spatiale 1 mm (3D)

Performances

TEP

Résolution spatiale

Portée du positon r
Acolinéarité $0{,}0022\ D$

Taille du détecteur d
Erreur de codage $b \sim d/3$

Erreur de parallaxe

$$p = \alpha \frac{r}{\sqrt{r^2 + R^2}}$$

Echantillonnage

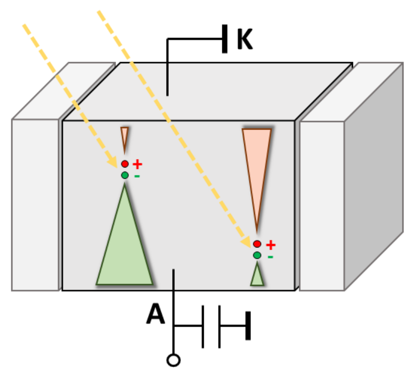

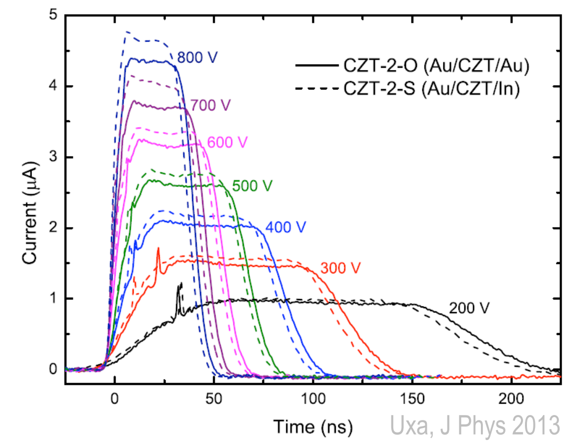

Uxa, J Phys 2013

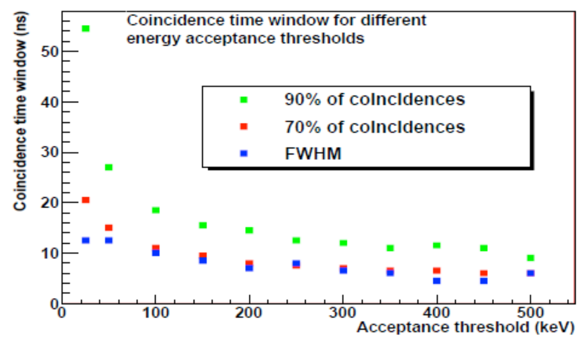

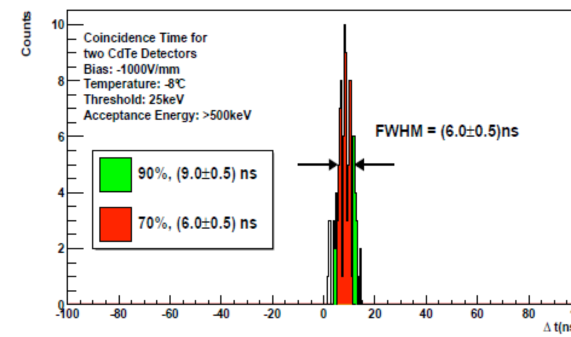

Arino, J Instrum 2013

Pouvoir d'arrêt : 86% à 4cm (LSO 82% à 2 cm)
ΔE/E ~ 2-3% (100000 e$^-$ / LSO 2500 e$^-$)
Résolution spatiale 1 mm (3D)
Résolution temporelle ~ 5-10 ns

Performances

TEP

Résolution spatiale

Portée du positon r
Acolinéarité $0{,}0022\,D$

Taille du détecteur d
Erreur de codage $b \sim d/3$

Erreur de parallaxe

$$p = \alpha \frac{r}{\sqrt{r^2 + R^2}}$$

Echantillonnage

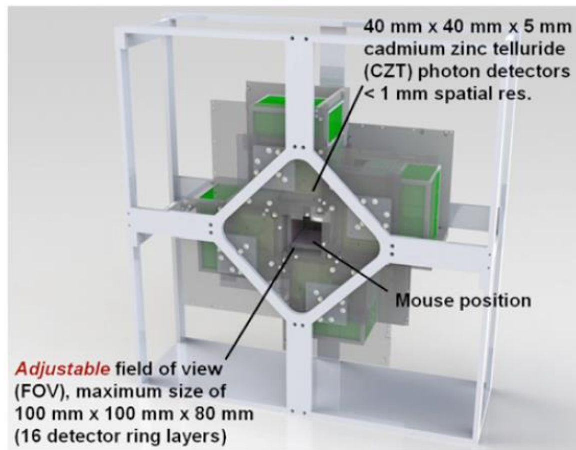

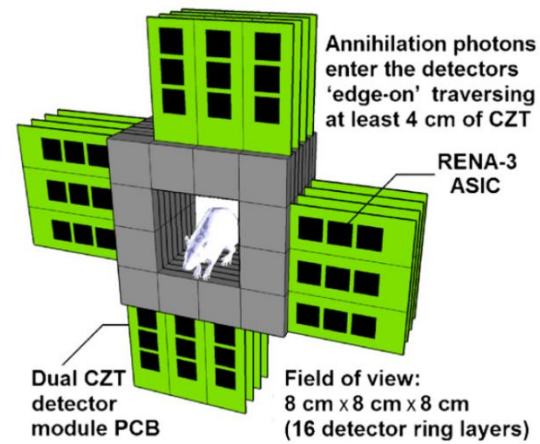

Gu, Phys Med Biol 2014

Pouvoir d'arrêt : 86% à 4cm (LSO 82% à 2 cm)
ΔE/E ~ 2-3% (100000 e^- / LSO 2500 e^-)
Résolution spatiale 1 mm (3D)
Résolution temporelle ~ 5-10 ns

Performances

TEP

Résolution en énergie

> Scintillation
> Transfert
> PMT

Rendement lumineux
Non-linéarité (ph-e/MeV)

Q_0 : ph-e
N: photons
p : transfert
M : gain PMT

$$\boxed{\overline{Q_0} = \overline{N}\overline{p}\overline{M}}$$

$$\left(\frac{\Delta E}{E}\right)_{FWHM} = 2.35\sqrt{v(Q_0)}.$$

$$v(Q_0) \approx \left[v(N) - \frac{1}{\overline{N}}\right] + v(p) + \frac{1 + v(M)}{\overline{N}\overline{p}}. \qquad \boxed{\sim \frac{1}{\overline{N}\,\overline{p}}}$$

Dorenbos, IEEE Trans Nucl Sci 1995

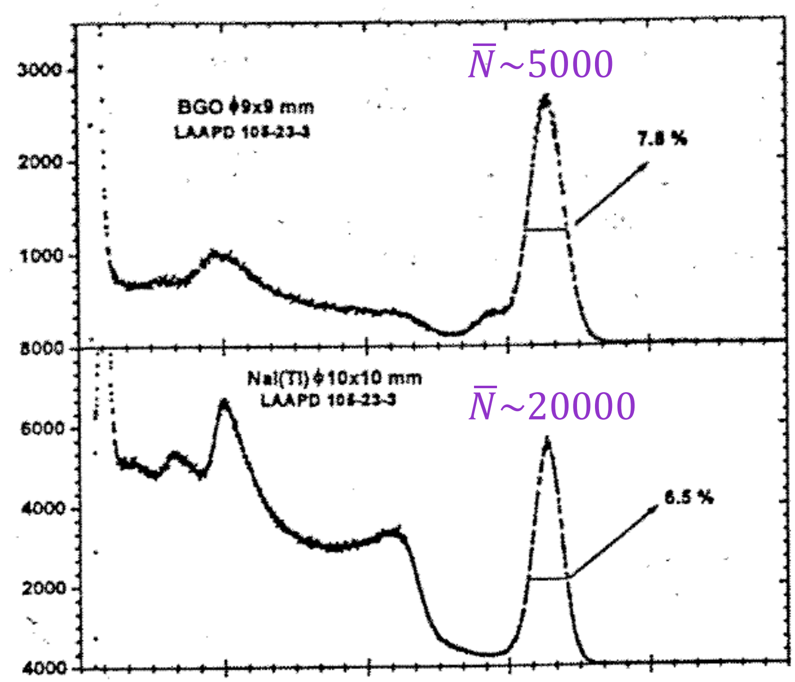

Moszynski, IEEE Nucl Sci Symp 1997

Performances

TEP

Résolution temporelle

Flux p-e : $\dfrac{N_{pe}}{\tau_d}$ (ns^{-1})

$$N_{ph} = E\ L\ F \quad \begin{cases} E \text{ énergie (MeV)} \\ L \text{ luminosité (ph / MeV)} \\ F \text{ efficacité de collection (\%)} \end{cases}$$

$$L = 10^6 \frac{R\ S}{\beta E_g} \quad \begin{cases} \beta E_g \text{ énergie d'ionisation (eV)} \\ S \text{ efficacité de transfert (\%)} \\ R \text{ efficacité de radiation (\%)} \end{cases}$$

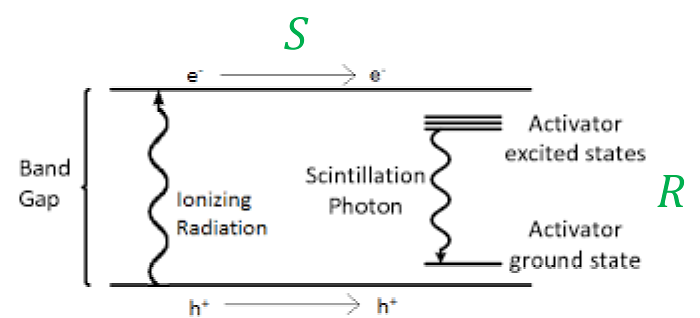

$$N_{pe} = Q N_{ph}$$ Q efficacité quantique photo-K (%)

TEP

Résolution temporelle

Flux p-e : $\frac{N_{pe}}{\tau_d}$

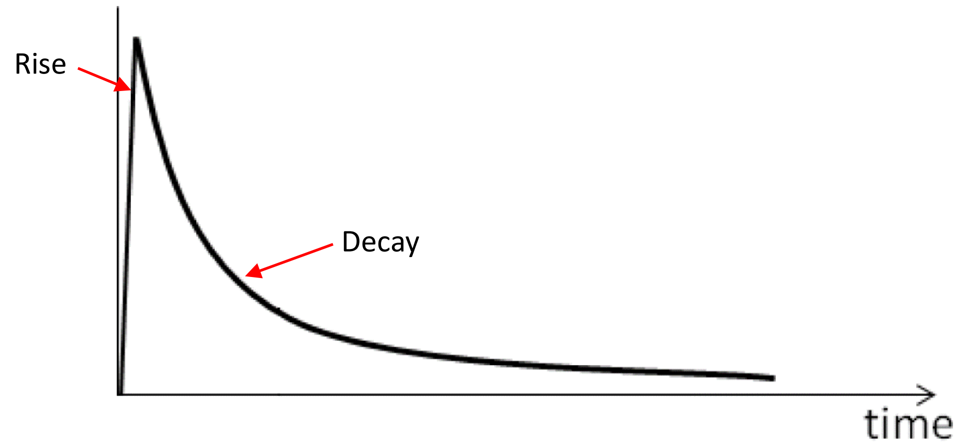

	NaI(Tl)	LSO	$LaBr_3$:Ce	BaF_2
Luminosity (photons MeV^{-1})	42 000	35 000	70 000	1800
Rise time τ_r (ns)	0.6	0.03	0.2[a]	0.0
Decay time τ_d (ns)	230	40	17[a]	0.8
Photoelectrons N_{pe}[b]	3000	2500	5000	130
N_{pe}/τ_d	13.0	62.5	294	162

Derenzo, Phys Med Biol 2014

Performances

TEP

Résolution temporelle

Flux p-e : $\frac{N_{pe}}{\tau_d}$

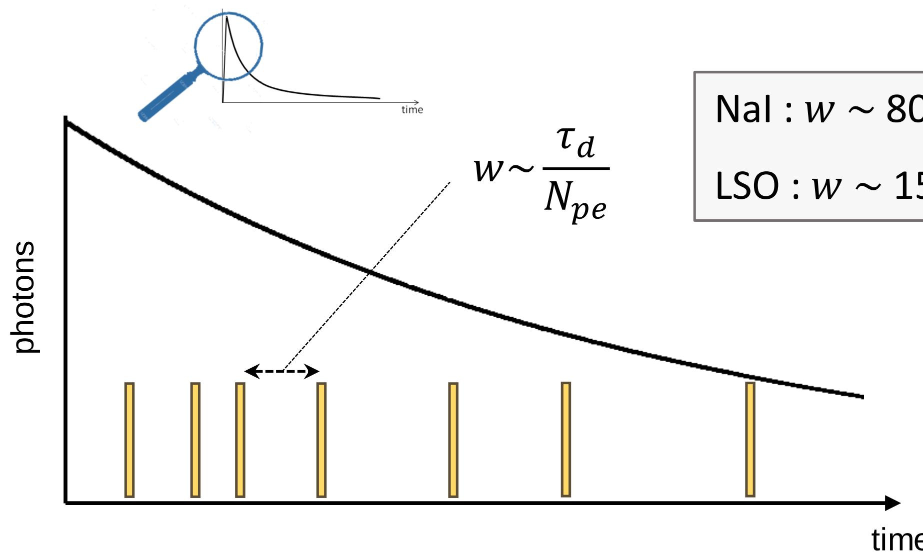

NaI : $w \sim$ 80 ps

LSO : $w \sim$ 15 ps

	NaI(Tl)	LSO	$LaBr_3$:Ce	BaF_2
Luminosity (photons MeV^{-1})	42 000	35 000	70 000	1800
Rise time τ_r (ns)	0.6	0.03	0.2	0.0
Decay time τ_d (ns)	230	40	17	0.8
Photoelectrons N_{pe}	3000	2500	5000	130
N_{pe}/τ_d	13.0	62.5	294	162

Derenzo, Phys Med Biol 2014

Performances

TEP

Résolution temporelle

Flux p-e : $\frac{N_{pe}}{\tau_d}$

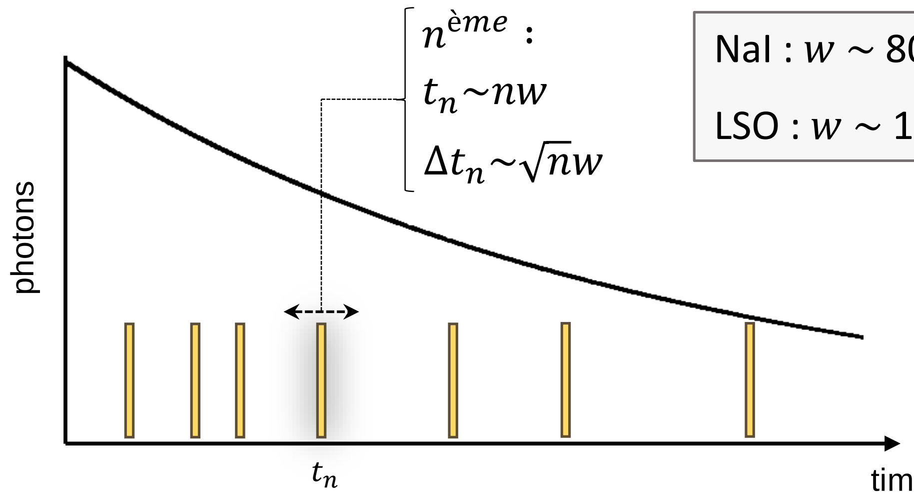

NaI : $w \sim$ 80 ps

LSO : $w \sim$ 15 ps

	NaI(Tl)	LSO	$LaBr_3$:Ce	BaF_2
Luminosity (photons MeV^{-1})	42 000	35 000	70 000	1800
Rise time τ_r (ns)	0.6	0.03	0.2	0.0
Decay time τ_d (ns)	230	40	17	0.8
Photoelectrons N_{pe}	3000	2500	5000	130
N_{pe}/τ_d	13.0	62.5	294	162

Derenzo, Phys Med Biol 2014

Performances

TEP

Résolution temporelle

Flux p-e : $\dfrac{N_{pe}}{\tau_d}$

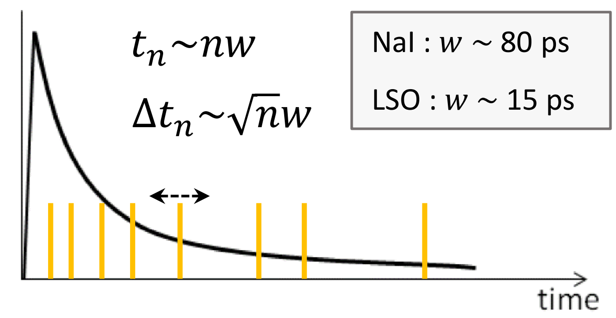

$\circledast$

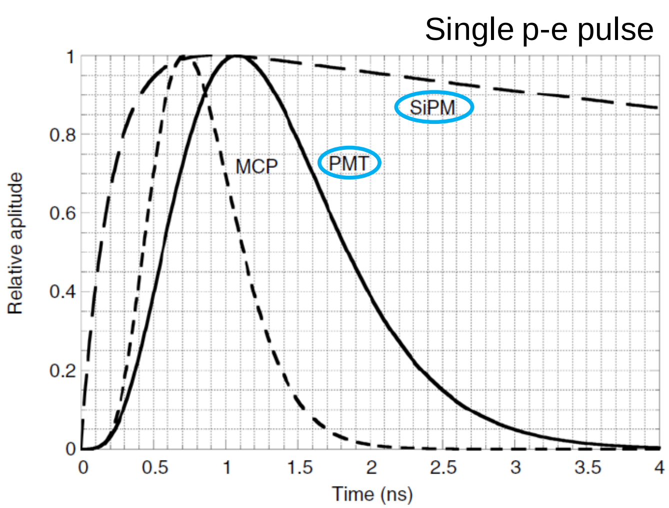

Derenzo, Phys Med Biol 2014

Performances

TEP

Résolution temporelle

Flux p-e : $\dfrac{N_{pe}}{\tau_d}$

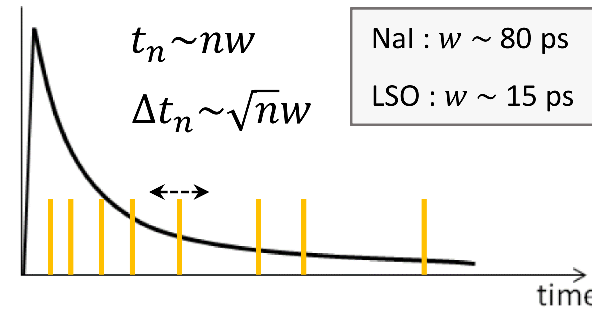

NaI : $w \sim 80$ ps

LSO : $w \sim 15$ ps

$\circledast$

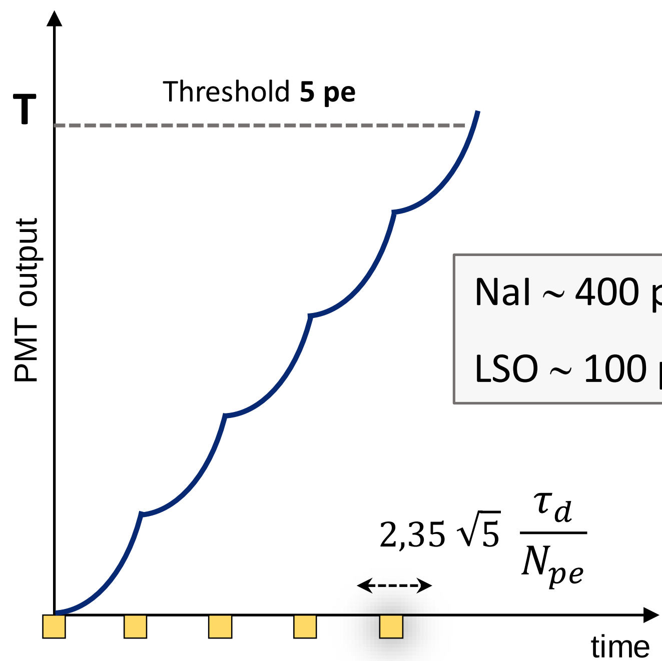

NaI ~ 400 ps

LSO ~ 100 ps

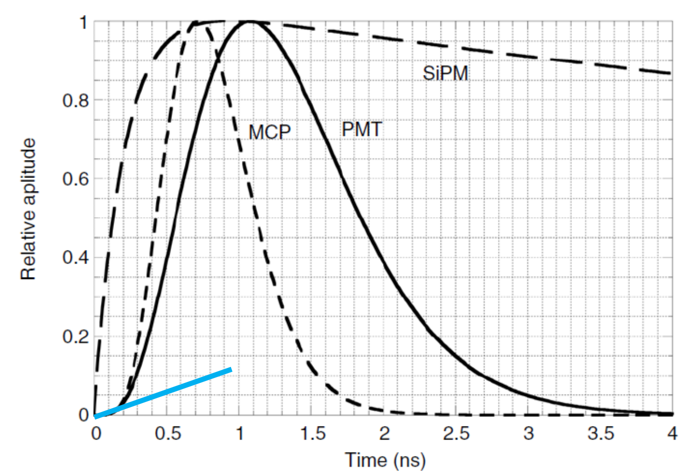

Performances

TEP

Résolution temporelle

Flux p-e : $\frac{N_{pe}}{\tau_d}$

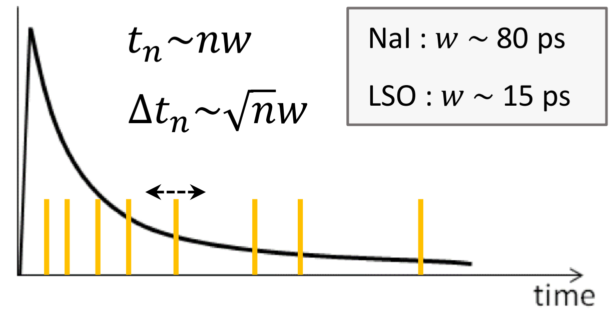

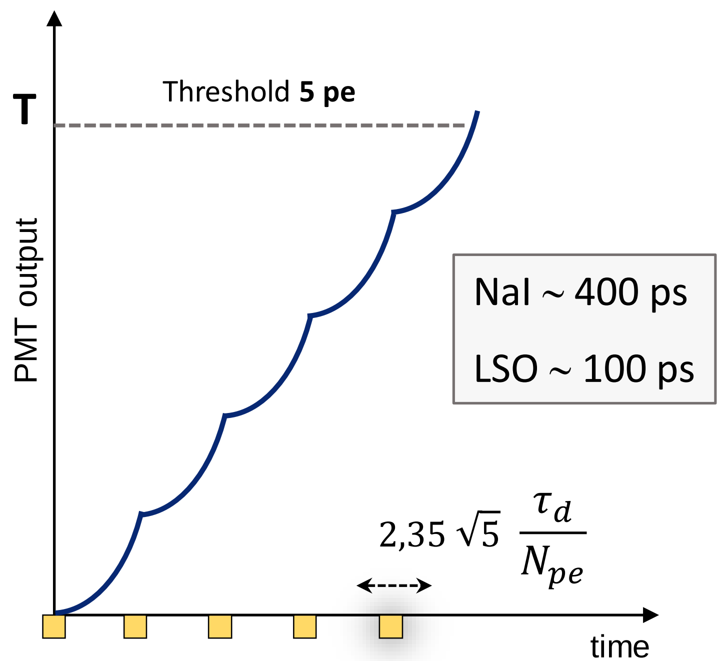

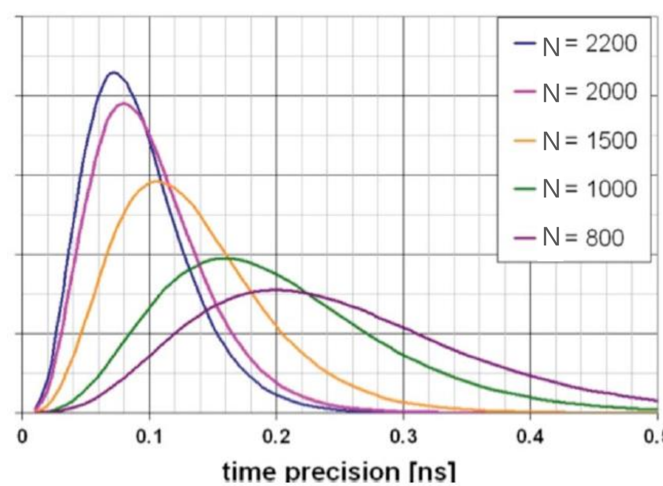

Lecoq, IEEE Trans Nucl Sci 2010

Performances

TEP

Résolution temporelle

Flux p-e

Cristal

Rise time

	NaI(Tl)	LSO	$LaBr_3$:Ce	BaF_2
Luminosity (photons MeV^{-1})	42 000	35 000	70 000	1800
Rise time τ_r (ns)	0.6	0.03	0.2[a]	0.0
Decay time τ_d (ns)	230	40	17[a]	0.8
Photoelectrons N_{pe}[b]	3000	2500	5000	130
N_{pe}/τ_d	13.0	62.5	294	162

Derenzo, Phys Med Biol 2014

Performances

TEP

Résolution temporelle

Flux p-e

Cristal
- **Rise time**
- **Profondeur d'interaction**

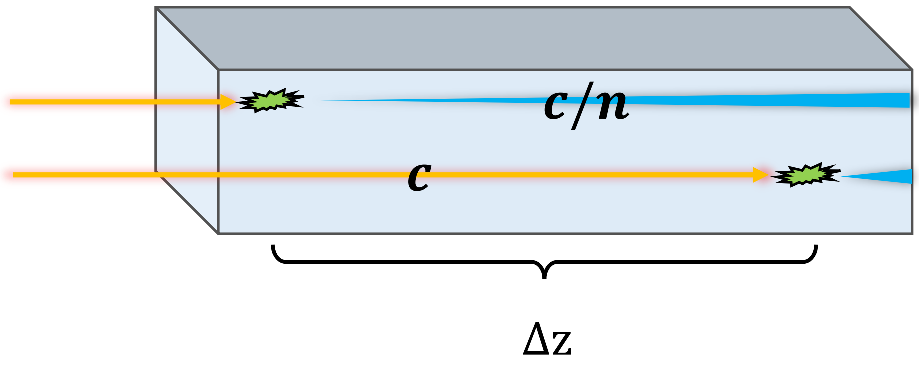

$$\Delta t = \Delta z \frac{n-1}{c} \sim \frac{\Delta z}{c}$$

~ 20 ps / cm

Performances

TEP

Résolution temporelle

Flux p-e

Cristal
- **Rise time**
- **Profondeur d'interaction**
- **Dispersion optique**

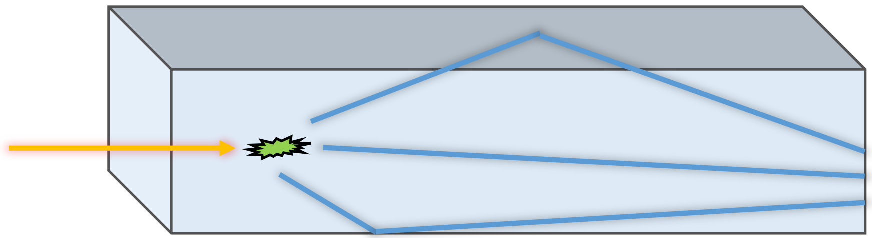

~ 100 ps

Performances

Institut National des Sciences et Techniques Nucléaires

TEP

Résolution temporelle

Flux p-e

Cristal
- **Rise time**
- **Profondeur d'interaction**
- **Dispersion optique**

PMT
- **Fluctuation TT**

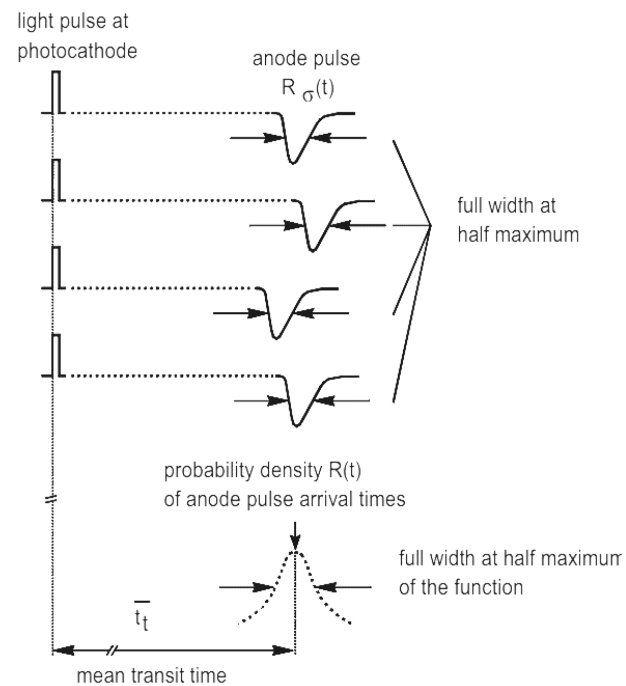

< 100 ps

Fig.21 Response-pulse jitter due to transit-time fluctuations.

lmu.web.psi.ch

Performances

TEP

Résolution temporelle

Flux p-e

Cristal
- **Rise time**
- **Profondeur d'interaction**
- **Dispersion optique**

PMT
- **Fluctuation TT**
- **Bruit**

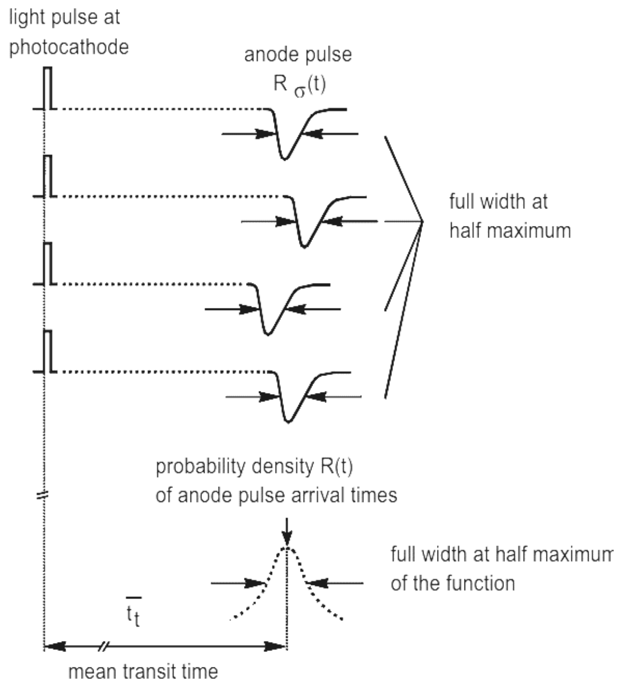

Fig.21 Response-pulse jitter due to transit-time fluctuations.

lmu.web.psi.ch

< 100 ps

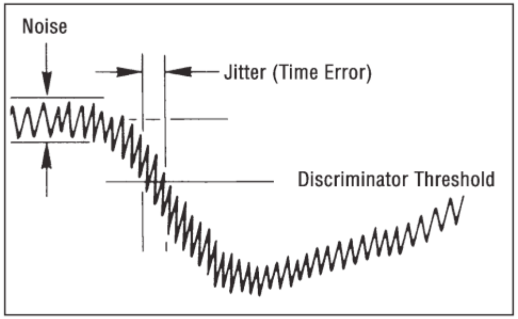

ortec-online.com

Performances

TEP

NECR **(noise equivalent count rate)**

True T
Random R
Scatter S
Prompt $P = T + R + S$

$T' = P - R - S$
$\langle T' \rangle = \langle P \rangle + \langle R \rangle + \langle S \rangle$

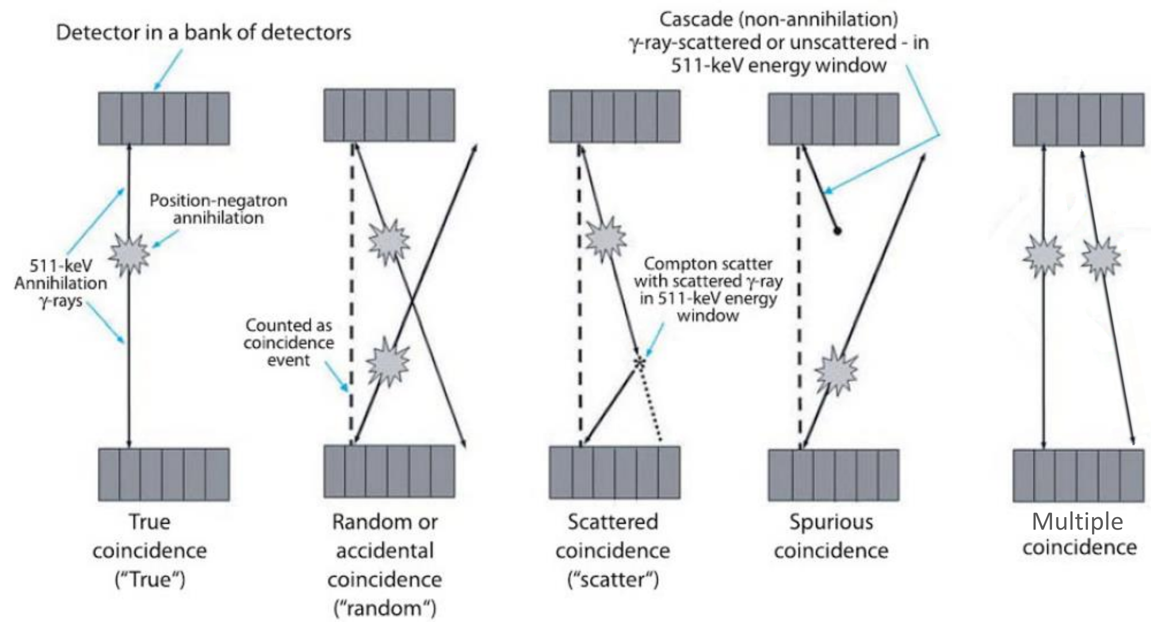

Biersack, Springer 2007

Performances

TEP

NECR

True T
Random R
Scatter S
Prompt $P = T + R + S$

$T' = P - R - S$
$\langle T' \rangle = \langle P \rangle + \langle R \rangle + \langle S \rangle$

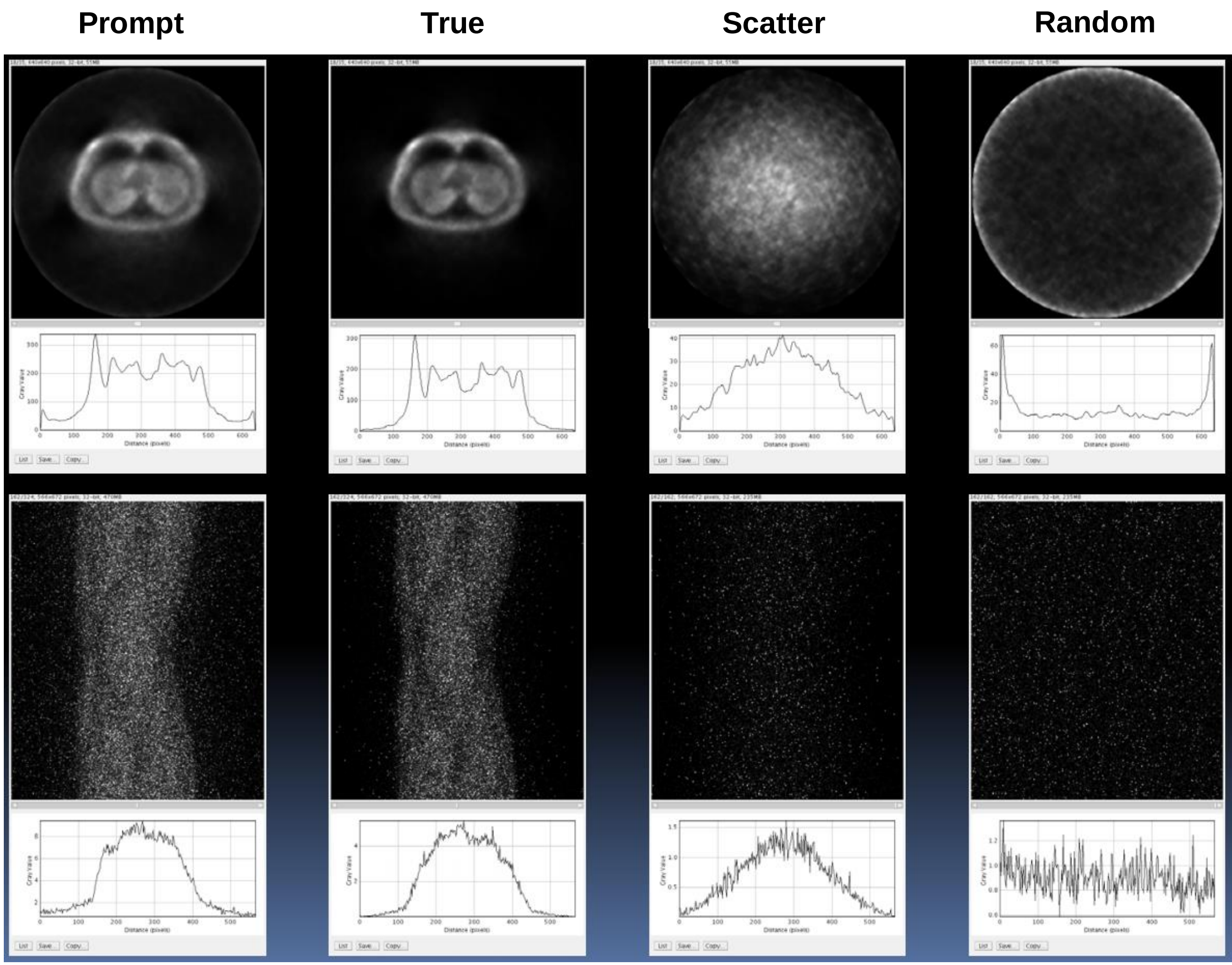

aapm.org

Performances

TEP

NECR **(noise equivalent count rate)**

True T
Random R
Scatter S
Prompt $P = T + R + S$

$$NECR = \frac{T^2}{T + S + kR}$$

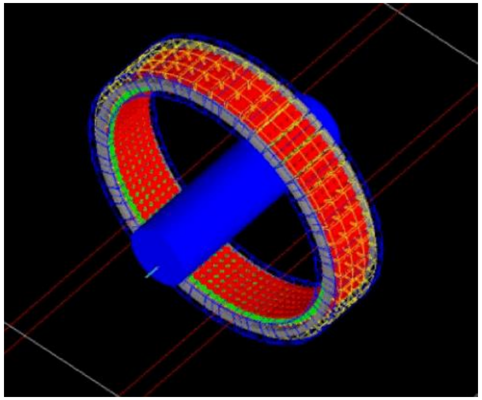

Nikolopoulos, J Nucl Med Radiat Ther 2014

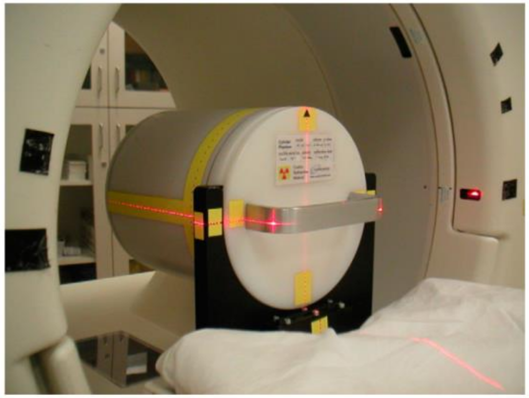

Lodge, J Nucl Med 2009

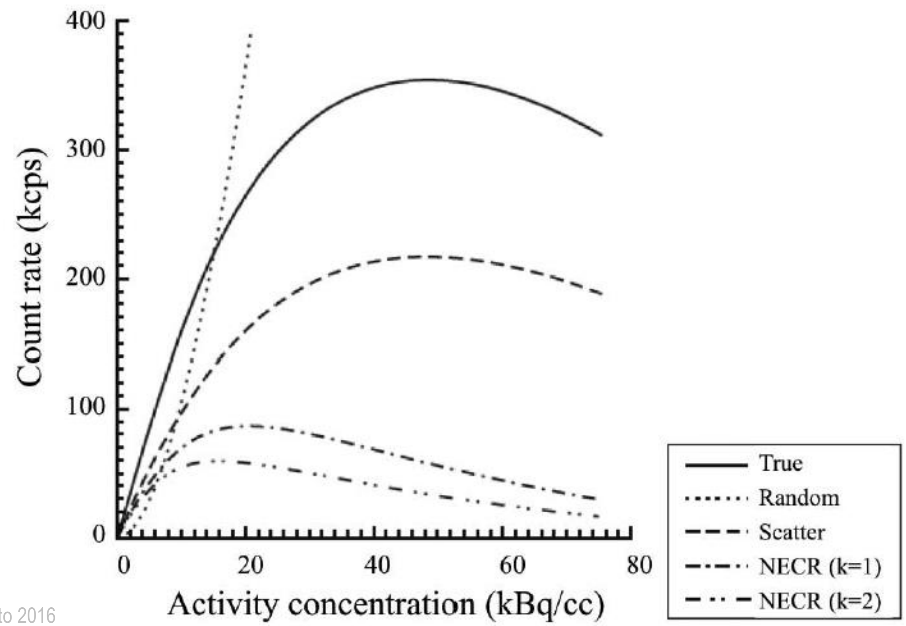

Del Guerra, Riv Nuov Cimento 2016

Performances

TEP

NECR **(noise equivalent count rate)**

True T
Random R
Scatter S
Prompt $P = T + R + S$

$$\boxed{NECR = \frac{T^2}{T + S + kR}}$$

$$R_{ij} = C_i \times C_j \times 2\tau$$

$$\boxed{R \propto A^2}$$

$$\boxed{T \,\&\, S \;\propto A}$$

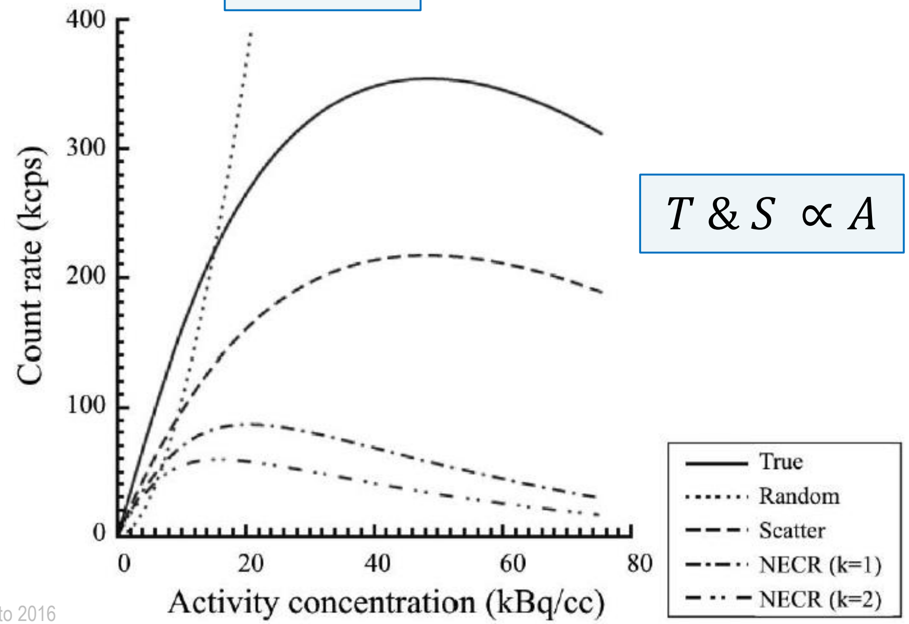

Del Guerra, Riv Nuov Cimento 2016

Performances

TEP

NECR **(noise equivalent count rate)**

True T
Random R
Scatter S
Prompt $P = T + R + S$

$$NECR = \frac{T^2}{T + S + kR}$$

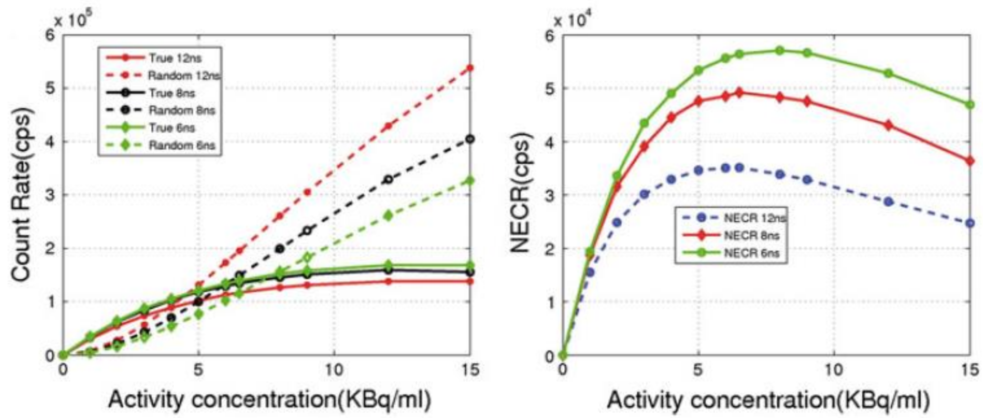

Saaidi, Bas Conc Nucl Phys 2016

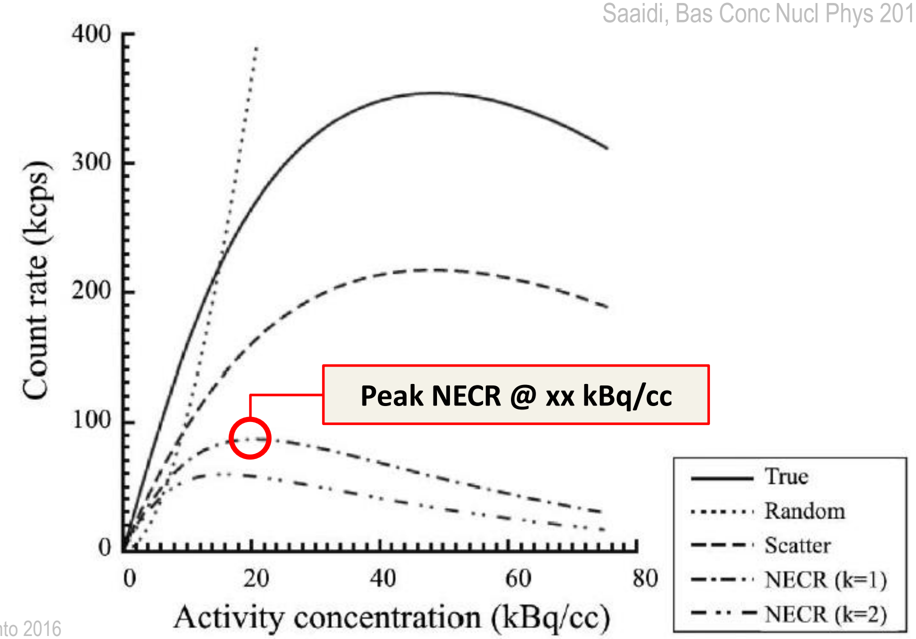

Del Guerra, Riv Nuov Cimento 2016

Performances

TEP

NECR (noise equivalent count rate)

True T
Random R
Scatter S
Prompt $P = T + R + S$

$$NECR = \frac{T^2}{T + S + kR}$$

$$\boxed{SNR^2 \propto NECR \times \Delta t}$$

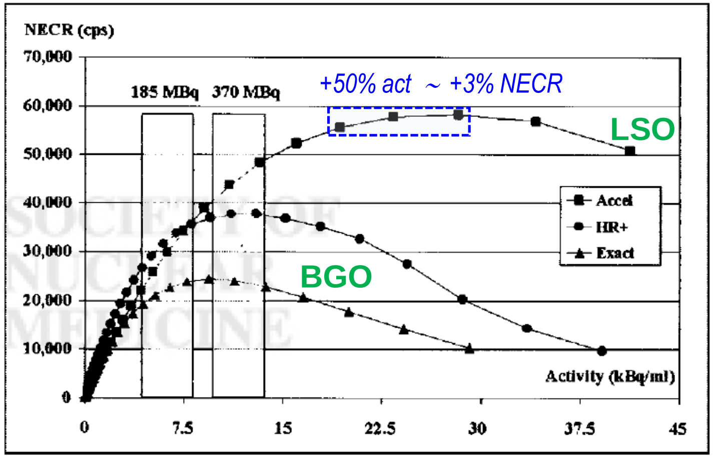

Tarantola, J Nucl Med 2003

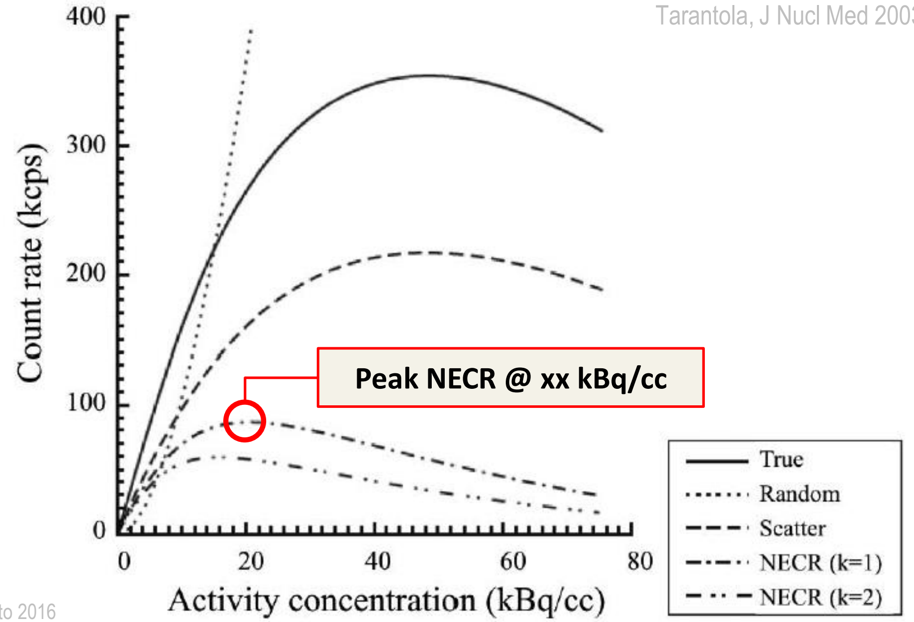

Del Guerra, Riv Nuov Cimento 2016

Performances

TEP

NECR **(noise equivalent count rate)**

True T
Random R
Scatter S
Prompt $P = T + R + S$

$$NECR = \frac{T^2}{T + S + kR}$$

SF **(scatter fraction)**

$$\boxed{SF = \frac{S}{T + S}}$$

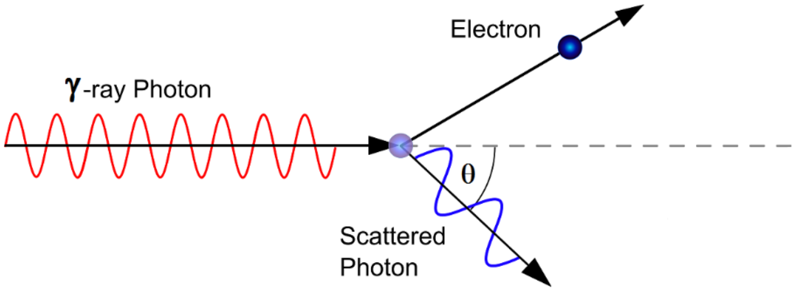

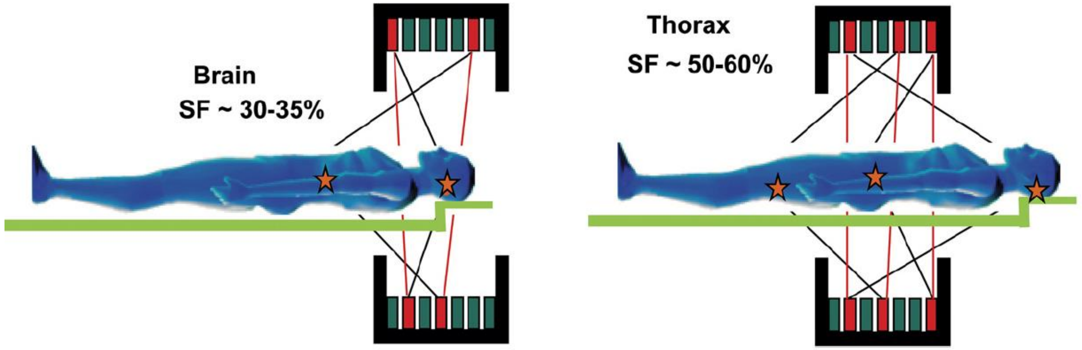

Zaidi, PET Clin 2007

Performances

TEP

NECR **(noise equivalent count rate)**

True T
Random R
Scatter S
Prompt $P = T + R + S$

$$NECR = \frac{T^2}{T + S + kR}$$

SF **(scatter fraction)**

$$\boxed{SF = \frac{S}{T + S}}$$

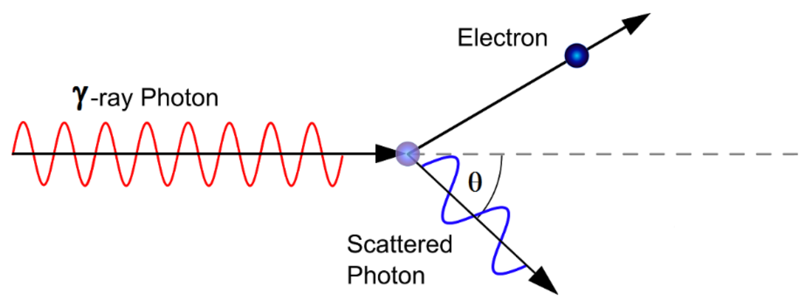

$$E'_\gamma(\theta) = \frac{E_\gamma}{1 + \left(\frac{E_\gamma}{m_e c^2}\right)(1 - \cos\theta)}$$

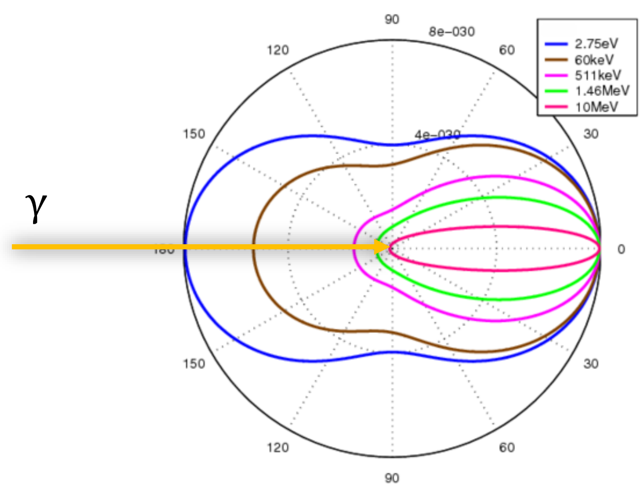

Performances

TEP

NECR **(noise equivalent count rate)**

True T
Random R
Scatter S
Prompt $P = T + R + S$

$$NECR = \frac{T^2}{T + S + kR}$$

SF **(scatter fraction)**

$$\boxed{SF = \frac{S}{T + S}}$$

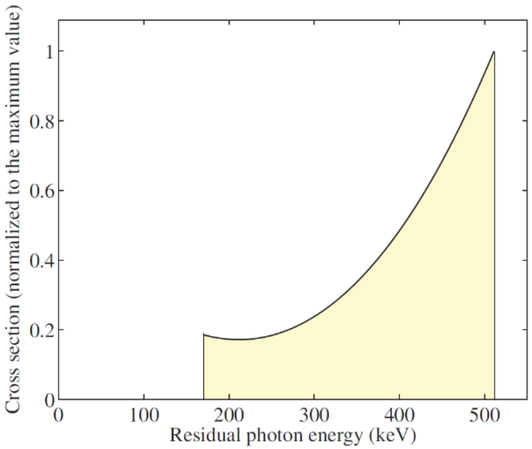

Del Guerra, Riv Nuov Cimento 2016

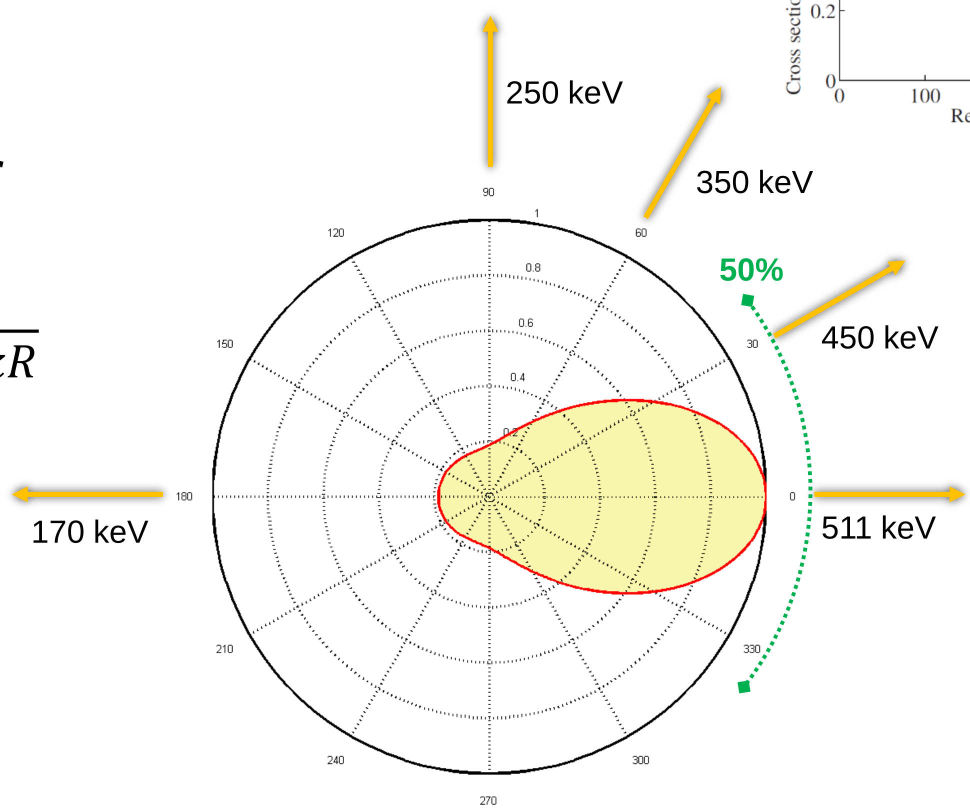

Performances

TEP

NECR **(noise equivalent count rate)**

True T
Random R
Scatter S
Prompt $P = T + R + S$

$$NECR = \frac{T^2}{T + S + kR}$$

SF **(scatter fraction)**

$$\boxed{SF = \frac{S}{T + S}}$$

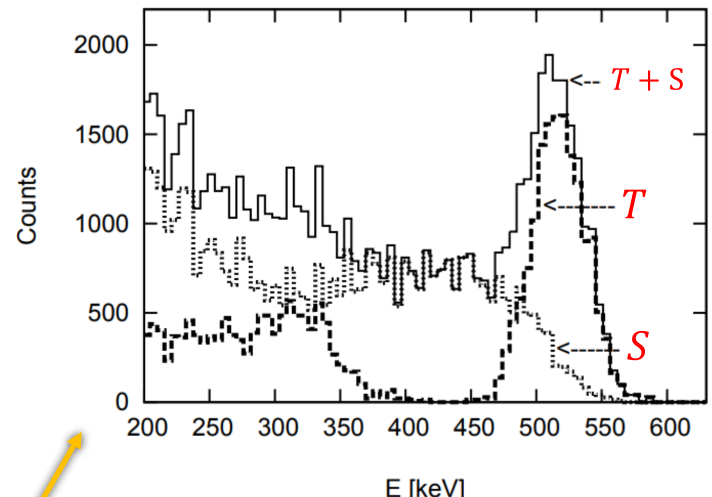

Popescu, Phys Med Biol 2006

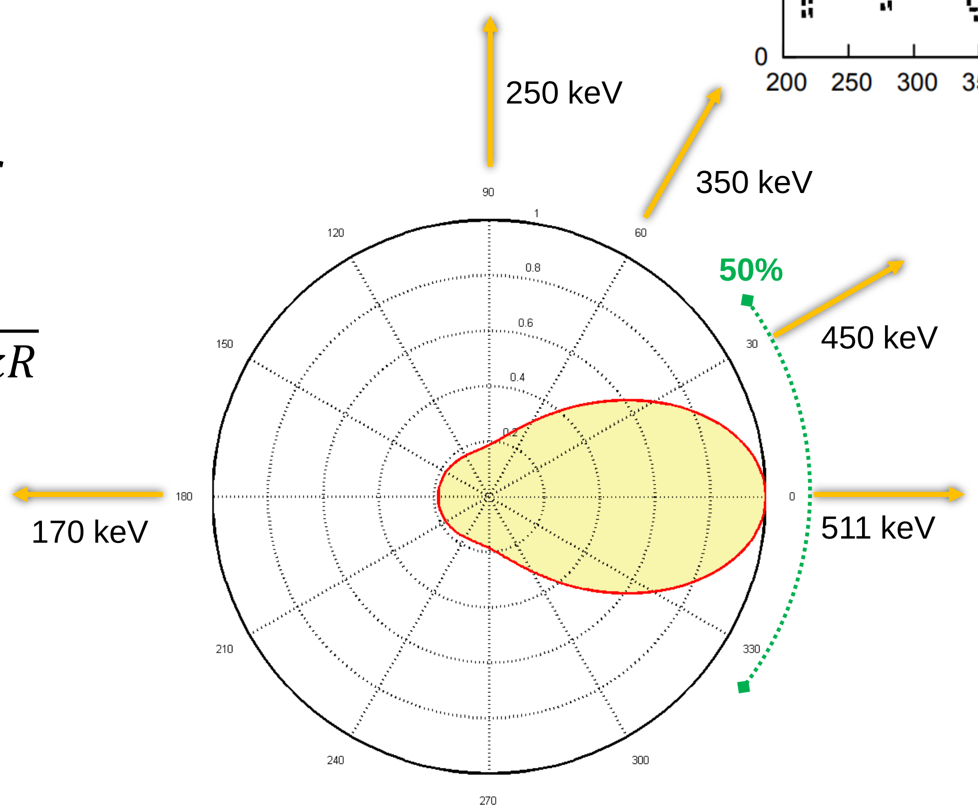

Performances

TEP

NECR **(noise equivalent count rate)**

True T
Random R
Scatter S
Prompt $P = T + R + S$

$$NECR = \frac{T^2}{T + S + kR}$$

SF **(scatter fraction)**

$$SF = \frac{S}{T + S}$$

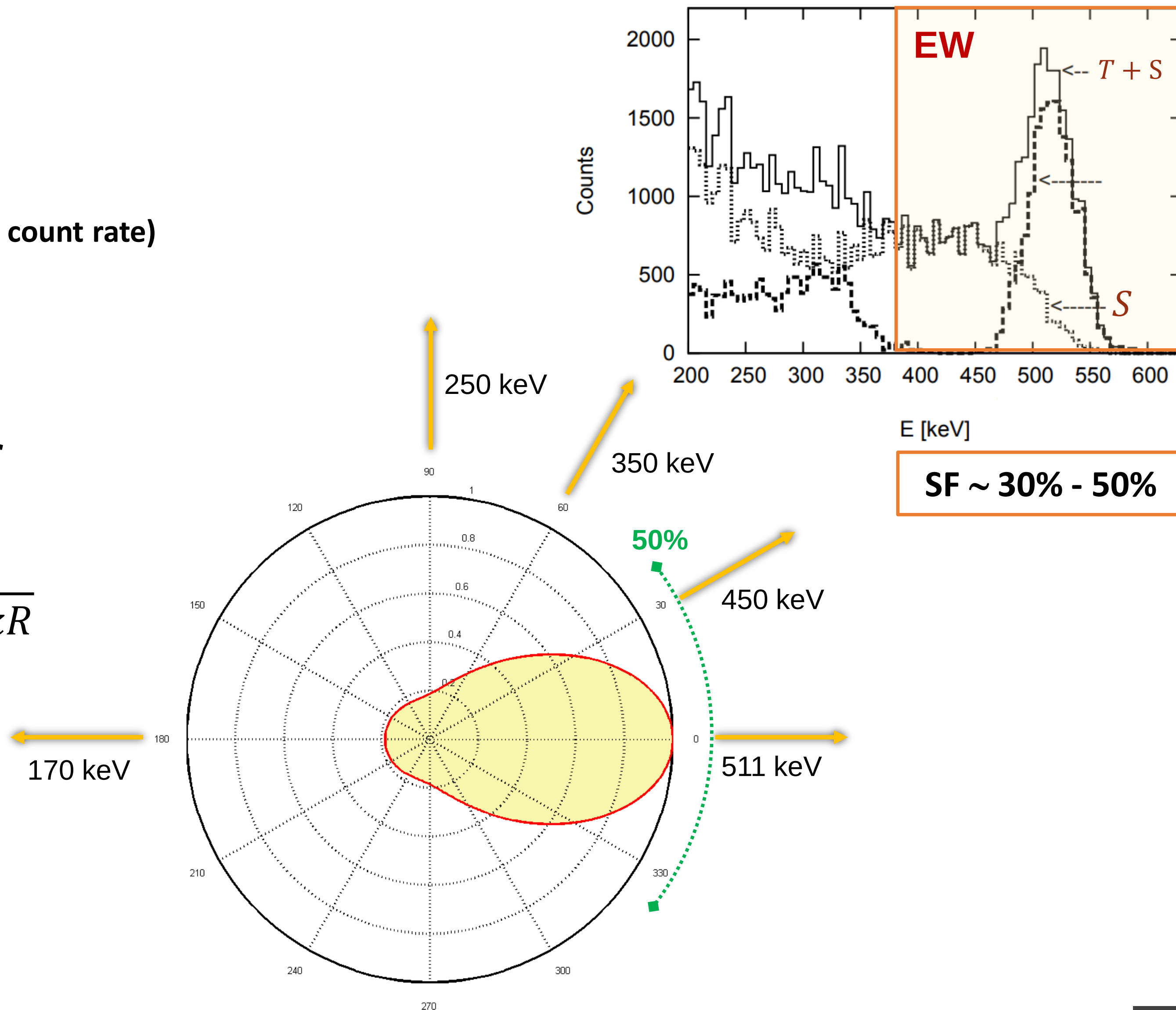

TEP

NECR (noise equivalent count rate)

True T
Random R
Scatter S
Prompt $P = T + R + S$

$$NECR = \frac{T^2}{T + S + kR}$$

SF (scatter fraction)

$$\boxed{SF = \frac{S}{T + S}}$$

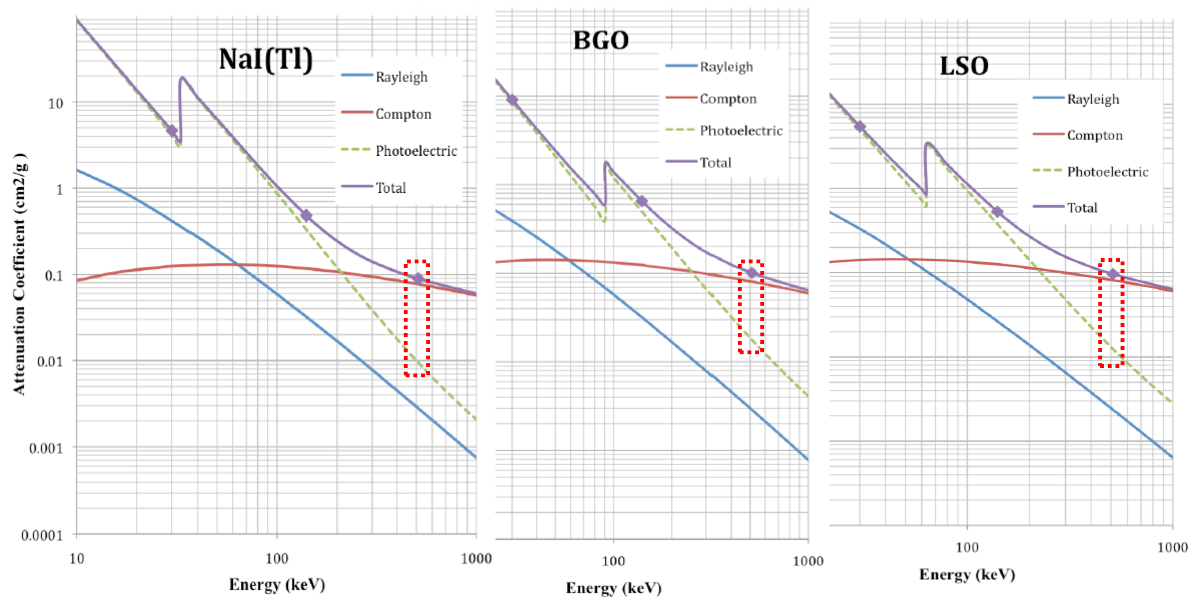

à 25 mm	PE 10% C 47%	PE 36% C 55%	PE 28% C 60%

Performances

TEP

NECR **(noise equivalent count rate)**

True T
Random R
Scatter S
Prompt $P = T + R + S$

$$NECR = \frac{T^2}{T + S + kR}$$

SF **(scatter fraction)**

$$\boxed{SF = \frac{S}{T + S}}$$

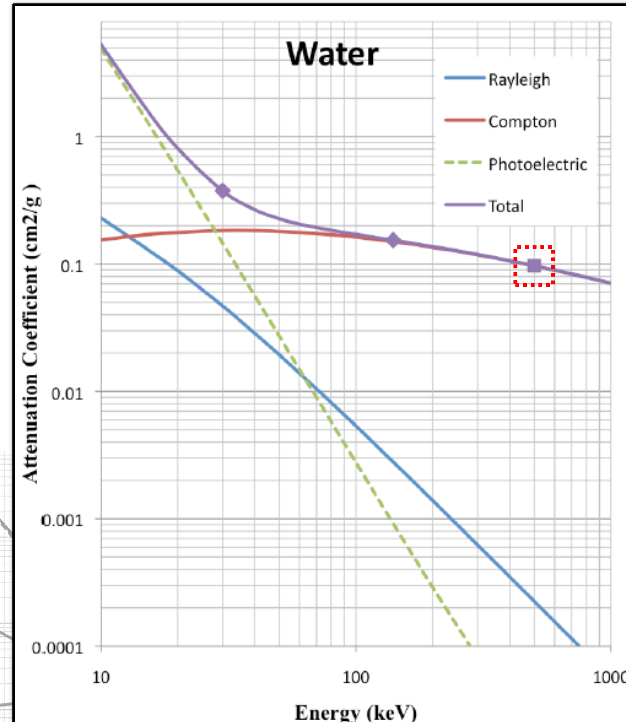

à 20 cm

PE 0,1%
C 85%

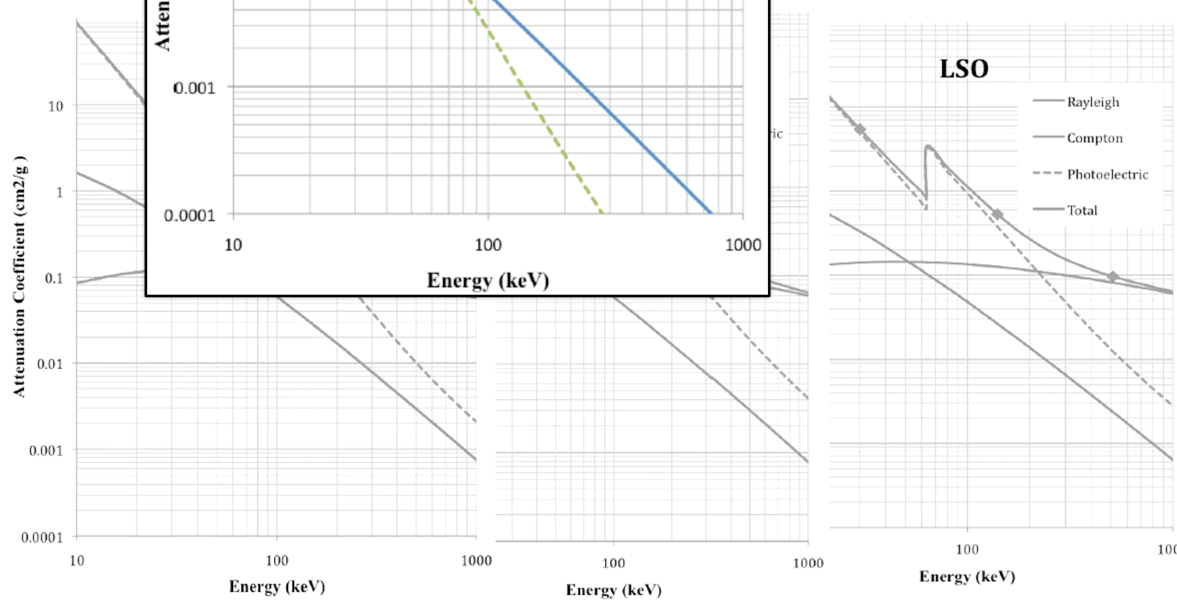

à 25 mm

PE 10% C 47%	PE 36% C 55%	PE 28% C 60%

Performances

TEP

NECR **(noise equivalent count rate)**

True T
Random R
Scatter S
Prompt $P = T + R + S$

$$NECR = \frac{T^2}{T + S + kR}$$

SF **(scatter fraction)**

$$SF = \frac{S}{T + S}$$

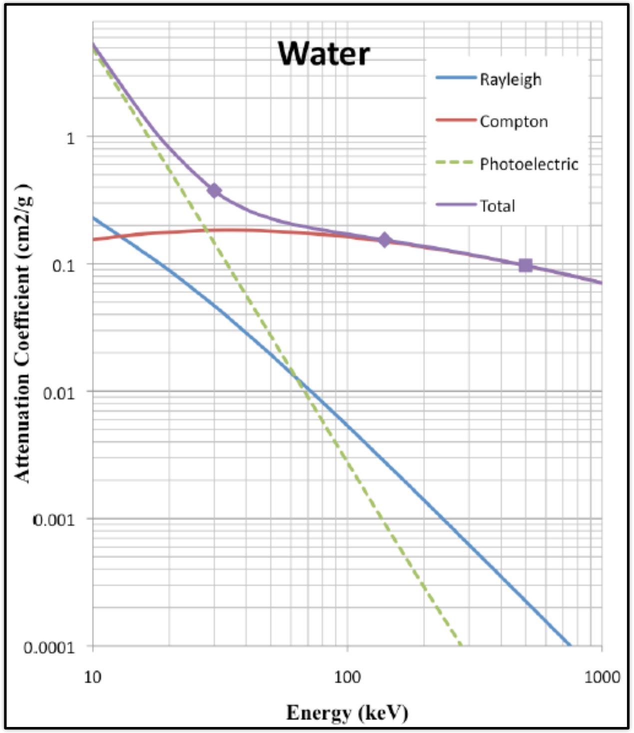

à 20 cm

PE 0,1%
C 85%

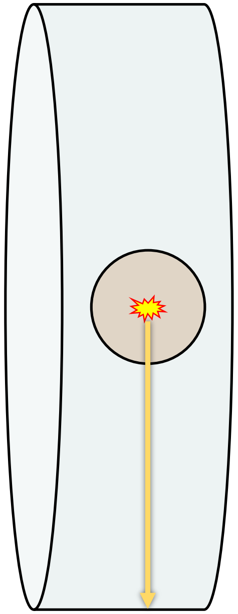

Performances

TEP

NECR **(noise equivalent count rate)**

True T
Random R
Scatter S
Prompt $P = T + R + S$

$$NECR = \frac{T^2}{T + S + kR}$$

SF **(scatter fraction)**

$$SF = \frac{S}{T + S}$$

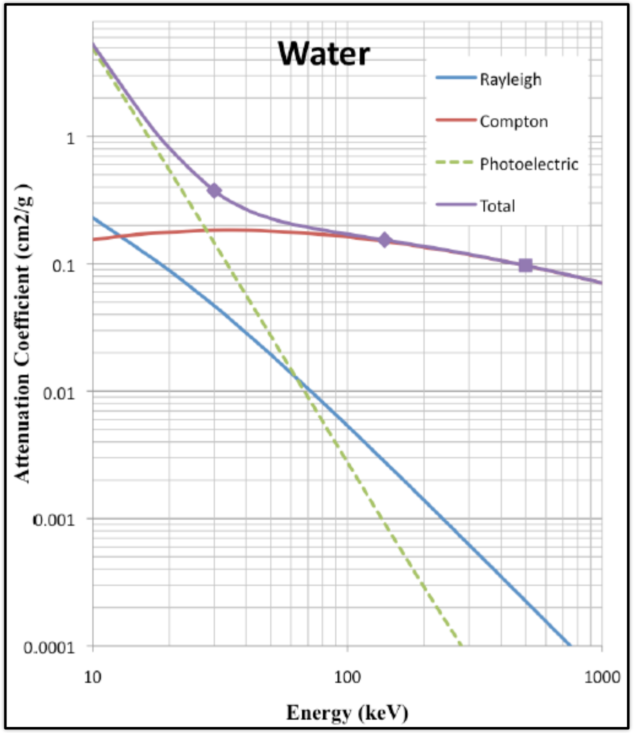

à 20 cm

PE 0,1%
C 85%

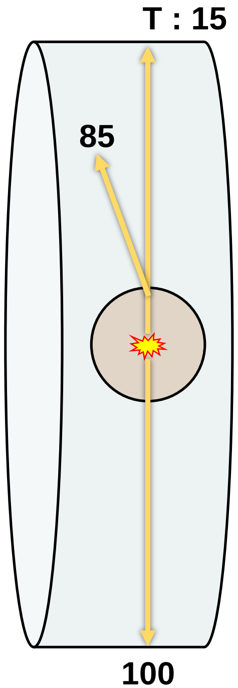

Performances

TEP

NECR **(noise equivalent count rate)**

True T
Random R
Scatter S
Prompt $P = T + R + S$

$$NECR = \frac{T^2}{T + S + kR}$$

SF **(scatter fraction)**

$$SF = \frac{S}{T + S}$$

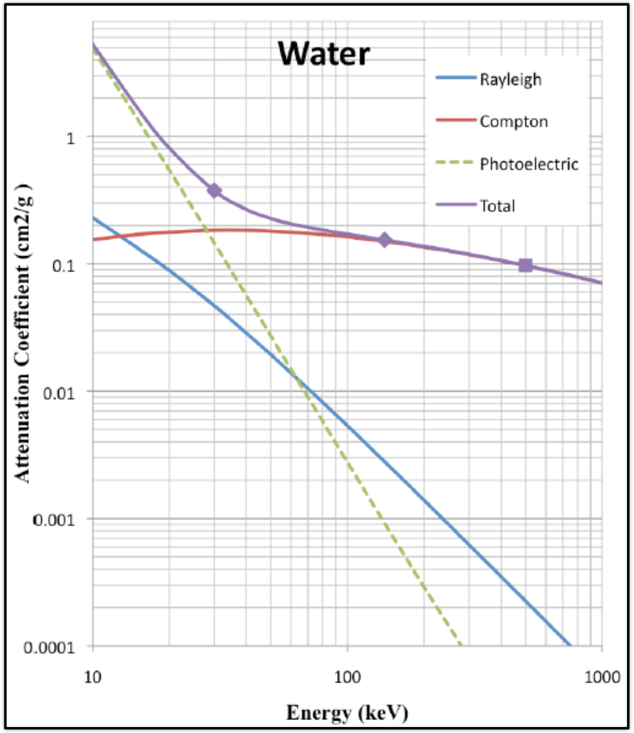

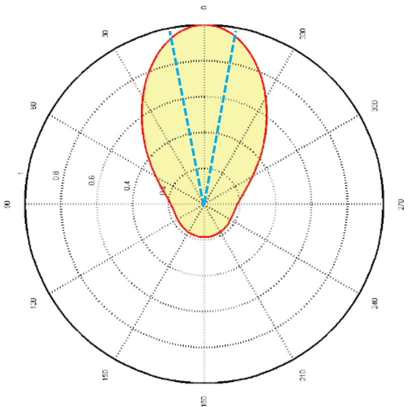

à 20 cm

PE 0,1%
C 85%

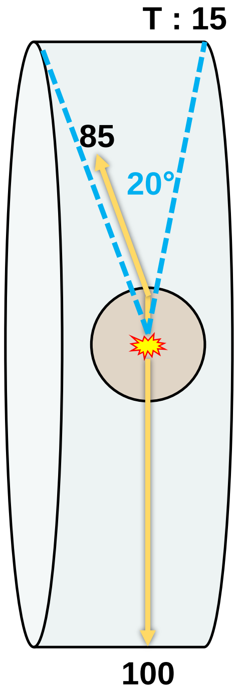

Performances

TEP

NECR **(noise equivalent count rate)**

True T
Random R
Scatter S
Prompt $P = T + R + S$

$$NECR = \frac{T^2}{T + S + kR}$$

SF **(scatter fraction)**

$$SF = \frac{S}{T + S}$$

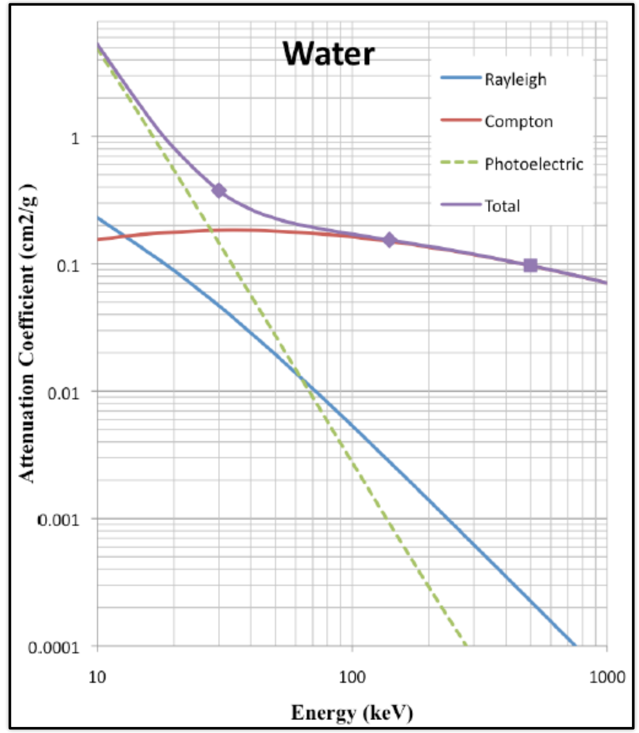

à 20 cm

PE 0,1%
C 85%

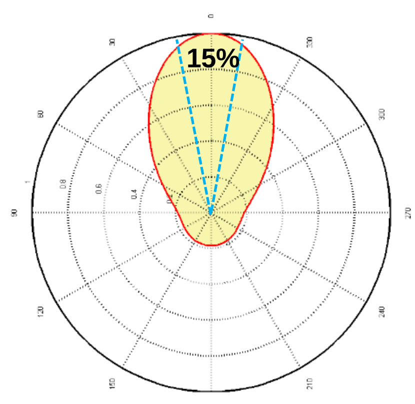

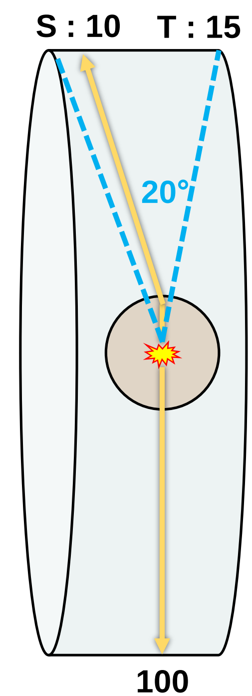

Performances

TEP

NECR (noise equivalent count rate)

True T
Random R
Scatter S
Prompt $P = T + R + S$

$$NECR = \frac{T^2}{T + S + kR}$$

SF (scatter fraction)

$$SF = \frac{S}{T + S}$$

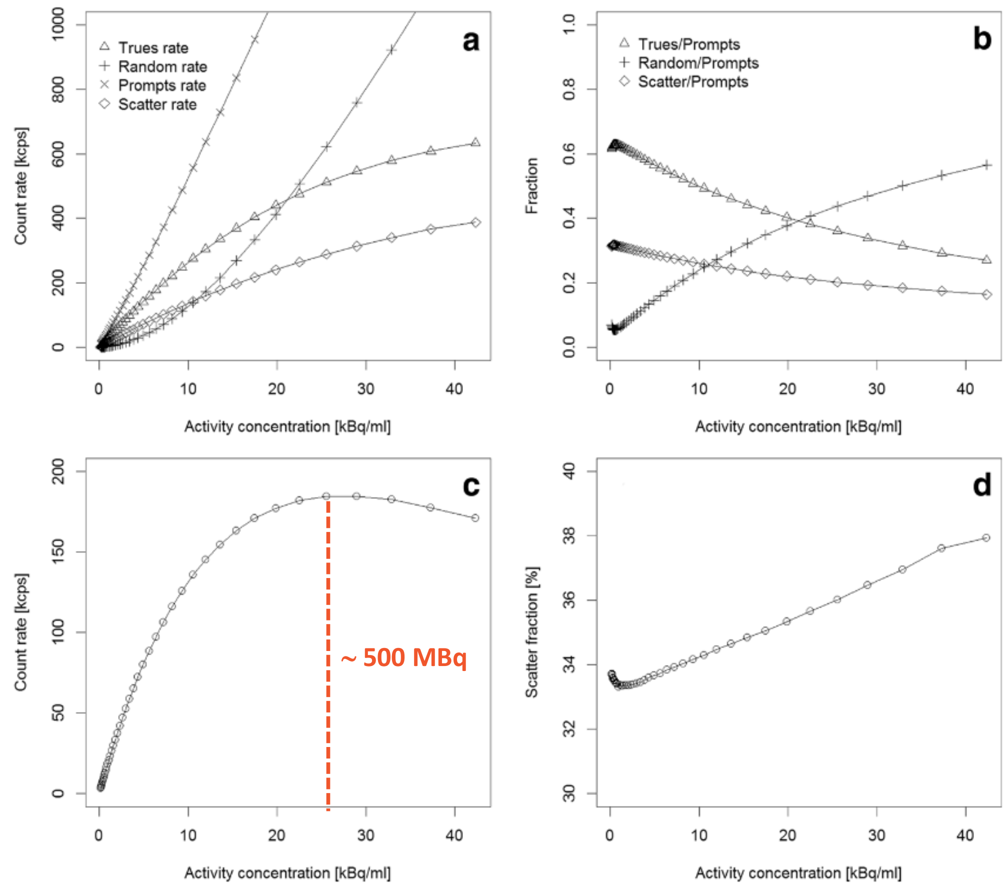

Fig. 3 mCT Flow. **a** Prompts, trues, randoms, and scatter count rates. **b** Fraction of trues, randoms, and scatter counts vs the total number of coincidences processed. **c** NECR curve for the measured range of activities. **d** Scatter fraction (in %) for the same range of activities

Rausch, EJNMMI Phys 2015

Performances

Table 2 Comparison of system characteristics across manufacturer PET/CT systems

Manufacture	GE	GE	Philips	Philips	Philips	Siemens	Siemens	Toshiba
PET/CT model	Discovery MI (4-ring) [51]	Discovery 690 [43]	Vereos (this work)	Ingenuity TF [44]	Gemini T [42]	Biograph mCT flow [45]	Biograph mCT [46, 47]	Celesteion [48–50]
Photo detector	SiPM	PMT	SiPM	PMT	PMT	PMT	PMT	PMT
Number of detectors	9792	256	23,040	420	560	768	768	480
Scintillator	LYSO	LYSO	LYSO	LYSO	LYSO	LSO	LSO	LYSO
Number of crystals	19,584	13,824	23,040	28,336	28,336	32,448	32,448	30,720
Crystal size (mm^3)	3.95 × 5.3 × 25	4.2 × 6.3 × 25	3.86 × 3.86 × 19	4 × 4 × 22	4 × 4 × 22	4 × 4 × 20	4 × 4 × 20	4 × 4 × 12
Ring diameter (cm)	74.4	81.0	76.4	90.0	90.3	84.2	84.2	88.0
Axial FOV (cm)	20.0	15.7	16.4	18.0	18.0	22.1	22.1	19.6
Plane spacing (mm)	n/a	n/a	1, 2, or 4	2 or 4	2 or 4	2	2	2
TOF Timing resolution (ps)	375	544	322	502	585	555	527	410
Sensitivity (cps/kBq)	13.7	7.4	5.7	7.3	6.6	9.6	9.7	4.0
Transverse resolution @ 1 cm (mm)	4.1	4.7	4.0	4.8	4.8	4.3	4.4	5.1
Transverse resolution @ 10 cm (mm)	5.0	5.1	4.4	5.1	5.2	4.9	4.9	5.1
Axial resolution @ 1 cm (mm)	4.5	4.7	4.0	4.7	4.8	4.3	4.4	5.0
Axial resolution @ 10 cm (mm)	6.0	5.6	4.8	5.2	4.8	5.9	5.7	5.4
Peak NECR (kcps @ kBq/mL)	193.4 @ 21.9	139.1 @ 29.0	171 @ 50.5	124.1 @ 20.3	125 @ 17.4	185 @ 29	156 @ 31.1	≥51 @ n/a
Energy resolution (%)	9.4	12.4	11.2	11.1	11.5	n/a	11.5	11.3
Scatter fraction at peak NECR (%)	40.6	37	30.8	36.7	27	33.4	32.7	42.7

Zhang, EJNMMI Res 2018

Contrôle qualité

Table 2 Routine QC tests for PET and PET/CT. *Equipment type*: coincidence, scintillator system (fixed and mobile systems)

Test	Purpose	Frequency	Comments
PET1. Physical inspection	To check gantry covers in tunnel and patient handling system	Daily	Inspect for mechanical and other defects that may compromise safety of patient or staff
PET2. Daily QC	To test and visualize proper functioning of detector modules; visual inspection of 2-D sinograms (automated)	Daily	To be performed with point or rod sources without attenuating object inside scanner field of view
PET3. Uniformity	To estimate axial uniformity across image planes 1−[max] by imaging a uniformly filled object	After maintenance/new setups/normalization	To be also performed after software upgrade or changes; the object could be a 20-cm diameter ^{68}Ge cylinder, or a refillable cylinder with ^{18}F
PET4. Normalization	To determine system response to activity inside the field of view	Variable (at least six-monthly)	Frequency of test depends on system reliability and service; must be performed after firmware upgrade and hardware service; use phantoms and instructions as recommended by manufacturer
PET5. Calibration	To determine calibration factor from image voxel intensity to true activity concentration	Variable (at least six-monthly)	Must follow a new normalization; follow the manufacturer's procedures
PET6. Spatial resolution	To measure spatial resolution of point source in sinogram and image space	Yearly	Use a ^{18}F point source (nonstandard) or linear source
PET7. Count rate performance	To measure count rate as a function of (decaying) activity over a wide range of activities	After new setups/normalization/recalibrations	To include count loss correction; and specific measurements of: (a) total/random/scatter/net true coincidences, and (b) noise equivalent count rate
PET8. Sensitivity	To measure the volume response of the system to a source of given activity concentration	Monthly	Perform according to NEMA NU2 standards with a set of sleeved rod sources [11]; an alternative method is given in NEMA-NU2 1994
PET9. Image quality	To check hot and cold spot image quality of standardized image quality phantom	Yearly	According to NEMA NU2 image quality test [11]; required after system installation, not mandatory during clinical operation

EANM, Eur J Nucl Med Mol Imaging 2010

Contrôle qualité

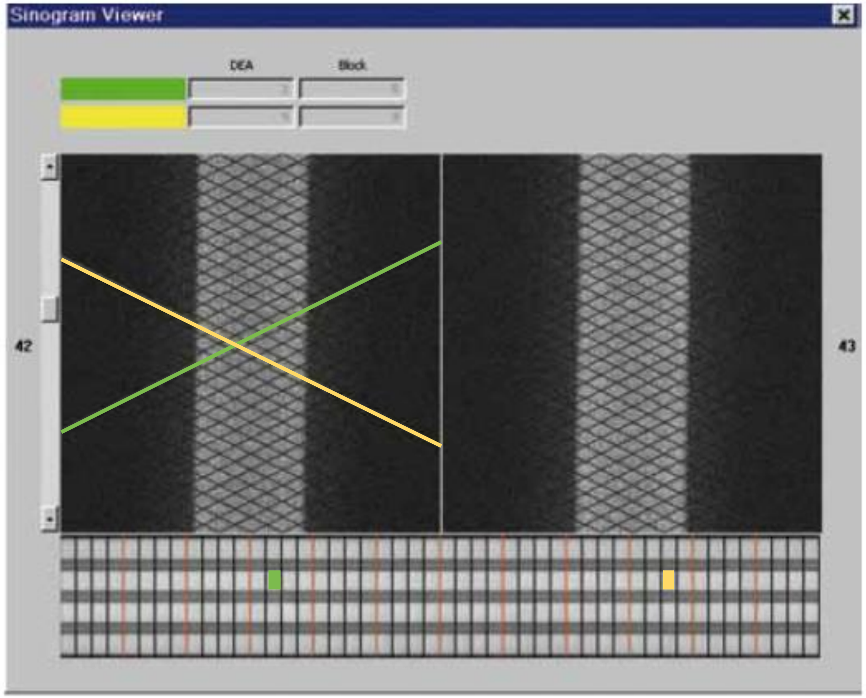

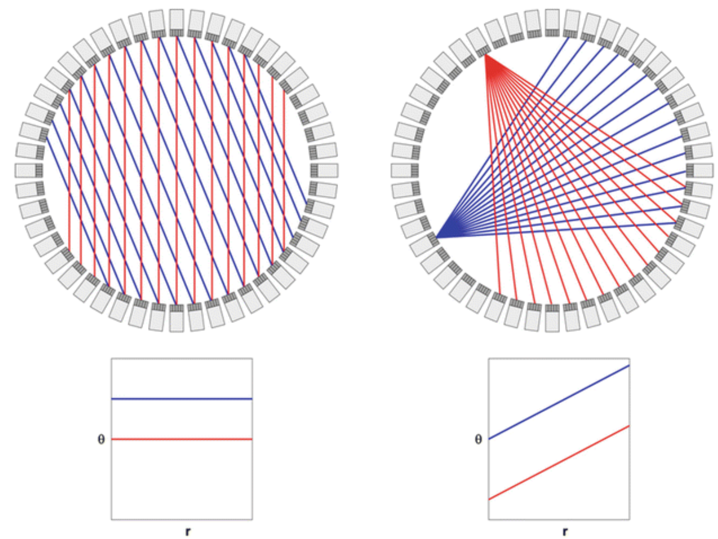

EANM 2010

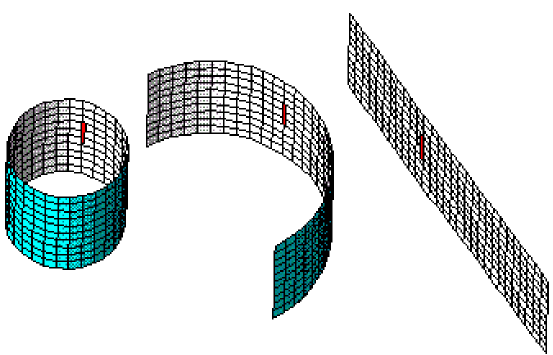

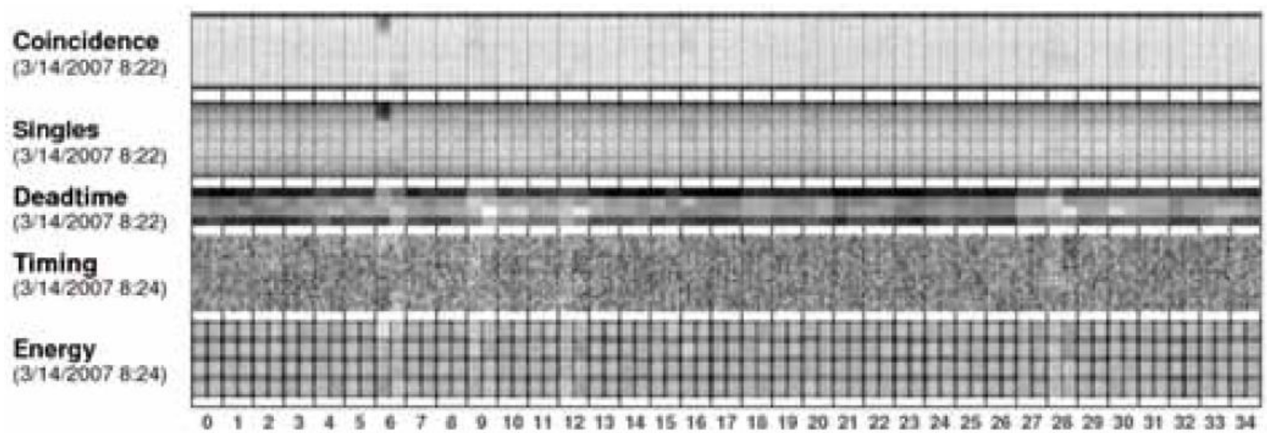

> Résolution

NEMA NU 2-2007

PERFORMANCE MEASUREMENTS OF POSITRON EMISSION TOMOGRAPHS

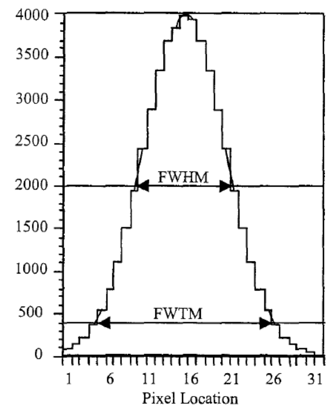

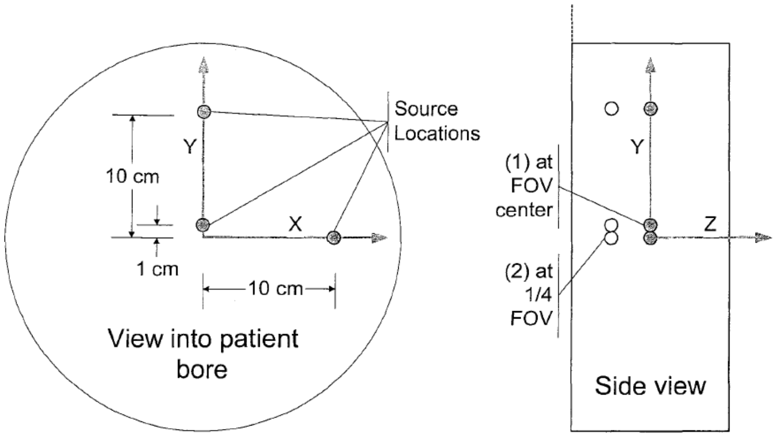

NEMA NU2, 2007

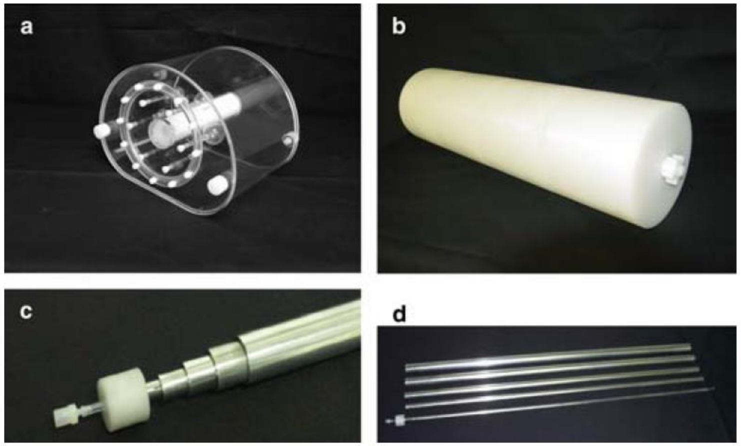

Saha, Springer 2015

	Description	Formula
At 1 cm radius		
Transverse	Average x & y for both z positions (4 numbers)	$\mathrm{RES}=\begin{pmatrix}\mathrm{RESx}_{x=0,y=1,z=center}+\mathrm{RESy}_{x=0,y=1,z=center}+\\ \mathrm{RESx}_{x=0,y=1,z=1/4FOV}+\mathrm{RESy}_{x=0,y=1,z=1/4FOV}\end{pmatrix}\Big/4$
Axial	Average of 2 z positions (2 numbers)	$\mathrm{RES}=\left(\mathrm{RESz}_{x=0,y=1,z=center}+\mathrm{RESz}_{x=0,y=1,z=1/4FOV}\right)/2$
At 10 cm radius		
Transverse radial	Average 2 transverse for both z positions (4 numbers)	$\mathrm{RES}=\begin{pmatrix}\mathrm{RESx}_{x=10,y=0,z=center}+\mathrm{RESy}_{x=0,y=10,z=center}+\\ \mathrm{RESx}_{x=10,y=0,z=1/4FOV}+\mathrm{RESy}_{x=0,y=10,z=1/4FOV}\end{pmatrix}\Big/4$
Transverse tangential	Average 2 transverse for both z positions (4 numbers)	$\mathrm{RES}=\begin{pmatrix}\mathrm{RESy}_{x=10,y=0,z=center}+\mathrm{RESx}_{x=0,y=10,z=center}+\\ \mathrm{RESy}_{x=10,y=0,z=1/4FOV}+\mathrm{RESx}_{x=0,y=10,z=1/4FOV}\end{pmatrix}\Big/4$
Axial resolution	Average 2 transverse for both z positions (4 numbers)	$\mathrm{RES}=\begin{pmatrix}\mathrm{RESz}_{x=10,y=0,z=center}+\mathrm{RESz}_{x=0,y=10,z=center}+\\ \mathrm{RESz}_{x=10,y=0,z=1/4FOV}+\mathrm{RESz}_{x=0,y=10,z=1/4FOV}\end{pmatrix}\Big/4$

Contrôle qualité

- > Résolution
- > NECR / SF
- > Sensibilité

NEMA NU 2-2007

PERFORMANCE MEASUREMENTS OF POSITRON EMISSION TOMOGRAPHS

$$C_n = C_0 \exp(-n\,\delta\,\mu)$$

$$\log(C_n) = \log(C_0) - n\,\delta\mu$$

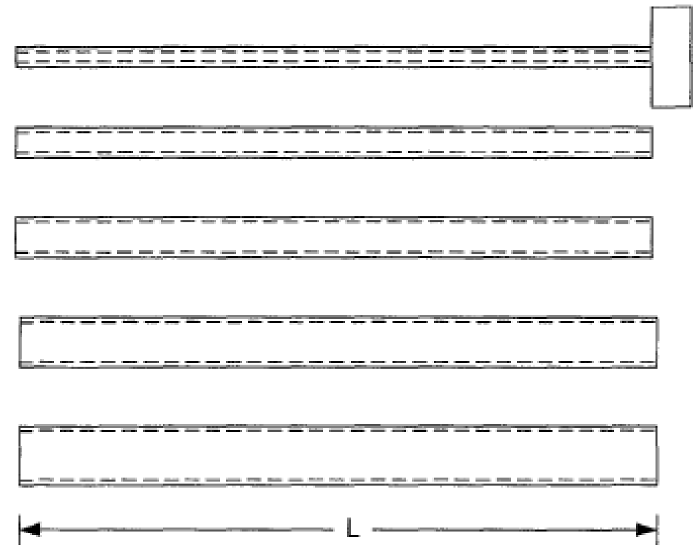

NEMA NU2, 2007

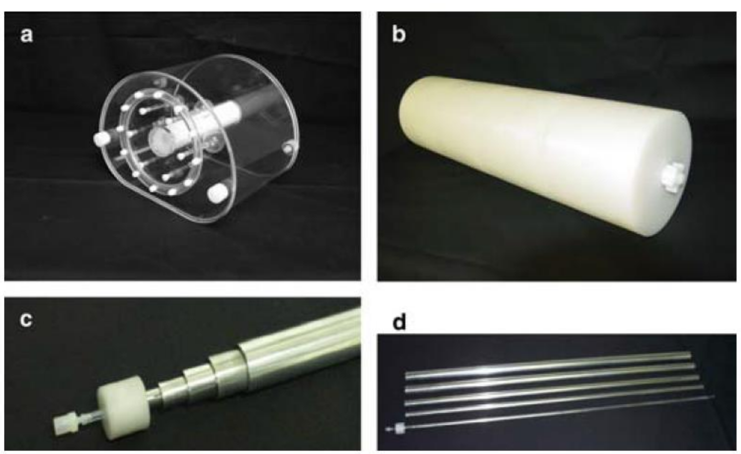

Saha, Springer 2015

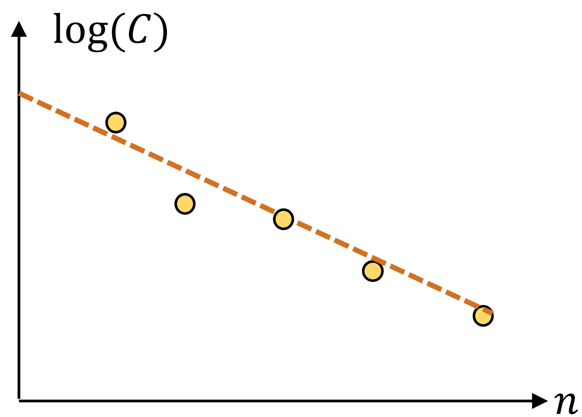

Contrôle qualité

- > **Résolution**
- > **NECR / SF**
- > **Sensibilité**
- > **Qualité / contraste**

NEMA NU 2-2007

PERFORMANCE MEASUREMENTS OF POSITRON EMISSION TOMOGRAPHS

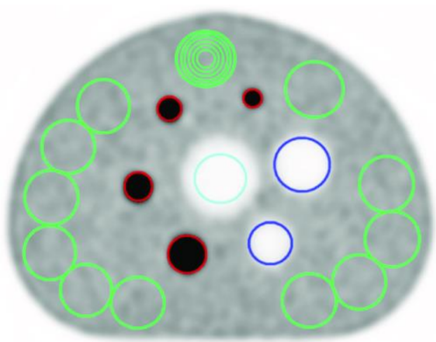

Karlberg, EJNMMI Phys 2016

$$Q_{H,j} = \frac{C_{H,j}/C_{B,j} - 1}{a_H/a_B - 1} * 100\% \qquad Q_{C,j} = \left(1 - \frac{C_{C,j}}{C_{B,j}}\right) * 100\%$$

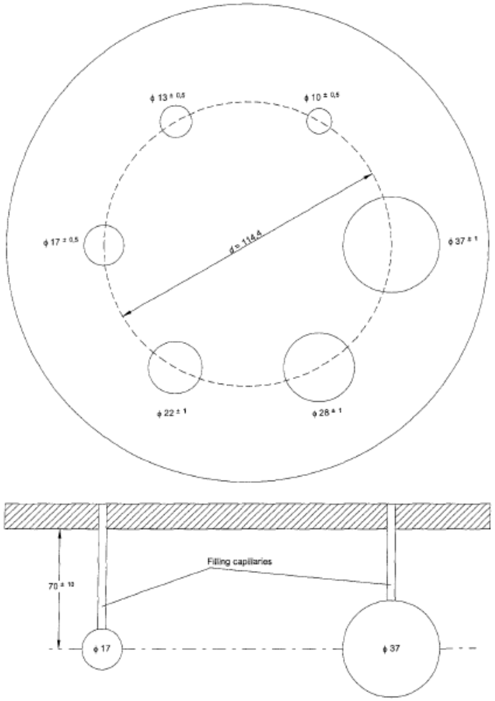

NEMA NU2, 2007

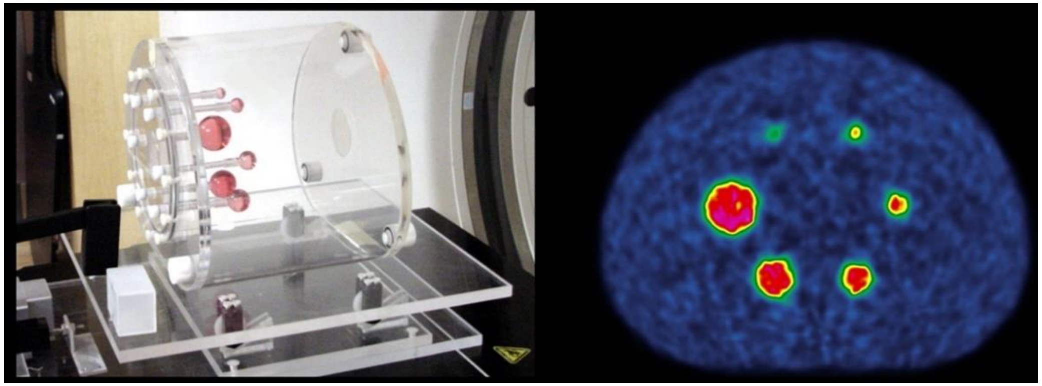

Vines, J Nucl Med Technol 2007

Reconstruction

Encodage SPECT

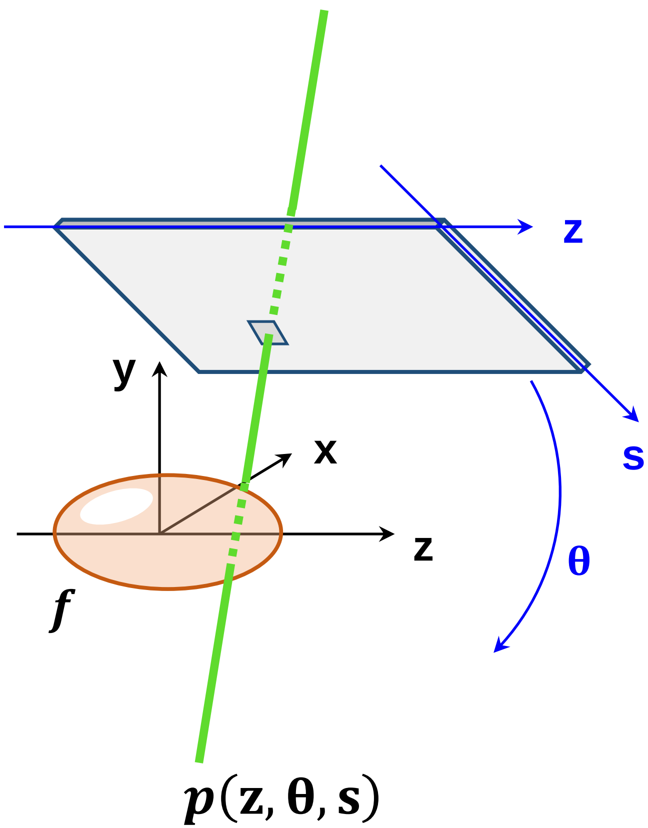

Reconstruction

Encodage SPECT

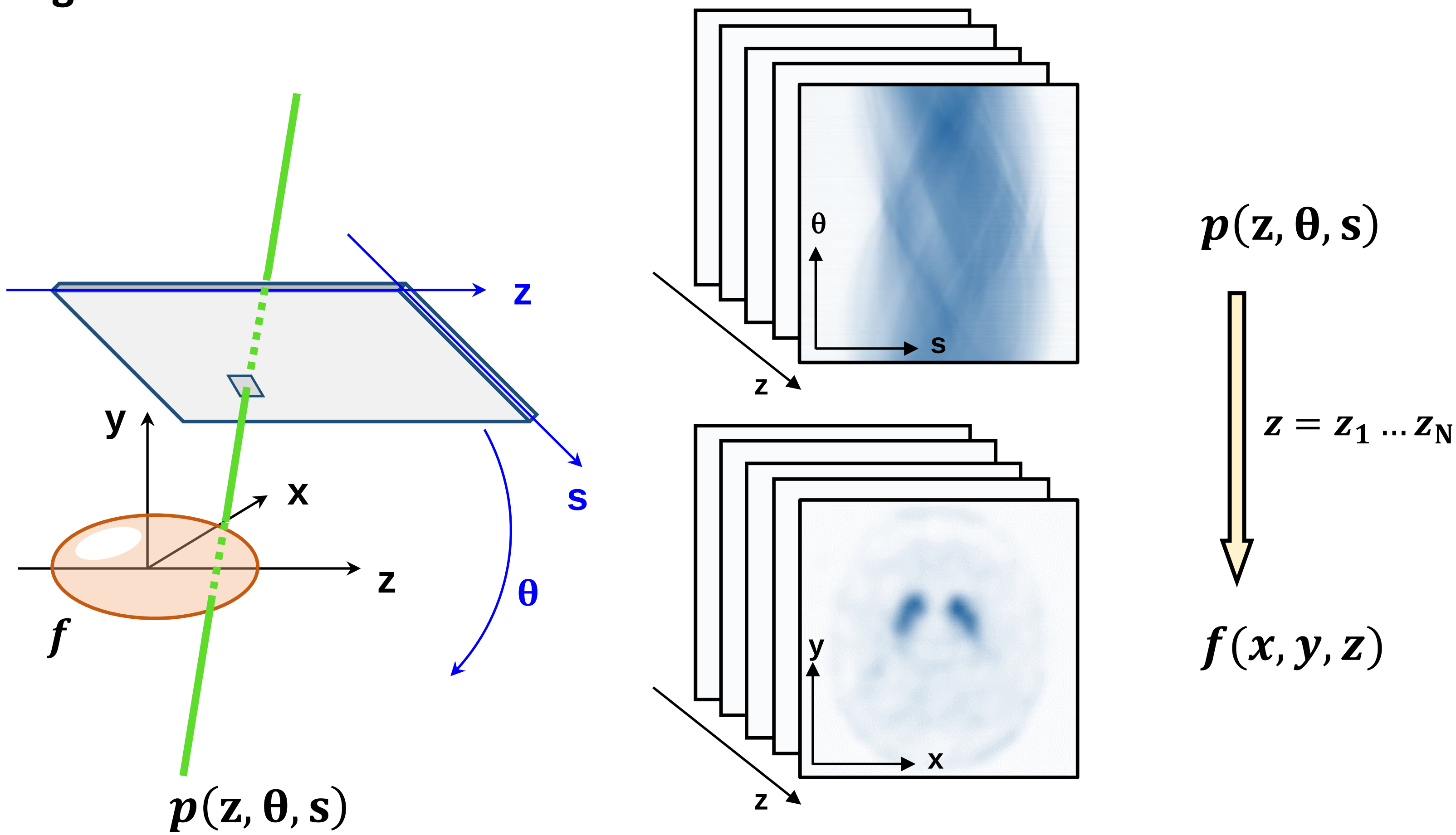

Encodage TEP

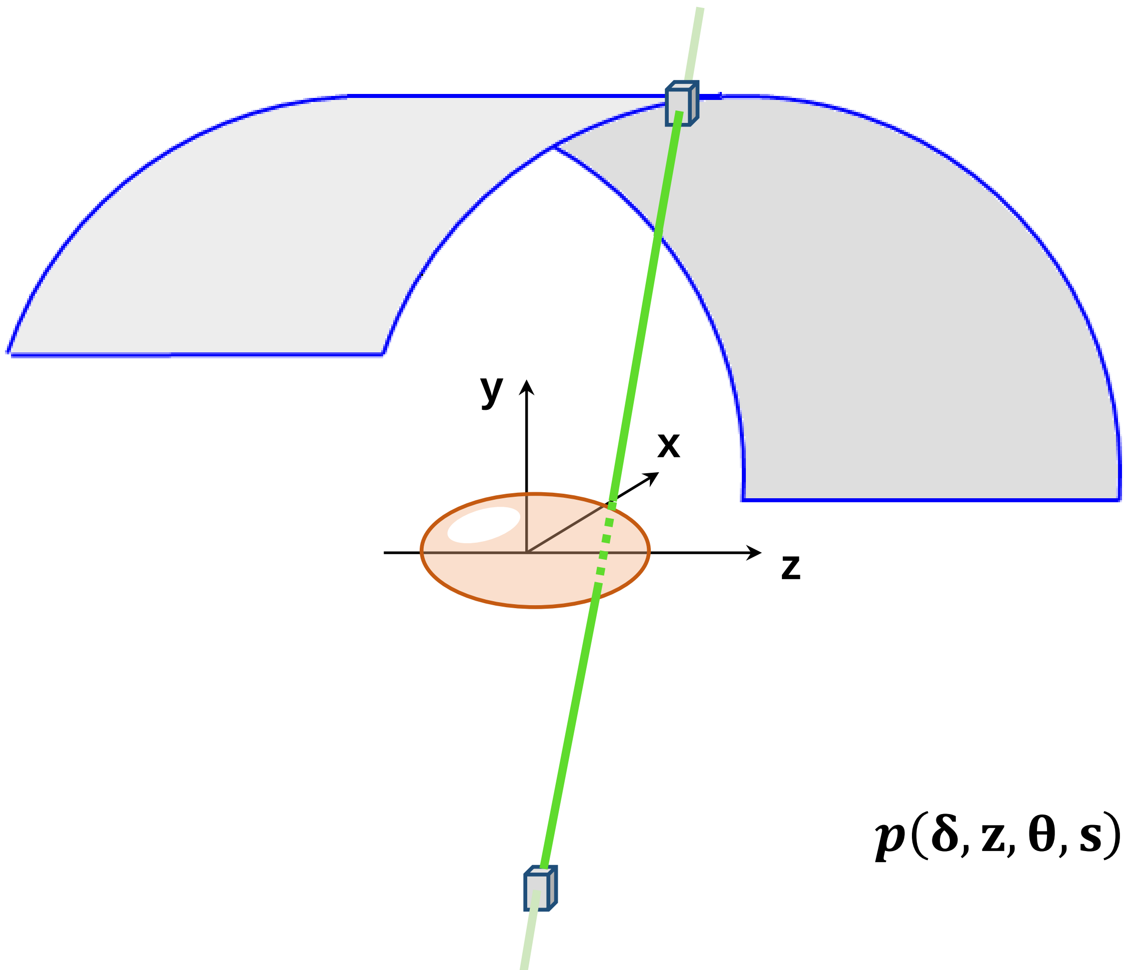

$$\boldsymbol{p(\delta, z, \theta, s)}$$

Reconstruction

Encodage TEP

$$p(\delta = tan\psi, z, \theta, s)$$

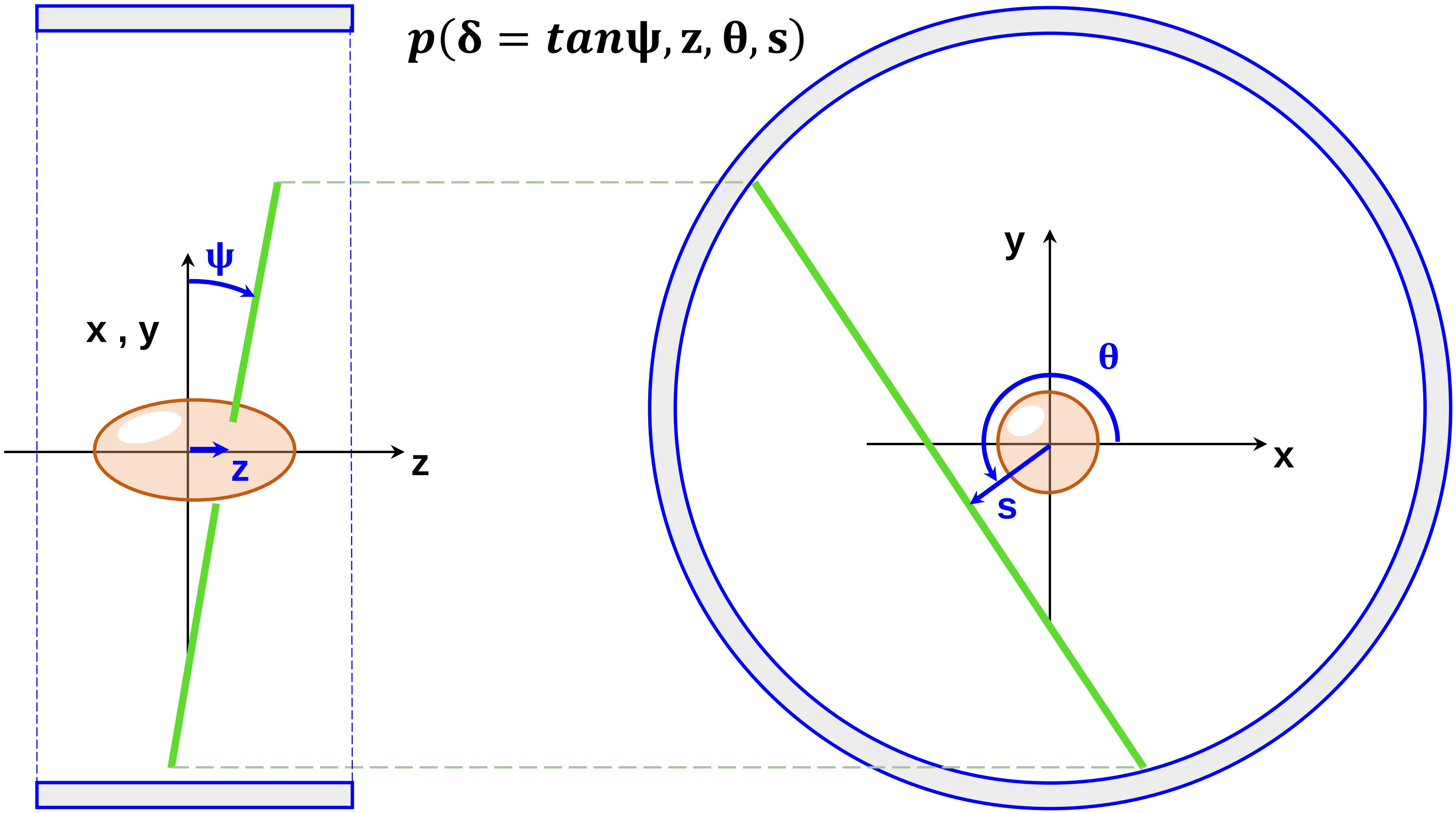

Reconstruction

Encodage TEP

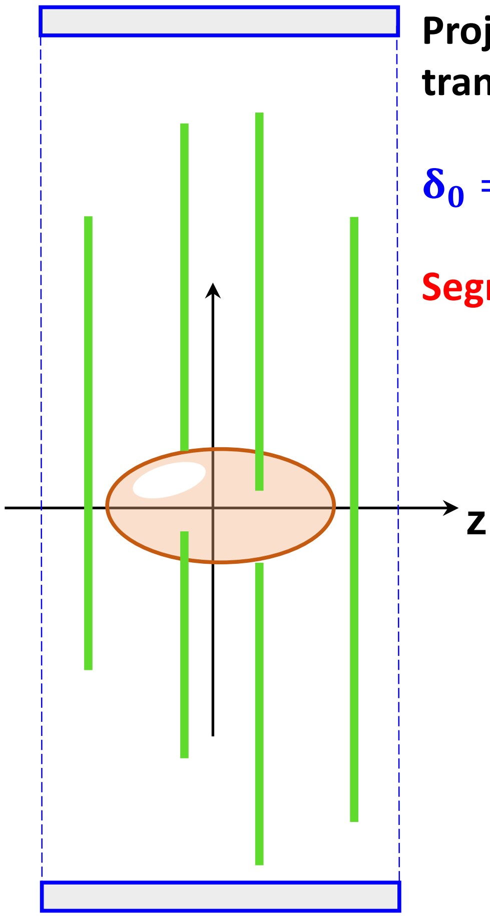

Projections transverses :

$\delta_0 = 0$

Segment 0

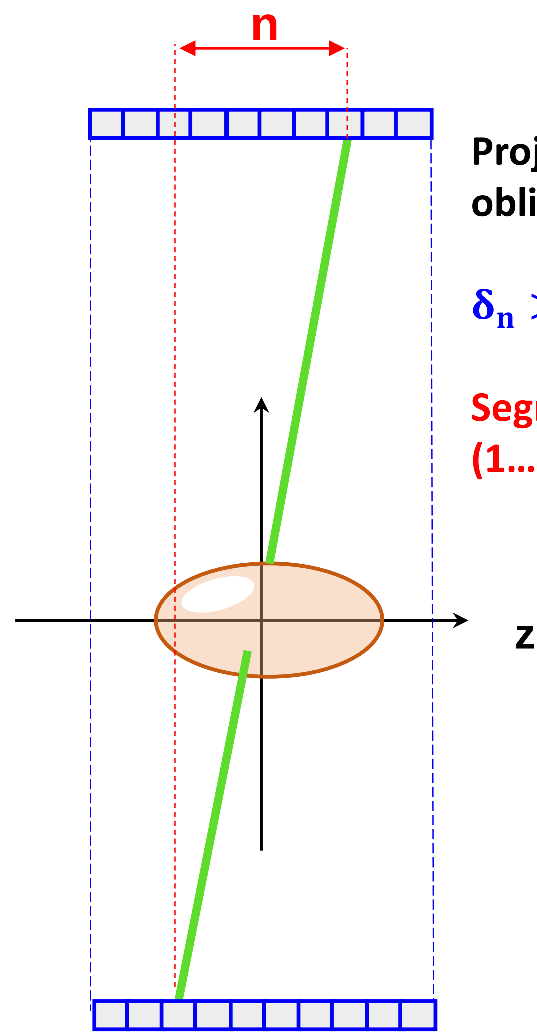

Projections obliques :

$\delta_n > 0$

Segment n (1…N)

Reconstruction

Encodage TEP

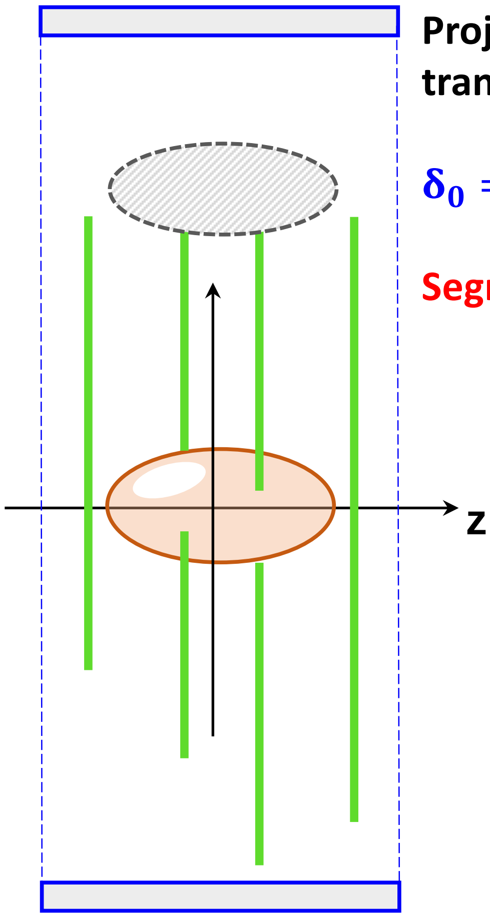

Projections transverses :

$\delta_0 = 0$

Segment 0

COMPLETES

&

SUFFISANTES

$$p(0, z, \theta, s) \rightarrow f(x, y, z)$$

Reconstruction

Encodage TEP

TRONQUEES

$$p(\delta_{n>0}, z, \theta, s) \nrightarrow f(x, y, z)$$

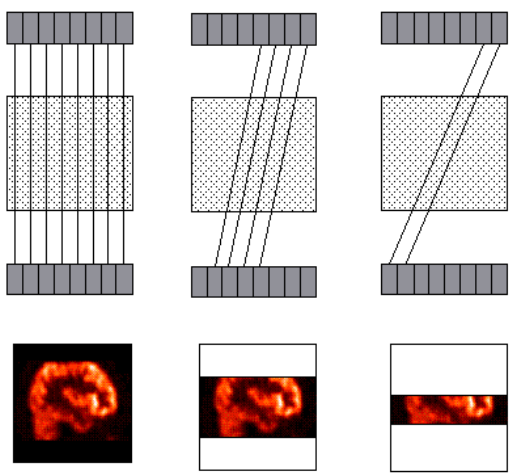

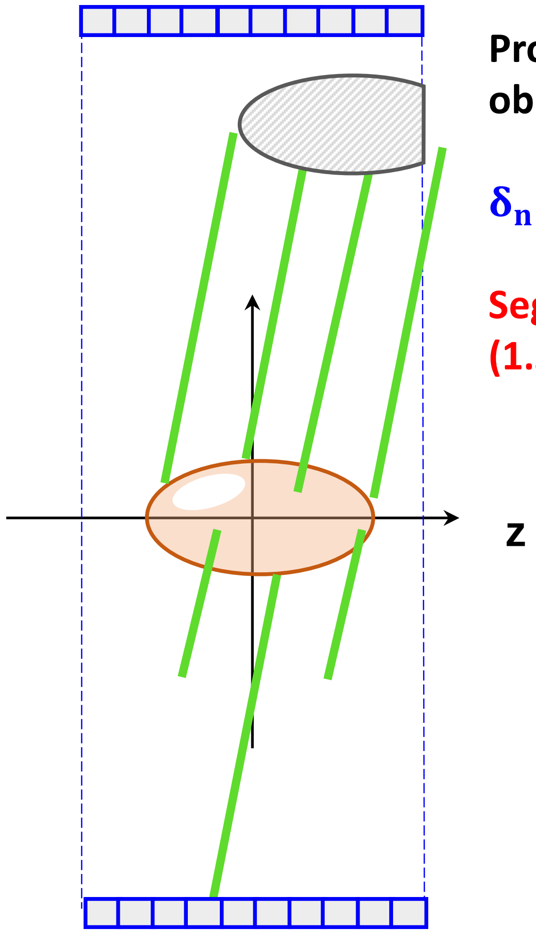

Projections obliques :

$\delta_n > 0$

Segment n (1…N)

Reconstruction

Encodage TEP

TRONQUEES

&

REDONDANTES

$$p(\delta_{n>0}, z, \theta, s) \nrightarrow f(x, y, z)$$

$$\left.\begin{array}{l} p(0, z, \theta, s) \\ p(\delta_1, z, \theta, s) \\ p(\delta_2, z, \theta, s) \\ p(\delta_3, z, \theta, s) \\ \vdots \end{array}\right\} \rightarrow f(x, y, z)$$

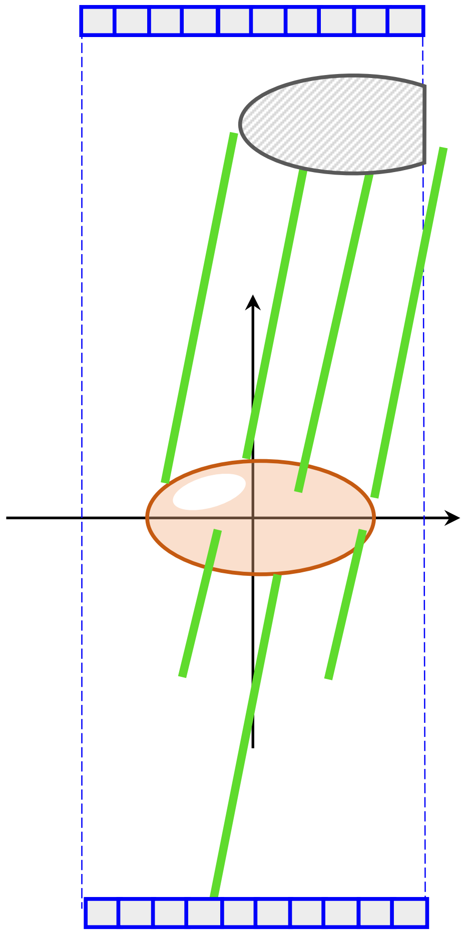

Projections obliques :

$\delta_n > 0$

Segment n (1…N)

Reconstruction

Acquisition 2D / Reconstruction 2D

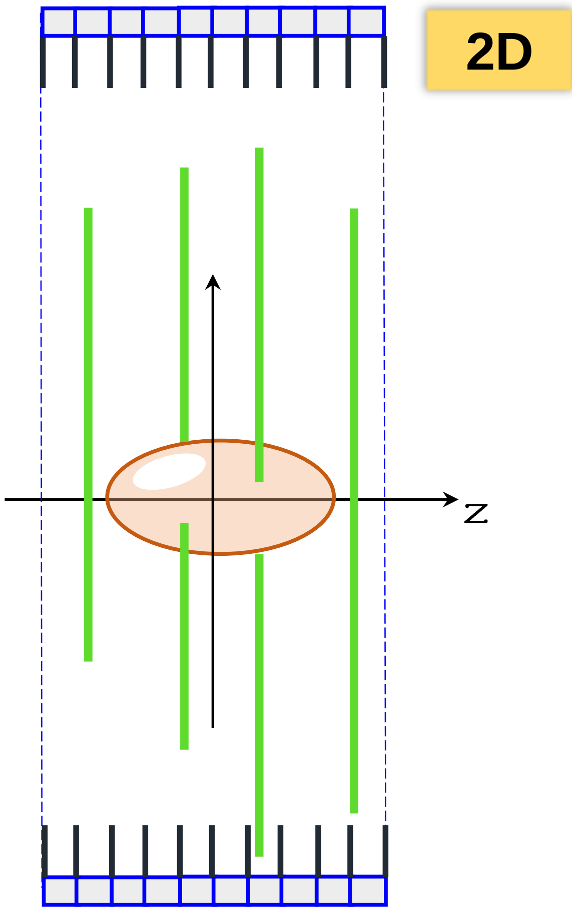

$$p(0, z, \theta, s) \rightarrow f(x, y, z)$$

Collimation

Très rapide

SNR ↘

Reconstruction

Acquisition 3D / Reconstruction 2D

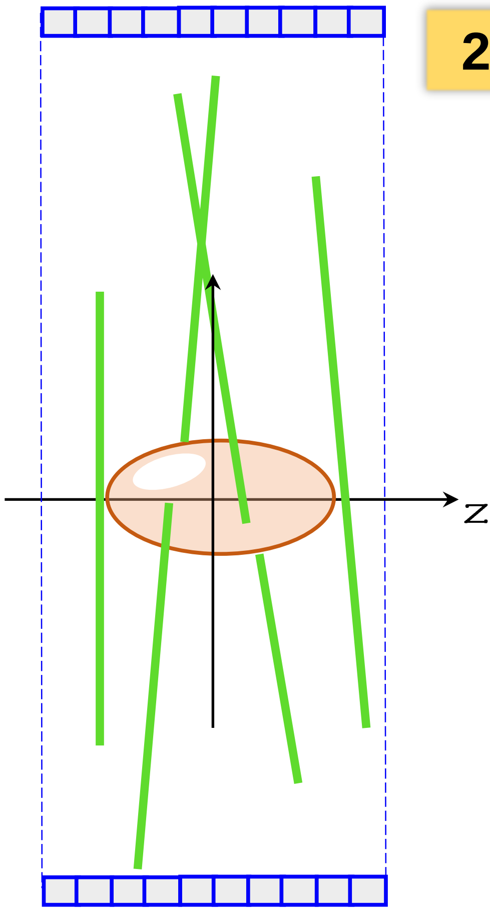

2D ½

$$\underbrace{p(0, z, \theta, s)\ , p(\delta_1, z, \theta, s)\ , p(\delta_2, z, \theta, s)\ , \ldots}$$

$$\downarrow$$

$$p(0, z, \theta, s)$$

$$\downarrow$$

$$f(x, y, z)$$

« Rebinning »

Rapide

Approximatif (FORE,…)

Acquisition 3D / Reconstruction 3D

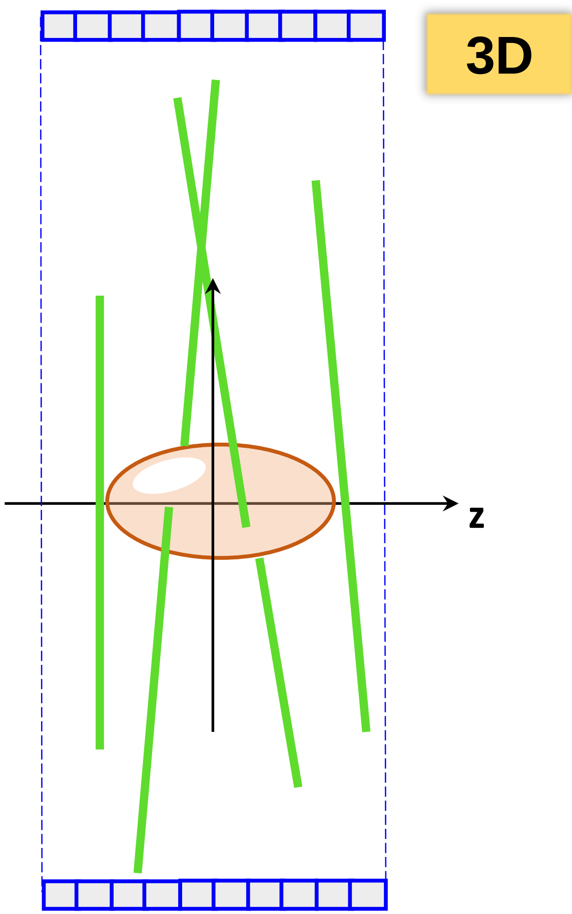

$$\left.\begin{array}{c} p(0, z, \theta, s) \\ p(\delta_1, z, \theta, s) \\ p(\delta_2, z, \theta, s) \\ p(\delta_3, z, \theta, s) \\ \vdots \end{array}\right\} \rightarrow f(x, y, z)$$

3D vrai

Reconstruction analytique ou itérative

SNR ↗

Reconstruction

Acquisition 3D / Reconstruction 3D

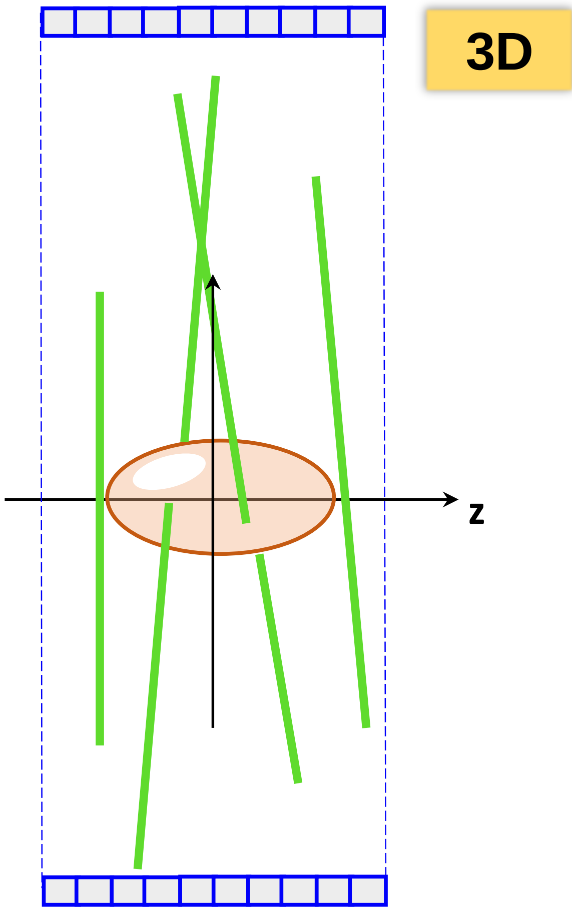

TABLE 5.2
PERFORMANCE CHARACTERISTICS OF COMMERCIALLY AVAILABLE PET SCANNERS

	GE Discovery ST	GE Discovery STE	Siemens Biograph
Description			
Available PET modes	2D & 3D	2D & 3D	3D
Detector material type	BGO	BGO	LSO
Detector crystal size (mm)	6.2×6.2×30	4.8×6.2×30	4×4×20
NEMA performance			
Sensitivity			
2D trues (cps/kBq)	2.0	2.0	N/A
3D trues (cps/kBq)	9.3	8.5	4.5
Scatter fraction			
2D	19%	19%	N/A
3D	44%	36%	36%
Count rate capability			
Peak NECR, 2D	84 kcps @ 49 kBq/mL	84 kcps @ 49 kBq/mL	N/A
Peak NECR, 3D	63 kcps @ 12 kBq/mL	80 kcps @ 12 kBq/mL	93 kcps @ 29 kBq/mL

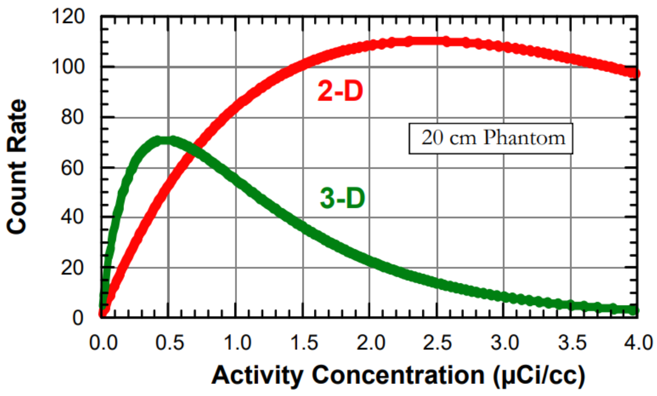

Reconstruction analytique

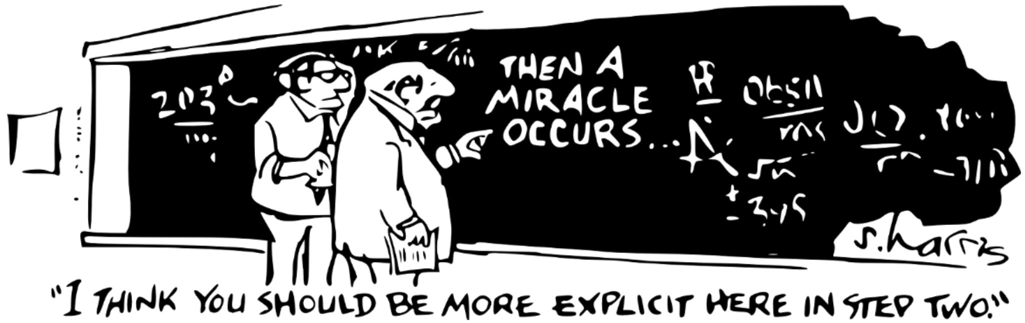

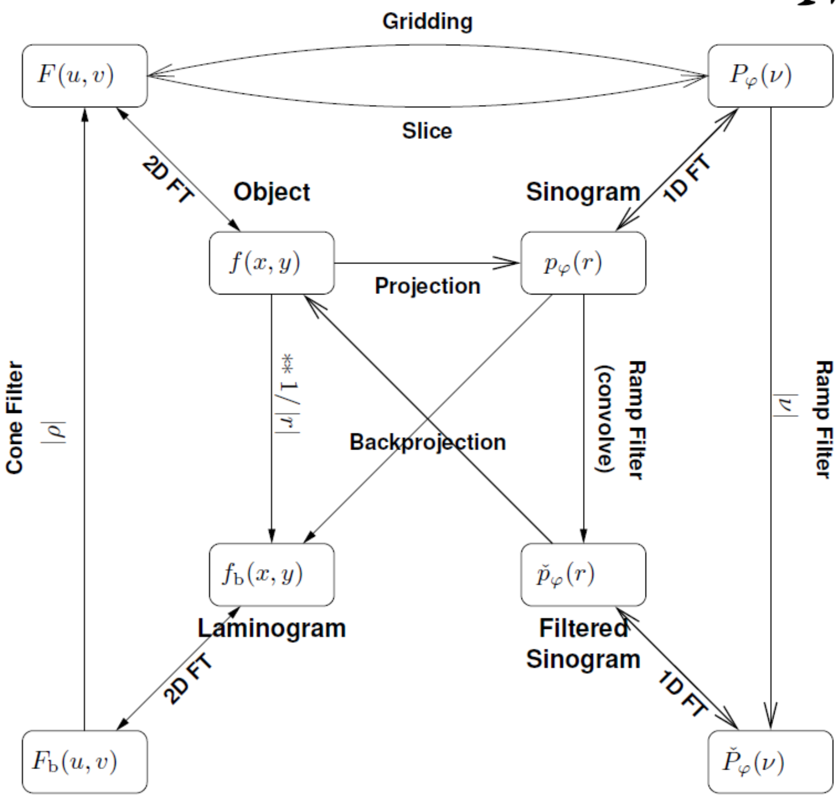

Fessler 2009 (web.eecs.umich.edu)

Reconstruction

Reconstruction analytique

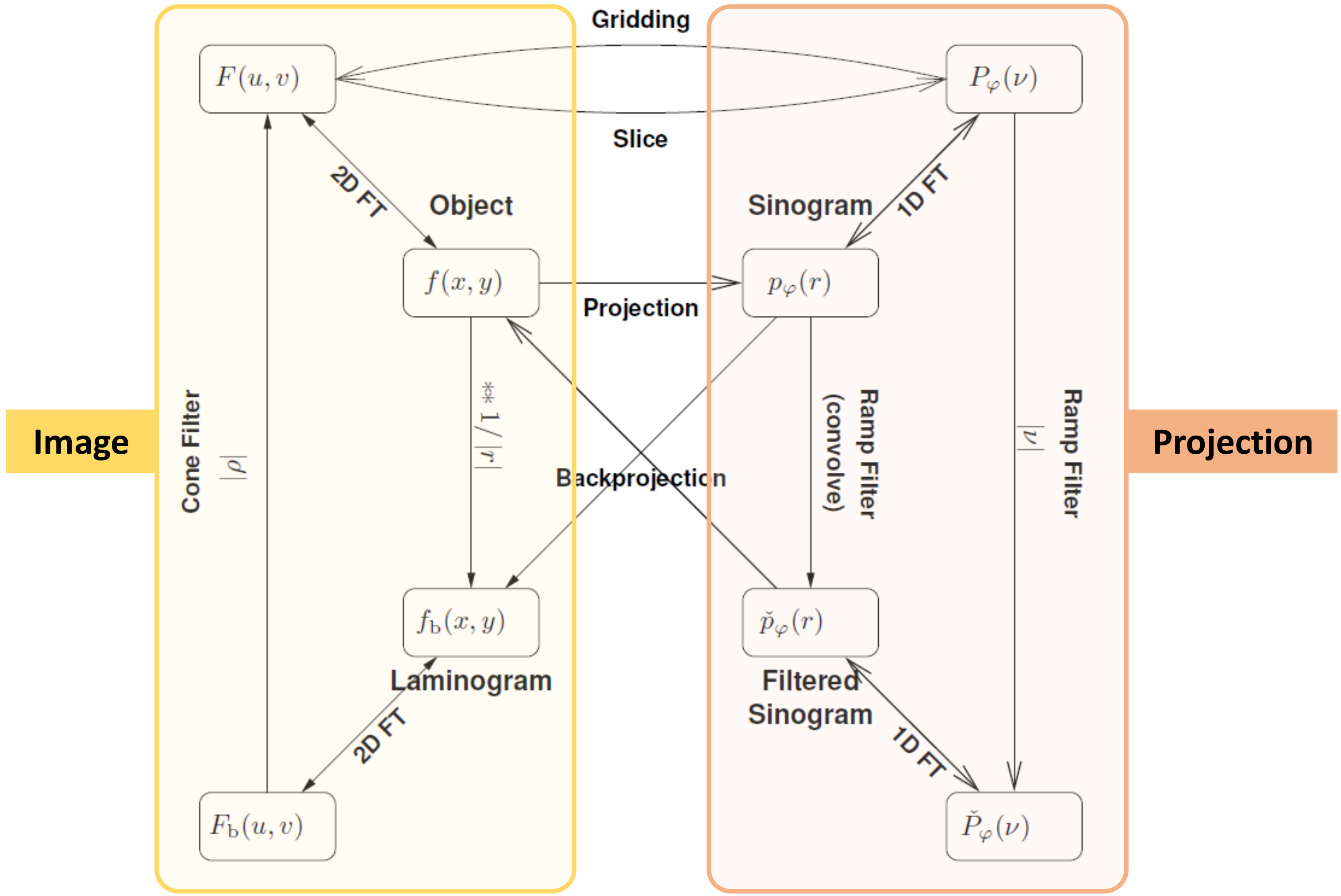

Reconstruction

Reconstruction analytique

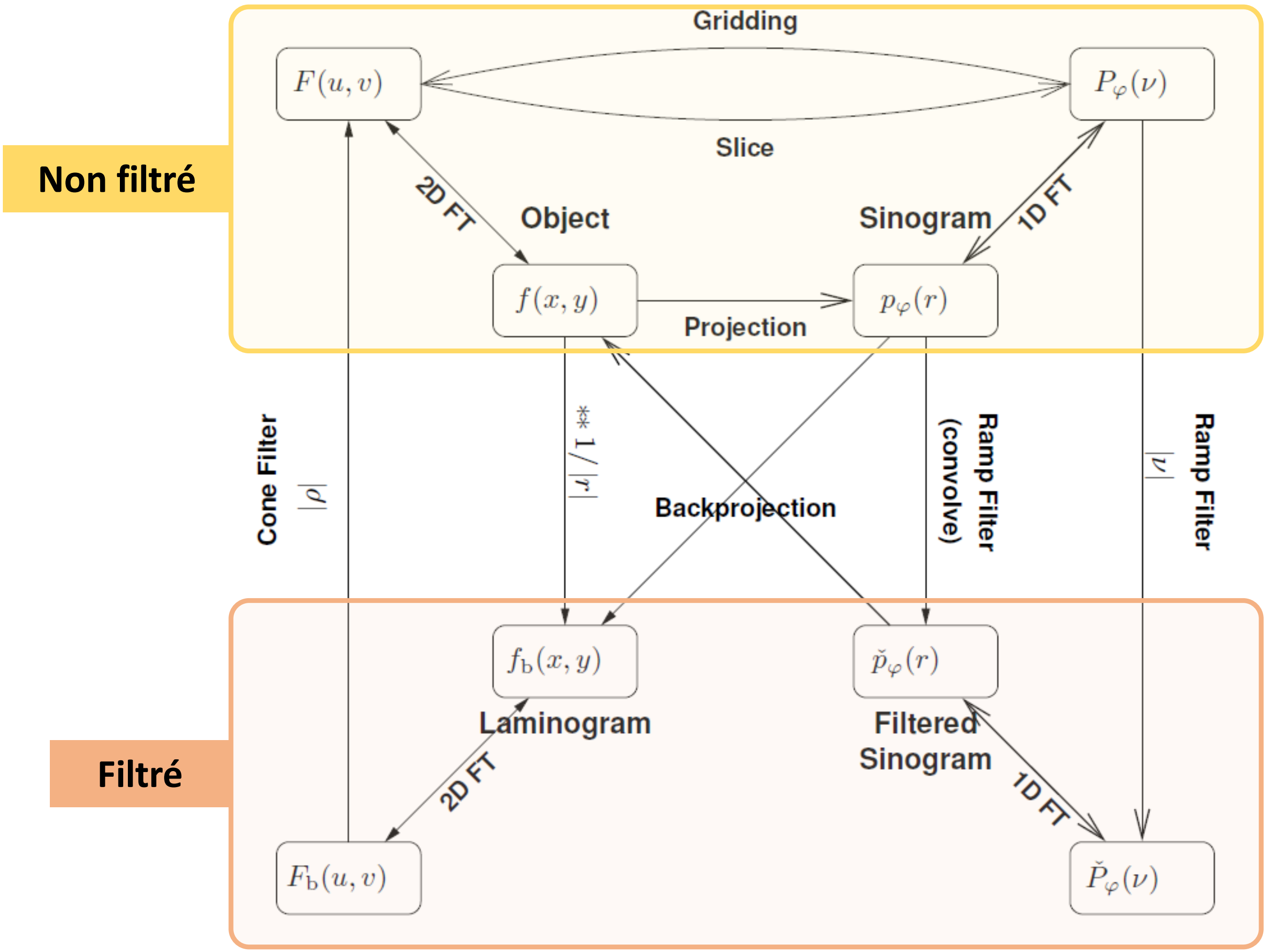

Reconstruction

Reconstruction analytique

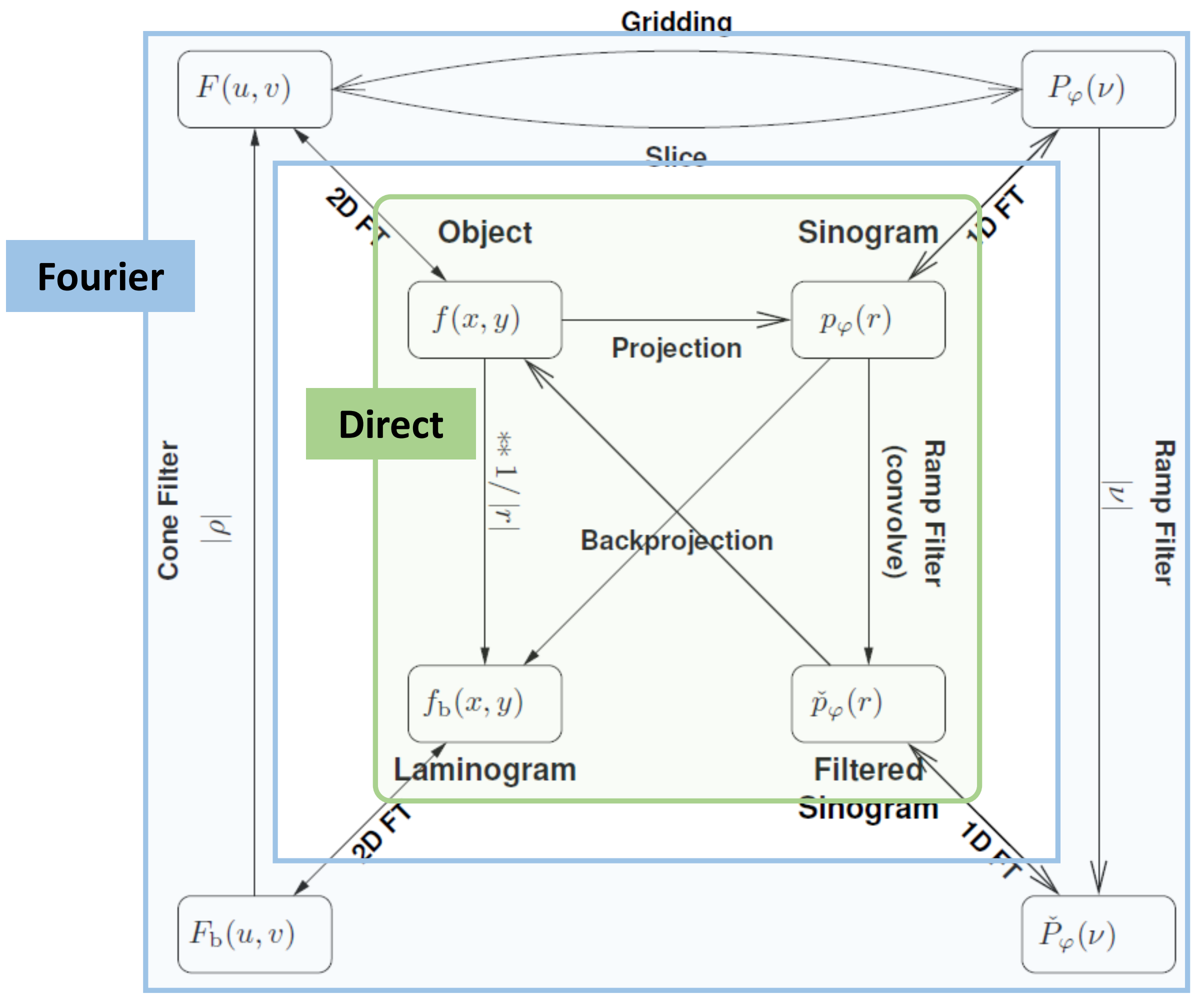

Institut National des Sciences et Techniques Nucléaires

Reconstruction analytique

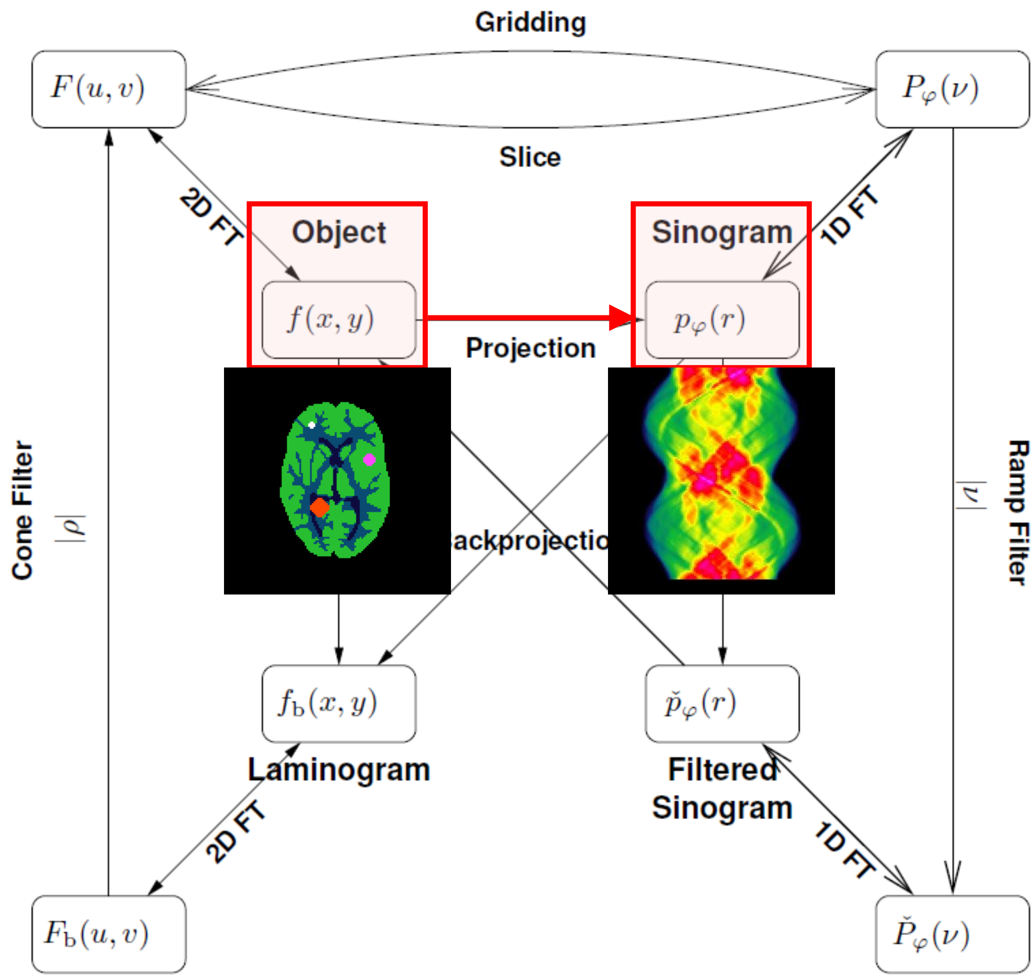

Reconstruction

Reconstruction analytique

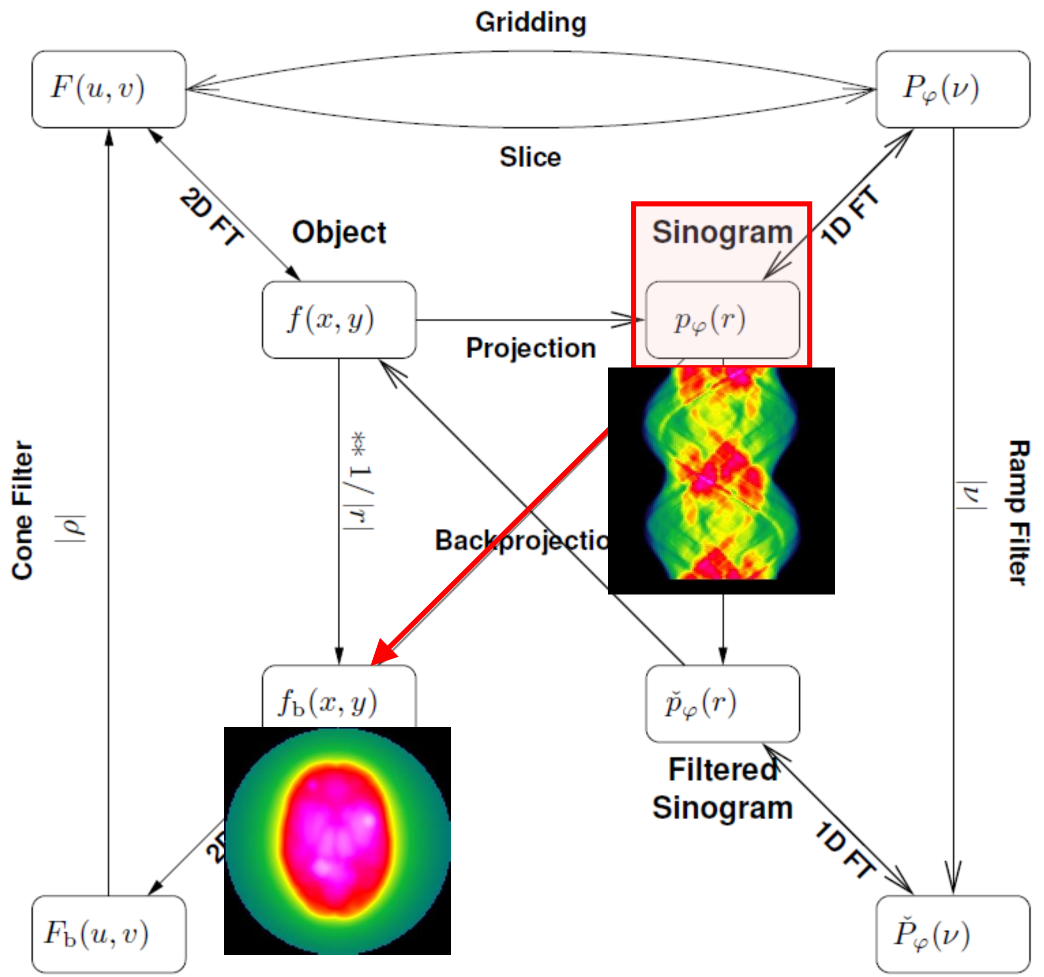

RP
rétroprojection

Reconstruction

Reconstruction analytique

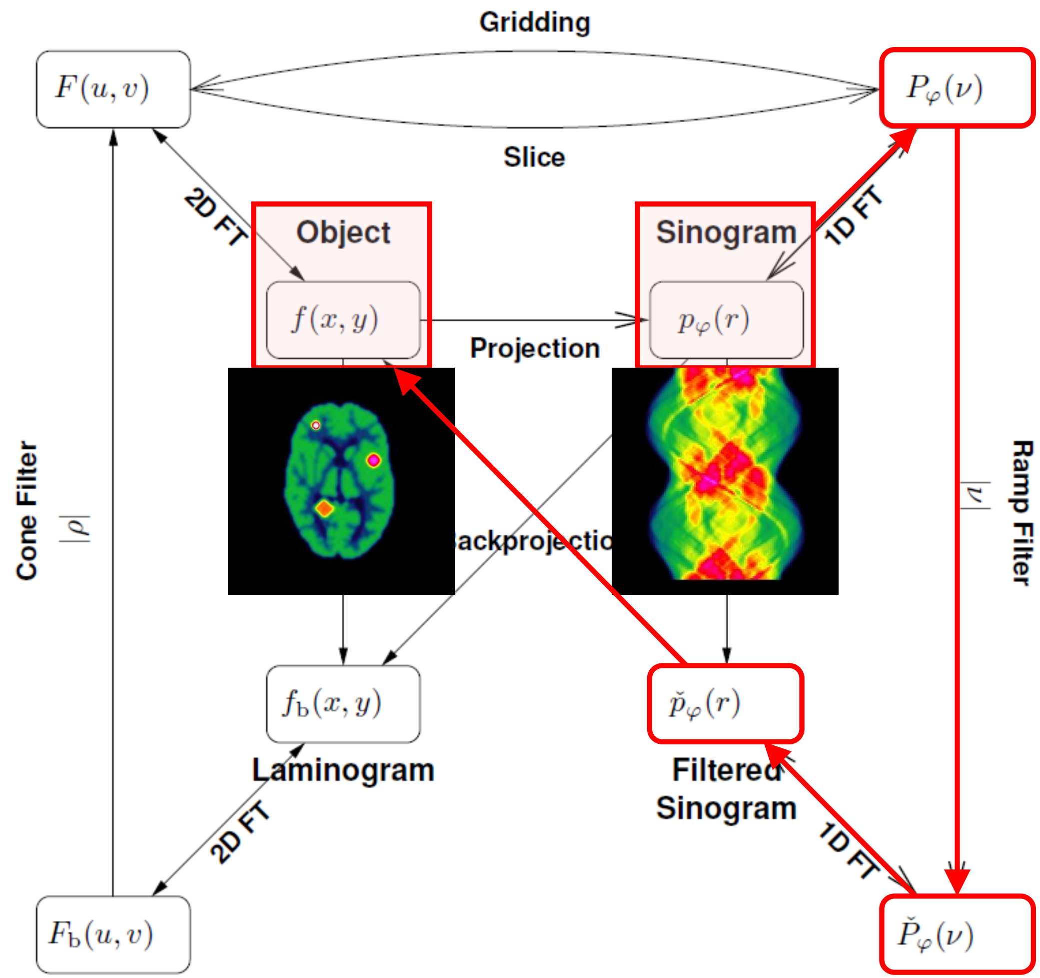

RPF
rétroprojection filtrée

Reconstruction

Reconstruction analytique

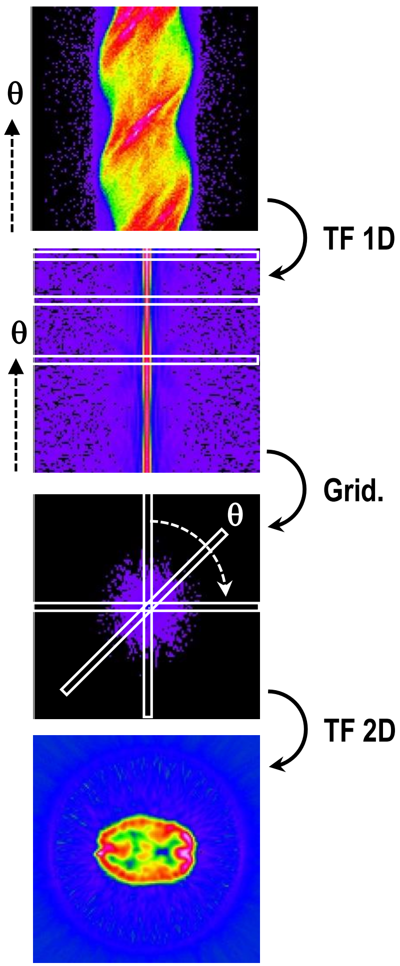

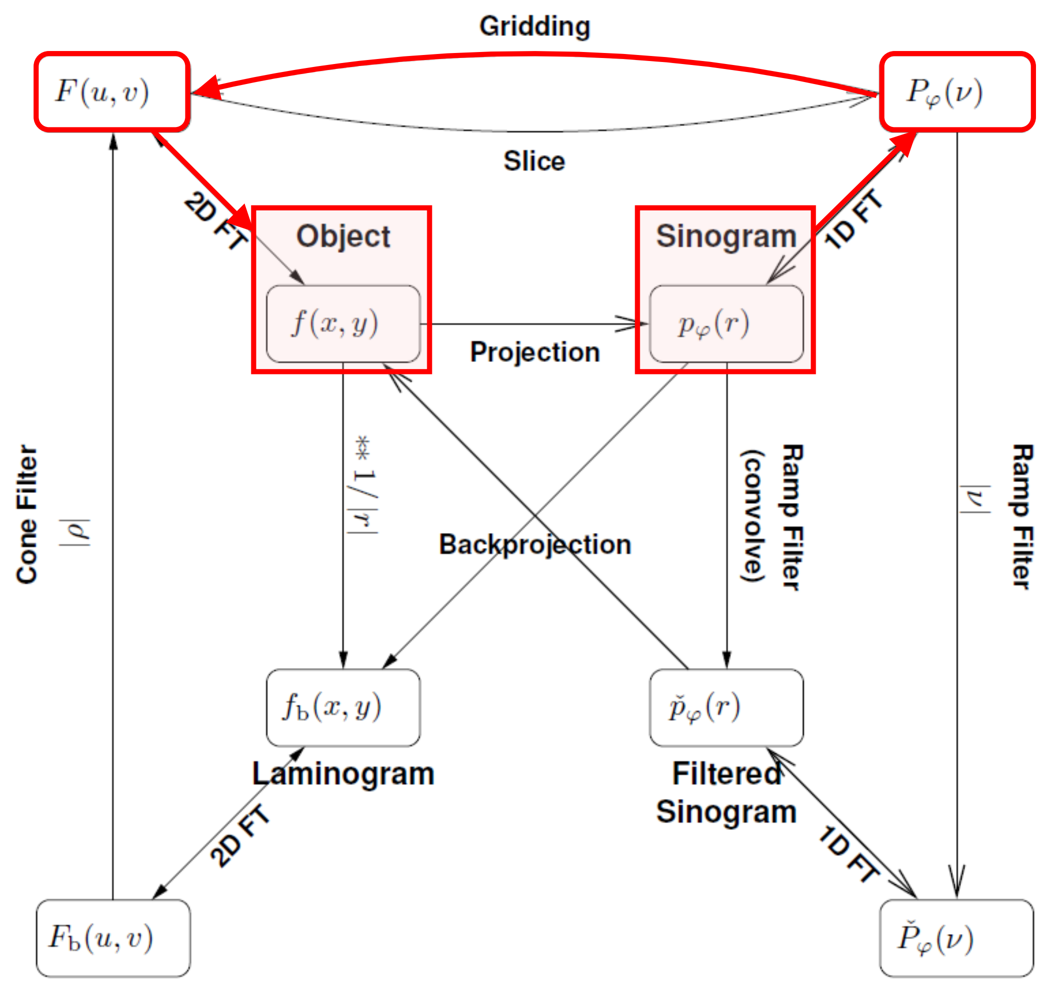

Synthèse de Fourier

Reconstruction

Reconstruction analytique

Limites

Troncature axiale

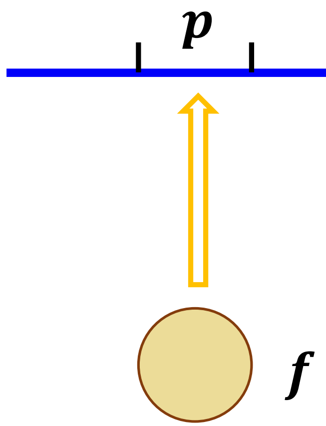

Reconstruction

Reconstruction analytique

Limites

Troncature axiale

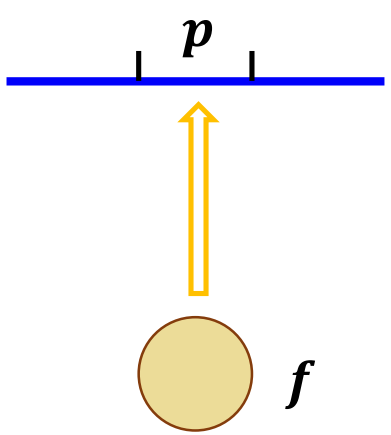

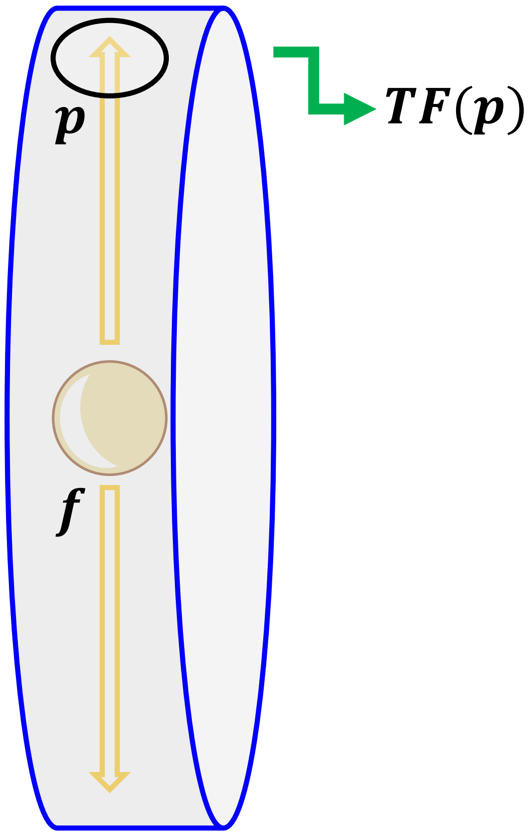

Reconstruction analytique

Limites

Troncature axiale

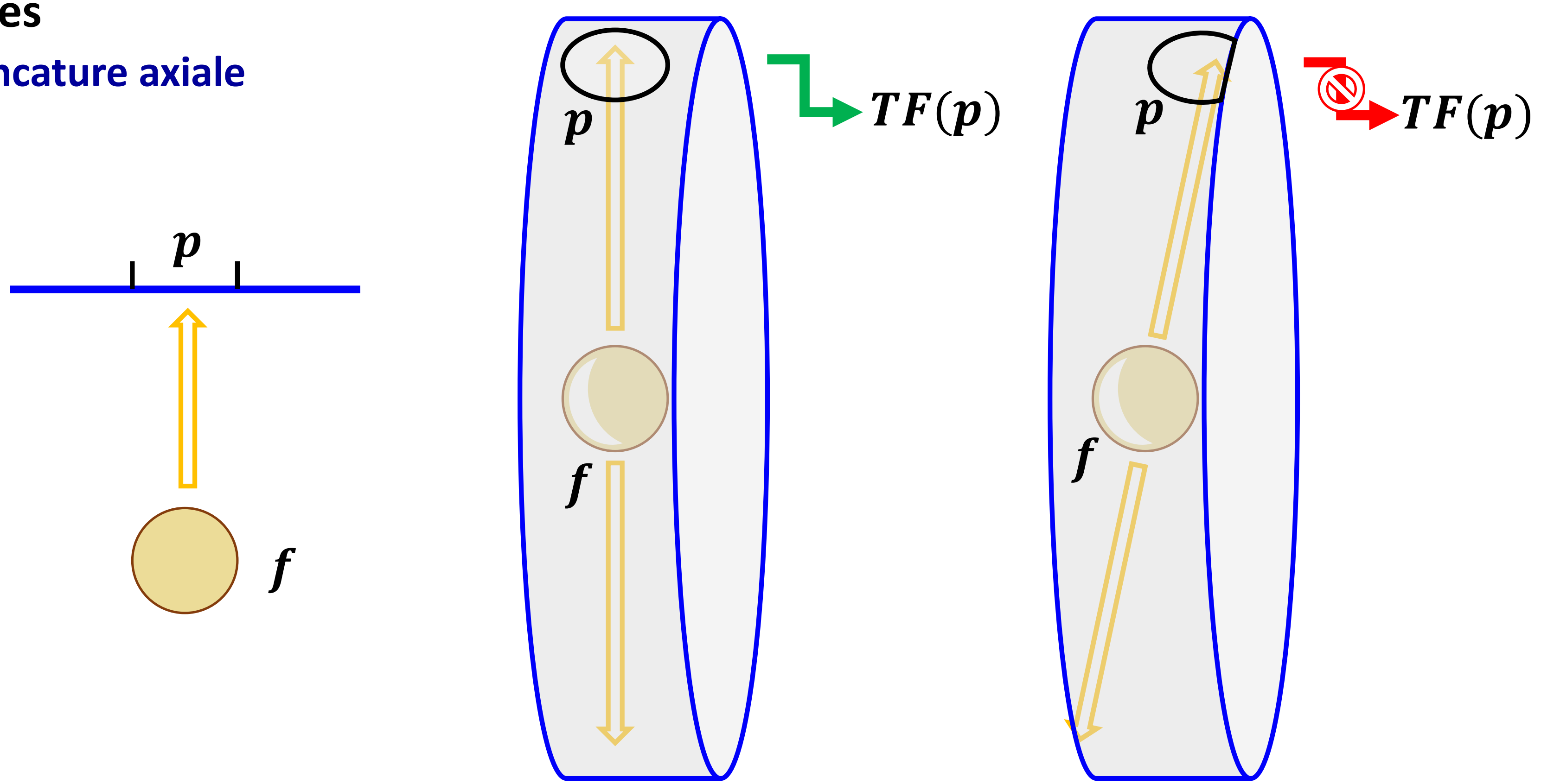

Reconstruction analytique

Limites

- Troncature axiale
- Interactions photon-matière

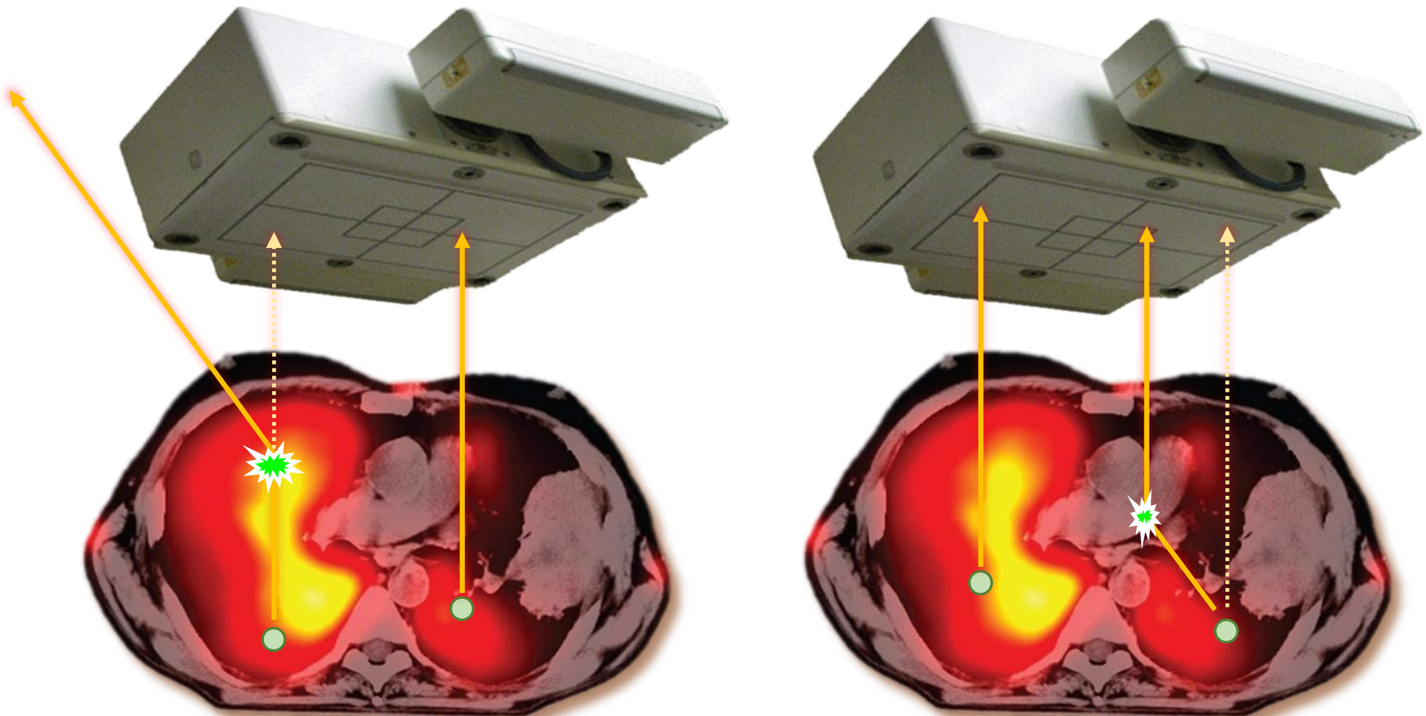

Reconstruction

Reconstruction analytique

Limites

- Troncature axiale
- Interactions photon-matière
- Réponse du détecteur (PSF)

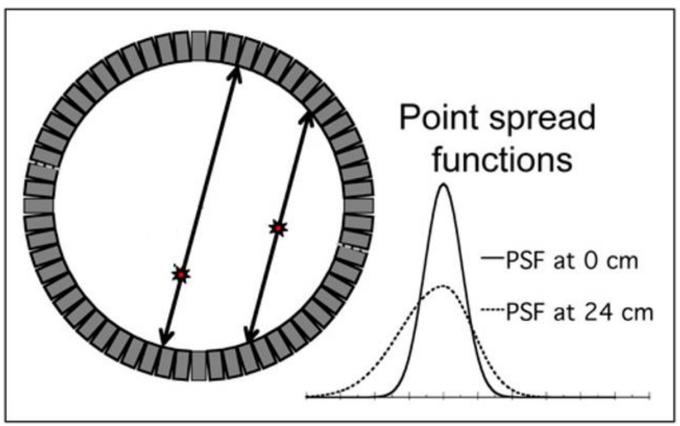

Kadrmas, J Nucl Med 2009

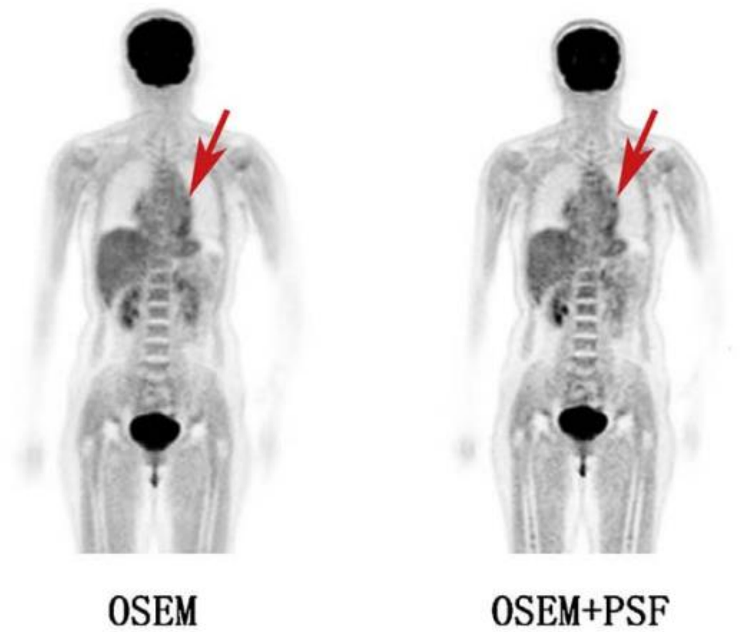

Shang, Eur J Radiol 2017

Reconstruction

Reconstruction analytique

Limites

- Troncature axiale
- Interactions photon-matière
- Réponse du détecteur (PSF)
- Bruit statistique

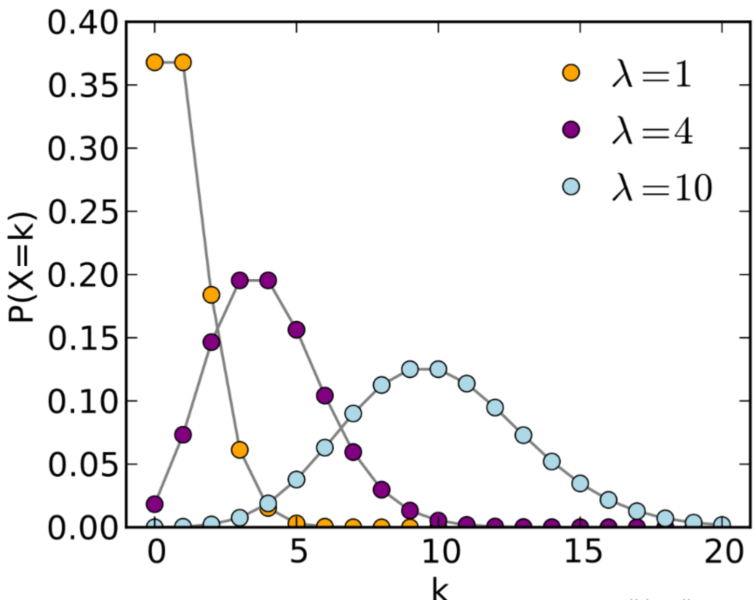

wikipedia.org

Reconstruction

Reconstruction itérative

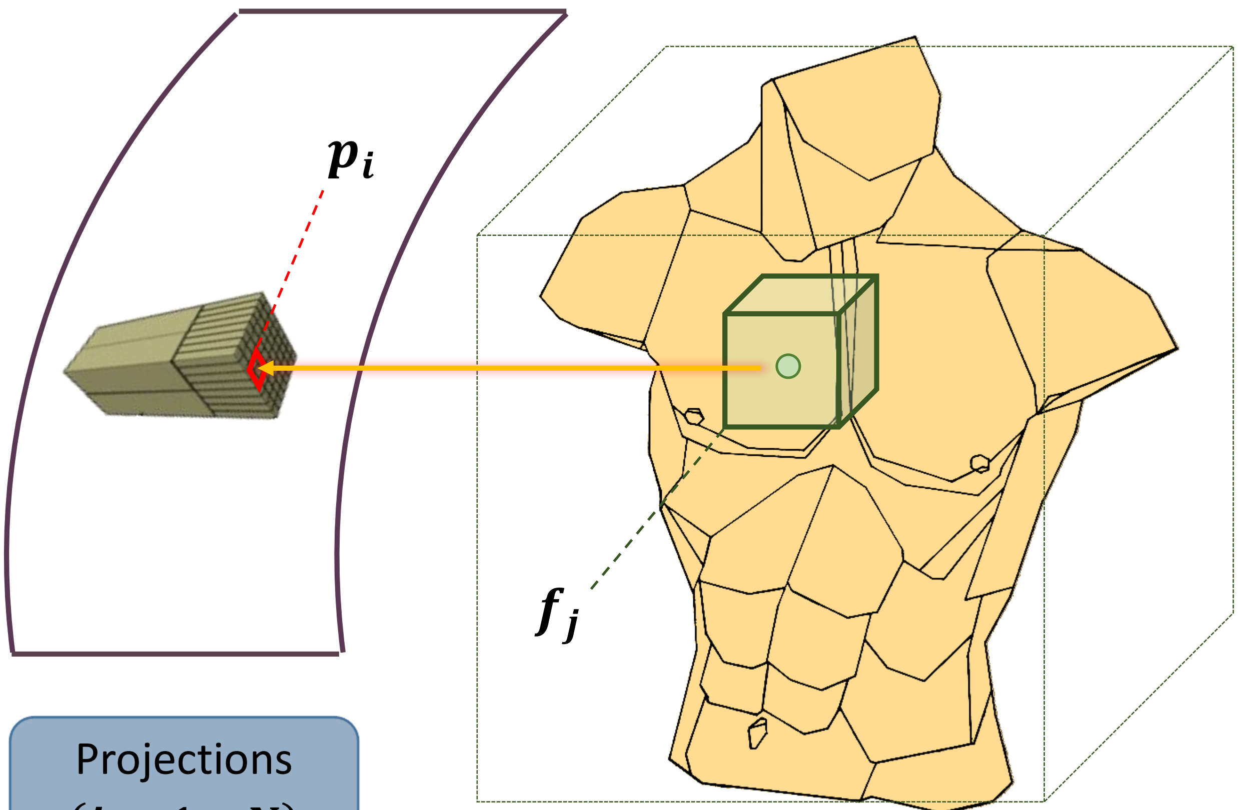

Projections
$(i = 1 \ldots N)$

Voxels / pixels $(j = 1 \ldots M)$

Reconstruction

Reconstruction itérative

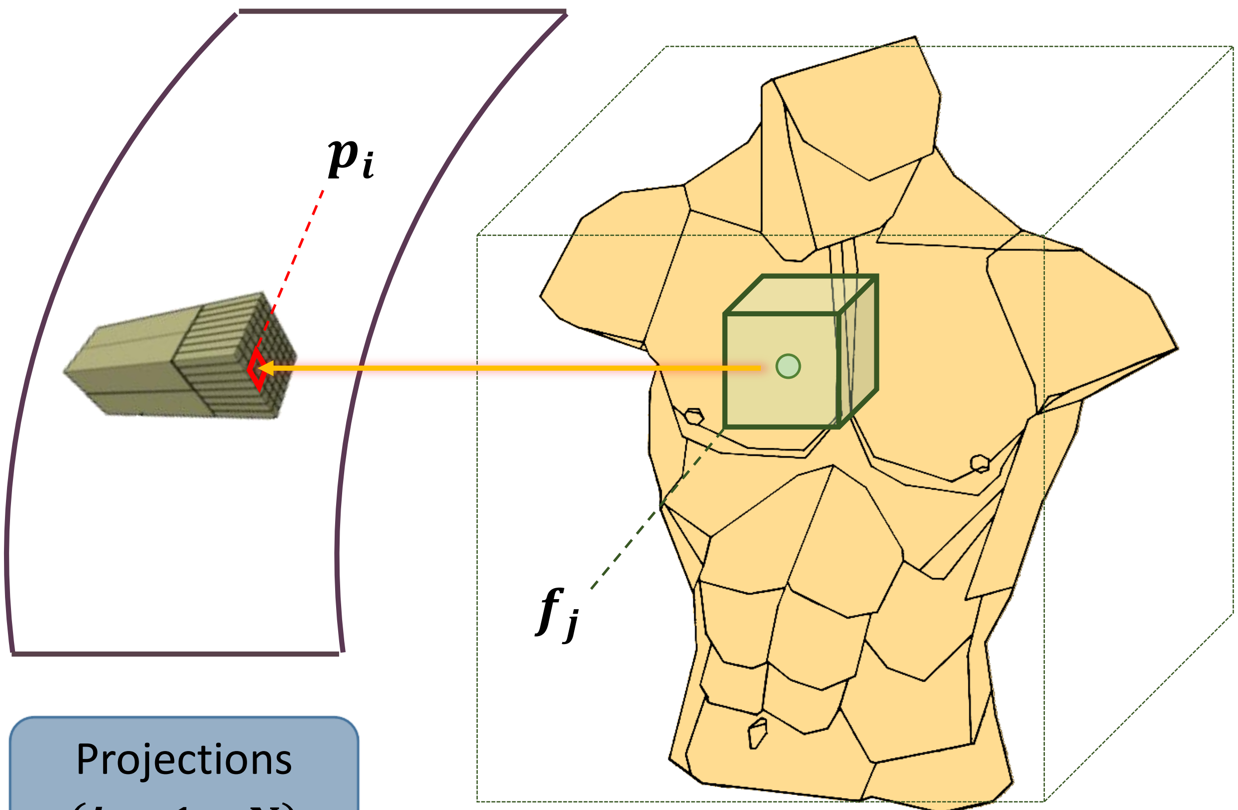

Projections
$(i = 1 \ldots \mathrm{N})$

Voxels / pixels $(j = 1 \ldots \mathrm{M})$

Matrice système

$$\mathbf{R} \in \mathbb{R}^{\mathbf{N} \times \mathbf{M}}$$

$$\mathbf{R}_{ij} = \wp(j \rightarrow i)$$

> Géométrie

> Atténuation

> Réponse du détecteur

Reconstruction

Reconstruction itérative

$$p = \mathbf{R}f + scat + rand + noise$$

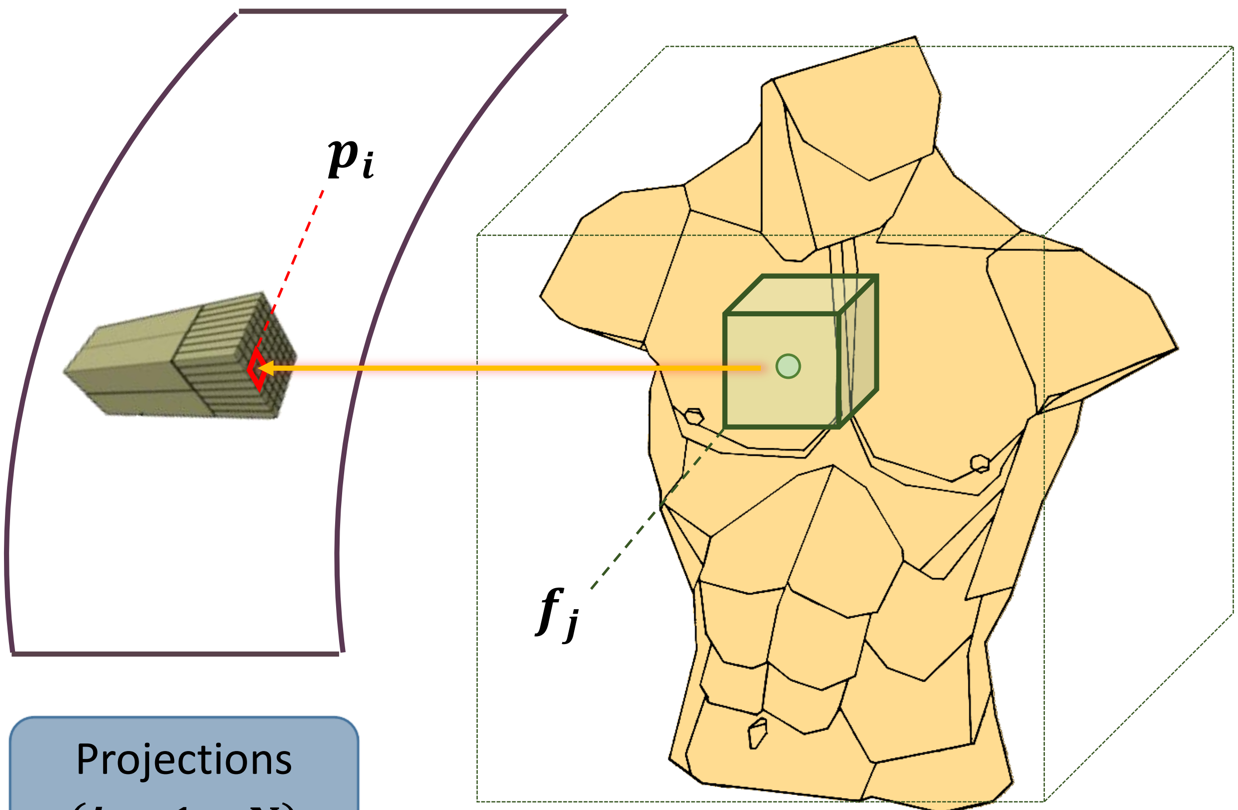

Projections
$(i = 1 \ldots \mathrm{N})$

Voxels / pixels $(j = 1 \ldots \mathrm{M})$

Matrice système

$$\mathbf{R} \in \mathbb{R}^{\mathbf{N \times M}}$$

$$\mathbf{R}_{ij} = \wp(j \to i)$$

> Géométrie
> Atténuation
> Réponse du détecteur

Reconstruction

Reconstruction itérative

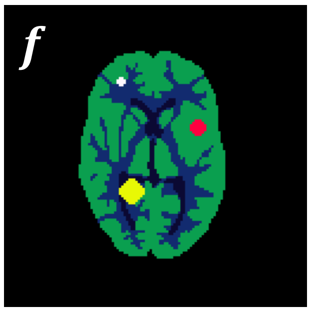

objet

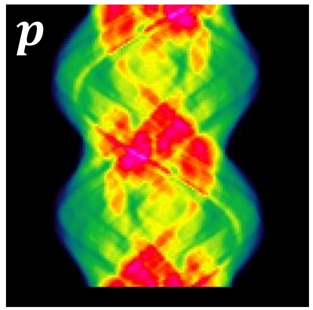

$$\boldsymbol{p} = \mathbf{R}\boldsymbol{f} \quad (+\boldsymbol{noise})$$

Reconstruction

Reconstruction itérative

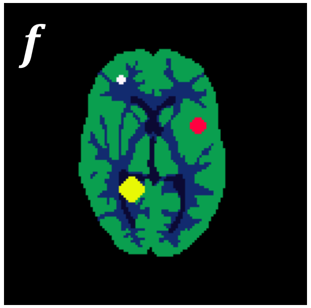

objet

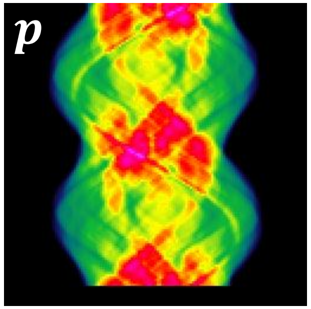

estimation

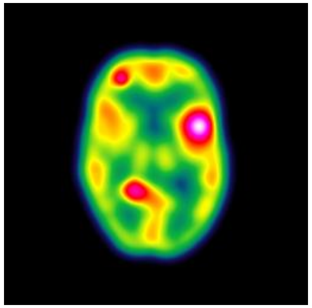

projection

$$\bar{p}^0 = \mathrm{R}\bar{f}^0$$

$\bar{f}^0$

Reconstruction

Reconstruction itérative

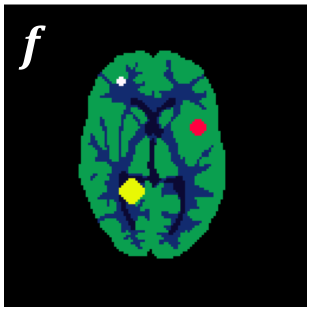

objet

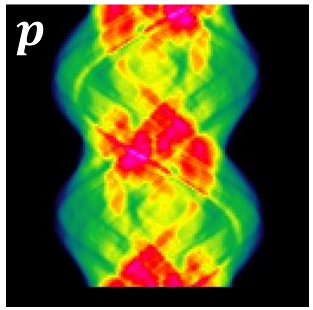

comparaison

estimation

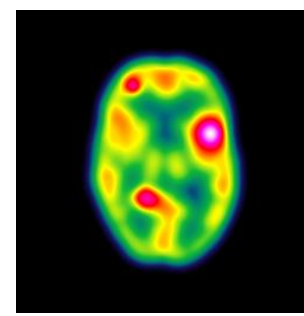

projection

$$\bar{p}^0 = \mathrm{R}\bar{f}^0$$

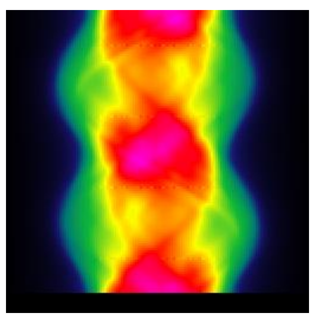

$\bar{p}^0$

$\bar{f}^0$

Reconstruction

Reconstruction itérative

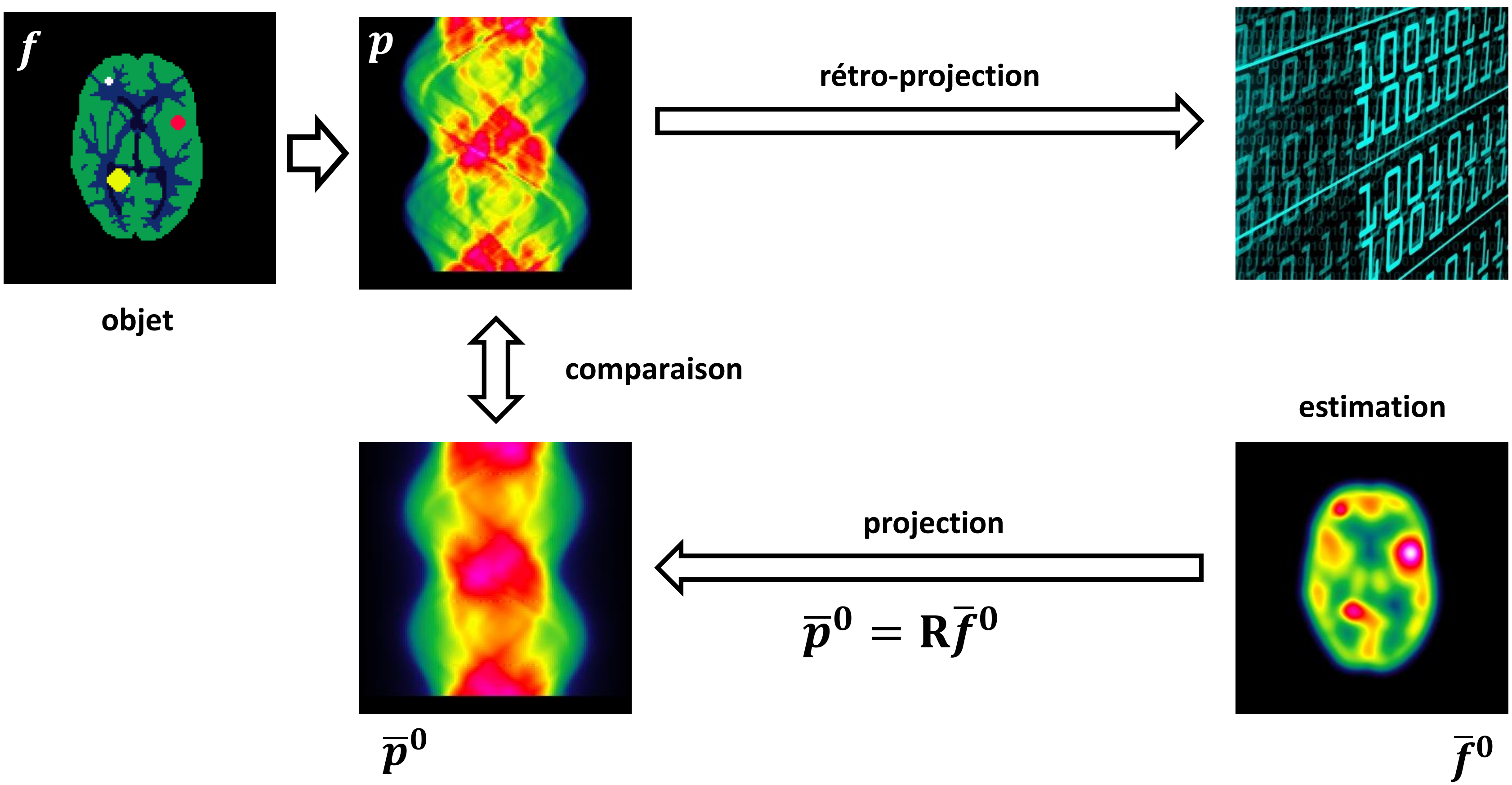

Reconstruction

Reconstruction itérative

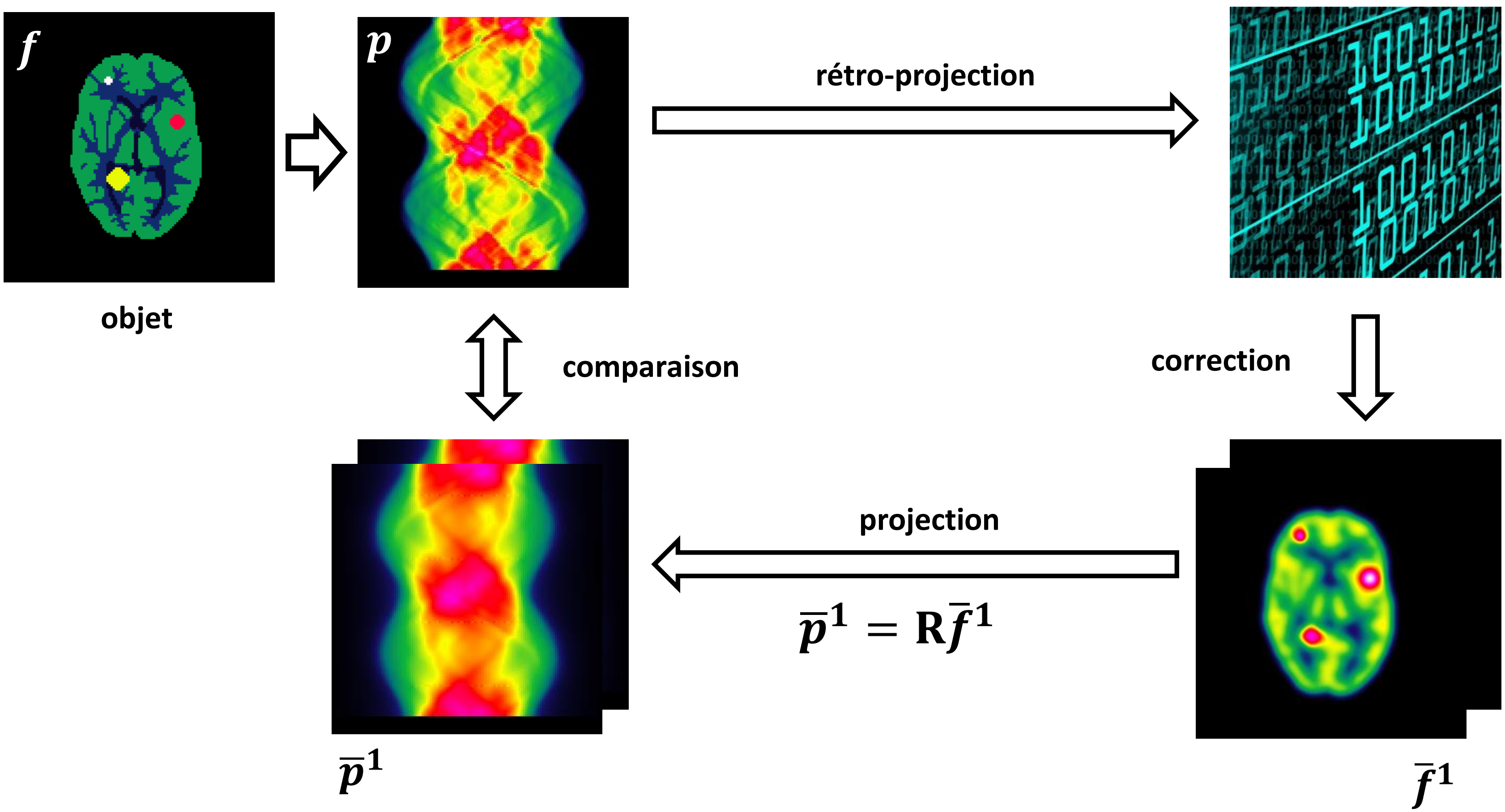

Reconstruction

Reconstruction itérative

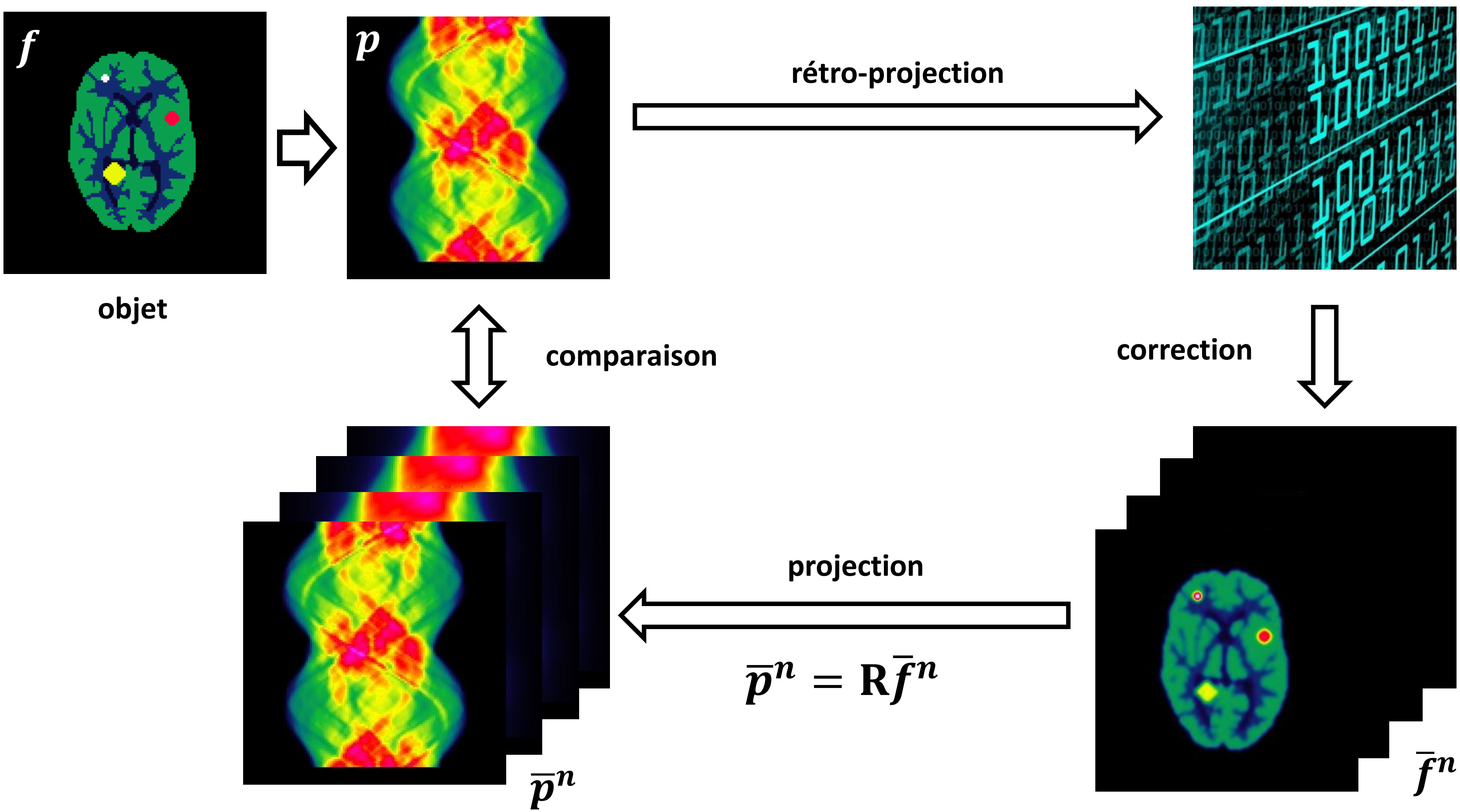

Reconstruction itérative

Many emission tomography ***papers discuss "image reconstruction algorithms" as if the algorithm is the estimator***

This is partially ***true if you use stopping rules, since then the specific characteristics of the iterations determine the image properties perhaps more than the objective function does****, since the user rarely iterates to convergence.*

With penalized objective functions, the estimator (as specified by the objective) determines the image properties, ***and the algorithm is merely a nuisance that is necessary for finding the maximizer of that objective.***

As others have argued before me, the choice of the objective and the algorithm ideally should be kept separate, i.e., ***the objective should be chosen based on statistical principles****, and then* ***the algorithm should be chosen based on how fast it maximizes*** *the chosen objective.*

All too frequently these two distinct issues have been blurred together.

JA Fessler (web.eecs.umich.edu)

Reconstruction

Reconstruction itérative

Fonction Objectif $\bar{\boldsymbol{f}} = \underset{\boldsymbol{f}\in\boldsymbol{\Omega}}{argmin}\ \{J(\boldsymbol{f},\boldsymbol{p})\}$

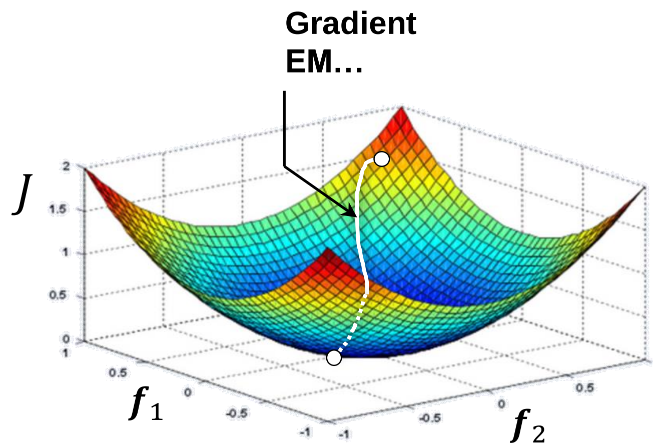

Moindres carrés (LS)

$$J(\boldsymbol{f},\boldsymbol{p}) = \ \|\mathbf{R}\boldsymbol{f} - \boldsymbol{p}\|^2$$

Maximum likelihood (ML)

$$J(\boldsymbol{f},\boldsymbol{p}) = -log\{\, \wp(\boldsymbol{p}|\boldsymbol{f})\,\}$$

Reconstruction

Reconstruction itérative

Fonction Objectif $\bar{\boldsymbol{f}} = \underset{\boldsymbol{f} \in \boldsymbol{\Omega}}{argmin} \{ J(\boldsymbol{f}, \boldsymbol{p}) \}$

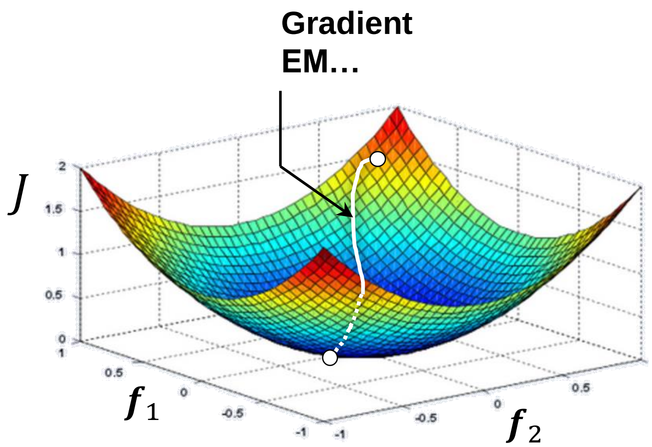

Moindres carrés (LS)

$$J(\boldsymbol{f}, \boldsymbol{p}) = \|\mathbf{R}\boldsymbol{f} - \boldsymbol{p}\|^2$$

Maximum likelihood (ML)

$$J(\boldsymbol{f}, \boldsymbol{p}) = -log\{ \wp(\boldsymbol{p}|\boldsymbol{f}) \}$$

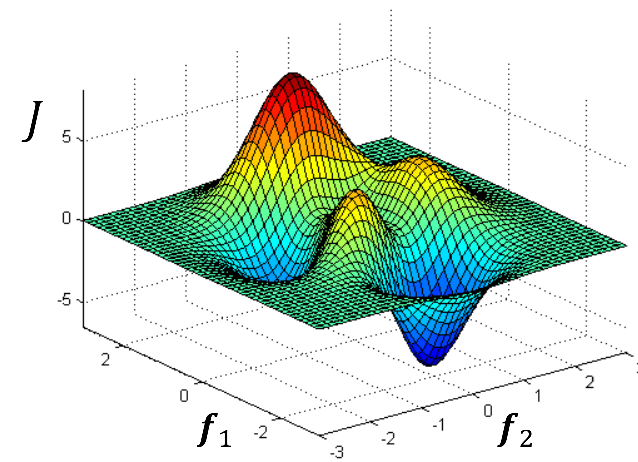

Reconstruction

Régularisation

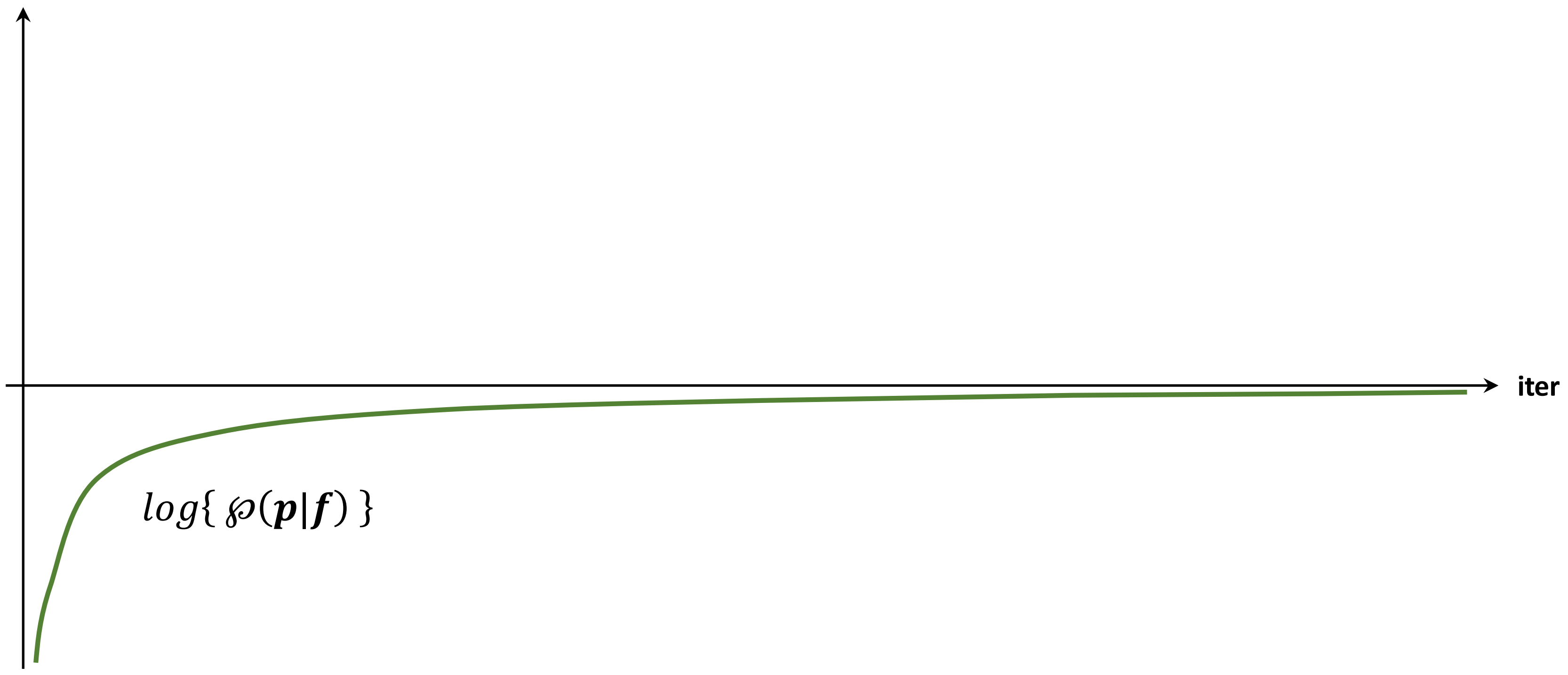

Reconstruction

Régularisation

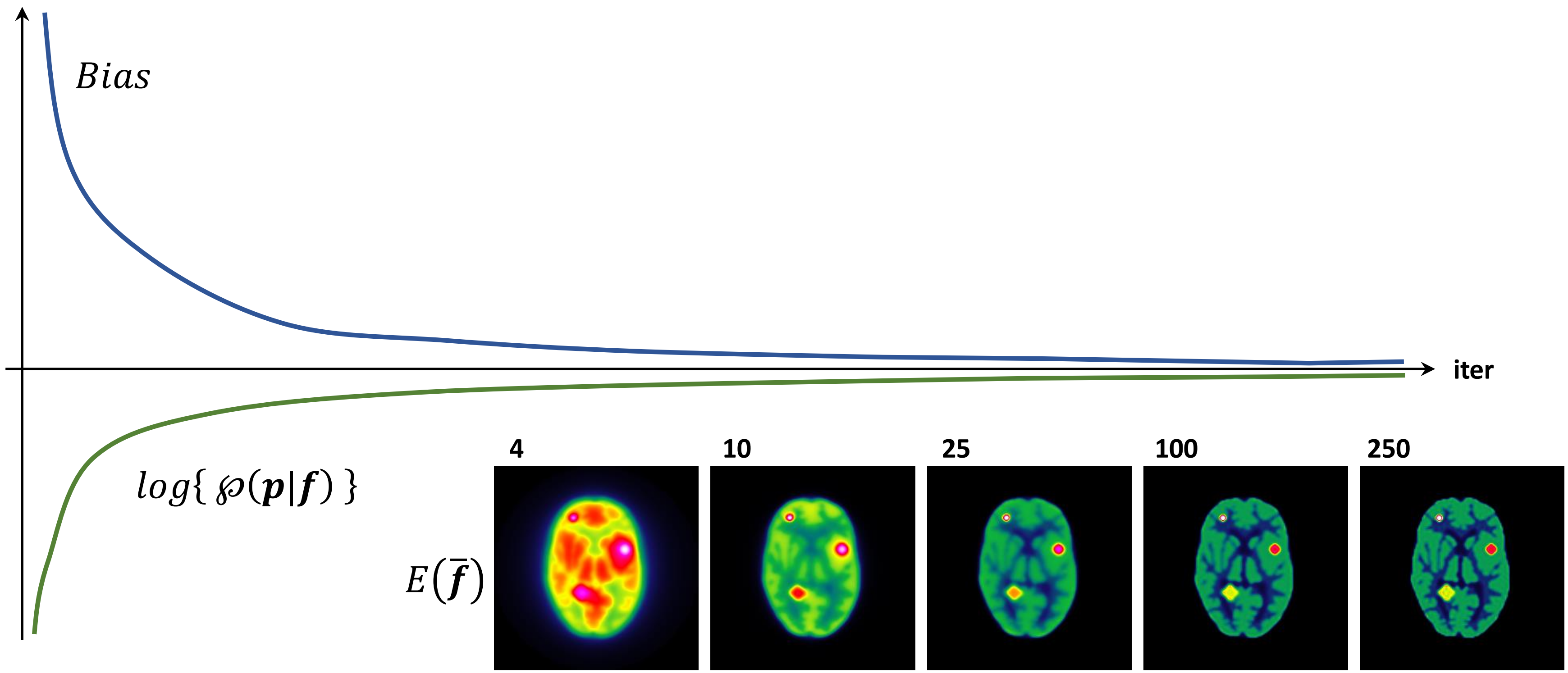

Reconstruction

Régularisation

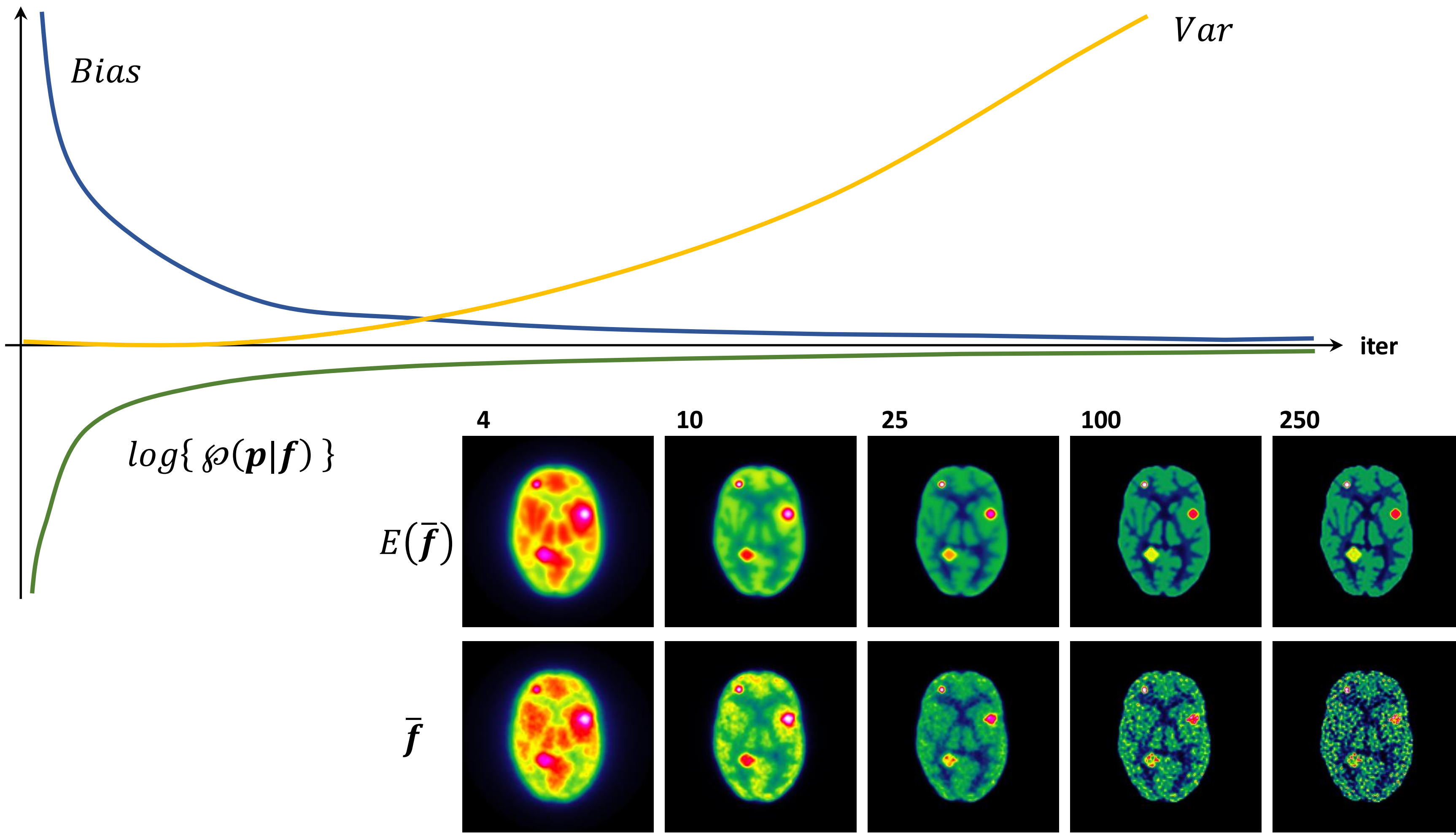

Reconstruction

Régularisation

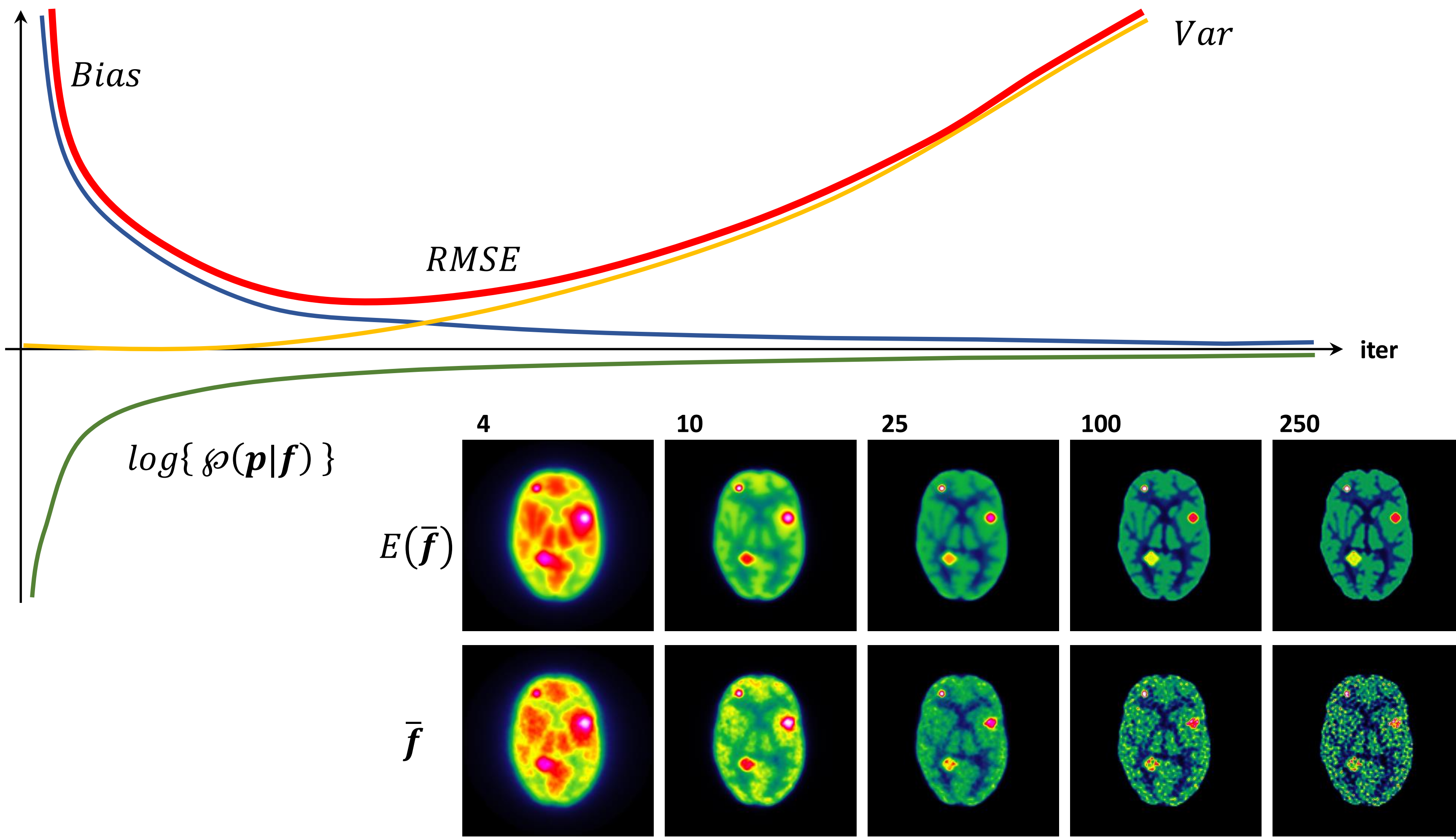

Régularisation

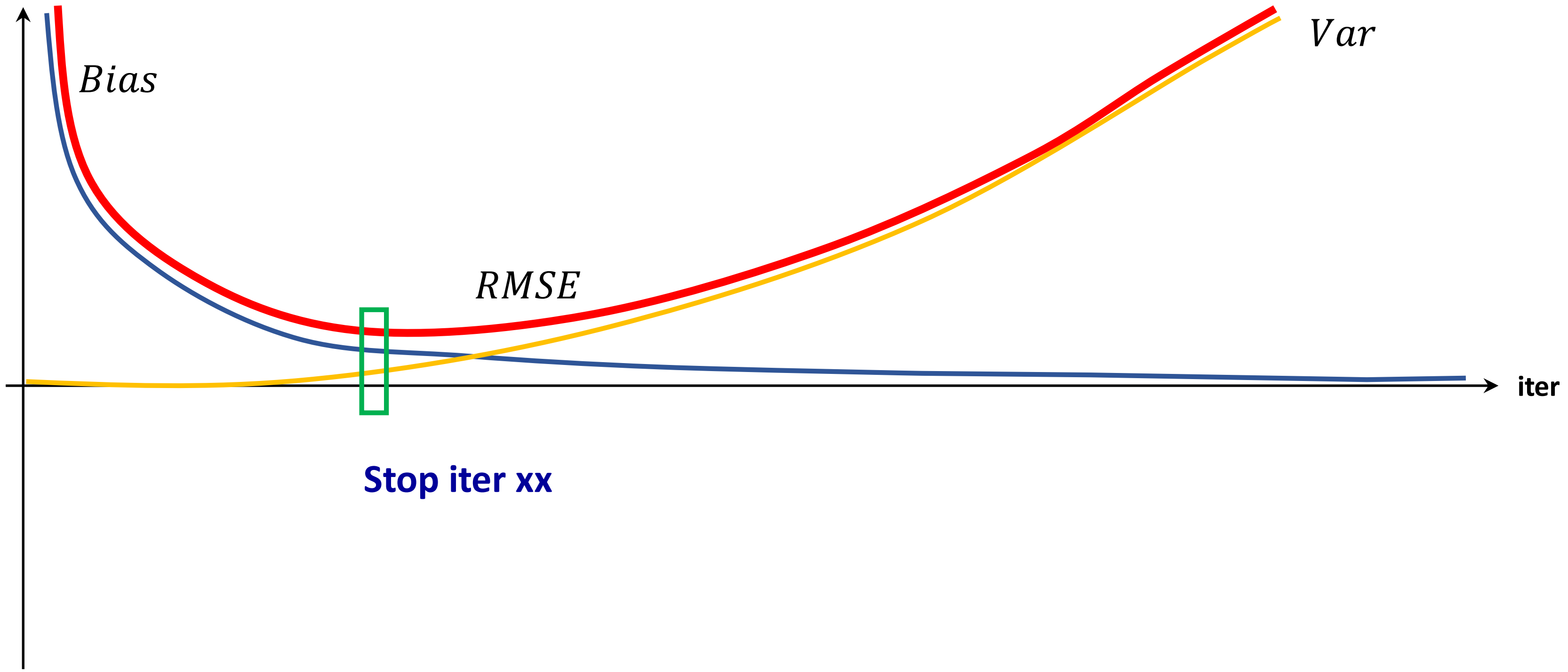

Reconstruction

Régularisation

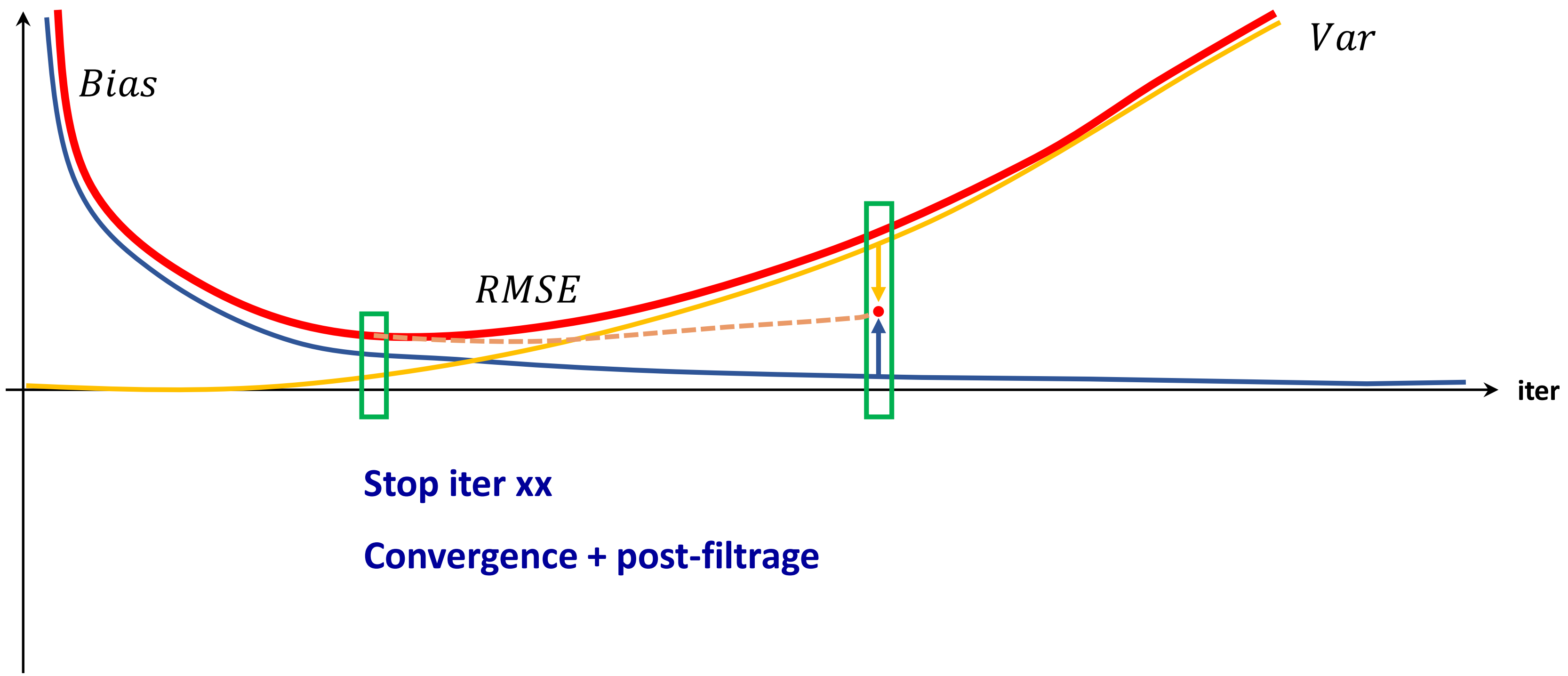

Stop iter xx

Convergence + post-filtrage

Régularisation

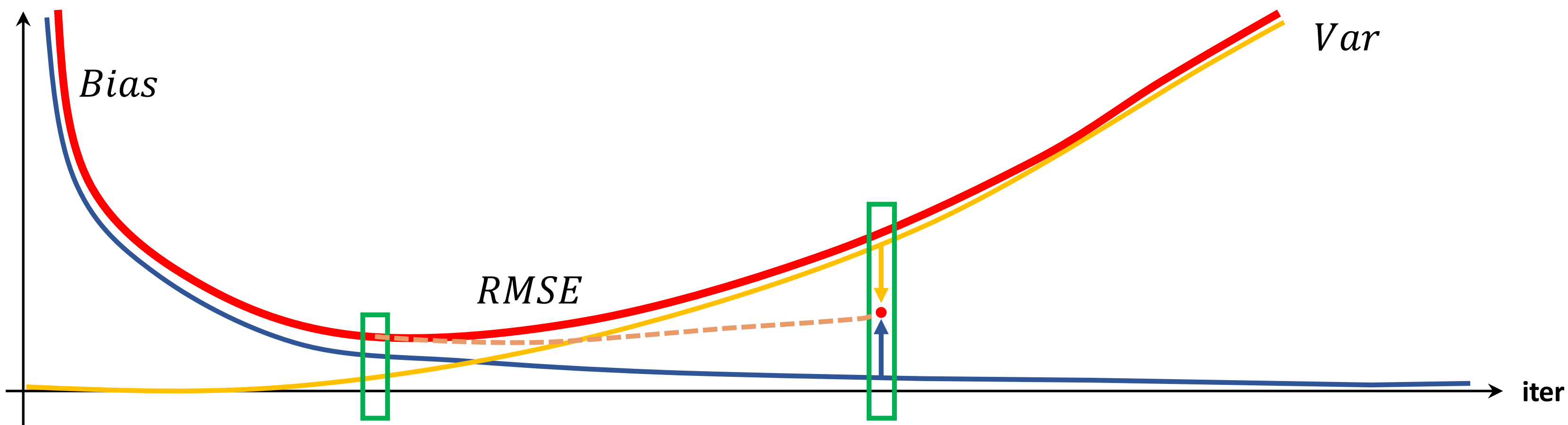

Stop iter xx

Convergence + post-filtrage

Relaxation

$$\bar{\boldsymbol{f}} = \underset{\boldsymbol{f} \in \Omega}{argmin} \left\{ J(\boldsymbol{f},\boldsymbol{p}) + \beta \, H(\boldsymbol{f},\boldsymbol{p}) \right\}$$

Adéquation
↓ biais

Régularisation
↓ variance

Régularisation

Post-filtrage

FWHM : 2 pix 3,5 pix 5 pix

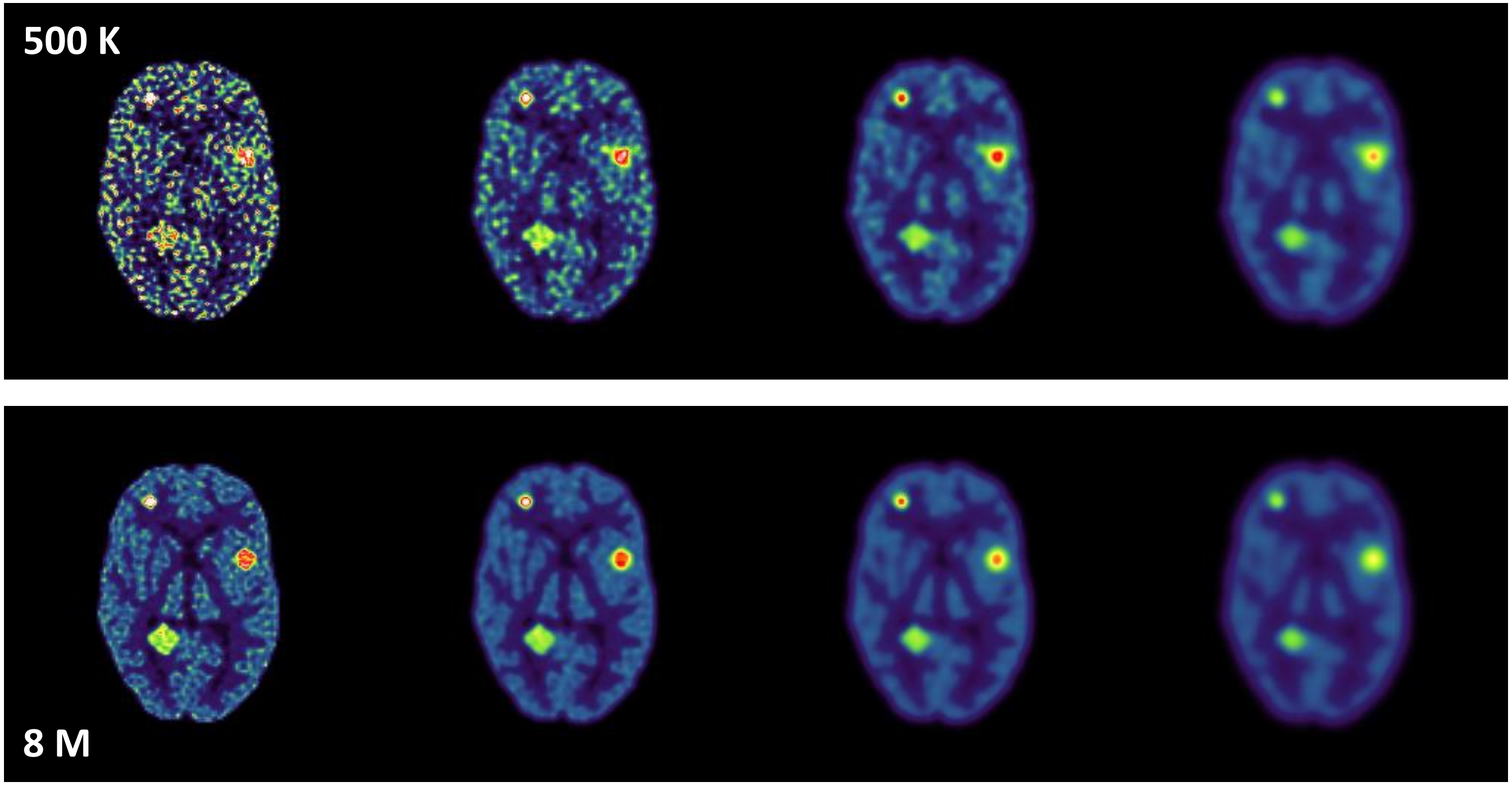

Reconstruction

Régularisation

Relaxation (MAP-EM)

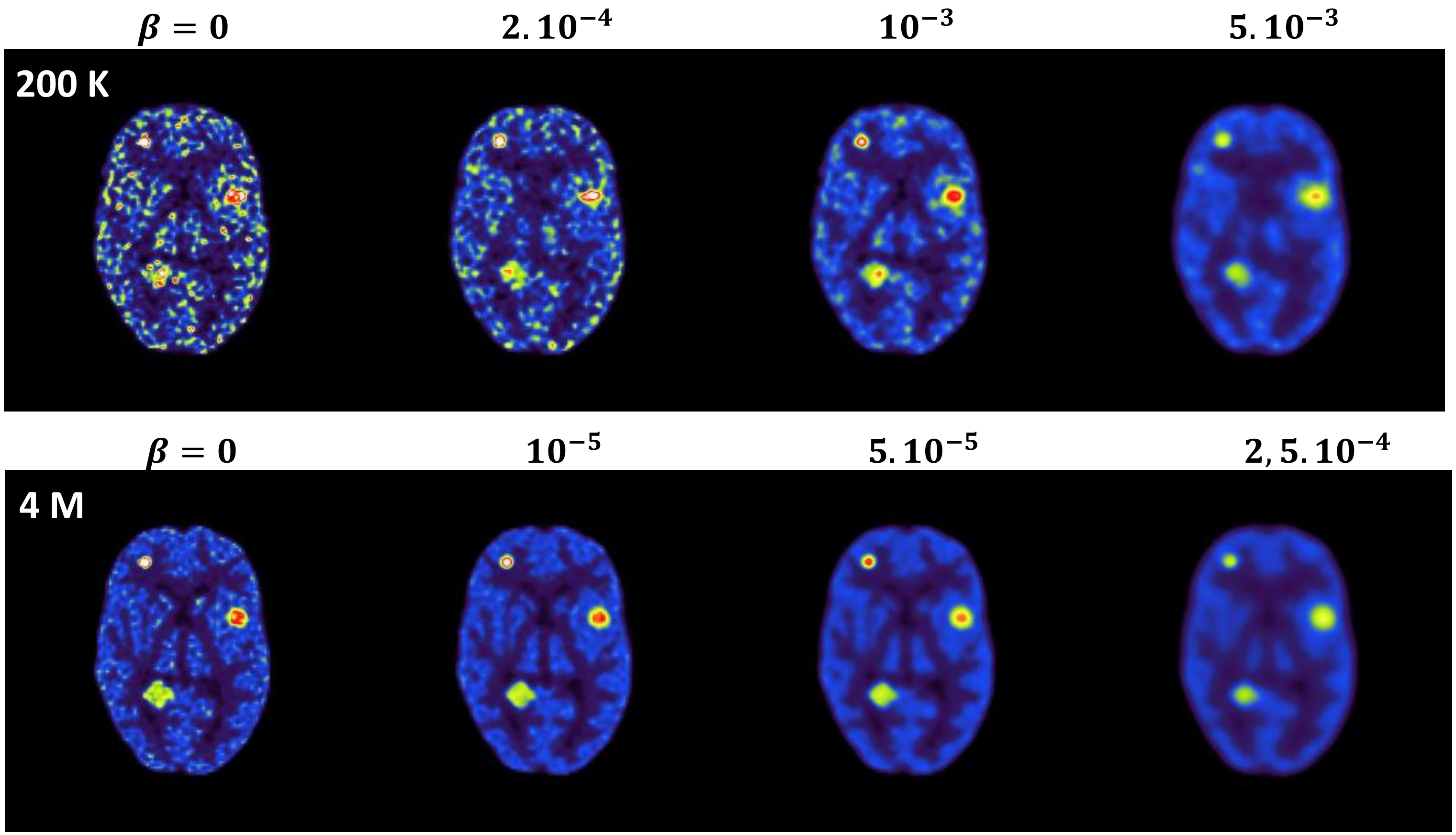

Corrections

$$\boldsymbol{p} = \mathbf{R}\boldsymbol{f} + \boldsymbol{scat} + \boldsymbol{rand} \ \ (+\boldsymbol{noise})$$

Corrections

$$p = \mathbf{R}f + scat + rand$$

$$\boxed{f \quad \text{t.q.} \quad \mathbf{R}f = p - scat - rand}$$

Corrections

$$\boldsymbol{p} = \mathbf{R}\boldsymbol{f} + \boldsymbol{scat} + \boldsymbol{rand}$$

$$\boldsymbol{f} \;\; \text{t.q.} \;\; \mathbf{R}\boldsymbol{f} = \boldsymbol{p} - \boldsymbol{scat} - \boldsymbol{rand}$$

$$\mathbf{R} = \mathbf{R}_{norm} \times \mathbf{R}_{blur} \times \mathbf{R}_{attn} \times \mathbf{R}_{geom}$$

Corrections

$$\boldsymbol{p} = \mathbf{R}\boldsymbol{f} + \boldsymbol{scat} + \boldsymbol{rand}$$

$$\boldsymbol{f} \quad \text{t.q.} \quad \mathbf{R}\boldsymbol{f} = \boldsymbol{p} - \boldsymbol{scat} - \boldsymbol{rand}$$

$$\mathbf{R} = \mathbf{R}_{norm} \times \mathbf{R}_{blur} \times \mathbf{R}_{attn} \times \mathbf{R}_{geom}$$

$$\boxed{\boldsymbol{f} \quad \text{t.q.} \quad \mathbf{R}_{geom}\,\boldsymbol{f} = \delta\, \mathbf{C}_{norm} \times \mathbf{C}_{blur} \times \mathbf{C}_{attn} \times (\boldsymbol{p} - \boldsymbol{scat} - \boldsymbol{rand})}$$

Corrections

$$f \quad \text{t.q.} \quad \boxed{\mathbf{R}_{geom}}\, \boldsymbol{f} = \delta\, \mathbf{C}_{norm} \times \mathbf{C}_{blur} \times \mathbf{C}_{attn} \times (\boldsymbol{p} - \boldsymbol{scat} - \boldsymbol{rand})$$

Géométrie

$$\mathbf{R}_{geom}(i,j) \propto \Lambda \cap \Pi$$

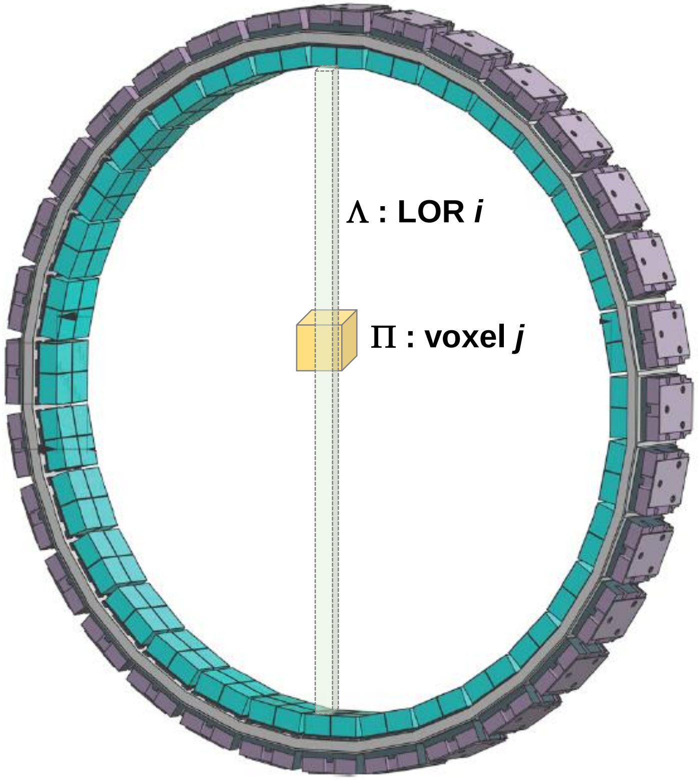

Borghi, Phys Med Biol 2018

Corrections

$$\boldsymbol{f} \quad \text{t.q.} \quad \boxed{\mathbf{R}_{geom}}\, \boldsymbol{f} = \delta\, \mathbf{C}_{norm} \times \mathbf{C}_{blur} \times \mathbf{C}_{attn} \times (\boldsymbol{p} - \boldsymbol{scat} - \boldsymbol{rand})$$

Géométrie

$$\mathbf{R}_{geom}(i,j) \propto \Lambda \cap \Pi$$

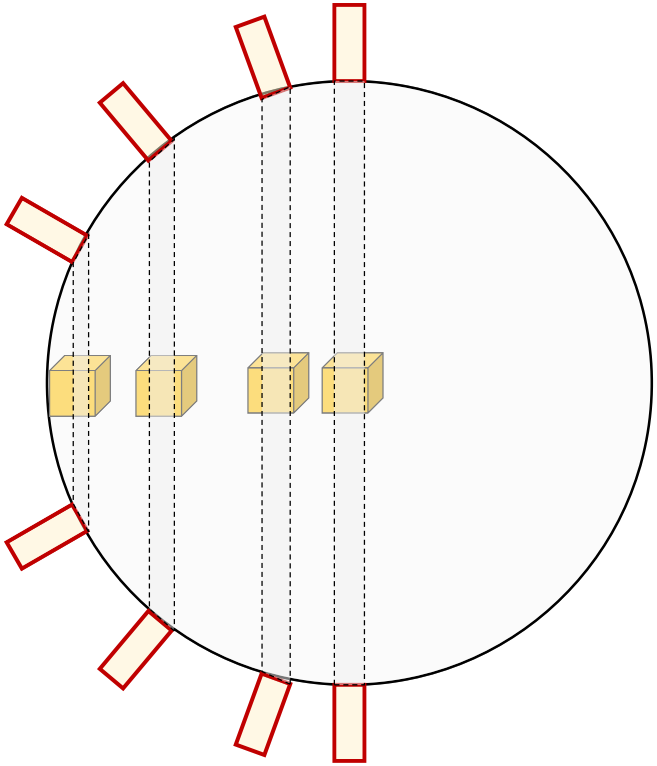

Corrections

$$\boldsymbol{f} \quad \text{t.q.} \quad \mathbf{R}_{geom}\,\boldsymbol{f} = \delta\,\mathbf{C}_{norm} \times \mathbf{C}_{blur} \times \mathbf{C}_{attn} \times (\boldsymbol{p} - \boldsymbol{scat} - \boxed{\boldsymbol{rand}})$$

Fortuits

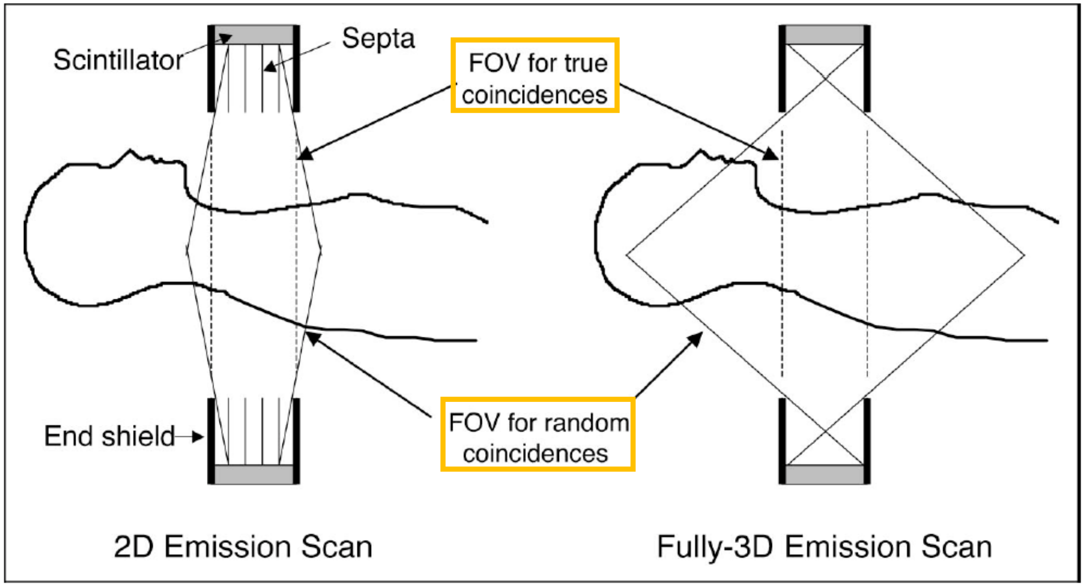

Brasse, J Nucl Med 2005

Corrections

$$\boldsymbol{f} \quad \text{t.q.} \quad \mathbf{R}_{geom}\, \boldsymbol{f} = \delta\, \mathbf{C}_{norm} \times \mathbf{C}_{blur} \times \mathbf{C}_{attn} \times (\boldsymbol{p} - \boldsymbol{scat} - \boxed{\boldsymbol{rand}})$$

Fortuits

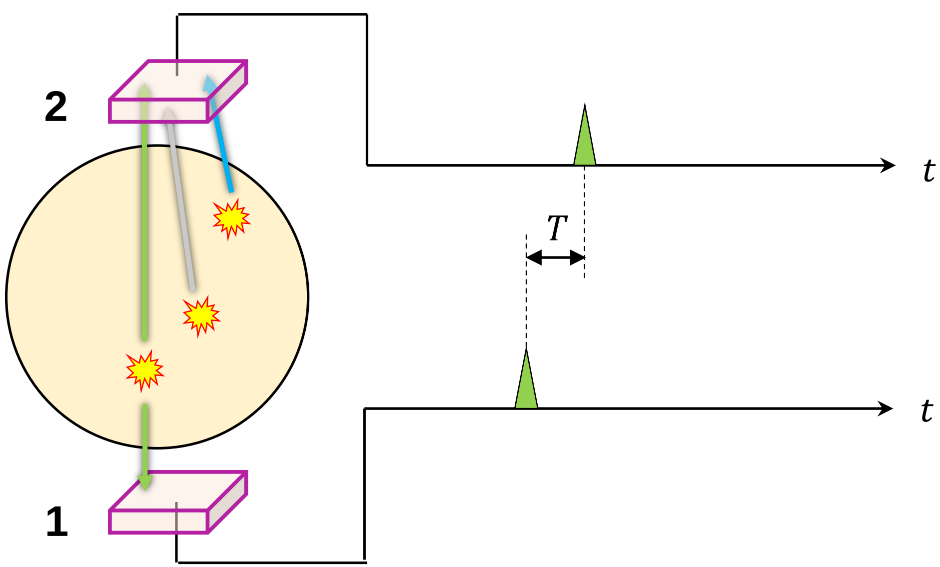

Corrections

$$\boldsymbol{f} \quad \text{t.q.} \quad \mathbf{R}_{geom}\,\boldsymbol{f} = \delta\, \mathbf{C}_{norm} \times \mathbf{C}_{blur} \times \mathbf{C}_{attn} \times (\boldsymbol{p} - \boldsymbol{scat} - \boxed{\boldsymbol{rand}})$$

Fortuits

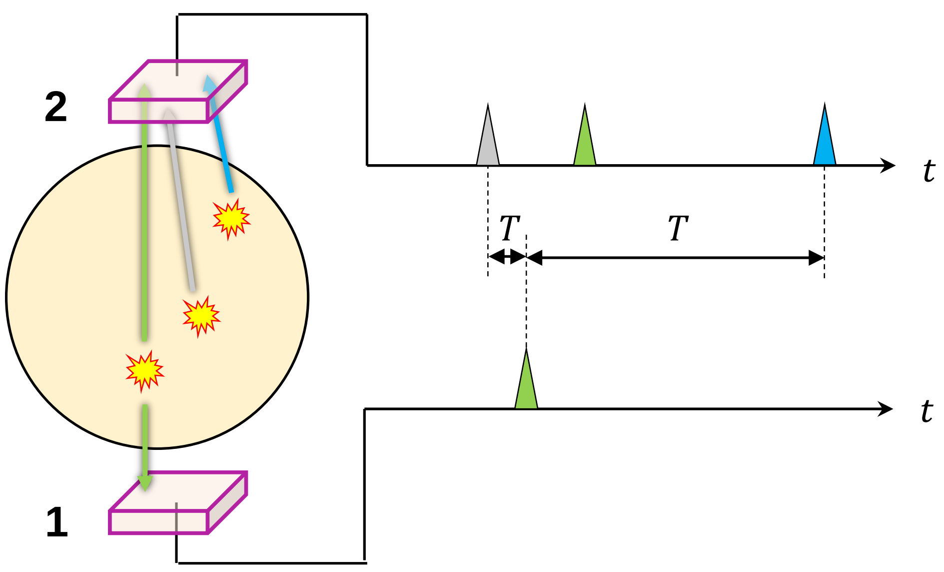

Corrections

$$\boldsymbol{f} \quad \text{t.q.} \quad \mathbf{R}_{geom}\,\boldsymbol{f} = \delta\,\mathbf{C}_{norm} \times \mathbf{C}_{blur} \times \mathbf{C}_{attn} \times (\boldsymbol{p} - \boldsymbol{scat} - \boxed{\boldsymbol{rand}})$$

Fortuits

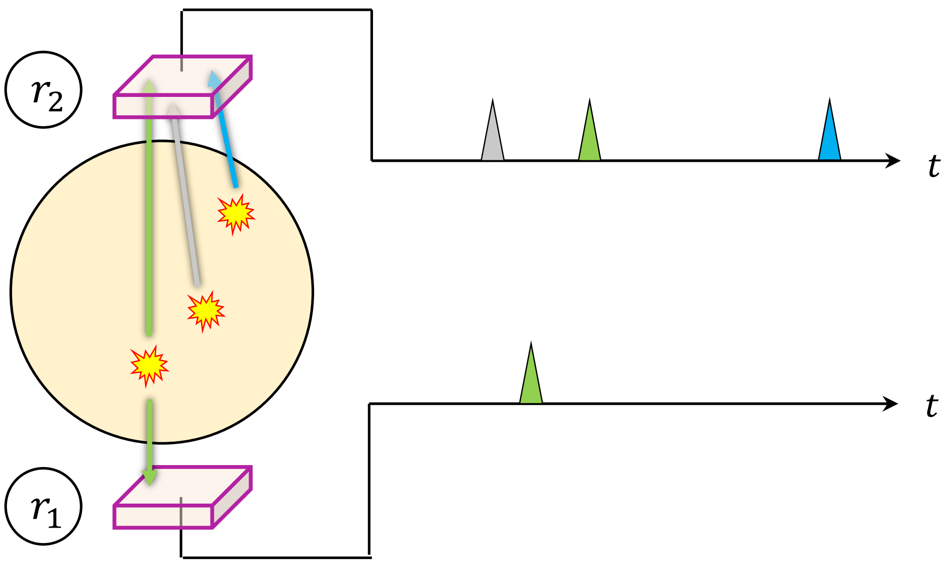

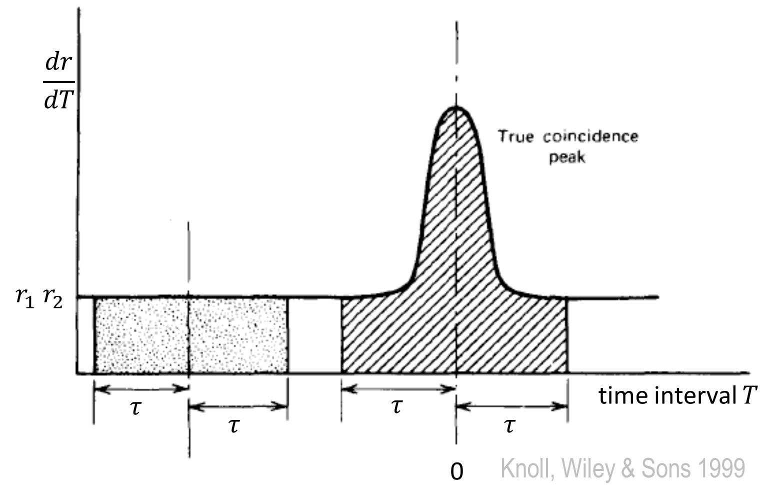

Corrections

$$\boldsymbol{f} \quad \text{t.q.} \quad \mathbf{R}_{geom}\,\boldsymbol{f} = \delta\,\mathbf{C}_{norm} \times \mathbf{C}_{blur} \times \mathbf{C}_{attn} \times (\boldsymbol{p} - \boldsymbol{scat} - \boxed{\boldsymbol{rand}})$$

Fortuits

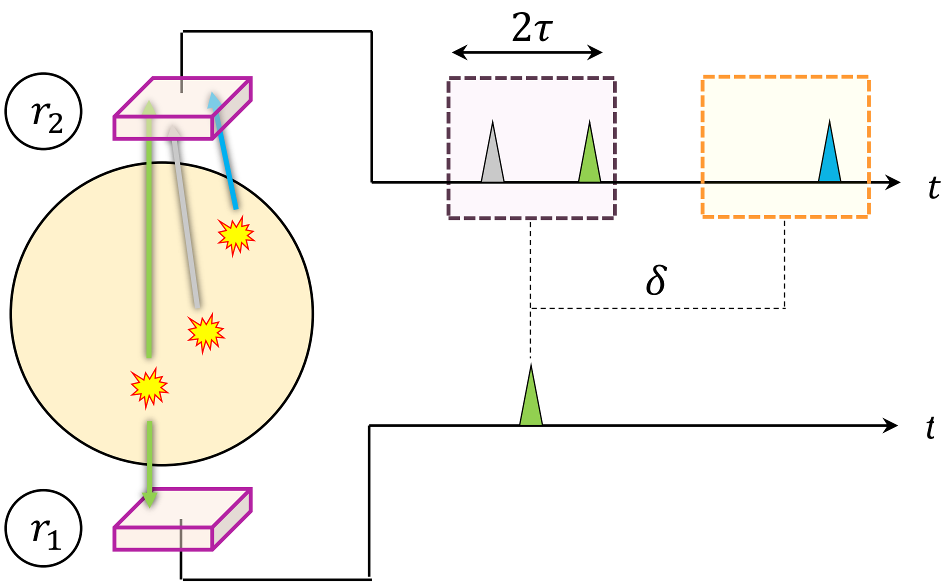

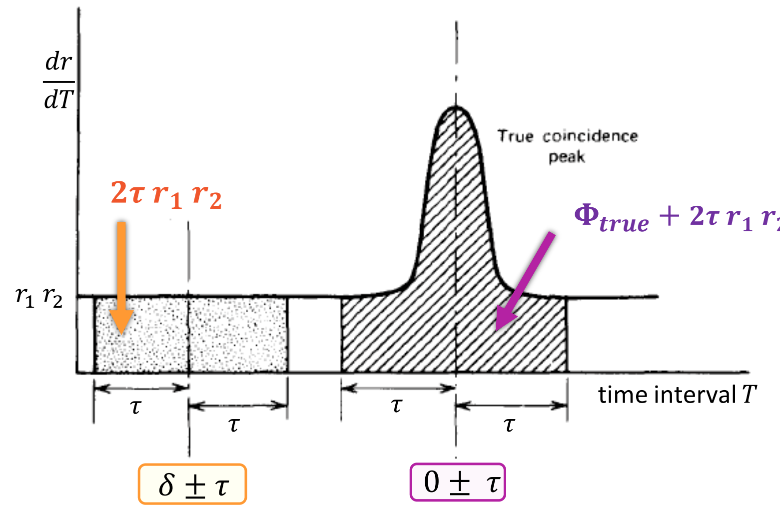

Corrections

$$\boldsymbol{f} \quad \text{t.q.} \quad \mathbf{R}_{geom}\,\boldsymbol{f} = \delta\,\mathbf{C}_{norm} \times \mathbf{C}_{blur} \times \mathbf{C}_{attn} \times (\boldsymbol{p} - \boldsymbol{scat} - \boxed{\boldsymbol{rand}})$$

Fortuits

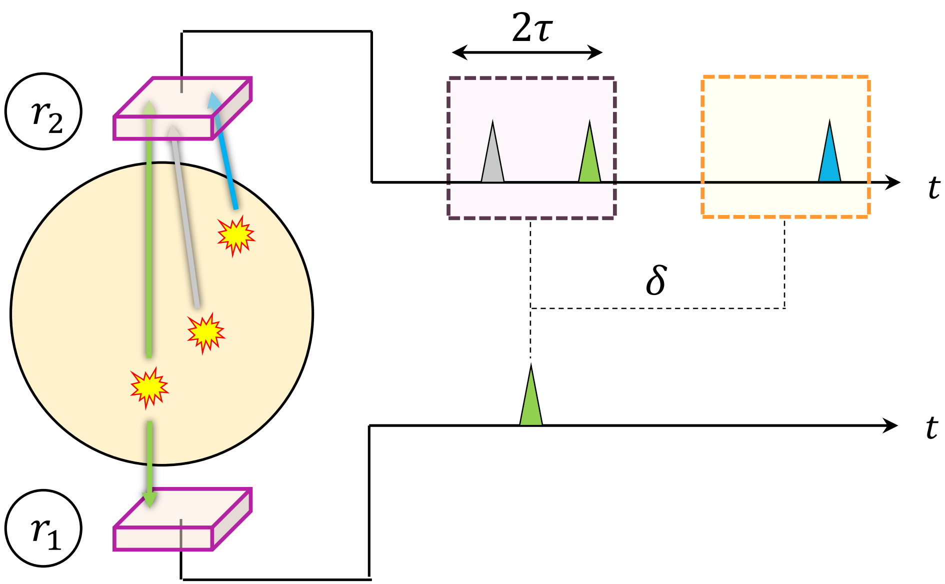

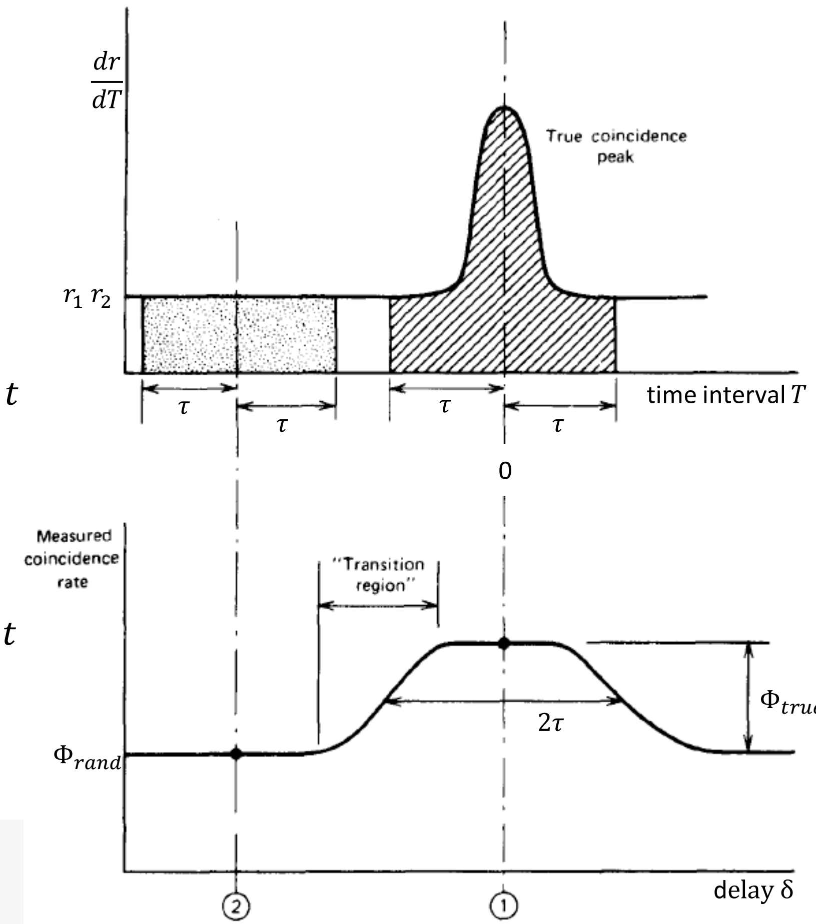

True : Φ_{true}
Random : $\Phi_{rand} = 2\tau\, r_1\, r_2$

Knoll, Wiley & Sons 1999

Corrections

$$\boldsymbol{f} \quad \text{t.q.} \quad \mathbf{R}_{geom}\,\boldsymbol{f} = \delta\, \mathbf{C}_{norm} \times \mathbf{C}_{blur} \times \mathbf{C}_{attn} \times (\boldsymbol{p} - \boldsymbol{scat} - \boxed{\boldsymbol{rand}})$$

Fortuits

Fenêtre de coïncidences

> *D/c < 2 ns*
> *résolution temporelle*
> *2 τ_{opt} ~ 10 ns*

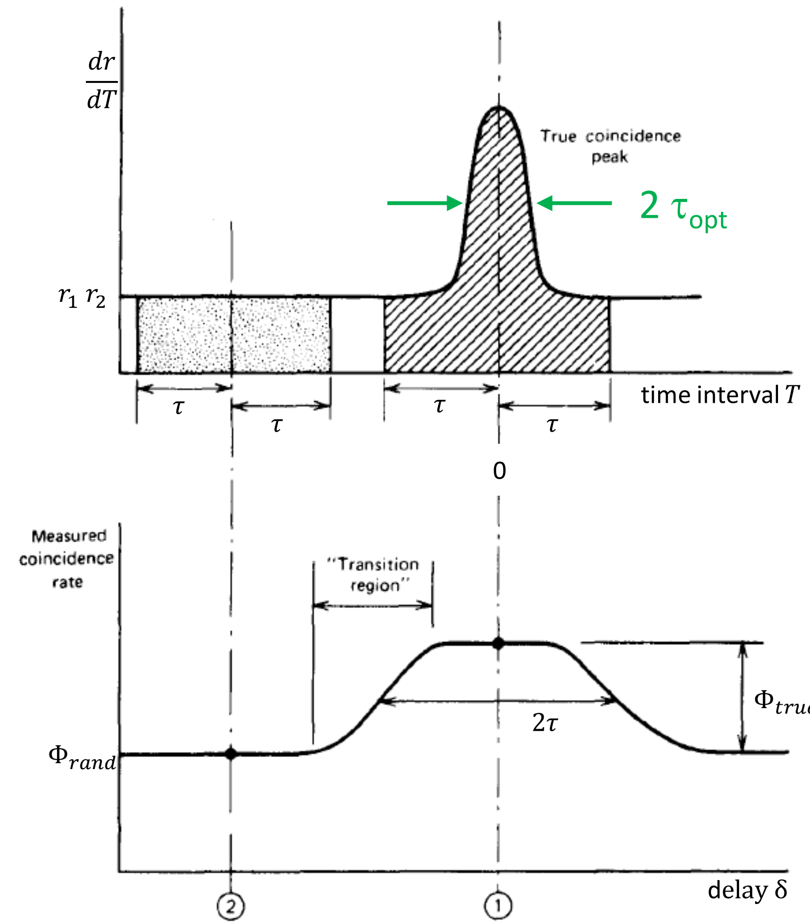

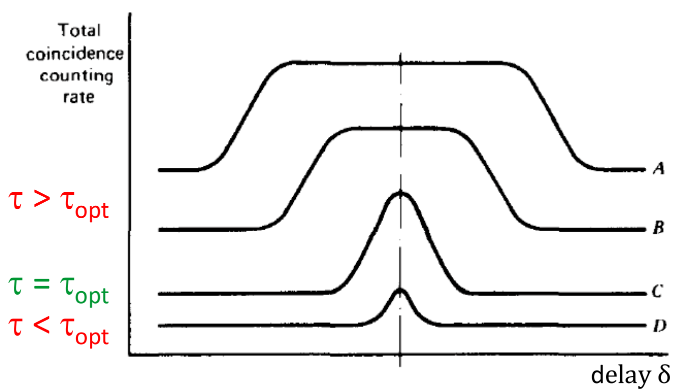

Knoll, Wiley & Sons 1999

Corrections

$$\boldsymbol{f} \quad \text{t.q.} \quad \mathbf{R}_{geom}\,\boldsymbol{f} = \delta\,\mathbf{C}_{norm} \times \mathbf{C}_{blur} \times \mathbf{C}_{attn} \times (\boldsymbol{p} - \boldsymbol{scat} - \boxed{\boldsymbol{rand}})$$

Fortuits

Tail-fitting
Singles

$$\Phi_{rand} = 2\tau\, r_1\, r_2$$

$$NECR = \frac{T^2}{T + S + kR}$$

$$k = 1$$

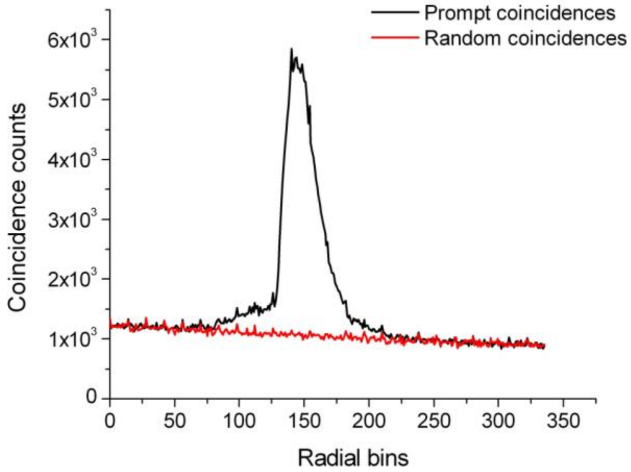

Carlier, Med Phys 2015

Corrections

$$\boldsymbol{f} \quad \text{t.q.} \quad \mathbf{R}_{geom}\, \boldsymbol{f} = \delta\, \mathbf{C}_{norm} \times \mathbf{C}_{blur} \times \mathbf{C}_{attn} \times (\boldsymbol{p} - \boldsymbol{scat} - \boxed{\boldsymbol{rand}})$$

Fortuits

Tail-fitting
Singles
Fenêtre décalée

$$NECR = \frac{T^2}{T + S + kR}$$

$$k = 2$$

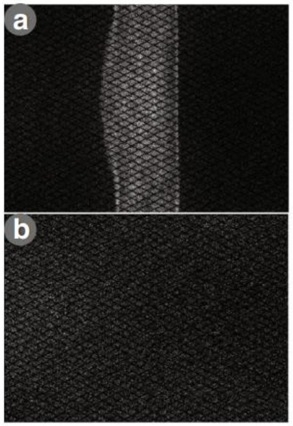

Markiewicz, Neuroinformatics 2018

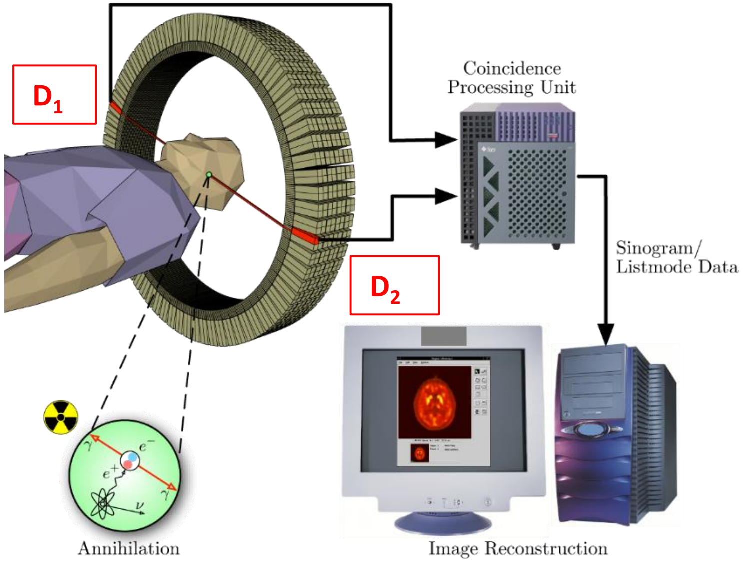

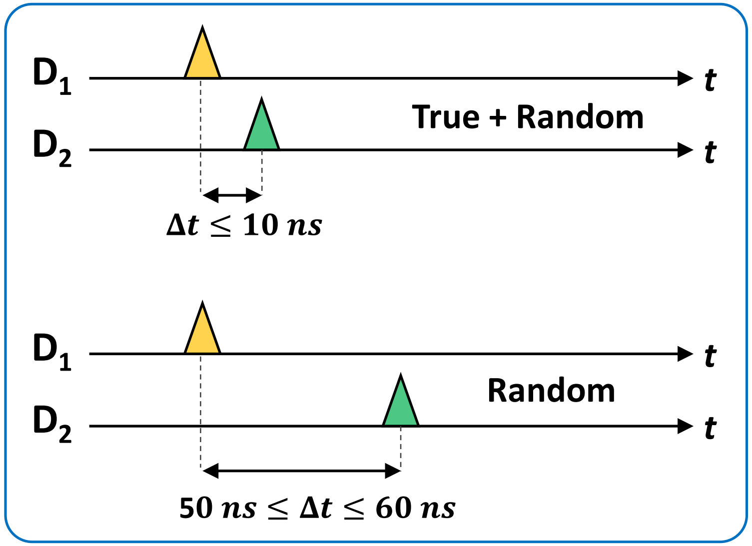

Corrections

$$\boldsymbol{f} \quad \text{t.q.} \quad \mathbf{R}_{geom}\,\boldsymbol{f} = \delta\,\mathbf{C}_{norm} \times \mathbf{C}_{blur} \times \mathbf{C}_{attn} \times (\boldsymbol{p} - \boldsymbol{scat} - \boxed{\boldsymbol{rand}})$$

Fortuits

$$NECR = \frac{T^2}{T + S + kR}$$

$$k \sim 1$$

Tail-fitting
Singles
Fenêtre décalée
+ filtrage

$$R_{ij} = \frac{R_{jA} \times R_{iB}}{R_{AB}}$$

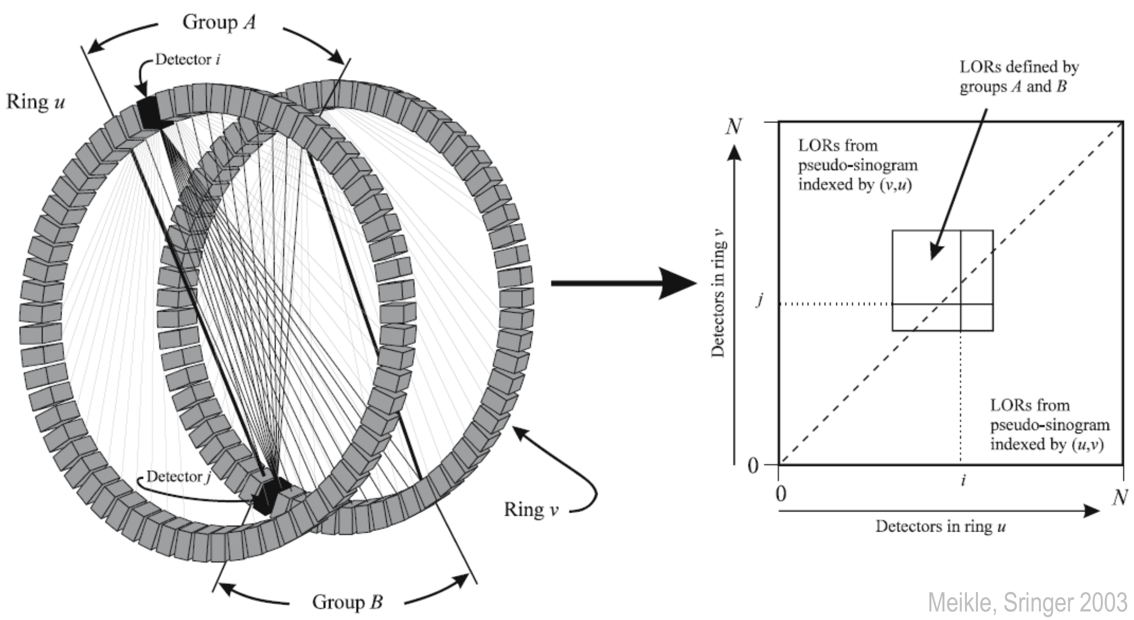

Meikle, Sringer 2003

Corrections

$$\boldsymbol{f} \quad \text{t.q.} \quad \mathbf{R}_{geom}\,\boldsymbol{f} = \delta\, \mathbf{C}_{norm} \times \mathbf{C}_{blur} \times \mathbf{C}_{attn} \times (\boldsymbol{p} - \boldsymbol{scat} - \boxed{\boldsymbol{rand}})$$

Fortuits

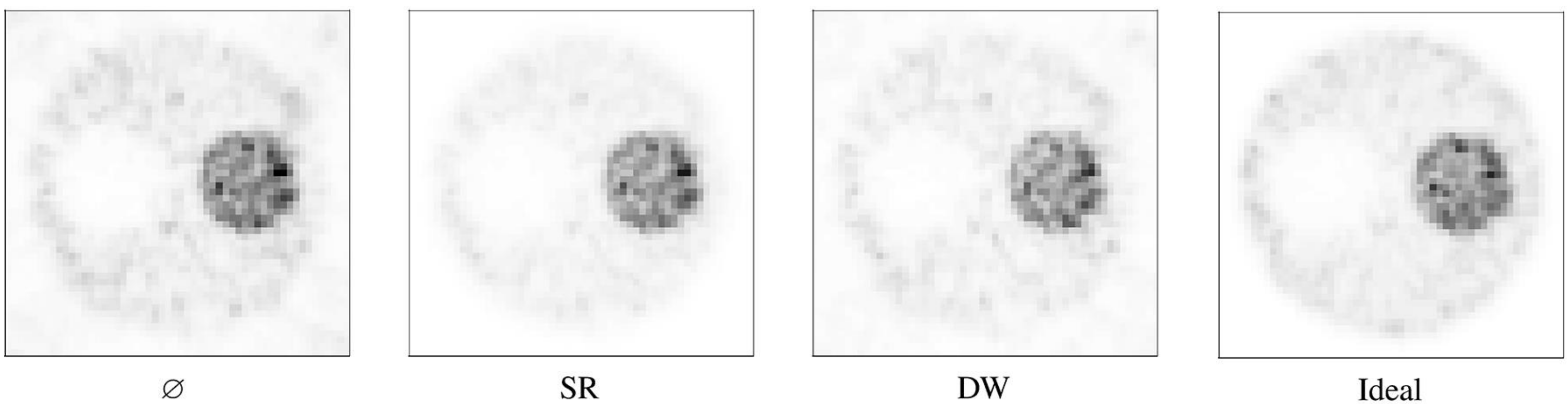

Oliver, Plos One 2016

Corrections

$$f \quad \text{t.q.} \quad \mathbf{R}_{geom}\, \boldsymbol{f} = \delta\, \mathbf{C}_{norm} \times \mathbf{C}_{blur} \times \mathbf{C}_{attn} \times (\boldsymbol{p} - \boxed{\boldsymbol{scat}} - \boldsymbol{rand})$$

Diffusé

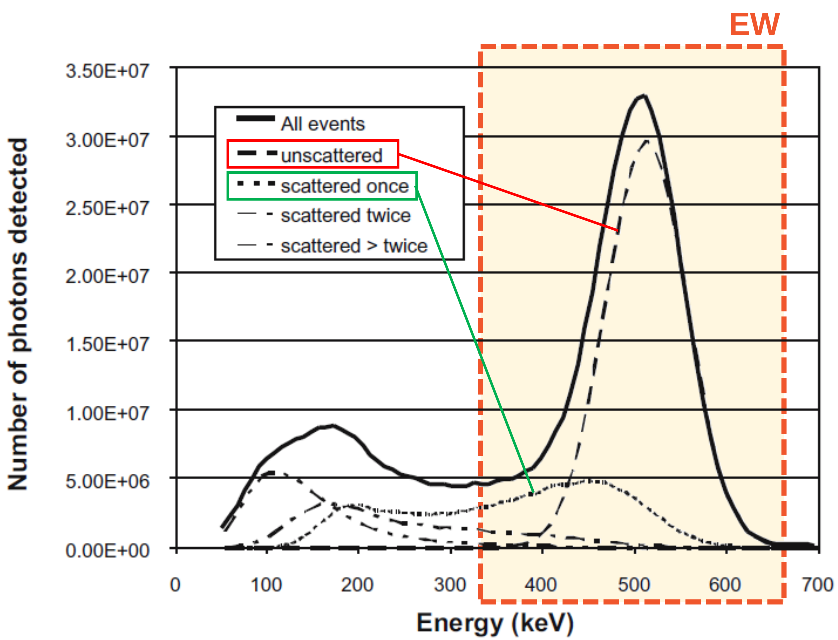

Meikle, Sringer 2003

Corrections

$$f \quad \text{t.q.} \quad \mathbf{R}_{geom}\, \boldsymbol{f} = \delta\, \mathbf{C}_{norm} \times \mathbf{C}_{blur} \times \mathbf{C}_{attn} \times (\boldsymbol{p} - \boxed{\boldsymbol{scat}} - \boldsymbol{rand})$$

Diffusé

> Tail-fitting

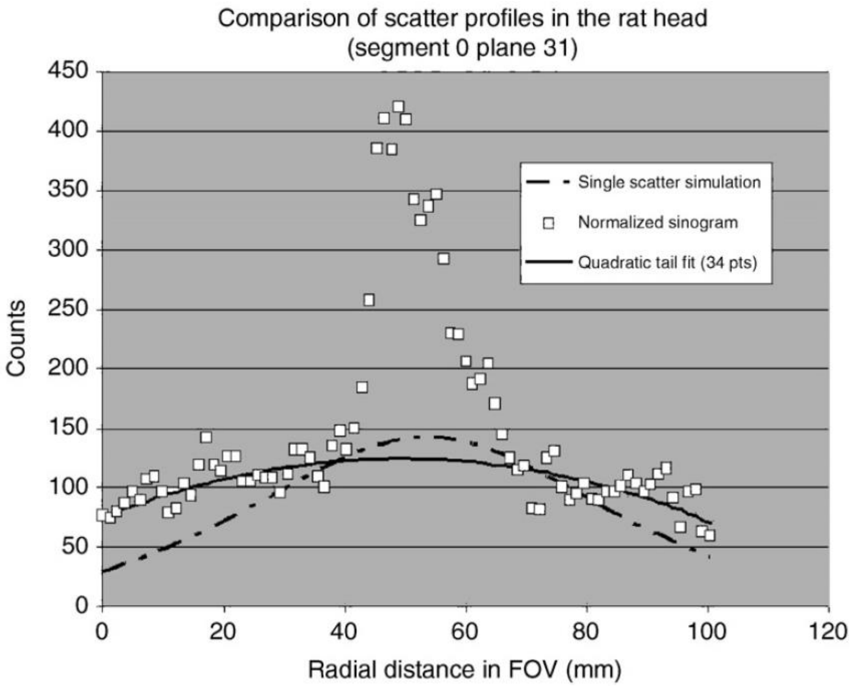

Vaska, Int Rev Neurobiol 2006

Corrections

$$\boldsymbol{f} \quad \text{t.q.} \quad \mathbf{R}_{geom}\,\boldsymbol{f} = \delta\,\mathbf{C}_{norm} \times \mathbf{C}_{blur} \times \mathbf{C}_{attn} \times (\boldsymbol{p} - \boxed{\boldsymbol{scat}} - \boldsymbol{rand})$$

Diffusé

> Tail-fitting
> Fenêtrage

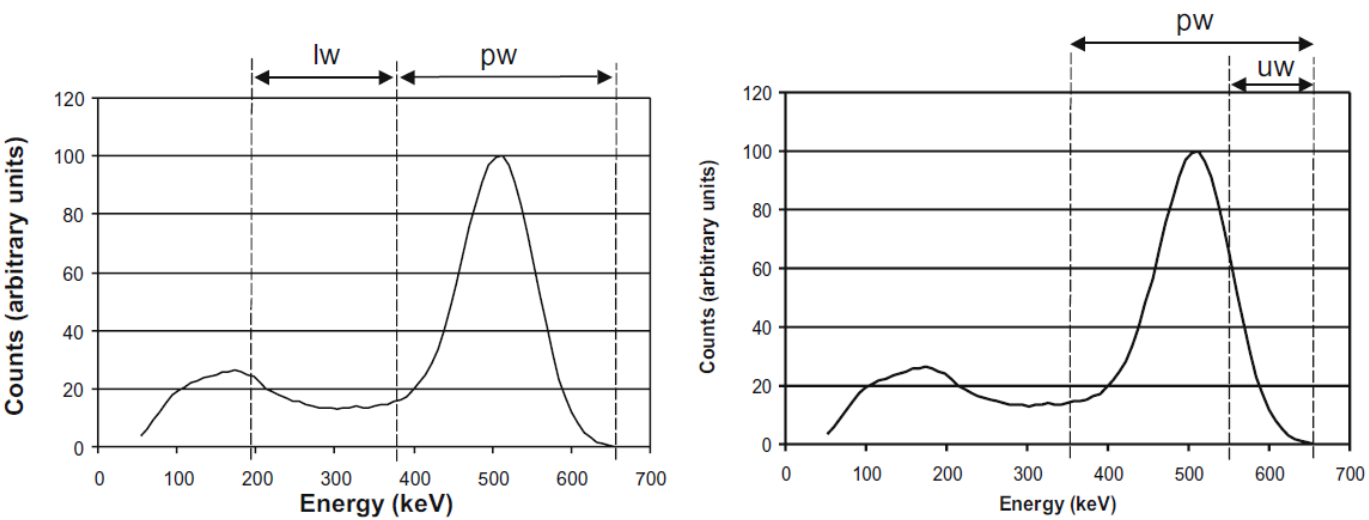

Meikle, Sringer 2003

Corrections

$$f \quad \text{t.q.} \quad \mathbf{R}_{geom}\, f = \delta\, \mathbf{C}_{norm} \times \mathbf{C}_{blur} \times \mathbf{C}_{attn} \times (p - \boxed{scat} - rand\,)$$

Diffusé

> Tail-fitting
> Fenêtrage

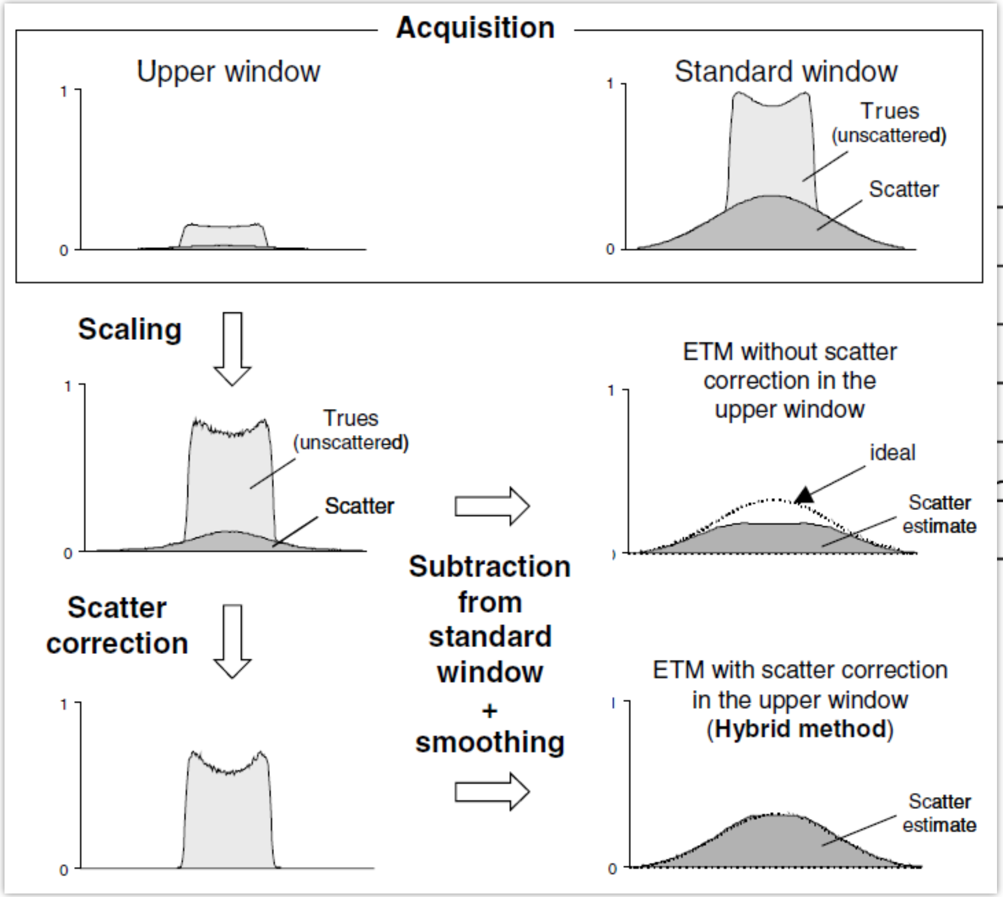

Ferreira, Phys Med Biol 2002

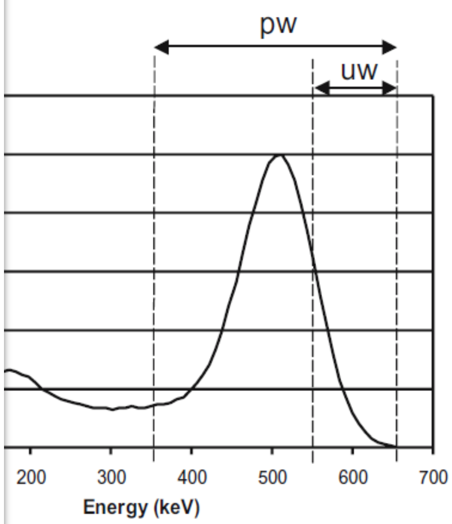

Meikle, Sringer 2003

Corrections

$$f \quad \text{t.q.} \quad \mathbf{R}_{geom}\, \boldsymbol{f} = \delta\, \mathbf{C}_{norm} \times \mathbf{C}_{blur} \times \mathbf{C}_{attn} \times (\boldsymbol{p} - \boxed{\boldsymbol{scat}} - \boldsymbol{rand})$$

Diffusé

- > Tail-fitting
- > Fenêtrage
- > (Dé-)convolution

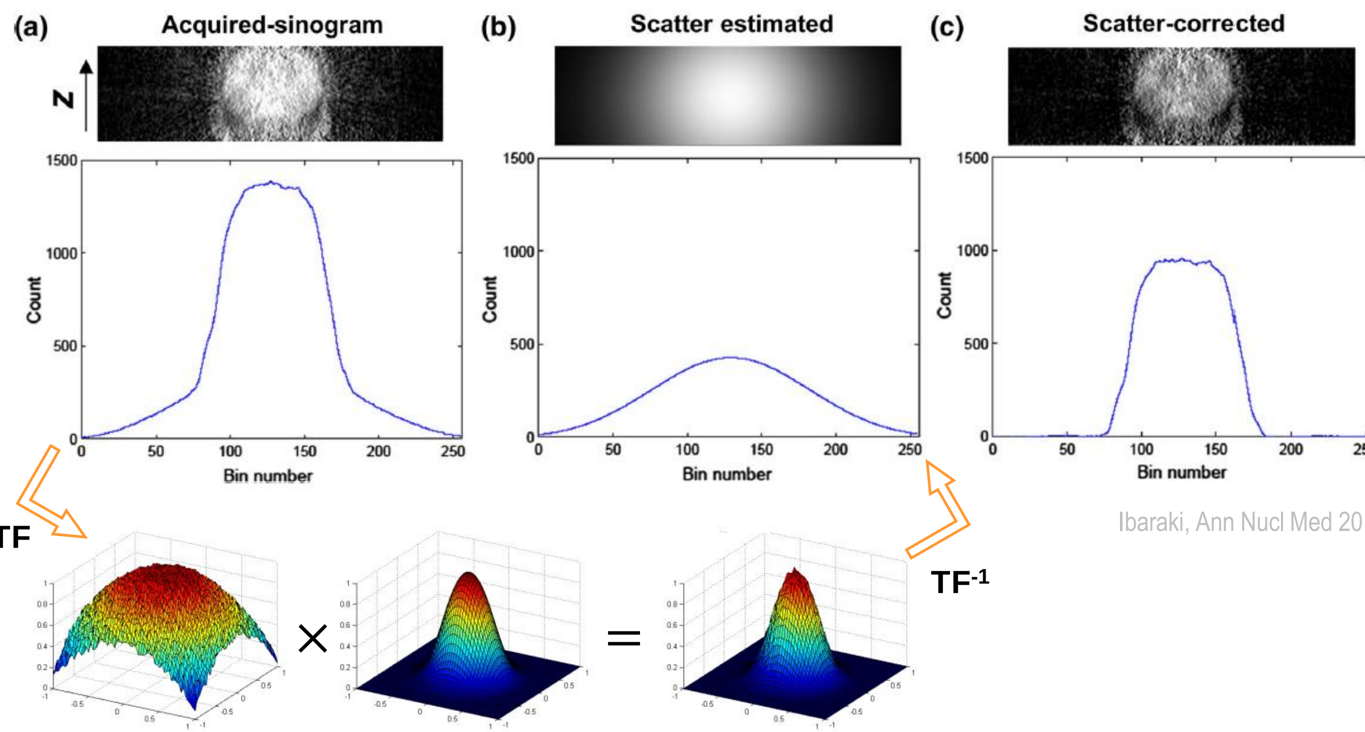

Ibaraki, Ann Nucl Med 2016

Corrections

$$\boldsymbol{f} \quad \text{t.q.} \quad \mathbf{R}_{geom}\,\boldsymbol{f} = \delta\,\mathbf{C}_{norm} \times \mathbf{C}_{blur} \times \mathbf{C}_{attn} \times (\boldsymbol{p} - \boxed{\boldsymbol{scat}} - \boldsymbol{rand}\,)$$

Diffusé

> Tail-fitting
> Fenêtrage
> (Dé-)convolution

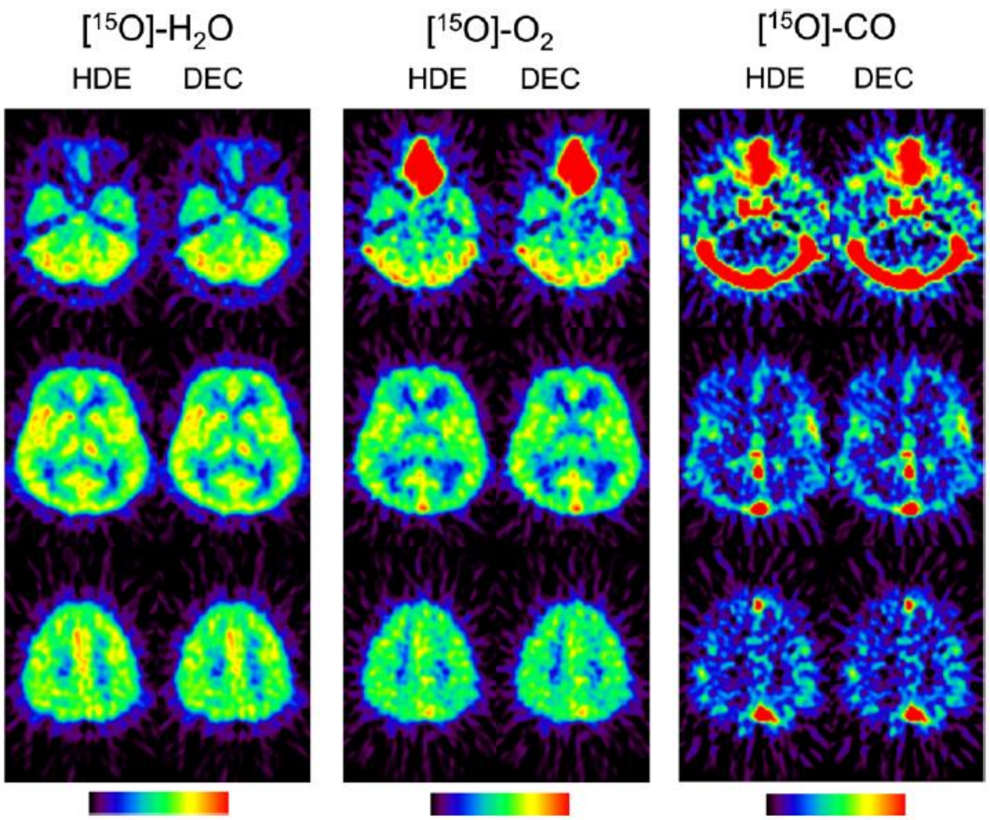

Ibaraki, Ann Nucl Med 2016

Corrections

$$f \quad \text{t.q.} \quad \mathbf{R}_{geom}\, \boldsymbol{f} = \delta\, \mathbf{C}_{norm} \times \mathbf{C}_{blur} \times \mathbf{C}_{attn} \times (\boldsymbol{p} - \boxed{\boldsymbol{scat}} - \boldsymbol{rand})$$

Diffusé

- > Tail-fitting
- > Fenêtrage
- > (Dé-)convolution
- > Simulation
  - *Analytique (SSS)*

$$\boxed{I_{A,S,B} = I_A + I_B}$$

with

$$I_A = \int_A^S \boxed{f(\vec{x})}\,\mathrm{d}\vec{x} \cdot \exp\left(-\int_A^S \mu(E,\vec{x})\,\mathrm{d}\vec{x}\right) \cdot \exp\left(-\int_B^S \mu(E',\vec{x})\,\mathrm{d}\vec{x}\right) \times \frac{\sigma_A \cdot \sigma_B}{r_A^2 \cdot r_B^2} \cdot \frac{\mathrm{d}\mu(\theta)}{\mathrm{d}\Omega} \cdot \varepsilon_A(E) \cdot \varepsilon_B(E')$$

and

$$I_B = \int_B^S f(\vec{x})\,\mathrm{d}\vec{x} \cdot \exp\left(-\int_B^S \mu(E,\vec{x})\,\mathrm{d}\vec{x}\right) \cdot \exp\left(-\int_A^S \boxed{\mu(E',\vec{x})}\,\mathrm{d}\vec{x}\right) \times \frac{\sigma_A \cdot \sigma_B}{r_A^2 \cdot r_B^2} \cdot \boxed{\frac{\mathrm{d}\mu(\theta)}{\mathrm{d}\Omega}} \cdot \varepsilon_A(E') \cdot \varepsilon_B(E).$$

Werling, Phys Med Biol 2002

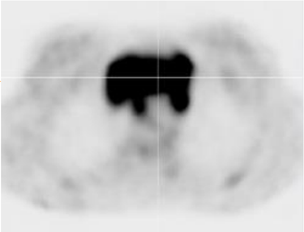

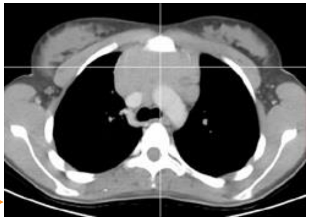

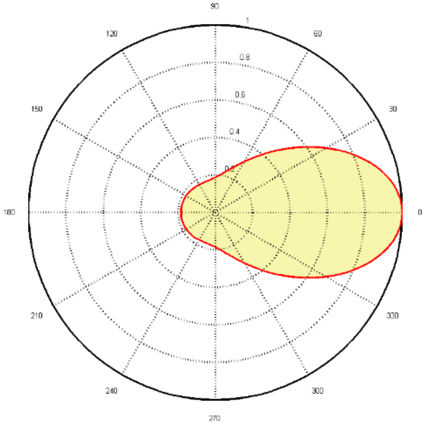

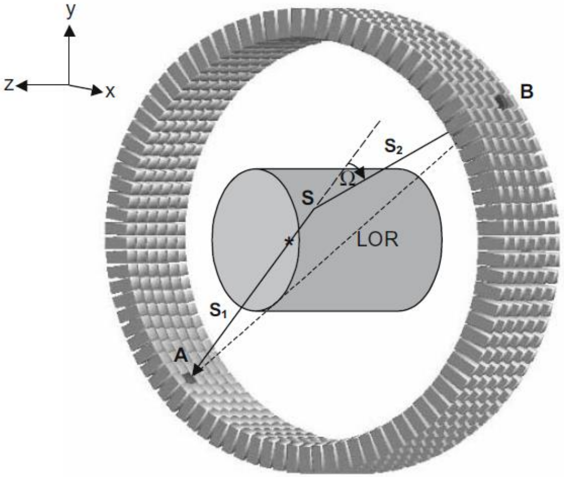

Meikle, Sringer 2003

Corrections

$$f \quad \text{t.q.} \quad \mathbf{R}_{geom}\, \boldsymbol{f} = \delta\, \mathbf{C}_{norm} \times \mathbf{C}_{blur} \times \mathbf{C}_{attn} \times (\boldsymbol{p} - \boxed{\boldsymbol{scat}} - \boldsymbol{rand})$$

Diffusé

> Tail-fitting
> Fenêtrage
> (Dé-)convolution
> Simulation
Analytique (SSS)

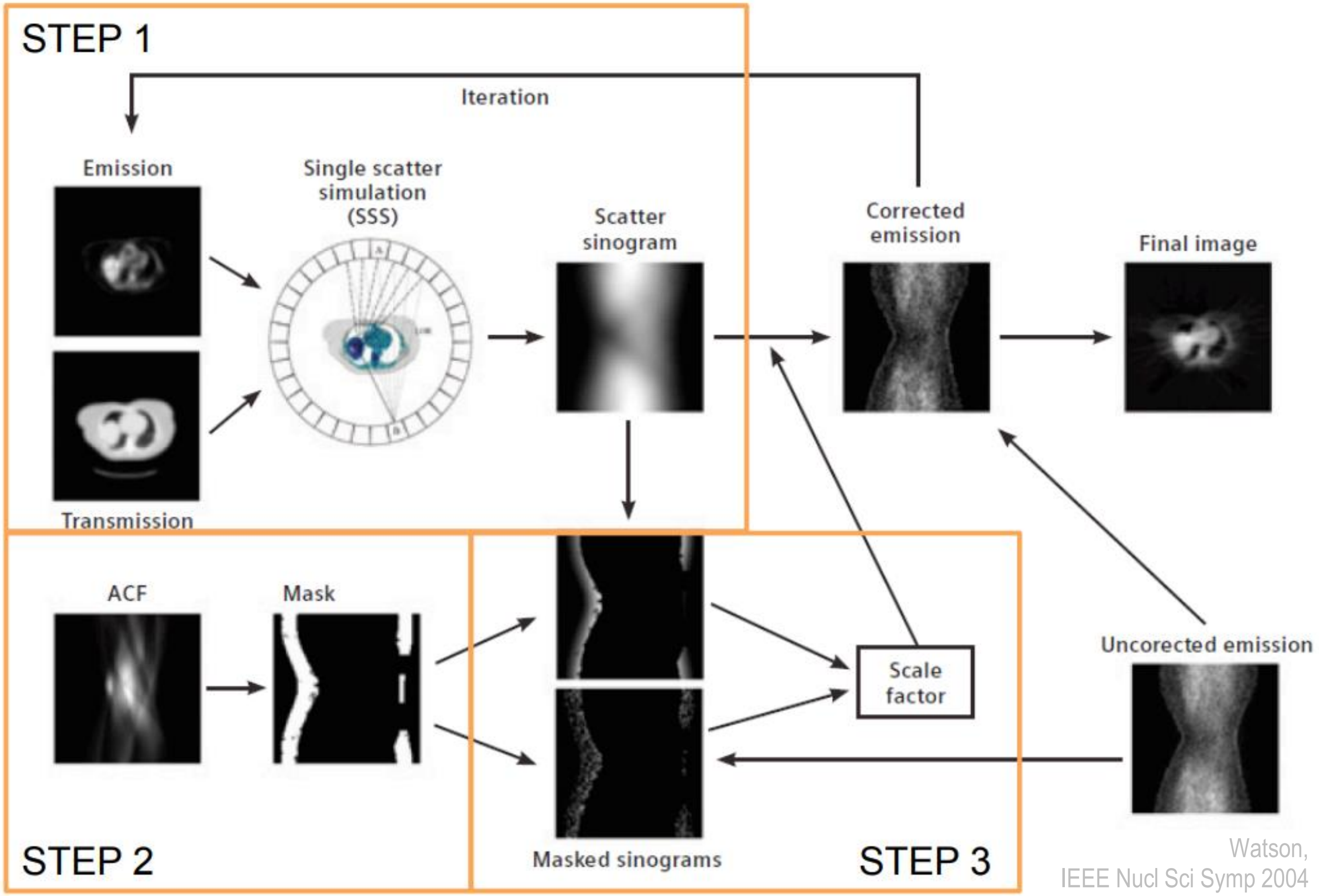

Watson, IEEE Nucl Sci Symp 2004

Corrections

$$\boldsymbol{f} \quad \text{t.q.} \quad \mathbf{R}_{geom}\, \boldsymbol{f} = \delta\, \mathbf{C}_{norm} \times \mathbf{C}_{blur} \times \mathbf{C}_{attn} \times (\boldsymbol{p} - \boxed{\boldsymbol{scat}} - \boldsymbol{rand})$$

Diffusé

$\boldsymbol{scat}$

> Tail-fitting
> Fenêtrage
> (Dé-)convolution
> Simulation
Analytique (SSS)
Monte-Carlo

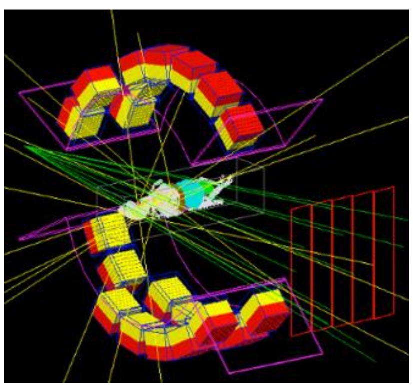

opengatecollaboration.org

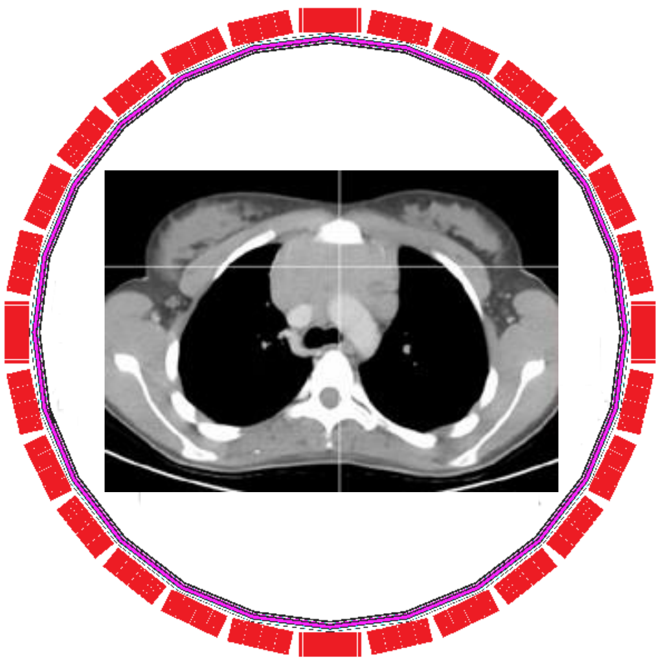

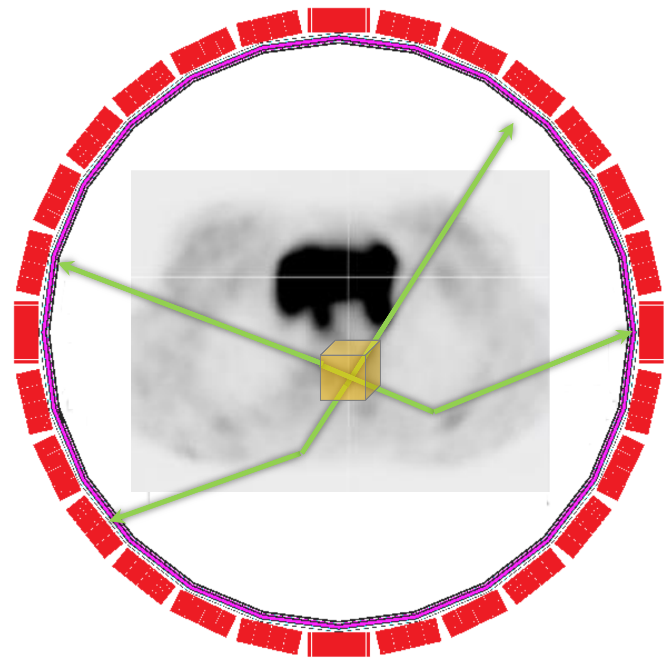

Corrections

$$\boldsymbol{f} \quad \text{t.q.} \quad \mathbf{R}_{geom}\, \boldsymbol{f} = \delta\, \mathbf{C}_{norm} \times \mathbf{C}_{blur} \times \mathbf{C}_{attn} \times (\boldsymbol{p} - \boxed{\boldsymbol{scat}} - \boldsymbol{rand}\,)$$

Diffusé

> Tail-fitting
> Fenêtrage
> (Dé-)convolution
> Simulation

Analytique (SSS)
Monte-Carlo

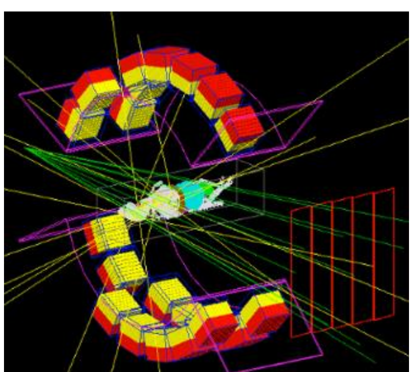

opengatecollaboration.org

$\mathbf{R}_{geom\,/\,attn\,/\,scat}$

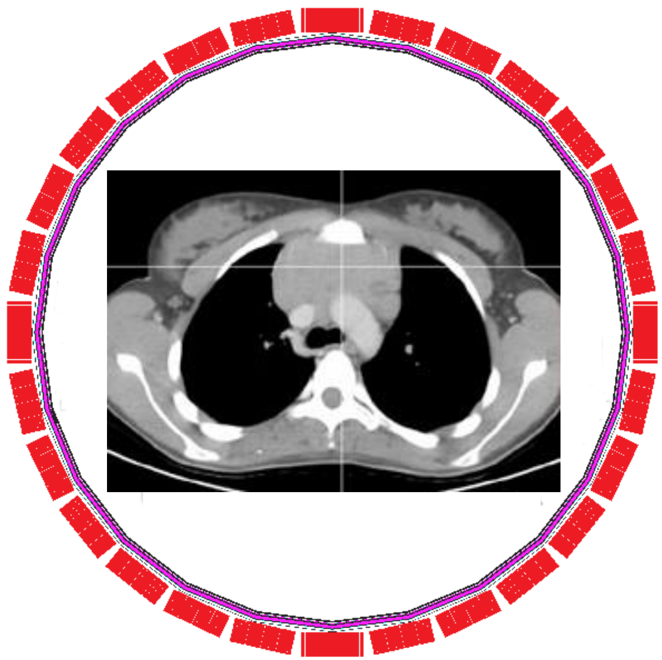

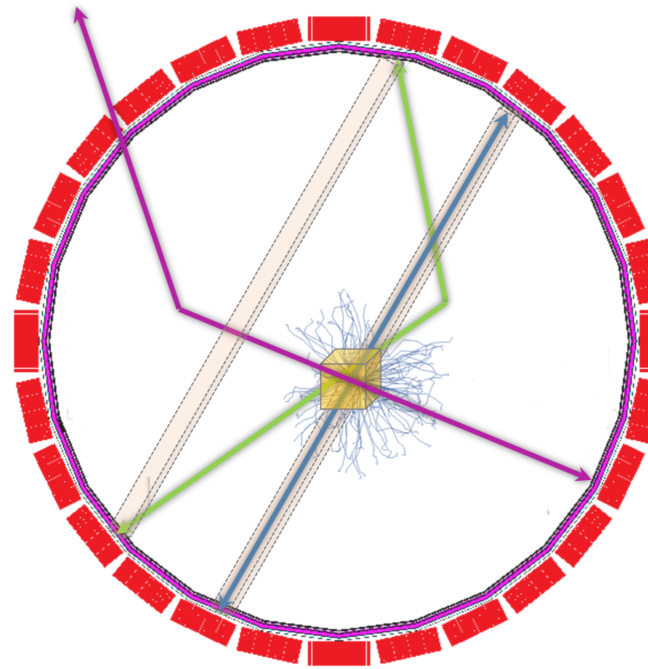

Corrections

$$\boldsymbol{f} \quad \text{t.q.} \quad \mathbf{R}_{geom}\, \boldsymbol{f} = \delta\, \mathbf{C}_{norm} \times \mathbf{C}_{blur} \times \mathbf{C}_{attn} \times (\boldsymbol{p} - \boxed{\boldsymbol{scat}} - \boldsymbol{rand})$$

Diffusé

- **> Tail-fitting**
- **> Fenêtrage**
- **> (Dé-)convolution**
- **> Simulation**
  - *Analytique (SSS)*
  - *Monte-Carlo*

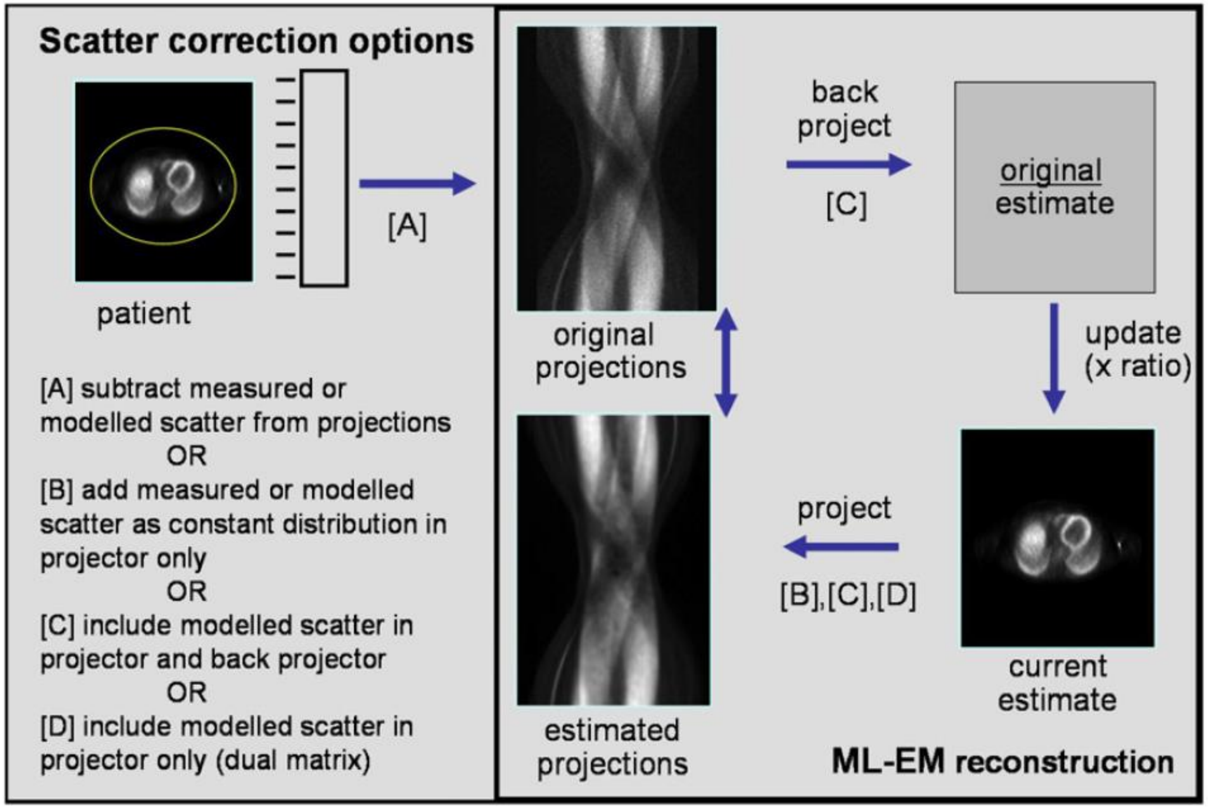

Hutton, Phys Med Biol 2011

Corrections

$$\boldsymbol{f} \quad \text{t.q.} \quad \mathbf{R}_{geom}\,\boldsymbol{f} = \delta\,\mathbf{C}_{norm} \times \mathbf{C}_{blur} \times \mathbf{C}_{attn} \times (\boldsymbol{p} - \boxed{\boldsymbol{scat}} - \boldsymbol{rand})$$

Diffusé

> Tail-fitting
> Fenêtrage
> (Dé-)convolution
> Simulation

Analytique (SSS)
Monte-Carlo

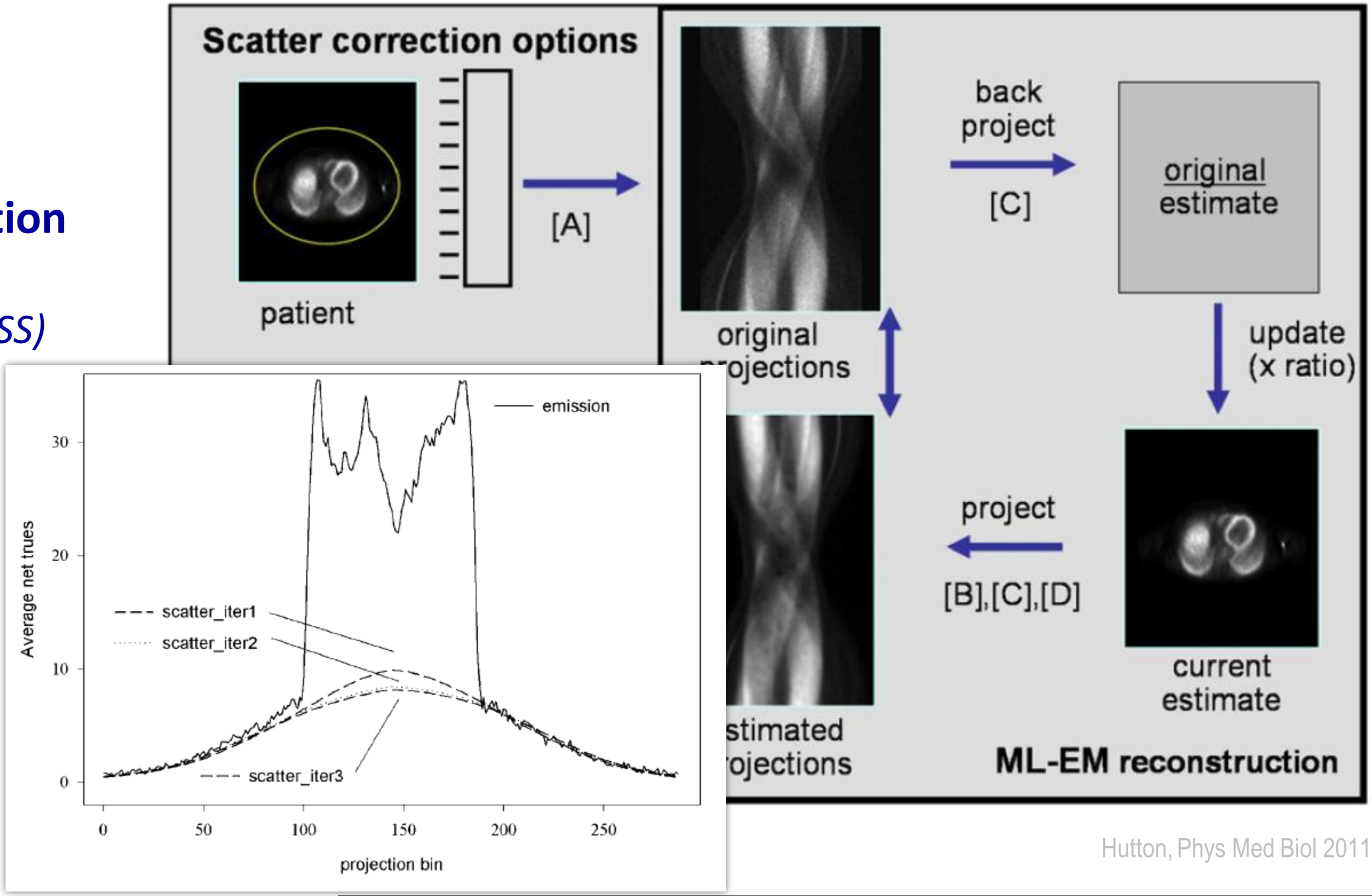

Hutton, Phys Med Biol 2011

Werling, Phys Med Biol 2002

Corrections

$$\boldsymbol{f} \quad \text{t.q.} \quad \mathbf{R}_{geom}\,\boldsymbol{f} = \delta\, \mathbf{C}_{norm} \times \mathbf{C}_{blur} \times \boxed{\mathbf{C}_{attn}} \times (\boldsymbol{p} - \boldsymbol{scat} - \boldsymbol{rand})$$

Atténuation

$$\mathbf{R}_{attn} \sim 15\% \times 15\% \sim 2\%$$

$d = 20\ cm$: $\mathbf{C}_{attn} \sim 7$

$d = 30\ cm$: $\mathbf{C}_{attn} \sim 20$

$d = 40\ cm$: $\mathbf{C}_{attn} \sim 50$

$d = 50\ cm$: $\mathbf{C}_{attn} \sim 150$

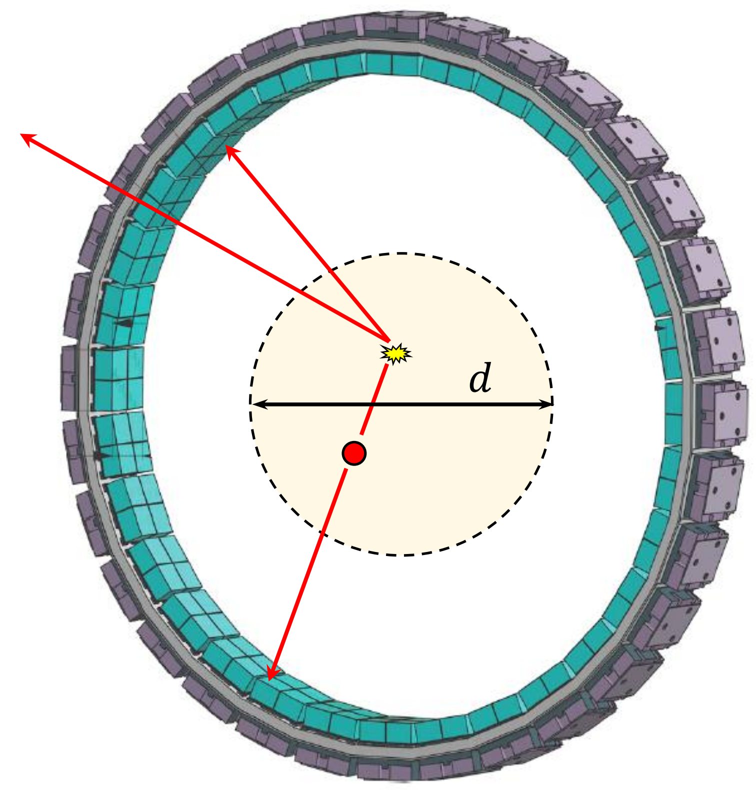

Borghi, Phys Med Biol 2018

Corrections

$$\boldsymbol{f} \quad \text{t.q.} \quad \mathbf{R}_{geom}\,\boldsymbol{f} = \delta\,\mathbf{C}_{norm} \times \mathbf{C}_{blur} \times \boxed{\mathbf{C}_{attn}} \times (\boldsymbol{p} - \boldsymbol{scat} - \boldsymbol{rand})$$

Atténuation

$$\wp(\boldsymbol{j1} \to \boldsymbol{i}) = \boldsymbol{e}^{-\int_A \mu\,dx}\,\boldsymbol{e}^{-\int_B \mu\,dx}$$

$$\wp(\boldsymbol{j2} \to \boldsymbol{i}) = \boldsymbol{e}^{-\int_A \mu\,dx}\,\boldsymbol{e}^{-\int_B \mu\,dx}$$

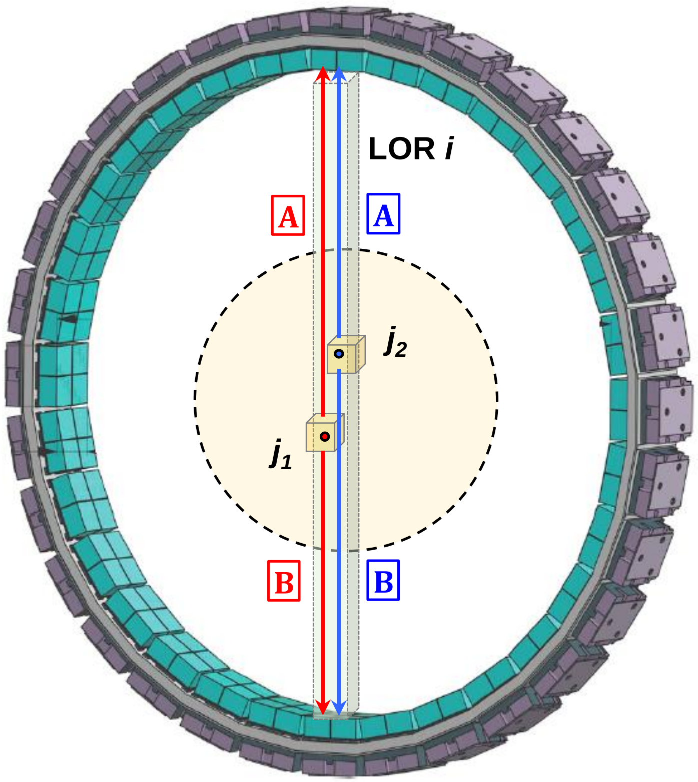

Borghi, Phys Med Biol 2018

Corrections

$$\boldsymbol{f} \quad \text{t.q.} \quad \mathbf{R}_{geom}\,\boldsymbol{f} = \delta\,\mathbf{C}_{norm} \times \mathbf{C}_{blur} \times \boxed{\mathbf{C}_{attn}} \times (\boldsymbol{p} - \boldsymbol{scat} - \boldsymbol{rand})$$

Atténuation

$$\wp(\boldsymbol{j1} \rightarrow \boldsymbol{i}) = \boldsymbol{e}^{-\int_{A} \boldsymbol{\mu}\,\boldsymbol{dx}}\boldsymbol{e}^{-\int_{B} \boldsymbol{\mu}\,\boldsymbol{dx}} = \boldsymbol{e}^{-\int_{LOR} \boldsymbol{\mu}\,\boldsymbol{dx}}$$

$$\wp(\boldsymbol{j2} \rightarrow \boldsymbol{i}) = \boldsymbol{e}^{-\int_{A} \boldsymbol{\mu}\,\boldsymbol{dx}}\boldsymbol{e}^{-\int_{B} \boldsymbol{\mu}\,\boldsymbol{dx}} = \boldsymbol{e}^{-\int_{LOR} \boldsymbol{\mu}\,\boldsymbol{dx}}$$

$$\mathbf{C}_{attn}(\boldsymbol{i}) = \boldsymbol{e}^{\int_{LOR} \boldsymbol{\mu}\,\boldsymbol{dx}}$$

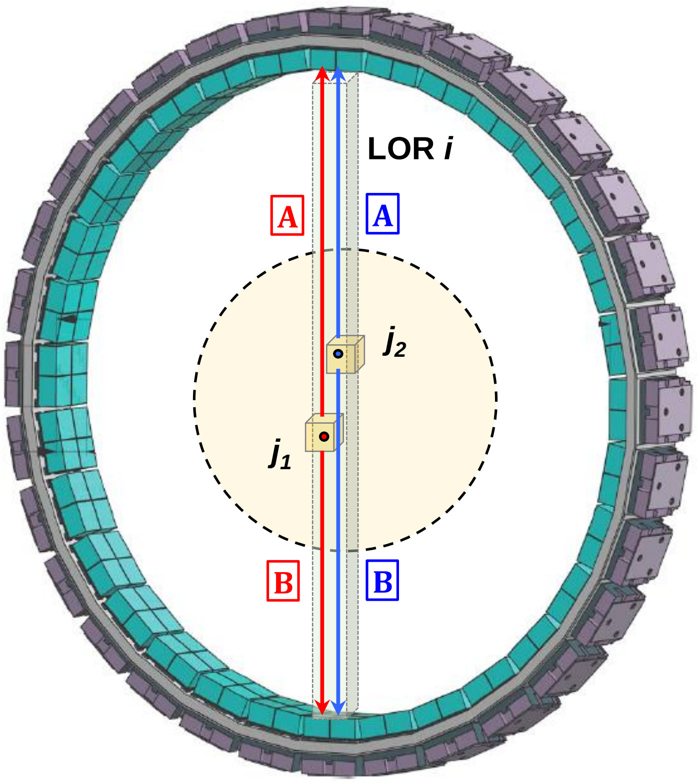

Borghi, Phys Med Biol 2018

Corrections

$$f \quad \text{t.q.} \quad \mathbf{R}_{geom}\, \boldsymbol{f} = \delta\, \mathbf{C}_{norm} \times \mathbf{C}_{blur} \times \boxed{\mathbf{C}_{attn}} \times (\boldsymbol{p} - \boldsymbol{scat} - \boldsymbol{rand})$$

Atténuation

$$\mathbf{C}_{attn}(\boldsymbol{i}) = \boldsymbol{e}^{\int_{\mathbf{LOR}} \boldsymbol{\mu}\, \boldsymbol{dx}}$$

> Chang $\mathbf{C}_{attn}(\boldsymbol{i}) \sim \boldsymbol{e}^{\boldsymbol{\mu}\, \boldsymbol{d_i}}$

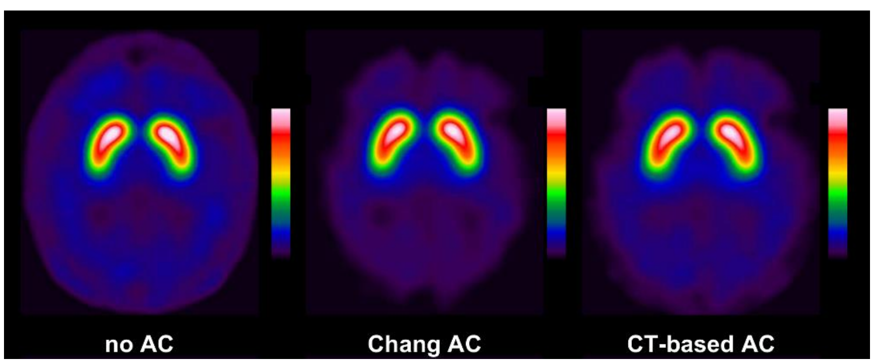

Lange, Plos One 2014

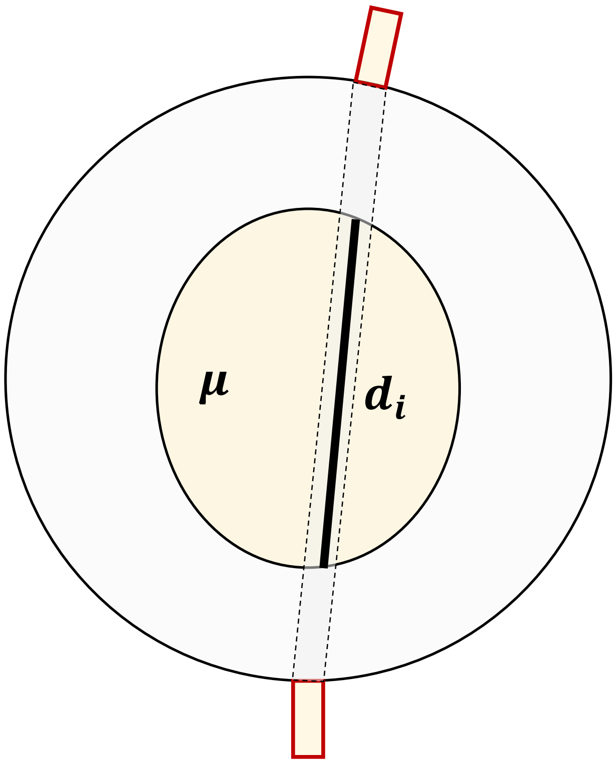

Corrections

$$f \quad \text{t.q.} \quad \mathbf{R}_{geom}\, \boldsymbol{f} = \delta\, \mathbf{C}_{norm} \times \mathbf{C}_{blur} \times \boxed{\mathbf{C}_{attn}} \times (\boldsymbol{p} - \boldsymbol{scat} - \boldsymbol{rand})$$

Atténuation

$$\mathbf{C}_{attn}(\boldsymbol{i}) = \boldsymbol{e}^{\int_{\mathrm{LOR}} \boldsymbol{\mu}\, \boldsymbol{dx}}$$

> Chang

> Scan transmission

$$\mathbf{C}_{attn}(\boldsymbol{i}) = \frac{\boldsymbol{blank}(\boldsymbol{i})}{\boldsymbol{trans}(\boldsymbol{i})}$$

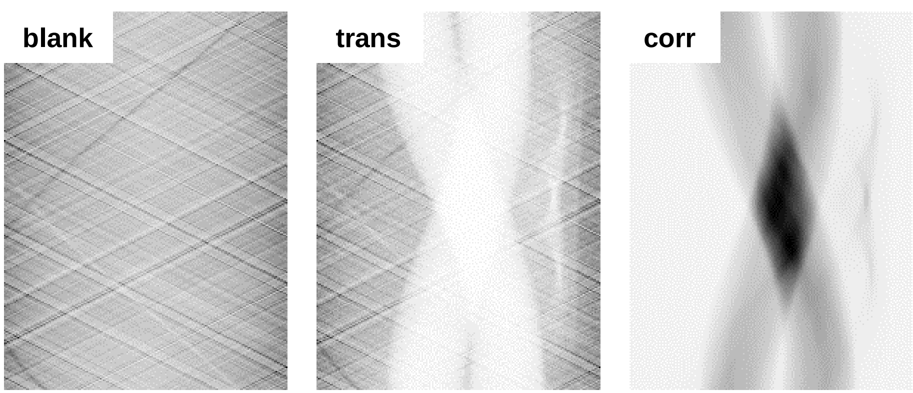

turkupetcentre.net

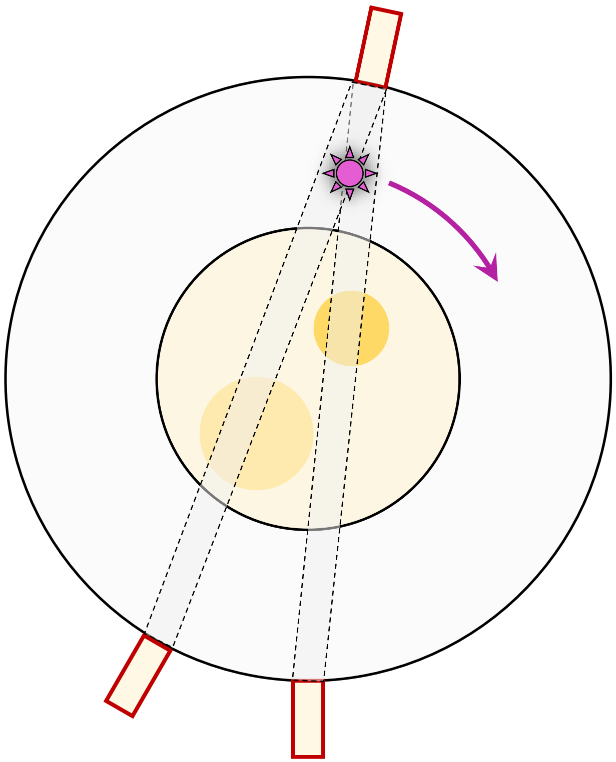

Corrections

$$f \quad \text{t.q.} \quad \mathbf{R}_{geom}\, \boldsymbol{f} = \delta\, \mathbf{C}_{norm} \times \mathbf{C}_{blur} \times \boxed{\mathbf{C}_{attn}} \times (\boldsymbol{p} - \boldsymbol{scat} - \boldsymbol{rand})$$

Atténuation

$$\mathbf{C}_{attn}(\boldsymbol{i}) = \boldsymbol{e}^{\int_{\mathrm{LOR}} \boldsymbol{\mu}\, \boldsymbol{dx}}$$

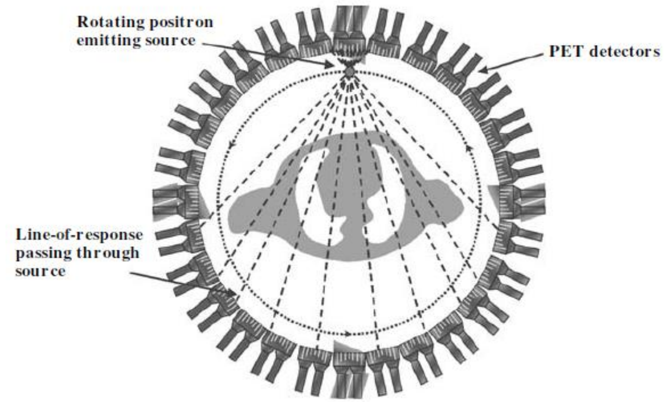

> Chang
> Scan transmission (^{68}Ge, ^{137}Cs)

$$\mathbf{C}_{attn}(\boldsymbol{i}) = \frac{\boldsymbol{blank}(\boldsymbol{i})}{\boldsymbol{trans}(\boldsymbol{i})}$$

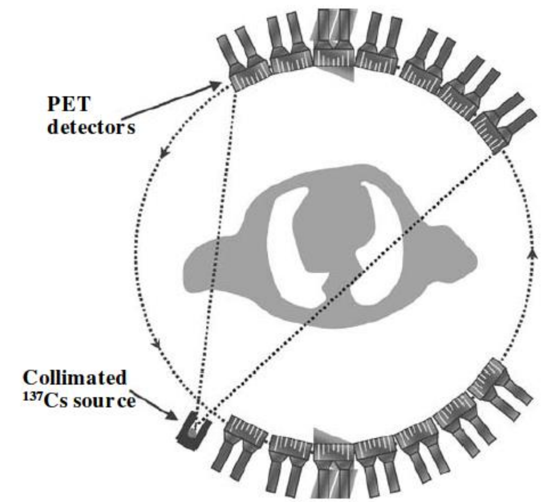

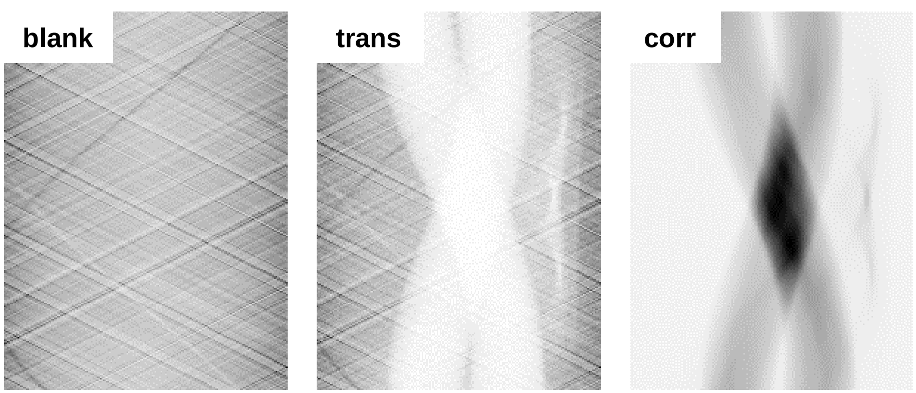

turkupetcentre.net

Meikle, Sringer 2003

Corrections

$$f \quad \text{t.q.} \quad \mathbf{R}_{geom}\, f = \delta\, \mathbf{C}_{norm} \times \mathbf{C}_{blur} \times \boxed{\mathbf{C}_{attn}} \times (p - scat - rand)$$

Atténuation

$$\mathbf{C}_{attn}(i) = e^{\int_{\mathrm{LOR}} \mu\, dx}$$

- > Chang
- > Scan transmission
- > CT-AC

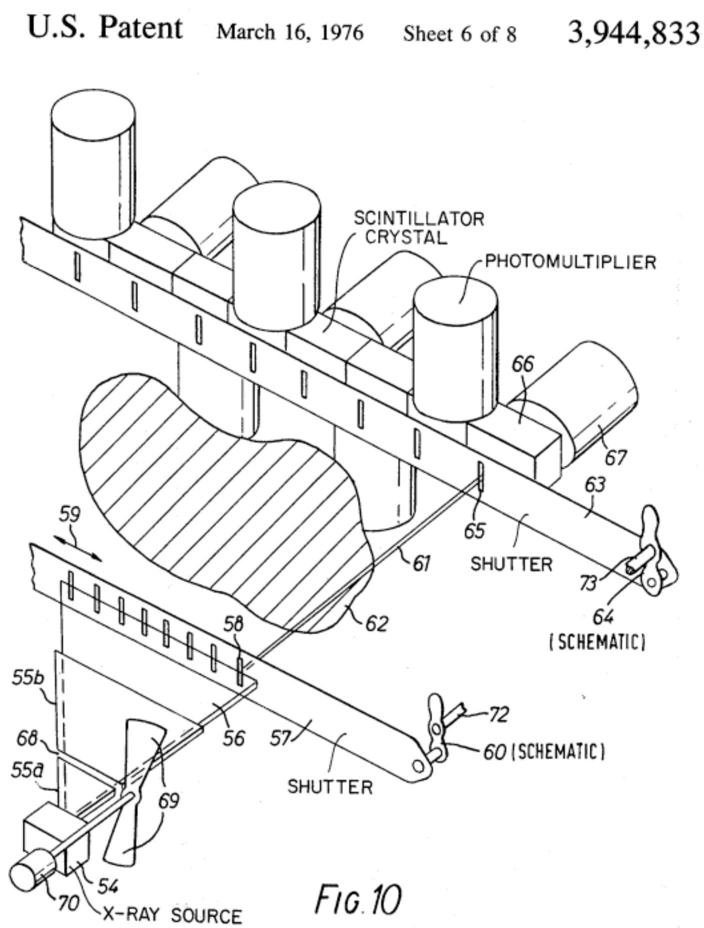

Hounsfield 1976 (patents.google)

Corrections

$$f \quad \text{t.q.} \quad \mathbf{R}_{geom}\, f = \delta\, \mathbf{C}_{norm} \times \mathbf{C}_{blur} \times \boxed{\mathbf{C}_{attn}} \times (p - scat - rand)$$

Atténuation

$$\mathbf{C}_{attn}(i) = e^{\int_{\mathrm{LOR}} \mu\, dx}$$

- > Chang
- > Scan transmission
- > CT-AC

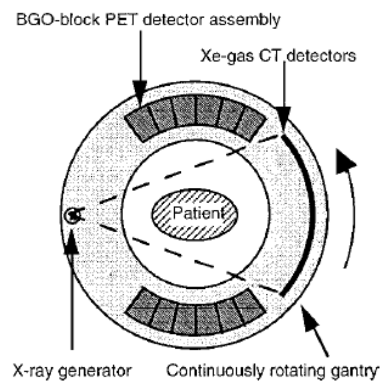

FIG. 1. Illustration of the PET/CT scanner operational principles. The continuous rotation of the detectors allows collection of full projection data sets for the PET and CT subsystems. With no septa, the PET detector arrays are operated in 3D (high-sensitivity) mode, and are mounted forward of the CT system on the same rotating support. Data will be acquired and read out during continuous rotation through optical slip-rings.

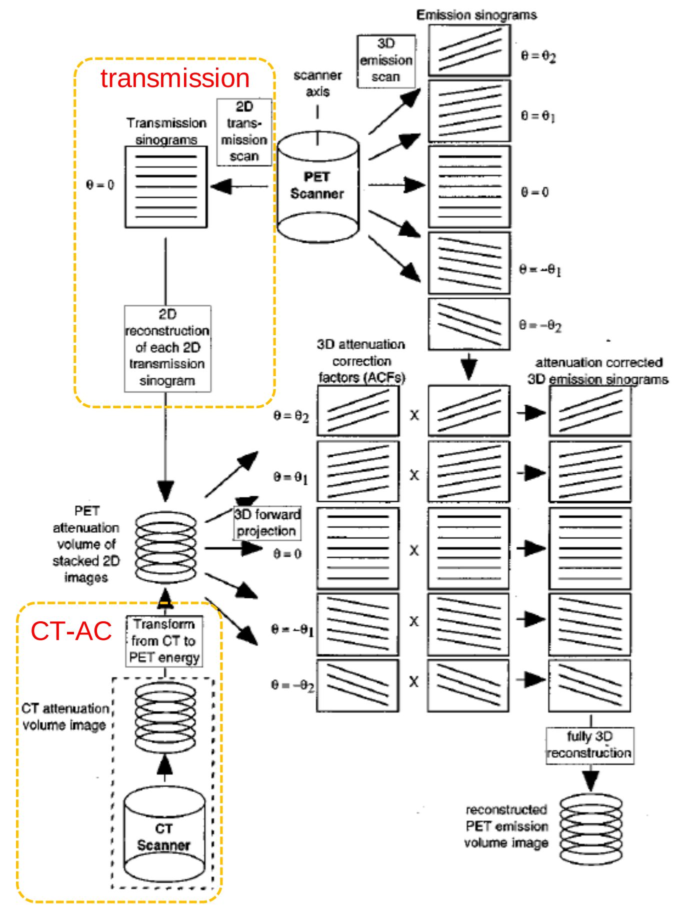

Kinahan, Med Phys 1998

Corrections

$$\boldsymbol{f} \quad \text{t.q.} \quad \mathbf{R}_{geom}\,\boldsymbol{f} = \delta\, \mathbf{C}_{norm} \times \mathbf{C}_{blur} \times \boxed{\mathbf{C}_{attn}} \times (\boldsymbol{p} - \boldsymbol{scat} - \boldsymbol{rand})$$

Atténuation

$$\mathbf{C}_{attn}(\boldsymbol{i}) = \boldsymbol{e}^{\int_{\text{LOR}} \boldsymbol{\mu}\, \boldsymbol{dx}}$$

> Chang
> Scan transmission
> CT-AC

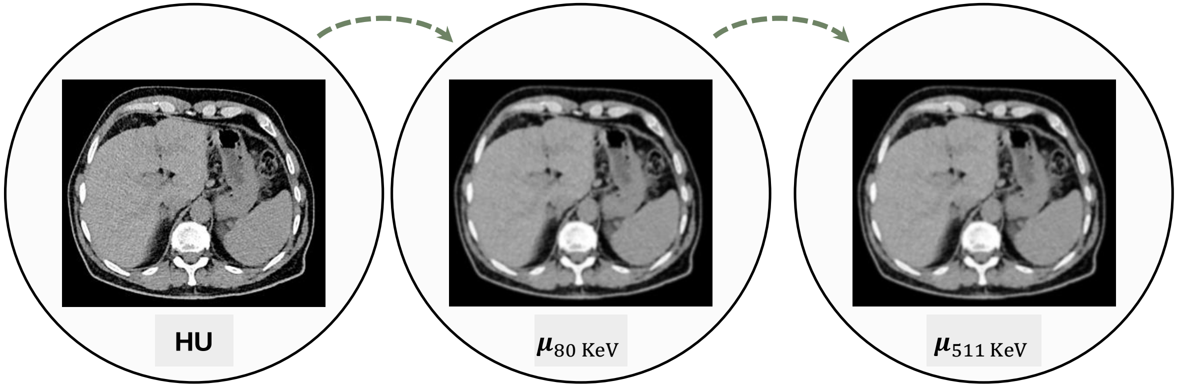

$$\mu_{\text{Com}} \propto \rho \qquad \mu_{\text{PE}} \propto \rho \frac{Z^3}{E^3}$$

TABLE I. Mass attenuation coefficients (linear attenuation coefficient/density) in cm^2/g. Data are from Hubbell (Ref. 9).

	80 keV			500 keV			Ratio of totals
Material	Photoelec.	Compton	Total	Photoelec.	Compton	Total	80 keV:500 keV
Air	0.006	0.161	0.167	<0.001	0.087	0.087	1.92
Water	0.006	0.178	0.184	<0.001	0.097	0.097	1.90
Muscle	0.006	0.176	0.182	<0.001	0.096	0.096	1.90
Bone	0.034	0.175	0.209	<0.001	0.093	0.093	2.26

Kinahan, Med Phys 1998

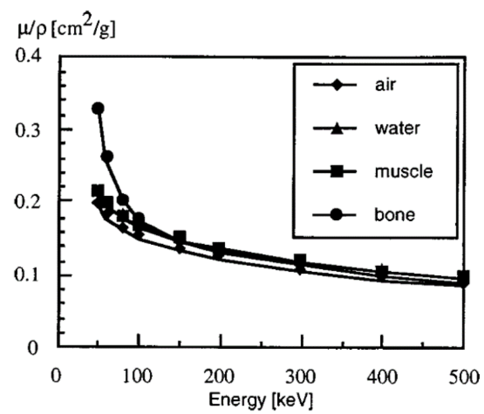

Corrections

$$\boldsymbol{f} \quad \text{t.q.} \quad \mathbf{R}_{geom}\,\boldsymbol{f} = \delta\, \mathbf{C}_{norm} \times \mathbf{C}_{blur} \times \boxed{\mathbf{C}_{attn}} \times (\boldsymbol{p} - \boldsymbol{scat} - \boldsymbol{rand})$$

Atténuation

$$\mathbf{C}_{attn}(\boldsymbol{i}) = \boldsymbol{e}^{\int_{\mathrm{LOR}} \boldsymbol{\mu}\, \boldsymbol{dx}}$$

- > Chang
- > Scan transmission
- > CT-AC

  Segmentation

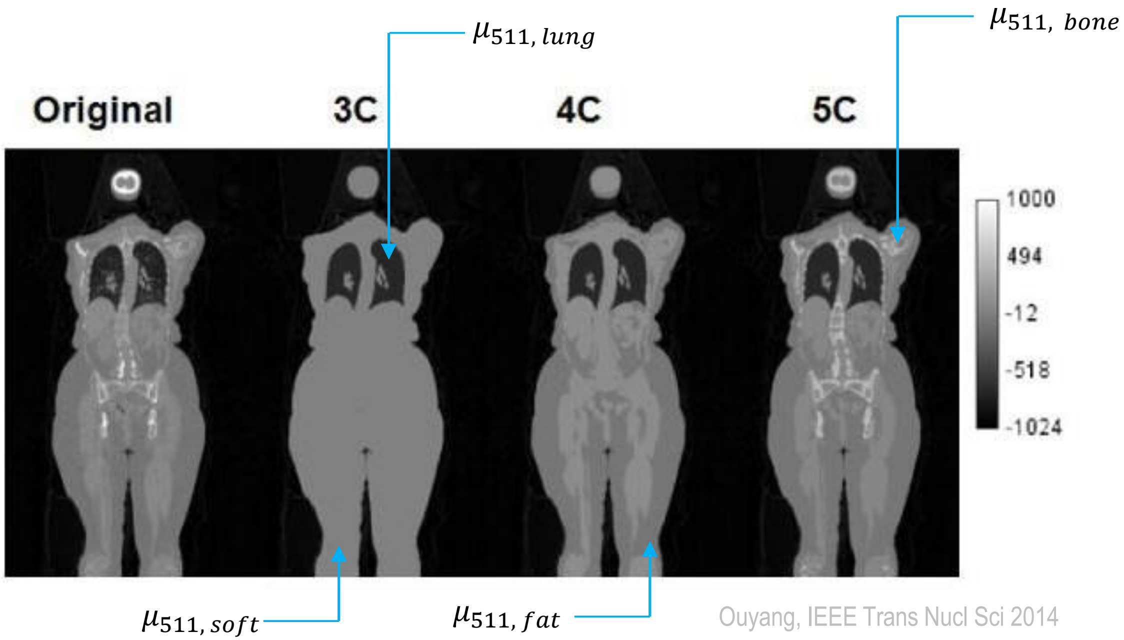

Ouyang, IEEE Trans Nucl Sci 2014

Corrections

$$f \quad \text{t.q.} \quad \mathbf{R}_{geom}\, f = \delta\, \mathbf{C}_{norm} \times \mathbf{C}_{blur} \times \boxed{\mathbf{C}_{attn}} \times (p - scat - rand)$$

Atténuation

$$\mu_{\mathrm{Com}} \propto \rho \qquad \mu_{\mathrm{PE}} \propto \rho \frac{\mathrm{Z}^3}{\mathrm{E}^3}$$

$$\mathbf{C}_{attn}(i) = e^{\int_{\mathrm{LOR}} \mu\, dx}$$

- > Chang
- > Scan transmission
- > CT-AC
  - *Segmentation*
  - *Conversion*

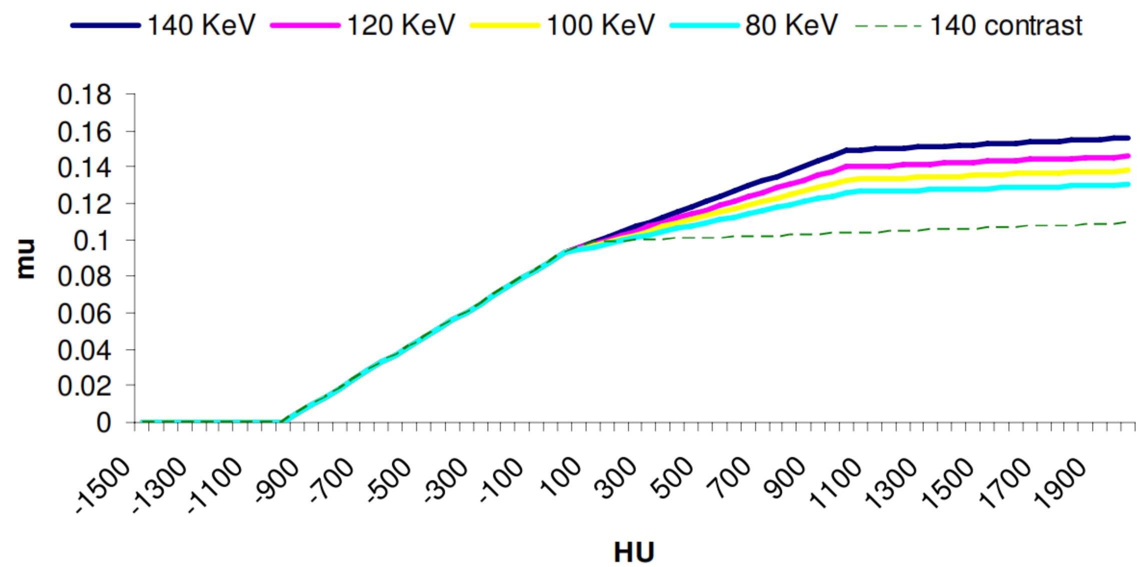

Abella, Nucl Sci Symp 2007

Corrections

$$f \quad \text{t.q.} \quad \mathbf{R}_{geom}\, \boldsymbol{f} = \delta\, \mathbf{C}_{norm} \times \mathbf{C}_{blur} \times \boxed{\mathbf{C}_{attn}} \times (\boldsymbol{p} - \boldsymbol{scat} - \boldsymbol{rand})$$

Atténuation

$$\mathbf{C}_{attn}(\boldsymbol{i}) = \boldsymbol{e}^{\int_{\mathrm{LOR}} \boldsymbol{\mu}\, \boldsymbol{dx}}$$

> Chang
> Scan transmission
> CT-AC

Segmentation
Conversion
Hybride

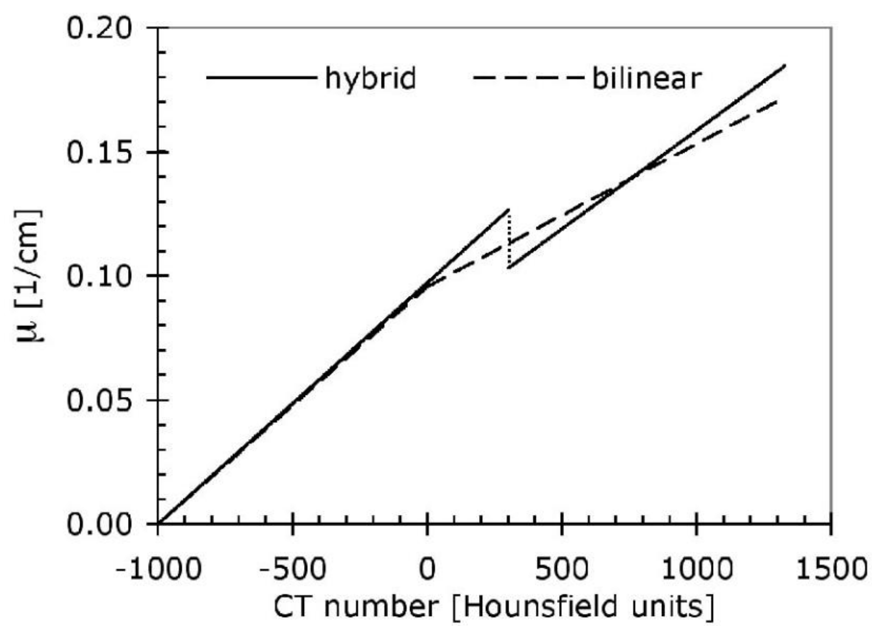

Kinahan, Semin Nucl Med 2003

Corrections

$$\boldsymbol{f} \quad \text{t.q.} \quad \mathbf{R}_{geom}\,\boldsymbol{f} = \delta\,\mathbf{C}_{norm} \times \mathbf{C}_{blur} \times \boxed{\mathbf{C}_{attn}} \times (\boldsymbol{p} - \boldsymbol{scat} - \boldsymbol{rand})$$

Atténuation

$$\mathbf{C}_{attn}(\boldsymbol{i}) = \boldsymbol{e}^{\int_{\mathbf{LOR}} \boldsymbol{\mu}\, \boldsymbol{dx}}$$

- > Chang
- > Scan transmission
- > CT-AC
  - *Segmentation*
  - *Conversion*
  - *Hybride*
  - *Dual energy*

$$\mu(x,y,z;E) = a_P(x,y,z)\ f_P(E) + a_C(x,y,z)\ f_C(E)$$

$$I_1 = \int S_1(E)\ \exp[-A_P f_P(E) - A_C f_C(E)]\ dE$$

$$I_2 = \int S_2(E)\ \exp[-A_P f_P(E) - A_C f_C(E)]\ dE$$

$$\mu(x,y,z;E_d) = a_P(x,y,z)\ f_P(E_d) + a_C(x,y,z)\ f_C(e_d)$$

Alvarez, IEEE Trans Nucl Sci 1979

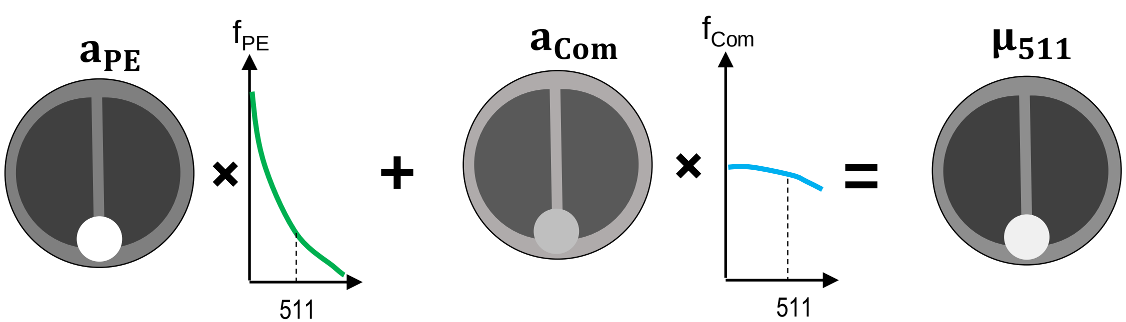

Corrections

$$f \quad \text{t.q.} \quad \mathbf{R}_{geom}\, \boldsymbol{f} = \delta\, \mathbf{C}_{norm} \times \mathbf{C}_{blur} \times \boxed{\mathbf{C}_{attn}} \times (\boldsymbol{p} - \boldsymbol{scat} - \boldsymbol{rand})$$

Atténuation

$$\mathbf{C}_{attn}(\boldsymbol{i}) = \boldsymbol{e}^{\int_{\mathrm{LOR}} \boldsymbol{\mu}\, \boldsymbol{dx}}$$

- **> Chang**
- **> Scan transmission**
- **> CT-AC**
  - *Segmentation*
  - *Conversion*
  - *Hybride*
  - *Dual energy*

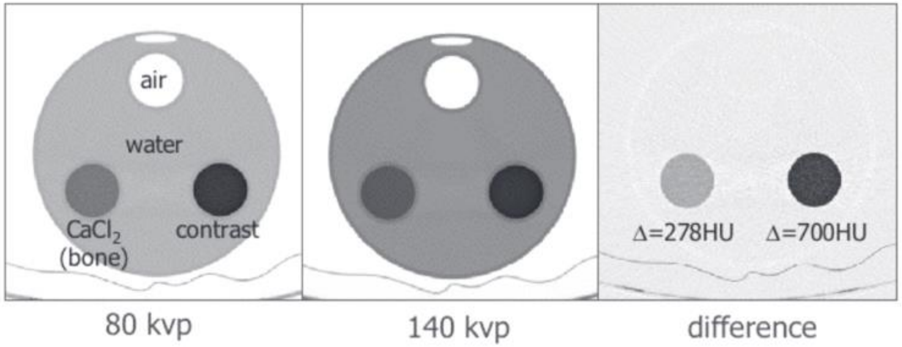

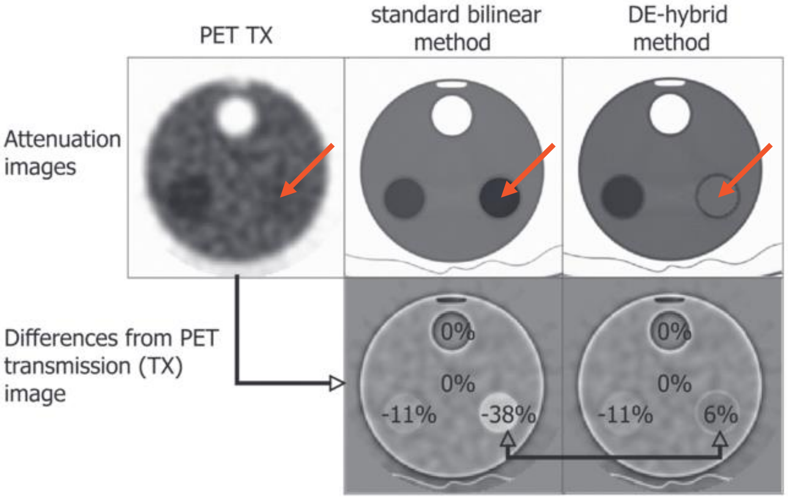

Kinahan, Technol Cancer Res Treat 2006

Corrections

$$\boldsymbol{f} \quad \text{t.q.} \quad \mathbf{R}_{geom}\,\boldsymbol{f} = \delta\, \mathbf{C}_{norm} \times \mathbf{C}_{blur} \times \boxed{\mathbf{C}_{attn}} \times (\boldsymbol{p} - \boldsymbol{scat} - \boldsymbol{rand})$$

Atténuation

$$\mathbf{C}_{attn}(\boldsymbol{i}) = \boldsymbol{e}^{\int_{\mathrm{LOR}} \boldsymbol{\mu}\, \boldsymbol{dx}}$$

> Chang
> Scan transmission
> CT-AC

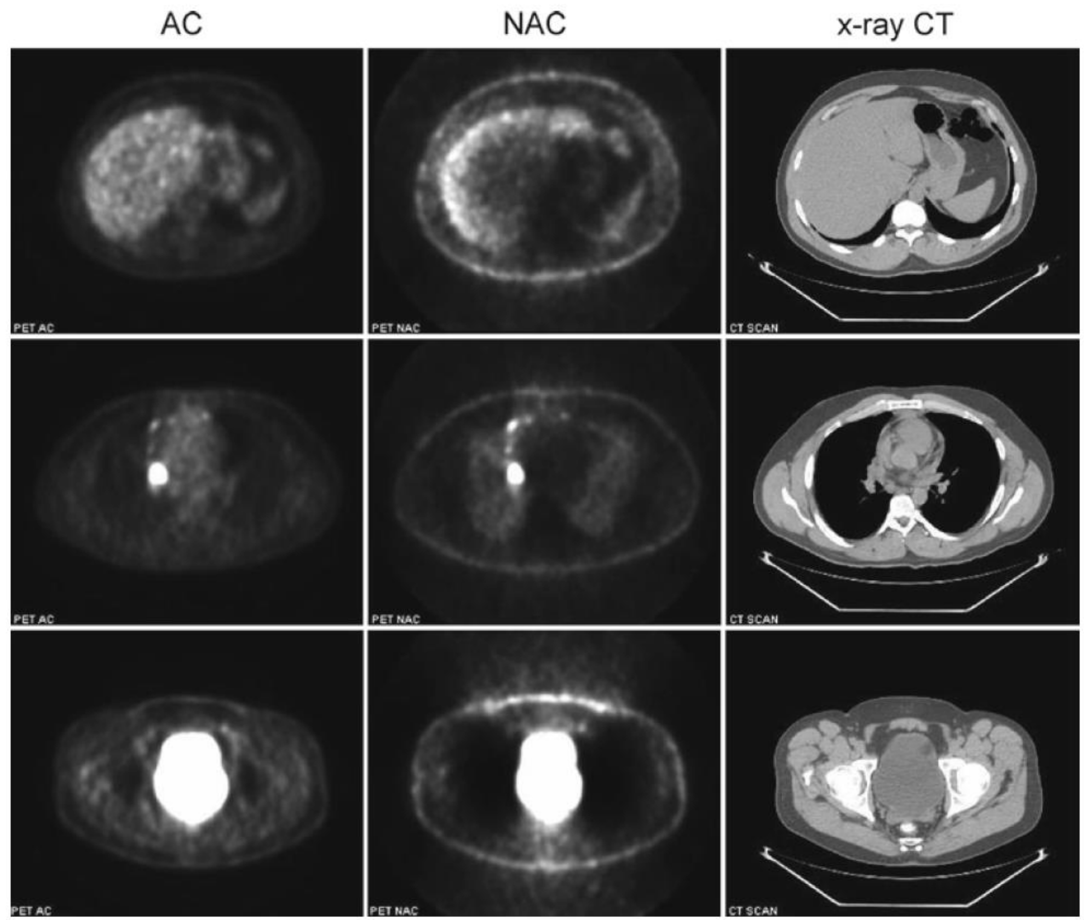

Turkington, Springer 2011

Corrections

$$\boldsymbol{f} \quad \text{t.q.} \quad \mathbf{R}_{geom}\, \boldsymbol{f} = \delta\, \mathbf{C}_{norm} \times \mathbf{C}_{blur} \times \boxed{\mathbf{C}_{attn}} \times (\boldsymbol{p} - \boldsymbol{scat} - \boldsymbol{rand})$$

Atténuation

$$\mathbf{C}_{attn}(\boldsymbol{i}) = \boldsymbol{e}^{\int_{\mathrm{LOR}} \boldsymbol{\mu}\, \boldsymbol{dx}}$$

- > Chang
- > Scan transmission
- > CT-AC

Mouvement respiratoire

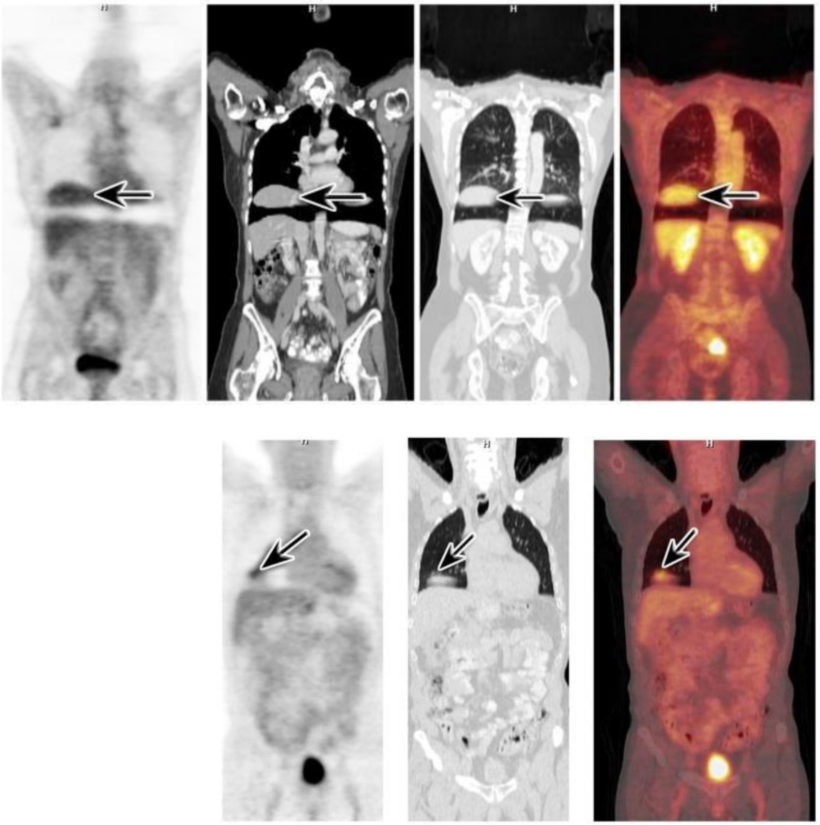

Blodgett, Clin Imaging 2014

Corrections

$$\boldsymbol{f} \quad \text{t.q.} \quad \mathbf{R}_{geom}\, \boldsymbol{f} = \delta\, \mathbf{C}_{norm} \times \mathbf{C}_{blur} \times \boxed{\mathbf{C}_{attn}} \times (\boldsymbol{p} - \boldsymbol{scat} - \boldsymbol{rand})$$

Atténuation

$$\mathbf{C}_{attn}(\boldsymbol{i}) = \boldsymbol{e}^{\int_{\mathbf{LOR}} \boldsymbol{\mu}\, \boldsymbol{dx}}$$

> Chang
> Scan transmission
> CT-AC

Mouvement respiratoire

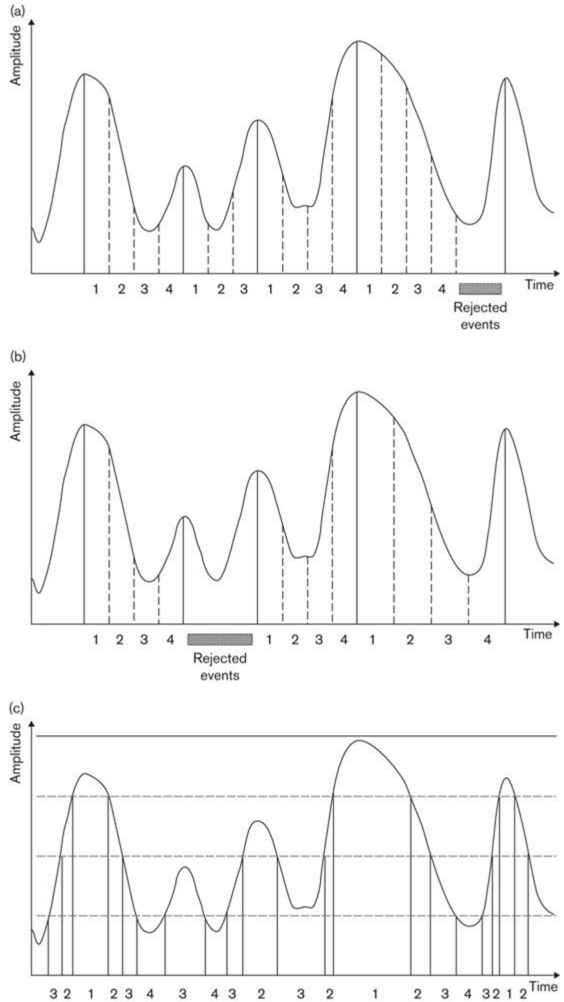

Pépin, Nucl Med Commun 2014

Corrections

$$\boldsymbol{f} \quad \text{t.q.} \quad \mathbf{R}_{geom}\, \boldsymbol{f} = \delta\, \mathbf{C}_{norm} \times \mathbf{C}_{blur} \times \boxed{\mathbf{C}_{attn}} \times (\boldsymbol{p} - \boldsymbol{scat} - \boldsymbol{rand})$$

Atténuation

$$\mathbf{C}_{attn}(\boldsymbol{i}) = \boldsymbol{e}^{\int_{\mathrm{LOR}} \boldsymbol{\mu}\, \boldsymbol{dx}}$$

- > Chang
- > Scan transmission
- > CT-AC

Mouvement respiratoire

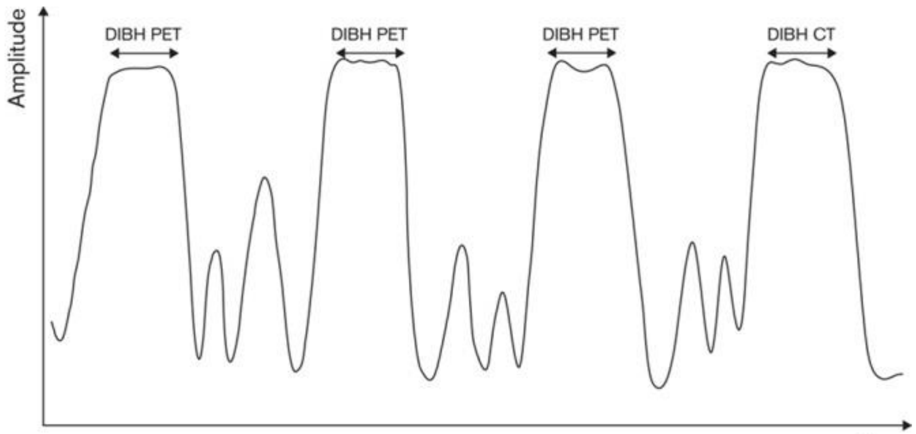

Pépin, Nucl Med Commun 2014

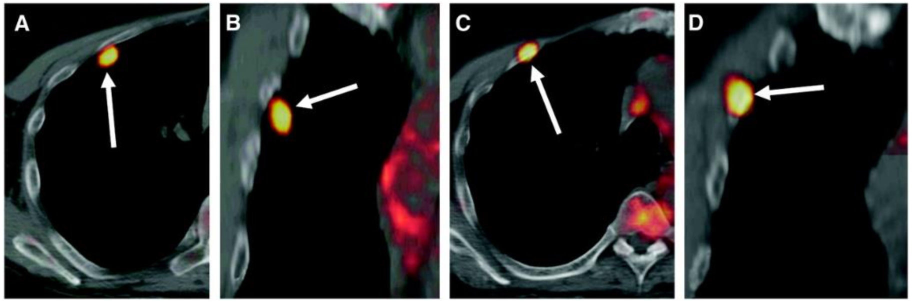

Meirelles, J Nucl Med 2007

Corrections

$$f \quad \text{t.q.} \quad \mathbf{R}_{geom}\, f = \delta\, \mathbf{C}_{norm} \times \mathbf{C}_{blur} \times \boxed{\mathbf{C}_{attn}} \times (\boldsymbol{p} - \boldsymbol{scat} - \boldsymbol{rand})$$

Atténuation

$$\mathbf{C}_{attn}(\boldsymbol{i}) = \boldsymbol{e}^{\int_{\mathrm{LOR}} \boldsymbol{\mu}\, \boldsymbol{dx}}$$

> Chang
> Scan transmission
> CT-AC

Mouvement respiratoire

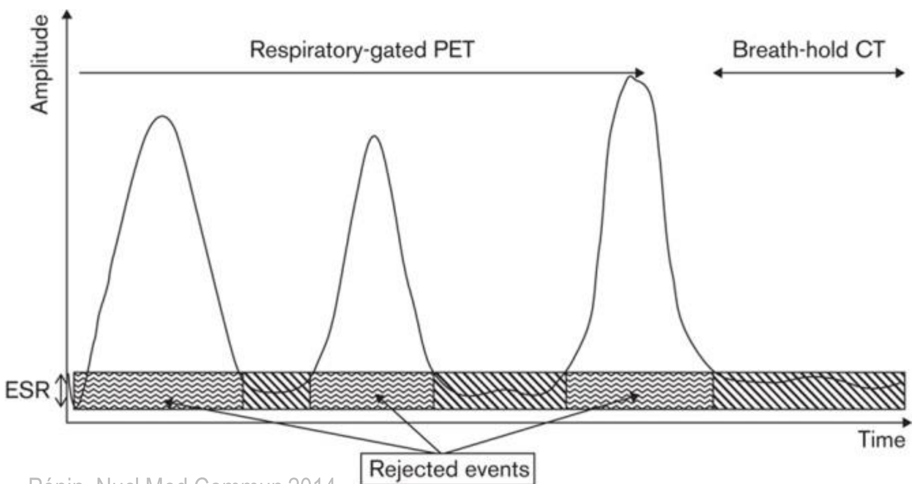

Pépin, Nucl Med Commun 2014

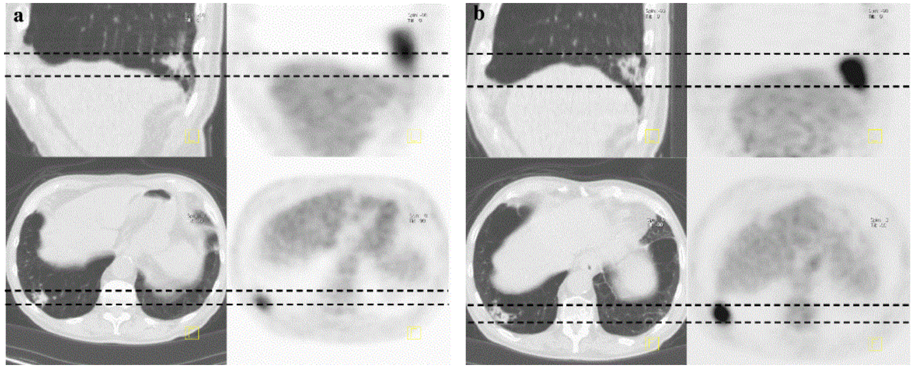

Fin, Eur J Nucl Med Mol Imaging 2008

Corrections

$$\boldsymbol{f} \quad \text{t.q.} \quad \mathbf{R}_{geom}\,\boldsymbol{f} = \delta\,\mathbf{C}_{norm} \times \mathbf{C}_{blur} \times \boxed{\mathbf{C}_{attn}} \times (\boldsymbol{p} - \boldsymbol{scat} - \boldsymbol{rand})$$

Atténuation

$$\mathbf{C}_{attn}(\boldsymbol{i}) = \boldsymbol{e}^{\int_{\mathrm{LOR}} \boldsymbol{\mu}\, \boldsymbol{dx}}$$

- > Chang
- > Scan transmission
- > CT-AC

  Mouvement respiratoire

  Décalage - données manquantes

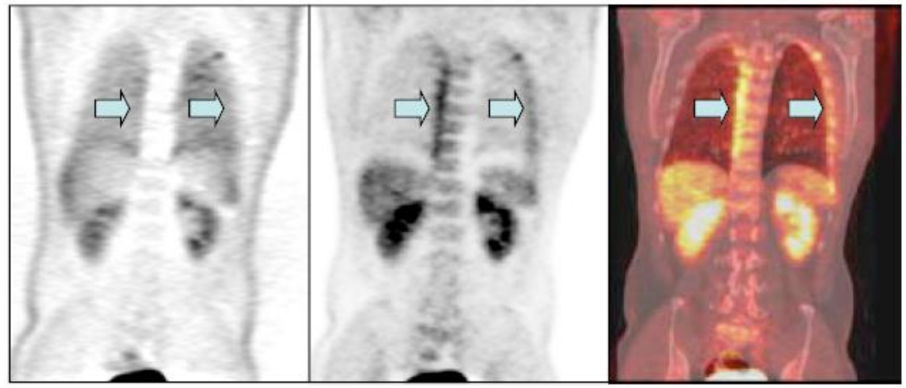

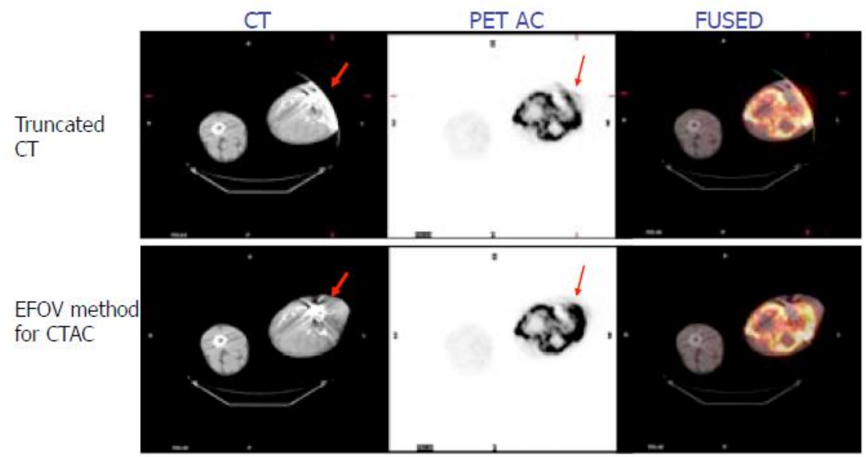

Max SUV changed from 3.4 to 12.7 with extended field of view CT

Kinahan (aapm.org)

Corrections

$$\boldsymbol{f} \quad \text{t.q.} \quad \mathbf{R}_{geom}\,\boldsymbol{f} = \delta\,\mathbf{C}_{norm} \times \mathbf{C}_{blur} \times \boxed{\mathbf{C}_{attn}} \times (\boldsymbol{p} - \boldsymbol{scat} - \boldsymbol{rand})$$

Atténuation

$$\mathbf{C}_{attn}(\boldsymbol{i}) = \boldsymbol{e}^{\int_{\text{LOR}} \boldsymbol{\mu}\, \boldsymbol{dx}}$$

- **> Chang**
- **> Scan transmission**
- **> CT-AC**

  Mouvement respiratoire
  Décalage - données manquantes
  Durcissement de faisceau

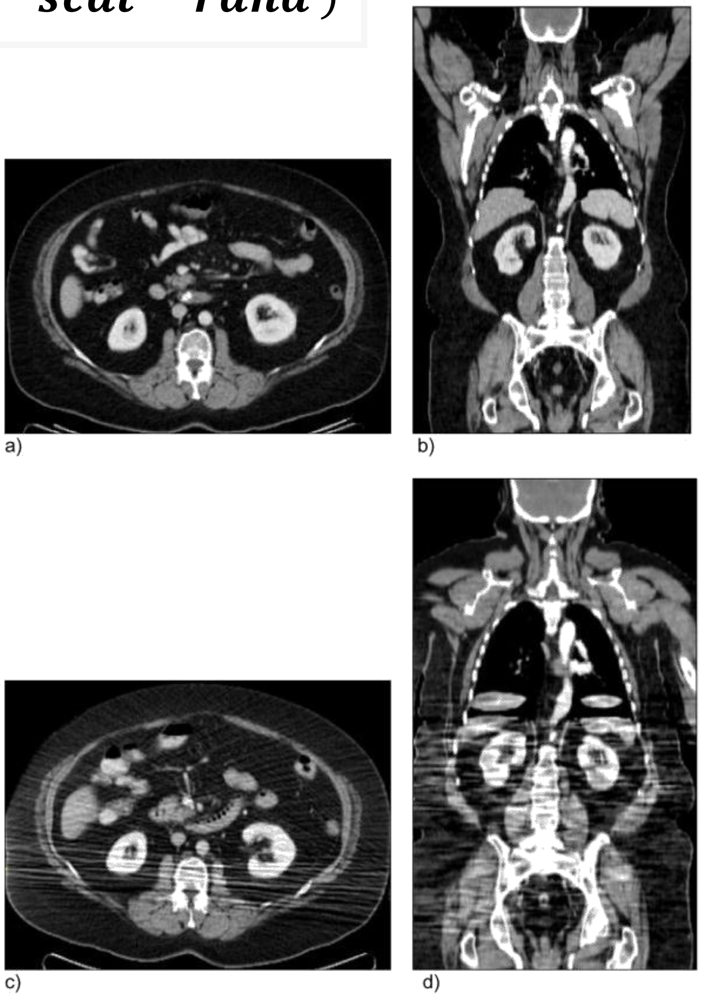

Simpson, Contemp Diag Radiol 2017

Corrections

$$f \quad \text{t.q.} \quad \mathbf{R}_{geom}\, f = \delta\, \mathbf{C}_{norm} \times \mathbf{C}_{blur} \times \boxed{\mathbf{C}_{attn}} \times (p - scat - rand)$$

Atténuation

$$\mathbf{C}_{attn}(i) = e^{\int_{\mathrm{LOR}} \mu\, dx}$$

- > Chang
- > Scan transmission
- > CT-AC
  - *Mouvement respiratoire*
  - *Décalage - données manquantes*
  - *Durcissement de faisceau*
  - *Matériel dense*

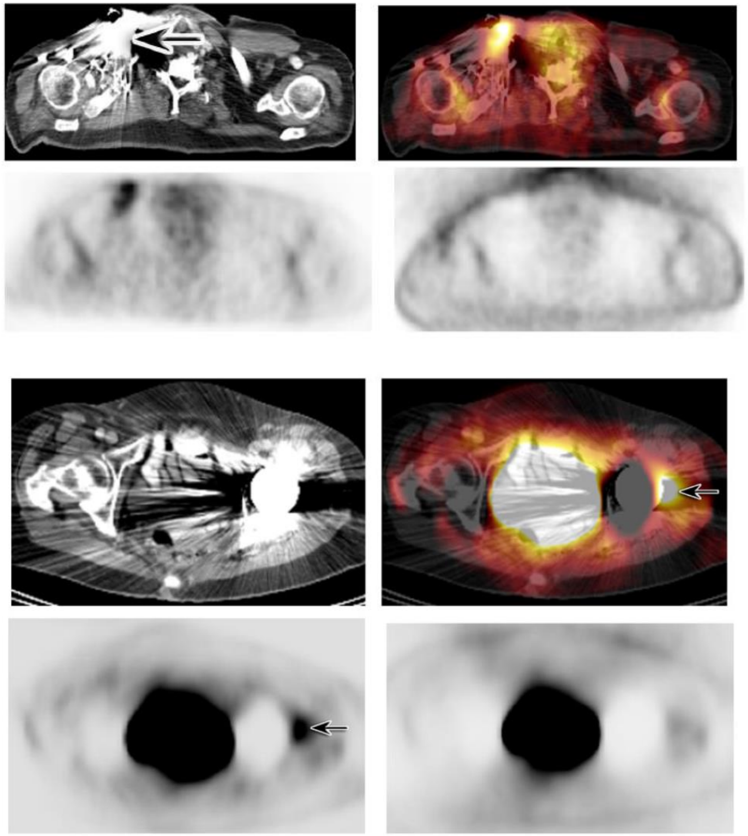

Blodgett, Clin Imaging 2014

Corrections

$$f \quad \text{t.q.} \quad \mathbf{R}_{geom}\, \boldsymbol{f} = \delta\, \mathbf{C}_{norm} \times \mathbf{C}_{blur} \times \boxed{\mathbf{C}_{attn}} \times (\boldsymbol{p} - \boldsymbol{scat} - \boldsymbol{rand})$$

Atténuation

$$\mathbf{C}_{attn}(\boldsymbol{i}) = \boldsymbol{e}^{\int_{\mathrm{LOR}} \boldsymbol{\mu}\, \boldsymbol{dx}}$$

- > Chang
- > Scan transmission
- > CT-AC

Mouvement respiratoire
Décalage - données manquantes
Durcissement de faisceau
Matériel dense

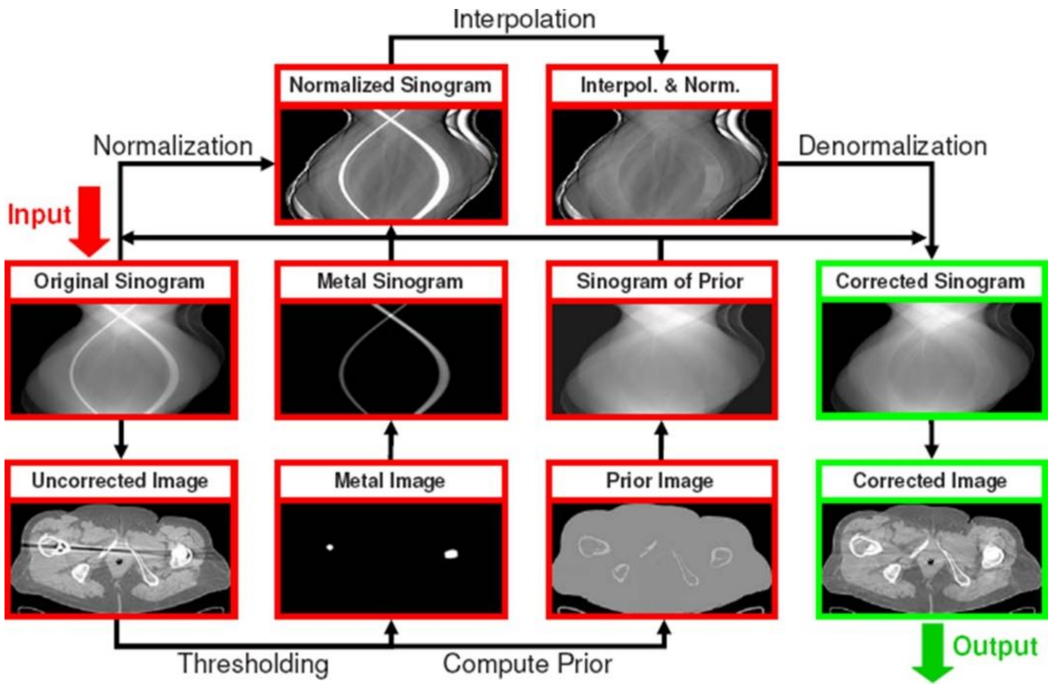

Meyer, Med Phys 2010

Corrections

$$\boldsymbol{f} \quad \text{t.q.} \quad \mathbf{R}_{geom}\,\boldsymbol{f} = \delta\,\mathbf{C}_{norm} \times \mathbf{C}_{blur} \times \boxed{\mathbf{C}_{attn}} \times (\boldsymbol{p} - \boldsymbol{scat} - \boldsymbol{rand})$$

Atténuation

$$\mathbf{C}_{attn}(\boldsymbol{i}) = \boldsymbol{e}^{\int_{\mathrm{LOR}} \boldsymbol{\mu}\, \boldsymbol{dx}}$$

- **> Chang**
- **> Scan transmission**
- **> CT-AC**
  - *Mouvement respiratoire*
  - *Décalage - données manquantes*
  - *Durcissement de faisceau*
  - *Matériel dense*

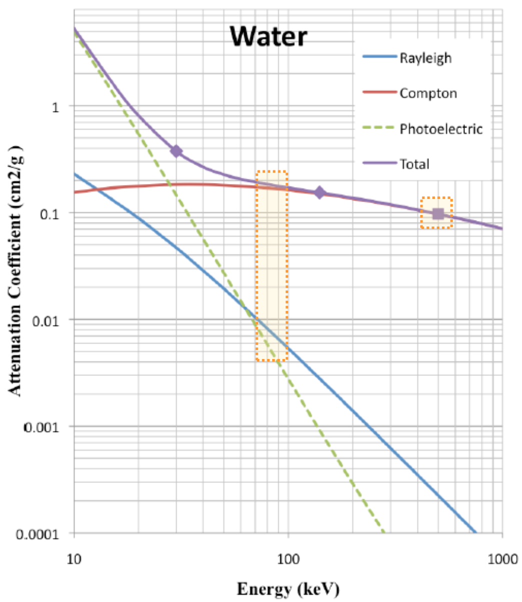

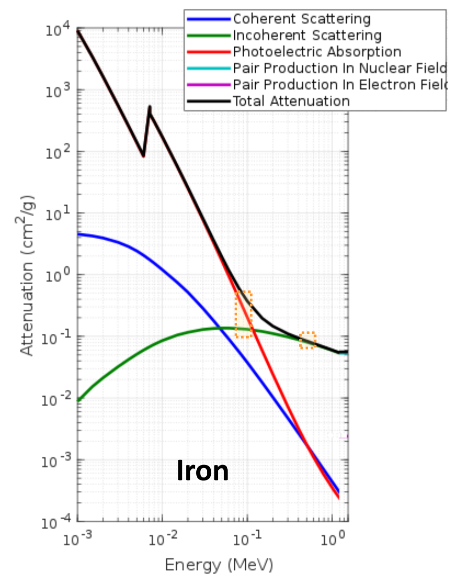

Corrections

$$f \quad \text{t.q.} \quad \mathbf{R}_{geom}\, \boldsymbol{f} = \delta\, \mathbf{C}_{norm} \times \mathbf{C}_{blur} \times \boxed{\mathbf{C}_{attn}} \times (\boldsymbol{p} - \boldsymbol{scat} - \boldsymbol{rand})$$

Atténuation

$$\mathbf{C}_{attn}(\boldsymbol{i}) = \boldsymbol{e}^{\int_{\mathrm{LOR}} \boldsymbol{\mu}\, \boldsymbol{dx}}$$

- > Chang
- > Scan transmission
- > CT-AC

  Mouvement respiratoire

  Décalage - données manquantes

  Durcissement de faisceau

  Matériel dense

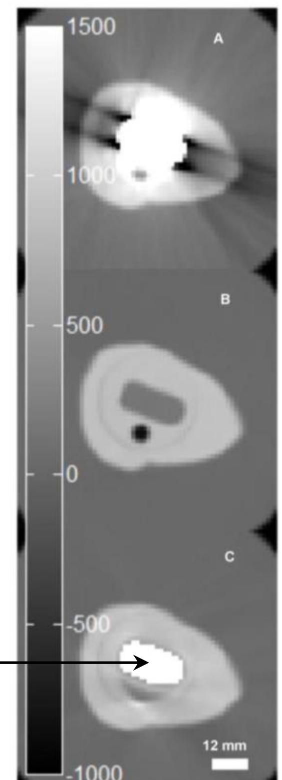

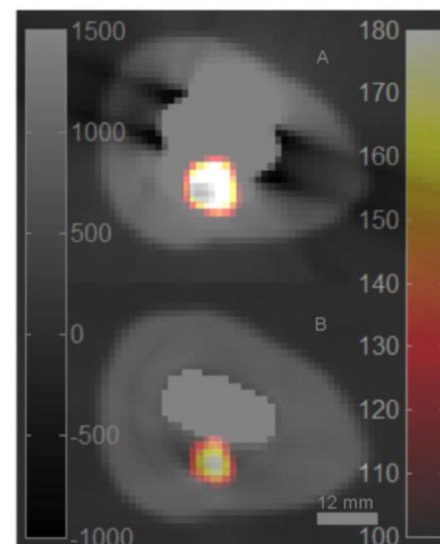

28% Cr, 66% Co, 6% Mo

$\rightarrow \mu_{511}$

Harnish, Ann Nucl Med 2015

Corrections

$$f \quad \text{t.q.} \quad \mathbf{R}_{geom}\, \boldsymbol{f} = \delta\, \mathbf{C}_{norm} \times \boxed{\mathbf{C}_{blur}} \times \mathbf{C}_{attn} \times (\boldsymbol{p} - \boldsymbol{scat} - \boldsymbol{rand}\,)$$

Modélisation de PSF

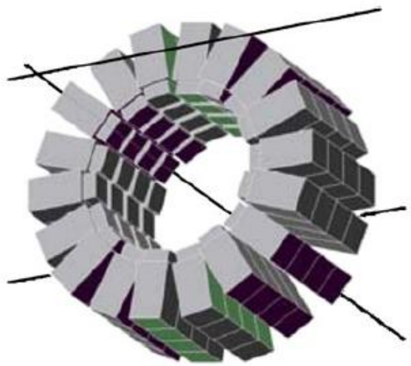

Lee, Phys Med Biol 2004

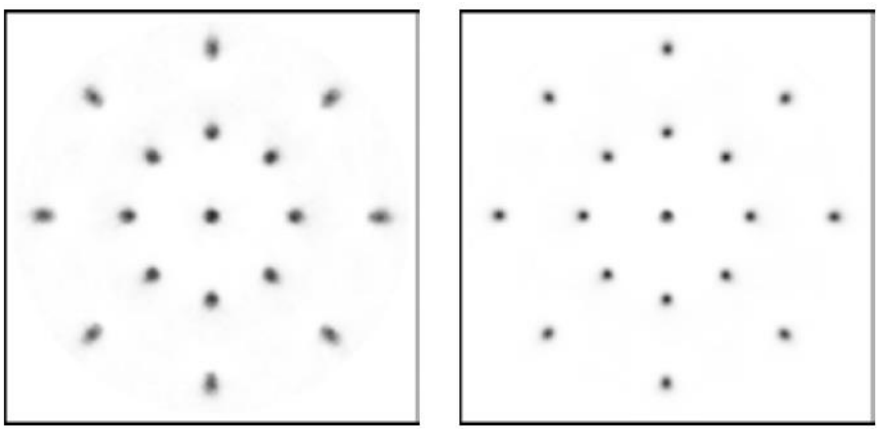

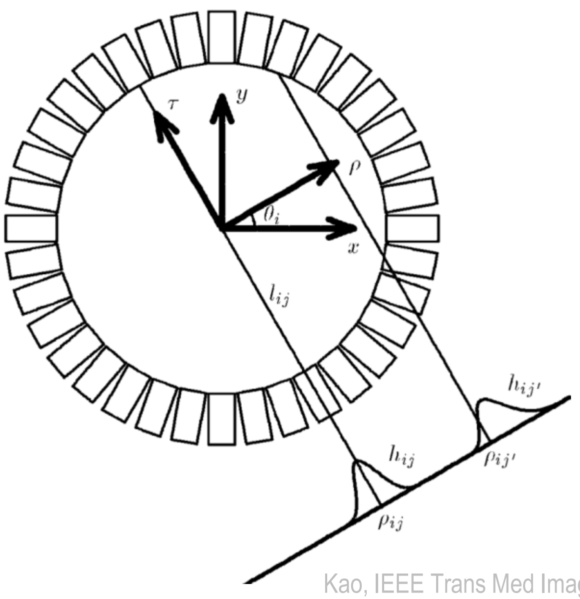

Kao, IEEE Trans Med Imaging 1997

Corrections

$$\boldsymbol{f} \quad \text{t.q.} \quad \mathbf{R}_{geom}\,\boldsymbol{f} = \delta\,\mathbf{C}_{norm} \times \boxed{\mathbf{C}_{blur}} \times \mathbf{C}_{attn} \times (\boldsymbol{p} - \boldsymbol{scat} - \boldsymbol{rand})$$

Modélisation de PSF

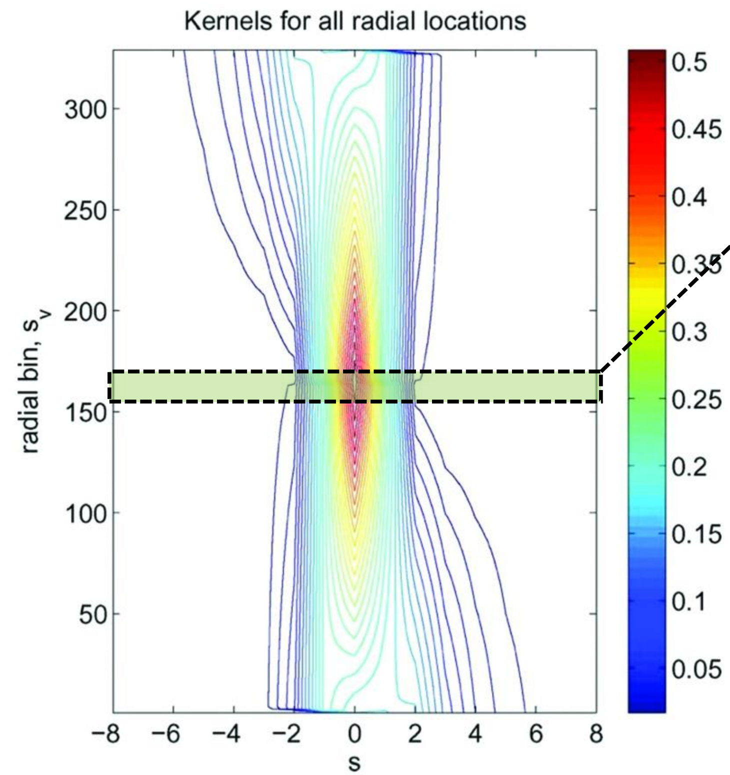

Alessio, IEEE Trans Med Imaging 2010

$\mathbf{C}_{blur}(i,:) =$

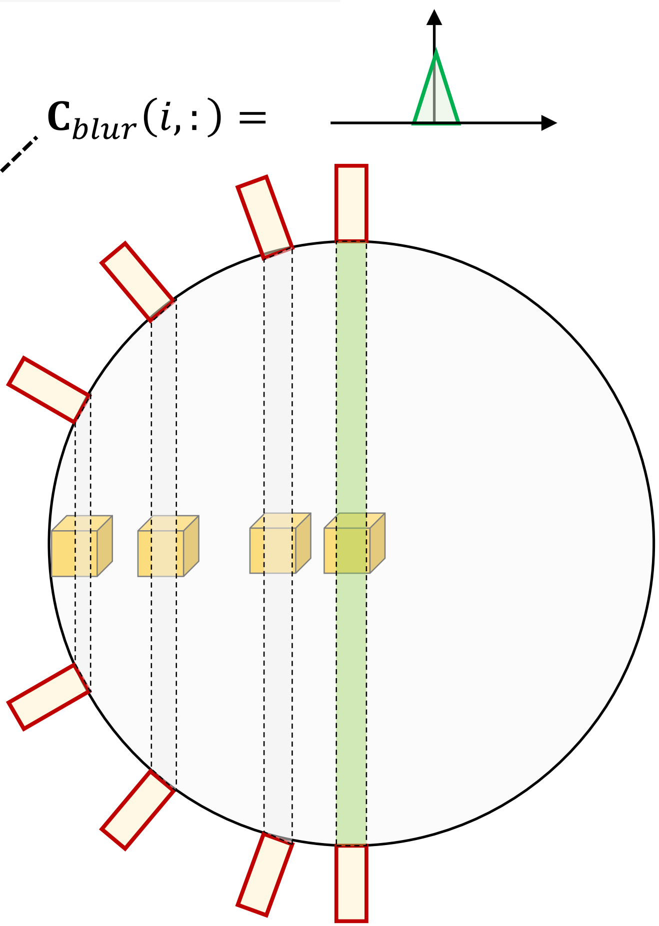

$$\boldsymbol{f} \quad \text{t.q.} \quad \mathbf{R}_{geom}\,\boldsymbol{f} = \delta\, \mathbf{C}_{norm} \times \boxed{\mathbf{C}_{blur}} \times \mathbf{C}_{attn} \times (\boldsymbol{p} - \boldsymbol{scat} - \boldsymbol{rand}\,)$$

Modélisation de PSF

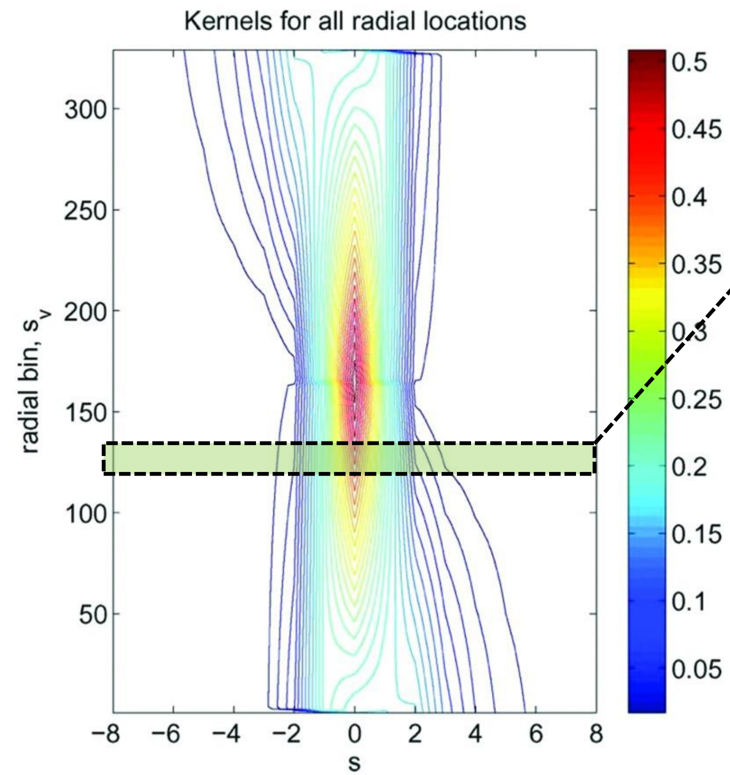

$\mathbf{C}_{blur}(i,:) =$

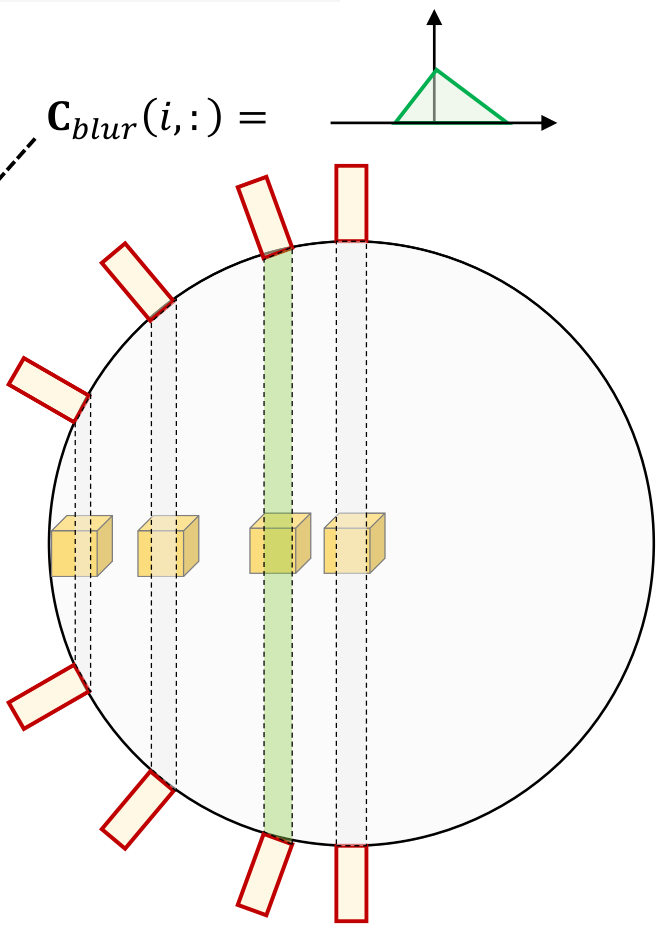

Alessio, IEEE Trans Med Imaging 2010

Corrections

$$\boldsymbol{f} \quad \text{t.q.} \quad \mathbf{R}_{geom}\, \boldsymbol{f} = \delta\, \mathbf{C}_{norm} \times \boxed{\mathbf{C}_{blur}} \times \mathbf{C}_{attn} \times (\boldsymbol{p} - \boldsymbol{scat} - \boldsymbol{rand})$$

Modélisation de PSF

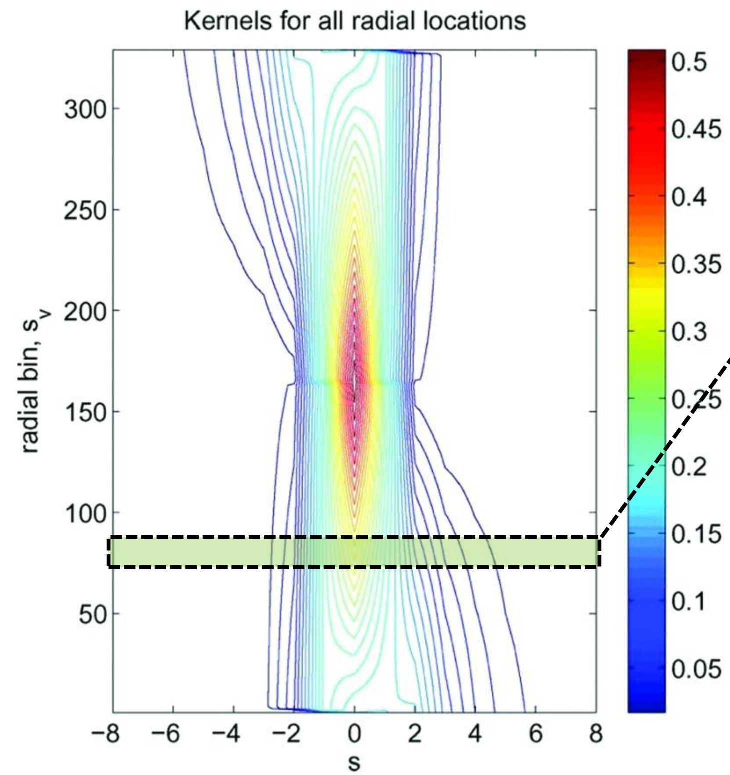

Alessio, IEEE Trans Med Imaging 2010

$\mathbf{C}_{blur}(i,:) =$

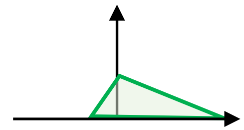

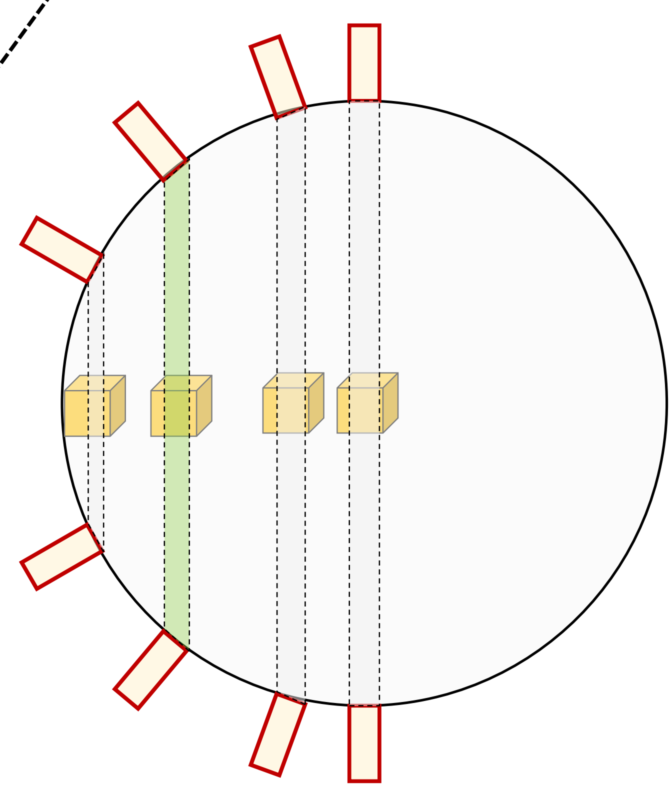

Corrections

$$\boldsymbol{f} \quad \text{t.q.} \quad \mathbf{R}_{geom}\,\boldsymbol{f} = \delta\,\mathbf{C}_{norm} \times \boxed{\mathbf{C}_{blur}} \times \mathbf{C}_{attn} \times (\boldsymbol{p} - \boldsymbol{scat} - \boldsymbol{rand}\,)$$

Modélisation de PSF

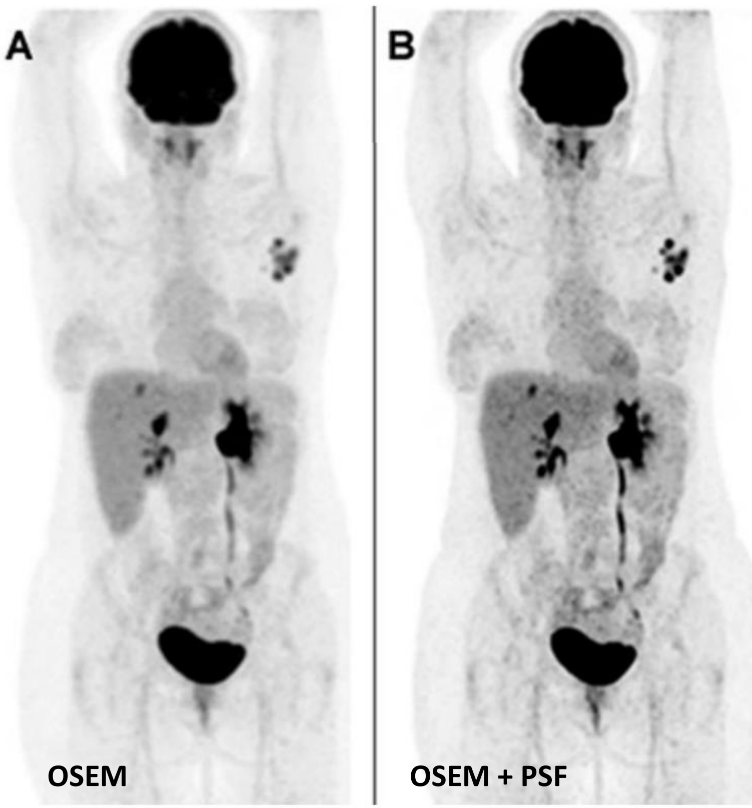

Rahmim, Med Phys 2013

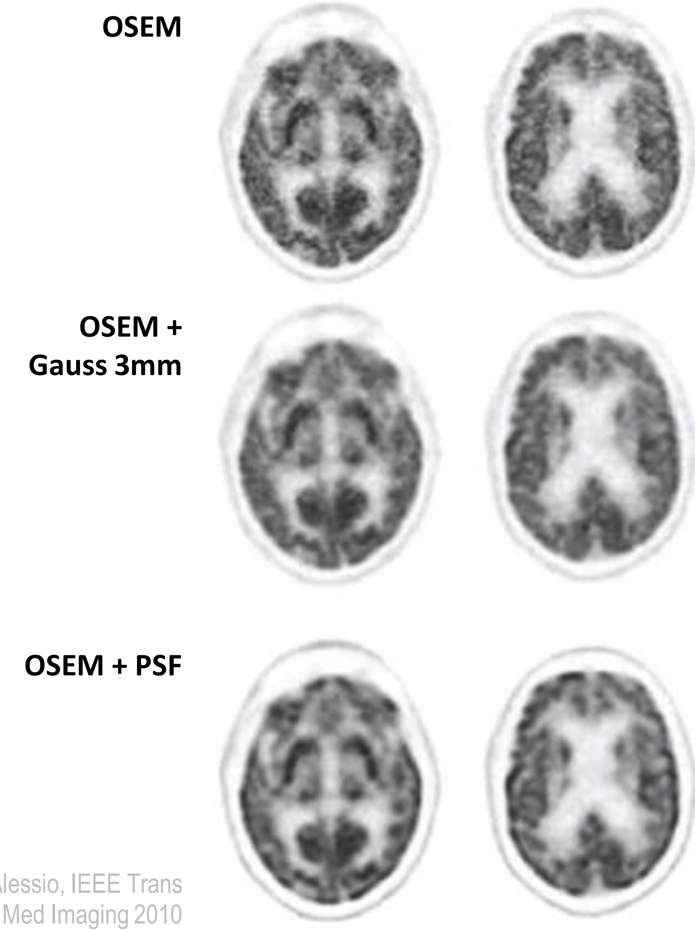

Alessio, IEEE Trans Med Imaging 2010

Corrections

$$\boldsymbol{f} \quad \text{t.q.} \quad \mathbf{R}_{geom}\, \boldsymbol{f} = \delta\, \mathbf{C}_{norm} \times \boxed{\mathbf{C}_{blur}} \times \mathbf{C}_{attn} \times (\boldsymbol{p} - \boldsymbol{scat} - \boldsymbol{rand})$$

Modélisation de PSF

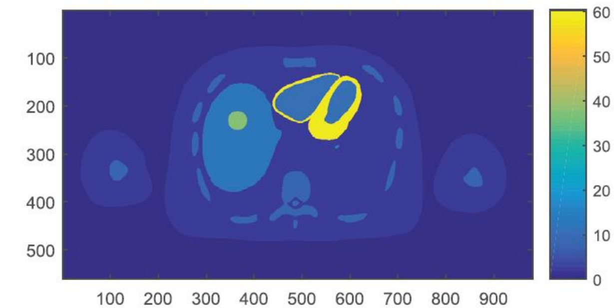

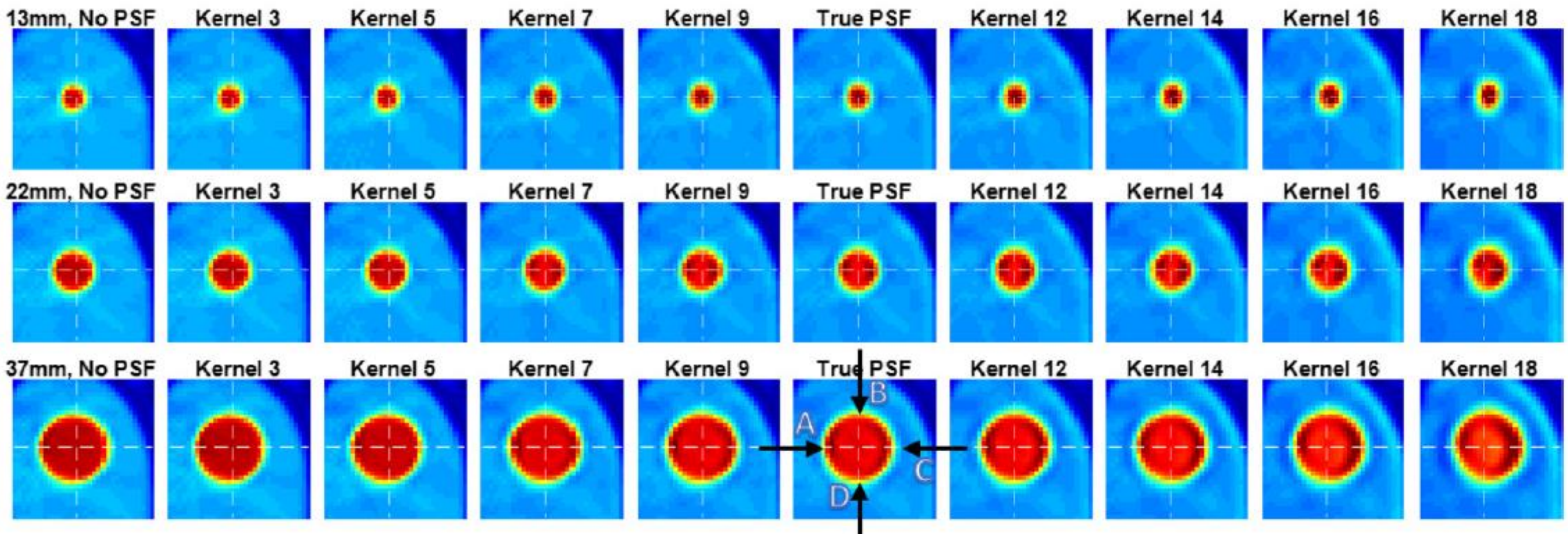

Ashrafinia, Phys Med Biol 2017

Corrections

$$\boldsymbol{f} \quad \text{t.q.} \quad \mathbf{R}_{geom}\,\boldsymbol{f} = \delta\,\mathbf{C}_{norm} \times \boxed{\mathbf{C}_{blur}} \times \mathbf{C}_{attn} \times (\boldsymbol{p} - \boldsymbol{scat} - \boldsymbol{rand})$$

Modélisation de PSF

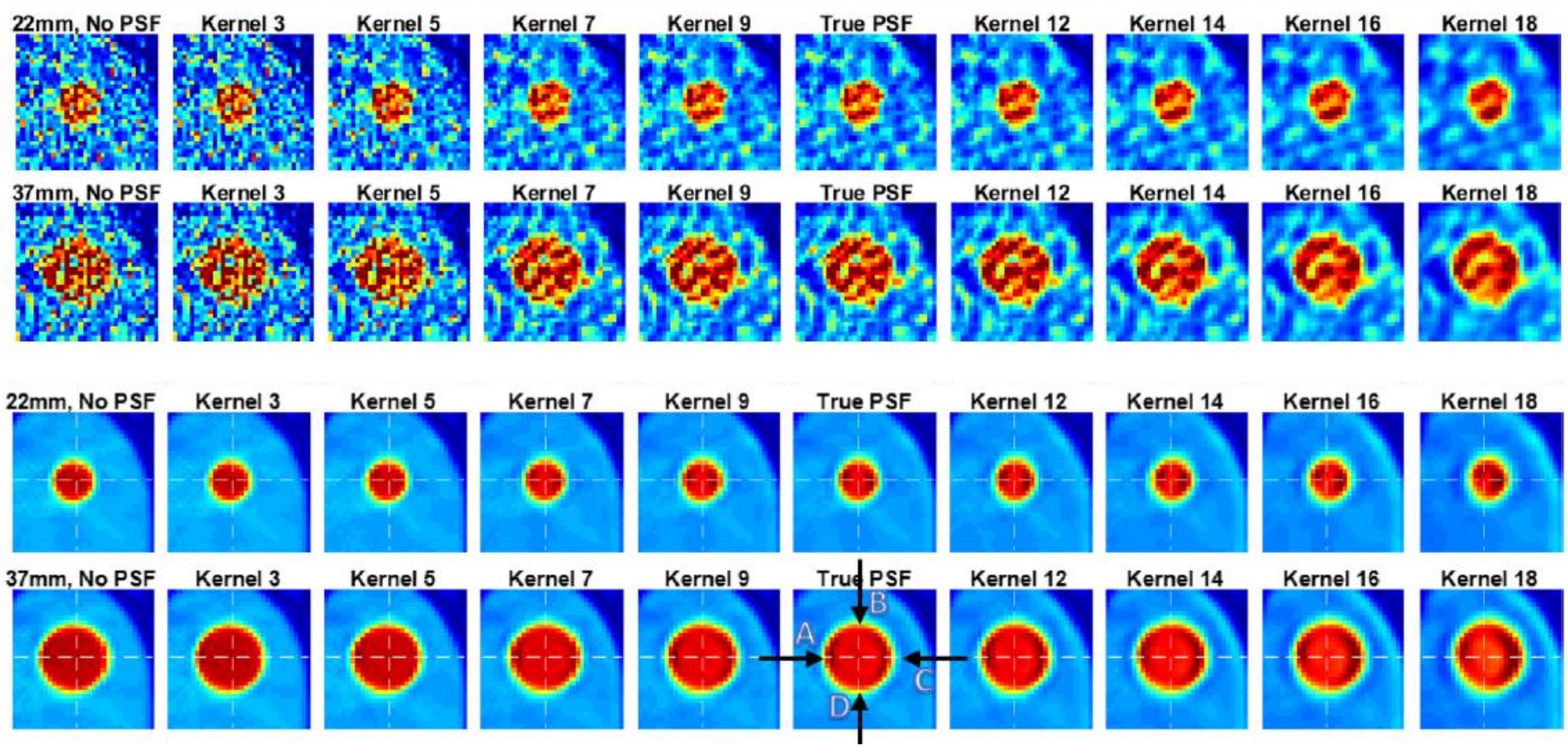

Ashrafinia, Phys Med Biol 2017

Corrections

$$f \quad \text{t.q.} \quad \mathbf{R}_{geom}\, f = \delta\, \mathbf{C}_{norm} \times \boxed{\mathbf{C}_{blur}} \times \mathbf{C}_{attn} \times (\boldsymbol{p} - \boldsymbol{scat} - \boldsymbol{rand})$$

Modélisation de PSF

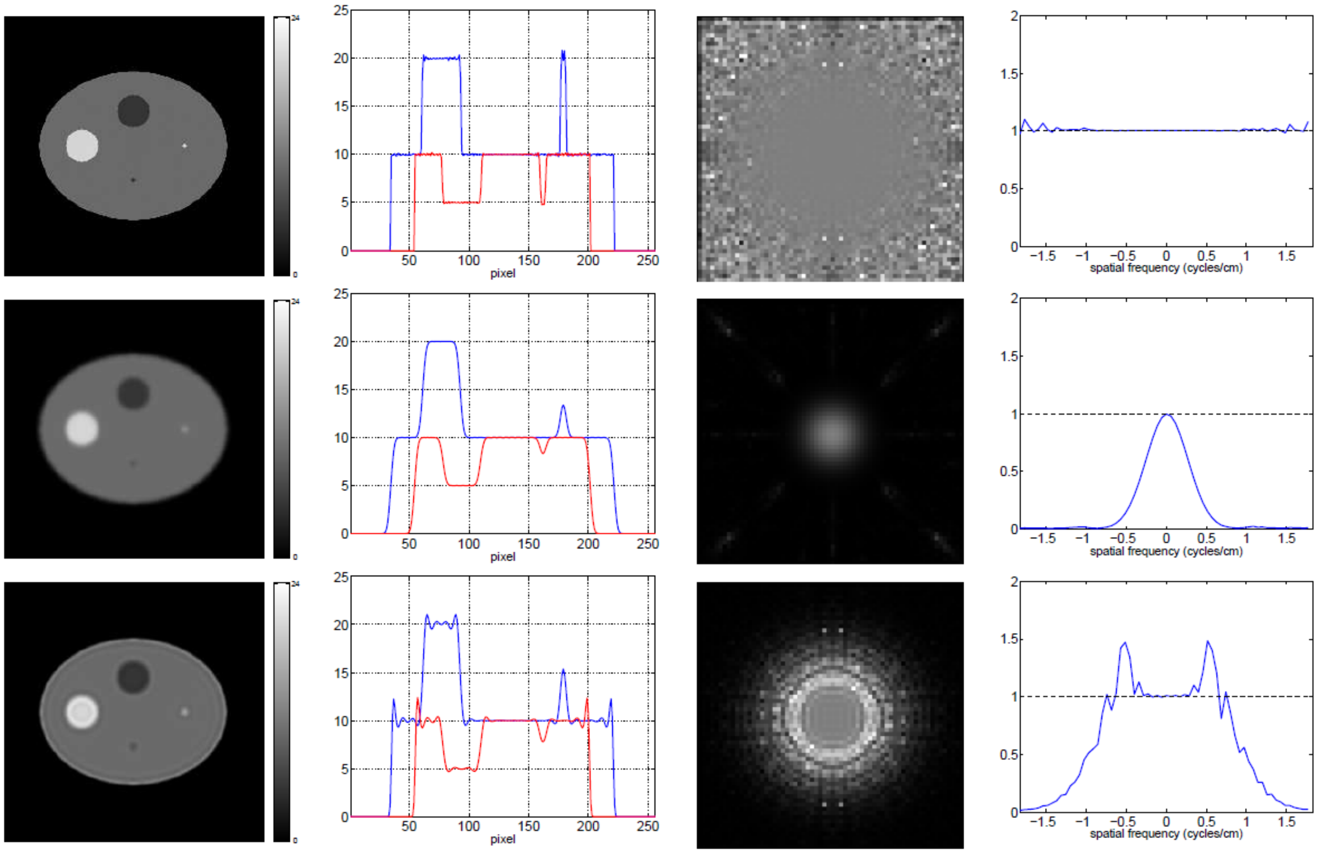

Tong, IEEE Nucl Sci Symp 2010

Corrections

$$\boldsymbol{f} \quad \text{t.q.} \quad \mathbf{R}_{geom}\,\boldsymbol{f} = \delta\,\mathbf{C}_{norm} \times \boxed{\mathbf{C}_{blur}} \times \mathbf{C}_{attn} \times (\boldsymbol{p} - \boldsymbol{scat} - \boldsymbol{rand})$$

Modélisation de PSF

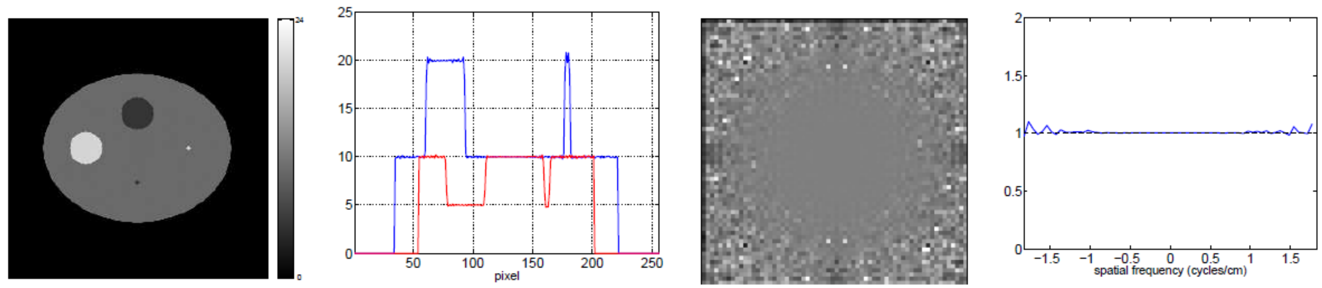

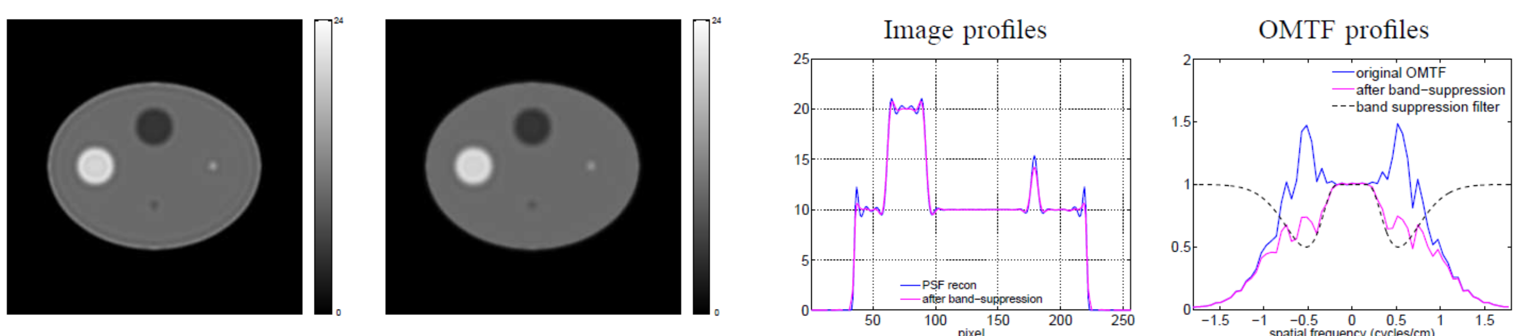

Tong, IEEE Nucl Sci Symp 2010

Corrections

$$f \quad \text{t.q.} \quad \mathbf{R}_{geom}\, \boldsymbol{f} = \delta\, \mathbf{C}_{norm} \times \boxed{\mathbf{C}_{blur}} \times \mathbf{C}_{attn} \times (\boldsymbol{p} - \boldsymbol{scat} - \boldsymbol{rand})$$

Modélisation de PSF

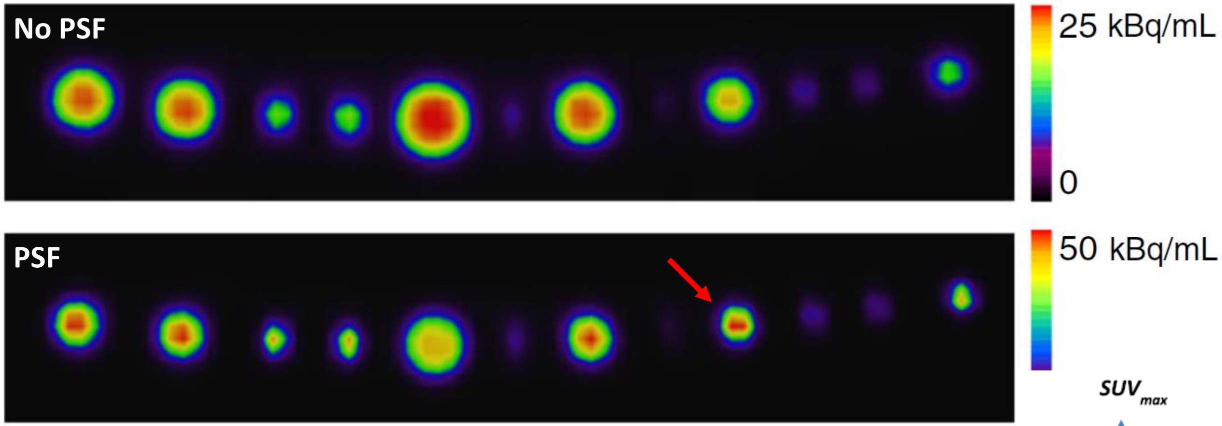

Munk, EJNMMI Phys 2017

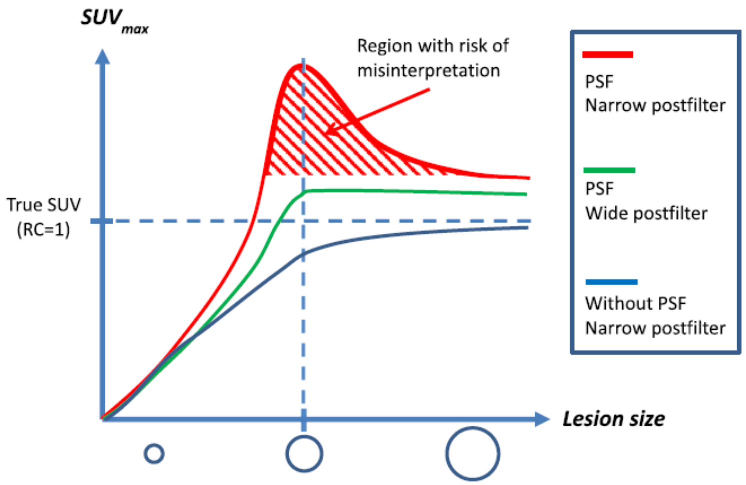

Corrections

$$f \quad \text{t.q.} \quad \mathbf{R}_{geom}\, \boldsymbol{f} = \delta\, \mathbf{C}_{norm} \times \boxed{\mathbf{C}_{blur}} \times \mathbf{C}_{attn} \times (\boldsymbol{p} - \boldsymbol{scat} - \boldsymbol{rand})$$

Modélisation de PSF

Alternative : correction PVE

Déconvolution

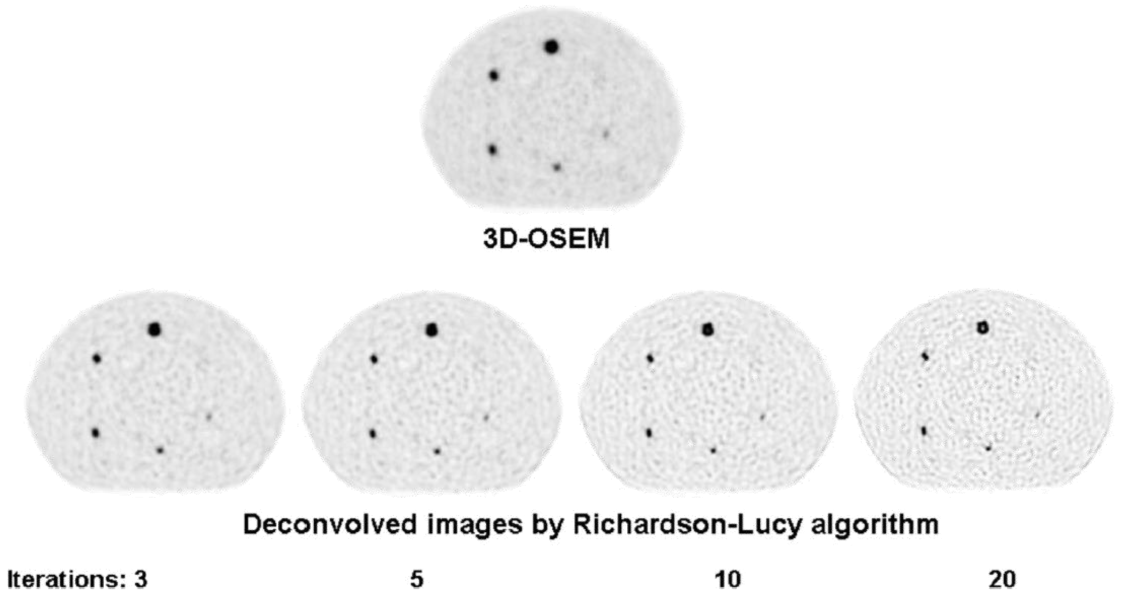

Bettinardi, Clin Transl Imaging 2014

Corrections

$$\boldsymbol{f} \quad \text{t.q.} \quad \mathbf{R}_{geom}\,\boldsymbol{f} = \delta\, \mathbf{C}_{norm} \times \boxed{\mathbf{C}_{blur}} \times \mathbf{C}_{attn} \times (\boldsymbol{p} - \boldsymbol{scat} - \boldsymbol{rand})$$

Modélisation de PSF

Alternative : correction PVE

Déconvolution

Partition (segmentation anatomique)

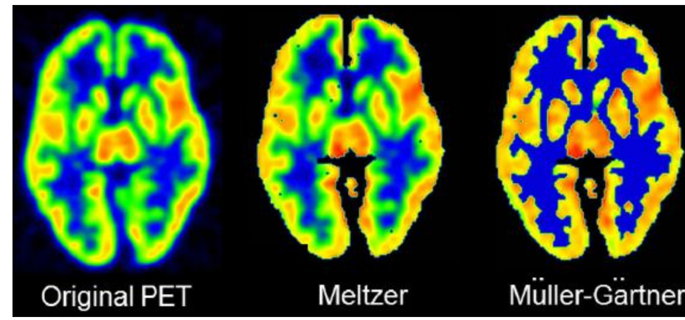

Bettinardi, Clin Transl Imaging 2014

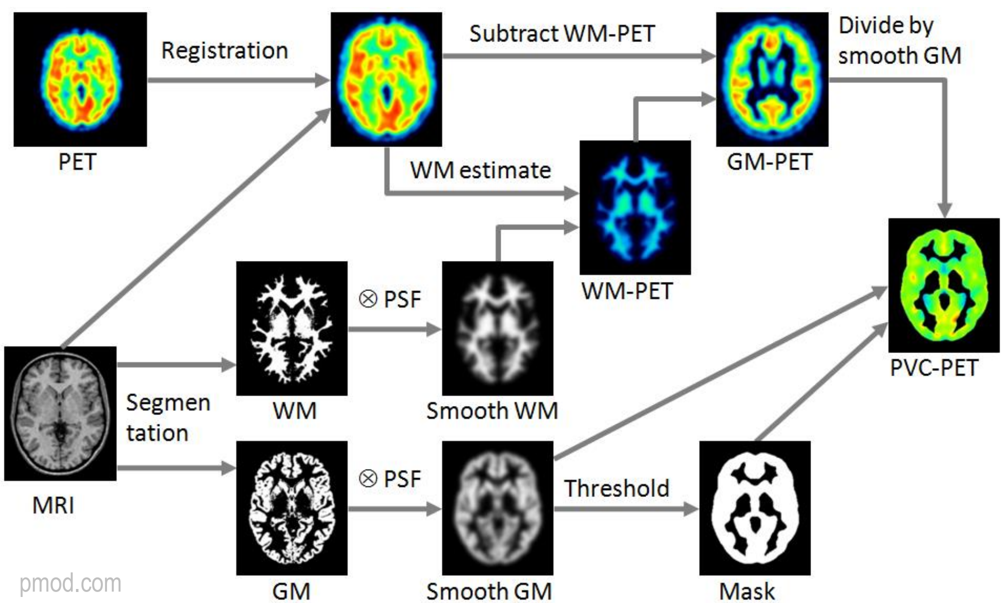

pmod.com

Müller-Gärtner

$$A_{GM\ corr} = \frac{A_{GM} - \overbrace{A_{WM}(WM * PSF)}^{\textit{Spill-in}}}{\underbrace{GM * PSF}_{\textit{Spill-out}}}$$

Meltzer

$$A_{corr} = \frac{A}{Brain * PSF}$$

Corrections

$$\boldsymbol{f} \quad \text{t.q.} \quad \mathbf{R}_{geom}\,\boldsymbol{f} = \delta\,\mathbf{C}_{norm} \times \boxed{\mathbf{C}_{blur}} \times \mathbf{C}_{attn} \times (\boldsymbol{p} - \boldsymbol{scat} - \boldsymbol{rand})$$

Modélisation de PSF

Alternative : correction PVE

Déconvolution
Partition
Multi-résolution

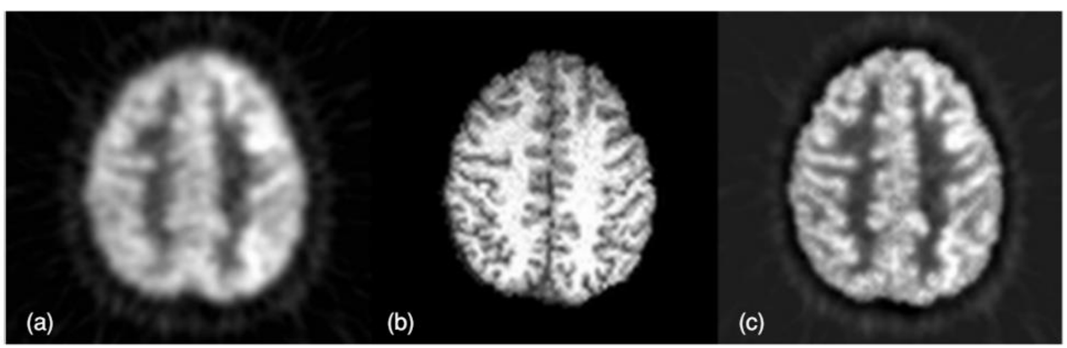

Bouisson, Phys Med Biol 2006

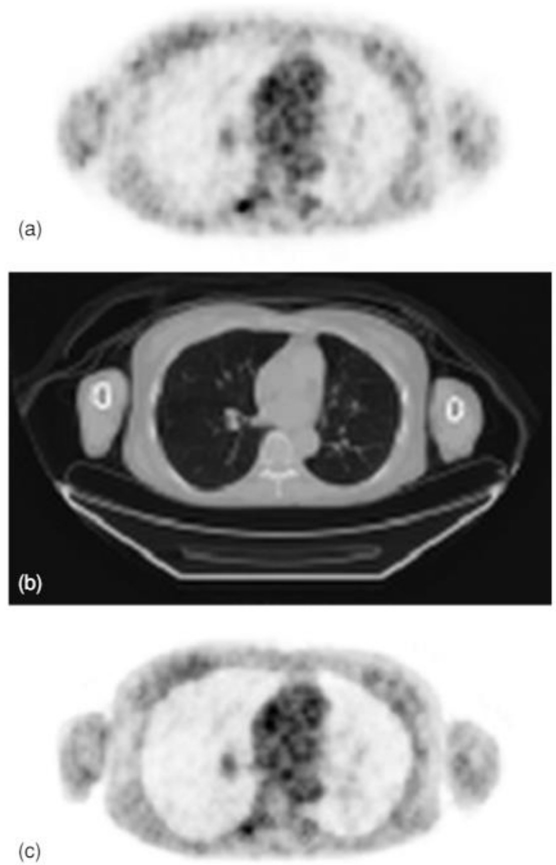

Corrections

$$\boldsymbol{f} \quad \text{t.q.} \quad \mathbf{R}_{geom}\,\boldsymbol{f} = \delta\,\boxed{\mathbf{C}_{norm}} \times \mathbf{C}_{blur} \times \mathbf{C}_{attn} \times (\boldsymbol{p} - \boldsymbol{scat} - \boldsymbol{rand})$$

Normalisation

Géométrie - profil radial

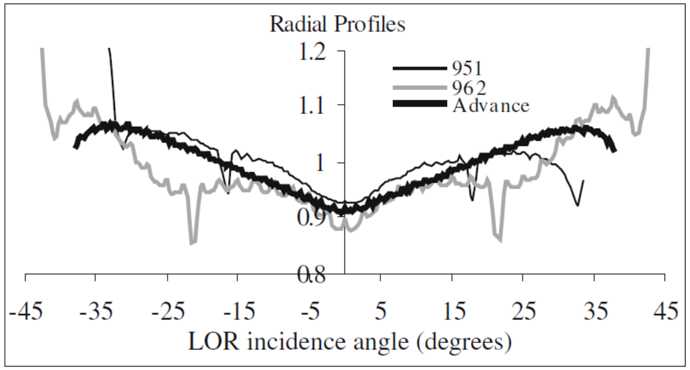

Meikle, Sringer 2003

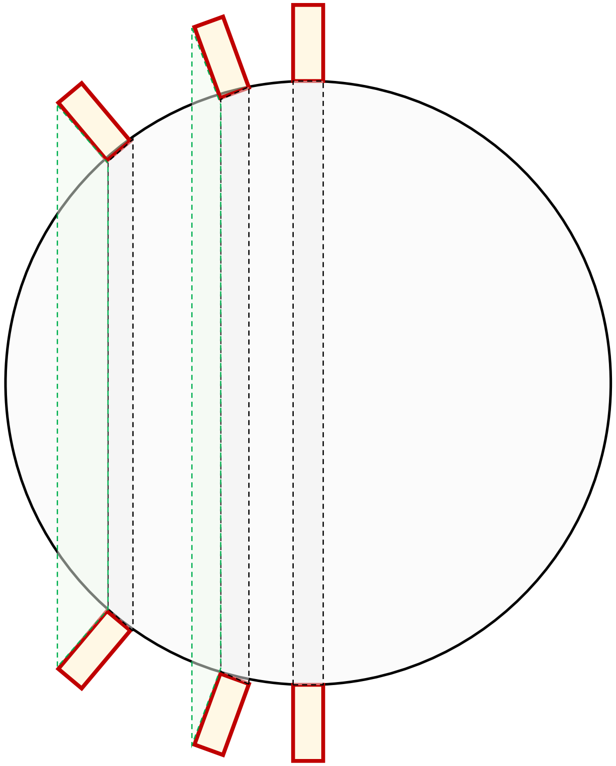

Corrections

$$\boldsymbol{f} \quad \text{t.q.} \quad \mathbf{R}_{geom}\, \boldsymbol{f} = \delta\, \boxed{\mathbf{C}_{norm}} \times \mathbf{C}_{blur} \times \mathbf{C}_{attn} \times (\boldsymbol{p} - \boldsymbol{scat} - \boldsymbol{rand})$$

Normalisation

Géométrie - profil radial

Profil de bloc

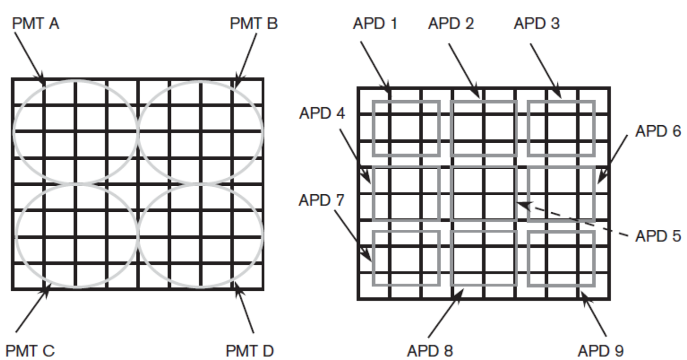

Theodorakis, Nucl Med Commun 2013

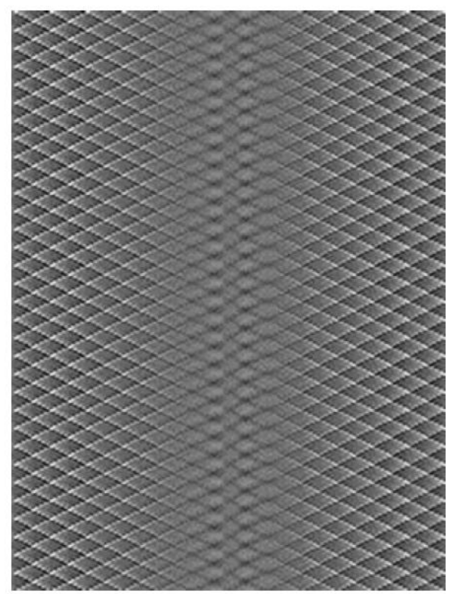

Meikle, Sringer 2003

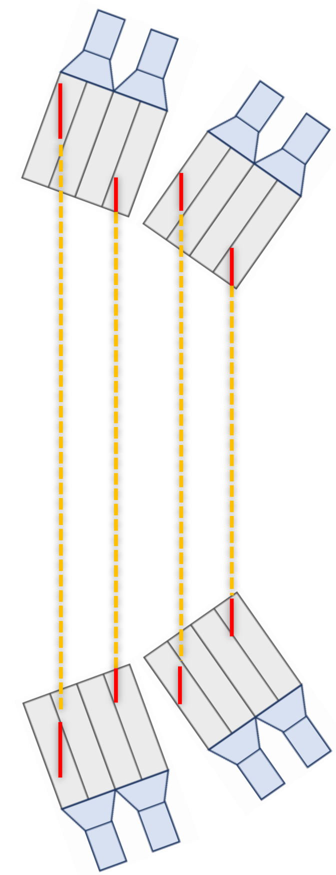

Corrections

$$\boldsymbol{f} \quad \text{t.q.} \quad \mathbf{R}_{geom}\, \boldsymbol{f} = \delta\, \boxed{\mathbf{C}_{norm}} \times \mathbf{C}_{blur} \times \mathbf{C}_{attn} \times (\boldsymbol{p} - \boldsymbol{scat} - \boldsymbol{rand})$$

Normalisation

- Géométrie - profil radial
- Profil de bloc
- Efficacité intrinsèque
- Synchronisation

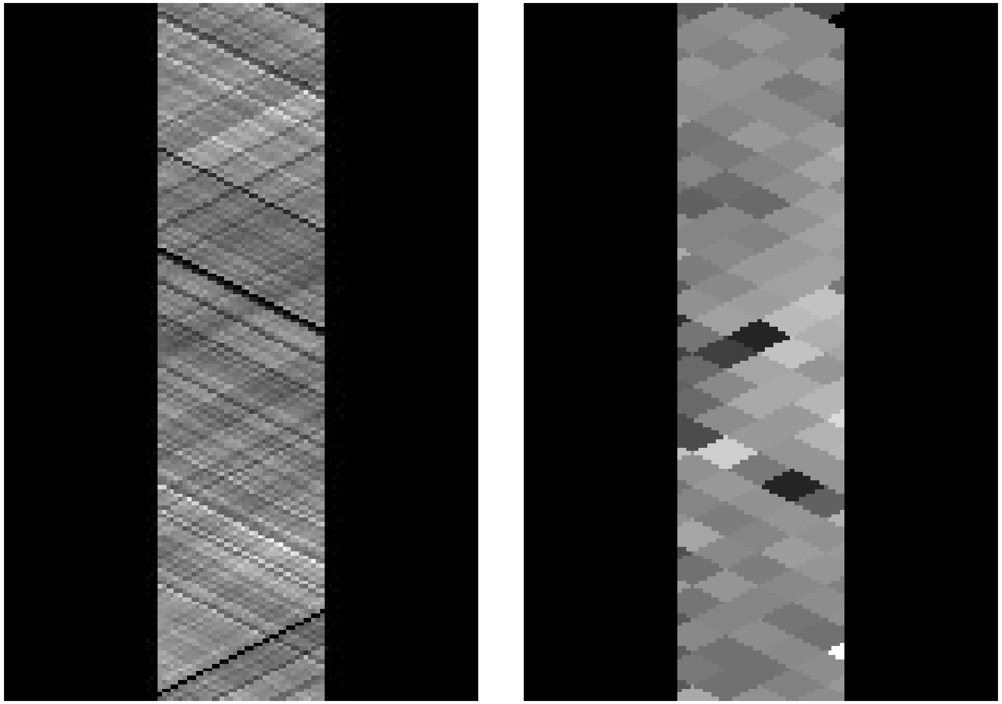

Bai, Phys Med Biol 2002

Corrections

$$f \quad \text{t.q.} \quad \mathbf{R}_{geom}\, f = \delta\, \boxed{\mathbf{C}_{norm}} \times \mathbf{C}_{blur} \times \mathbf{C}_{attn} \times (\boldsymbol{p} - \boldsymbol{scat} - \boldsymbol{rand})$$

Normalisation

Géométrie - profil radial
Profil de bloc
Efficacité intrinsèque
Synchronisation
Alignement structurel

$$\mathbf{C}_{norm}(a,b) = \varepsilon_a\, \varepsilon_b\, g_{ab}\, b_{ab}\, t_{ab}\, m_{ab}$$

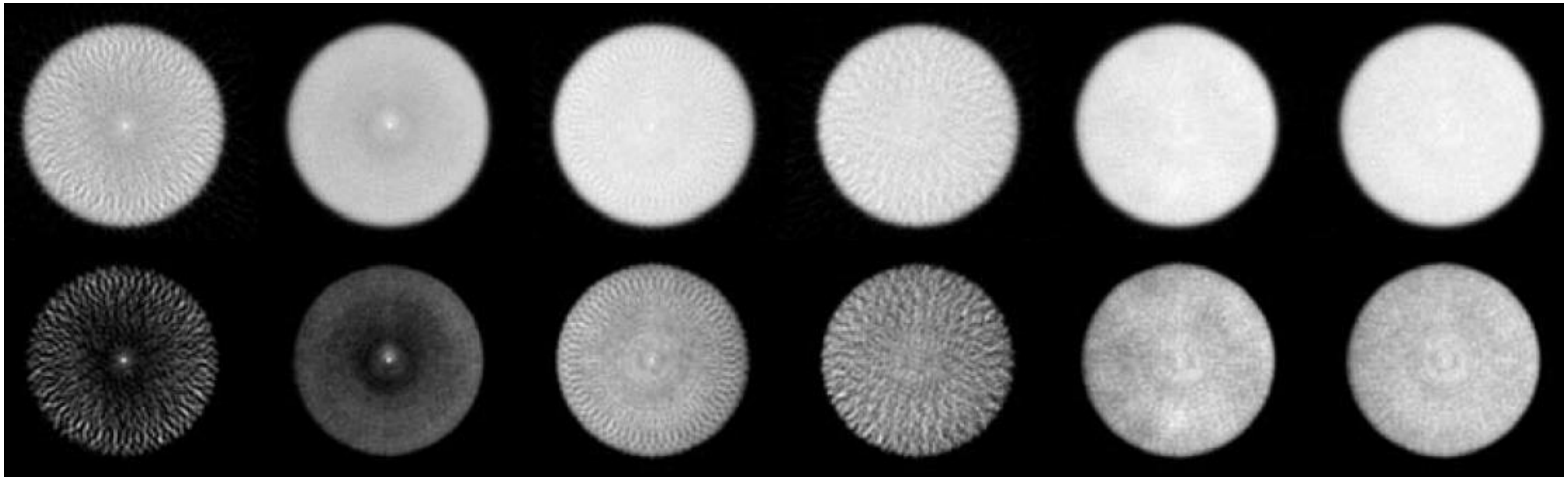

Meikle, Sringer 2003

Corrections

$$\boldsymbol{f} \quad \text{t.q.} \quad \mathbf{R}_{geom}\,\boldsymbol{f} = \boxed{\delta}\,\mathbf{C}_{norm} \times \mathbf{C}_{blur} \times \mathbf{C}_{attn} \times (\boldsymbol{p} - \boldsymbol{scat} - \boldsymbol{rand})$$

Effet temps mort

Temps d'intégration
Empilement

paralysable

Electronique

non paralysable

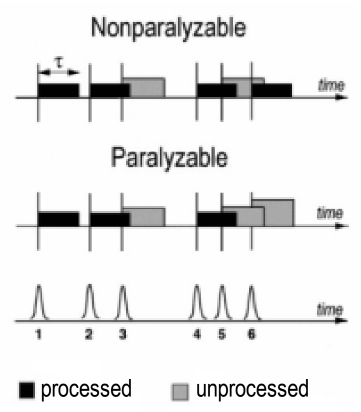

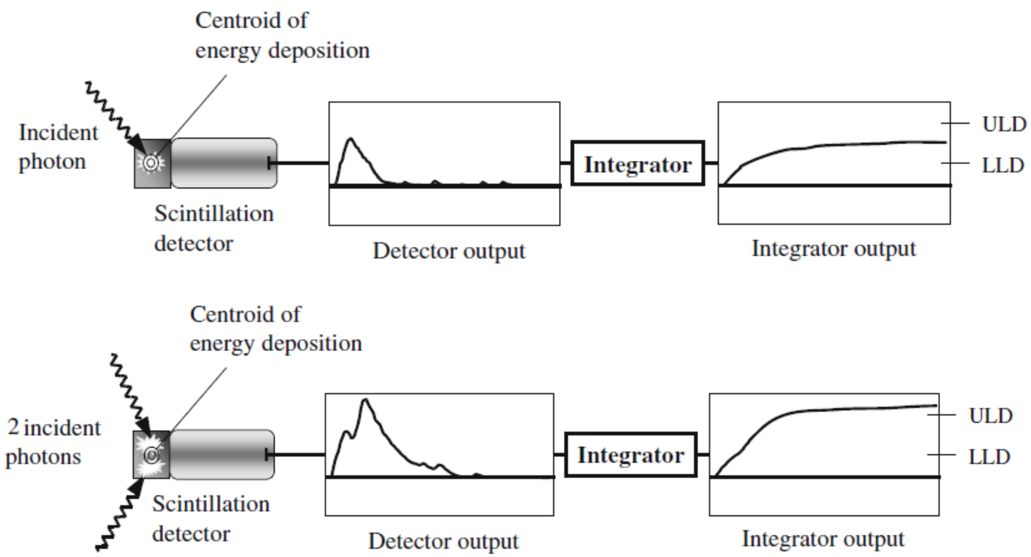

Meikle, Sringer 2003

Corrections

$$\boldsymbol{f} \quad \text{t.q.} \quad \mathbf{R}_{geom}\,\boldsymbol{f} = \boxed{\delta}\,\mathbf{C}_{norm} \times \mathbf{C}_{blur} \times \mathbf{C}_{attn} \times (\boldsymbol{p} - \boldsymbol{scat} - \boldsymbol{rand})$$

Effet temps mort

Temps d'intégration
Empilement

paralysable $m = ne^{-n\tau}$

Electronique *non paralysable* $m = \dfrac{n}{1 + n\tau}$

Fractional dead-time

$$\delta(m) = \frac{m}{n}$$

Idéalement

$$\delta(m, \boldsymbol{f})$$

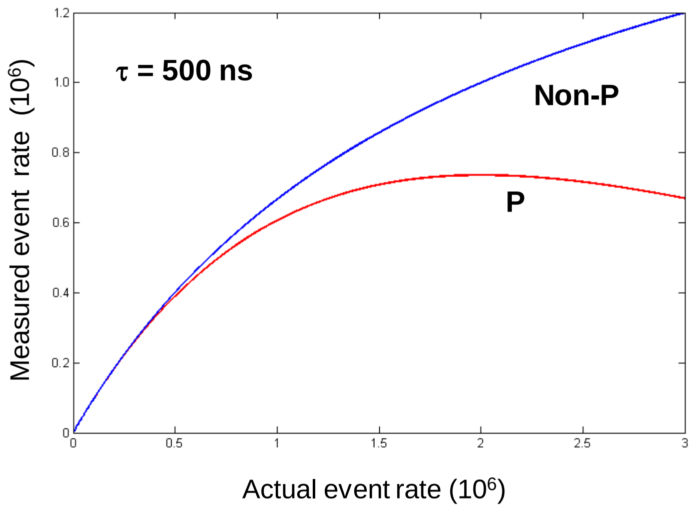

Corrections

$$f \quad \text{t.q.} \quad \mathbf{R}_{geom}\, \boldsymbol{f} = \boxed{\delta}\, \mathbf{C}_{norm} \times \mathbf{C}_{blur} \times \mathbf{C}_{attn} \times (\boldsymbol{p} - \boldsymbol{scat} - \boldsymbol{rand})$$

Effet temps mort

Temps d'intégration
Empilement
paralysable

Electronique *non paralysable*

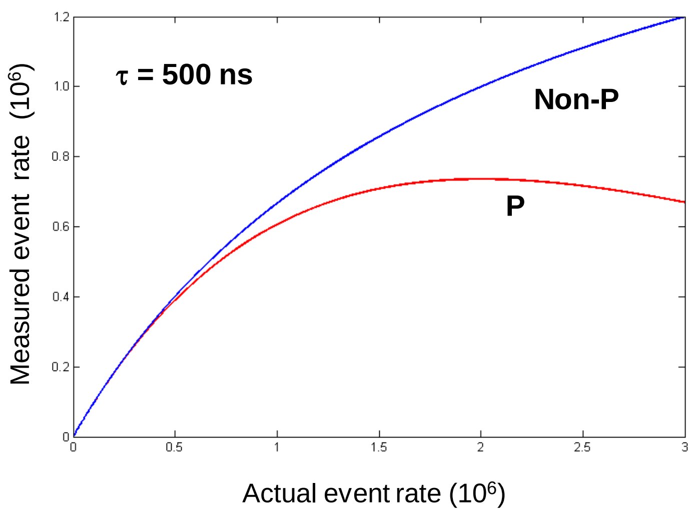

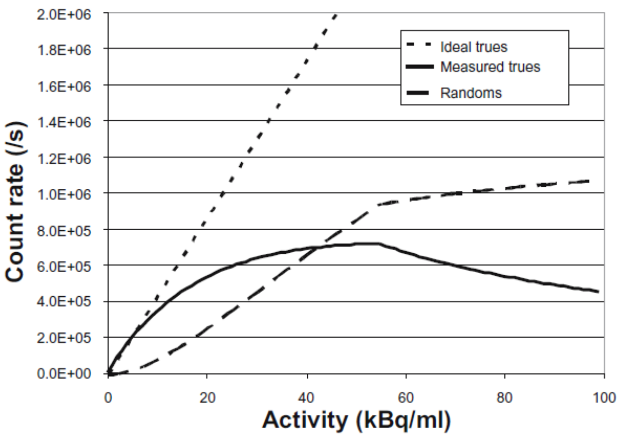

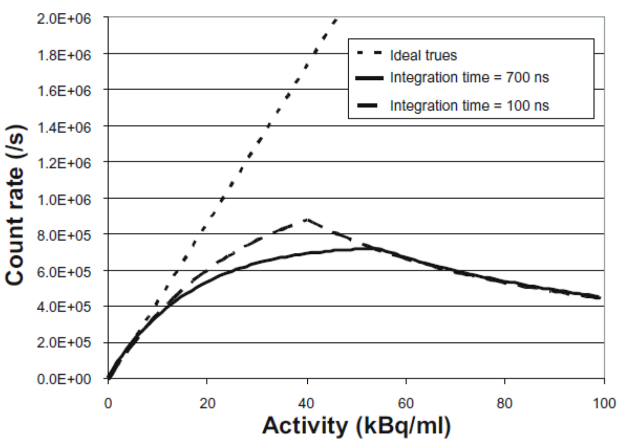

Meikle, Sringer 2003

Corrections

$$\boldsymbol{f} \quad \text{t.q.} \quad \mathbf{R}_{geom}\,\boldsymbol{f} = \boxed{\delta}\,\mathbf{C}_{norm} \times \mathbf{C}_{blur} \times \mathbf{C}_{attn} \times (\boldsymbol{p} - \boldsymbol{scat} - \boldsymbol{rand})$$

Effet temps mort

Temps d'intégration
Empilement

paralysable

Electronique

non paralysable

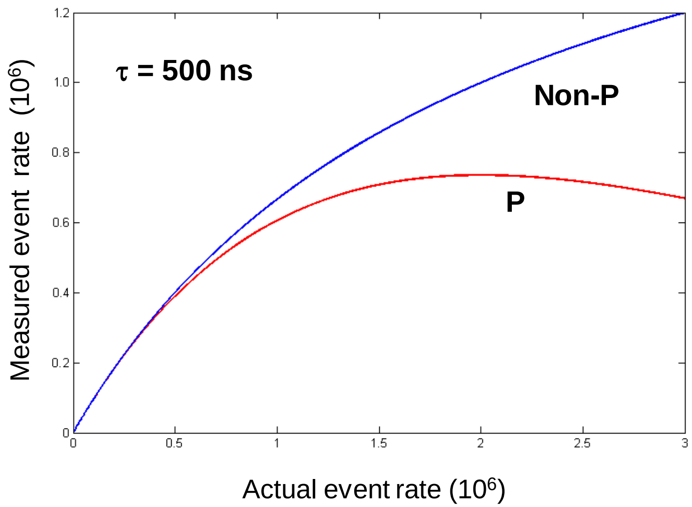

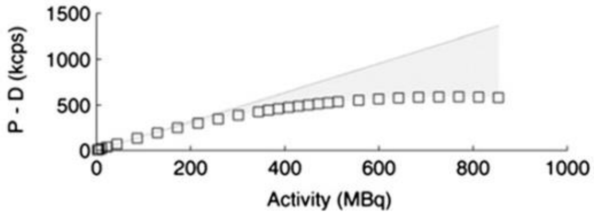

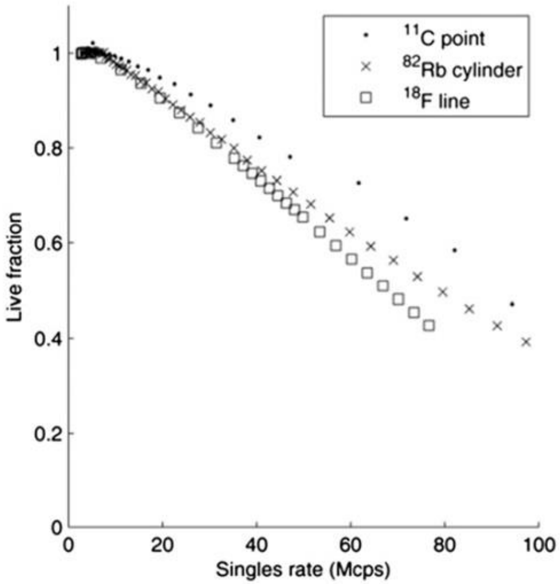

Kolthammer, Phys Med Biol 2015

Evolutions récentes

Temps de vol (ToF)

$$t_1 = \frac{R - \Delta x}{c} \qquad t_2 = \frac{R + \Delta x}{c}$$

$$\Delta t = \frac{2\,\Delta x}{c}$$

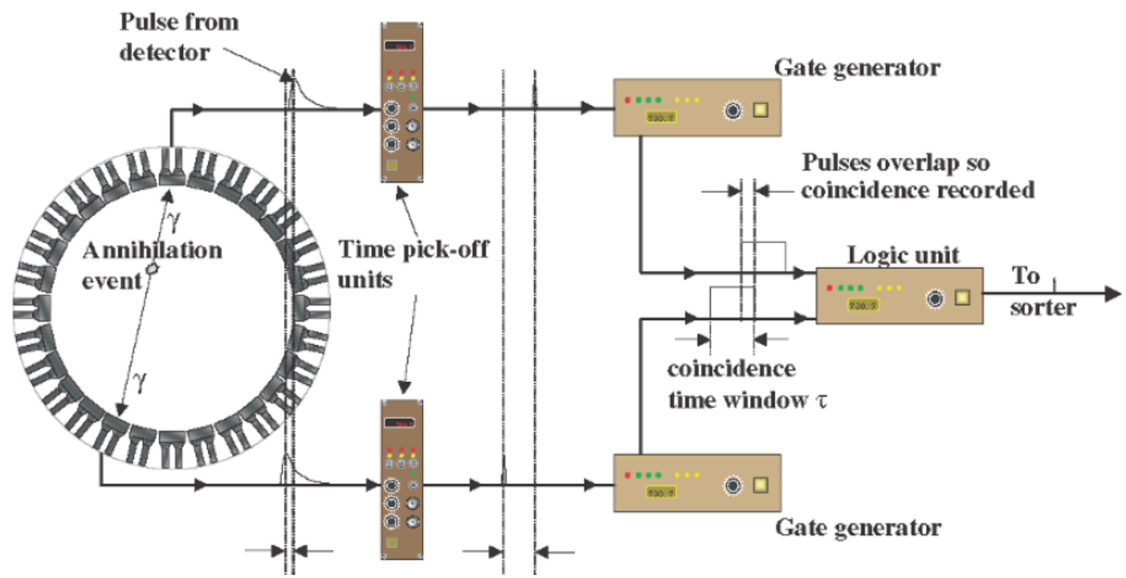

Δt

$\Delta t \pm \frac{\sigma_t}{2}$

Meikle, Sringer 2003

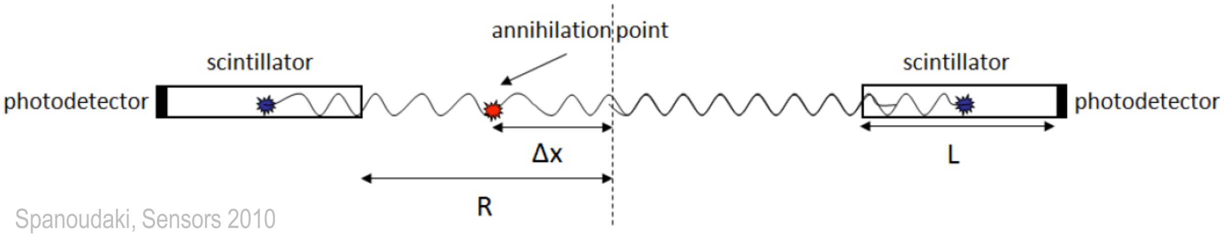

Spanoudaki, Sensors 2010

Evolutions récentes

Temps de vol (ToF)

$$t_1 = \frac{R - \Delta x}{c} \qquad t_2 = \frac{R + \Delta x}{c}$$

$$\Delta t = \frac{2\,\Delta x}{c} \qquad \Delta x = \frac{c\,\Delta t}{2}$$

$$\boxed{\sigma_x = \frac{c\,\sigma_t}{2}}$$

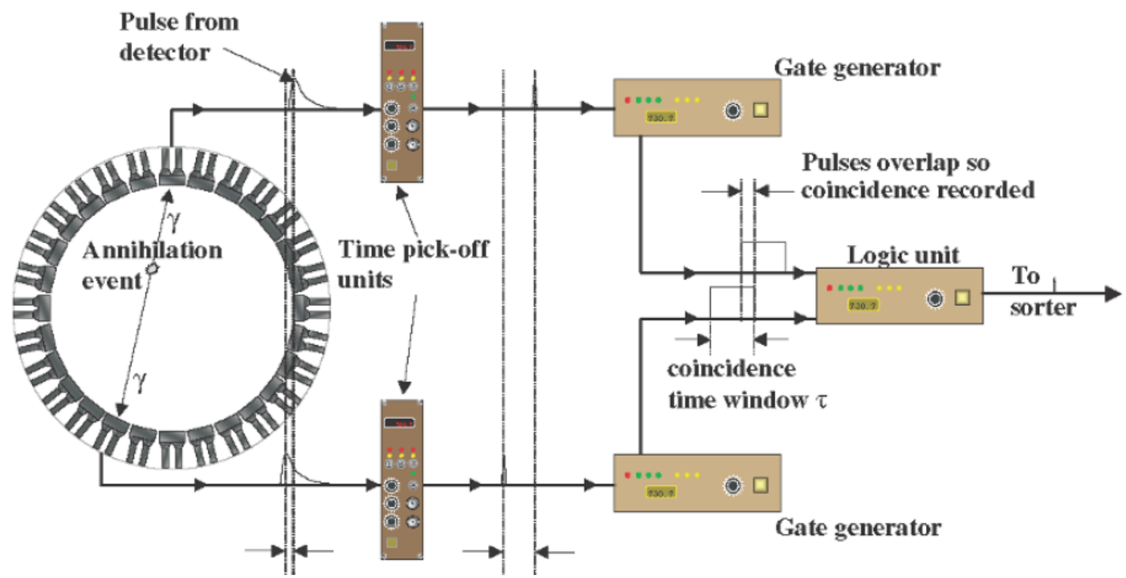

Δt $\qquad$ $\Delta t \pm \frac{\sigma_t}{2}$

Meikle, Sringer 2003

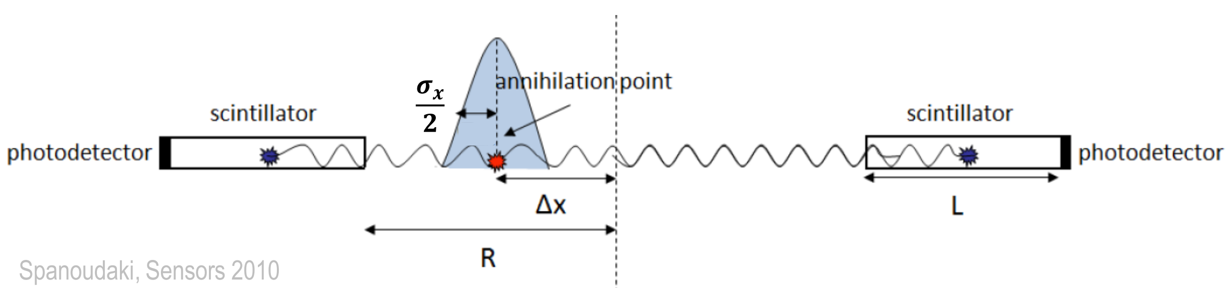

Spanoudaki, Sensors 2010

Evolutions récentes

Temps de vol (ToF)

$$t_1 = \frac{R - \Delta x}{c} \qquad t_2 = \frac{R + \Delta x}{c}$$

$$\Delta t = \frac{2\,\Delta x}{c} \qquad \Delta x = \frac{c\,\Delta t}{2}$$

$$\boxed{\sigma_x = \frac{c\,\sigma_t}{2}}$$

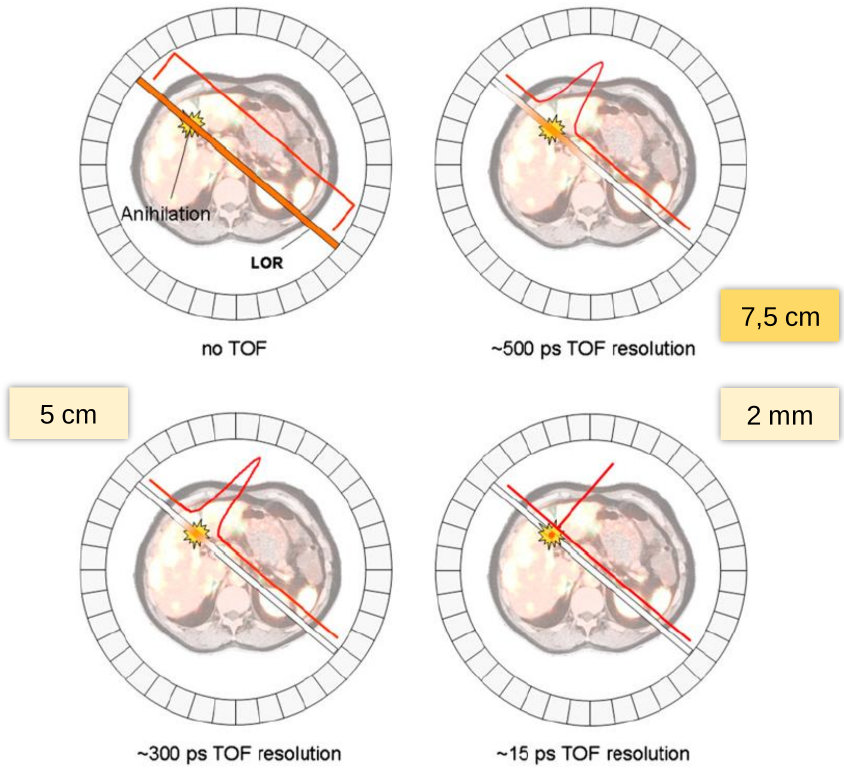

Pichler, J Nucl Med 2008

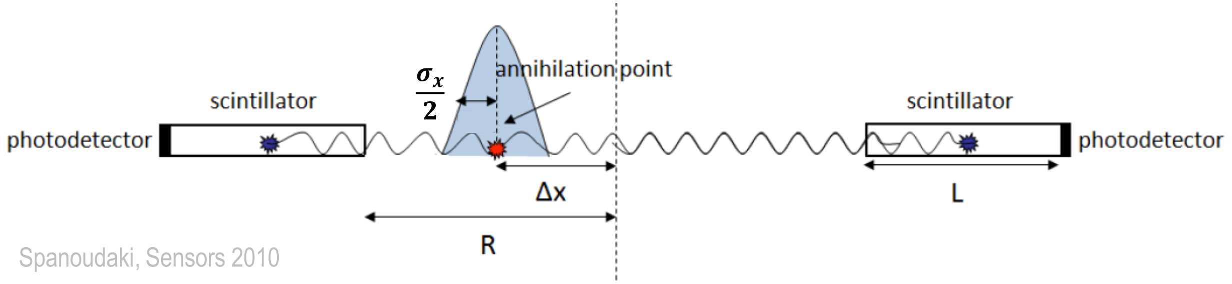

Spanoudaki, Sensors 2010

Evolutions récentes

Temps de vol (ToF)

$$t_1 = \frac{R - \Delta x}{c} \qquad t_2 = \frac{R + \Delta x}{c}$$

$$\Delta t = \frac{2\,\Delta x}{c} \qquad \Delta x = \frac{c\,\Delta t}{2}$$

$$\boxed{\sigma_x = \frac{c\,\sigma_t}{2}}$$

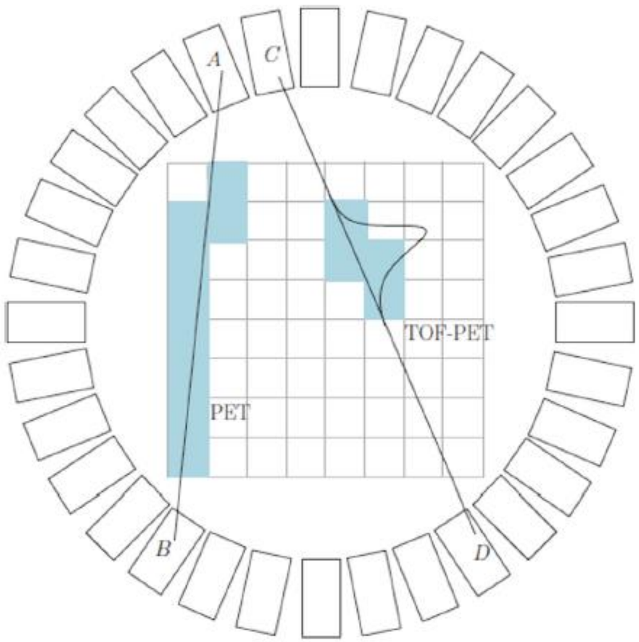

Slomka, Semin Nucl Med 2016

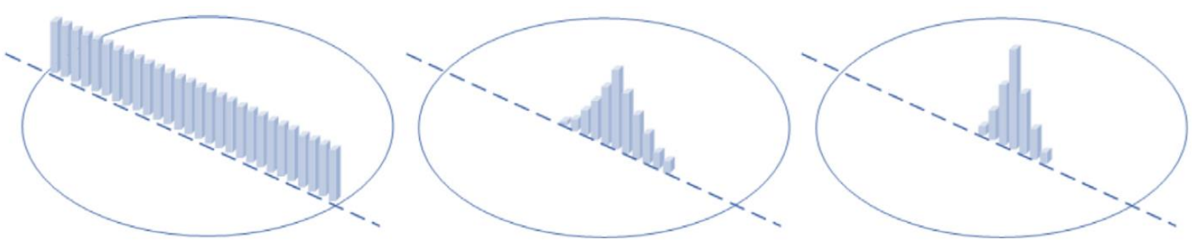

$\mathbf{R}_{geom}$

Slomka, Prog Cardiovasc Dis 2015

Evolutions récentes

Temps de vol (ToF)

$$t_1 = \frac{R - \Delta x}{c} \qquad t_2 = \frac{R + \Delta x}{c}$$

$$\Delta t = \frac{2\,\Delta x}{c} \qquad \Delta x = \frac{c\,\Delta t}{2}$$

$$\sigma_x = \frac{c\,\sigma_t}{2}$$

$$NECR_{TOF} = \frac{D}{\sigma_x}\,\beta\,NECR$$

$$SNR_{TOF} = \sqrt{\frac{D}{\sigma_x}}\,SNR$$

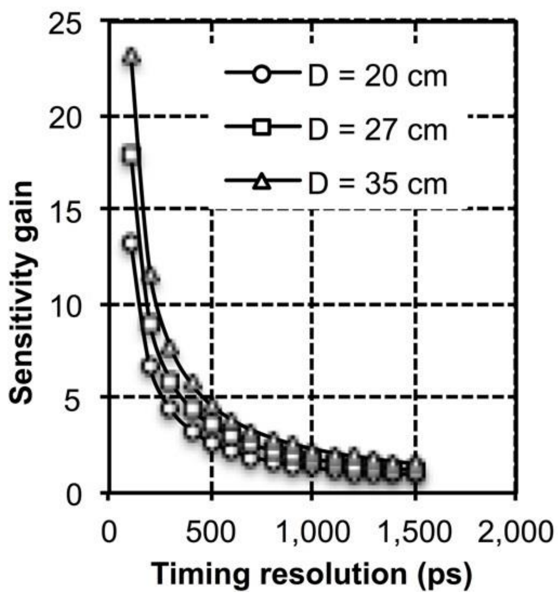

Surti, J Nucl Med 2015

Table 1 Time resolution, spatial uncertainty and estimated TOF gain for a 40-cm effective diameter patient

Time resolution (ns)	Δx (cm)	TOF NEC gain	TOF SNR gain
0.1	1.5	26.7	5.2
0.3	4.5	8.9	3.0
0.6	9.0	4.4	2.1
1.2	18.0	2.2	1.5
2.7	40.0	1.0	1.0

Conti, Eur J Nucl Med Mol Imaging 2011

Evolutions récentes

Temps de vol (ToF)

Table 2 Comparison of system characteristics across manufacturer PET/CT systems

Manufacture	GE	GE	Philips	Philips	Philips	Siemens	Siemens
PET/CT model	Discovery MI (4-ring) [51]	Discovery 690 [43]	Vereos (this work)	Ingenuity TF [44]	Gemini T [42]	Biograph mCT flow [45]	Biograph mCT [46, 47]
Photo detector	SiPM	PMT	SiPM	PMT	PMT	PMT	PMT
Number of detectors	9792	256	23,040	420	560	768	768
Scintillator	LYSO	LYSO	LYSO	LYSO	LYSO	LSO	LSO
Number of crystals	19,584	13,824	23,040	28,336	28,336	32,448	32,448
Crystal size (mm^3)	3.95 × 5.3 × 25	4.2 × 6.3 × 25	3.86 × 3.86 × 19	4 × 4 × 22	4 × 4 × 22	4 × 4 × 20	4 × 4 × 20
Ring diameter (cm)	74.4	81.0	76.4	90.0	90.3	84.2	84.2
Axial FOV (cm)	20.0	15.7	16.4	18.0	18.0	22.1	22.1
Plane spacing (mm)	n/a	n/a	1, 2, or 4	2 or 4	2 or 4	2	2
TOF Timing resolution (ps)	375	544	322	502	585	555	527
Sensitivity (cps/kBq)	13.7	7.4	5.7	7.3	6.6	9.6	9.7
Transverse resolution @ 1 cm (mm)	4.1	4.7	4.0	4.8	4.8	4.3	4.4
Transverse resolution @ 10 cm (mm)	5.0	5.1	4.4	5.1	5.2	4.9	4.9
Axial resolution @ 1 cm (mm)	4.5	4.7	4.0	4.7	4.8	4.3	4.4
Axial resolution @ 10 cm (mm)	6.0	5.6	4.8	5.2	4.8	5.9	5.7
Peak NECR (kcps @ kBq/mL)	193.4 @ 21.9	139.1 @ 29.0	171 @ 50.5	124.1 @ 20.3	125 @ 17.4	185 @ 29	156 @ 31.1
Energy resolution (%)	9.4	12.4	11.2	11.1	11.5	n/a	11.5
Scatter fraction at peak NECR (%)	40.6	37	30.8	36.7	27	33.4	32.7

Zhang, EJNMMI Res 2018

Evolutions récentes

Temps de vol (ToF)

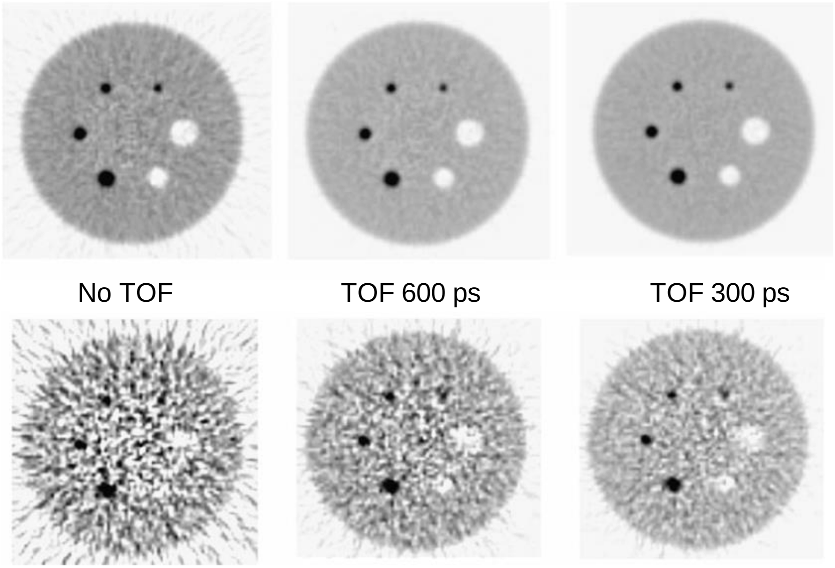

Conti, Eur J Nucl Med Mol Imaging 2011

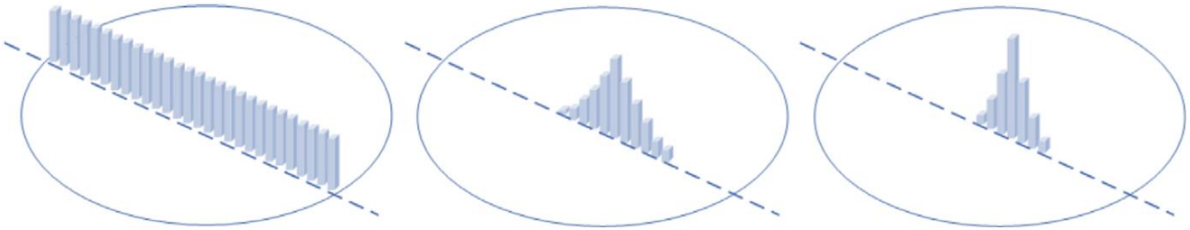

Slomka, Prog Cardiovasc Dis 2015

- **Synchronisation temporelle**
- **Modélisation du kernel ToF**
- **Correction de diffusé (ToF-SSS)**

Evolutions récentes

Temps de vol (ToF)

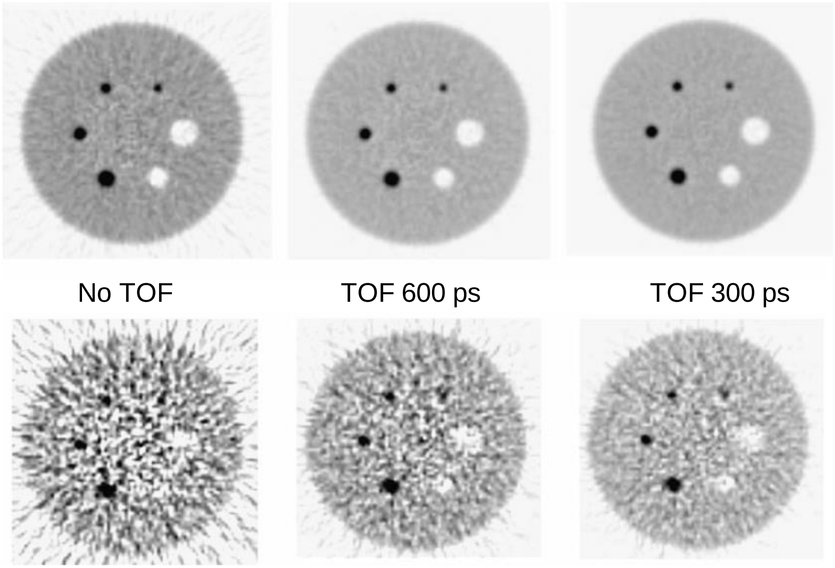

Conti, Eur J Nucl Med Mol Imaging 2011

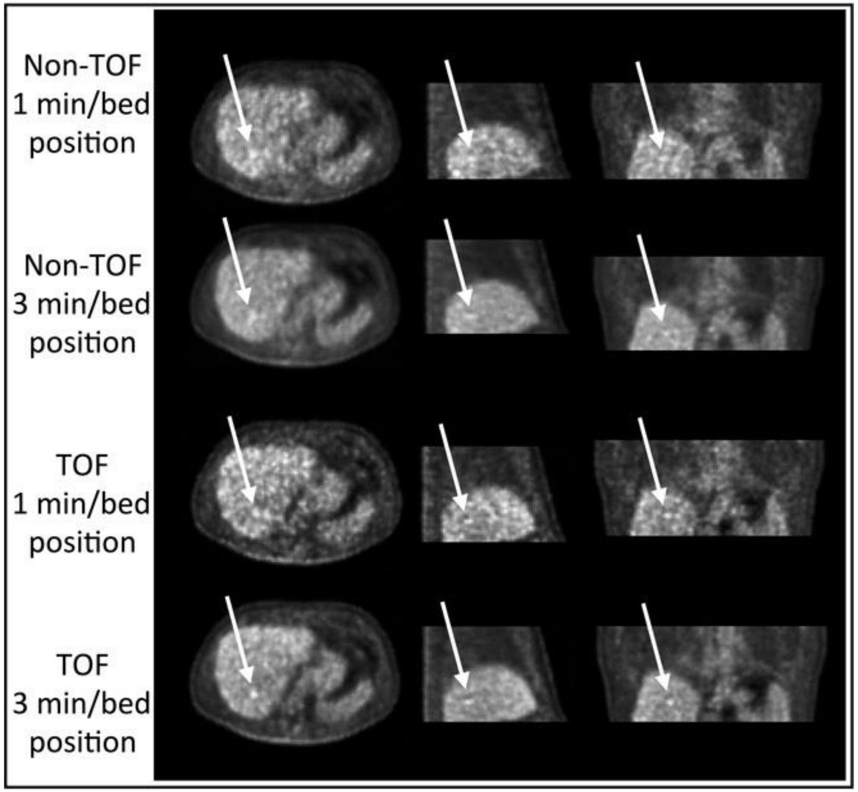

Surti, J Nucl Med 2015

Evolutions récentes

Temps de vol (ToF)

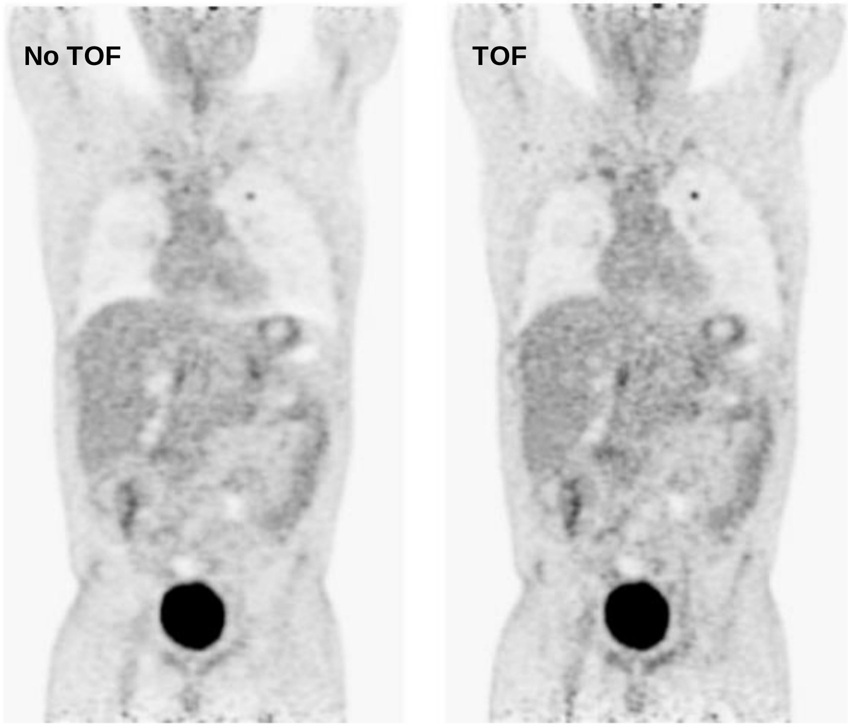

Conti, Eur J Nucl Med Mol Imaging 2011

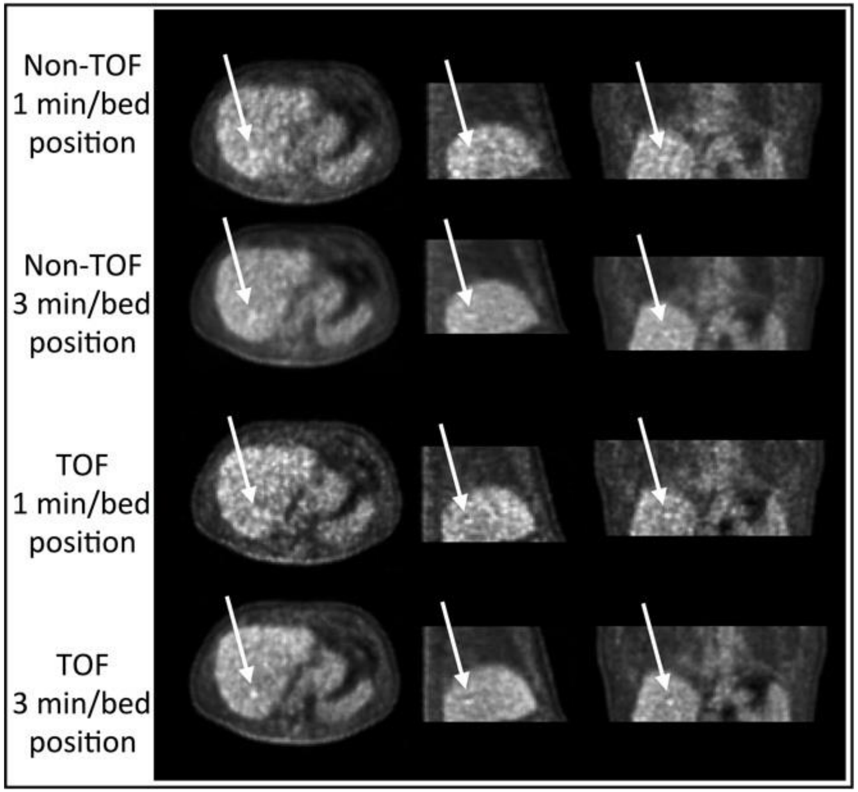

Surti, J Nucl Med 2015

Evolutions récentes

Temps de vol (ToF)

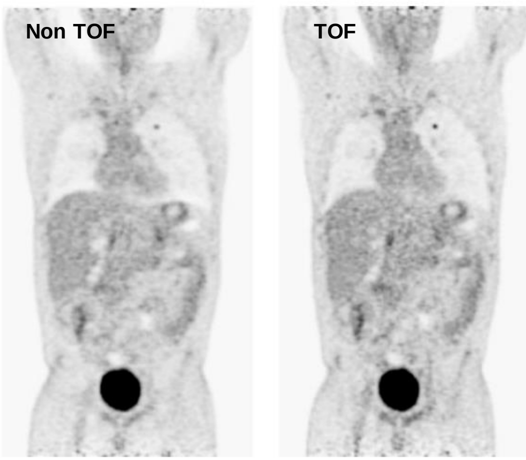

Conti, Eur J Nucl Med Mol Imaging 2011

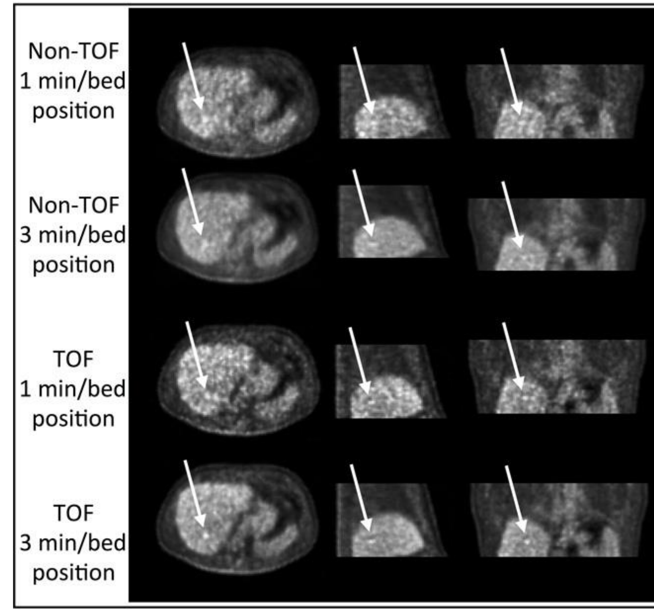

Surti, J Nucl Med 2015

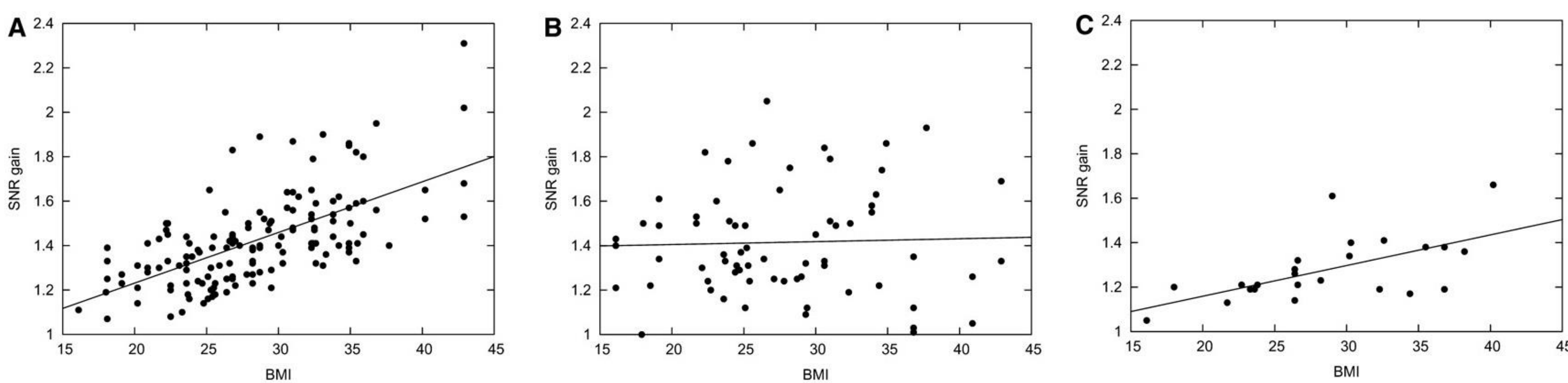

Lois, J Nucl Med 2010

Evolutions récentes

Temps de vol (ToF)

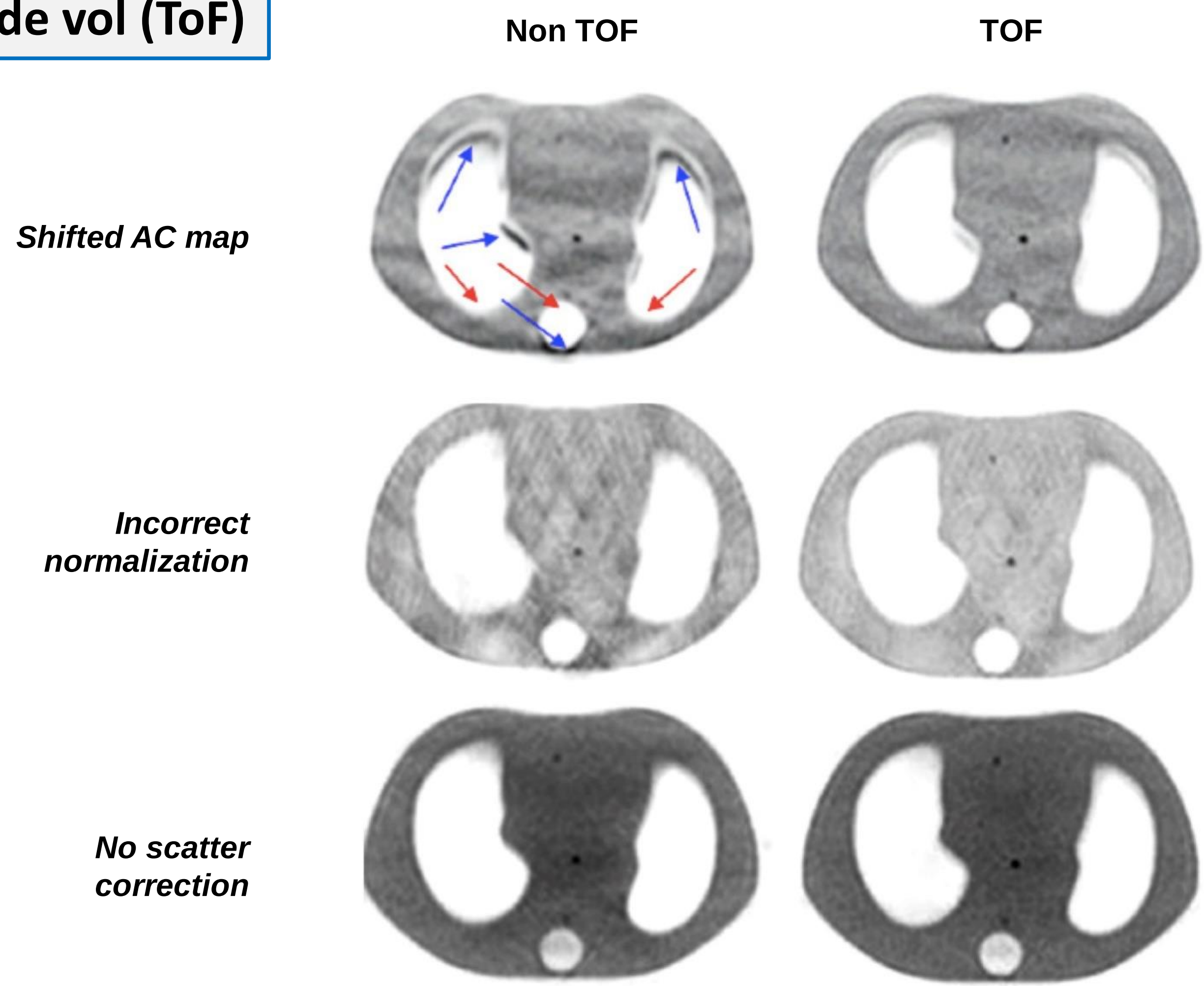

Conti, Phys Med Biol 2010

Temps de vol (ToF)

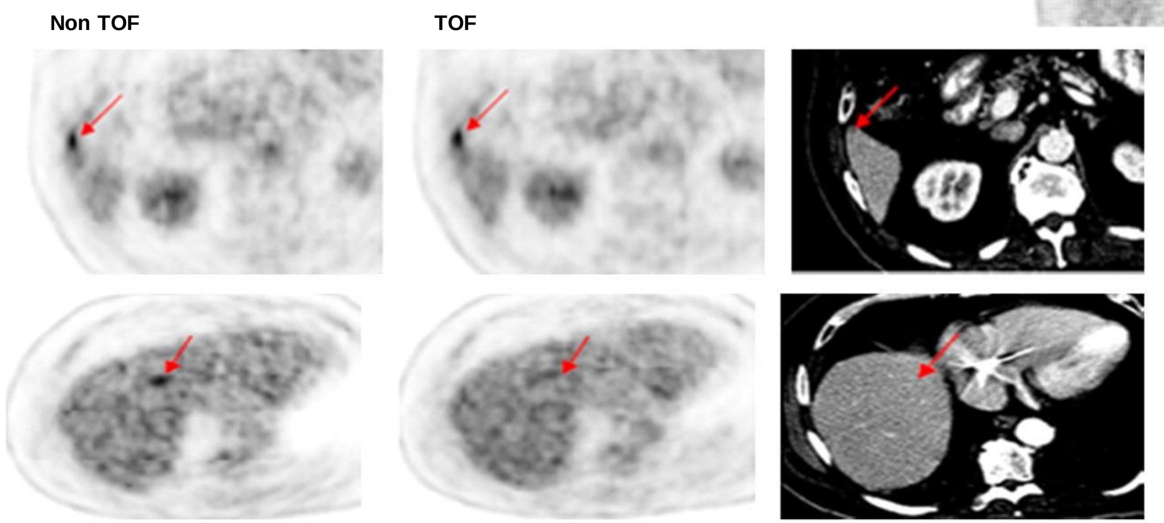

Lois,
J Nucl Med
2010

Evolutions récentes

Temps de vol (ToF)

Applications potentielles

> *Basse statistique*

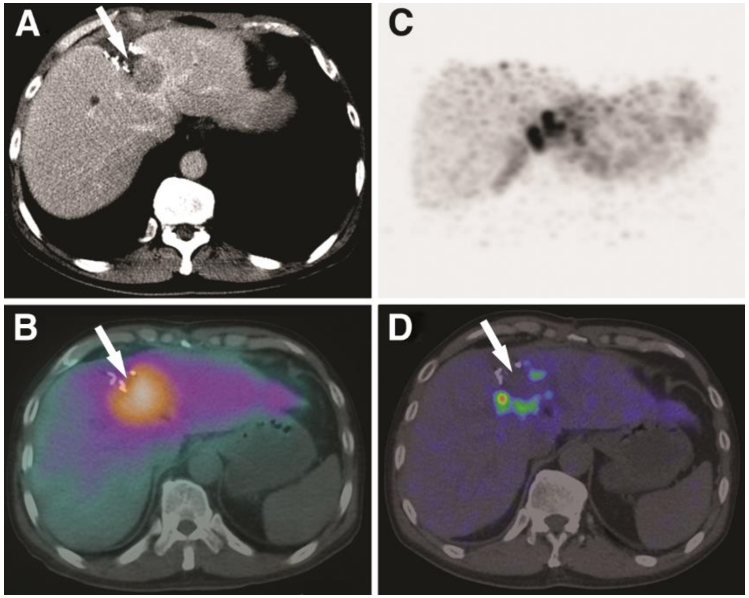

Kao, Clin Nucl Med 2011

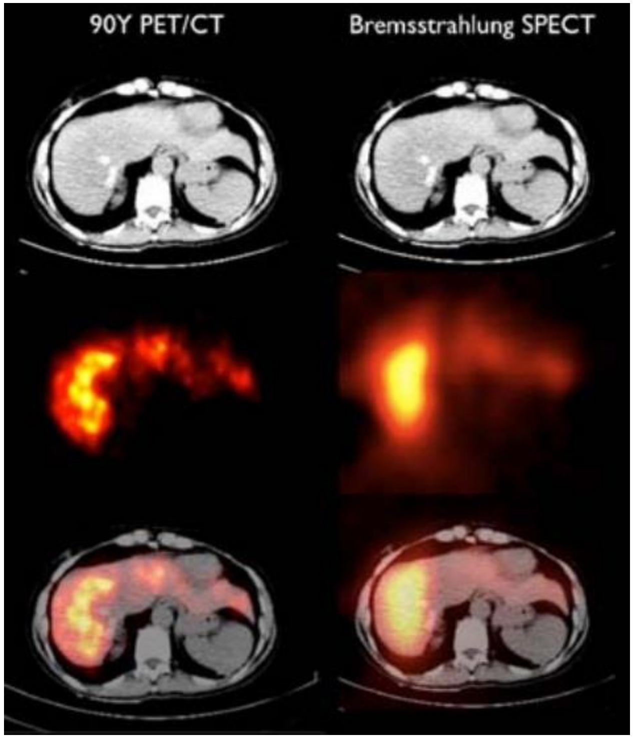

Lhommel, Eur J Nucl Med Mol Imaging 2009

Evolutions récentes

Temps de vol (ToF)

Applications potentielles

> Basse statistique
> Tomographie intérieure / à angle limité

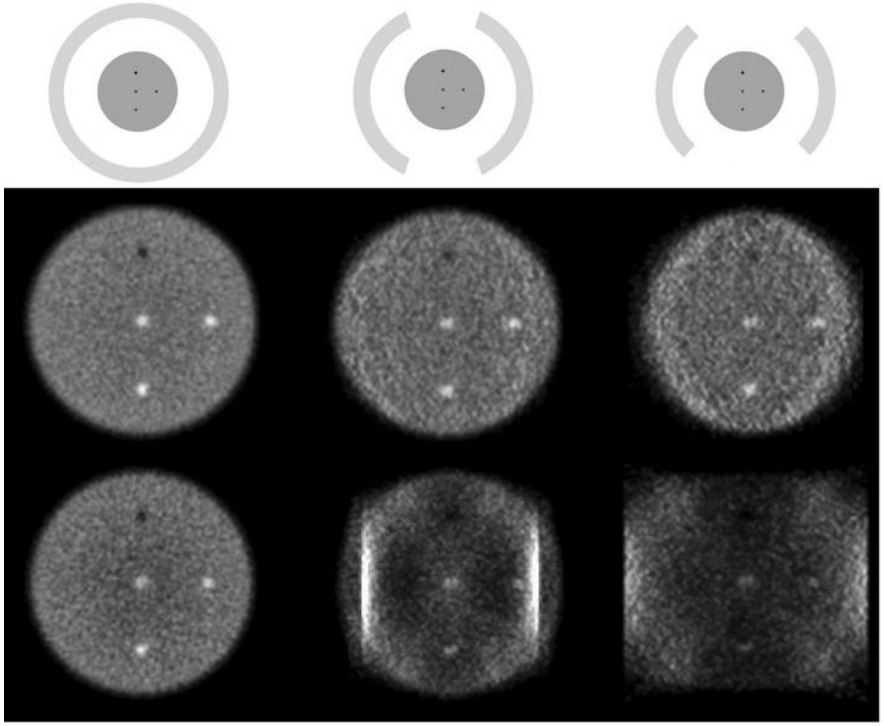

Surti, Phys Med Biol 2009

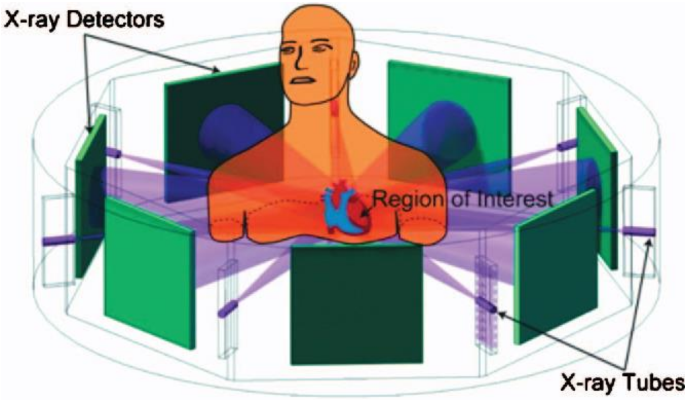

Wang, Med Phys 2009

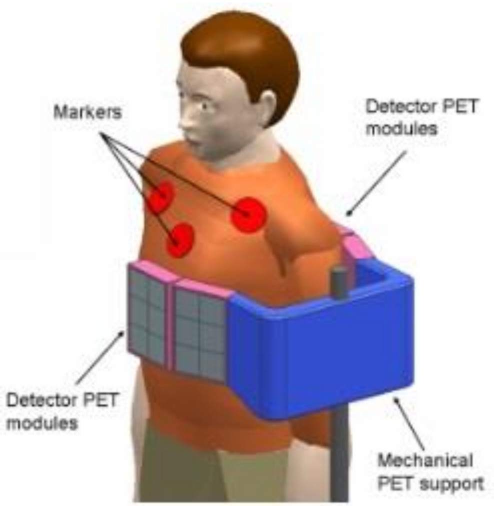

i3m-detectors.com

Evolutions récentes

Temps de vol (ToF)

Applications potentielles

> *Basse statistique*
> *Tomographie intérieure / à angle limité*
> *Hadron-thérapie*

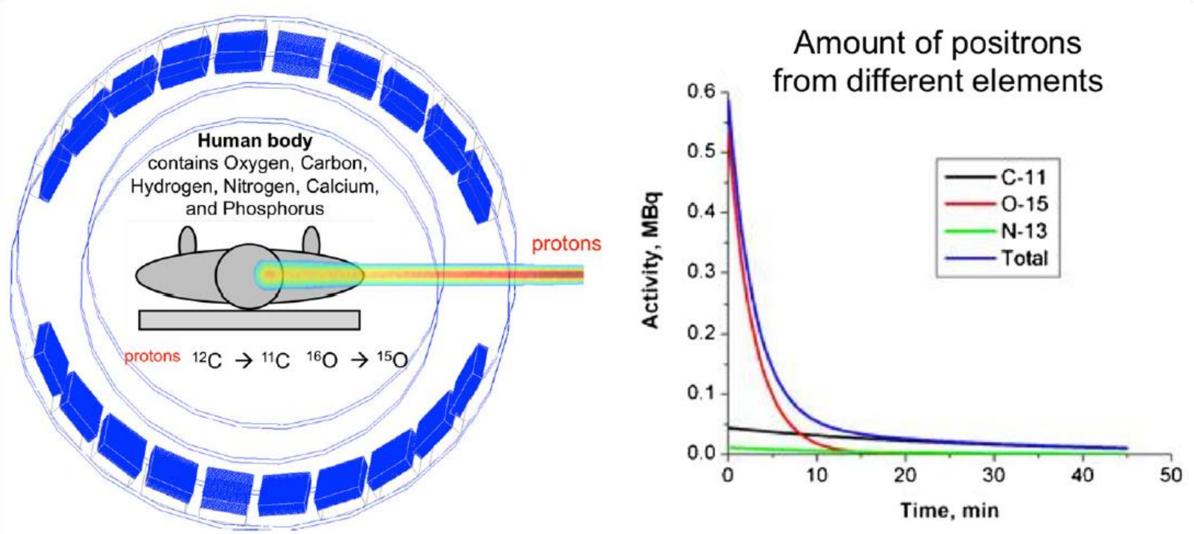

Fig. 10 Open ring design of in-beam PET

Vandenberghe, EJNMMI Physics 2016

Evolutions récentes

Temps de vol (ToF)

Applications potentielles

> Basse statistique
> Tomographie intérieure / à angle limité
> Hadron-thérapie
> Séparation émission / transmission

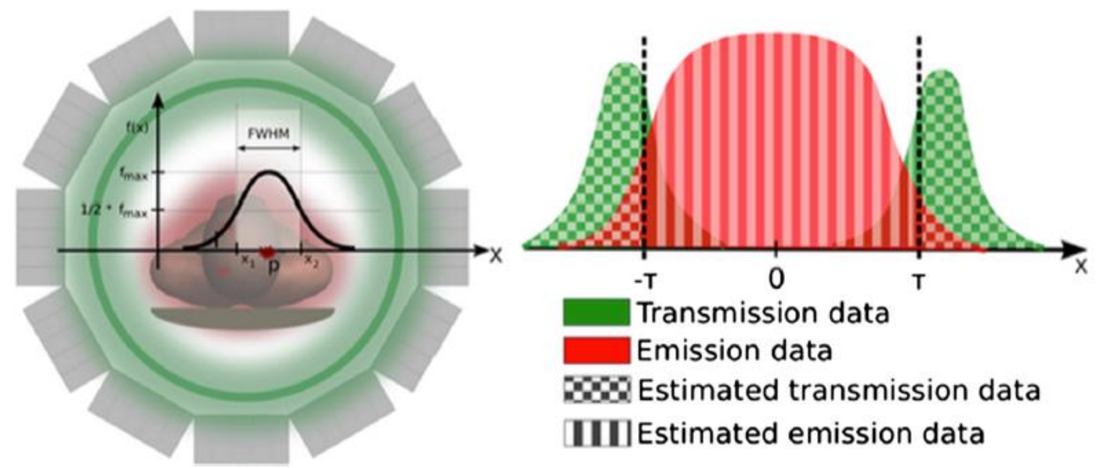

Fig. 7 TOF-based extraction of transmission data on a particular LOR for a threshold radius τ

Vandenberghe, EJNMMI Physics 2016

Evolutions récentes

TEP-IRM

Motivations

> *Dosimétrie*
> *Contraste tissus mous*
> *Corrections (mvt, PVE)*
> *Imagerie multi-paramétrique*
> *Métabolisme / fonction*

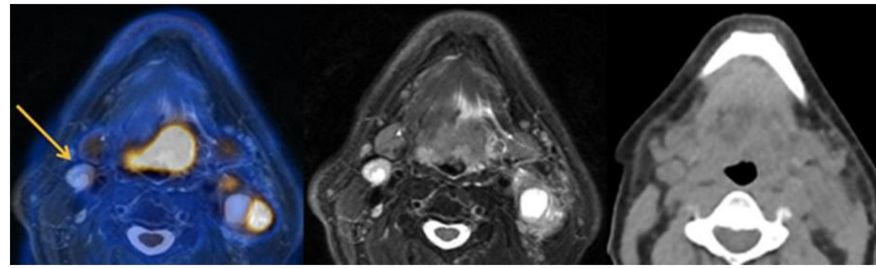

Kuhn, J Nucl Med 2014

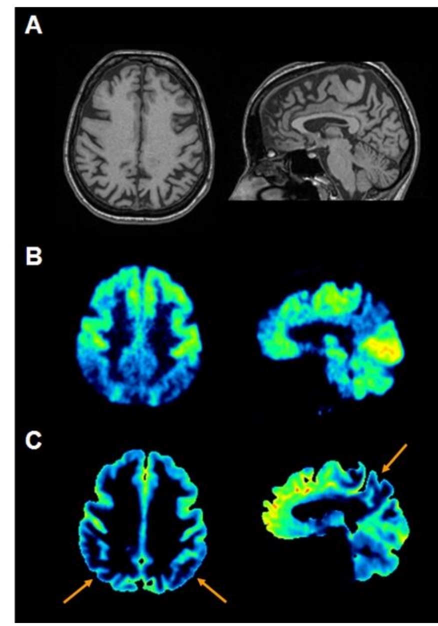

Zaidi, Med Phys 2011

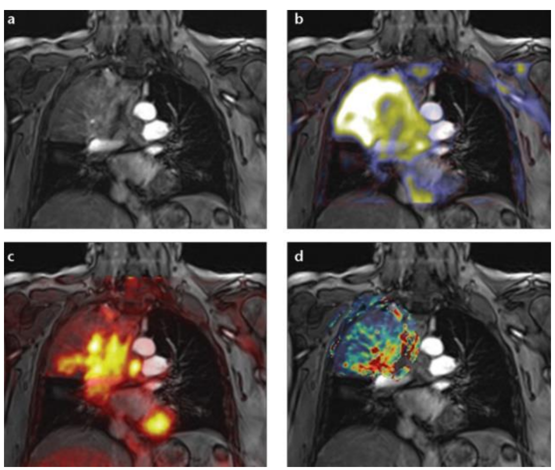

Nensa, Diagn Interv Radiol 2014

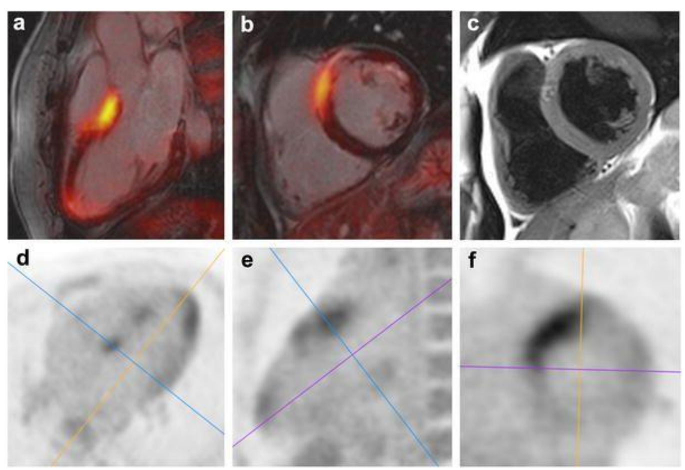

Krumm, Jpn J Radiol 2018

Evolutions récentes

TEP-IRM

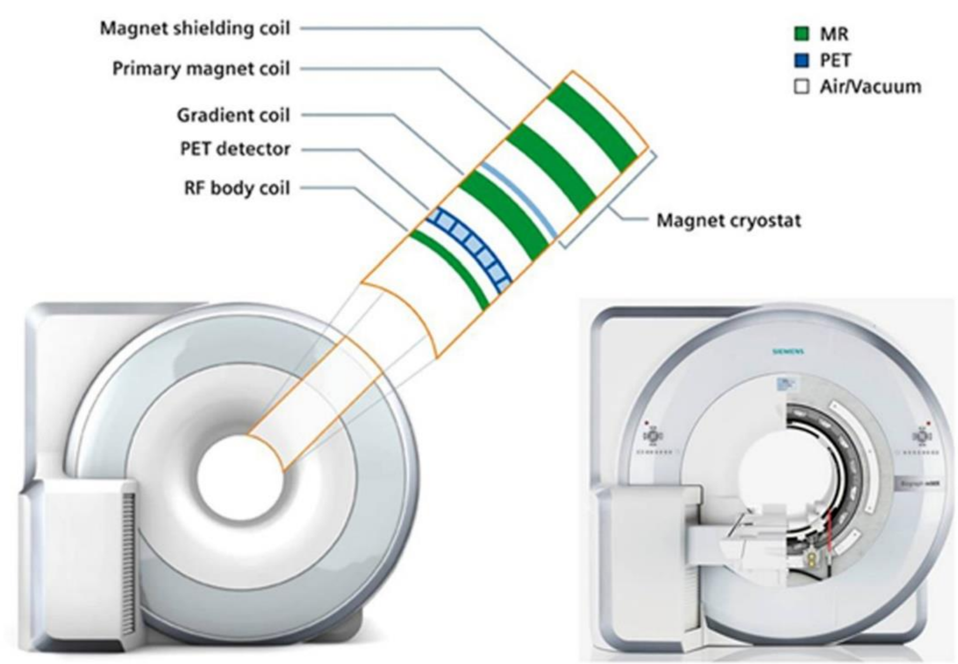

Zaidi, Med Phys 2011

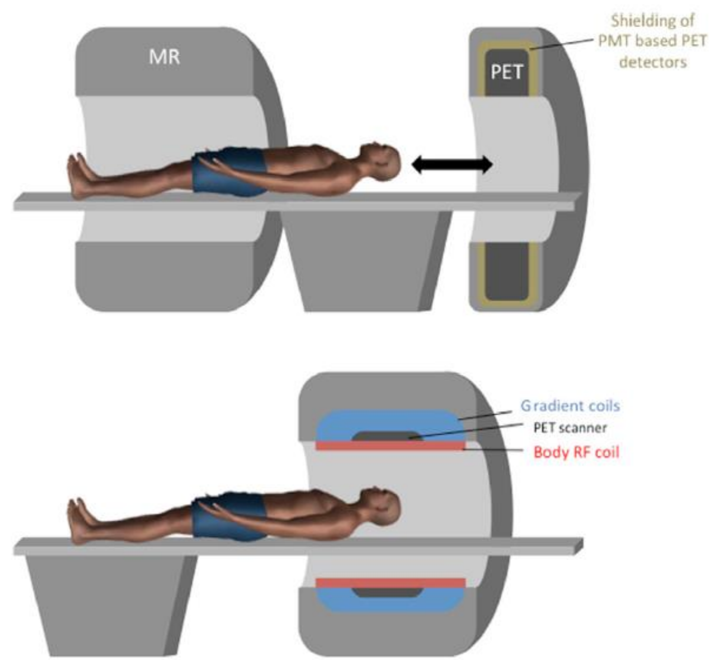

Vandenberghe, Phys Med Biol 2015

Evolutions récentes

TEP-IRM

Contraintes

Table 1. Interference effects of MRI on PET performance.

MRI	Effect on PET	Solutions	Consequences
B_0	Changes path of electrons	Replace PMTs by APDs, SiPMs	Higher cost
	in readout		More channels Reduced timing (APD)
B_1	Heating, vibration	Redesign of electronics (no conductive components) Temperature control	Additional complexity
RF	Interference with electronics	RF shielding around PET	Increased eddy currents and heating

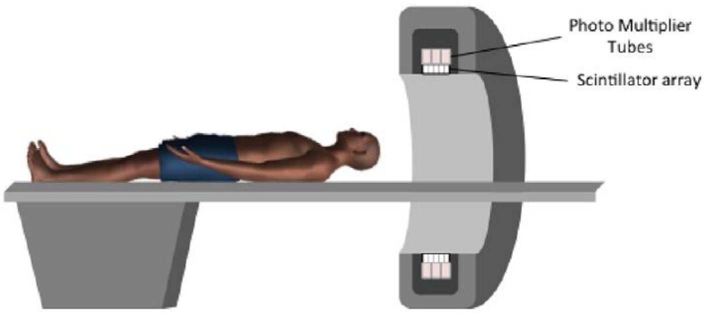

Table 2. Interference effects of PET on MRI.

PET component	Effect on MRI	Solutions	Consequences
Scintillators	B_0 non-uniformities	Use of MRI compatible PET scintillators	
Gamma shielding	Eddy currents lead to distortion and non-linearity	Alternative gamma shielding materials	Higher cost
PET electronics and power cables	Interference with RF detection	RF shielding around PET	

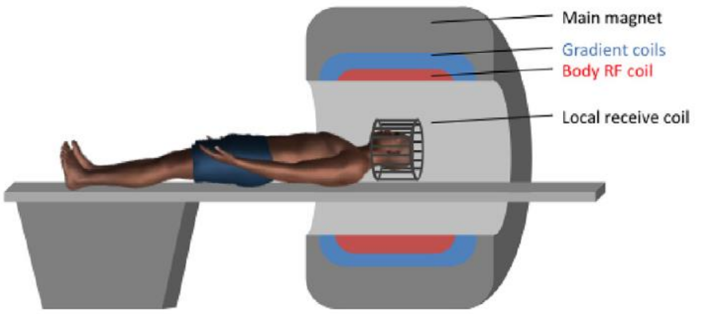

Vandenberghe, Phys Med Biol 2015

Evolutions récentes

TEP-IRM

Contraintes

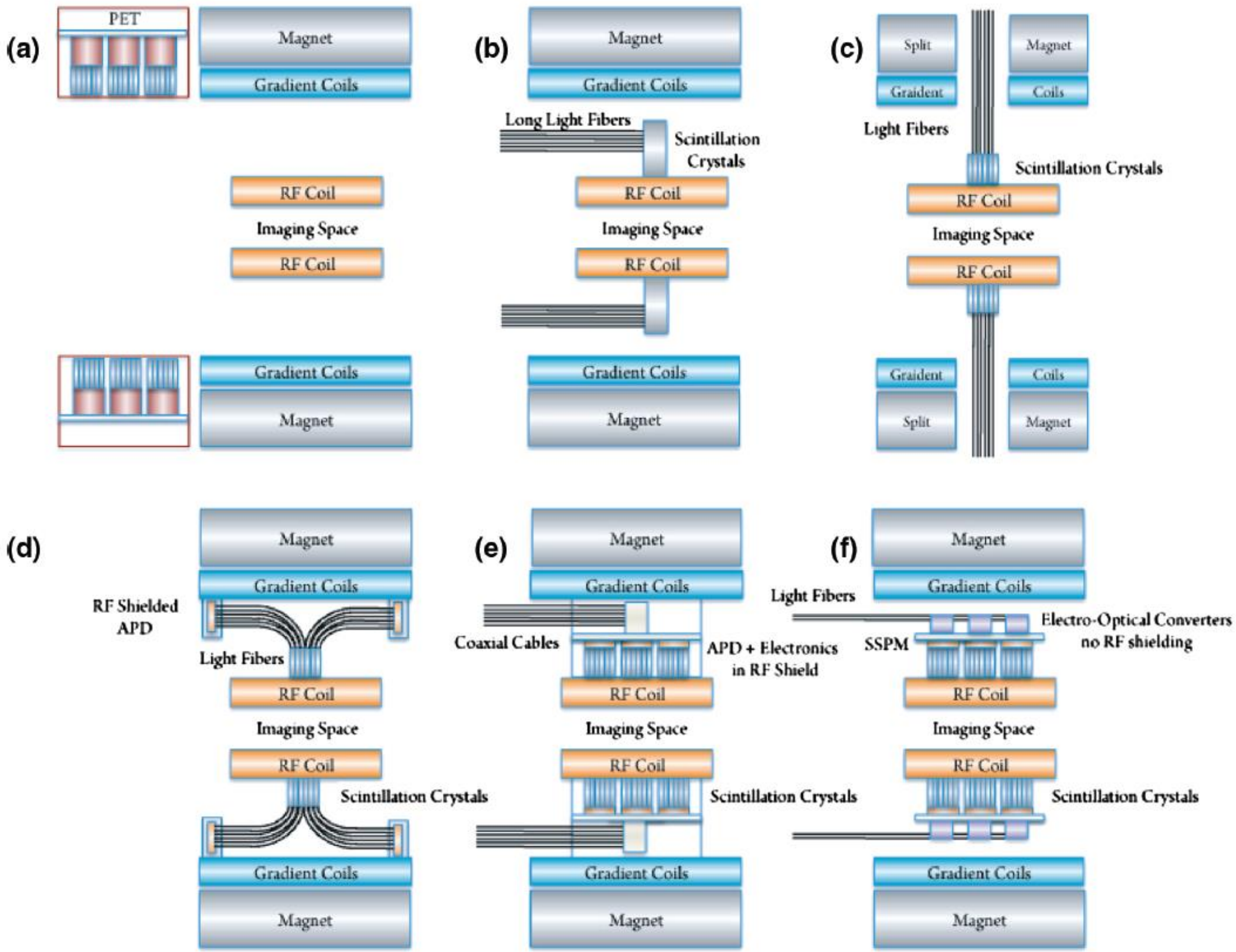

Wherl, Cancer Res Treat 2010

Evolutions récentes

TEP-IRM

Philips

GE

Siemens

Aiello, Int Rev Neurobiol 2018

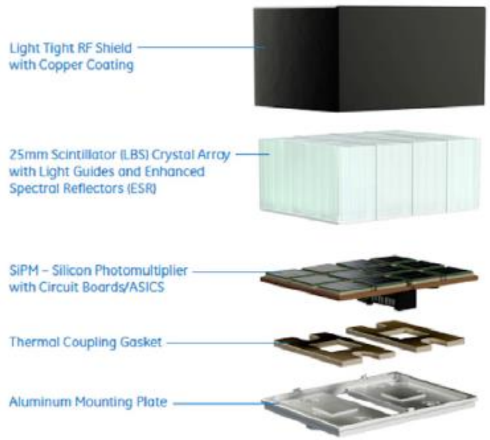

GE

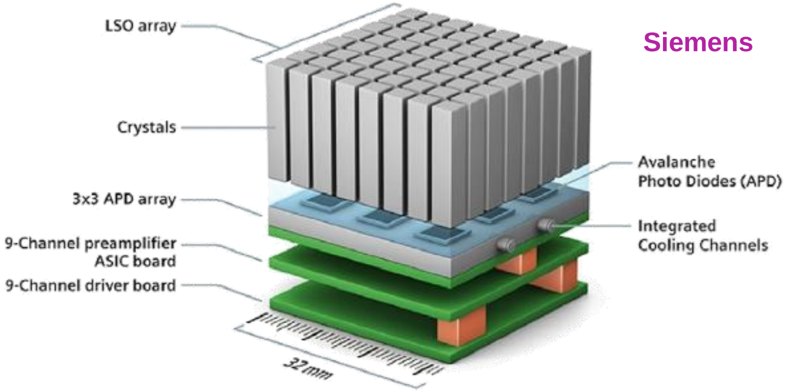

Siemens

Slomka, Semin Nucl Med 2016

Evolutions récentes

TEP-IRM

PET/MR Model	GE Signa	mMR
Patient port (cm)	60	60
MR model (3 T)	Discovery 750 w (3 T)	Verio
Patient scan range (cm)	188 (PET)/205(MR)	200
Maximum patient weight (kg [lb])	226 (500)	200 (441)
Acquisition modes	3D S&S	3D S&S
Number of image planes	89	127
Plane spacing (mm)	2.8	2
Crystal size (mm^3)	$4 \times 5.3 \times 25$	$4 \times 4 \times 20$
Number of crystals	20,160	28,672
Number of PMTs	SiPM	APD
Physical axial FOV (cm)	25	25.8
Detector material	LYSO	LSO
System sensitivity @ 0 cm (%)*	2.1	1.5
Transaxial resolution @ 1 cm (mm)*	4.2	4.1
Transaxial resolution @ 10 cm (mm)*	5.2	5.2
Axial resolution @ 1 cm (mm)*	5.8	4.3
Axial resolution @ 10 cm (mm)*	7.1	6.6
Peak NECR (kcps)*	210 @ 17.5 kBq/ml	175 @ 21.8 kBq/ml
Time-of-flight resolution (picoseconds)	400	n.a.
Time-of-flight localization (cm)	6.0	n.a.
Coincidence window (nanoseconds)	4.6	5.9

Slomka, Semin Nucl Med 2016

Evolutions récentes

TEP-IRM

PET/MR Model	GE Signa	mMR
Patient port (cm)	60	60
MR model (3 T)	Discovery 750 w (3 T)	Verio
Patient scan range (cm)	188 (PET)/205(MR)	200
Maximum patient weight (kg [lb])	226 (500)	200 (441)
Acquisition modes	3D S&S	3D S&S
Number of image planes	89	127
Plane spacing (mm)	2.8	2
Crystal size (mm^3)	4 × 5.3 × 25	4 × 4 × 20
Number of crystals	20,160	28,672
Number of PMTs	SiPM	APD
Physical axial FOV (cm)	25	25.8
Detector material	LYSO	LSO
System sensitivity @ 0 cm (%)*	2.1	1.5
Transaxial resolution @ 1 cm (mm)*	4.2	4.1
Transaxial resolution @ 10 cm (mm)*	5.2	5.2
		4.3
		6.6
	kBq/ml	175 @ 21.8 kBq/ml
		n.a.
		n.a.
		5.9

Slomka, Semin Nucl Med 2016

Table 1 Performance characteristics of the Biograph mMR and Biograph mCT

Parameter	mMR	mCT
Resolution (mm)		
Axial FWHM/FWTM @ 1 cm	4.1/8.2	4.4/8.8
Transverse FWHM/FWTM @ 1 cm	4.0/8.0	4.4/8.3
Axial FWHM/FWTM @ 10 cm	6.4/11.8	5.7/10.7
Transverse FWHM/FWTM @ 10 cm	5.0/10.8	4.9/9.3
Average sensitivity (kcps/MBq)	13.3	10.0
Peak NECR (kcps)	196 @ 24.4 kBq/mL	186 @ 30.1 kBq/mL
Scatter fraction (peak NECR)	37.9 %	37.7 %
Count rate accuracy (mean bias, peak NECR)	4.9 %	1.9 %

Karlberg, EJNMMI Phys 2016

Evolutions récentes

TEP-IRM

Correction d'atténuation

- >> *Info de densité*
- >> *Signal air / poumon / os*
- >> *Troncature FOV*
- >> *Atténuation coils*
- >> *Synchronisation*

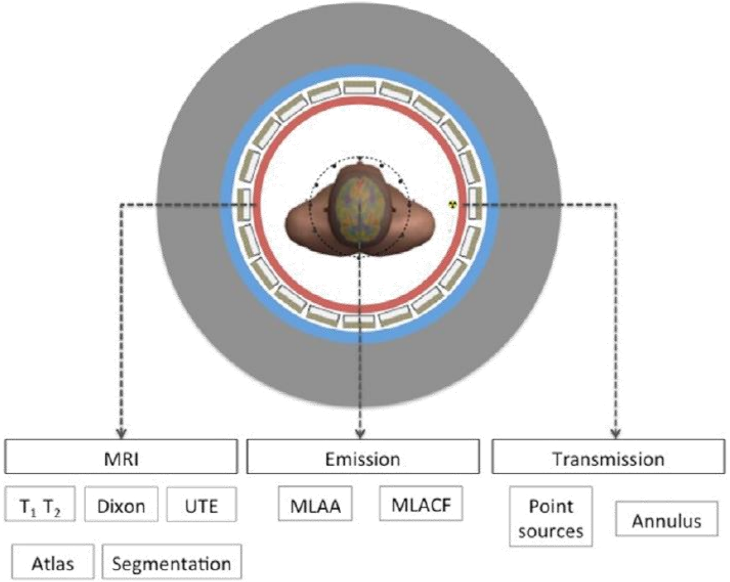

Table 3. Performance of methods for attenuation correction in PET-MRI.

Method	Advantages	Disadvantages
MRI(Segmentation)	Fast No dose	Segmentation errors No signal in bone One AC value per tissue Need for templates for coils Truncated FOV
MRI(Atlas)	Fast No dose	Anatomical abnormalities Difficult for body imaging Templates for coils Truncated FOV
MRI(UTE)	Identification of bone	Additional MRI acquisition time needed Not tested for whole body imaging
PET(Emission)	No additional acquisition time	Limited to tracers with distributed uptake (like FDG) Need for templates for coils
PET(Transmission)	Works for any object in FOV	Additional sources and dose Noisy attenuation maps Limited spatial resolution

Vandenberghe, Phys Med Biol 2015

Evolutions récentes

TEP-IRM

Correction d'atténuation

> *Segmentation T_1*

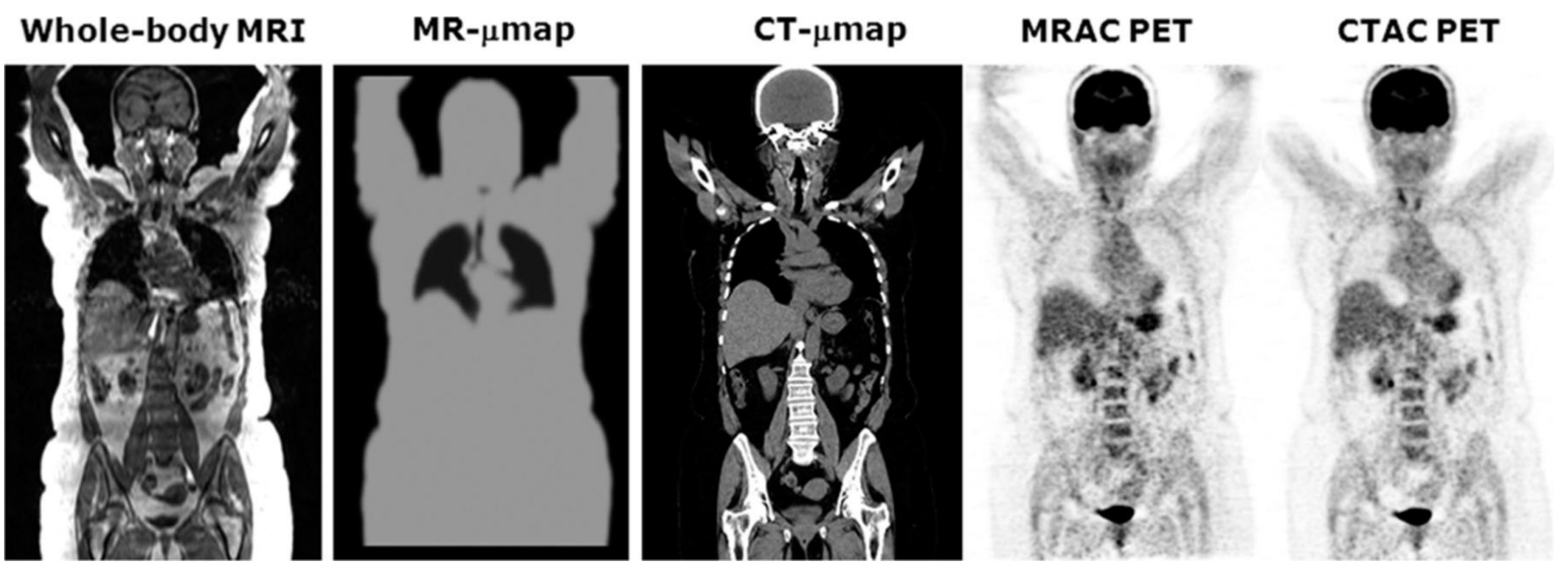

Zaidi, Med Phys 2011

Evolutions récentes

TEP-IRM

Correction d'atténuation

> *Segmentation T_1*
> *Segmentation Dixon*

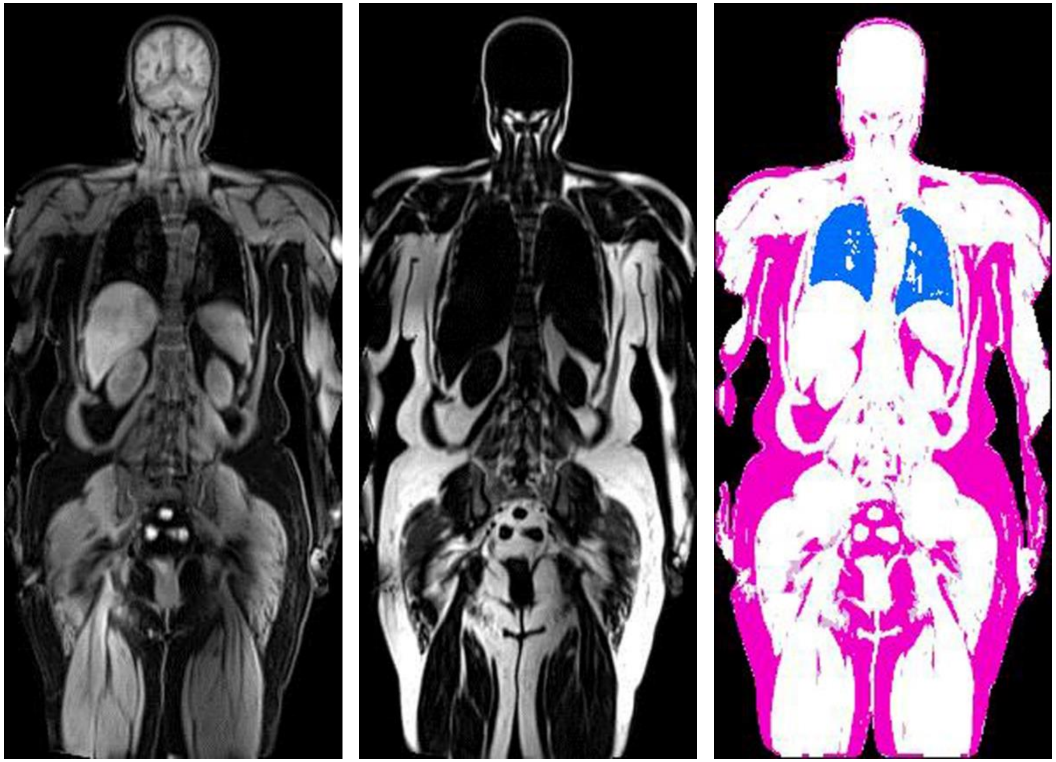

Muzik, Semin Roentgenol 2014

Evolutions récentes

TEP-IRM

Correction d'atténuation

> Segmentation T_1
> Segmentation Dixon
> Segmentation UTE

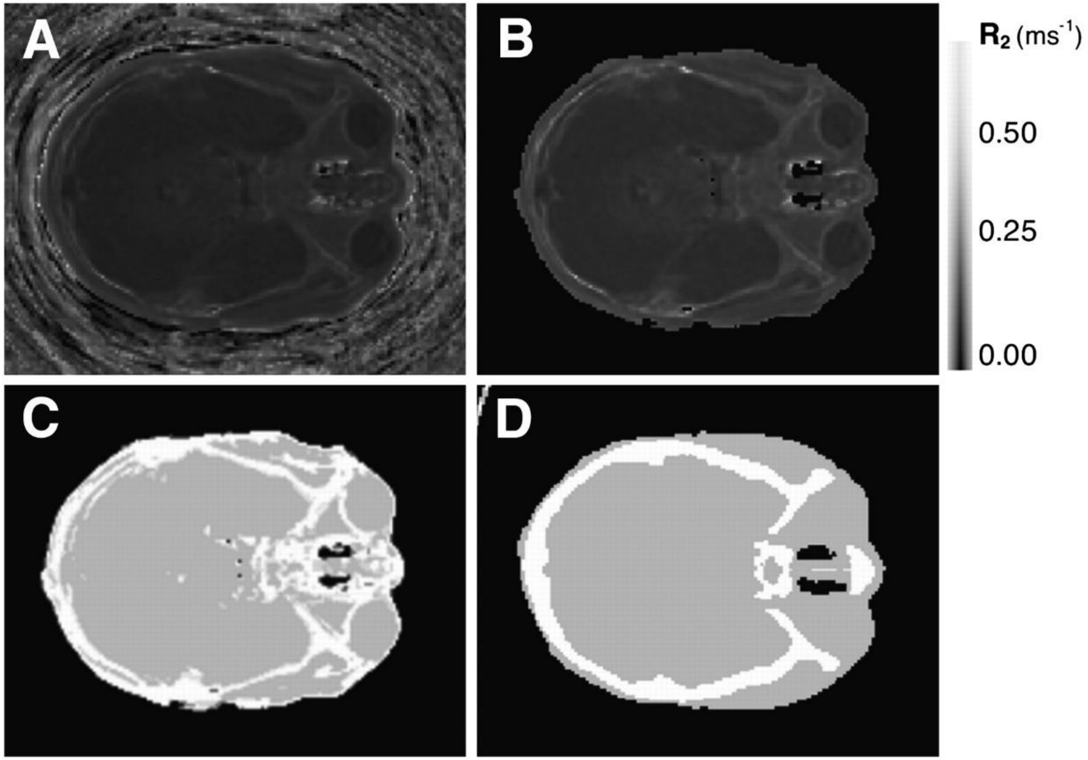

Keereman, J Nucl Med 2010

Evolutions récentes

TEP-IRM

Correction d'atténuation

> *Segmentation T_1*
> *Segmentation Dixon*
> *Segmentation UTE*
> *Atlas / template*

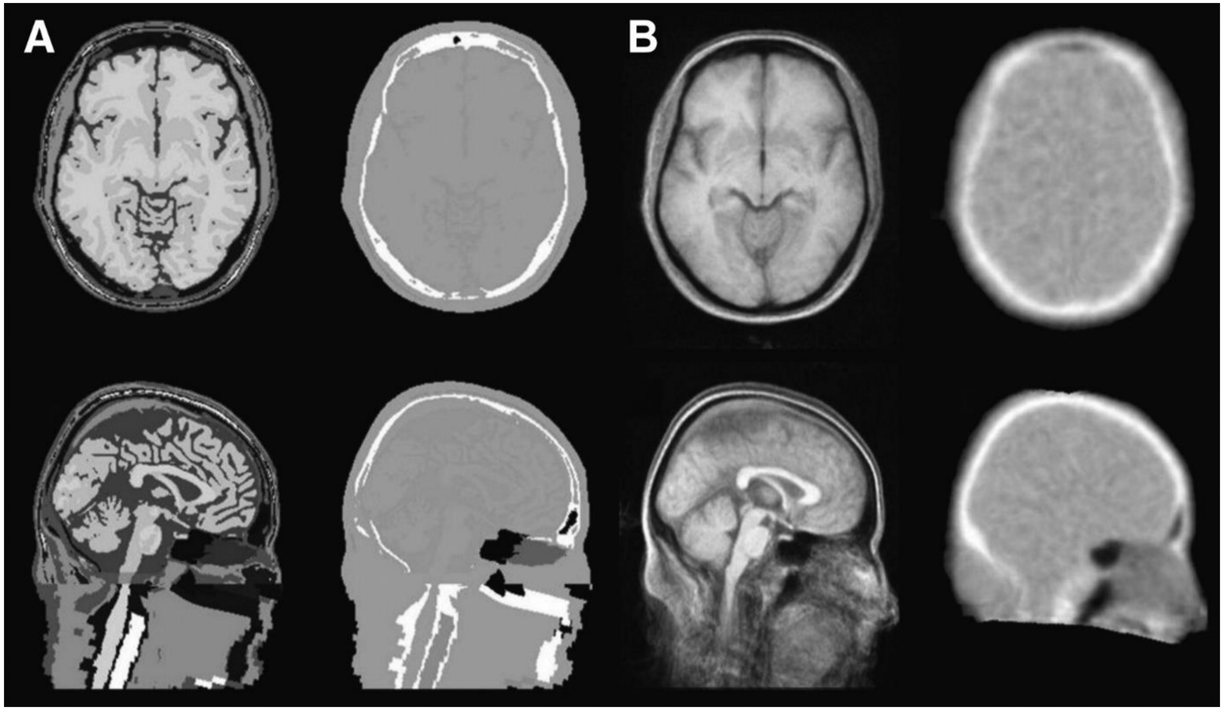

Malone, J Nucl Med 2011

Perspectives

Imagerie Compton

$$\cos\omega = 1 + m_0c^2\,(E_1^{-1} - E_2^{-1})$$

Compton scattering kinetics

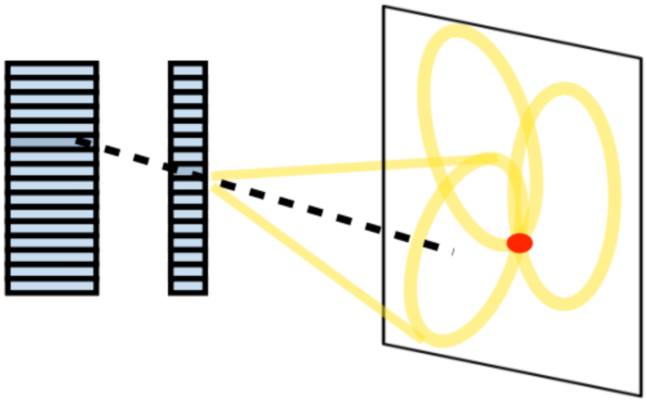

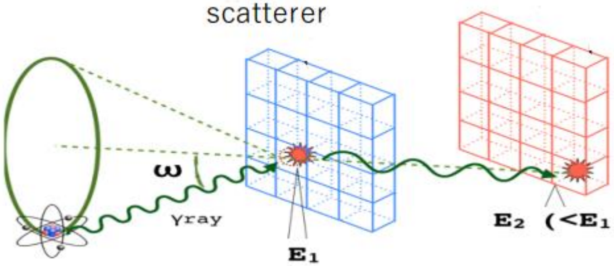

Shimazoe 2017 (indico.cern.ch)

Perspectives

Imagerie Compton

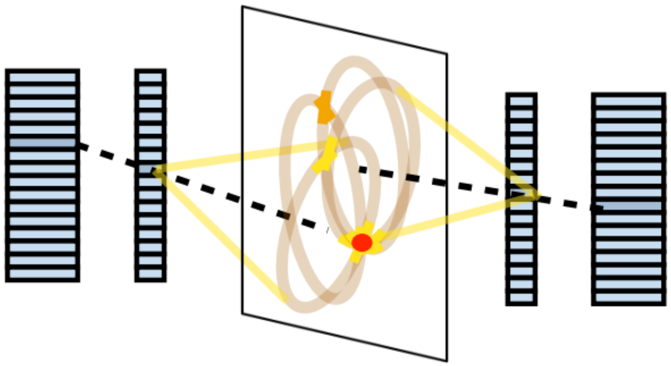

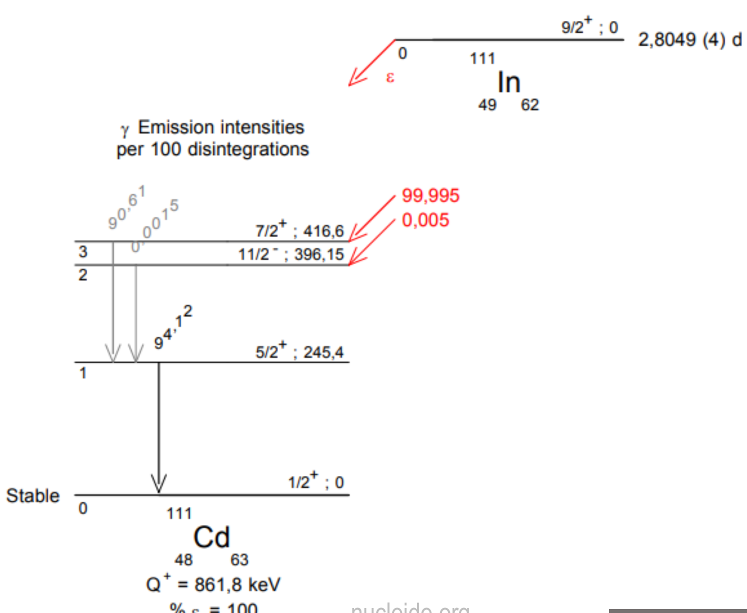

nucleide.org

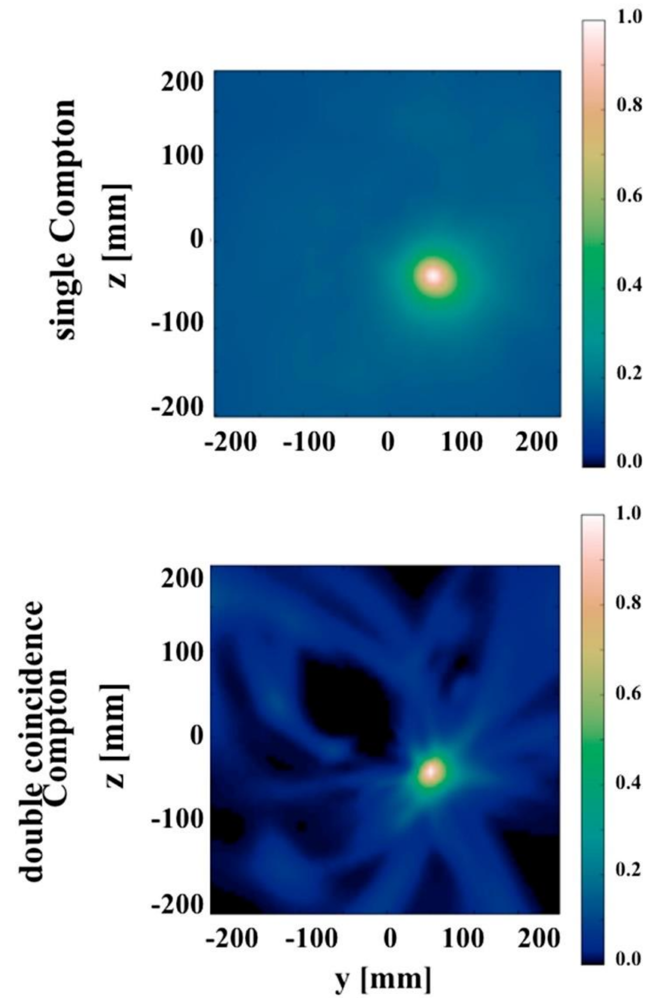

Yoshihara, Nucl Inst Met Phys 2017

Perspectives

Imagerie Compton

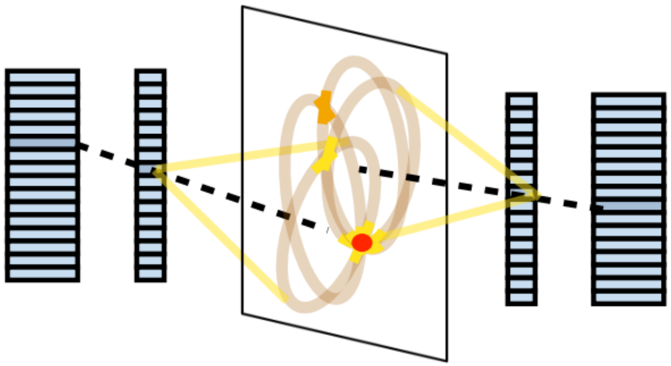

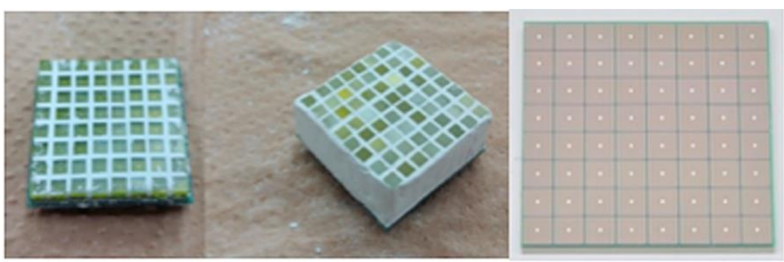

Scatterer GAGG 1.5 mm	Absorber GAGG 10 mm	SiPM

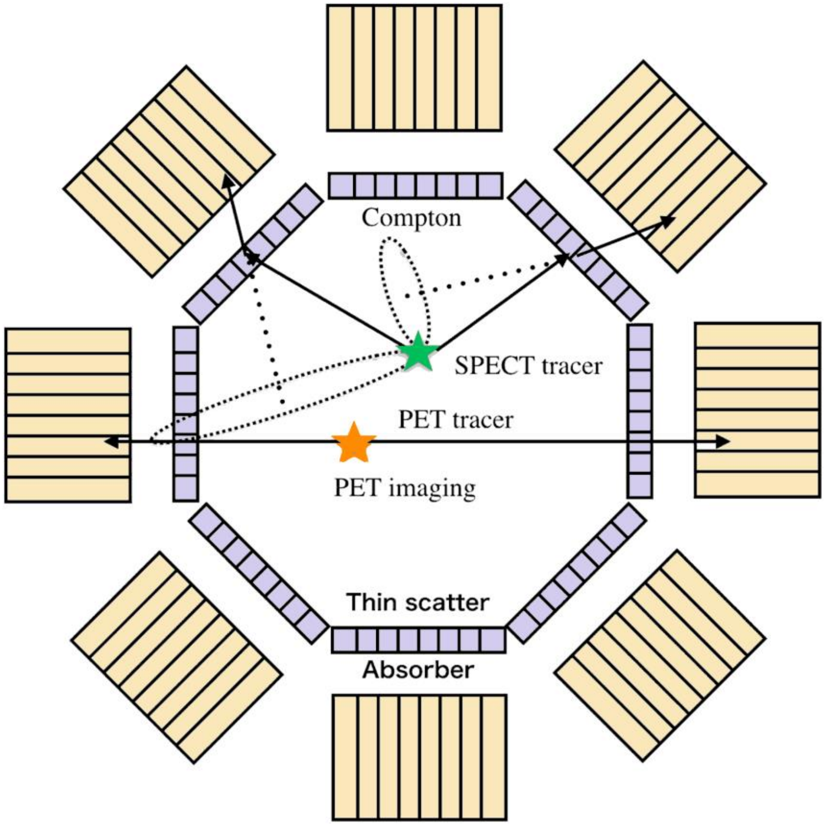

Shimazoe, Nucl Inst Met Phys 2018

Perspectives

Imagerie Compton

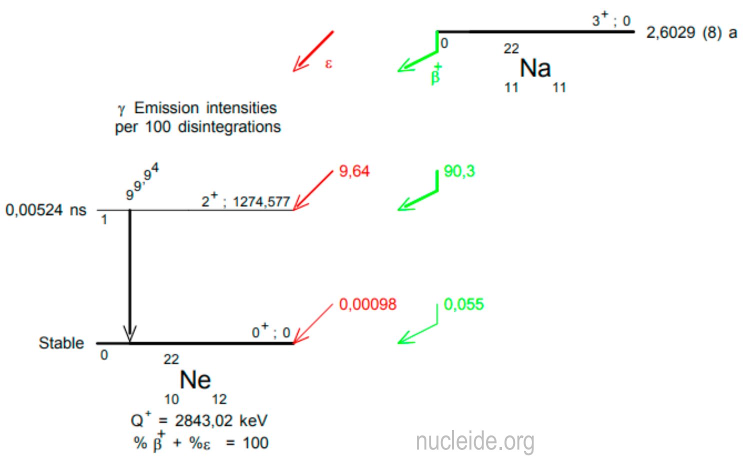

nucleide.org

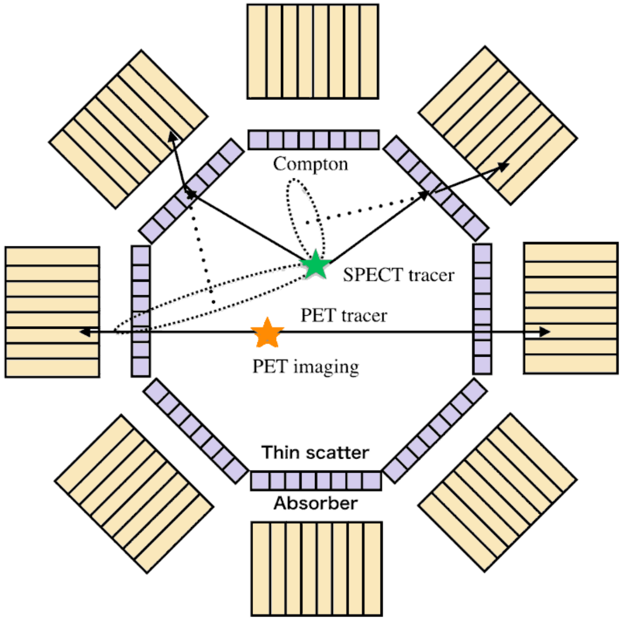

Shimazoe, Nucl Inst Met Phys 2018

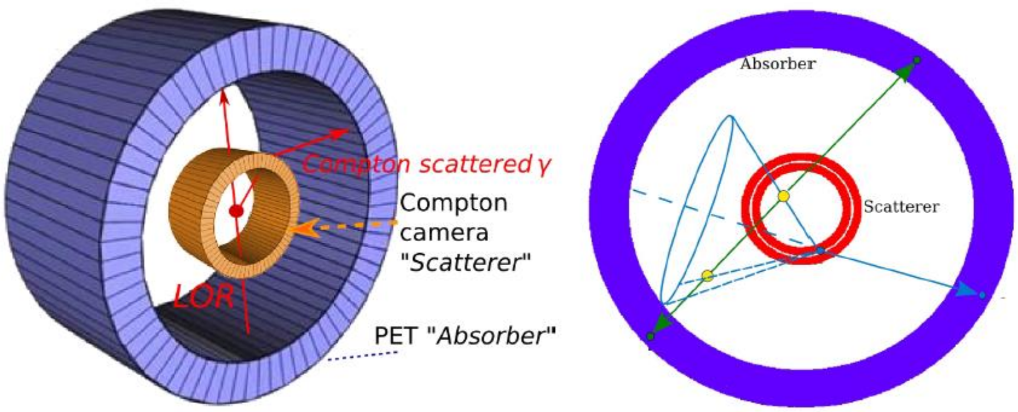

Kolstein, J Instrum 2016

Perspectives

Imagerie Compton

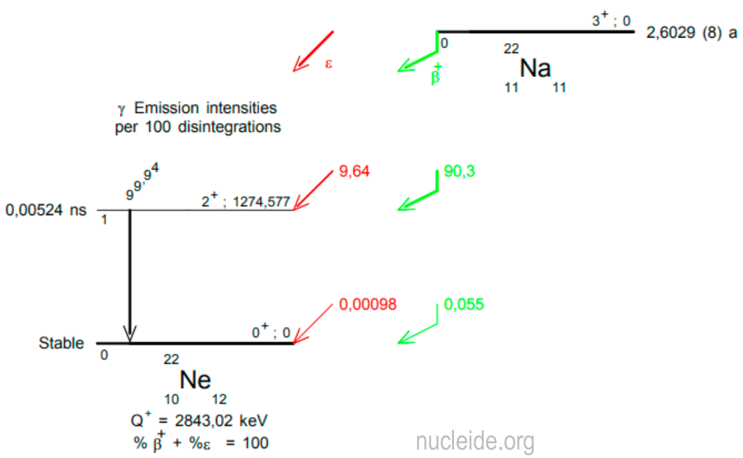

nucleide.org

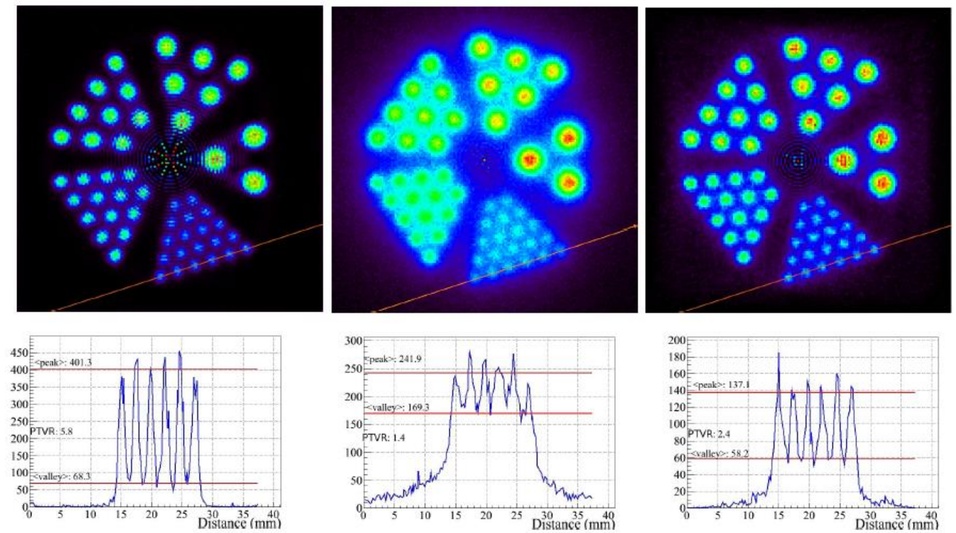

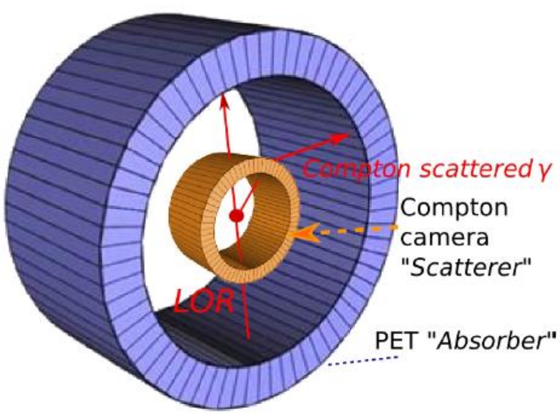

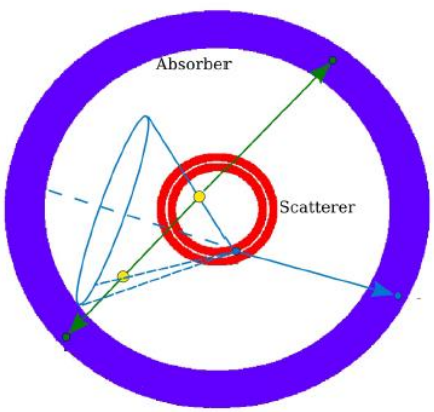

Kolstein, J Instrum 2016

Perspectives

TEP Cerenkov

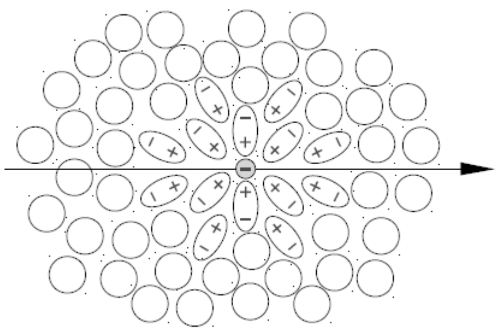

$v < c_0/n$

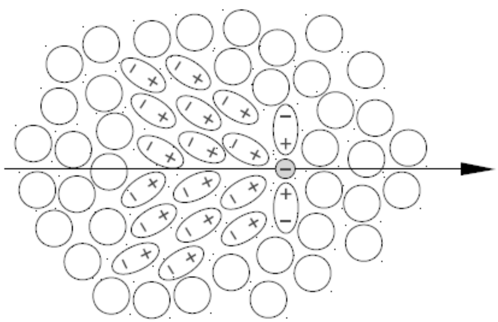

$v > c_0/n$

$$v > \frac{c}{n}$$

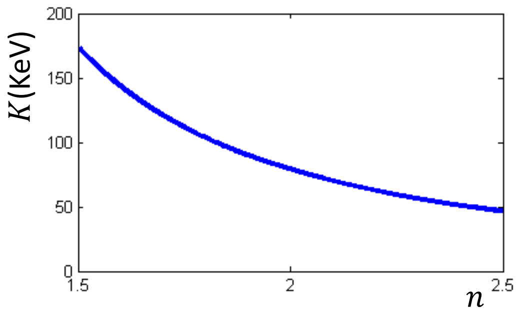

$$K > 511\left(\frac{n}{\sqrt{n^2-1}} - 1\right)$$

Perspectives

TEP Cerenkov

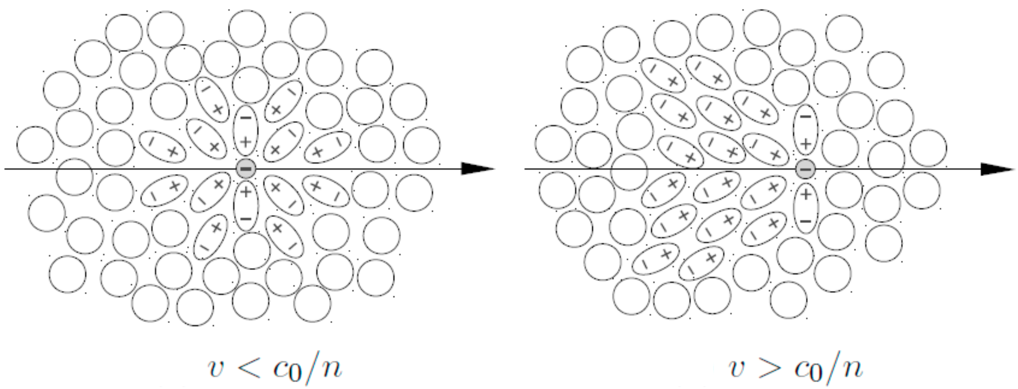

$$v > \frac{c}{n}$$

$$K > 511\left(\frac{n}{\sqrt{n^2-1}} - 1\right)$$

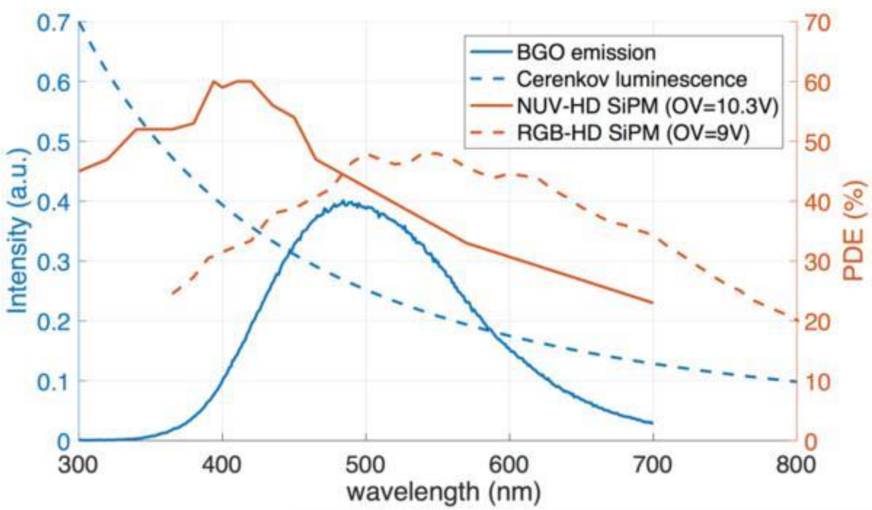

Kwon, Phys Med Biol 2016

- n
- Fraction PE (Z)
- Transparence
- Photodétecteur sensible UV & rapide

BGO : ~ 16 photons
Res temp < 300 ps

TEP Cerenkov

	BGO	LSO	$LaBr_3(Ce)$	PbF_2
Density (g/cm^3)	7.1	7.4	5.1	7.77
μ_{511keV} (cm^{-1})	0.96	0.87	0.43	1.06
Photofraction for 511 keV (*)	0.41	0.32		0.46
Decay time (ns)	300	40	17	-
Light yield (/511 keV)	3,000	15,000	30,000	10 (‡)

(*) [XCOM: Photon Cross Sections Database] (‡) in 250-800 nm wavelength interval

Dolenec 2012

Zhu, Physics Procedia 2012

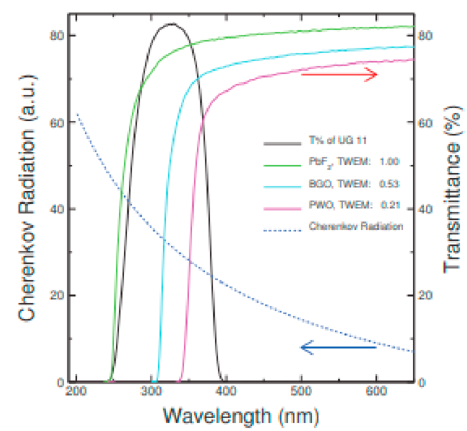

Perspectives

TEP Cerenkov

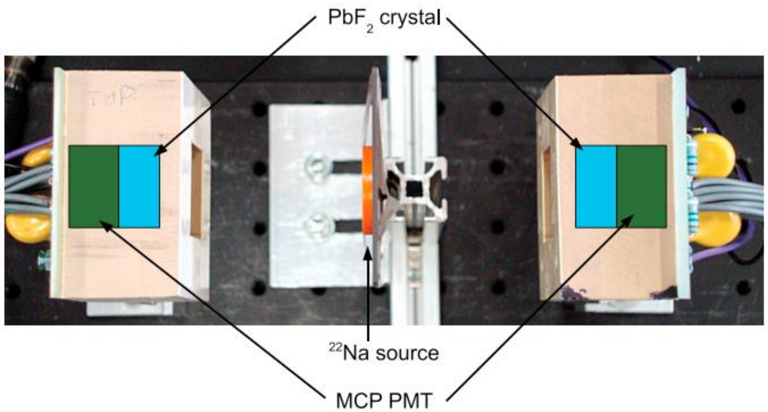

Korpar, Physics Procedia 2012

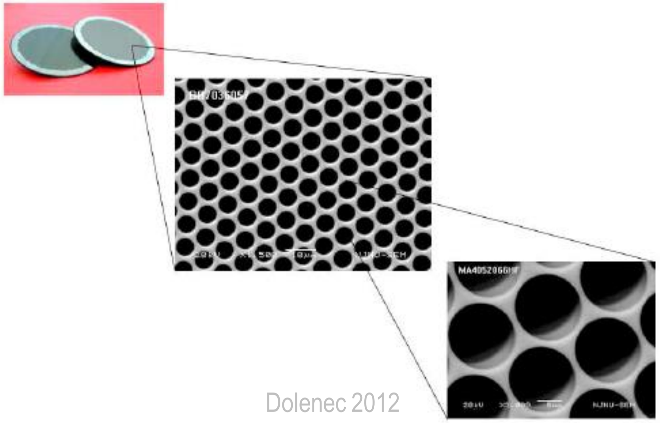

Dolenec 2012

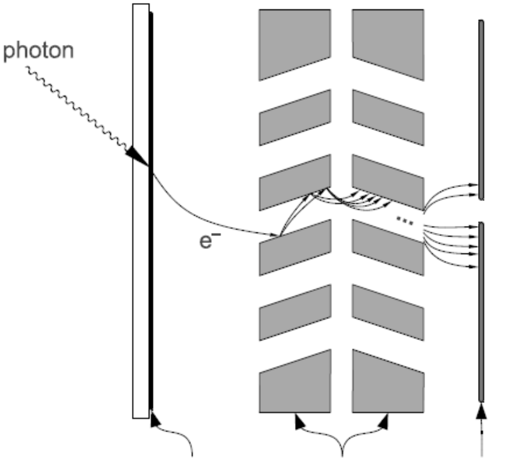

Perspectives

TEP Cerenkov

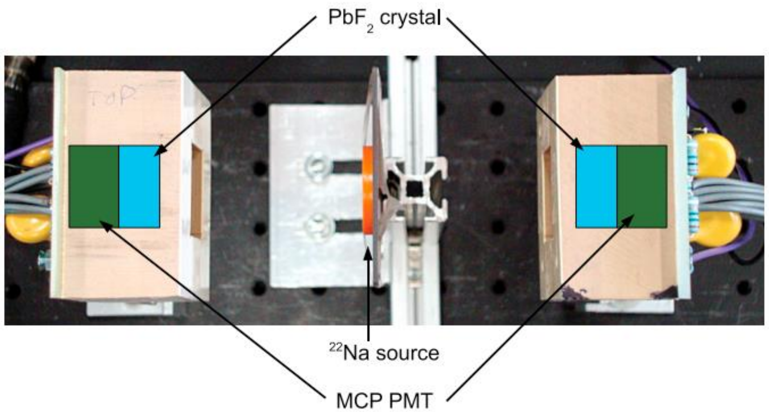

Res temp ~ 100 ps

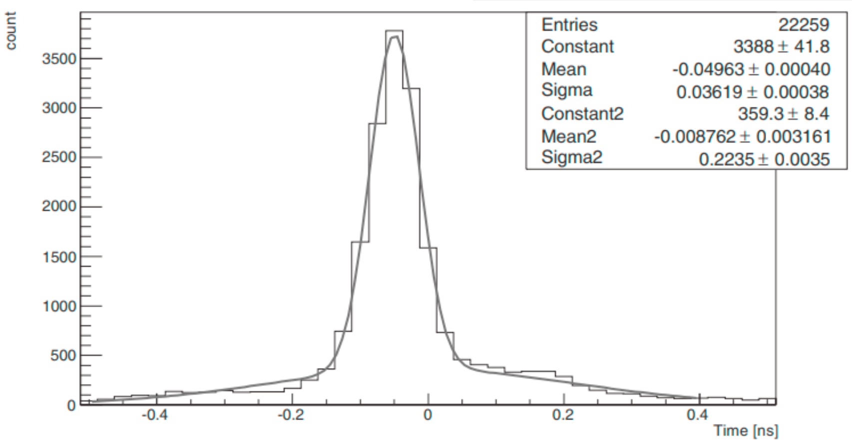

Efficacité ~ 8%
(LSO 30%)

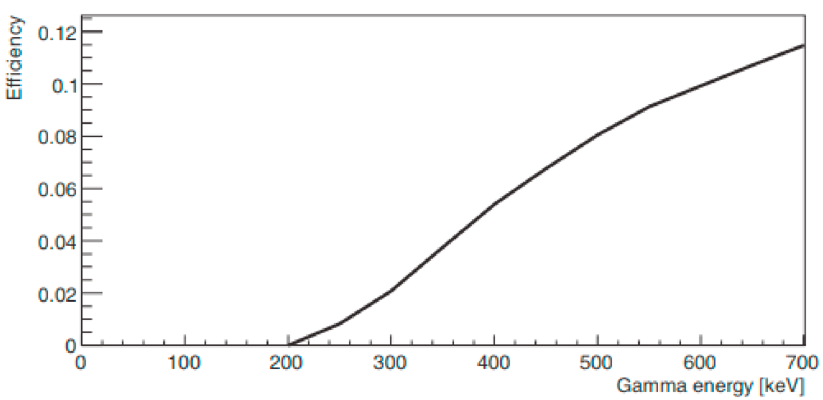

Korpar, Physics Procedia 2012

Perspectives

TEP Cerenkov

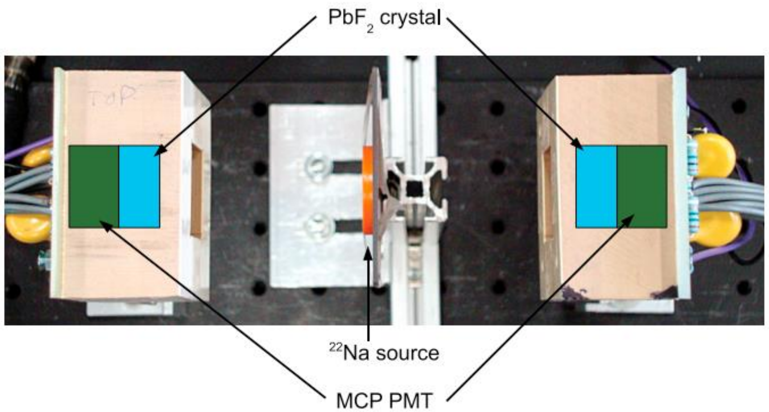

Efficacité ~ 25%
Res temp ~ 300 ps

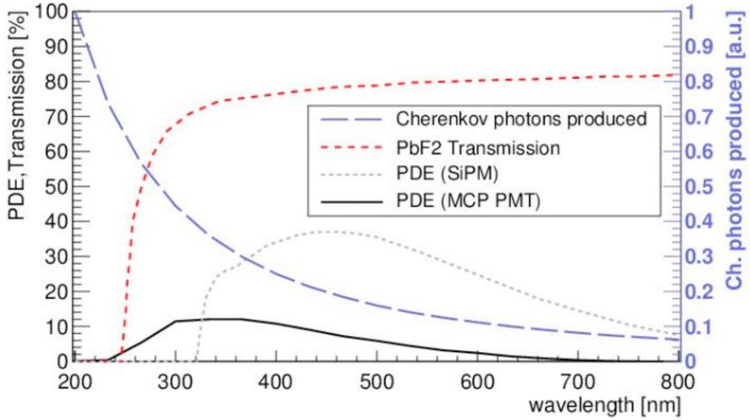

Res temp ~ 100 ps

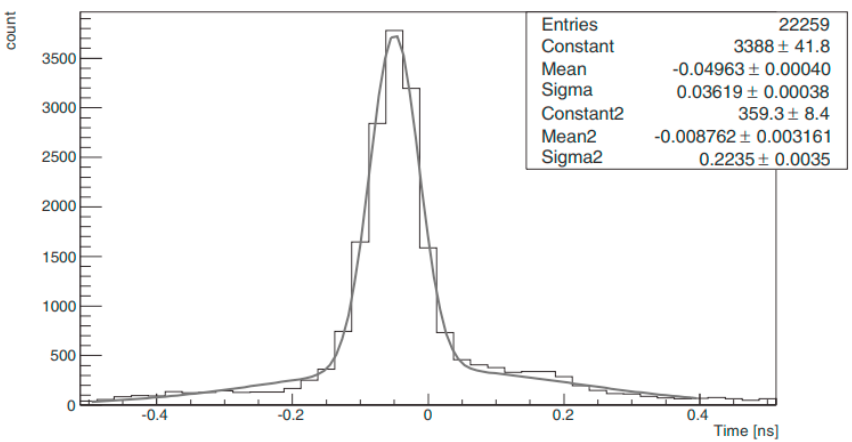

Efficacité ~ 8%
(LSO 30%)

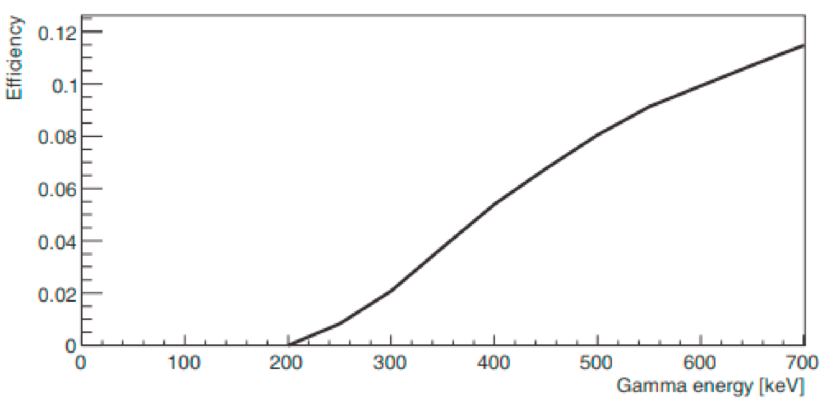

Korpar, Physics Procedia 2012

Perspectives

TEP corps entier

- Modular “Block” Detectors
- ~3.1 x 3.1 x 20 mm L(Y)SO (16 x16)
- PMT (possibly SiPM) readout
- Time of flight and 1-bit DOI
- 40 rings, 48 detectors/ring
- ~78.6 cm ring diameter
- 215 cm axial FOV

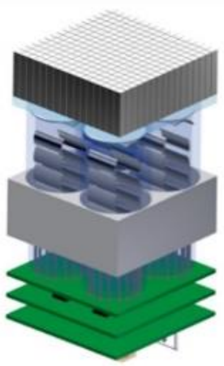

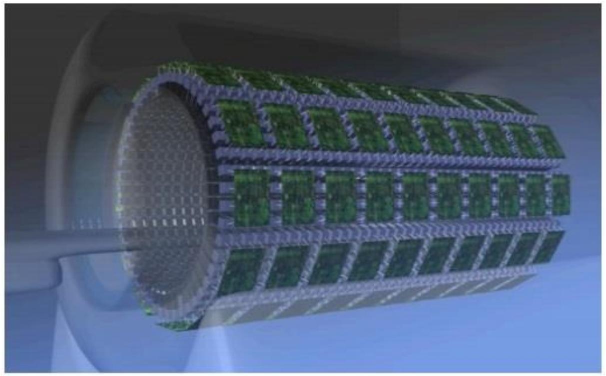

Cherry, J Nucl Med 2018

Perspectives

TEP corps entier

- Modular “Block” Detectors
- ~3.1 x 3.1 x 20 mm L(Y)SO (16 x16)
- PMT (possibly SiPM) readout
- Time of flight and 1-bit DOI
- 40 rings, 48 detectors/ring
- ~78.6 cm ring diameter
- 215 cm axial FOV

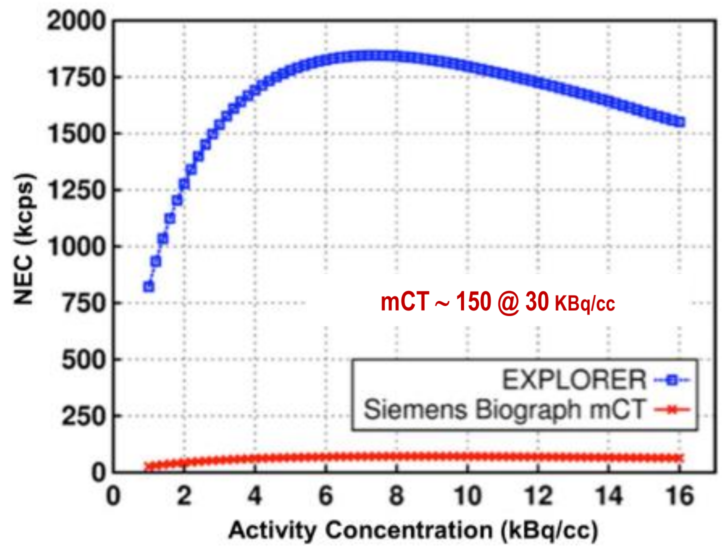

Acceptance ~ 1/5 $\rightarrow$ 1
FOV axial ~ 1/8 $\rightarrow$ 1

Sensibilité ~ × 40

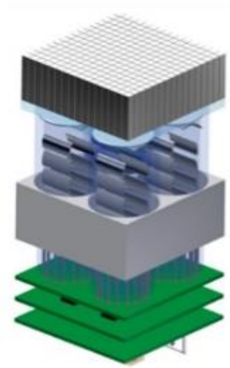

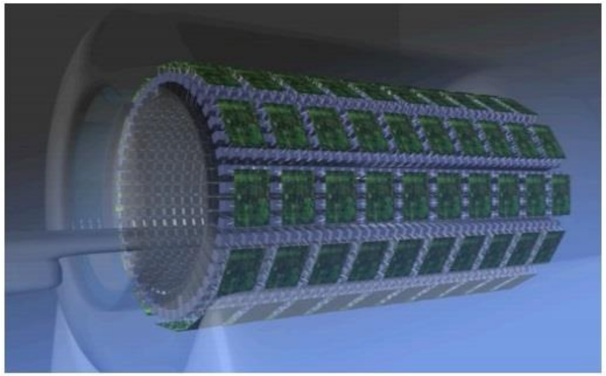

Cherry, J Nucl Med 2018

Perspectives

TEP corps entier

- Modular “Block” Detectors
- ~3.1 x 3.1 x 20 mm L(Y)SO (16 x16)
- PMT (possibly SiPM) readout
- Time of flight and 1-bit DOI
- 40 rings, 48 detectors/ring
- ~78.6 cm ring diameter
- 215 cm axial FOV

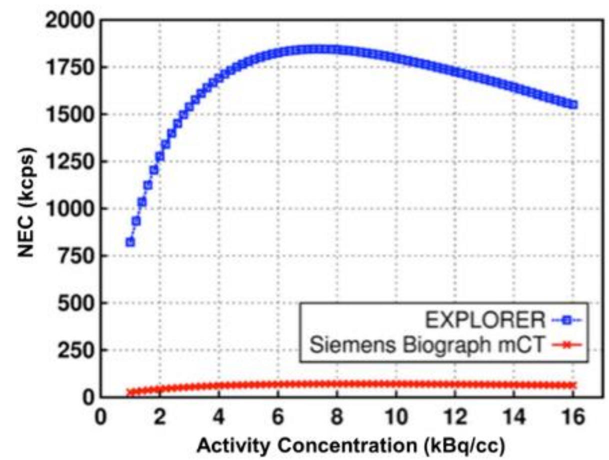

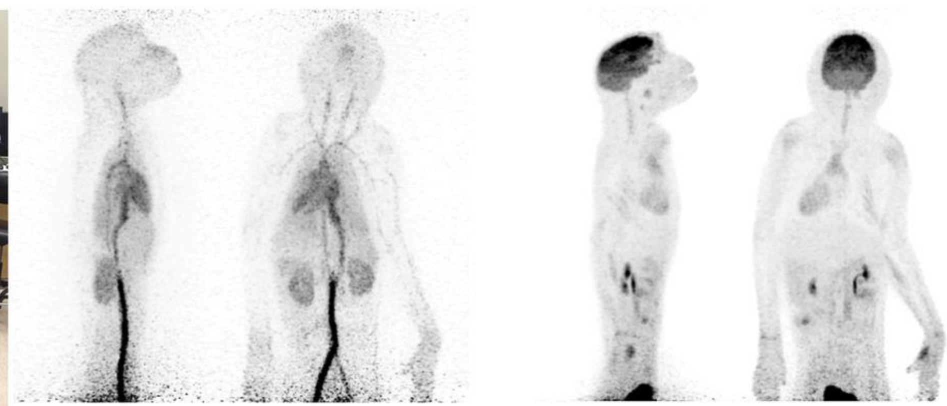

0- to 30-s scan

55- to 60-min scan

Cherry, J Nucl Med 2018

Perspectives

TEP corps entier

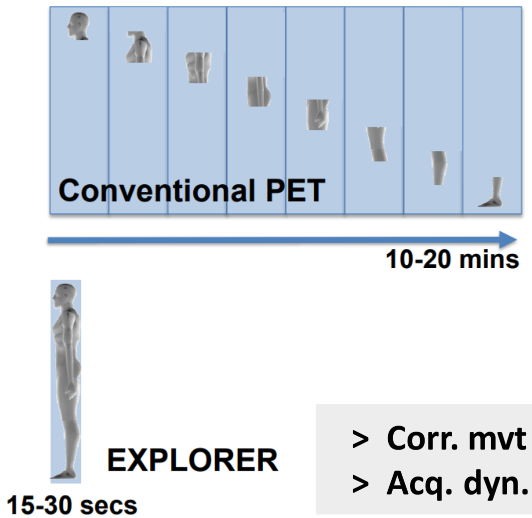

> Corr. mvt
> Acq. dyn.

Perspectives

TEP corps entier

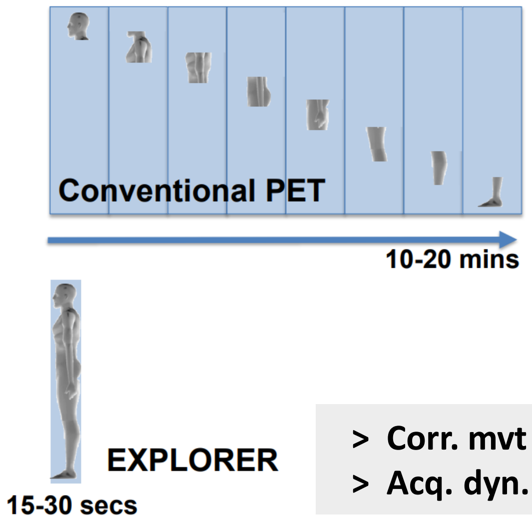

> Corr. mvt
> Acq. dyn.

Conventional PET EXPLORER

Major increase in dynamic range

can image for 5 more half lives

^{11}C
> 3 hours

^{18}F
> 16 hours

^{89}Zr
> 30 days

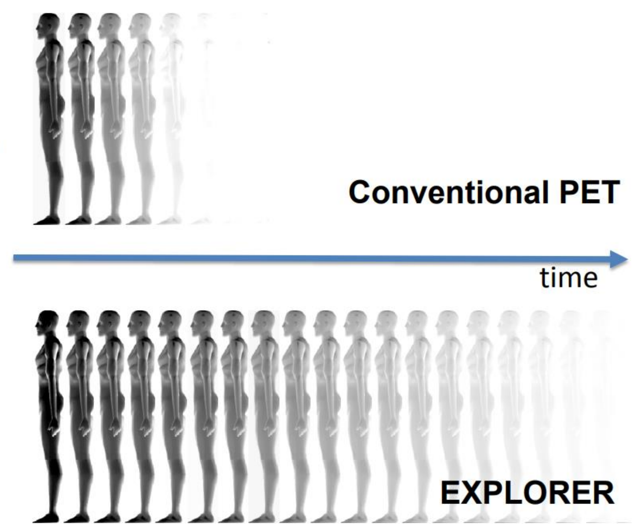

Perspectives

J-PET

Isotope	Half-life	β^+ decay	E_γ (MeV)
^{22}Na	2.6 (years)	$^{22}\mathrm{Na} \rightarrow ^{22}\mathrm{Ne} + e^+ + \nu_e + \gamma$	1.27
^{68}Ga	67.8 (min)	$^{68}\mathrm{Ga} \rightarrow ^{68}\mathrm{Zn} + e^+ + \nu_e + \gamma$	1.08
^{44}Sc	4.0 (h)	$^{44}\mathrm{Sc} \rightarrow ^{44}\mathrm{Ca} + e^+ + \nu_e + \gamma$	1.16

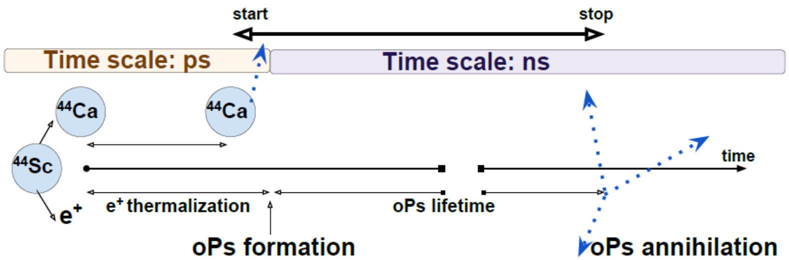

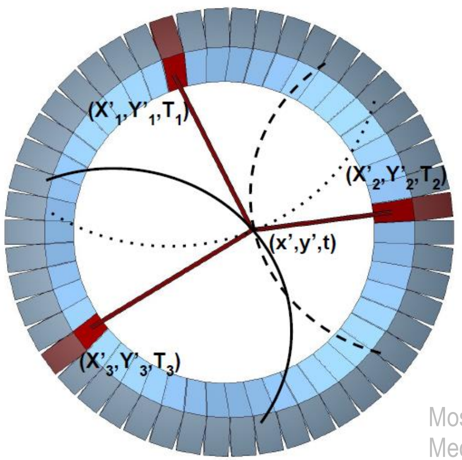

Moskal, Phys Med Biol 2019

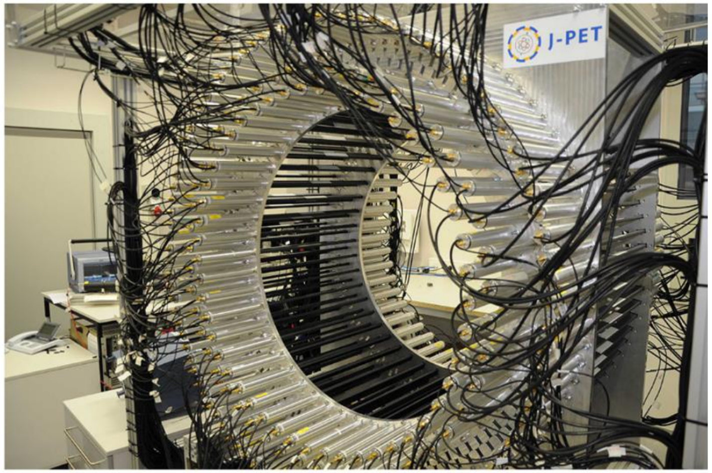

Kaminska, Eur Phys J 2016

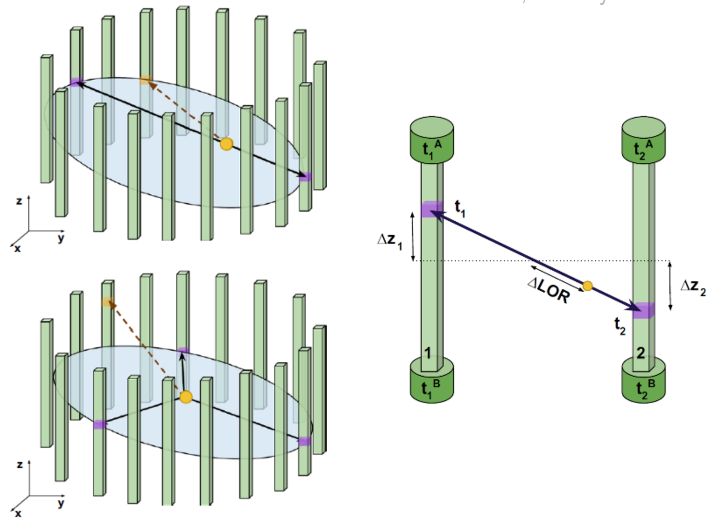

Références

- A Del Guerra et al. Positron Emission Tomography: Its 65 years. Riv Nuov Cimento 2016.
- D Groheux et al. FDG PET-CT for solitary pulmonary nodule and lung cancer: Literature review. Diagn Interv Imaging 2016.
- TC El-Galaly et al. PET/CT for Staging; Past, Present, and Future. Semin Nucl Med 2018.
- Q Han et al. Understanding the role of PET CT in lymphoma management: The era of Lugano Classification. J Nucl Med 2017.
- S Carkaci et al. Retrospective Study of 18F-FDG PET/CT in the Diagnosis of Inflammatory Breast Cancer: Preliminary Data. J Nucl Med 2009.
- B Tantiwongkosi et al. Role of 18F-FDG PET/CT in pre and post treatment evaluation in head and neck carcinoma. World J Radiol 2014.
- EL Martin-Macintosh et al. Multimodality Imaging of Neurodegenerative Processes: Part 1, The Basics and Common Dementias. Am J Roentgenol 2016.
- AF Schinkel et al. Assessment of myocardial viability in patients with heart failure. J Nucl Med 2007.
- FL Besson et al. Diagnostic performance of 18F-fluorodeoxyglucose positron emission tomography in giant cell arteritis: a systematic review and meta-analysis. Eur J Nucl Med Mol Imaging 2011.
- KA Quinn et al. Comparison of magnetic resonance angiography and 18F-fluorodeoxyglucose positron emission tomography in large-vessel vasculitis. Ann Rheum Dis 2018.
- S Schwarzenböck et al. Choline PET and PET/CT in Primary Diagnosis and Staging of Prostate Cancer. Theranostics 2012.
- JN Talbot et al. Use of choline PET for studying hepatocellular carcinoma. Clin Transl Imaging 2014.
- WP Kluijfhout et al. 18F-Fluorocholine PET–CT enables minimal invasive parathyroidectomy in patients with negative sestamibi SPECT–CT and ultrasound: A case report. Int J Surg Case Rep 2015.
- W Langsteger et al. 18F-NaF-PET/CT and 99mTc-MDP Bone Scintigraphy in the Detection of Bone Metastases in Prostate Cancer. Semin Nucl Med 2016.
- SA Eshuis et al. Direct comparison of FP-CIT SPECT and F-DOPA PET in patients with Parkinson’s disease and healthy controls. Eur J Nucl Med Mol Imaging 2009.
- J Schwarzenberg et al. Treatment Response Evaluation using 18F-FDOPA PET in Patients with Recurrent Malignant Glioma on Bevacizumab Therapy. Clin Cancer Res 2015.
- C Lussey-Lepoutre et al. The current role of 18F-FDOPA PET for neuroendocrine tumor imaging. Médecine Nucléaire 2016.
- V Ambrosini et al. Comparison between 68Ga-DOTA-NOC and 18F-DOPA PET for the detection of gastro-entero-pancreatic and lung neuro-endocrine tumours. Eur J Nucl Med Mol Imaging 2008.
- F Lococo et al. Multicenter comparison of 18F-FDG and 68Ga-DOTA-peptide PET/CT for pulmonary carcinoid. Clin Nucl Med 2015.
- JJ Morigi et al. Prospective Comparison of 18F-Fluoromethylcholine Versus 68Ga-PSMA PET/CT in Prostate Cancer Patients Who Have Rising PSA After Curative Treatment and Are Being Considered for Targeted Therapy. J Nucl Med 2015.
- S Han et al. Impact of 68Ga-PSMA PET on the Management of Patients with Prostate Cancer: A Systematic Review and Meta-analysis. Eur Urol 2018.
- MC Williams et al. Computed tomography myocardial perfusion vs 15O-water positron emission tomography and fractional flow reserve. Eur Radiol 2017.
- P Mukherjee et al. Measurement of cerebral blood flow in chronic carotid occlusive disease: comparison of dynamic susceptibility contrast perfusion MR imaging with positron emission tomography. AJNR Am J Neuroradiol 2003.
- HA Hofman et al. Measurement of left ventricular volumes and function with O-15-labeled carbon monoxide gated positron emission tomography: comparison with magnetic resonance imaging. J Nucl Cardiol 2005.

Références

• VL Murthy et al. Clinical Quantification of Myocardial Blood Flow Using PET: Joint Position Paper of the SNMMI Cardiovascular Council and the ASNC. J Nucl Med 2018.
• TH Schindler et al. Cardiac PET imaging for the detection and monitoring of coronary artery disease and microvascular health. JACC Cardiovasc Imaging 2010.
• ME Murray et al. Clinicopathologic and 11C-Pittsburgh compound B implications of Thal amyloid phase across the Alzheimer's disease spectrum. Brain 2015.
• JW Park et al. A prospective evaluation of 18F-FDG and 11C-acetate PET/CT for detection of primary and metastatic hepatocellular carcinoma. J Nucl Med 2008.
• AW Glaudemans et al. Value of 11C-methionine PET in imaging brain tumours and metastases. Eur J Nucl Med Mol Imaging 2013.
• V Preylowski et al. Is the Image Quality of I-124-PET Impaired by an Automatic Correction of Prompt Gammas? Plos One 2013.
• J Cal-Gonzalez et al. Positron range estimation with PeneloPET. Phys Med Biol 2013.
• L Jødal et al. Positron range in PET imaging: an alternative approach for assessing and correcting the blurring. Phys Med Biol 2012.
• M Conti et al. Physics of pure and non-pure positron emitters for PET: a review and a discussion. EJNMMI Physics 2016.
• EL Cole et al. Radiosyntheses using Fluorine-18: the Art and Science of Late Stage Fluorination. Curr Top Med Chem 2014.
• J Marganiec-Galazka et al. Activity determination of 68Ge/68Ga by means of 4πβ(Č)-γ coincidence counting. Appl Radiat Isot 2018.
• TF Budinger. PET instrumentation: what are the limits? Semin Nucl Med 1998.
• WH Sweet. The uses of nuclear disintegration in the diagnosis and treatment of brain tumor. N Engl J Med 1951.
• WH Blahd. Ben Cassen and the development of the rectilinear scanner. Semin Nucl Med 1996.
• S Baum et al. Brain scanning in the diagnosis of acoustic neuromas. J Neurosurg 1972.
• GL Brownell. A history of PET. 1999.
• ME Phelps et al. Design Considerations for a Positron Emission Transaxial Tomograph (PETT III). IEEE Trans Nucl Sci 1976.
• ZH Cho et al. Circular Ring Transverse Axial Positron Camera for 3-Dimensional Reconstruction of Radionuclides Distribution. IEEE Trans Nucl Sci 1976.
SE Derenzo et al. The Donner 280-Crystal High Resolution Positron Tomograph. IEEE Trans Nucl Sci 1979.
• FA Kotasidis et al. Single scan parameterization of space-variant point spread functions in image space via a printed array: the impact for two PET/CT scanners. Phys Med Biol 2011.
• PJ Slomka et al. Advances in SPECT and PET Hardware. Prog Cardiovasc Dis 2015.
• Mao et al. Optical and Scintillation Properties of Inorganic Scintillators in High Energy Physics. IEEE Nucl Sci Symp 2007.
• VC Spanoudaki et al. Photo-Detectors for Time of Flight Positron Emission Tomography (ToF-PET). Sensors 2010.
• Q Wei Intrinsic Radiation in Lutetium Based PET Detector: Advantages and Disadvantages. Arxiv.org.
• JJ De Lima. Nuclear medicine physics. CRC Press 2010.
• Szczesniak et al. microPMT–A New Photodetector for Gamma Spectrometry and Fast Timing? IEEE Nucl Sci Symp 2013,
• S Sasaki et al. Ws Values in Several Inorganic Scintillation Crystals for Gamma Rays. IEEE Trans Nucl Sci 2010.
• BJ Pichler et al. Latest Advances in Molecular Imaging Instrumentation. J Nucl Med 2008.
• Y Zou et al. Planar CMOS analog SiPMs: design, modeling, and Characterization. J Mod Opt 2015.
• AJ Chaudhari et al. Crystal identification in positron emission tomography using nonrigid registration to a Fourier-based template. Phys Med Biol 2008.

Références

- EP Visser et al. Spatial Resolution and Sensitivity of the Inveon Small-Animal PET Scanner. J Nucl Med 2009.
- H Zaidi et al. Towards enhanced PET quantification in clinical oncology. Br J Radiol 2018.
- WW Moses. Fundamental Limits of Spatial Resolution in PET. Nucl Instrum Methods Phys Res 2011.
- FM Bengel et al. Cardiac emission positron tomography. JACC 2009,
- H Sy et al. The Effect of Magnetic Field on Positron Range and Spatial Resolution in an Integrated Whole-Body Time-Of-Flight PET/MRI System. IEEE Nucl Sci Symp 2014.
- G Soultanidis et al. Study of the effect of magnetic field in positron range using GATE simulation toolkit. J Phys Conf Ser 2011.
- J Zhang et al. Performance evaluation of the next generation solid-state digital photon counting PET/CT system. EJNMMI Res 2018.
- T Yamaya et al. A SiPM-based isotropic-3D PET detector X'tal cube with a three-dimensional array of 1 mm3 crystals. Phys Med Biol 2011.
- http://www.phys.utk.edu/labs/modphys/Compton%20Scattering%20Experiment.pdf
- MS Lee et al. Novel inter-crystal scattering event identification method for PET Detectors. Phys Med Biol 2018.
- JR Stickel et al. High-resolution PET detector design: modelling components of intrinsic spatial resolution. Phys Med Biol 2005.
- BH Peng et al. Recent Developments in PET Instrumentation. Curr Pharm Biotechnol 2010.
- TK Lewellen. Recent developments in PET detector technology. Phys Med Biol 2010.
- AJ Gonzalez et al. A PET Design Based on SiPM and Monolithic LYSO Crystals: Performance Evaluation. IEEE Trans Nucl Sci 2016.
- M Streun et al. Pulse Shape Discrimination of LSO and LuYAP Scintillators for Depth of Interaction Detection in PET. IEEE Trans Nucl Sci 2003.
- N Zhang et al. Anode position and last dynode timing circuits for dual-layer BGO scintillator with PS-PMT based modular PET detectors. IEEE Trans Nucl Sci 2002.
- AMK Foudray et al. Characterization of Two Thin Postion-Sensitive Avalanche Photodiodes on a Single Flex Circuit for Use in 3-D Positioning PET Detectors. IEEE Nucl Sci Symp 2006.
- F Ben Bouallègue et al. Actualités en cardiologie isotopique : Applications des nouvelles caméras CZT. Med Nucl 2015.
- Y Gu et al. Study of electrode pattern design for a CZT-based PET detector. Phys Med Biol 2014.
- M Moszynski et al. Energy resolution of scintillation detectors with large area avalanche photodiodes and photomultipliers light readout. IEEE Nucl Sci Symp 1997.
- P Dorenbos et al. Non-proportionality in the scintillation response and the energy resolution obtainable with scintillation crystals. IEEE Trans Nucl Sci 1995.
- S Uxa et al. Effect of contact preparation on the profile of the electric field in CdZnTe detectors. J Phys 2013.
- G Arino et al. Energy and coincidence time resolution measurements of CdTe detectors for PET. J Instrum 2013.
- SE Derenzo et al. Fundamental limits of scintillation detector timing precision. Phys Med Biol 2014.
- P Lecoq et al. Factors Influencing Time Resolution of Scintillators and Ways to Improve Them. IEEE Trans Nucl Sci 2010.
- http://lmu.web.psi.ch/docu/manuals/bulk_manuals/PMTs/Photonis_PMT_basics.pdf
- HJ Biersack et al. Clinical nuclear medicine. Springer 2007.
- https://www.aapm.org/meetings/amos2/pdf/49-14363-4210-81.pdf
- MA Lodge et al. A Practical, Automated Quality Assurance Method for Measuring Spatial Resolution in PET. J Nucl Med 2009.
- D Nikolopoulos et al. GATE Simulation of the Biograph 2 PET/CT Scanner. J Nucl Med Radiat Ther 2014.

Références

- R Saaidi et al. A Monte Carlo Study of Clinical PET ECAT EXACT HR+ Using GATE. Bas Conc Nucl Phys 2016.
- G Tarantola et al. PET instrumentation and reconstruction algorithms in whole-body applications. J Nucl Med 2003.
- H Zaidi et al. Scatter Compensation Techniques in PET. PET Clin 2007.
- LM Popescu et al. PET Energy-based Scatter Estimation and Image Reconstruction with Energy-dependent Correction. Phys Med Biol 2006.
- I Rausch et al. Performance evaluation of the Biograph mCT Flow PET/CT system according to the NEMA NU2-2012 standard. EJNMMI Phys 2015.
- EB Sokole et al. Routine quality control recommendations for nuclear medicine instrumentation. Eur J Nucl Med Mol Imaging 2010.
- EANM. Principles and Practice of PET/CT Part 1. A Technologist‘s Guide. EANM 2010.
- National Electrical Manufacturers Association. NEMA NU 2. Performance measurements of positron emission tomographs. Rosslyn, VA: National Electrical Manufacturers Association; 1994, 2001, 2007.
- GB Saha. Performance Characteristics of PET Scanners. In Basics of PET imaging (Chapter 6). Springer 2015.
- DC Vines et al. Quantitative PET Comparing Gated with Nongated Acquisitions Using a NEMA Phantom with Respiratory-Simulated Motion. J Nucl Med Technol 2007.
- https://web.eecs.umich.edu/~fessler/course/516/l/c-tomo.pdf
- K Shang et al. Clinical evaluation of whole-body oncologic PET with time-of-flight and point-spread function for the hybrid PET/MR system. Eur J Radiol 2017.
- DJ Kadrmas et al. Impact of time-of-flight on PET tumor detection. J Nucl Med 2009.
- G Borghi et al. Sub-3 mm, near-200 ps TOF/DOI-PET imaging with monolithic scintillator detectors in a 70 cm diameter tomographic setup. Phys Med Biol 2018.
- D Brasse et al. Correction Methods for Random Coincidences in Fully 3D Whole-Body PET: Impact on Data and Image Quality. J Nucl Med 2005.
- GF Knoll. Radiation Detection and Measurement. Wiley & Sons 1999.
- T Carlier et al. 90Y-PET imaging: Exploring limitations and accuracy under conditions of low counts and high random fraction. Med Phys 2015.
- PJ Markiewicz et al. NiftyPET: a High-throughput Software Platform for High Quantitative Accuracy and Precision PET Imaging and Analysis. Neuroinformatics 2018.
- SR Meikle et al. Quantitavie techiques in PET. In Positron Emission Tomography (Chapter 5). Sringer 2003.
- JF Oliver et al. Modelling Random Coincidences in Positron Emission Tomography by Using Singles and Prompts: A Comparison Study. Plos One 2016.
- P Vaska et al. Quantitative imaging with the micro-PET small-animal PET tomograph. Int Rev Neurobiol 2006.
- NC Ferreira et al. A hybrid scatter correction for 3D PET based on an estimation of the distribution of unscattered coincidences: implementation on the ECAT EXACT HR+. Phys Med Biol 2002.
- M Ibaraki et al. Validation of a simplified scatter correction method for 3D brain PET with 15O. Ann Nucl Med 2016.
- CC Watson et al. Advances in scatter correction for 3D PET/CT. IEEE Nucl Sci Symp 2004.
- BF Hutton et al. Review and current status of SPECT scatter correction. Phys Med Biol 2011.
- A Werling et al. Fast implementation of the single scatter simulation algorithm and its use in iterative image reconstruction of PET data. Phys Med Biol 2002.
- C Lange et al. CT-Based Attenuation Correction in I-123-Ioflupane SPECT. Plos One 2014.
- GN Hounsfield. Method of and apparatus for examining a body by radiation such as x or gamma radiation. United States patent 3919552, 1976.
- PE Kinahan et al. Attenuation correction for a combined 3D PET/CT scanner. Med Phys 1998.
- J Ouyang et al. Bias atlases for segmentation-based PET attenuation correction using PET-CT and MR. IEEE Trans Nucl Sci 2014.

Références

• M Abella et al. Accuracy of CT-Based Attenuation Correction in Bone Imaging with PET/CT. IEEE Nucl Sci Symp 2007.
• PE Kinahan et al. X-ray-based attenuation correction for positron emission tomography/computed tomography scanners. Semin Nucl Med 2003.
• R Alvarez et al. A Comparison of Noise and Dose in Conventional and Energy Selective Computed Tomography. IEEE Trans Nucl Sci 1979.
• PE Kinahan et al. Dual energy CT attenuation correction methods for quantitative assessment of response to cancer therapy with PET/CT imaging. Technol Cancer Res Treat 2006.
• TG Turkington. PET imaging basics. In Clinical PET-CT in Radiology: Integrated Imaging in Oncology (Chapter 2). Springer 2011.
• TM Blodgett et al. PET/CT Artifacts. Clin Imaging 2014.
• A Pépin et al. Management of respiratory motion in PET/computed tomography: the state of the art. Nucl Med Commun 2014.
GS Meirelles et al. Deep-inspiration breath-hold PET/CT: clinical findings with a new technique for detection and characterization of thoracic lesions. J Nucl Med 2007.
• L Fin et al. Initial clinical results for breath-hold CT-based processing of respiratory-gated PET acquisitions. Eur J nucl Med Mol Imaging 2008.
• PE Kinahan. PET/CT Issues: CT-based attenuation correction (CTAC), Artifacts, and Motion Correction. https://www.aapm.org/meetings/08ss/documents/Kinahan.pdf.
• DL Simpson et al. FDG PET/CT: Artifacts and Pitfalls. Contemp Diag Radiol 2017.
• E Meyer et al. Normalized metal artifact reduction (NMAR) in computed tomography. Med Phys 2010.
• R Harnish et al. The effect of metal artefact reduction on CT-based attenuation correction for PET imaging in the vicinity of metallic hip implants: A phantom study. Ann Nucl Med 2015.
• CM Kao et al. Image Reconstruction for Dynamic PET Based on Low-Order Approximation and Restoration of the Sinogram. IEEE Trans Med Imaging 1997.
• K Lee et al. Pragmatic fully 3D image reconstruction for the MiCES mouse imaging PET scanner. Phys Med Biol 2004.
• AM Alessio et al. Application and Evaluation of a Measured Spatially Variant System Model for PET Image Reconstruction. IEEE Trans Med Imaging 2010.
• A Rahmim. Resolution modeling in PET imaging: Theory, practice, benefits, and pitfalls. Med Phys 2013.
• S Ashrafinia et al. Generalized PSF modeling for optimized quantitation in PET imaging. Phys Med Biol 2017.
• S Tong et al. Properties of Edge Artifacts in PSF-Based PET Reconstruction. IEEE Nucl Sci Symp 2010.
• OL Munk et al. Point-spread function reconstructed PET images of sub-centimeter lesions are not quantitative. EJNMMI Phys 2017.
• V Bettinardi et al. PET quantification: strategies for partial volume correction. Clin Transl Imaging 2014.
• N Bouisson et al. A multiresolution image based approach for correction of partial volume effects in emission tomography. Phys Med Biol 2006.
• L Theodorakis et al. A review of PET normalization: striving for count rate Uniformity. Nucl Med Commun 2013.
• B Bai et al. Model-based normalization for iterative 3D PET image reconstruction. Phys Med Biol 2002.
• JA Kolthammer et al, Performance evaluation of the Ingenuity TF PET/CT scanner with a focus on high count-rate conditions. Phys Med Biol 2015.
• PJ Slomka et al. Recent Advances and Future Progress in PET Instrumentation. Semin Nucl Med 2016.
• S Surti et al. Update on time-of-flight PET imaging. J Nucl Med 2015.
• M Conti. Focus on time-of-flight PET: the benefits of improved time Resolution. Eur J Nucl Med Mol Imaging 2011.
• C Lois et al. An Assessment of the Impact of Incorporating Time-of-Flight Information into Clinical PET/CT Imaging. J Nucl Med 2010.

Références

- M Conti. Why is TOF PET reconstruction a more robust method in the presence of inconsistent data? Phys Med Biol 2010.
- R Lhommel et al. Yttrium-90 TOF PET scan demonstrates high-resolution biodistribution after liver SIRT. Eur J Nucl Med Mol Imaging 2009.
- YH Kao et al. Yttrium-90 Time-of-Flight PET/CT Is Superior to Bremsstrahlung SPECT/CT for Postradioembolization Imaging of Microsphere Biodistribution. Clin Nucl Med 2011.
- G Wang et al. A scheme for multisource interior tomography. Med Phys 2009.
- S Surti et al. Design considerations for a limited-angle, dedicated breast, TOF PET scanner. Phys Med Biol 2009.
- S Vandenberghe et al. Recent developments in time-of-flight PET. EJNMMI Physics 2016.
- H Zaidi et al. An outlook on future design of hybrid PET/MRI systems. Med Phys 2011.
- FP Kuhn et al. Contrast-Enhanced PET/MR Imaging Versus Contrast-Enhanced PET/CT in Head and Neck Cancer: How Much MR Information Is Needed? J Nucl Med 2014.
- F Nensa et al. Clinical applications of PET/MRI: current status and future perspectives. Diagn Interv Radiol 2014.
- P Krumm. Clinical use of cardiac PET/MRI: current state-of-the-art and potential future applications. Jpn J Radiol 2018.
- S Vandenberghe et al. PET-MRI: a review of challenges and solutions in the development of integrated multimodality imaging. Phys Med Biol 2015.
- HF Wherl et al. Combined PET/MR imaging--technology and applications.Technol Cancer Res Treat 2010.
- M Aiello et al. Hybrid PET/MRI Methodology. Int Rev Neurobiol 2018.
- AM Karlberg et al. Quantitative comparison of PET performance—Siemens Biograph mCT and mMR. EJNMMI Phys 2016.
- RF Muzik et al. PET/MRI – Technical Review. Semin Roentgenol 2014.
- V Keereman et al. MRI-Based Attenuation Correction for PET/MRI Using Ultrashort Echo Time Sequences. J Nucl Med 2010.
- IB Malone et al. Attenuation Correction Methods Suitable for Brain Imaging with a PET/MRI Scanner: A Comparison of Tissue Atlas and Template Attenuation Map Approaches. J Nucl Med 2011.
- K Shimazoe et al 2017. Double Photon Emission Compton Imaging based on event-driven SOI and GAGG-SiPM detectors (https://indico.cern.ch/event/577879/contributions/2741631/attachments/1575285/2487382/shimazoe_20171214SOIPIX2017.pdf).
- K Shimazoe et al. Development of simultaneous PET and Compton imaging using GAGG-SiPM based pixel detectors. Nucl Inst Met Phys 2018.
- Y Yoshihara et al. Evaluation of double photon coincidence Compton imaging method with GEANT4 simulation. Nucl Inst Met Phys 2017.
- M Kolstein et al, Using triple gamma coincidences with a pixelated semiconductor Compton-PET scanner: a simulation study. J Instrum2016
- SI Kwon et al. Bismuth germanate coupled to near ultraviolet silicon photomultipliers for time-of-flight PET. Phys Med Biol 2016.
- R Dolenec. Time-of-Flight Positron Emission Tomography Using Cherenkov Radiation. Doctoral Thesis 2012.
- R Zhu. Crystal calorimeters in the next decade. Physics Procedia 2012.
- S Korpar et al. Study of TOF PET using Cherenkov light. Physics Procedia 2012.
- SR Cherry et al. Total-Body PET: Maximizing Sensitivity to Create New Opportunities for Clinical Research and Patient Care. J Nucl Med 2018.
- D Kaminska et al. A feasibility study of ortho-positronium decays measurement with the J-PET scanner based on plastic scintillators. Eur Phys J 2016.
- P Moskal et al. Feasibility study of the positronium imaging with the J-PET tomograph. Phys Med Biol 2019.